Ministerie van Klimaat en
Groene Groei

> Retouradres Postbus 20401 2500 EK Den Haag

De Voorzitter van de Eerste Kamer
der Staten-Generaal
Kazernestraat 52
2514 CV DEN HAAG

Klimaat en groene Groei

Bezoekadres
Bezuidenhoutseweg 73
2594 AC Den Haag

Postadres
Postbus 20401
2500 EK Den Haag

Overheidsidentificatienr
00000003952069570000

T 070 379 8911 (algemeen)
F 070 378 6100 (algemeen)
www.rijksoverheid.nl/kgg

Ons kenmerk
KGG / 99657850

Bijlage(n)
5

Datum 17 juli 2025
Betreft Aardbevingen in en rondom het Groningenveld

Geachte Voorzitter,

Met deze brief wil het kabinet de Kamer informeren over de recente ontwikkelingen van de seismiciteit in en rondom het Groningenveld. Een belangrijke conclusie is dat de seismiciteit in 2024 op het laagste niveau lag van de afgelopen 20 jaar. De neerwaartse trend in aardbevingen die is ingezet in 2014 houdt aan en de verwachting is dat de afname de aankomende jaren doorzet.

Het is ruim een jaar geleden dat het Groningenveld formeel is gesloten[1]. Dat de gaskraan dicht is, betekent echter niet dat de aandacht van het kabinet voor Groningen verslapt. Het ministerie van Binnenlandse Zaken en Koninkrijksrelaties met NCG en het IMG werkt voortdurend aan de versterkingsoperatie, de schadeafhandeling en via de Sociale en Economische agenda aan het herstel van Groningen. Het ministerie van Klimaat en Groene Groei houdt in samenwerking met Staatstoezicht op de Mijnen (SodM), de Nederlandse Organisatie voor toegepast-natuurwetenschappelijk onderzoek (TNO) en het Koninklijk Nederlands Meteorologisch Instituut (KNMI) het aantal, de locaties en de grootte van de aardbevingen in en rondom het Groningenveld in de gaten. Met deze brief geeft het kabinet (i) een update over aardbevingen in het afgelopen jaar en de verwachtingen voor de aankomende jaren, en (ii) informeert het de Kamer over recent uitgekomen onderzoeken die betrekking hebben op aardbevingen in het Groningenveld. Een daarvan is het onderzoek over stikstofinjectie in het Groningenveld, welke tijdens het debat met de Eerste Kamer op 16 april 2024 is toegezegd[2]. (iii) Ten slotte wordt de Kamer kort geïnformeerd over toekomstige ontwikkelingen rondom monitoren van seismiciteit. Een gelijke brief zal worden verzonden naar de Tweede Kamer.

I. Ontwikkeling seismiciteit in het Groningenveld in 2024

Begin dit jaar heeft de NAM haar ‘Rapportage seismiciteit Groningen gasveld – kalender jaar 2024’ gedeeld (bijlage 1). Dit is de eerste halfjaarlijkse rapportage van 2025 die NAM in een vernieuwd systeem twee keer per kalender jaar opstelt, in plaats van twee keer per gasjaar, zoals voorheen gebruikelijk was. SodM heeft

[1] Wet sluiting Groningenveld gaat per 19 april 2024 in | Nieuwsbericht | Rijksoverheid.nl
[2] Verslag van de plenaire vergadering van dinsdag 16 april 2024 - Eerste Kamer der Staten-Generaal

deze rapportage beoordeeld. Deze beoordeling vindt u in bijlage 2. Uit deze rapportage en de website van het KNMI[3] komt naar voren dat in 2024 36 geïnduceerde aardbevingen zijn gemeten in het Groningenveld. Zes hiervan hadden een magnitude groter dan 1,5 en twee een magnitude groter dan 2,0. De grootste beving in 2024, met een magnitude van 2,2, vond plaats in Garsthuizen op 31 oktober. Ter vergelijking, in 2023 vonden er 43 geïnduceerde aardbevingen plaats in het Groningenveld, waarvan negen met een magnitude van 1,5 of hoger. In de jaren 2021 en 2022 lagen deze aantallen hoger, en vonden bovendien aardbevingen plaats met magnitudes van boven de 3,0 (zie figuur 1). De laatste keer dat het aantal en de intensiteit van aardbevingen vergelijkbaar was met afgelopen jaar, was in 2004. Toen vonden ook zes aardbevingen plaats met magnitudes groter dan 1,5, waarvan één met een magnitude groter dan 2,0 (namelijk 2,1). We zien dat de trend van het afnemende aantal aardbevingen groter dan 1,5 in 2024 doorzet. Deze observatie komt overeen met de verwachting uit de publieke Seismische Dreiging en Risico Analyse (pSDRA)[4], het model van TNO wat het aantal aardbevingen voorspelt en aan de hand daarvan het risico inschat.

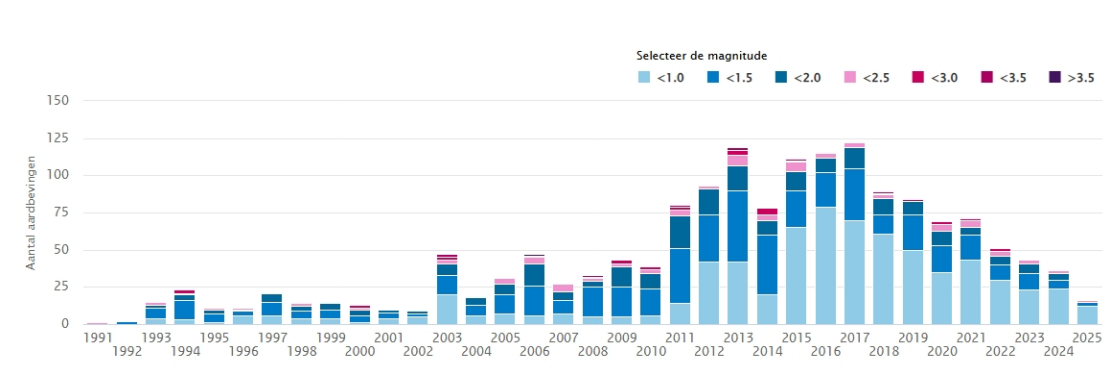

Figuur 1. Aantal gemeten aardbevingen in het Groningenveld per jaar.

De meeste aardbevingen in 2024 vonden plaats in het noordwesten van het Groningenveld. Dit is al jaren seismisch het meest actieve gebied. Dit komt omdat de druk in het Groningenveld niet gelijkmatige verdeeld is over het veld, doordat er de laatste jaren niet uit het cluster Loppersum is gewonnen. Nu de gaswinning is gestopt kan de druk in het veld weer langzaam egaliseren. Hierdoor vermindert de druk in het noordwesten van het veld nog wel, wat in die gebieden kan leiden tot aanhoudende seismiciteit. Desondanks is ook in die gebieden de seismiciteit in 2024 afgenomen[5].

De verwachting uit de modellen van de pSDRA 2023 voor de aankomende vijf jaar (2025-2030) is dat het aantal aardbevingen met een magnitude hoger dan 1,5 rond de vier (± drie) per jaar zal liggen. Dit beeld wordt in de eerste maanden van 2025 bevestigd. Op het moment van schrijven hebben in 2025 twee aardbevingen met een magnitude van 2,0[6] of hoger in en rondom het Groningenveld

[3] KNMI - Aardbevingscatalogus
[4] Publieke SDRA Groningen | NLOG
[5] Dashboard Groningen
[6] Er zijn geen aardbevingen geweest met magnitudes tussen de 1,5 en 2,0.

plaatsgevonden, in Usquert (2,2) en Warffum (2,1)[7,8]. Hoewel het niet direct de verwachting is, is het niet uitgesloten dat nog een enkele aardbeving in de aankomende jaren een magnitude hoger dan 3,0 zal hebben.

II. Onderzoeken naar aardbevingen in en rondom het Groningenveld

In het Kennisprogramma Effecten Mijnbouw (KEM) wordt o.a. onderzoek gedaan naar aardbevingen in en rondom het Groningenveld. Afgelopen jaar zijn twee onderzoeken uitgevoerd die direct betrekking hebben op seismiciteit in of rondom het Groningenveld; (i) een onderzoek naar de mogelijkheid om het aantal aardbevingen te verminderen door stikstof te injecteren (KEM-24b, bijlage 3) en (ii) een onderzoek naar seismiciteit in de aquifer (watervoerende laag) ten zuidwesten van het Groningenveld, door drukvermindering als gevolg van de (inmiddels gestopte) gaswinning uit het Groningenveld en andere omliggende gasvelden (KEM-19b, bijlage 4 en 5).

KEM-24b

In KEM-24b heeft TNO onderzocht of het injecteren van stikstof in het Groningenveld een positief effect zou kunnen hebben op de seismiciteit. Dat wil zeggen of stikstofinjectie het aantal en de grootte van aardbevingen zou kunnen verminderen. Hiervoor zijn de modellen van pSDRA, die gebruikt wordt om het seismisch risico door de gaswinning Groningen te berekenen, ingezet om in plaats van een drukverlaging in het reservoir (door gaswinning) een drukverhoging (door injectie) te modelleren. Zo kon theoretisch onderzocht worden wat het effect van injectie kan zijn op het aantal aardbevingen en op het risico waar gebouwen aan worden blootgesteld. Uit dit onderzoek blijkt dat injectie *in theorie* het aantal aardbevingen inderdaad kan verminderen. Met name injectie in de regio Loppersum kan mogelijk al relatief snel het risico doen verminderen omdat de druk juist in deze regio de komende jaren nog afneemt.

Echter is in dit onderzoek alleen gekeken naar positieve effecten van injectie, en in eerste instantie niet naar de mogelijk *negatieve* (seismiciteit verhogende) effecten. TNO geeft bijvoorbeeld aan dat injectie de temperatuur in het reservoir zal verlagen, wat juist aardbevingen kan veroorzaken. Het effect hiervan is niet meegenomen omdat de huidige modellen ongeschikt zijn om dit te kunnen berekenen. Het aanpassen van de modellen zou veel tijd hebben gekost waardoor resultaten langer op zich hadden laten wachten. De resultaten van deze studie dienen daarom gelezen te worden als een theoretische verkenning voor de potentie van injectie voor aardbevingsvermindering en zeker niet als een definitief resultaat. Daarnaast is in deze studie geen rekening gehouden met de beschikbare hoeveelheid stikstofgas in Nederland en evenmin met de benodigde infrastructuur om dit gas op locatie te kunnen krijgen en te kunnen injecteren. Het is belangrijk te realiseren dat het dus praktisch onhaalbaar is om op korte termijn de hoeveelheid stikstof te injecteren waarmee in dit onderzoek is gerekend.

Gezien de afnemende seismiciteit, de voortgang van de versterkingsoperatie, het gebrek aan stikstof en injectie infrastructuur, het feit dat het Groningenveld heropend zou moeten worden[9] en, wellicht het belangrijkst, gezien de kans op

---

[7] Beide bevingen vonden niet plaats in het Groningenveld maar in de aangrenzende watervoerende laag (aquifer). Deze bevingen worden niet direct veroorzaakt door drukvereffening in het Groningenveld, maar door aanhoudende drukdaling in de aquifer als gevolg van eerdere gaswinning.

[8] Van de beving in Warffum is het niet mogelijk deze met zekerheid aan het Groningenveld toe te schrijven, maar het is wel mogelijk dat deze beving (deels) is veroorzaakt door drukdaling als gevolg van gaswinning uit het Groningenveld. Voor de volledigheid wordt hij daarom hier wel genoemd.

[9] Dit zou noodzakelijk zijn om de putten en andere infrastructuur open en functioneel te houden voor injectie.

door injectie veroorzaakte aardbevingen, zet het kabinet niet in op verder onderzoek naar stikstofinjectie voor toepassing in het Groningenveld[10].

Een goed begrip van de relatie tussen injectie van gassen of vloeistoffen en aardbevingen is van groot belang voor het toekomstige gebruik van de Nederlandse bodem. Denk hierbij aan bijvoorbeeld het gebruik van aardwarmte en de opslag van CO_2. KEM-24b vormt daarom een waardevolle toevoeging aan de kennis over injectie in de aardbodem, en laat zien hoe de kennis opgedaan in Groningen kan bijdragen aan kennisverdieping in bredere zin, binnen en buiten Groningen. Het ministerie van Klimaat en Groene Groei zal zich inzetten om de gaten in onze kennis van injectie en de relatie met aardbevingen zo veel mogelijk (verder) te dichten, in lijn met Nij Begun (maatregel 49). Hierbij kan worden ingezet in verder modelmatig onderzoek, bijvoorbeeld een vervolgonderzoek op KEM-24b waarin de effecten van temperatuur wel worden gemodelleerd, wat zou kunnen worden ingebracht bij het KEM. Daarnaast is het ook belangrijk om meer data te verzamelen, zodat de huidige kennis getoetst kan worden en de modellen geverifieerd. Daarom is het van groot belang om goed te monitoren bij projecten waarbij sprake is van injectie, zoals de opslag van CO_2 in de Noordzee.

KEM-19b
In KEM-19b is in detail gekeken naar mogelijke aardbevingen in de zuidwestelijke aquifer naast het Groningenveld, zowel door drukverlaging vanwege eerdere gaswinning als door mogelijke toekomstige ondergrondse activiteiten. Deze aquifer staat in directe verbinding met het Groningenveld en andere kleine gasvelden, zoals Roden, Vries-Noord, Pasop, Faan, Boerakker, en Bedum. Door de eerdere gaswinning uit deze omliggende velden neemt de druk in het waterhoudende gedeelte van de gesteentelaag waarin ook de gasvelden zich bevinden nog steeds af. Net als bij gaswinning zou deze drukverlaging kunnen leiden tot aardbevingen. De afgelopen jaren zijn hier dan ook lichte aardbevingen geobserveerd door het meetnetwerk van het KNMI.

In dit onderzoek heeft TNO de breuken in de aquifer beter in kaart gebracht en de modellen van de pSDRA uitgebreid naar deze regio. Zo is de relatie tussen de drukvereffening in de aquifer en het seismisch risico onderzocht. Hieruit bleek dat hoewel er grote onzekerheden zijn in de toekomstige drukken in de aquifer, het seismisch risico in de aquifer klein is en blijft. De berekeningen laten zien dat de kans op schade aan gebouwen en infrastructuur boven de aquifer afneemt als functie van de afstand tot het Groningenveld. Dit komt omdat de kans op schadeveroorzakende bevingen in het Groningenveld nog steeds veel groter is dan in de aquifer.

In een tweede onderdeel van het onderzoek (bijlage 5) heeft TNO gekeken naar mogelijk toekomstige activiteiten in de zuidwestelijke aquifer en de bijbehorende seismische risico's[11]. Er is onderzocht hoe en waar de kans op bevingen als gevolg van deze activiteiten het grootst zou zijn. TNO concludeert dat in het noorden van de aquifer (de regio net ten noorden van de stad Groningen) de kans op bevingen het grootst is, en dat vooral eventuele koeling van de ondergrond en de breuken rondom een project goed in kaart gebracht moeten worden om het seismisch risico van het project goed te kunnen inschatten.

Hogere dan verwachte seismiciteit 2020-2022

---

[z] Injectie in het Groningen-gasveld | Voormalige gaswinning Groningen-gasveld | Staatstoezicht op de Mijnen

[11] Het is goed hierbij te vermelden dat er momenteel geen specifieke plannen zijn voor ondergrondse activiteiten in deze aquifer.

In 2020 tot 2023 werden er in Groningen meer aardbevingen geobserveerd dan aan de hand van de modellen van de pSDRA werd verwacht. Om te achterhalen waar dit verschil vandaan kwam heeft SodM in april 2022 de NAM verzocht hier onderzoek naar te doen. Het ministerie van Klimaat en Groene Groei heeft gelijktijdig TNO verzocht hetzelfde te doen. Zowel NAM als TNO hebben daarna verschillende mogelijke oorzaken onderzocht om te kijken welke processen het verschil tussen de modellen en de observaties het beste verklaart. Medio 2024 zijn (tussentijdse) resultaten van dit onderzoek[12] gedeeld met SodM en het ministerie. Uit de resultaten bleek dat het verschil met de observaties mogelijk te wijten is aan te eenvoudige modellen, waarin o.a. de vertraging tussen gaswinning en aardbevingen mogelijk onderschat is. SodM heeft het KEM-subpanel gevraagd deze onderzoeken te evalueren. SodM geeft aan na de zomer van 2025 in een breder advies met een appreciatie te komen van deze onderzoeken van de NAM. Het ministerie van Klimaat en Groene Groei wacht dit advies van SodM af voordat zij verdere vervolgstappen zet met betrekking tot deze onderzoeken.

III. Uitbreiding KNMI netwerk naar aanleiding van PEGA

In het kader van maatregel 49 van de kabinetsreactie Nij Begun op de parlementaire enquête Groningen, zal het seismologisch meetnetwerk van het KNMI worden uitgebreid. Zoals in eerdere communicatie is aangegeven, zal bij deze uitbreiding de focus liggen op gebieden waar ondergrondse activiteiten plaatsvinden[13]. De ambitie is dat in deze gebieden alle aardbevingen met een magnitude van 1,5 of groter zullen worden geregistreerd. Het gebied boven het Groningenveld voldoen al ruim aan deze eis. Hier worden namelijk aardbevingen vanaf een magnitude van 0,5 geregistreerd. Boven de aquifer is dit echter nog 1,0. Het ministerie zal dit jaar in een brief aan de Tweede Kamer meer duiding geven over de specifieke plannen van het KNMI over de uitbreiding van het netwerk, zowel in Groningen als in de rest van Nederland.

Tot slot

Uit de update over de aardbevingen in en rondom het Groningenveld in 2024 blijkt duidelijk dat de seismiciteit in 2024 op het laagste niveau lag van de afgelopen 20 jaar. De neerwaartse trend die is ingezet in 2014 houdt aan en de verwachting is dat het aantal aardbevingen de aankomende jaren verder zal afnemen. Met het volledig beëindigen van de gaswinning uit het Groningenveld is de oorzaak van de aardbevingen weggenomen. Uiteraard zijn de ontstane problemen daar nog niet mee opgelost, maar de positieve ontwikkeling in seismiciteit biedt perspectief voor de bewoners van het aardbevingsgebied.

Sophie Hermans
Minister van Klimaat en Groene Groei

[12] Onderzoeksrapporten | Nederlandse Aardolie Maatschappij
[13] https://open.overheid.nl/documenten/0c5df99b-7d39-441c-9d22-088608809430/file

RAPPORTAGE SEISMICITEIT GRONINGEN GASVELD

-

KALENDER JAAR 2024

Contents

1 Overzicht

1.1 Inleiding

Deze rapportage is opgesteld om te voldoen aan Mijnbouwregeling artikel 1.3a.5 waarin staat dat de houder van de winningsvergunning Groningen-gasveld twee keer per kalenderjaar een rapportage opstelt over ontwikkelingen van de seismiciteit. In dit rapport met peildatum 1 januari 2025 zal de seismiciteit in het Groningen-gasveld voor het volledige kalenderjaar 2024 worden toegelicht.

In dit artikel van de Mijnbouwregeling staat ook dat de seismiciteit wordt gemonitord door middel van het continu bijhouden van vier parameters. Deze vier parameters zijn onderverdeeld in twee zogenoemde trendparameters en in twee zogenoemde incidentparameters (Ref. 1). De maximale aardbevingsdichtheid en het aantal aardbevingen per jaar ('activity rate') zijn de trendparameters. Deze parameters worden gebruikt om vroegtijdig een lokale of veld-brede toename of afname van de seismiciteit te signaleren over de afgelopen 6 maanden[1]. De trendparameters worden berekend over een periode van 6 maanden en gerapporteerd op jaarbasis. De piek grondversnellingen (PGA) en piek grondsnelheden (PGV) van de aardbevingen zijn de incidentparameters. Daarnaast is ook de aardbevingsmagnitude van belang in de Mijnbouwregeling.

1.2 Belangrijkste conclusies van dit rapport

- De daling van de seismiciteit in het Groningen gasveld heeft zich ook in 2024 voortgezet.
- Er zijn in 2024 zes aardbevingen in het Groningen gasveld geregistreerd met een magnitude $M_L \geq 1{,}5$. Het aantal aardbevingen per kalenderjaar met magnitude $M_L \geq 1{,}5$ is sinds 2004 niet zo laag geweest. Dit aantal ligt ook dicht bij de prognose gebaseerd op de Dreigings- en Risicoinschatting (HRA).
- Het aantal aardbevingen met een magnitude $M_L \geq 1{,}2$ ligt met zeven aardbevingen in 2024 lager dan de 10 verwachte aardbevingen, gebaseerd op de HRA.
- Deze aardbevingen hadden het epicentrum in het uiterste noordwesten van het Groningen gasveld. Ook dat komt overeen met de prognose van de HRA.
- De grootste van deze aardbevingen had een magnitude van $M_L = 2{,}2$.

1.3 Aantal aardbevingen (activity rate)

Het aantal aardbevingen in 2024 met een magnitude groter dan of gelijk aan $M_L \geq 1{,}2$ was zeven en het aantal aardbevingen met een magnitude groter dan of gelijk aan $M_L \geq 1{,}5$ was zes. De hoogste magnitude van een aardbeving in 2024 was $M_L = 2{,}2$.

Laagste activity rate in 2024 was 6 aardbevingen per jaar. Sinds 2004 is de activity rate niet zo laag geweest. Echter in de periode tussen 2004 en 2014 zijn er misschien aardbevingen met magnitude $1{,}2 \leq M_L < 1{,}5$ opgetreden die door het destijds geïnstalleerde monitoringsnetwerk niet zijn opgemerkt.

De ontwikkeling van de seismiciteit in Groningen wordt in meer detail beschreven in paragrafen 4.1 tot 4.4.

[1] De Mijnbouwregeling hanteert een observatieperiode van 6 maanden; dus bijvoorbeeld van 00:00 uur op 1 november tot 00:00 uur op 1 mei. Door het jaar varieert hierdoor de duur van de observatieperiode. Als februari bijvoorbeeld binnen de observatieperiode valt dan is deze korter. De duur van de observatieperiode varieert tussen de 181 en 184 dagen.

Tabel 1-1 Aardbevingen in Groningen met een kracht $M_L \geq 1,2$ geregistreerd in 2024 door het KNMI seismisch monitoringsnetwerk. Locatie van het hypocentrum is gebaseerd op de KNMI-aardbevingscatalogus.

Plaats	Datum	Time hh:mm:ss UTC	Magnitude	Diepte km	Easting	Northing
Eerste helft 2024						
Luddeweer	28-Jan-24	01:47:05	1,2	3	244171	584985
Zeerijp	11-Apr-24	09:10:24	2,1	3	245078	597136
Lageland	14-Apr-24	14:08:51	1,6	3	242503	584955
Usquert	29-Apr-24	11:42:14	1,5	3	234322	603180
Tweede helft 2024						
Kantens	09-Aug-24	18:00:20	1,7	3	239906	599602
Usquert	19-Okt-24	09:12:35	1,7	3	237453	602899
Garsthuizen	31-Okt-24	15:15:26	2,2	3	242511	598419

1.4 Aardbevingsdichtheid

Aardbevingsdichtheid is gedefinieerd als het aantal geobserveerde aardbevingen per vierkante kilometer per jaar en wordt berekend voor het hele Groningen-gasveld. Deze dichtheid is berekend op basis van de aardbevingen, geregistreerd gedurende de voorafgaande 6 maanden, met een magnitude $M_L \geq 1,2$.

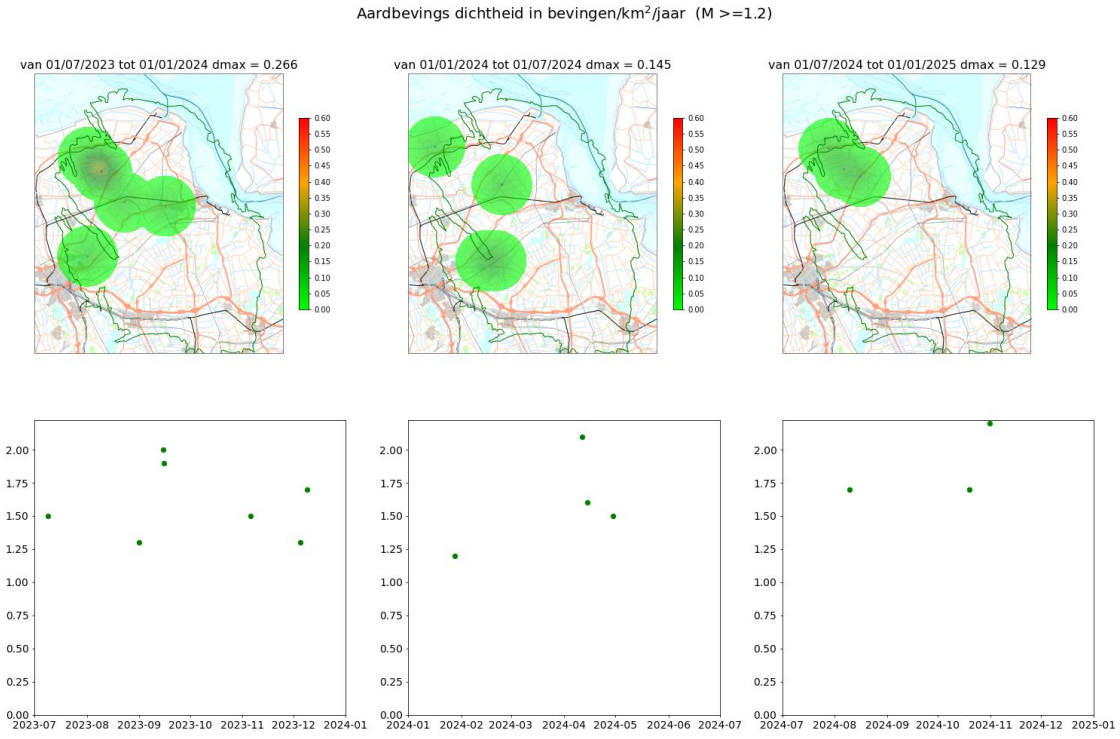

Figuur 1-1 Kaarten van aardbevingsdichtheid gebaseerd op aardbevingen met magnitude $M_L \geq 1,2$ gedurende 2024. De aardbevingsdichtheid is omgerekend naar jaarbasis. De grafieken onder de kaarten tonen de magnitude van de aardbevingen in tijd. De kaarten en grafieken zijn voor peildatum 1 Januari 2024, 1 July 2024 en 1 Januari 2025.

De epicentra van de drie aardbevingen in deze rapportage periode met een magnitude $M_L \geq 1,2$ liggen in het noordwesten van het Groningen-gasveld. De aardbevingsdichtheid is in dit gebied daarom

relatief hoog vergeleken met de rest van het gasveld. De maximale aardbevingsdichtheid is gedaald tot 0,129 aardbevingen per (km^2 · jaar), zie figuur 1-1.

1.5 Trend in seismiciteit

Het aantal aardbevingen per jaar laat vanaf 2014 een dalende trend zien. In 2024 zijn er zeven aardbevingen met een magnitude $M_L \geq 1{,}2$ geregistreerd. Het aantal aardbevingen per kalenderjaar met magnitude $M_L \geq 1{,}2$ is sinds 2002 niet zo laag geweest. Echter in de periode tussen 2003 en 2014 zijn er misschien aardbevingen met magnitude $1{,}2 \leq M_L < 1{,}5$ opgetreden die door het, destijds geïnstalleerde, monitoringsnetwerk niet zijn opgemerkt. Dat zou betekenen dat het aantal aardbevingen in 2002 met een magnitude $M_L \geq 1{,}2$ mogelijk hoger is geweest dan was geobserveerd en we nog verder terug moeten gaan in de tijd voor het jaar dat het aantal aardbevingen met magnitude $M_L \geq 1{,}2$ lager was dan in 2024.

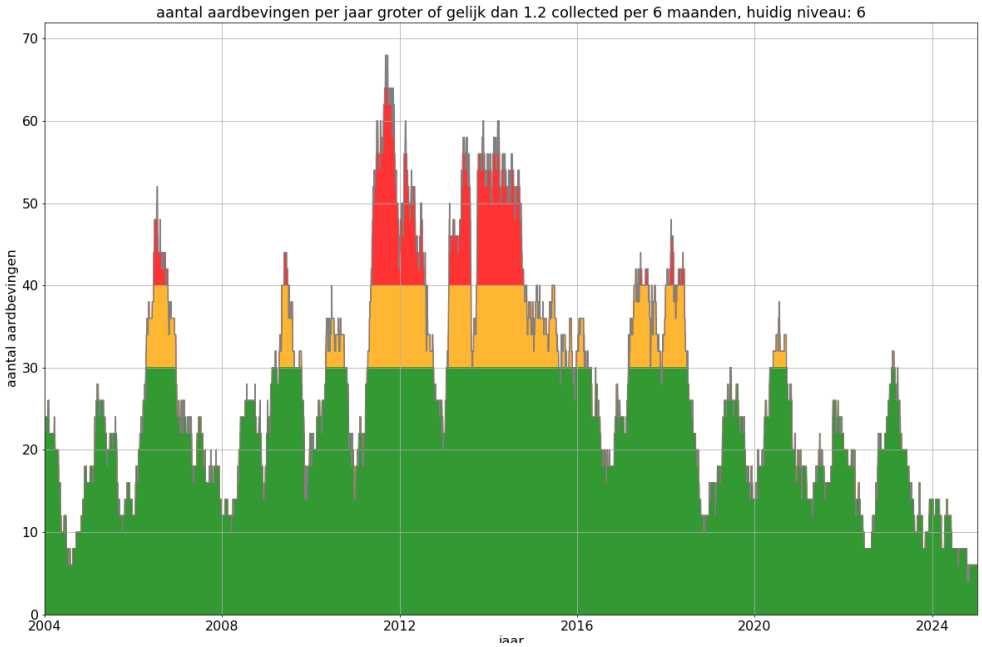

Figuur 1-2 Aantal aardbevingen per jaar berekend als aangegeven in de Mijnbouwregeling artikel 1.3a.5. Aangegeven in de figuur zijn aardbevingen met een magnitude $M_L \geq 1{,}2$ gedurende een voorgaande 6-maanden periode geconverteerd naar jaarbasis.

1.6 Aardbevingen met hoogste magnitude

De aardbevingen met de grootste magnitude in 2024, nabij Garsthuizen. Deze had een magnitude van $M_L = 2{,}2$. Deze geregistreerde magnitude is lager dan de grenswaarden voor deze signaalparameter.

1.7 Incidentparameters PGA en PGV

Het Rapport '*Defining criteria for semi-annual earthquake reporting of PGV and PGA in Groningen*' (Ref. 2) bevat een analyse van de piek grondsnelheid en piek grondversnelling die is geobserveerd voor aardbevingen met verschillende magnitudes. De waargenomen magnitude van de aardbevingen in 2024 geeft aan dat de piek grondversnellingen en piek grondsnelheden lager zijn dan de grenswaarden voor deze signaalparameters.

2 Inleiding en leeswijzer

2.1 Inleiding

Dit halfjaarlijkse rapport beschrijft een analyse van de ontwikkeling van de seismiciteit in het Groningen-gasveld zoals benoemd in Artikel 1.3a.5 van de Mijnbouwregeling. Hierin staat dat de houder van de winningsvergunning Groningen-gasveld twee keer per kalenderjaar een rapportage opstelt over ontwikkelingen in de seismiciteit (Ref. 1). Ook na het insluiten van de gasproductie uit het Groningen-gasveld zal NAM doorgaan met uitgeven van deze rapportages als onderdeel van de nazorg.

In de afgelopen jaren heeft NAM twee keer per jaar een 'Rapportage Seismiciteit Groningen' uitgebracht, gebaseerd op alle aardbevingsgegevens tot respectievelijk 1 mei en 1 november. Nu het gasveld is gesloten op 1 oktober 2023 brengt NAM de rapportage periode in overeenstemming met het kalenderjaar. De door de Mijnbouwregeling voorgeschreven twee rapportages per jaar zullen dan gebaseerd zijn op alle aardbevingsgegevens tot respectievelijk 1 januari en 1 juli. De seismiciteit gedurende een vol kalenderjaar wordt daarmee beschreven in twee seismische monitoringsrapportages. Dit maakt de rapportage van de seismische monitoring in Groningen eenvoudiger en daarmee transparanter. In dit rapport met peildatum 1 januari 2025 zal de seismiciteit in het volledige kalenderjaar 2024 worden toegelicht.

Seismische gegevens in dit rapport zijn bijgewerkt tot en met 31 december 2024. De productie gegevens zijn bijgewerkt tot de sluiting van het Groningen-gasveld. Het rapport kijkt in principe een jaar terug, maar daar waar relevant wordt verder teruggekeken om seismische ontwikkelingen in hun bredere historische context te plaatsen. Een tabel met de aardbevingen die in Groningen zijn geregistreerd in het afgelopen jaar, door het seismisch monitoringsnetwerk geopereerd door KNMI, is in dit rapport opgenomen onder Appendix B.

2.2 Monitoring van het Groningen gasveld in de Mijnbouwregeling

In de Mijnbouwregeling (artikel 1.3a.6.1a tot en met f) staat beschreven welke actie moet worden genomen, wanneer het waarnemingsniveau van een trendparameter wordt overschreden. Dit is samengevat in Tabel 2.1. In Mijnbouwregeling artikelen 1.3a.8 en 1.3a.9 is beschreven welke actie genomen moet worden bij overschrijding van het waarnemingsniveau van een signaalparameter, zie hiervoor tabel 2.2.

Tabel 2-1 Beschrijving van welke actie ondernomen wordt bij overschrijding van een waarnemingsniveau voor een trendparameter volgens Mijnbouwregeling artikel 1.3a.6. Meldingen worden gedaan aan de Minister van Klimaat en Groene Groei en de Inspecteur-generaal der Mijnen (SodM).

Trendparameter	Waarnemings-Niveau	Melding	Analyse
Aantal aardbevingen $M_L \geq 1,2$	30	Waarneming melden binnen 48 uren.	-
	40	Idem	Analyse van de ontwikkeling van seismiciteit binnen 14 dagen.
Aardbevingsdichtheid	0,30	Waarneming melden binnen 48 uren.	-
	0,40	Idem	Analyse van de ontwikkeling van seismiciteit binnen 14 dagen.

Tabel 2-2 Beschrijving van welke actie ondernomen wordt bij overschrijding van een signaalparameter waarnemingsniveau volgens Mijnbouwregeling artikel 1.3a.8 (Grondversnelling en Grondsnelheid) en artikel 1.3a.9 (Magnitude). Meldingen worden gedaan aan de Minister van Klimaat en Groene Groei en de Inspecteur-generaal der Mijnen (SodM).

Signaalparameter	Waarnemings-niveau	Melding	Analyse
Grondversnelling	> 0,08 g	Terstond waarneming melden	Eerste analyse binnen 48 uren, nadere analyse binnen 14 dagen.
Grondsnelheid	50 mm/s	Idem	Idem
Magnitude	≥ 3,0	Terstond waarneming melden	Eerste analyse binnen 48 uren, nadere analyse binnen 14 dagen.

2.3 Leeswijzer

Voor de in dit rapport besproken analyses wordt de dataset van geregistreerde aardbevingen onderverdeeld in vier magnitude-klassen. Dit is gedaan vanwege de verschillen in compleetheid en omvang van de vier sub-sets, die daardoor statistisch niet direct vergelijkbaar zijn. Om de leesbaarheid te vergroten wordt voor elke klasse de volgende vaste kleur gebruikt in de verschillende figuren.

- Groen: Aardbevingen met een magnitude[2] groter of gelijk aan $M_L = 1,0$
- Paars: Aardbevingen met een magnitude groter of gelijk aan $M_L = 1,2$
- Blauw: Aardbevingen met een magnitude groter of gelijk aan $M_L = 1,5$
- Rood: Aardbevingen met een magnitude groter of gelijk aan $M_L = 2,0$

Voor het bepalen van de monitoringsparameters voor het aantal aardbevingen en aardbevingsdichtheid zijn aardbevingen met een magnitude $M_L \geq 1,2$ van belang. Het seismisch model dat gebruikt wordt voor het inschatten van dreiging en risico is gekalibreerd op basis van de aardbevingen met een magnitude $M_L \geq 1,5$.

[2] De sterkte van de aardbevingen worden in dit rapport aangeduid in Local Magnitude Scale of M_L (Ref. 3).

In dit rapport wordt een , (komma) gebruikt als scheidingsteken voor decimalen, en een . (punt) voor duizendtallen.

2.4 Meetnetwerk en meetnauwkeurigheid

Het seismische meetnetwerk is eigendom van en wordt geopereerd en onderhouden door het KNMI. Elk seismisch meetstation bestaat uit een bovengronds geplaatste accelerometer voor het meten van grondversnellingen en vier ondergronds geplaatste geofoons voor een nauwkeurige bepaling van het epi- en hypocentrum en de bepaling van de aardbevingssterkte. Deze geofoons zijn in een put op 50, 100, 150 en 200 meter diepte geplaatst. Daarnaast zijn er ook oude geofoon stations van vóór de uitbreiding en nieuw geplaatste stations (vooral ten westen en zuiden van het gasveld) die alleen grondversnelling meten. Alle in dit hoofdstuk gerapporteerde meetgegevens zijn ontleend aan het KNMI en terug te vinden op de website van het KNMI.

Het seismische meetnetwerk boven het Groningen-gasveld is in 2014 uitgebreid met 69 nieuwe seismische meetstations. Hierdoor is de gevoeligheid van het meetnetwerk toegenomen. In de periode van 2003 tot en met 2014 werden alle aardbevingen in het Groningen-gasveld met een magnitude groter dan $M_L \geq 1{,}5$ op de schaal van Richter geregistreerd. Vanaf 2014 worden door de uitbreiding van het monitoringsnetwerk alle aardbevingen met een magnitude groter dan $M_L \geq 1{,}0$ op de schaal van Richter boven het Groningen-gasveld geregistreerd. Vóór 2014 werden ook enkele aardbevingen met een magnitude boven de $M_L \geq 1{,}0$ geregistreerd, maar door de lagere gevoeligheid van het meetnetwerk is het niet zeker of alle aardbevingen met een magnitude tussen de $M_L = 1{,}0$ en de $M_L = 1{,}5$ geregistreerd zijn. Daardoor kan in die periode het werkelijke aantal aardbevingen vanaf $M_L = 1{,}0$ onderschat zijn.

2.5 Magnitude van compleetheid

De magnitude van compleetheid (magnitude of completeness of ook wel MoC) is de laagste magnitude M_L waarvoor elke aardbeving waargenomen kan worden, ongeacht locatie in het Groningen-gasveld. Aardbevingen met een magnitude kleiner dan de MoC kunnen waargenomen worden wanneer deze zich voordoen op een voor het meetnetwerk ‘gunstige’ locatie. Wanneer de aardbeving zich voordoet op een andere locatie zou deze mogelijk niet worden waargenomen. Voor aardbevingen met een magnitude groter dan de MoC geldt dat deze worden waargenomen, ongeacht de locatie in het gasveld. De MoC wordt afgeleid uit de waarnemingen en is onderhevig aan een bepaalde mate van onzekerheid.

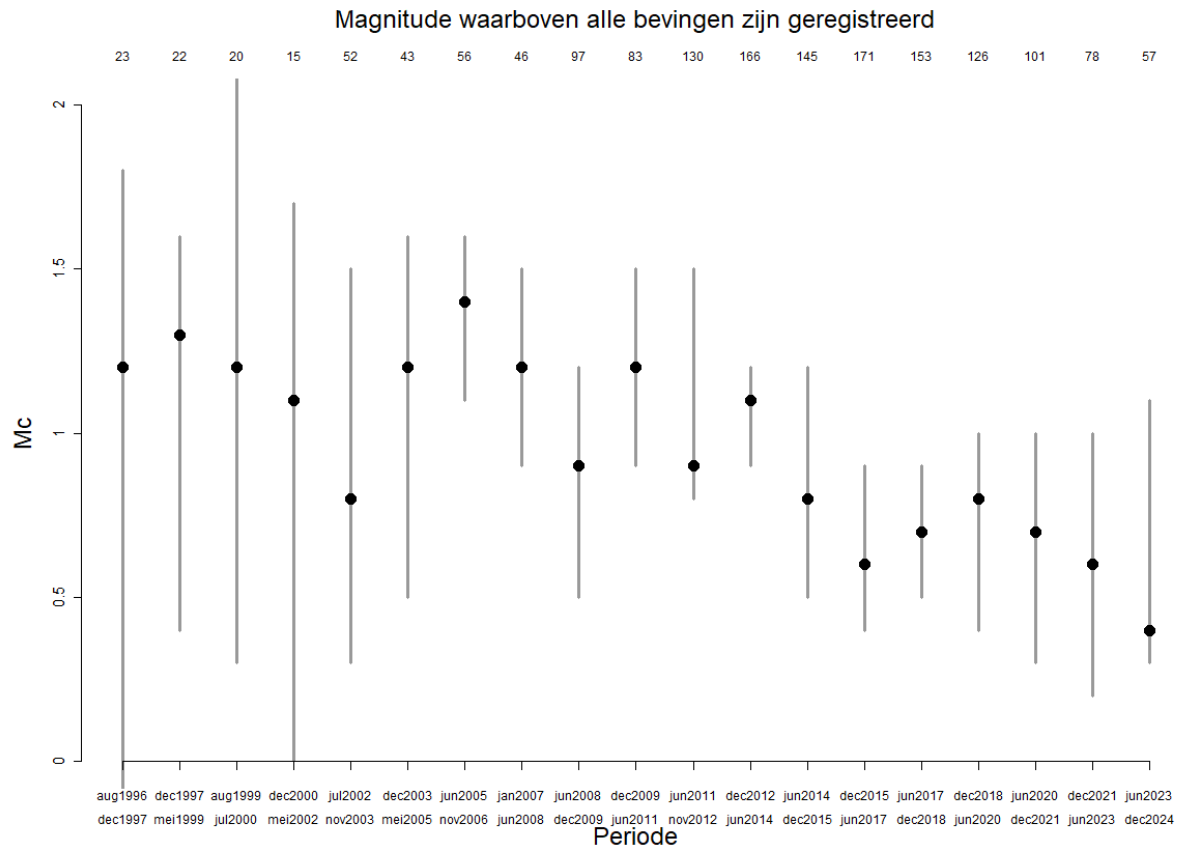

Figuur 2-1 Magnitude of Completeness met onzekerheidsintervallen voor verschillende periodes, met de stip wordt de P50 waarde aangegeven.

Voor statistisch onderzoek is het van belang een goede MoC te veronderstellen. Is de veronderstelde MoC te hoog dan wordt de dataset kleiner dan mogelijk en is het moeilijker statistisch relevante conclusies aan de data te verbinden. Is de MoC te laag aangenomen dan is de dataset incompleet en worden mogelijkerwijs foutieve conclusies uit de dataset afgeleid.

De MoC is afgeleid volgens de maximum curvature method (Ref. 3 en 4) en de resultaten met het 95% betrouwbaarheidsinterval zijn weergegeven in figuur 2-1. In het figuur is duidelijk zichtbaar dat vanaf 2014 de MoC afneemt (ook kleinere aardbevingen worden geregistreerd). Dit is en direct gevolg van de uitbreiding van het seismisch monitoringsnetwerk. Vanaf 2014 zijn aardbevingen met een magnitude $M_L \geq 1{,}0$ bruikbaar voor statistisch onderzoek. In de periode voorafgaand aan 2014 is de dataset waarschijnlijk compleet voor aardbevingen met een magnitude $M_L \geq 1{,}2$ en zeer waarschijnlijk compleet voor aardbevingen met een magnitude $M_L \geq 1{,}5$. In deze rapportage wordt een MoC van 1,0, 1,2 of 1,5 verondersteld, onder meer afhankelijk van hoe ver teruggekeken wordt in de tijd. Deze hogere MoC in de periode voor 2014 is de reden dat we voorzichtig moeten zijn wanneer we het aantal aardbevingen met $M_L \geq 1{,}2$ in 2024 vergelijken met die in jaren voor 2014.

3 Trendparameters

3.1 Waarnemingen en lange termijn trend

Het aantal aardbevingen en de maximale aardbevingsdichtheid zijn de trendparameters. Zowel het aantal aardbevingen als de maximale aardbevingsdichtheid zijn stabiel op een historisch laag niveau gedurende de huidige rapportage periode en vallen onder het laagste waarnemingsniveau. In Tabel 3-1 wordt voor het afgelopen jaar de activity rate, het aantal aardbevingen op jaarbasis met een magnitude $M_L \geq 1{,}2$ en de maximale aardbevingsdichtheid in het Groningen gasveld getoond.

Tabel 3-1 Trendparameter overzicht voor 2024. Aantal aardbevingen ($M_L \geq 1{,}2$) in de maand en aardbevingsdichtheid (aantal aardbevingen per jaar en vierkante kilometer) zijn berekend op het einde van de maand.

	jan	feb	mrt	apr	mei	juni	juli	aug	sep	okt	nov	dec
Aantal aardbevingen in de maand ($M_L \geq 1{,}2$)	1	0	0	3	0	0	0	1	0	2	0	0
Aardbevings-dichtheid	0,27	0,27	0,13	0,15	0,15	0,15	0,08	0,08	0,08	0,13	0,13	0,13
Activity Rate: Aantal aardbevingen per jaar ($M_L \geq 1{,}2$)	14	12	8	14	12	8	6	8	8	6	6	6

De trendparameters worden continu bijgehouden in de vorm van een trendlijngrafiek, zie figuur 3-1. In beide grafieken van de trendparameters is de periode waarin de aardbevingen verzameld worden zes maanden. De getallen zijn omgerekend naar een jaarlijks aantal aardbevingen/dichtheid. De achtergrondkleur geeft het niveau van de seismiciteit weer, groen: lage activiteit, geel: bovengemiddelde activiteit en oranje: hoge activiteit.

In de maanden juli tot september 2024 daalde de maximale aardbevingsdichtheid tot 0,08 aardbevingen per $km^2 \cdot$ jaar. Ook in 2023 is de aardbevingsdichtheid zo laag geweest. De laatste keer dat de aardbevingsdichtheid daar voor ook zo laag is geweest was in 2003.

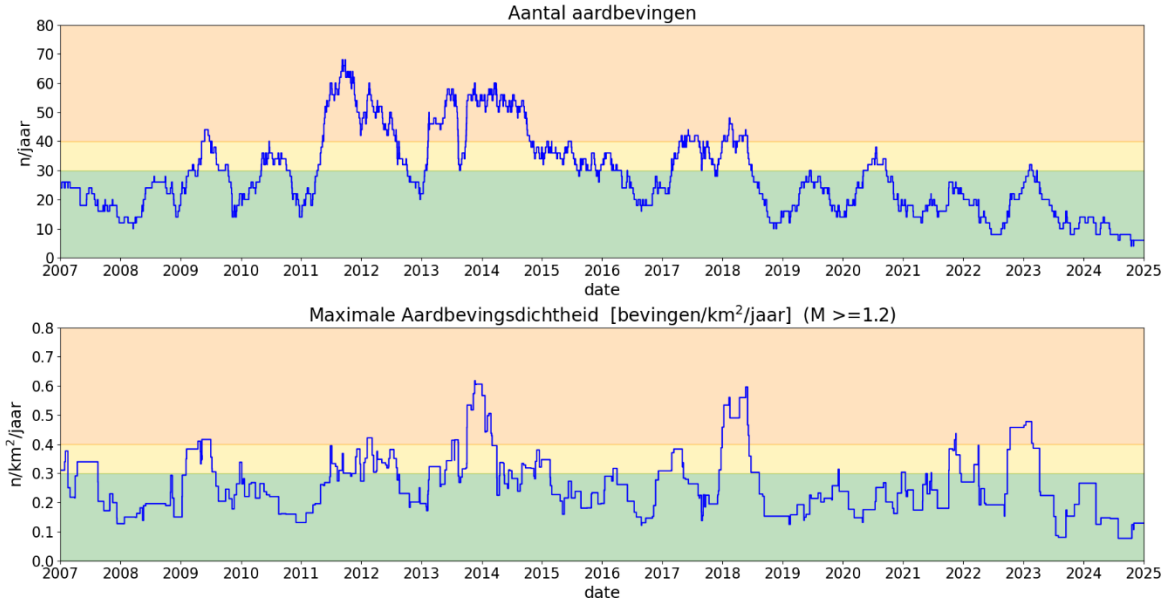

Figuur 3-1 Trendparameters: In de bovenste grafiek wordt het aantal waargenomen aardbevingen met een magnitude M_L = 1,2 of groter per twaalf maanden getoond. In de onderste grafiek wordt de maximale aardbevingsdichtheid (voor aardbevingen met een magnitude van M_L = 1,2 of groter) per twaalf maanden getoond.

3.2 Trendparameter aantal aardbevingen

De trendparameter 'aantal aardbevingen' toont het aantal waargenomen aardbevingen met een magnitude M_L=1,2 of groter in het voorgaande jaar. Dit wordt ook het rollende aantal of 12-maandsgetal genoemd. Dit wordt berekend over de voorgaande zes maanden. Het 12-maandsgetal van 1 januari 2025 is dus de som van het aantal aardbevingen van een bepaalde magnitude in de voorafgaande periode van 1 juli 2024 tot en met 31 december 2024 omgerekend naar één jaar.

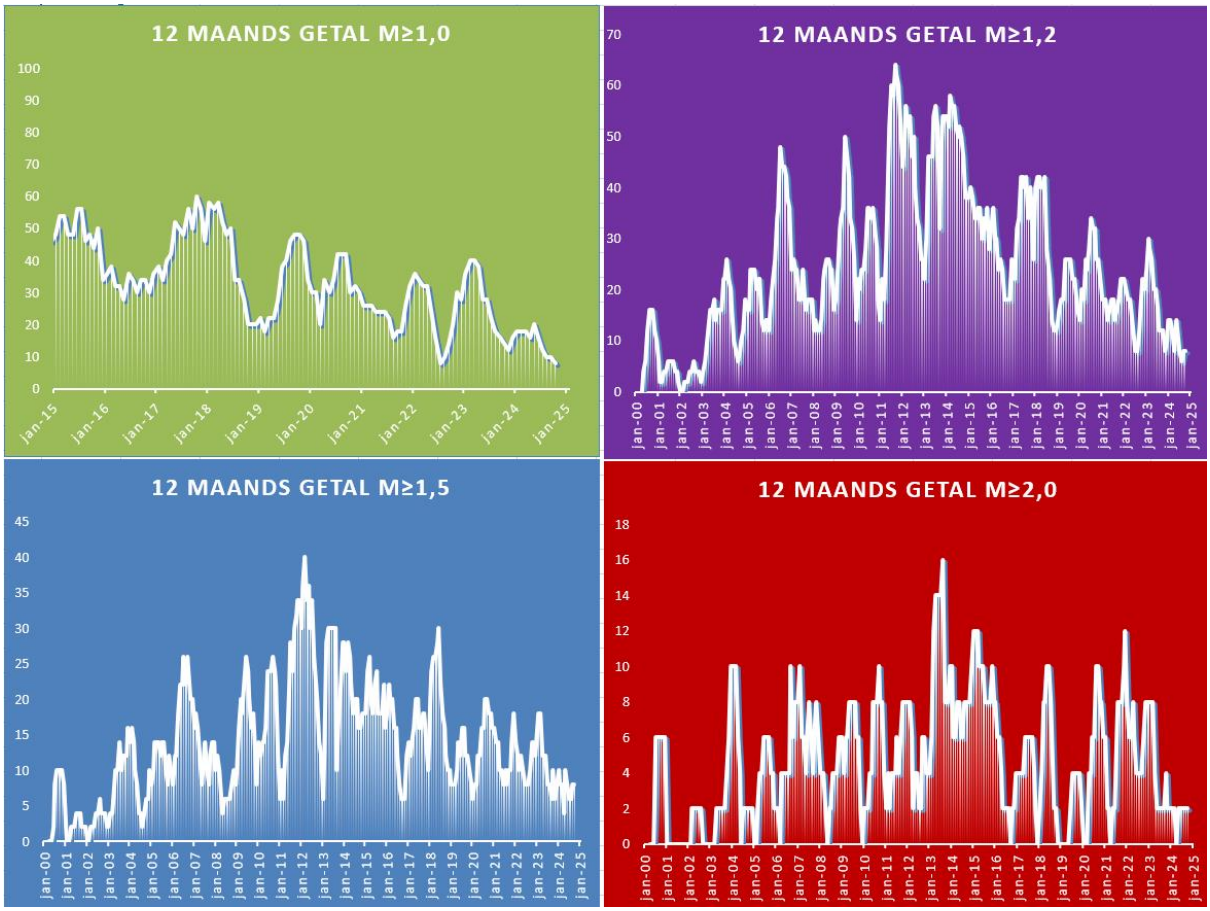

Figuur 3-2 12-maandsgetallen voor vier magnitude-klassen; waarnemingen voor ML ≥ 1,0 weergegeven vanaf 2014, de overige waarnemingen sinds 2000. Deze trend is gebaseerd op aardbevingsobservaties tijdens de voorgaande 6 maanden. Deze zijn omgerekend naar jaarbasis.

Figuur 3-2 laat het 12-maandsgetal zien over een langere periode voor vier magnitude-klassen. Hierbij geldt dat de dataset van aardbevingen met een magnitude onder de $M_L \geq 1,0$ in de periode voor 2014 mogelijk incompleet is vanwege beperkingen in het meetsysteem in die periode, zie ook hoofdstuk 2.4. De dalende trend in het aantal aardbevingen (met magnitude groter dan of gelijk aan $M_L = 1,0$, $M_L = 1,2$ en $M_L = 1,5$) is het gevolg van de afbouw van de gas-productie en daarna het insluiten van het gasveld.

3.3 Aardbevingsdichtheid

Figuur 3-3 toont een kaart met de aardbevingsdichtheid en de epicentra van de in deze rapportage periode geregistreerde aardbevingen. Aardbevingsdichtheid wordt berekend met de Quartic Kernel functie. Alle geregistreerde aardbevingen met een magnitude van $M_L = 1,2$ en groter zijn hierin opgenomen. De berekende aardbevingsdichtheid wordt getoond door middel van een kleurenschaal. Als trendparameter wordt de maximale waarde van de berekende aardbevingsdichtheid over de voorgaande zes maanden gebruikt.

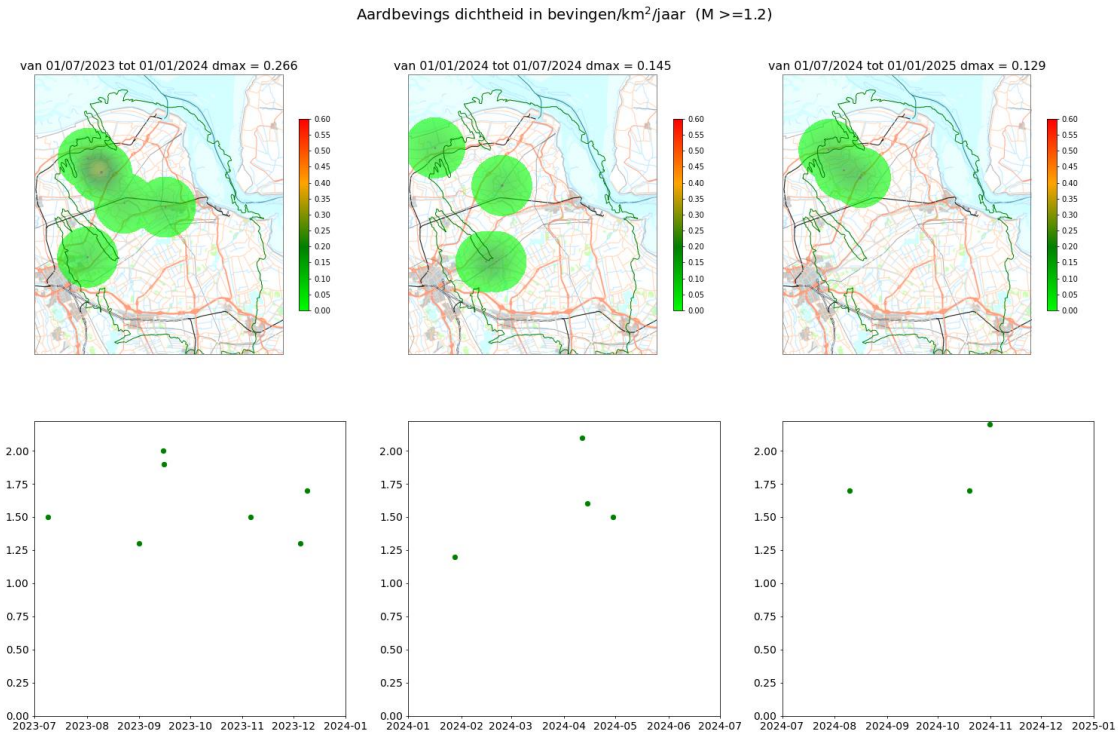

Figuur 3-3 Boven: Kaarten van aardbevingsdichtheid gebaseerd op aardbevingen met magnitude $M_L \geq 1,2$ gedurende de er aan voorafgaande 6 maanden. De aardbevingsdichtheid is omgerekend naar jaarbasis. Onder: Grafieken met de magnitude van de aardbevingen in tijd. De kaarten en grafieken zijn voor peildatum 1 Januari 2024, 1 July 2024 en 1 Januari 2025.

In de huidige rapportage periode vallen de drie aardbevingen met $M_L \geq 1,2$ allen in het uiterste noordwesten van het Groningen gasveld. Het gebied waar aardbevingsdichtheid wordt geëvalueerd is duidelijk te zien in figuur 3-3.

4 Nadere analyse van de geobserveerde seismiciteit

In dit hoofdstuk zijn de resultaten van een nadere analyse van de trends en patronen van de trendparameters opgenomen, te weten het verloop van het aantal aardbevingen in de tijd en de regionale ontwikkeling van de seismiciteit.

4.1 Aantal aardbevingen

In 2024 zijn er in totaal zeven aardbevingen geregistreerd met een magnitude groter of gelijk aan $M_L \geq 1{,}2$. Figuur 4-1 toont duidelijk de dalende trend in het aantal aardbevingen sinds 2012. De laatste keer dat het aantal aardbevingen (activity rate) zo laag was is twintig jaar geleden in 2004.

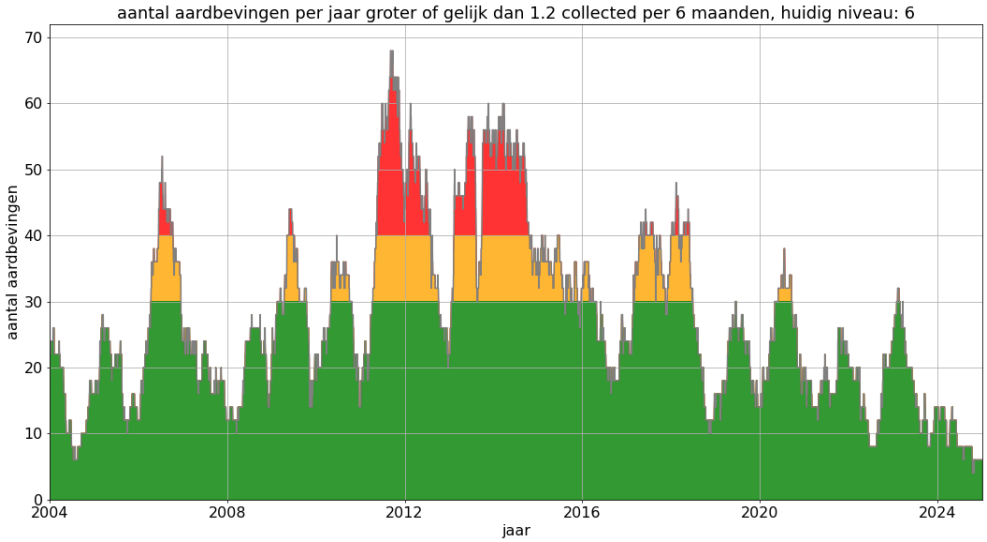

Figuur 4-1 Aantal aardbevingen berekend per jaar zoals aangegeven in Mijnbouwregeling artikel 1.3a.5. Dit betreft de aardbevingen met een kracht van $M_L \geq 1{,}2$ in de voorgaande 6 maanden omgerekend naar jaarbasis.

Het aantal aardbevingen per maand onderverdeeld in vijf magnitudeklassen is opgenomen in tabel 4.1. In de eerste helft van 2024 zijn er 4 aardbevingen geregistreerd met een magnitude $M_L \geq 1{,}2$. In de huidige periode, de tweede helft van 2024, zijn er 3 aardbevingen met een magnitude $M_L \geq 1{,}2$ geregistreerd. Deze hadden alle drie een magnitude $M_L \geq 1{,}5$.

Tabel 4-1 Aantal waargenomen aardbevingen per maand het afgelopen jaar verdeeld over vijf magnitude klassen.

Maand	$1{,}0 \leq M_L < 1{,}2$	$1{,}2 \leq M_L < 1{,}5$	$1{,}5 \leq M_L < 2{,}0$	$2{,}0 \leq M_L < 2{,}5$	$M_L \geq 2{,}5$	Totaal $M_L \geq 1{,}2$
jan-24	0	1	0	0	0	1
feb-24	1	0	0	0	0	0
mrt-24	1	0	0	0	0	0
apr-24	0	0	2	1	0	3
mei-24	0	0	0	0	0	0
jun-24	0	0	0	0	0	0
jul-24	0	0	0	0	0	0
aug-24	0	0	1	0	0	1
sep-24	0	0	0	0	0	0
okt-24	1	0	1	1	0	2
nov-24	0	0	0	0	0	0
Dec-24	2	0	0	0	0	0
Eerste helft 2024	2	1	2	1	0	4
Tweede helft 2024	3	0	2	1	0	3
2024	5	1	4	2	0	7

Figuur 4-2 laat de ontwikkeling van het aantal aardbevingen per jaar zien voor vier verschillende magnitude-klassen. Het panel linksboven (groene kleur) laat het jaarlijks aantal aardbevingen zien voor $M_L \geq 1{,}0$ (waarbij opgemerkt moet worden dat er vanwege incompleetheid geen data van vóór 2014 getoond zijn voor $M_L \leq 1{,}0$). Er zijn statistische aanwijzingen dat de dataset boven de $M_L = 1{,}2$ wel compleet zou kunnen zijn (ook voor de periode voor 2014), zie hiertoe ook de uiteenzetting in sectie 2.5. Dit is de reden dat deze geplot is vanaf het jaar 2000 (paneel rechtsboven, paarse kleur). Het linker paneel beneden (blauwe kleur) laat aardbevingen zien met een magnitude van $M_L \geq 1{,}5$. Deze dataset is vrijwel zeker compleet vanaf 2000 en kan dus goed gebruikt worden om een historisch overzicht te geven van de seismische ontwikkeling. Het paneel rechts beneden tenslotte (in de rode kleuren), toont het aantal aardbevingen met een magnitude $M_L \geq 2{,}0$.

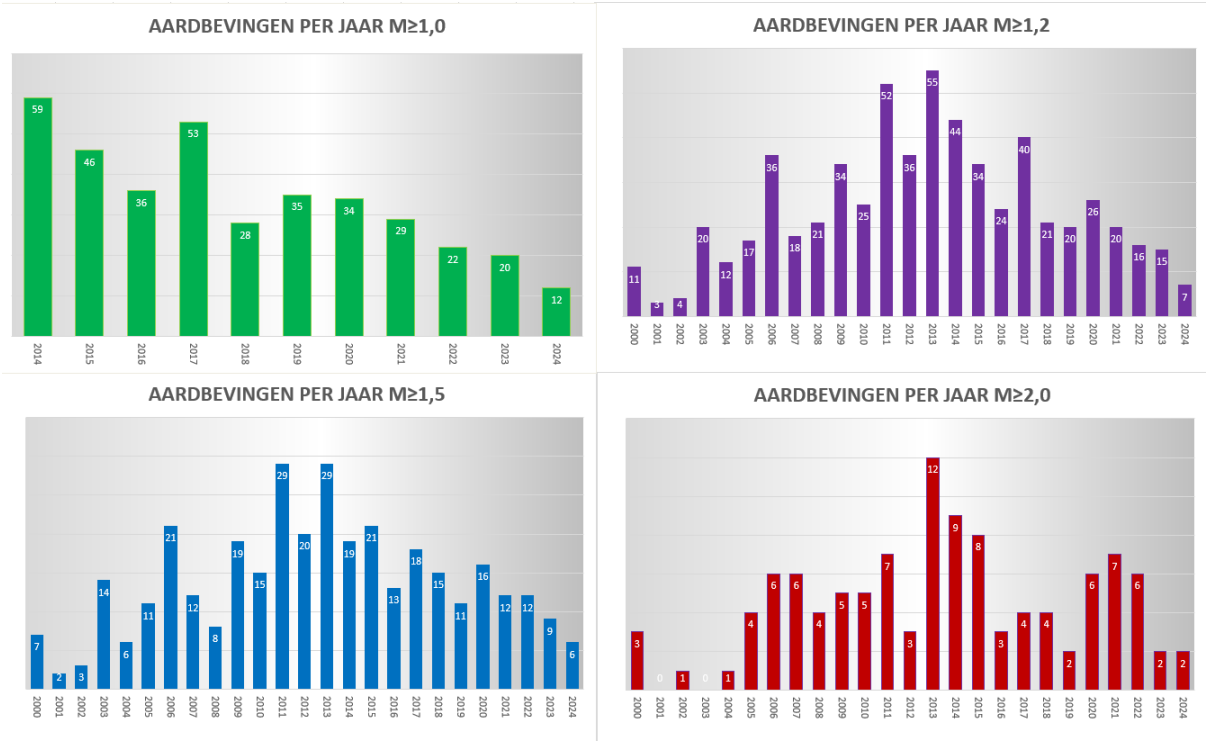

Figuur 4-2 Aantal aardbevingen per jaar voor vier verschillende magnitude-klassen. Het aantal aardbevingen in 2024 is aangegeven voor de eerste tien maanden van het jaar.

4.2 Distributie van aardbevingen over het Groningen-gasveld

De distributie van aardbevingen over het Groningen-gasveld is getoond op de kaart in Figuur 4-3 en Figuur 4-4. In deze figuren wordt de kaart van het gasveld met de epicentra van alle (dus ook de aardbevingen met een magnitude kleiner dan de MoC waarde) aardbevingen. De locaties van de in 2024 geregistreerde aardbevingen zijn in rood weergegeven. De aardbevingen die plaats vonden voor 2024 zijn in geel weergeven. Alle zeven aardbevingen met een magnitude $M_L \geq 1{,}2$ in 2024 hebben een epicentrum binnen het meest seismisch actieve gebied ten noordwesten van Loppersum. Dit komt overeen met de voorspelling; dat door de voortgaande drukvereffening in het Groningen-gasveld de reservoirdruk in dit gebied nog steeds daalt. De zwaarste aardbeving met een magnitude $M_L = 2.2$ vond plaats bij Garsthuizen op 31 oktober 2024.

4.3 Gas-productie gedurende 2024

Om 6 uur in de ochtend op 1 oktober 2023 is het Groningen gasveld ingesloten. De laatste gas-productie was van 8 januari tot 10 januari 2024 toen, op verzoek van het ministerie van Klimaat en Groene Groei, vanuit twee locaties van het Groningen gasveld, Spitsbergen en Scheemderzwaag, voor korte tijd geproduceerd werd op het waakvlam niveau. In totaal is gedurende deze korte periode nog ca. 8 mln m^3 aardgas geproduceerd uit het Groningen gasveld (Ref. 5 tot 7n). In de daarop volgende maanden van 2024 is het gasveld niet geproduceerd.

4.4 Ontwikkeling van de aardbevingsdichtheid over tijd

De maximumwaarde van de aardbevingsdichtheid als functie van de tijd over het gehele veld en per deelgebied is weergegeven in Figuur 4-5. De gebieden tussen de verschillende grenswaarden voor rapportage en analyse op basis van aardbevingsdichtheid volgens de Mijnbouwwet zijn aangegeven in de kleuren groen, geel en rood.

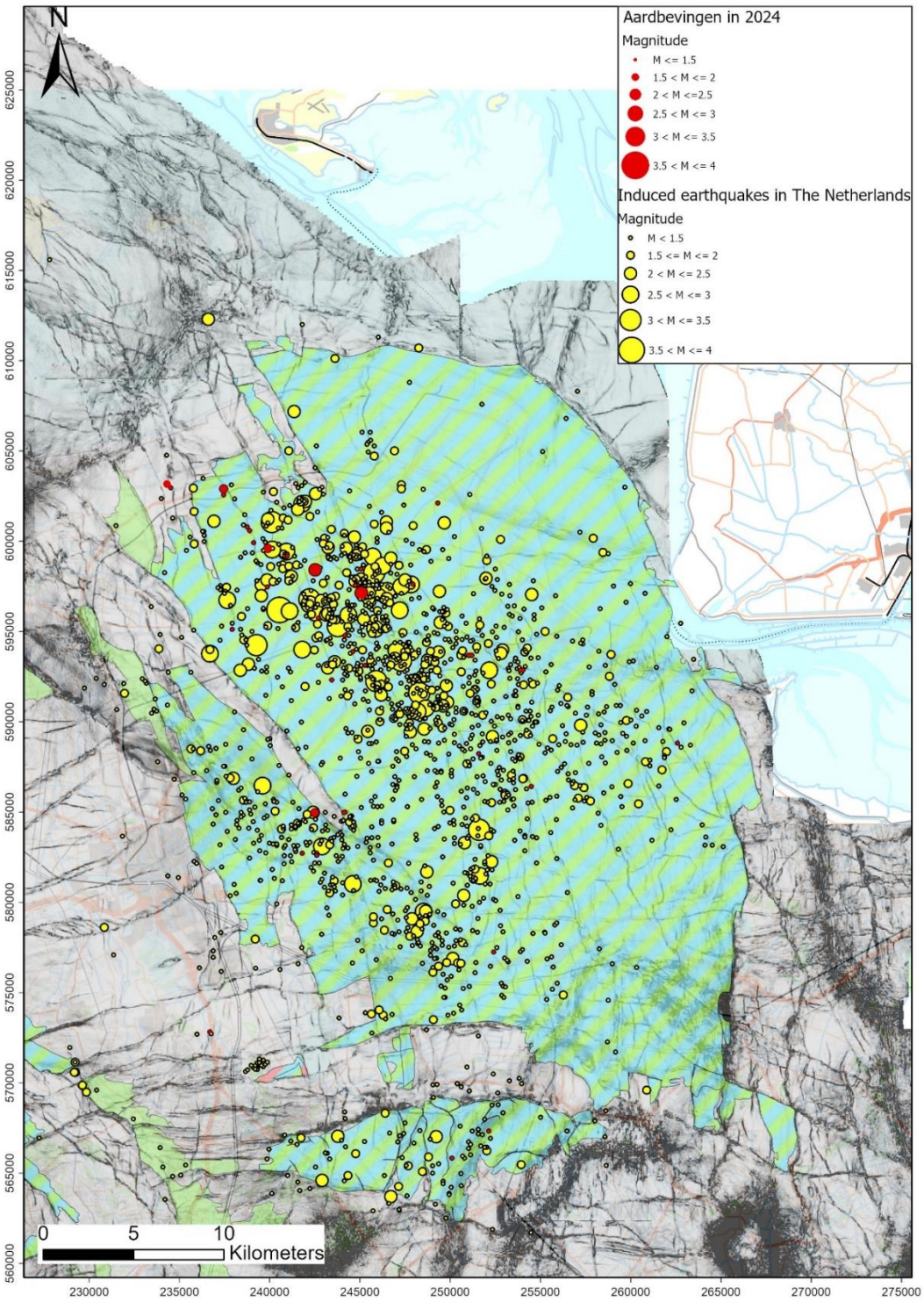

Figuur 4-3 Kaart van de diepe ondergrond met daarop in groen het Groningen-gasveld en de omliggende gasvelden. Met rode stippen zijn alle aardbevingen geregistreerd in 2024 aangegeven. Alle aardbevingen vóór 2024 zijn aangegeven met gele cirkels. De grootte van de cirkel is een maat voor de magnitude van de aardbeving.

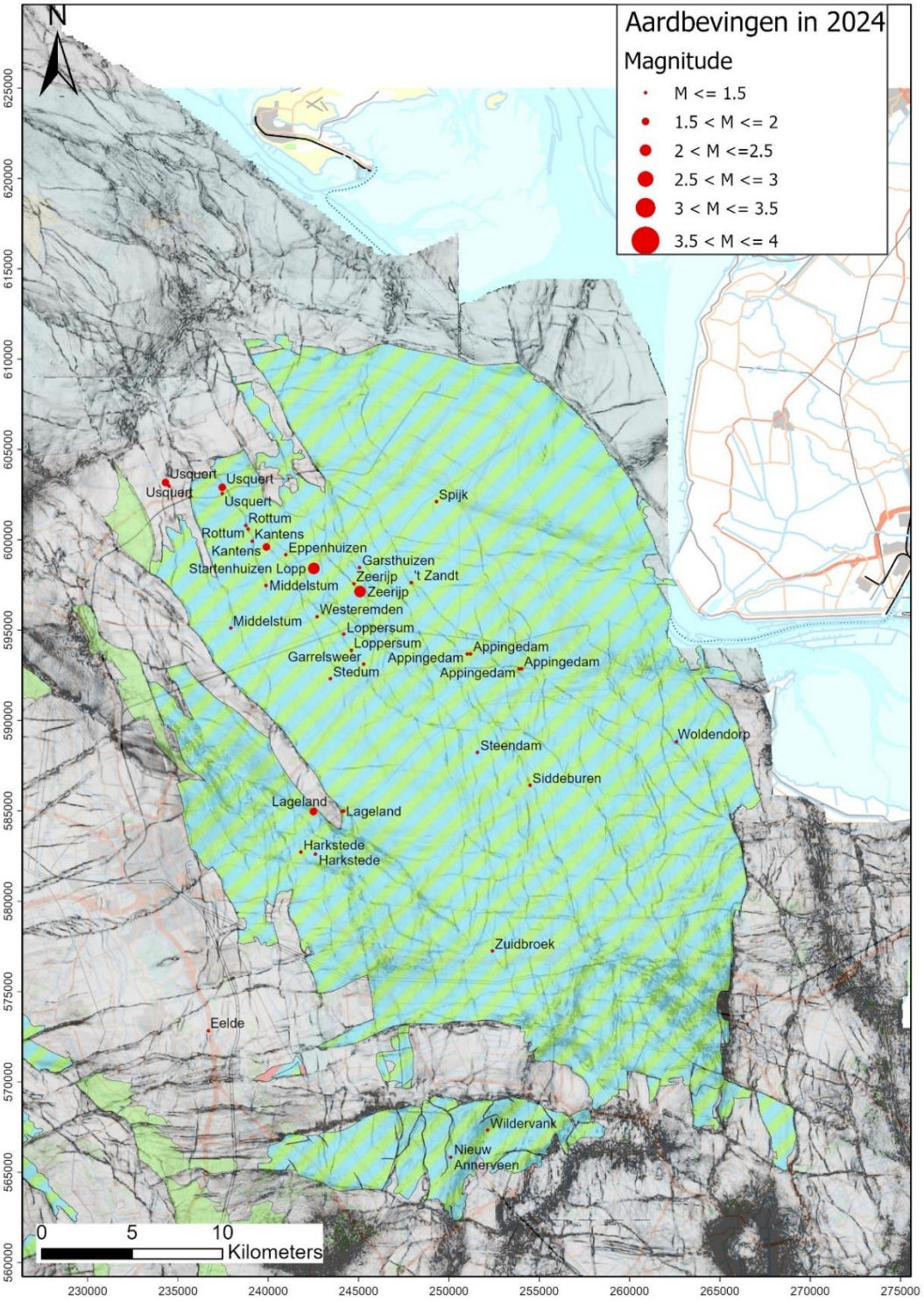

Figuur 4-4 Kaart van de diepe ondergrond met daarop in groen het Groningen-gasveld en de omliggende gasvelden. Met rode stippen zijn alle in 2024 geregistreerde aardbevingen aangegeven. De grootte van de cirkel is een maat voor de magnitude van de aardbeving.

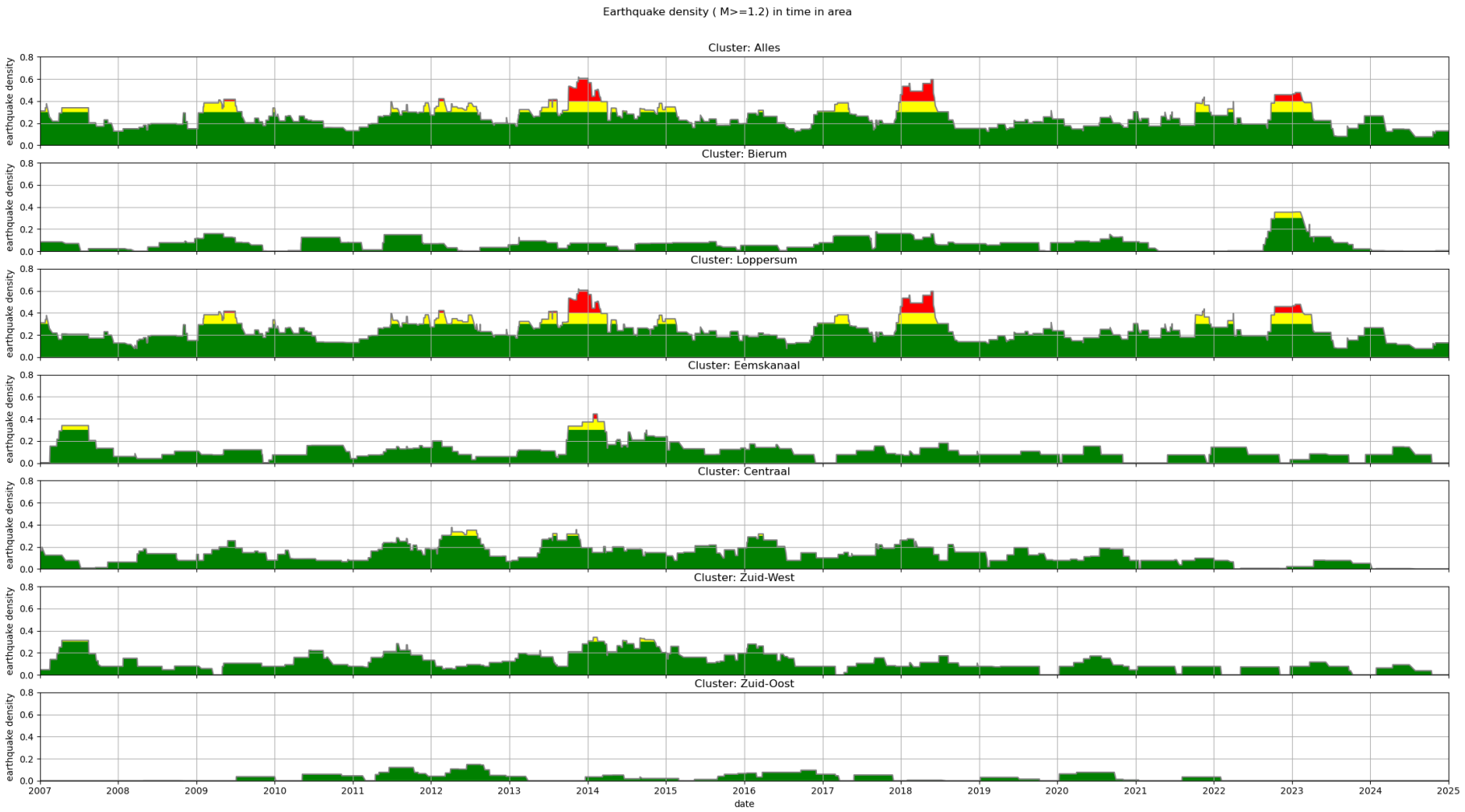

Figuur 4-5 De ontwikkeling van de maximale aardbevingsdichtheid over de jaren in het gehele Groningen-gasveld en kleinere gebieden binnen het Groningen-gasveld, weergegeven in aantal aardbevingen met een M_L>1,2 per km^2 per jaar. De achtergrondkleur geeft het relatieve niveau van de seismiciteit weer, groen: lage activiteit, geel: bovengemiddelde activiteit en rood: hoge activiteit.

Duidelijk zichtbaar in figuur 4-5 is de hogere maximale aardbevingsdichtheid in de periode van 2013 tot 2014 en de periodes 2018 en 2022 over het gasveld en in het gebied Loppersum in het bijzonder. Omdat de aardbevingen in het Loppersum-gebied vaak minder dan 5 km van de grens van het Bierum cluster plaatsvonden, was door de manier waarop de aardbevingsdichtheid wordt berekend in het verleden ook in het Bierum cluster de aardbevingsdichtheid hoger. Ook eind 2022 tot begin 2023 was de maximale aardbevingsdichtheid in het Loppersum Cluster hoog. Dat kwam door de zwermen aardbevingen in heel kleine gebieden ten noordwesten van Loppersum.

In alle gebieden is de maximale aardbevingsdichtheid sindsdien gedaald. In het laatste jaar daalt ook in het Loppersum gebied de aardbevingsdichtheid aanzienlijk. De maximale aardbevingsdichtheid voor het totale Groningen gasveld wordt nu bijna uitsluitend bepaald door de aardbevingsdichtheid in het Loppersum gebied. Dit komt goed overeen met de modellering van de seismiciteit. Door het vanaf begin 2014 sterk verlagen van productie en later insluiten van de vijf productieclusters rond Loppersum is de reservoir druk hier hoog gebleven ten opzichte van de reservoirdruk in de rest van het gasveld. Hierdoor vindt nu drukvereffening plaats waardoor de reservoirdruk in het noordwesten van het Groningen gasveld blijft dalen.

4.5 Statistische analyse naar de ontwikkeling aardbevingen

Deze analyse is uitgevoerd om de statistische significantie van de ontwikkeling van de trend van het aantal aardbevingen per kwartaal te duiden. Om dit inzichtelijk te maken zijn twee grafieken gemaakt van het aantal aardbevingen per kwartaal met betrouwbaarheidsintervallen van de te verwachten hoeveelheid aardbevingen; één onder de aanname dat de seismische events Poisson verdeeld zijn (Figuur 4-6); één onder de aanname dat de events quasi-Poisson verdeeld zijn (Figuur 4-7). De betrouwbaarheidsintervallen helpen bij de interpretatie van de data. Een seismisch relatief rustige periode kan het gevolg zijn van veranderingen in geproduceerde volumes, maar kan ook op toeval berusten.

De Poisson verdeling geeft een redelijke beschrijving van de data onder de aanname dat de aardbevingen ongecorreleerd zijn. Deze aanname is echter niet geheel correct omdat naschokken plaatsvinden. De quasi-Poisson verdeling kan gebruikt worden om een hogere mate (ten opzichte van de Poisson verdeling) van variabiliteit in aantallen aardbevingen tussen kwartalen te beschrijven. Deze hogere variabiliteit kan ontstaan door een bepaalde mate van correlatie tussen de aardbevingen door naschokken. De statistische analyse gebaseerd op de quasi-Poisson verdeling is meer robuust en resulteert in grotere onzekerheidsmarges voor het aantal aardbevingen in een kwartaal.

Beide plots bevatten de volgende informatie:

- Blauwe stippen voor het aantal seismische events per kwartaal.
- Een blauwe lijn die de trendlijn van het aantal te verwachten seismische events weergeeft.
- Een donkergrijze band; het 95% betrouwbaarheidsinterval van de trendlijn.
- Een lichtgrijze band; het 95% voorspellingsinterval van het aantal te verwachten events in dat kwartaal.

Beide manieren van beschouwen van de data geven grofweg hetzelfde beeld. Het aantal aardbevingen nam toe in de periode van 2001 tot een maximum in 2012. Hierna laat het aantal aardbevingen een neergaande trend zien in de periode van 2013 tot 2024. Merk op dat de onzekerheidsbanden in 2022 – 2024 mogelijk toenemen door grotere variatie van het aantal aardbevingen per kwartaal, maar dat de onzekerheid rondom de trend sowieso toeneemt, omdat er simpelweg minder datapunten nabij

zijn om de trend uit af te leiden. De trend voor de laatste maanden is met minder zekerheid af te leiden dan de trend op een punt waar alle data twee jaar ervoor en erna bekend is.

Uit deze analyse is te concluderen dat er statistisch bewijs is dat de frequentie van het voorkomen van aardbevingen een neergaande trend laat zien.

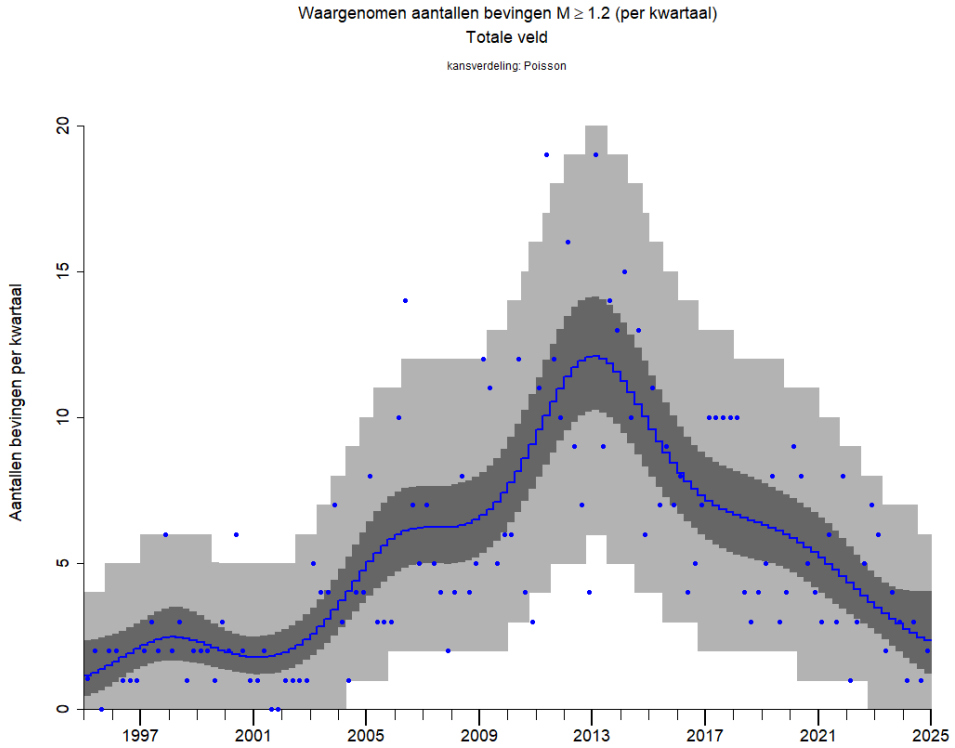

Figuur 4-6: Trend en betrouwbaarheidsinterval van het aantal aardbevingen per kwartaal, bij Poisson verdeelde seismische events.

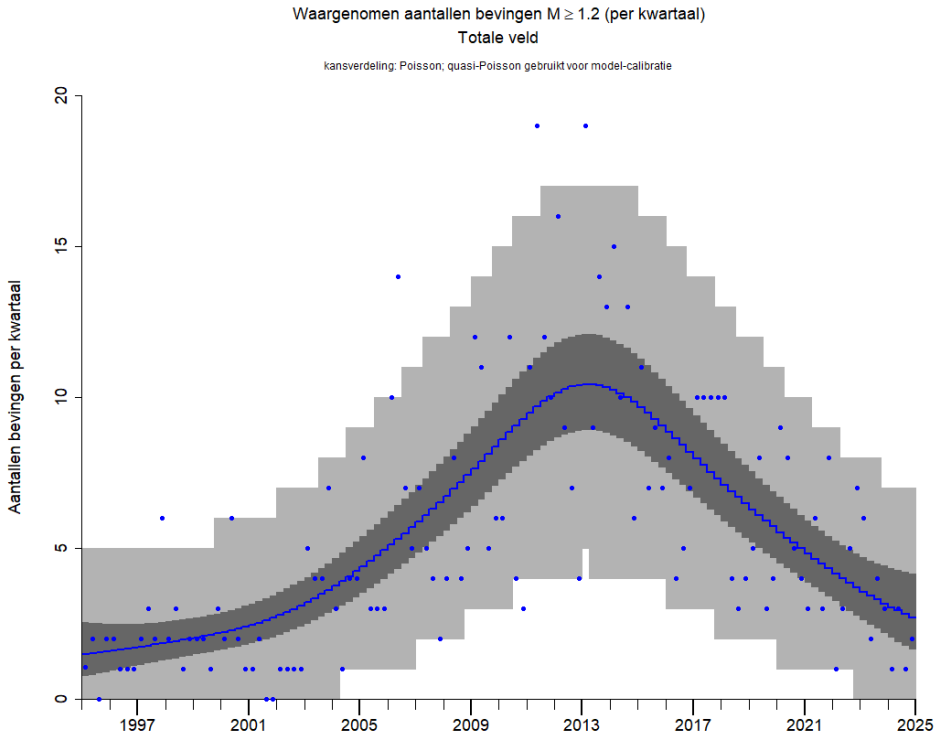

Figuur 4-7: Trend en betrouwbaarheidsinterval van het aantal aardbevingen per kwartaal, bij quasi-Poisson verdeelde seismische events.

4.6 Vergelijking aantal geobserveerde en voorspelde aardbevingen

4.6.1 Kalibratie seismologisch model

In 2024 heeft TNO geen seismische risicoinschatting gepubliceerd. De vergelijking van het geobserveerde aantal aardbevingen is daarom gebaseerd op de Hazard and Risk Assessment (HRA). Deze inschatting is geijkt aan de aardbevingencatalogus van alle aardbevingen in Groningen met een magnitude van $M_L \geq 1{,}5$ tot 1 januari 2024.

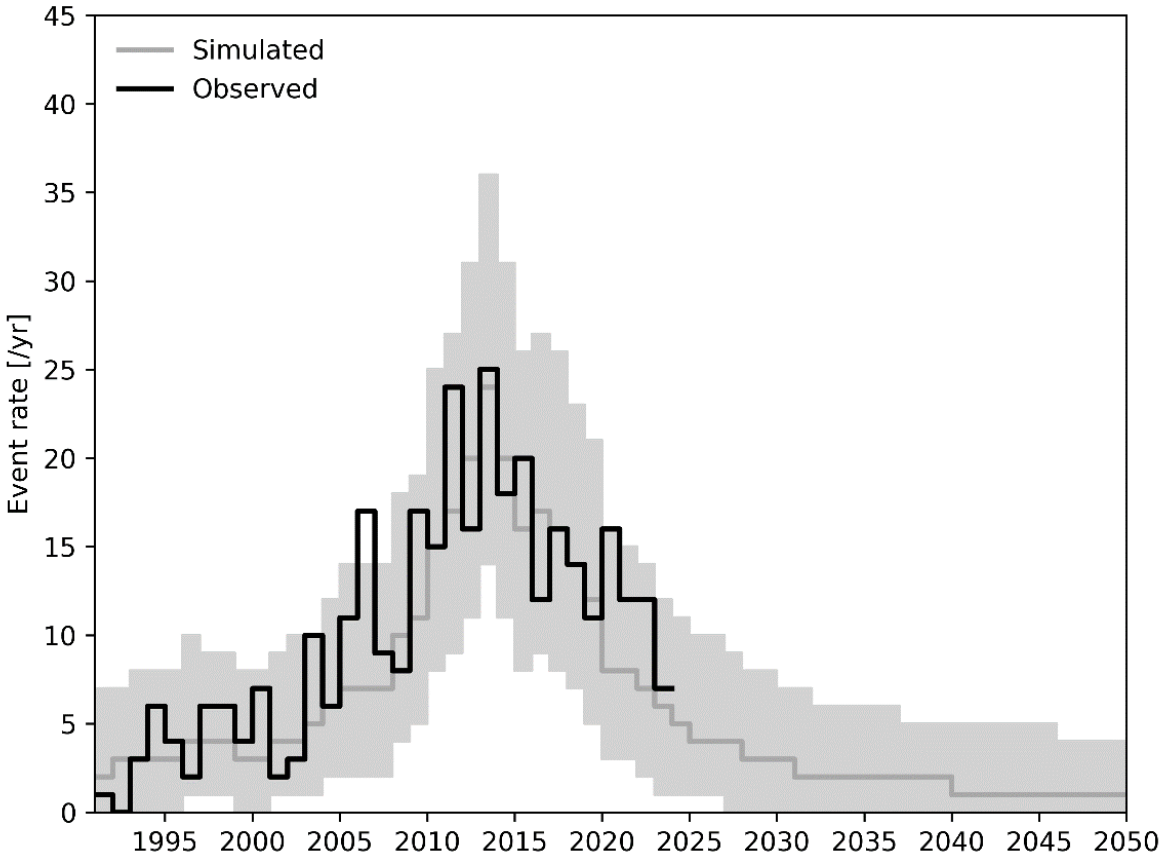

Figuur 4-8 Kalibratie van het seismologisch model gebaseerd op de aardbevingen met een magnitude $M_L \geq 1{,}5$ tot 1 januari 2024.

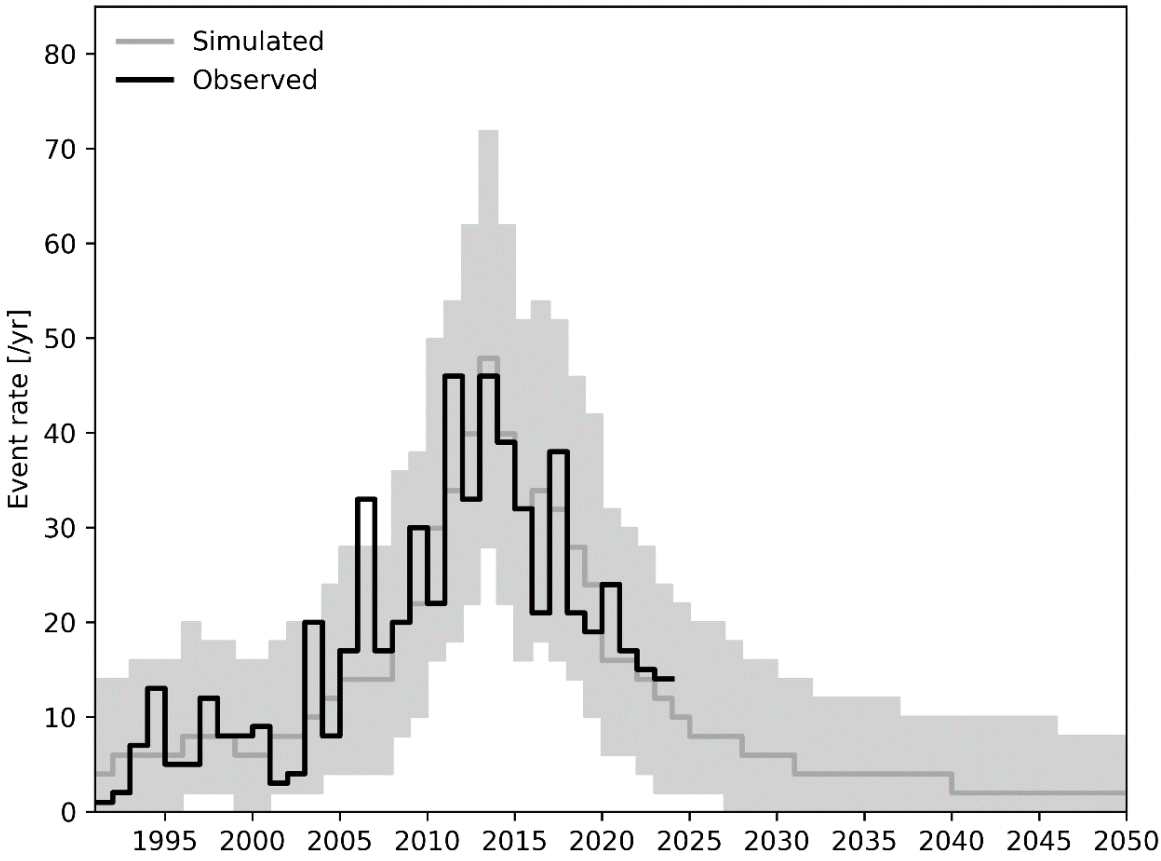

Figuur 4-9 Aantal geregistreerde aardbevingen met een magnitude $M_L \geq 1,2$ vergeleken met het seismologisch model gebaseerd op de aardbevingen tot 1 januari 2024.

4.6.2 Tellen van het aantal aardbevingen

Het KNMI rapporteert twee versies van de waargenomen Groningse aardbevingsmagnitudes, de eerste is tot 5 cijfers achter de komma en dus zonder afronding. De tweede versie (beschikbaar als een tabel in pdf format) geeft de magnitude van aardbevingen, na afronding tot 1 cijfer achter de komma. In de eerdere hoofdstukken (1 tot en met 4.5) van deze periodieke rapportage maakt NAM gebruik van de tweede versie van de KNMI aardbevingscatalogus met afronding.

Echter voor de vergelijking tussen het opgetreden aantal aardbevingen met de voorspeling van het seismologisch model moet gebruik worden gemaakt van een aardbevingencatalogus waarin de waarden van de magnitude niet zijn afgerond (de eerste versie). Daardoor zal een aardbeving met een magnitude van 1,50 wel worden meegeteld als een aardbeving met M ≥ 1,5 maar bijvoorbeeld een aardbeving met een magnitude van 1,49 niet.

Afronding vertekent het aantal aardbevingen boven een overschrijdingswaarde (zoals bijvoorbeeld een overschrijdingswaarde van M ≥ 1,5). Door deze afronding worden aardbevingen met een magnitude tussen 1,45 en 1,5 (1,45 ≤ M < 1,5) ook meegeteld bij de aardbevingen met een magnitude M ≥ 1,5. Sommige aardbevingen met een magnitude kleiner van 1,5 worden door de afronding dus toch meegeteld met M ≥ 1,5. Voor een exacte vergelijking tussen aantallen geobserveerde aardbevingen en het aantal voorspelde aardbevingen wordt daarom de niet-afgeronde versie van de aardbevingencatalogus gebruikt.

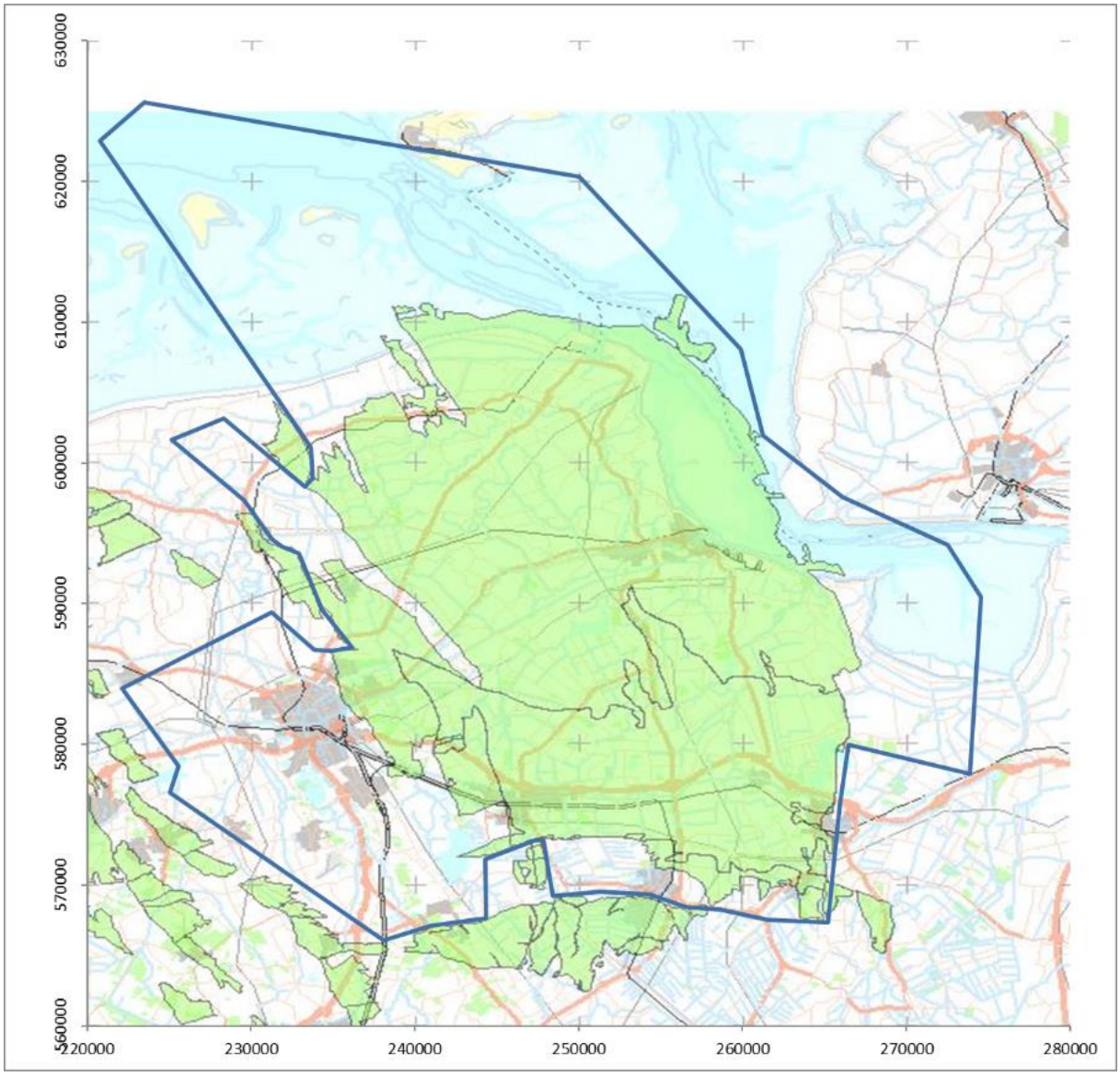

Figuur 4-10 De polygoon rond het Groningen gasveld. Aardbevingen met het epicentrum binnen deze polygoon worden toegewezen aan het Groningen gasveld. Ten zuiden van de polygoon is het Annerveen gasveld te zien.

Voor het tellen van het aantal aardbevingen voor seismische rapportage van het Groningen gasveld is ook de toewijzing van aardbevingen aan het Groningen gasveld of een van de er omheen liggende gasvelden belangrijk. Een aardbeving kan bijvoorbeeld zijn oorsprong hebben in het Annerveen gasveld dat ten zuiden van het Groningen gasveld ligt. Hiervoor wordt door NAM de polygoon (in blauw) in onderstaande figuur gebruikt. Aardbevingen met het epicentrum binnen deze polygoon worden toegewezen aan het Groningen gasveld.

Voor de aardbevingen in 2024 is de afronding van belang voor de aardbevingen op 28 januari 2024 bij Luddeweer. De afgeronde magnitude gerapporteerd door KNMI is M_L = 1,2. Echter de magnitude is naar boven afgerond. De magnitude van deze aardbeving was dus M_L < 1,2 en telt in deze vergelijking daarom niet mee.

4.6.3 Vergelijking aantal geobserveerde aardbevingen met modelvoorspelling

Het HRA-model wordt geijkt aan de aardbevingen met een magnitude $M_L \geq 1{,}5$. Daarom tonen we de vergelijking tussen met model en de werkelijk opgetreden aantal aardbevingen voor aardbevingen met magnitude $M_L \geq 1{,}5$. Figuur 4-11 laat zien dat in kalender jaar 2023 er zeven aardbevingen zijn geobserveerd met een magnitude $M_L \geq 1{,}5$. Dit lag dicht tegen het voor dat jaar verwachte aantal aardbevingen. In 2024 zijn er zes aardbevingen geweest met een magnitude $M_L \geq 1{,}5$. Drie hiervan waren in april. Dit valt binnen de onzekerheidsband, en ligt heel dicht bij de verwachtingswaarde.

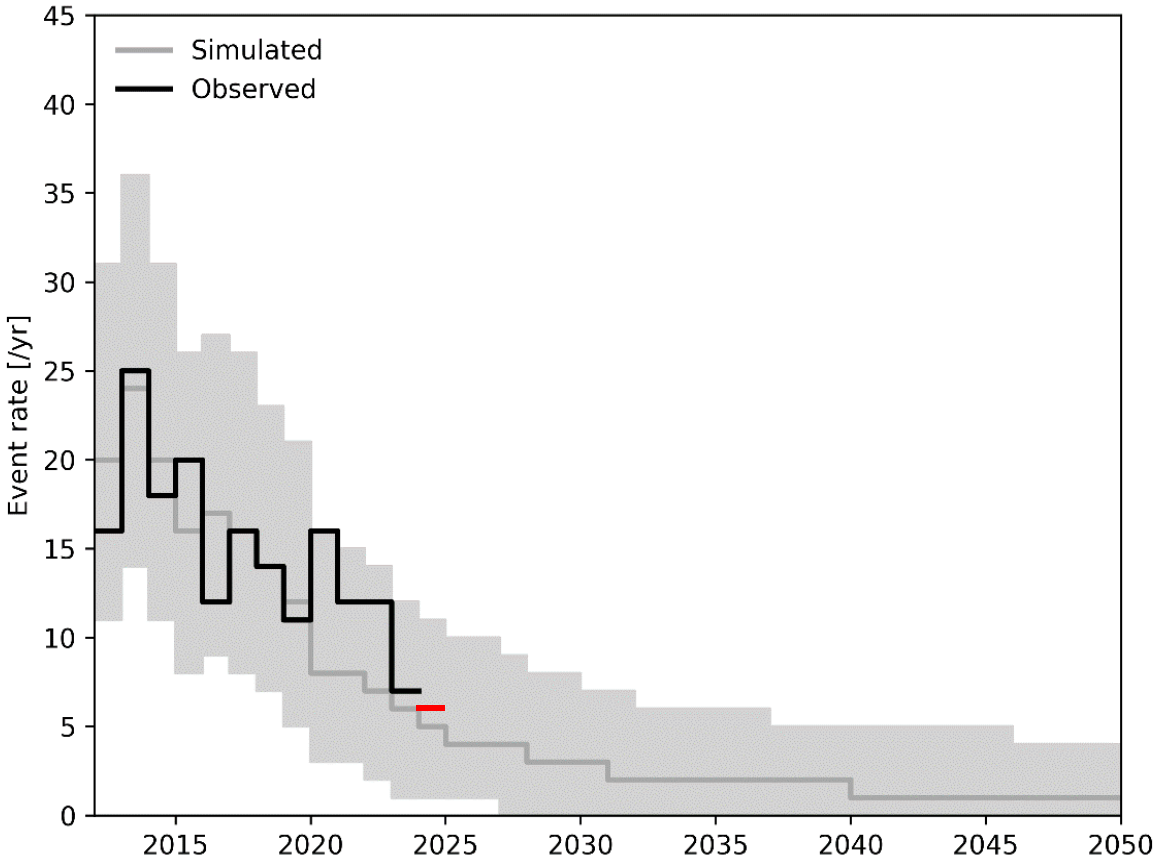

Figuur 4-11 Voorspelde aantal aardbevingen in het Groningen gasveld met een magnitude $M_L \geq 1{,}5$. Het aantal geobserveerde aardbevingen in 2024 is aangegeven in rood.

De Mijnbouwregeling schrijft voor dat de aardbevingenrapportage wordt gebaseerd op aardbevingen met magnitude $M_L \geq 1{,}2$. Omdat het verwachte aantal aardbevingen met $M_L \geq 1{,}2$ groter is, is ook de vergelijking hiervoor tussen voorspelde en geobserveerde aantal aardbevingen betrouwbaarder. Figuur 4-12 laat zien dat in kalender jaar 2023 er veertien aardbevingen zijn geobserveerd met een magnitude $M_L \geq 1{,}2$. Dit ligt dicht tegen het verwachte aantal aardbevingen voor 2023 aan. In 2024 zijn er zes aardbevingen geweest met een magnitude $M_L \geq 1{,}2$. Dit ligt onder het verwachte aantal aardbevingen in 2024 (de voorspelling is 10 aardbevingen in 2024).

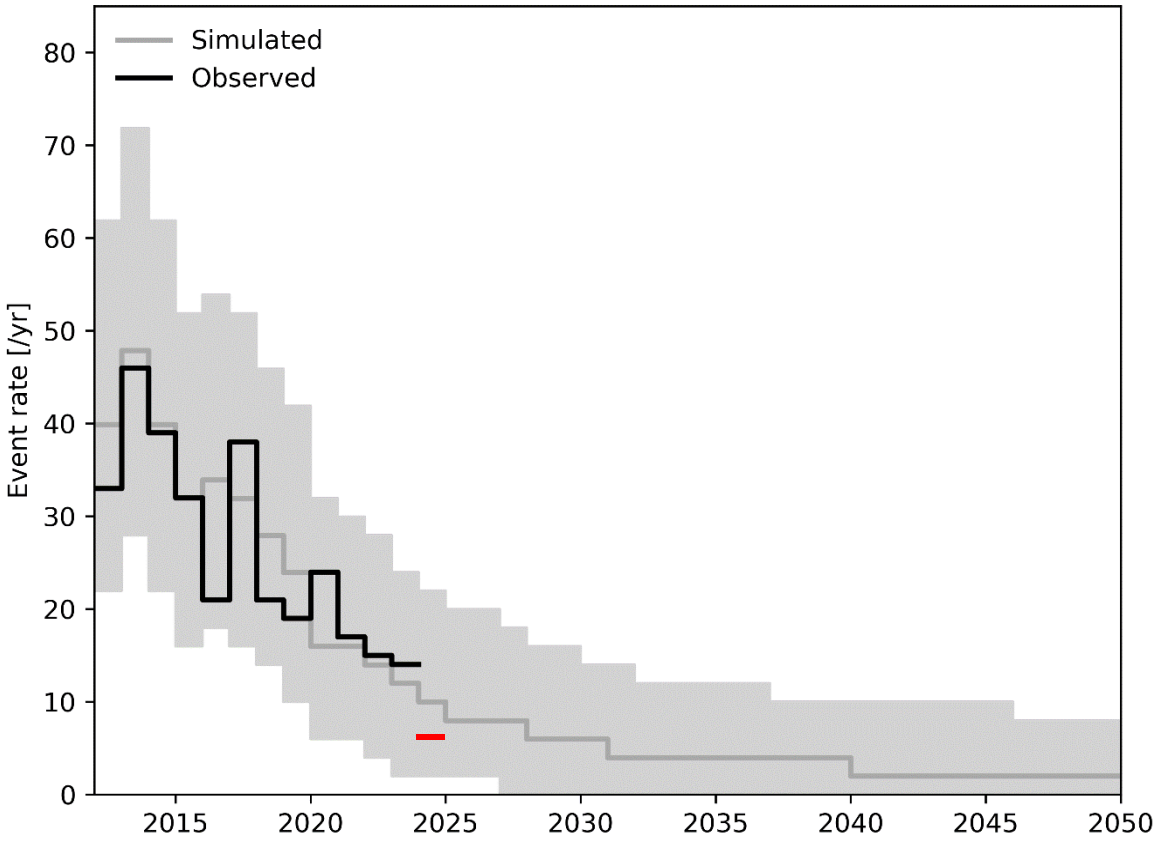

Figuur 4-12 Voorspelde aantal aardbevingen in het Groningen gasveld met een magnitude $M_L \geq 1{,}2$. Het aantal geobserveerde aardbevingen in 2024 is aangegeven in rood.

Referenties

1. Advies over de actualisatie van de trendparameters en de bijbehorende grenswaarden in artikel 1.3a van de Mijnbouwregeling, SodM, 16 juni 2020.
2. Defining criteria for semi-annual earthquake reporting of PGV and PGA in Groningen, Michail Ntinalexis, April 2024.
3. Magnitude and Energy of Earthquakes. B. Gutenberg, C.F. Richter. Annali di Geofisica. 9: 1-15, 1956.
4. Minimum Magnitude of Completeness in Earthquake Catalogs: Examples from Alaska, the Western United States, and Japan. Wiemer, Stefan en Wyss, Max. 4, 2000, Bulletin of the Seismological Society of America, pp. 859-869.
5. Opstarten Productie Groningen gasveld, 8 januari 2024, Persbericht NAM.
6. Productie Groningen gasveld gestopt, 10 januari 2024, Persbericht NAM.
7. Kamerbrief: Twee productielocaties Groningenveld op waakvlam, , 8 januari 2024, J.A. Vijlbrief Staatssecretaris van Economische Zaken en Klimaat.

Appendix A – Overzicht periodieke rapportages en speciale rapportages seismiciteit Groningen

Titel	Datum
Rapportage recente aardbevingen Wirdum en Garsthuizen 2016/2017	mei 2017
Ground Motions from the M_L 2.6 Slochteren Earthquake of 27th May 2017	juni 2017
Special Report on the earthquake density and activity rate following the earthquakes in Appingedam (M_L=1.8) and Scharmer (M_L=1.5) in August 2017	sept 2017
Special Report on the Loppersum earthquakes – December 2017	dec 2017
Special Report on the Zeerijp Earthquake	jan 2018
Short special report Exceedance Activity Rate - February 2018	feb 2018
Special Report - Westerwijtwerd Earthquake - 22nd May 2019	mei 2019
Analyse overschrijding MRP-grenswaarde Aardbevingsdichtheid 9 september 2019	sept 2019
Analyse overschrijding aardbevingsdichtheid - 3 december 2019	dec 2019
Special Report on the Zijldijk M_L = 2.5 Earthquake of 2nd May 2020	mei 2020
Special Report on the Loppersum M_L=2.7 earthquake of 14th June 2020	aug 2020
Special Report on the Zeerijp Earthquake Swarm starting 4th October 2021	okt 2021
Supplement to special Report on the Zeerijp Earthquake Swarm starting 4th October 2021	nov 2021
Special Report on the Garrelsweer Earthquake 16th November 2021 with Magnitude M_L = 3.2	nov 2021
Special Report on the Earthquakes near Uithuizen in August, September and October 2022	okt 2022
Special Report on the Wirdum Earthquake 8th October 2022 with Magnitude M_L=3.1	okt 2022
Special Report on the two Zandeweer Earthquakes on 15th September 2023 with Magnitude M_L = 2.0 and M_L = 1.9 respectively	okt 2023
Special Report on the earthquake near Zeerijp on 11th April 2024 with a magnitude M_L 2.1	mei 2024

Tabel A.1 Rapportages van opmerkelijke seismische gebeurtenissen zoals aardbevingen met een grotere kracht of aardbevingszwermen.

Title	Date
Analyse seismiciteit	nov 2016
Rapportage Seismiciteit Groningen - November 2017	nov 2017
Rapportage Seismiciteit Groningen - Juni 2018	juli 2018
Rapportage Seismiciteit Groningen - November 2018	nov 2018
Rapportage Seismiciteit Groningen - Mei 2019	mei 2019
Rapportage Seismiciteit Groningen - November 2019	nov 2019
Rapportage Seismiciteit Groningen - Mei 2020	apr 2020
Rapportage Seismiciteit Groningen - November 2020	nov 2021
Rapportage Seismiciteit Groningen - Mei 2021	juni 2021
Rapportage Seismiciteit Groningen - November 2021	nov 2021
Rapportage Seismiciteit Groningen - Mei 2022	juni 2022
Rapportage Seismiciteit Groningen - November 2022	dec 2022
Rapportage Seismiciteit Groningen - Mei 2023	juni 2023
Rapportage Seismiciteit Groningen - November 2023	dec 2023
Rapportage Seismiciteit Groningen - Mei 2024	juni 2024
Rapportage Seismiciteit Groningen – Eerste helft 2024	juli 2024
Rapportage Seismiciteit Groningen - November 2024	Nov 2024
Rapportage Seismiciteit Groningen - Kalenderjaar 2024	Jan 2025

Tabel A.2 Halfjaarlijkse monitoringsrapportages voor de seismiciteit in het Groningen gasveld.

Appendix B – Aardbevingscatalogus (door KNMI) voor kalenderjaar 2024

Plaats	Datum	Time hh:mm:ss	Magnitude	Diepte km	Easting	Northing
Zuidbroek	04-jan-24	22:43:33	0,5	3	252408	577242
Luddeweer	28-Jan-24	01:47:05	1,2	3	244171	584985
Eppenhuizen	11-Feb-24	07:17:13	0,4	3	240979	599176
Appingedam	12-Feb-24	13:41:37	1,1	3	251209	593693
Appingedam	12-Feb-24	14:06:46	0,3	3	251009	593689
Woldendorp	05-Mar-24	13:23:37	0,5	3	262583	588813
Stedum	06-Mar-24	00:29:52	0,4	3	243435	592319
Usquert	08-Mar-24	12:42:18	1,0	3	237459	602565
Westeremden	13-Mar-24	13:10:52	0,5	3	242706	595756
Steendam	19-Mar-24	13:21:09	0,8	3	251585	588246
Garrelsweer	01-Apr-24	06:46:39	0,2	3	245287	593132
Lageland	04-Apr-24	14:32:45	0,6	3	244105	584984
Zeerijp	08-Apr-24	00:54:43	0,3	3	244737	597575
Zeerijp	11-Apr-24	09:10:24	2,1	3	245078	597136
Lageland	14-Apr-24	14:08:51	1,6	3	242503	584955
Usquert	29-Apr-24	11:42:14	1,5	3	234322	603180
’t Zandt	05-Mei-24	19:14:45	0,3	3	247933	597636
Siddeburen	12-Mei-24	11:38:16	0,8	3	254492	586412
Harkstede	13-Mei-24	23:11:10	0,4	3	242612	582619
Garsthuizen	18-Mei-24	01:52:34	0,8	3	245053	598471
Loppersum	06-Jul-24	7:39:58	0,4	3	244606	593899
Middelstum	06-Jul-24	16:57:40	0,5	3	237920	595114
Kantens	19-Jul-24	20:19:49	0,6	3	239102	599922
Kantens	09-Aug-24	18:00:20	1,7	3	239906	599602
Appingedam	24-Sep-24	23:50:53	0,8	3	253892	592857
Usquert	09-Oct-24	22:14:33	0,7	3	234525	602960
Rottum	11-Oct-24	11:26:22	0,9	3	238753	600806
Usquert	19-Oct-24	09:12:35	1,7	3	237453	602899
Eelde	21-Oct-24	05:17:09	0,9	3	236699	572831
Loppersum	22-Oct-24	00:24:36	0,3	3	244190	594782
Rottum	30-Oct-24	10:22:29	1,1	3	238890	600586
Garsthuizen	31-Oct-24	15:15:26	2,2	3	242511	598419
Appingedam	09-Nov-24	00:40:57	0,4	3	254025	592860
Spijk	23-Nov-24	22:03:14	0,9	3	249309	602116
Middelstum	13-Dec-24	06:32:07	1,1	3	239877	597486
Harkstede	15-Dec-24	11:46:10	1,1	3	241809	582716

Tabel B Aardbevingen geregistreerd door het seismisch monitoring netwerk tussen 1 januari 2024 en 1 januari 2025 (huidige en de vooraf gaande rapportage periodes).

Staatstoezicht op de Mijnen
Ministerie van Klimaat en Groene Groei

> Retouradres Postbus 24037 2490 AA Den Haag

De minister van Klimaat en Groene Groei
drs. S. Th. M. Hermans
Postbus 20401
2500 EK Den Haag

Staatstoezicht op de Mijnen

Bezoekadres
Henri Faasdreef 312
2492 JP Den Haag

Postadres
Postbus 24037
2490 AA Den Haag

T 070 379 8400 (algemeen)
F 070 379 8455 (algemeen)

info@sodm.nl
www.sodm.nl

Datum 14 maart 2025
Betreft Beoordeling SodM periodieke rapportage seismiciteit Groningen-gasveld kalenderjaar 2024

Ons kenmerk
96858342

Uw kenmerk

Bijlage(n)
1

Hooggeachte mevrouw Hermans,

De Nederlandse Aardolie Maatschappij B.V. (verder: NAM) heeft mij op 30 januari 2025 de periodieke rapportage van de seismiciteit in het Groningen-gasveld over het jaar 2024 toegestuurd (conform artikel 1.3a.5 van de Mijnbouwregeling). Ik heb deze rapportage beoordeeld en ben van mening dat die een volledig overzicht en een goede analyse geeft van de waargenomen bevingen. De seismische activiteit is in 2024 verder afgenomen en in lijn met de verwachtingen. In deze brief licht ik dat verder toe.

<u>Rapportage vanaf 2025 op basis van kalenderjaren</u>
In de afgelopen jaren bracht de NAM twee keer per jaar een 'Rapportage Seismiciteit Groningen' uit die het ritme van de gasjaren (lopende van 1 oktober tot en met 31 september) volgde. Aangezien het Groningen-gasveld is gesloten en er dus geen sprake meer is van gasjaren, heeft SodM in overleg met uw ambtenaren de NAM gevraagd de rapportage vanaf 1 januari 2025 weer aan te laten sluiten op het kalenderjaar. Dit sluit beter aan op de wettelijk vastgelegde systematiek van jaarlijkse meetplannen voor de bodembeweging en op de jaaroverzichten die het KNMI publiceert. Bovendien is het overzichtelijker voor geïnteresseerden. De NAM zal de door de Mijnbouwregeling voorgeschreven halfjaarlijkse rapportages vanaf nu baseren op alle aardbevingsgegevens tot en met respectievelijk 30 juni en 31 december van het kalenderjaar. De op 30 januari aangeleverde rapportage is daarmee de eerste jaarrapportage in dit nieuwe ritme en geeft een overzicht van de ontwikkeling van de seismiciteit in het Groningen-gasveld voor het volledige kalenderjaar 2024.

<u>De seismische activiteit is verder afgenomen</u>
De huidige seismische activiteit in het Groningen-gasveld is vooral het gevolg van drukvereffening. De jarenlange gaswinning heeft voor drukverschillen gezorgd in het veld. Het aardgas stroomt nu van plekken met een hoge druk naar plekken met een lage druk. Daar waar de drukken nog dalen veroorzaakt dit proces (extra) spanningen op breuken in de diepe ondergrond, die tot bevingen kunnen leiden.

De daling van de seismiciteit in het Groningen-gasveld heeft zich in 2024 voortgezet. De rapportage laat zien dat ten opzichte van het kalenderjaar 2023 er een halvering is geweest in het aantal bevingen met een sterkte van 1,2 of zwaarder: zeven in 2024 t.o.v. veertien in 2023. Ook het aantal bevingen met een

sterkte van 1,5 of zwaarder is licht afgenomen: zes bevingen in 2024 t.o.v. zeven in 2023. Sinds 2004 is dit aantal niet zo laag geweest.
De zwaarste beving had een magnitude van 2,2 en vond op 31 oktober plaats bij Garsthuizen. Vijf van de zes bevingen met magnitudes ≥ 1,5 hadden een epicentrum in het seismisch meest actieve gebied, ten noordwesten van Loppersum. Desondanks is de maximale aardbevingsdichtheid in alle gebieden in 2024 verder gedaald.

In 2024 is tussen 8 en 10 januari kortstondig gas gewonnen vanwege een periode van lage weerstemperaturen. Gedurende deze dagen is 8 miljoen m^3 gas gewonnen. Het effect van deze winning op de druk in het gasveld en het proces van drukvereffening is verwaarloosbaar. Deze winning heeft dan ook geen waarneembaar effect gehad op de seismische activiteit. Op 19 april 2024 is de gaswinning uit het Groningen-gasveld definitief beëindigd.

Waargenomen seismische activiteit komt overeen met de verwachting
De Nederlandse organisatie voor Toegepast-Natuurwetenschappelijk Onderzoek (verder: TNO) voorspelt het aantal en de zwaarte van de te verwachten bevingen in de seismische dreiging en risicoanalyse (SDRA). De meest recente SDRA is van 20 maart 2023 en was uitgevoerd voor het gasjaar 2023/2024.[1] In die rapportage wordt in scenario 1 uitgegaan van het insluiten van het Groningen-gasveld per 1 oktober 2023. Aangezien de rapportages per 1 januari 2025 uitgaan van kalenderjaren, heeft SodM op 28 januari 2025 TNO verzocht om de bij deze SDRA behorende voorspelling van de seismische activiteit per kalenderjaar in kaart te brengen. TNO heeft de nieuwe weergave van deze voorspelling op 4 februari 2025 bij SodM aangeleverd.[2] SodM stelt aan de hand daarvan vast dat het aantal van zes bevingen met een sterkte van 1,5 of groter overeenkomt met de verwachting zoals berekend in de SDRA voor het kalenderjaar 2024.[3]

Ik hoop u hiermee voldoende te hebben geïnformeerd.

Hoogachtend,

[redacted]

Manager afdeling Toezicht: Gasnetten en Voormalige Gaswinning Groningen
Coördinerend Manager Energietransitie

---

[1] TNO, Publieke Seismische dreigings- en risicoanalyse Publieke Seismische Dreigings- en Risicoanalyse Groningen Gasveld 2023; Scenario 1.
[2] TNO heeft desgevraagd op 4 februari 2025 de voorspelling van de seismische activiteit volgens de vigerende SDRA per kalenderjaar als figuur toegestuurd. Daaruit blijkt dat er vijf aardbevingen met magnitude 1,5 of zwaarder voorspeld werden voor kalenderjaar 2024 met een onzekerheidsband van 0 tot 7 bevingen.
[3] De NAM heeft in de rapportage van 2024 de gemeten seismiciteit vergeleken met de voorspellingen van de eigen HRA, omdat in de laatst gepubliceerde SDRA van TNO de seismische activiteit alleen per gasjaar en niet per kalenderjaar in kaart is gebracht.

TNO innovation for life

KEM-24b
Preliminary assessment of beneficial effects of nitrogen injection in depleted reservoirs

TNO Public › TNO 2024 R11366
10 October 2024

Energy & Materials Transition
www.tno.nl
+31 88 866 42 56
info@tno.nl

TNO 2024 R11366 – 10 October 2024

KEM-24b
Preliminary assessment of beneficial effects of nitrogen injection in depleted reservoirs

Author(s)	Osinga, S., Leeuwenburgh, O., Vogelaar, B., Pena Clavijo, S., Bottero, S.
Classification report	TNO Public
Title	KEM-24b: Preliminary assessment of beneficial effects of nitrogen injection in depleted reservoirs
Report text	TNO
Number of pages	92 (excl. front and back cover)
Number of appendices	2
Sponsor	The Dutch Ministry of Economic Affairs and Climate
Programme name	Kennisprogramma Effecten van Mijnbouw - KEM program
Project name	KEM-24b
Project number	060.58402

Executive summary

This report documents the results of the KEM-24b project conducted by TNO as part of the "Kennisprogramma Effecten van Mijnbouw" (KEM programme), which was initiated by The Dutch Ministry of Economic Affairs and Climate.

The KEM-24b project is a scientific study into effects that are associated with re-pressurization of the Groningen gas field by large-scale post-production injection of nitrogen. This has previously been identified as a possible means to decrease the number of earthquakes, and consequently the seismic hazard and risk. In particular nitrogen gas (N_2) has been identified as a suitable fluid since it is largely inert, readily available, and does not show complex phase behaviour. The project has focussed on beneficial effects on seismicity only and has not considered economic, practical and societal aspects of such an injection campaign, nor the potential negative effects on seismicity due to cooling-induced reservoir compaction.

A literature review highlighted the unique character of the Groningen case and re-confirmed the need for a dedicated approach. The study was therefore conducted with the existing model chain Groningen (used for the Seismic Hazard and Risk Analysis by TNO), into which a recently developed publicly available reservoir simulation model of the Groningen field was included. It was first verified and confirmed that the reservoir model produces results that are largely consistent with historic gas production data. Different scenarios for availability and injection of gas were subsequently evaluated with the model chain and compared to a scenario where no nitrogen is injected (the base case). Two scenarios were considered for gas availability, one based on an estimate of the current national nitrogen generation capacity, and one hypothetical scenario meant to investigate the theoretical potential of gas injection. Since the effect of cold gas injection on reservoir cooling and associated compaction and stresses is currently not included in the model chain an investigation was additionally performed on how such effects can be included in the future. Including these cooling effects will lead to a seismic source model where N_2 injection has both beneficial effects on seismicity (by reducing or reverting compaction through increasing pore pressures) and negative effects on seismicity (by increasing reservoir compaction through cooling). The updated seismic source model has not been implemented as part of this study and therefore the relative magnitude of these competing positive and negative effects has not been investigated here.

The results of KEM-24b are as follows:

Model chain:

- Basic notions about the expected pressure equilibration and gas flow after the cessation of production without any injection of gas are reproduced by the new reservoir simulation model that has been adopted for this study to replace the previously used proprietary NAM model.
- The model chain incorporating the new reservoir model is able to produce base case reference seismicity predictions that are consistent with observed seismicity as well as with earlier results obtained with the previously used reservoir model.
- A relatively simple way was outlined to include the potentially adverse effects of reservoir cooling and compaction (leading to more seismicity) in a possible update of the seismic source model.

Expected impact of nitrogen injection:

- The potential reduction in number of earthquakes, seismic hazard, and seismic risk compared to the 'no injection' base case, can be considerable, mostly depending on the amount of nitrogen injected. For example, our model results show that the number of buildings exposed to a risk level above the Meijdam norm goes down from approximately 500 to 200 after 1 year of N_2 injection (amounting to a total volume of 1.58 bcm of nitrogen) in the Loppersum well cluster.
- The potential positive effects of injection increase with the amount of injected nitrogen and is dependent on the spatial and temporal distribution of nitrogen over the field.
- Under the modelling assumptions used in this study, these positive effects could disappear again, depending on when injection is stopped.

While the effects of gas injection on pressure as simulated with the model chain can be considered realistic, possible effects of composition and temperature of the injected gas were not explicitly considered in the scenario evaluation. Furthermore, several simple assumptions were made about availability and distribution of nitrogen across the field. A follow-up study could be conceived in which potential negative effects are quantified, and possibly minimized, while optimizing beneficial effects.

Contents

1 Introduction

1.1 Background

The production of gas from the Groningen gas field has caused seismic events whose impact have ultimately led to the decision to cease production in October 2023. It is generally accepted that the seismicity is largely the consequence of compaction at reservoir level, caused by lowering of the gas pressure in the reservoir, in turn leading to critically stressed faults.

It is expected that this form of induced seismicity will continue for some time also after production has stopped, because of the existing pressure gradients in the field and the time that it will take for gas to re-distribute and pressure to equilibrate. Such equilibration implies pressure increases in some parts of the field and pressure decreases in other parts of the field. These decreases in pressure could cause further compaction and therefore potentially new seismic events. A more favourable pressure state that could lead to a reduction in seismicity could be actively created by strategic injection of gas. The objective of injection would be to reduce or prevent pressure decline in crucial parts of the field, leading to a more stable stress state and less seismicity. Pressure maintenance by fluid injection is therefore considered as a possible safety measure to the Groningen field, along with the ongoing reinforcement of buildings after the recent cessation of gas production.

As part of the initial KEM-24 project (2022), research was performed into the effectivity of nitrogen gas injection for reduction of seismicity in the Groningen field following the end of production. It was concluded that nitrogen gas injection is the most promising option. Conclusions about the effectiveness of such injection were difficult to judge with confidence due to characteristics of the model available for that study.

1.2 Objectives

The current study aims to deliver useful insights into the potential to reduce the number of seismic events in the Groningen field post production by injection of nitrogen gas. In particular, it aims to answer the following questions:

1. What can be learned from examples of fluid injection in reservoirs similar to the Groningen reservoir?

2. Which injection scenarios for mitigating seismicity could be applied after production has stopped?

3. How can the existing SHRA (Seismic Hazard and Risk Assessment, https://www.nlog.nl/publieke-sdra-groningen) model chain be adapted to include fluid injection?

4. What is the potential beneficial effect of fluid injection on the overall seismic risk?

1.3 Scope and approach

Learnings from gas injection operations are collected and discussed in a literature review (Chapter 2) that will consider both national and international projects. Special attention is given to gas storage projects in the Netherlands as these are most similar to the Groningen case in terms of geology and injected gas.

Scenarios for injection of nitrogen are designed with reference to currently available nitrogen generation capacity in the Zuidbroek II facility, and to the distribution of well clusters in the Groningen field. We will simulate these scenarios with the reservoir simulation model developed and released for public use by NAM. Since the model does not support simulation of different gas compositions, we will consider injection of gas with the same properties as the Groningen gas. These simulations will therefore show the effect of re-pressurization of the reservoir. The volumetric effects of gas composition will be investigated in a separate box model experiment with a compositional simulator. Furthermore, we will assume that nitrogen is available to be injected at all wells that are potentially operational in the field. That is, the availability and/or suitability of the surface infrastructure and the sourcing and distribution of the nitrogen are not explicitly considered and studied. The results of the reservoir simulations are presented in Chapter 3.

The reservoir flow simulations produce snapshots over time of the pressure conditions in the reservoir. These pressure states can be used as input to a hazard calculation involving the quantification of expected seismicity. In this study, the modelling of seismicity will be performed using the current seismic source model that is available in the Groningen model chain (TNO, 2022). This model considers the relation between pressure decrease and compaction to be elastic and immediate, and the relation between compaction and seismicity to be immediate as well. The source model can also capture the reverse process, in which pressure increases lead to decompaction, stabilization of faults and a reduction of seismicity. The projected seismicity, seismic hazard and risk can be calculated for all injection scenarios with the TNO model chain. The impact on seismicity will be reported both in terms of total seismicity rate through time (number of events per year) and the spatial distribution of seismicity through time. The impact on hazard will be reported as spatial difference maps for ground motions at 475 and 2475 year return period for a range of spectral periods. The impact on risk will be quantified using an aggregated risk metric: the mean LPR of the total building stock of the exposure database. The number of buildings exceeding the Meijdam norm through time will be reported for each case. Results from application of the model chain to different injection scenarios will be described in Chapter 4.

The seismic source model does not account for potentially destabilizing (seismicity enhancing) effects related to pressure increase, or temperature decrease. Since the injection of nitrogen will primarily lead to pressure increases, in the seismic source model, nitrogen injection is expected to lead to a reduction in overall seismicity. Potentially adverse (seismicity enhancing) effects of nitrogen injection are not quantified in this study. However, this study will investigate possible future adjustments that can be made to the current seismic source model to include the potentially destabilizing (seismicity enhancing) effects related to pressure increase, or temperature decrease. A proposal for such adjustment is provided in Chapter 5.

We end the report with Conclusions and Recommendations.

2 Literature review

2.1 Introduction

The aim of current literature study is threefold: 1) summarize the available knowledge on injection-induced seismicity and risk mitigation strategies. 2) provide analogous cases (e.g., gas storage), provide lessons learned and determine its relevance for the Groningen case. 3) comment on differences with other injection techniques (e.g., wastewater disposal) and what those differences imply for mitigation strategies.
This literature review covers a brief overview of the Groningen Pressure Maintenance (GPM) study program by NAM (2016), including research by TNO (2015a, 2015b, 2015c) and Shell Global Solutions. We summarize induced seismicity by geomechanical stress changes by water injection in geothermal fields (Buijze et al., 2019) and the mechanism-based assessment of induced seismicity related to fluid injection (and gas production). Next, several examples of possible injection-induced seismicity in the Netherlands are presented as lessons learned. Field cases of cyclic injection in Underground Gas Storage (UGS) facilities, production water injection in depleted gas fields and aquifers, and geothermal operations may serve as possible analogues to fluid injection in the Groningen gas field. Where possible, example field cases of injection and/or fluid circulation with a geological setting comparable to the Groningen field have been chosen. In addition, differences with fluid-injection operations outside the Netherlands are given.

2.2 Previous injection studies Groningen

2.2.1 The Groningen Pressure Maintenance study

NAM (2016) has assessed possibilities for pressure maintenance in the Groningen gas field by injection through the Groningen Pressure Maintenance (GPM) study program since early 2013. Pressure maintenance was considered as a possible safety measure with regard to the Groningen gas field, along with reducing (and ceasing) of gas production and reinforcing buildings. The GPM program includes research by Shell Global Solutions as well as research by external academics and consultants (NAM, 2016). TNO (2014, 2015a, 2015b, 2015c) did a generic study on injection-induced seismicity by means of literature studies and the modelling of geomechanical effects of nitrogen injection on fault stability. Shell Global Solutions did research into the technical feasibility of gas injection into the Groningen field with the objective to reduce seismicity and subsidence by sustaining the reservoir pressure. The local group ‘Groningen 2.0’ did research into alternative options and potential synergies between GPM and local economic or industrial developments in the Groningen area (NAM, 2016).
The study (NAM, 2016) showed that injection of nitrogen into the Groningen field is technically feasible and can reduce the rate of pressure decline or stabilize pressures. However, the seismic hazard for GPM could not be calculated (back in 2016) and it remained uncertain whether large scale injection will have a significant positive or negative effect on seismicity. Finally, NAM (2016) indicated that a field test in Groningen and additional research would be required to establish whether GPM is effective in reducing seismicity.

2.2.2 Initial KEM-24 study

The initial KEM-24 study by Fugro (2022a, 2022b) investigated the effect of fluid injection on seismicity using the Groningen reservoir as an example. The main conclusions on induced seismicity of the KEM-24 study by Fugro were that N_2 injection appeared to be much more effective than CO_2 injection and that injection should be avoided near the critically-stressed Loppersum fault system (Fugro, 2022a). Therefore, Fugro (2022b) concluded that, from the seismic hazard point of view the "best action" for induced seismicity is to allow the Groningen reservoir system to re-equilibrate pressures in a natural way. In addition, Fugro (2022b) concluded that fluid injection would lead to an increase in the seismicity rate and to an increase of the seismic hazard.

The KEM-panel evaluated the results from the initial KEM-24 study by Fugro. KEM (2022) found that the conclusions and recommendations by Fugro were based on somewhat incomplete results, since the Fugro model was incapable to simultaneously mimic historic changes in the reservoir pressure and observed seismicity. As such, the forecasting potential of the Fugro model could not be validated.

As part of the original KEM-24 project, it was concluded that nitrogen gas injection is the most promising option (KEM, 2022). The KEM-panel has suggested a follow-up that resulted in issuing this study.

2.3 Reviews of fluid injection-related induced seismicity

Following McGarr et al. (2015), fluid injection-related induced seismicity from human operations can be classified in five different broad classes. Injection activities that are distinguished are (1) disposal of wastewater into deep formations, (2) injection of water or CO_2 into depleted reservoirs for enhanced oil recovery, (3) hydraulic fracturing to enable production of oil and gas from low-permeability rock, (4) injection of CO_2 for permanent carbon capture and storage, and (5) development of (enhanced) geothermal systems (Zang et al., 2019).

Review articles are available for the different classes of fluid injection-related induced seismicity (Zang et al., 2019). For example, Suckale (2009) and Davies et al. (2013) reviewed induced seismicity in hydrocarbon fields. Warpinski et al. (2012) elaborated on induced seismicity related to hydraulic fracture operations in shale-gas extraction. At European scale, Evans et al. (2012) separated crystalline from sedimentary environments, and reviewed induced seismicity from fluid-injection into geothermal reservoirs and CO_2 storage sites. For the US, Ellsworth (2013) focused on injection-induced earthquakes caused by wastewater disposal. Zang et al. (2014) gave an overview of induced seismicity in geothermal operations with emphasis on Enhanced Geothermal Systems (EGS), where fluid is injected to re-open pre-existing fractures, but also in comparison to other classes of fluid-induced seismicity. Rubinstein and Mahani (2015) discussed fluid-induced seismicity related to wastewater injection, hydraulic fracturing, and enhanced oil recovery.

All reviews above, including the recent one by Foulger et al. (2018), beside from monitoring strategies and traffic light systems, do not discuss innovative technologies how to actually reduce fluid injection-related induced seismicity, e.g., by advanced injection schemes (Zang et al., 2019). Better knowledge of the stress and pressure conditions at depth; the hydrogeologic framework, including the presence and geometry of faults; and the location and mechanisms of natural seismicity will be needed to develop a predictive understanding of the hazard posed by induced earthquakes (Zang et al., 2019). We will first discuss the stress and pressure mechanisms that may cause induced seismicity.

2.4 Mechanisms of induced seismicity

Buijze et al. (2019) point at stress changes as the key mechanisms causing induced seismicity in geothermal fields by e.g., fluid injection: stress changes due to 1) pore pressure increase; 2) poro-elastic stressing; and 3) thermoelastic stressing. First, an increase in pressure on a fault due to e.g. fluid injection reduces the effective normal stress on the fault and brings the fault closer to failure. The elevated pressure diffuses away from the injection well as a function of time, raising pressures and inducing seismic events further away from the source (e.g., Shapiro and Dinske, 2009). Second, a change in pore pressure also causes a volumetric strain (volume change) of the rock mass experiencing a pressure change. This volume change causes a change in stress within the rock mass itself controlled by pore pressure changes, and in the surrounding rock formations, i.e., poro-elastic stressing. Third, analogous to poro-elasticity, changes in temperature cause volumetric strain of the rock mass, which leads to stress changes within and around the volume experiencing a temperature change. The thermoelastic stress changes are opposite to those resulting from a pressure increase, because cooling leads to a decrease in total stresses (Buijze et al., 2019). NAM (2023a) identified five different mechanisms that may lead to induced seismicity:

2.4.1 Increase of shear stress during depletion

Gas production causes a decrease of pore pressure and a possible increase of shear stress on existing faults in the reservoir leading to fault reactivation and induced seismicity. Depletion induced earthquakes are for example observed in Groningen, Roswinkel and Bergermeer. These earthquakes demonstrate that some of the faults in and bounding the reservoir reached a critical state, where small stress perturbations may lead to seismic activity. The shear stress increase by depletion is dictated by the amount of depletion, the fault geometry, and the mechanical properties of the reservoir rock. Although gas production from the Groningen field is ceased since October 2023, it is foreseen that autonomous fieldwide pore pressure equilibration (i.e., without fluid injection) will continue to lead to local pore pressure decrease in some areas, which can therefore continue to cause future earthquakes in the field.

2.4.2 Fieldwide pressure increase by fluid injection

As described by mechanism 2.4.1, fieldwide pore pressure equilibration decreases the local pore pressure leading to an increase of shear stress along existing faults. However, in the case of pore pressure restoration by fieldwide equilibration by local fluid injections, the stress path would revert to its initial condition with a decrease of the shear stress as a state that is less critical for fault reactivation. As noted by NAM (2023a), it is however, likely that reservoirs deform during depletion with partial plastic behavior, with permanent deformation and stress change as a result (stress hysteresis). This could lead to the development of higher shear stresses when compared to the fully elastic response.

2.4.3 Near-wellbore contraction due to thermal cooling

Studies into geothermic systems have shown that the injection of relatively cold fluids into a relatively warm reservoir may trigger seismicity. Injection of a cold fluid causes a portion of the reservoir to cool down. This temperature reduction is accompanied by thermal contraction of the reservoir rock, potentially activating nearby faults changing the local stress state.

Besides pressure increase by fluid injection as described by mechanism 2.4.2, the stress state in the reservoir near the well bore can be changed by rock contraction due to the injection of relatively cold fluid. During cold fluid injection, both the pore pressure increase (mechanism 2.4.2) and temperature decrease (mechanism 2.4.3) are largest in magnitude in the near-wellbore area. Consequently, in this near-wellbore area cold fluid injection has the largest impact on the stress state and on possible fault reactivation. However, the volume of cooled rock near the well bore (temperature front) is significantly smaller than the volume of reservoir rock exhibiting an increased pore pressure value (pressure front) due to cold fluid injection (NAM, 2023a).

2.4.4 Near-wellbore pressure increase in a fault

As described by mechanism 2.4.2, fieldwide pore pressure increase would (partially) revert the stress path compared to depletion and decrease the shear stress to a state that is less critical for fault reactivation. However, if the fluid pressure inside a fault increases more than the pressure in the host rock, this situation might cause a direct decrease of the effective normal stresses on the fault (NAM, 2023a). This situation occurs when the permeability in the fault is relatively high compared to the host rock and when a conductive path from the injection well to the fault exists. Fluid injection directly into the fault rock should be avoided by not using candidate injection wells that penetrate faults in the reservoir.

2.4.5 Chemical weakening of the fault strength

Chemical weakening is translated to a decrease of the friction in a fault. Chemical weakening is, however, relatively uncommon (NAM, 2023a).

2.4.6 Aseismic slip

Aseismic slip is also known to affect seismicity, but its exact contribution remains elusive. To address this, Mandal and Lui (2022) performed numerical modelling to understand the effects of injection volume and rate on long-term seismic and aseismic fault slip behavior. Their results suggest that both parameters can affect fault behavior, and, in some cases, their roles are interdependent, thus they should be examined simultaneously in order to fully characterize their effects on triggered fault responses.

2.5 Examples of possible injection-induced seismicity in the Netherlands

Below we list examples of *possible* injection-induced events in the Netherlands for underground gas storage (UGS), production water injection, and geothermal operations.

2.5.1 UGS in the northern Netherlands

In the Netherlands, four former natural gas reservoirs are used for underground gas storage: Norg, Grijpskerk, Bergermeer and Alkmaar. Only UGS Alkmaar has never registered any seismic activity.

The Dutch UGS sites in the Rotliegend sandstone are of interest as an analogue to GPM in the Groningen field (NAM, 2016). Although these fields are much smaller in size than the Groningen field, the reservoir rocks have the same geologic age (Permian Rotliegend sandstone) and are also cut by faults. Most importantly, the pore pressure changes during UGS are >100 bar and should thus bring about similar or even higher compaction and dilation (volume decrease and increase, respectively) and stress changes to faults and reservoir rock as during pressure maintenance in the Groningen field. Notably, injection at UGS sites in the north of the Netherlands did not give rise to large earthquakes (TNO, 2014). An injection-induced earthquake (M1.1) during UGS in the Netherlands was an recorded in 1999 at Norg at a pore pressure of 309 bar, after it was increased by about 125 bar above the pore pressure of the depleted field (about 185 bar) to values just 20 bar below the virgin pore pressure of 328 bar.
Of interest is also UGS Bergermeer in the province of Noord-Holland. In 1994 and 2001, during primary depletion of this reservoir, four seismic events were recorded with magnitudes varying between M3.0 and 3.5. The largest seismic event recorded during injection of gas was the 2013 M0.7 Bergermeer event, interpreted to be located close to the central fault (TNO, 2015b). At UGS Grijpskerk, an 1997 M1.3 event was observed during production. Fifteen years after conversion and start of UGS Grijpskerk operation, a second 2015 M1.5 event was recorded by the KNMI network during cyclic operation (Muntendam-Bos et al., 2022).
In summary, UGS data from three Dutch storage fields do not indicate large (e.g. M > 1.5) earthquakes during gas injection, although the pore pressure was increased by 90 to 129 bar after depletion of 150 to 200 bar (TNO, 2015b).

2.5.2 Water injection Borgsweer, Groningen

State Supervision of the Mines (SodM, 2023) has no indications that water injection in Borgsweer poses a danger to people and the environment or that water injection increases the risk of earthquakes in this specific case. Since 1972 production water is injected in the eastern flank of the Groningen gas field at the NAM location Borgsweer. The total injected volume through several injectors accumulates to 20-25 million m^3 to date. Injection target is the deeper Lower Slochteren aquifer, which is separated from the overlaying Ameland Claystone and the Upper Slochteren Sandstone gas bearing reservoir. The Groningen gas field around the Borgsweer injection site is in eastern direction connected to the Rysum aquifer (NAM, 2023b). A fault system in western direction restricts fluid flow from the Borgsweer site to the former production locations. As a result, the reservoir pressure at the Borgsweer injection site is several tens of bar higher than the adjacent Groningen gas field. Due to the flow-restricting presence of the fault system and the overlying Ameland Claystone, injection of production water at Borgsweer has no or limited impact on the reservoir pressure of the Groningen gas field. This interpretation is supported by measurements of the nearby Delfzijl-1 observation well (DLZ-1), situated west of the fault system. Since the pressure development in the Groningen reservoir is not or very limited influenced by Borgsweer water injection, it is expected that seismic activity due to water injection is limited.

2.5.3 Water injection in Weststellingwerf gas field, Friesland

Bois et al. (2013) tested five triggering mechanisms in a study to identify whether water injection in a relative distant well could have caused the so-called Weststellingwerf fault to slip leading to the 2009 M2.8 De Hoeve earthquake in southwestern Friesland, the Netherlands. These mechanisms include: 1) Pressure depletion during gas production; 2) Re-pressurization due to water injection; 3) Thermal stresses due to cold water injection; 4) Salt dissolution; and 5) Fault weakening due to water injection (chemical alteration).
The 2009 M2.8 De Hoeve earthquake occurred during injection of production water in the depleted gas field of Weststellingwerf, about 1 to 1.5 km to the north. At the time of the event, the De Hoeve gas field was not yet discovered and so no gas had been produced. Bois et al. (2013) connected the 2009 De Hoeve earthquake to fault lubrication by the water-weakening effect and/or a decrease in capillary pressure in the fault gouge material upon first contact with water. Since the rates of injected water were very low, both pressure increase (mechanism 2) and temperature decrease of the host rock (mechanism 3) resulted in low values, leaving the authors to conclude that strength weakening of the fault (fault lubrication) as the most plausible failure mechanism.

2.5.4 Water injection the Schoonebeek-Zechstein gas field

Recently, NAM (2023a) presented a mechanism-based assessment of induced seismicity related to gas production and water injection in the Schoonebeek-Zechstein gas field using a Mohr-Coulomb analysis. The 2017 M1.2 and 2018 M1.1 Schoonebeek events coincide with a period of injection of produced water in the SCH-597 injector. Since the epicenter of the 2017 M1.2 event is much closer to multiple gas production wells, this event is most likely associated with ongoing gas production in the field. The epicenter of the 2018 M1.1 Schoonebeek event is located close to ongoing gas production in the German part of the Schoonebeek field. The relatively nearby injection well ENZ-7 did not inject in 2018, but a possible relation between the 2018 event and transient pressure and temperature effects related to this injection cannot be completely ruled out (NAM, 2023a).
The 2000 M1.3 Dalen event coincided with a period of injection and gas production (NAM, 2023a). Since the epicenter is 5 km distant from the injector and at proximity to a gas production well, this event is not expected to be related to water injection activities but rather to the gas production.

2.5.5 Geothermal operation at Kwintsheul, South-Holland

In 2018, a geothermal doublet began operations in Kwintsheul, the Netherlands, aiming to supply heat to 64 hectares of greenhouses (Draganov et al., 2023). The reservoir used for the geothermal operation allows the extraction, circulation and reinjection of the fluid at a depth of 2.4 km. A case study review (Buijze et al., 2019) concluded that this kind of geothermal operations in the West Netherlands Basin (Lower Cretaceous and Upper Jurassic sandstones) are unlikely to generate felt seismicity.
Muntendam-Bos et al. (2022) reported on the 2019 M0.0 Kwintsheul event soon after a temporary special dense seismic monitoring array had been installed at the geothermal site in South-Holland. Despite the significant level of background noise in this highly populated part of the Netherlands, the signal was recorded by all 30 seismometers in the array.

A preliminary analysis of the event yielded a hypocenter relatively close to the tip of the injector at a depth estimate of 2.46 km. Muntendam-Bos et al. (2022) noted that the depth estimate is subject to a large uncertainty of more than a kilometer. Consequently, the event cannot unambiguously be attributed to the geothermal operation, since it cannot be excluded that the event is of tectonic origin.

2.5.6 Geothermal doublets in North-Limburg

Although the tectonic activity of the Ruhr Valley Graben and reservoir formation (Carboniferous Limestone Group) are not comparable to Groningen stress and gas field, two geothermal doublets in North-Limburg, the Netherlands, experienced seismicity, when fluid was produced and injected near the Tegelen fault zone, which intersects the reservoir formation. The largest hazard was inferred to result from thermo-elastic stresses, originating from cold water injection close to the Tegelen fault. Natural earthquake activity was observed in the vicinity of the geothermal systems. The hypocenter of the main M1.7 event was estimated to be in the depth interval of 4 to 6 km (Muntendam-Bos et al., 2022), well below the geothermal reservoir (located at 2–2.5 km depth). However, the uncertainty in the depth estimate is large and an occurrence at 2.5– 3.0 km (just below reservoir level) cannot be excluded, which led to the conclusion that the geothermal operations are a possible cause of the events. However, again it cannot be excluded that the event is of tectonic origin. Furthermore, a plausible explanation for the physical mechanism is hampered by the limited available geological information. Validation and refinement of the poorly constraint seismic velocity model and subsequent reassessment of the hypocenter locations as well as improved imaging of the geological structure in the area could provide important information towards a causal explanation (Muntendam-Bos et al., 2022). Vörös and Baisch (2022) relocated the hypocenters aligned along the Tegelen fault close to the CWG wells approximately at reservoir depth. At the moment, operations in both systems remain suspended.
Just south of the Dutch border, the same carbonates, but significantly deeper buried, are targeted at Balmatt geothermal site, near Mol, Belgium. Here, seismic events up to M2.2 occurred and were attributed to water injection/production (Buijze et al., 2023). The events led to suspension of operations.

2.6 Lessons learned from injection-induced seismicity in the Netherlands

2.6.1 Geothermal fields in the West Netherlands Basin

Most geothermal doublets in the Netherlands are located in relatively shallow, porous, sedimentary aquifers at 2–2.7 km depth with fluid temperatures of 60–100 °C (Mijnlieff, 2020). A case study review (Buijze et al., 2019) concluded that these systems are unlikely to generate felt seismic events (M > 2.0). The study suggested that especially geothermal operations in the shallow porous sandstones of the West Netherlands Basin (Lower Cretaceous and Upper Jurassic sandstones) are unlikely to generate seismicity. The study investigated 85 cases in various geothermal plays world-wide to assess the seismogenic potential of these systems.

Their assessment showed no cases of geothermal doublet projects in shallow, porous sandstone formations with reported seismicity of M > 2.0. Buijze et al., (2019) related this absence to the fact that these systems are 1) far away from a seismogenic basement, which is more prone to seismicity, 2) the pore pressure changes are very limited spatially as no stimulation is required. In addition, the intercalation of the sandstone formations with clay and shale layers would hydraulically isolate these formations from deeper layers (Muntendam-Bos et al., 2022).

2.6.2 Underground Gas Storage (UGS)

The relation between induced seismicity and underground gas storage (UGS) operations in Dutch gas reservoirs has been studied extensively. The general consensus of the studies of Dutch field cases of UGS (e.g., Muntendam-Bos et al., 2022) is that induced seismicity in the Rotliegend sandstone reservoirs is possible during the (re-)injection of cushion gas and the cyclic storage phase in which only the volume of working gas is produced and reinjected. Magnitudes are expected to remain well below those observed during depletion.

2.7 Differences with injection-induced seismicity outside the Netherlands

Ongoing interest in developing (deep) geothermal systems, hydraulic stimulation, and the sequestration of large quantities of CO_2 underground has prompted the need to identify factors that influence the different seismogenic responses to fluid injection. Recently, Kivi et al. (2023) collected worldwide data for 158 cases of injection-induced seismicity from 7 geologic gas storage projects (two natural gas and five carbon storage sites), 15 research projects, 54 tight and shale gas hydraulic fracturing projects, 58 deep geothermal programs, and 24 wastewater disposal activities. Their numbers show that geothermal operations contribute the most to their induced seismicity database (36.5 %), closely followed by hydraulic fracturing operations (34.6 %), wastewater disposal (15.1 %), research projects (9.4 %) and underground gas storage (4.4 %). Factors identified by Kivi et al. (2023) are, among others, host rock properties (e.g., porosity, Young's modulus, etc.), site characterization (e.g., depth of basement, temperature, etc.), fault properties (dip, type, etc.) and operational data (e.g., injection rate, maximum bottom-hole pressure, etc.).

Recently, Cheng et al. (2023) made an inventory of induced seismicity related to CO_2 injection. Compared with wastewater injection, shale gas hydraulic fracturing and EGS, the CGS (CO_2 Geological Storage) usually operates in high permeability reservoirs. For long-term CO_2 migration and storage, the injection pressure is easier to dissipate and the increase of injection pressure is always smaller under the same injection volume. CO_2 in CGS migrates further due to high reservoir permeability and the spatial distribution of the induced seismicity in CGS is usually wider. Although most seismic events related to CO_2 injection are M < 3, large magnitude events are occasionally recorded (Cheng et al., 2023).

Evans et al. (2012) document a study at various sites that seeks to determine where fluid injection has taken place without generating seismic events that were felt by the local population, as well as cases where it has. Evans et al. (2012) document 41 European case histories that describe the seismogenic response of crystalline and sedimentary rocks to fluid injection. The data generally support the view that injection in sedimentary rocks tends to be less seismogenic than in crystalline rocks. Examples of injection in crystalline rock, e.g., performed during Enhanced Geothermal System (EGS) projects are omitted in this literature review because of the lack of relecance to the Groningen case. Evans et al. (2012) acknowledge that the coverage of injection into sedimentary rocks is not complete, especially

for non-geothermal injections that did not produce felt earthquakes. Nevertheless, several sites where CO_2 is injected into sedimentary rock are included here.

2.7.1 CO_2 injection in Ketzin test site, Germany

The Ketzin test site in Germany is designed to monitor the behavior of CO_2 injected into the Triassic Stuttgart formation (Evans et al., 2012). Natural seismicity is very low. The highly heterogeneous reservoir is an 80 m thick fluvial sandstone saline aquifer that has its top at 630 m depth. The CO_2 is a gas under formation P-T conditions. The caprock consists of fine-grained, clay-rich clastic sediments and mudstone, which served as the caprock to a gas storage reservoir that was seasonally operated from 1960s until 2000. There are no observed faults within the CO_2 reservoir.
The reservoir is penetrated by three vertical wells drilled in 2007: one injection well and two monitoring wells. The CO_2 is injected through screens at a depth of 650 m. CO_2 injection commenced in 2008 and the pressure at the formation depth increased steadily to 81 bar after 1 year, which is 17 bar above the formation pressure. A seismic network has been operational at the site since 2009. No seismic events have been felt at the site (Evans et al., 2012).

2.7.2 CO_2 injection in Sleipner, North Sea, Norway

This is a pioneering project of Statoil to remove CO_2 from natural gas produced from the Sleipner-Vest gas reservoir underlying the Sleipner-A platform in the Norwegian part of the North Sea. CO_2 is injected into the extensive, high-permeability, 200 m thick saline aquifer that lies at a depth of 800–1100 m (Evans et al., 2012). Several events of magnitude M2–3 have occurred within 50 km of the platform over the past 20 years. The unconsolidated formation is hydrostatically-pressured. Injection began in 1996. The CO_2 is injected at a wellhead temperature of 25 C and a pressure 62–64 bar, and is thus close to the liquid/gas phase boundary. The downhole injection pressure above hydrostatic is uncertain (Evans et al., 2012). A value of 35 bar above hydrostatic pressure is probably an upper bound: other evidence suggests pressure may be only marginally above hydrostatic (Evans et al., 2012). Possible local seismic activity is not monitored at the site. However, there is no evidence from the regional networks of seismicity associated with the CO_2 injection operations (Evans et al., 2012).

2.7.3 Castor gas storage, Spain

Aforementioned studies of Dutch UGS field cases showed that induced seismicity in the Rotliegend sandstone reservoirs is possible during the (re-)injection of cushion gas and the cyclic storage phase in which gas is produced and reinjected. Magnitudes are expected to remain well below the level observed during depletion of the gas fields.
However, the observations at the Castor project in the old Amposta oil field, Spain, appear to contradict the conclusions from the Dutch field cases, as a cluster of events was observed during gas injection, while no induced seismicity was previously recorded during production (Muntendam-Bos et al., 2022). The Castor project aimed to convert the old, depleted oil field into a gas storage facility. Similar to the observations at Bergermeer, induced seismicity commenced shortly after the onset of cushion gas injection (Cesca et al., 2021). In contrast to Bergermeer, events up to magnitude 2.6 occurred during the injection in the Amposta field, and after 12 days injection was stopped. After the cessation of injection, the earthquakes continued to occur for some time and magnitudes increased up to M4.1.

There are a few important differences to consider between Amposta and the Dutch storage fields. First of all, the Amposta field is located in karstic, fractured and brecciated Lower Cretaceous dolomitic limestone (Cesca et al., 2021). The Dutch seismically active storage sites are located in the Rotliegend sandstone. Secondly, the Amposta field was characterized by a strong water drive during depletion, rendering enhanced oil recovery unnecessary. None of the Dutch storage fields showed substantial water drive during depletion. The lack of a proper seismic monitoring at the Castor site was previously recognized and potential monitoring solutions for offshore industrial operations proposed (Grigoli et al., 2017). Finally, the hypocenter depths of the Amposta earthquakes ranged from the injection depth to several kilometers deeper (Cesca et al., 2021, 2022; Vilarrasa et al., 2022). Considering that the field is located in the active Catalon-Valencian normal faulting extensional region (Muntendam-Bos et al., 2022), this may indicate that these earthquakes also contain an important tectonic component. In the Dutch studies, a non-critical subsurface stress state prior to depletion is assumed.

2.7.4 Injection-induced earthquakes in the U.S.

Ellsworth (2013) reviewed induced seismic activity in the United States (U.S.) that may be associated with industrial activity, with a focus on the disposal of wastewater by injection in deep wells and by hydraulic fracturing (“fracking”) to increase permeability. The earthquakes involved can be induced as part of the process to stimulate the production from tight shale formations, or by deep wastewater disposal. These latter operations are not commercialized in the Netherlands.

2.8 Monitoring and mitigating actions of injection-induced seismicity

2.8.1 Monitoring of U.S. regulated wells

Wells used in the U.S. petroleum industry to inject fluids are regulated (Ellsworth, 2013). Approximately 110,000 of these wells are used for enhanced oil recovery. In addition, 30,000 regulated wells in the U.S. are used for wastewater disposal. Of these wells, most have no detected seismicity within tens of kilometers, although a few are correlated with seismicity. However, this can be said with confidence only for earthquakes $M \geq 3$, as smaller earthquakes in the U.S. are not routinely reported or below the magnitude of completeness threshold.
Conclusions about the cause of many of the recent earthquakes suspected of being induced by injection are complicated by incomplete information on the hydrogeology, the initial state of stress and pore pressure, the pumping history of the well(s), and where pressure changes are being communicated at depth. Routine earthquake locations with uncertainties of 5 to 10 km and a high magnitude-detection threshold are of limited use. Particularly well-documented cases of injection-induced seismicity through a dedicated monitoring network illustrate what can be learned when more is known about the pre-injection stress state and seismicity, as well as the injection history (Ellsworth, 2013).

2.9 Conclusions

A review of the available knowledge on injection-induced seismicity suggests that the injection of nitrogen in the Groningen field with the aim of reducing seismicity would be unique in the world. The closest analogous cases to the Groningen case (in terms of expected possible geomechanical failure mechanisms, injection depth, and reservoir properties) show that magnitudes of the events observed at underground gas storage, geothermal heat production, and production water disposal projects in the Netherlands have so far been of relatively small (magnitudes ≤ 1.7). The relevance of these cases for the Groningen case is however limited, as their analogy with the Groningen gas field is often limited. The Groningen gas field is a unique case in many ways, for example because of its physical size and its history of seismicity during depletion, which took approximately 30 years after the start of production to initiate in terms of recorded events. Although the mechanical mechanisms at play in the Groningen gas field are likely not different than those in Dutch UGS operations, in the end it is the relative importance of all mechanisms, in combination with the geological and operational history of a field that determines the behavior in terms of seismicity. The Groningen gas field is also a unique case in the sense that it has a calibrated/history-matched model for its induced seismicity that appears to forecast reasonably well. It is therefore believed that application of the existing Groningen Seismic Risk and Hazard Analysis (SHRA) framework is a more suitable way to obtain a first indication of expected effects of gas injection in the Groningen field, rather than relying on similarities with other field cases.

3 Scenarios for nitrogen injection

3.1 Introduction

The estimation of hazard and risk associated with future scenario's for the Groningen field requires the use of predictive models. Hazard and Risk Assessment (HRA) tools established by NAM and TNO connect a series of physical-statistical models that include a reservoir dynamical model, a seismic source model, a ground motion model, and a fragility and consequence model. The first element of this model chain simulates the pressure distribution in the Groningen field resulting from historic production using the proprietary Shell reservoir simulator MoReS. In support of the transition of the Groningen HRA to the public domain, NAM has developed and released an Eclipse 100 simulation model. This chapter describes modifications implemented in the Eclipse model to make it suitable for prediction of the effects of re-pressurization by gas injection, scenarios for available gas injection volumes, and scenarios for the distribution of those volumes over space and time. Results from simulations of some of these scenarios are presented to validate the model. We also investigate the possible impact of the neglect of gas compositional effects in the Eclipse 100 model by separate simulations with the compositional simulator Eclipse 300.

3.2 Model description

An Eclipse 100 (Schlumberger) reservoir simulation model of the Groningen gas field has been developed by NAM, based on the existing MoReS model, and was made publicly available through https://public.yoda.uu.nl/geo/UU01/8JYW40.html together with a Petrel geo-model. The model simulates the gas production from the Groningen gas field and from several neighboring small fields between December 1955 and 1 January 2023. A basic quality check was performed by TNO to assess the suitability of the model for the purpose of this study. A summary of the main findings is provided here.

The main regional characteristics of the MoReS model appear to be reproduced by the model, as discussed in the document accompanying the Eclipse model[1]. Regional differences in pressure behaviour are reported for the Harkstede and Oldorp regions in the western periphery of the field. No extensive comparison was reported for individual wells. Poor well matches appear to be primarily associated with several small fields that are also included in the model. An important difference between the MoReS and Eclipse models is that the latter assumes dry gas, while the former includes water vapour in the gas phase. While this will mean that produced water rates in the Eclipse model are too low, water production in Groningen is known to be low, so the overall impact of reservoir volumes should be limited.

[1] Dynamic model (Eclipse version) to predict the formation pressure response to gas extraction in the Groningen gas field, The Netherlands, P. Tummala, NAM, 2023.

In the Eclipse model, wells are operated at combined observed gas and water production targets, presumably to ensure that the correct reservoir volumes are extracted, but this is not discussed in the document provided with the model.
The analytical aquifers implemented in the Eclipse model are different from the proprietary method available in MoReS. No discussion of differences or comparison of e.g. aquifer inflow volumes are available. It could be verified that specified gas rate targets are consistent with production volumes reported under normal conditions (nlog.nl). Pore volumes are explicitly defined by values imported from the Dynamo platform (the Shell proprietary model software framework). While fault transmissibility multipliers have been implemented in the MoRes model, no such multipliers are used in the Eclipse model. The history matching process and the resulting model modifications, e.g. to pore volume values, are not documented.

A few relatively small issues were identified (e.g. some erroneous grid connections in an unconnected aquifer and an incorrect end date, see Figure 8) but overall, the model is deemed appropriate for large-scale studies such as those currently executed as part of the KEM programme. In the following we provide further details of the model.

The Eclipse model made available by NAM contains the complete MoReS (model version GFR2022_HM_vV7_Jan23_clean1) time series of gas and water production data for 335 gas production wells of the Groningen field up to 1 January 2023. Gas production is given in Nm3/day whereas water production is given in bbl/day. It is not clear if water rates are specified for standard or normal conditions but differences in volumes should be very small and therefore have an insignificant impact on the outcome of the simulation.

The model grid is based on the Petrel geo-model that has also been made available by NAM. The model grid is divided into 45 equilibration regions and 20 fluid-in-place regions. Inflow into and outflow out of the modelled domain are determined by conditions specified at the boundaries. 4681 Carter-Tracy type aquifers are defined in the model to represent the connection to the Moewensteert, Rodewolt, and Usquert aquifers to the north and the Rysum aquifer to the east. The Groningen field is connected in the south-west to the Lauwersee aquifer. This aquifer is experiencing pressure decline as a result of both gas production from the Groningen field and from the nearby Roden, Vries, Faan and Pasop gas fields located to the (south)west. The contribution of these small fields is represented in the Groningen model by 10 pseudo production wells positioned along the south-west edge of the model that operate at specified water production rates. 11 wells represent gas and water production from four small gas fields that are included within the confines of the model boundaries: Bedum, Saaksum, Kiel-Windeweer and Warffum. Of these four, only Kiel-Windeweer is no longer in production. The remaining three fields are located to the (north)west of the Groningen field. No history matching has been performed to match history production from the small fields. Finally, 5 water injection wells of the Borgsweer location near the Eems-Dollard estuary are included in the model. The total number of wells in the model is therefore 365.

As part of the HRA workflow, simulated 3D pressure fields are vertically upscaled to 2D grids and interpolated to a regular map. Since earlier maps obtained with MoRes are still available we can compare the Eclipse maps to the MoReS maps (Figure 1). It is noted that the Eclipse-based maps are much smoother, indicative of much stronger pressure dissipation across faults in the model and consistent with the absence of any fault transmissibility multipliers in the NAM Eclipse model.

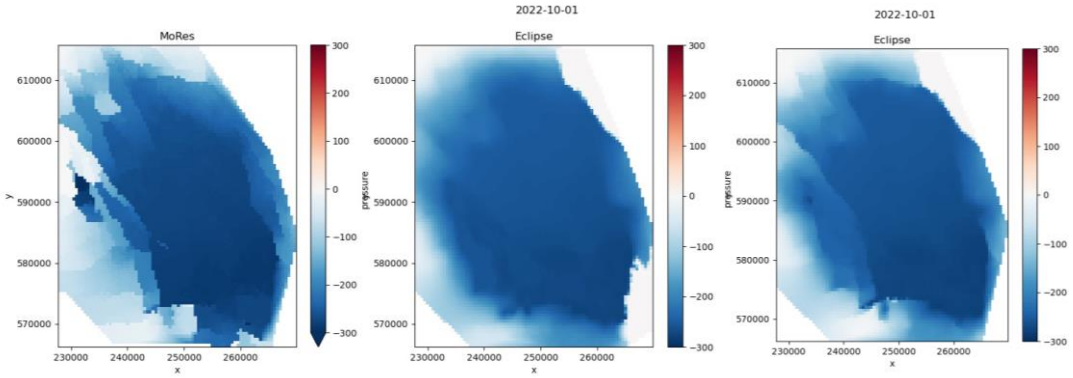

Figure 1 Pressure change at 2022-10-01 relative to initial pressure. Results are shown from simulations with the MoRes model (left) and with the Eclipse model without fault multipliers (middle) and with fault multipliers (right).

In order to obtain simulation results that are closer to the earlier MoReS results, fault multipliers were implemented that were taken from Table 12-1 of the 2016 Groningen model review report (SGS Horizon, 2016). While these multipliers were determined at the time for the MoReS model, and not tuned for use with the new Eclipse model, simulated pressures obtained with the latter model suggest a closer similarity to both the most recent available MoReS results and to pressure data when the multipliers are included (see Figure 2, Figure 3 and Figure 7 below). We therefore include these multipliers in all our simulations.

3.3 Production period

Production data for the period 1 January 2023 to 1 October 2023 were extracted from NLOG (nlog.nl) and used to extend the simulation schedule up to the end-of-production. Figure 2 to Figure 7 illustrate the performance of the simulation model in comparison to historic data obtained over the period of gas production from the Groningen field. Observed gas rates are very well matched on both field scale and for individual wells (we show results for one representative well only) for both versions of the Eclipse model (Figure 2 and Figure 3).
Examples of simulated flowing bottom-hole pressures (BHP) are shown for 4 wells from 4 different production regions in Figure 4 to Figure 7. Production regions and well cluster locations are shown in Figure 9. Simulated BHP values are similar for both versions of the Eclipse model, but the version with fault multipliers appears to produce slightly lower pressures, closer to the results obtained with the extensively history matched MoReS model.

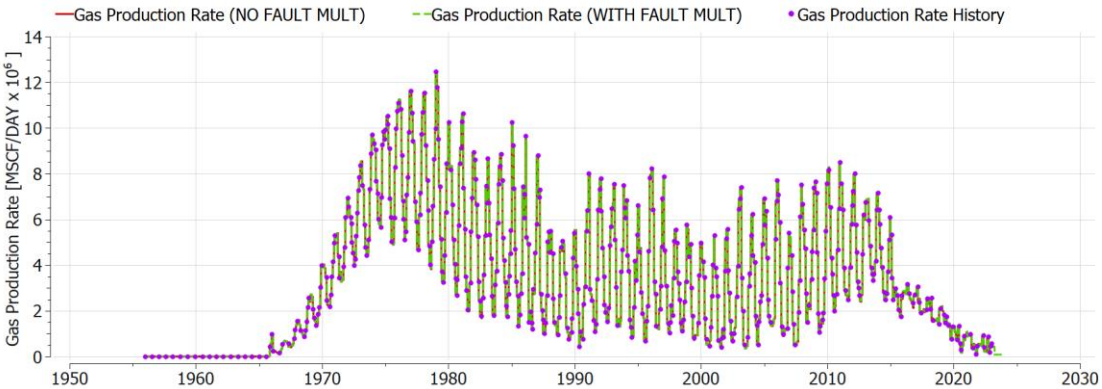

Figure 2 Field gas production rate simulated with the NAM Eclipse model without fault multipliers (red solid line) and the modified version with fault multipliers (green dashed line).

The dots indicate observed values. Note that the simulated rates (red solid and green dashed lines) overlap

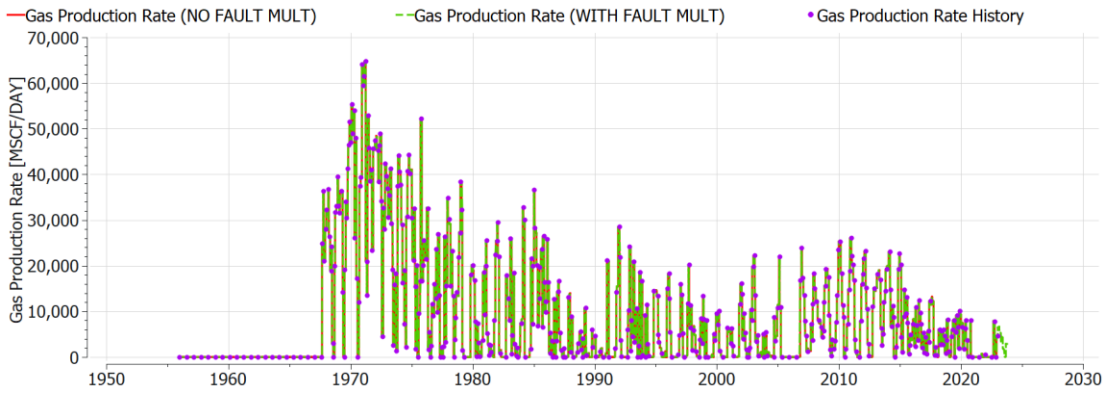

Figure 3 Well gas production rate for the Spitsbergen 3 well. Lines and colours are as in Figure 2.

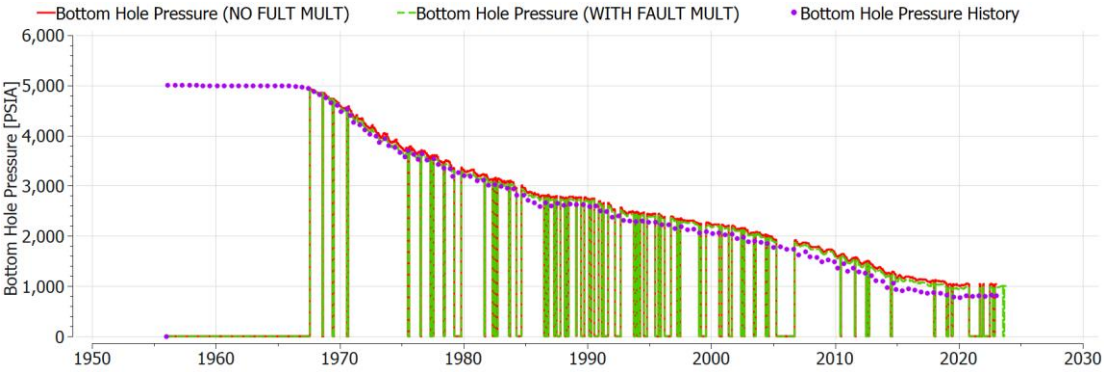

Figure 4 Simulated bottom hole pressures over the gas production period for the Spitsbergen 3 well obtained with the NAM Eclipse model without fault multipliers (red solid line) and the modified version with fault multipliers (green dashed line). The dots (labelled Bottom Hole Pressure History) indicate values simulated with the MoReS model. Vertical lines indicate times as which wells were closed.

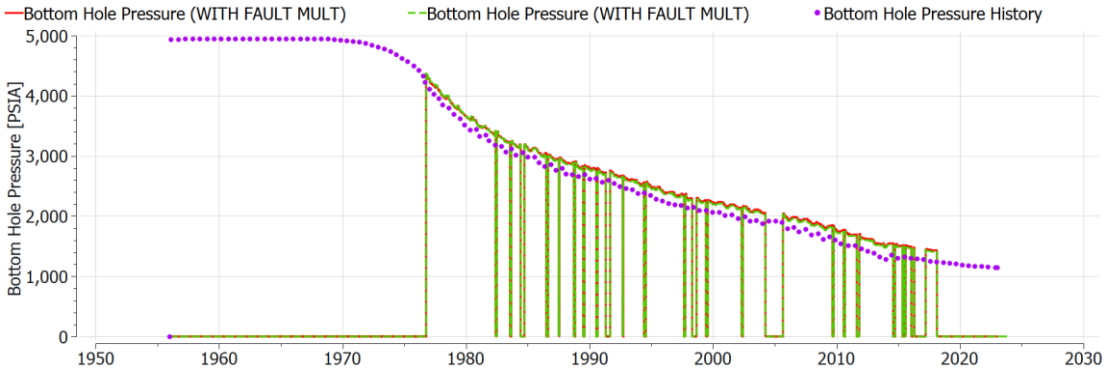

Figure 5 Simulated bottom hole pressures over the gas production period for the ‘t Zandt 3 well. Colors are as used in Figure 4.

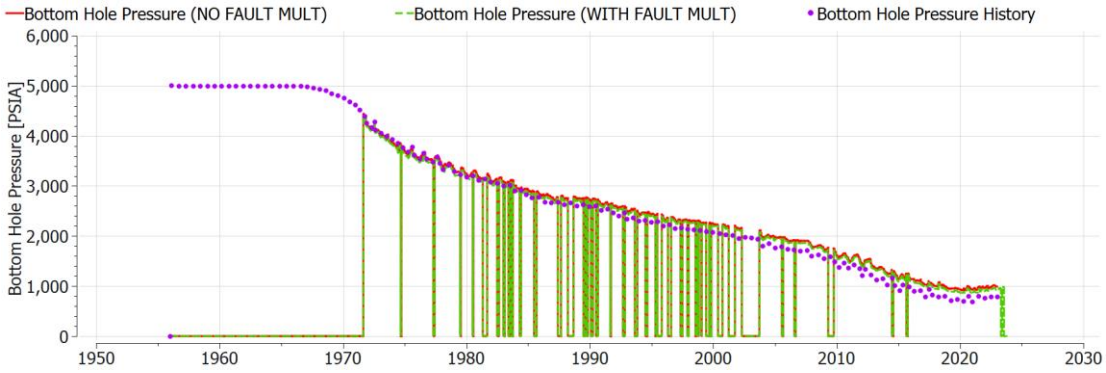

Figure 6 Simulated bottom hole pressures over the gas production period for the Zuidpolder 11 well. Colors are as used in Figure 4.

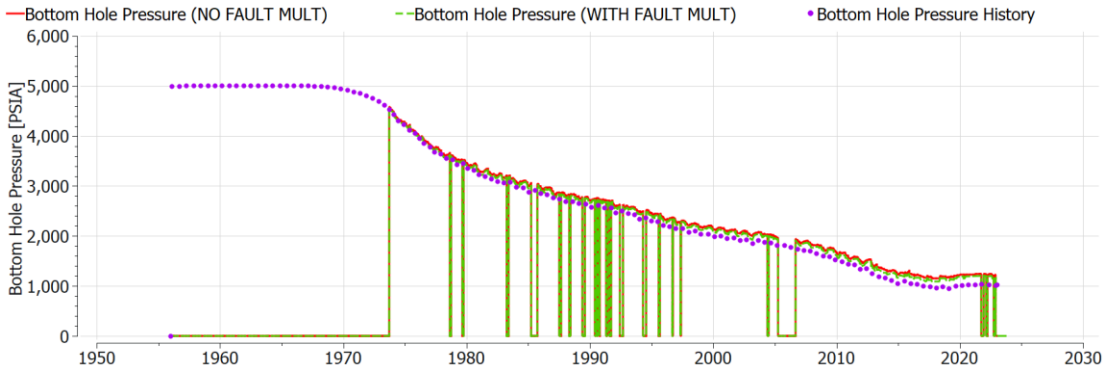

Figure 7 Simulated bottom hole pressures over the gas production period for the Amsweer 1 well. Colors are as used in Figure 4.

Figure 8 shows top views of the model grid and some basic results from simulation of the model over the production period. Clearly visible are the relatively pressure connection to the aquifer towards the south-west of the field, and the large pressure decline in especially the south-east of the field. The pressure in surrounding aquifers that are not dynamically connected with the gas reservoir remain unchanged.

3.4 Injection scenarios

The Eclipse 100 simulator is based on a so-called black-oil formulation in which fluid phases water and (dry) gas are given bulk properties consistent with their composition. Individual molecular components of the gas are not explicitly distinguished, as would be done in a compositional simulator. It is therefore not possible with this model to simulate injection of a gas with properties that are different from the gas that is already present in the reservoir. The focus of this simulation study is therefore primarily on the impacts of re-pressurization, where, for the practical reasons explained, we will assume that injected gas has the same properties as the natural gas present in the Groningen reservoir. The volumetric effects of gas composition will be investigated in a separate box model experiment with a compositional simulator.

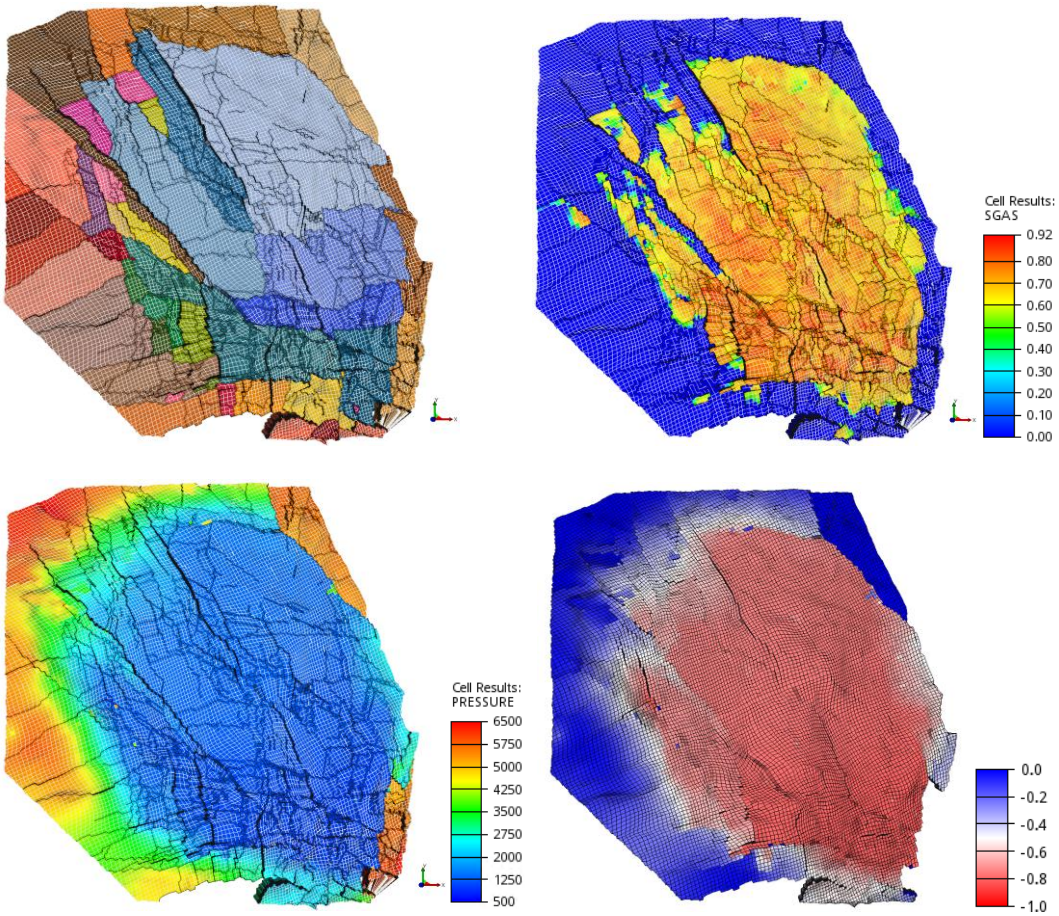

Figure 8 Top views of the NAM Eclipse 100 Groningen model grid. Top left: Fluid-in-place/equilibration regions. Top right: Initial gas saturation. Bottom left: Pressure [psi] in October 2023. Bottom right: Fractional pressure change in October 2023 relative to January 1965 (note that the aquifer region in the bottom-right part of the grid is de-activated).

Different scenarios for gas injection will be considered in which a given total volume rate is distributed in different ways over available clusters of injection wells. This includes not only the geographical distribution associated with the locations of these clusters, but also the distribution over time. The 335 Groningen gas wells are grouped into clusters which are listed in Table 1 and shown in Figure 9. We assume that closed-in wells are directly available, that suspended wells have been temporarily closed, but could be made available again if desired, and that abandoned wells are not available anymore.

Well clusters are themselves grouped according to production regions (Figure 9). Scenarios will be defined that distribute injection gas volumes over all active clusters in one or more production regions by different defined proportions. Individual well injection rates are calculated by the simulator using the well group target functionality of Eclipse and the injection potential of each well. Well rates are limited by historic production rates (e.g. well must have produced more than some minimum to be used as injection wells, and wells cannot inject at a rate higher than the maximum production rate).

We define four base scenarios for spatial distribution of gas injection: No injection, Injection in the Loppersum (LOPPZ) production region, Injection in the South-East production region, and simultaneous injection in the Loppersum and South-East production regions. These scenarios are motivated by the current understanding that seismicity in the field can be associated primarily to pressure decline and the associated reservoir compaction and changes to the stress field. Injection could reduce or even reverse pressure decline and therefore lead to a reduction in seismicity. In the following we discuss the various scenarios in more detail.

Figure 9 Overview of gas well clusters and past production regions in the Groningen field Source: NAM (2020). The status of wells in these clusters is summarized in Table 1.

Table 1 Status of well clusters in the Groningen field in October 2023 (End of Production).

Cluster	Well name abbreviation	Production region	Number of wells	Status (October 2023)
Amsweer	AMR	East-Central	12	Closed-in
Bierum	BIR	North	13	Suspended
Eemskanaal	EKL	Eemskanaal	12	Suspended
Eemskanaal 13	EKL	Eemskanaal	1	Suspended
De Eeker 1	EKR	South-East	11	Closed-in
De Eeker 2	EKR	South-East	10	Closed-in
Froombosch	FRB	South-West	8	Closed-in
Kooipolder	KPD	South-West	12	Closed-in
Leermens	LRM	LOPPZ	11	Suspended
Midwolda	MWD	n.a.	9	Abandoned
Noordbroek	NBR	n.a.	9	Abandoned
Nieuw Scheemda	n.a.	n.a.	9	Abandoned
Overschildt	OVS	LOPPZ	11	Suspended
Oudeweg	OWG	East-Central	11	Closed-in
De Paauwen	PAU	LOPPZ	5	Suspended
Ten Post	POS	LOPPZ	11	Abandoned
Sappemeer	SAP	South-West	9	Closed-in
Schaapbulten	SCB	East-Central	11	Closed-in
Siddeburen	SDB	East-Central	11	Suspended
Slochteren	SLO	South-West	8	Closed-in
Spitsbergen 1	SPI	South-West	10	Closed-in
Spitsbergen 2	SPI	South-West	9	Closed-in
Scheemderzwaag 1	SZW	South-East	10	Closed-in
Scheemderzwaag 2	SZW	South-East	10	Closed-in
Tjuchem	TJM	East-Central	11	Suspended
Tusschenklappen	TUS	South-West	10	Closed-in
Uiterburen	UTB	n.a.	10	Abandoned
't Zandt	ZND	LOPPZ	10	Suspended
Zuiderpolder	ZPD	South-East	12	Closed-in
Zuiderveen	ZVN	South-West	11	Closed-in

In the 'no injection' base case scenario, no gas injection is assumed to take place. However, redistributive flow of gas will still occur due to the existing pressure gradients in the field, that result from uneven production in the past. This scenario provides the baseline expectation for seismicity.

The area around Loppersum has experienced the highest seismic activity, including the largest event registered to date, at Huizinge. While production from this area was stopped already years ago, production continued from the south of the field. The resulting pressure gradient towards the south-east of the field (see Figure 8) will still cause flow of gas away from the Loppersum region, and therefore result in local lowering of the pressure and compaction of the reservoir. Injection in this area could potentially deliver direct beneficial effects on seismicity by, at least temporarily, maintaining pressure. At the same time, this would maintain or even strengthen the existing large-scale pressure gradient and thus cause gas to flow away from the injection area. Retaining any positive impacts would therefore require sustained injection over a long period until large-scale pressure equilibration has been established.

As soon as injection is stopped, local pressure may be expected to start to decline again, but possibly at a slower pace than before.

The south-east region of the field has depleted most strongly (i.e. pressure is lowest here), since gas production in recent years has primarily occurred here, and therefore will be the main driver for redistributive large-scale flow in the field. An increase in pressure in this region should reduce the large-scale pressure gradient across the field and thus permanently reduce the trend towards further pressure decline in regions further north. However, beneficial effects in the Loppersum area can be expected to occur slower and later than if gas were injected there. A compromise scenario that could deliver both short-term direct benefits as well as slower but long-term ones, is therefore to inject in both the Loppersum and South-East regions.

All presented simulations are variations of the above scenario's, where either the total injection volume rate, the distribution over the regions (and thus clusters), or the duration of injection is varied (see Table 2).

The total availability of injection gas used in the scenarios will be based on assumptions about the capacity of factories for nitrogen generation. One of these facilities is the recently completed phase II extension of the Zuidbroek factory, which has a reported capacity of 180.000 m^3/hour (https://zuidbroek.gasunie.nl/het-project). A rough estimate of total volume capacity based on possible contributions from all nitrogen factories in the Netherlands suggests that the Zuidbroek Phase II capacity might be a reasonable basis (from a technical and procedural point of view) for the comparison of various capacity scenarios, as further detailed below. For brevity we will sometimes refer to the Zuidbroek capacity as 1ZB, i.e. 1ZB = 180.000 m^3/hour (or, equivalently, 122 MSCF/day, or 1.58 x 10^9 Nm^3/year, where 10^9 Nm^3 = 1 BCM). To provide some context, this capacity can be compared to the historic field production rates of natural gas from the Groningen field and corresponds to about one fifth of daily natural gas production in the gas year 2020-2021. Total gas production from Groningen over the past 50 years amounts to more than 75 x 10^{12} SCF (or 2130 x 10^9 Nm^3). Complete replacement of that volume at the Zuidbroek nitrogen production rate, would take around 1350 years, which would clearly be infeasible. However, seismicity has not been an issue in the Groningen field from the start, and it may therefore be possible to influence current and future seismic activity by much lower injection volumes. This is the focus of the experiments that we will report here.

The definition of meaningful scenarios will require some assumptions about the future availability of nitrogen generation capacity and the future availability of wells in the Groningen field. Both of these will depend on (geo)political, market and societal developments that must be considered highly uncertain. Rather than speculating on possible outcomes, we will consider scenarios for injection of nitrogen that are based on the currently available nitrogen generation capacity, and on the distribution of available well clusters in the Groningen field at the time of end of production (end of 2023). In addition we will consider a more scientifically motivated set of scenarios that assumes a very high nitrogen generation. We will assume that nitrogen is available to be injected at all wells that are potentially operational in the field. That is, the availability and/or suitability of the surface infrastructure and the sourcing and distribution of the nitrogen are not explicitly considered and studied.

The first set of scenarios that we consider assumes a continuous nitrogen generation capacity of 1 ZB. This is based on a rough estimate of the spare capacity of all combined nitrogen generation facilities in the country (the total capacity is estimated to be roughly 3.2 ZB or 5.1 BCM/year). With spare capacity we mean the capacity not immediately needed to meet the current requirements for conversion of high-caloric imported gas to Groningen-grade gas. For the year 2023 Gasunie Transport Services (GST) reported using 2.84 BCM of nitrogen. This would suggest a spare capacity of about 2.2 BCM/year, or 1.4 ZB. We will consider the scenario that 1 ZB of this capacity is available for continuous injection throughout the year. We stress that the actual value is uncertain and may be even lower.

Since it is likely that injection of gas with this relatively modest volume rate (the reader is reminded of the earlier provided comparison with the historic gas production) does not lead to very significant reduction of seismicity in the short term, we will also consider a more scientifically motivated set of scenarios that assume a nitrogen injection capacity of 10 ZB. These scenarios will help to understand and illustrate fundamental mechanisms associated with repressurization and its impact on seismicity and also provide an indication of what might be achievable if there were no practical limitations. The 1ZB and 10ZB scenarios represent two cases; one of injection of an amount of N_2 that is currently being produced in the Netherlands (although not necessarily available for this specific purpose), and one case that would require a significant increase in the national N_2 production.

The complete set of scenarios considered in this study is summarized in Table 2.In this table, the abbreviation LO stands for Loppersum and SE stands for South-East. Scenarios 2 to 4 are based on a total nitrogen generation and injection capacity of 1 ZB, while scenarios 5 to 7 are the corresponding scenarios for a capacity of 10 ZB. Scenario's 8 and 9 are informed by results obtained for scenario's 5 and 6 and are meant to investigate the hypothesis of re-bouncing of seismicity after cessation of injection due to pressure equilibration throughout the field. In scenarios 8 and 9, injection is stopped at the time that model-predicted seismicity is reduced to zero in scenario's 5 and 6 respectively.

As an explanation of the Volume factors listed in Table 1, consider e.g. scenario 4. The total injected rate corresponds to 1 ZB, and this volume is divided equally over the LOPPZ and South-East regions. So 0.5 ZB is injected in LOPPZ and 0.5 ZB is injected in the South-East region.

For simplicity we assume that all gas production from nearby small fields ends on 1 October 2023. As a result both the small field wells and the pseudo aquifer wells are shut in at that time. Keeping these wells active during the injection scenarios would require that we include projected production rates for these fields, including expected dates for the end of operations of each of these fields. This would introduce a speculative element into the scenarios. Secondly, the production from the small fields has not been history matched and its impact is most likely not accurately represented anyway. Thirdly, the impact on seismicity in the Groningen field **is** expected to be insignificant.

During the period 1 January 2023 to 1 October 2023 the small fields and pseudo aquifer wells are operated in the model at the targets specified on 1 December 2022. The only pseudo aquifer well open during this period is the one representing production from the Faan field.

Table 2 Overview of injection scenarios. All injection scenarios are simulated until 2054. Injection is started in October 2025 in all cases except scenario 1. Volume factors express the total injected surface volume rate in terms of the of Zuidbroek Phase II nitrogen production capacity (180.000 m^3/hour). The time to stop injection in scenario 8 (9) is based on the results from scenario 5 (6) and corresponds to the time that model-predicted seismicity is reduced to zero.

Scenario	Name	Active clusters	Volume factors	Strategy
1	Base Case	None	0	no injection
2	LO	LOPPZ	1	continuous injection until 2054
3	SE	South-East	1	continuous injection until 2054
4	LO_SE	LOPPZ, South-East	0.5, 0.5	continuous injection until 2054
5	LO-10ZB	LOPPZ	10	continuous injection until 2054
6	SE-10ZB	South-East	10	continuous injection until 2054
7	LO_SE-10ZB	LOPPZ, South-East	5, 5	continuous injection until 2054
8	LO-10ZB-7Y	LOPZZ	10	stop injection after 7 years
9	SE-10ZB-11Y	South-East	10	stop injection after 11 years

3.5 Results

Figure 10 shows time series of the near-well pressure (averaged over 9 grid blocks) for all the scenarios listed in Table 2. Pressure curves are provided for the Amsweer 1, Eemskanaal 1, Ten Post 1, and Spitsbergen 1 wells, which are located in the Central-East, Eemskanaal, Loppersum and South-West production regions respectively. All four wells are inactive during the forecast (injection) period.

For the wells WEKL1 and WPOS1, located in the Eemskanaal and Loppersum regions respectively (Figure 10b and Figure 10c), the pressure tends to decline if no gas is injected due to pressure equilibration (see the red lines). Since pressure in these regions is initially higher than in the regions towards the east and south, the resulting pressure gradient will drive a gas flow that would ultimately result in a more or less homogeneous pressure throughout the field. At the Eemskanaal cluster location this tendency is observed for the first 6 to 20 years also when gas is injected in the Loppersum or South-East regions. The pressure decline stops later (around 2044) and at a lower value (about 1280 psi) when the total injected volume is lower.

As may be expected, the pressure increases much faster when gas is injected with a higher volume rate. Considering, for example, the location of the Amsweer 1 well (WAMR1), pressure is increased by up to 90 psi (6 bar) over the 30 year injection period for an injection rate of 1 ZB, while an increase of about 700 psi is observed over that same period for a rate of 10 ZB (Figure 10a). For context, these values compare to a historical pressure decline at this location of about 3800 psi (262 bar) over the production period (compare e.g. the change in BHP for WAMR1 as shown in Figure 7). Since this well is somewhat closer to the Loppersum region than to the South-East region, the pressure increase is somewhat delayed if the gas is injected in the South-East region (compare e.g. the blue and yellow lines).

At the Ten Post 1 (WPOS1) well location (Figure 10c) interesting behaviour is observed for scenario 8 (LO_10ZB_7Y, green line). Pressure decreases during the first few years after the end of production and before the start of injection. Pressure builds up quickly for a period of 7 years when large volumes of gas are injected using wells in the same production region.

When the injected is stopped after 7 years pressure starts to decline again immediately, reaching its lowest value at the end of the forecast period in 2054. If gas is injected in the South-East region (scenario 9, SE_10ZB_11Y, the black line), the initial pressure decline takes somewhat longer to reverse, but no second period of pressure decline is observed in this case, also not after 11 years, when injected is stopped.

Similar behaviour can be observed at the Spitsbergen 1 (WSPI1) well location as shown in (Figure 10d). This location is fairly close to the South-East production region and a clear decline of pressure is observed when injection is stopped after 11 years for scenario 9 (SE_10ZB_11Y, black line). No initial decrease in pressure is expected at this location due to the fact that pressure is already very low in the south of the field at the end of production. Gas will therefore tend to flow towards this location, especially from further north where the pressure is higher, even in the case that no gas is injected.

Several curves are reproduced in Figure 11, which also shows the pressure decline as a result of the production of gas, at two of these four locations. As can be clearly seen, even continuous injection at a rate of 10 ZB will not lead to complete re-pressurization of the Groningen field. However, more relevant for seismicity may be the elimination of spatial pressure gradients within the field.

A spatial impression of the pressure effect of several example injection scenarios is provided in Figure 12. Each panel shows the difference in pressure in 2054 between one injection scenario and the base case (no injection). Injection in the South-East region with a rate corresponding to 1 ZB results in limited pressure increases that are primarily limited to that region (panel b). In contrast, an even distribution of 10 times that rate over the Loppersum and South-East regions (panel e) results in significant increases in pressure throughout the field. Some pressure gradients remain between the two regions (not clearly visible due to the color scale), due to the existing pressure gradient across the field at the end of production, which means that further pressure equilibration would take place if injection is stopped.

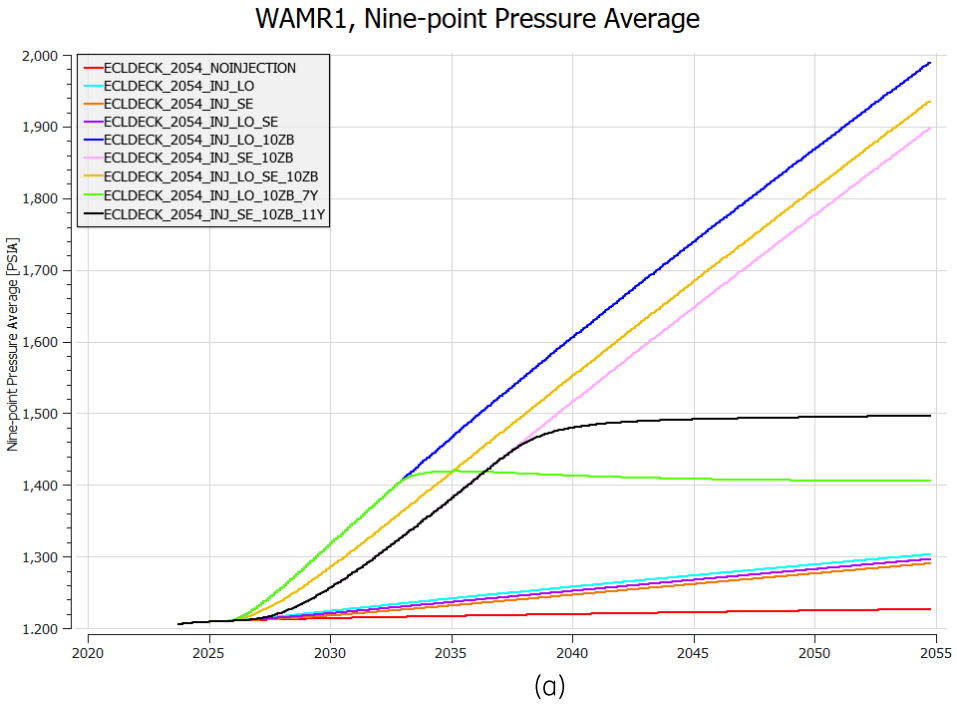
WAMR1, Nine-point Pressure Average
ECLDECK_2054_NOINJECTION
ECLDECK_2054_INJ_LO
ECLDECK_2054_INJ_SE
ECLDECK_2054_INJ_LO_SE
ECLDECK_2054_INJ_LO_10ZB
ECLDECK_2054_INJ_SE_10ZB
ECLDECK_2054_INJ_LO_SE_10ZB
ECLDECK_2054_INJ_LO_10ZB_7Y
ECLDECK_2054_INJ_SE_10ZB_11Y
Nine-point Pressure Average [PSIA]
2,000
1,900
1,800
1,700
1,600
1,500
1,400
1,300
1,200
2020
2025
2030
2035
2040
2045
2050
2055

(a)

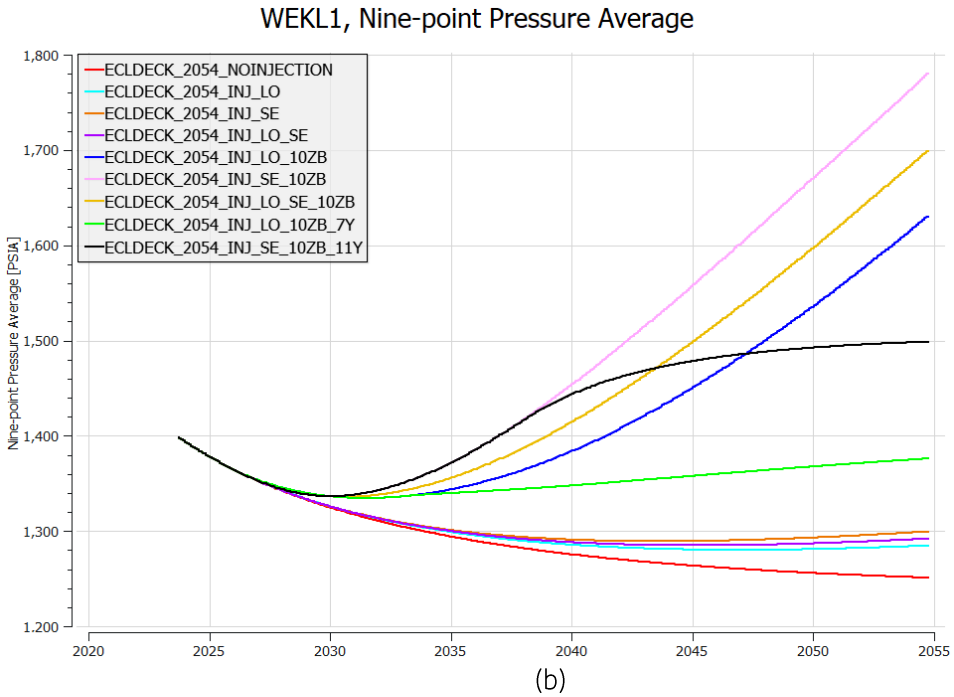
WEKL1, Nine-point Pressure Average
ECLDECK_2054_NOINJECTION
ECLDECK_2054_INJ_LO
ECLDECK_2054_INJ_SE
ECLDECK_2054_INJ_LO_SE
ECLDECK_2054_INJ_LO_10ZB
ECLDECK_2054_INJ_SE_10ZB
ECLDECK_2054_INJ_LO_SE_10ZB
ECLDECK_2054_INJ_LO_10ZB_7Y
ECLDECK_2054_INJ_SE_10ZB_11Y
Nine-point Pressure Average [PSIA]
1,800
1,700
1,600
1,500
1,400
1,300
1,200
2020
2025
2030
2035
2040
2045
2050
2055

(b)

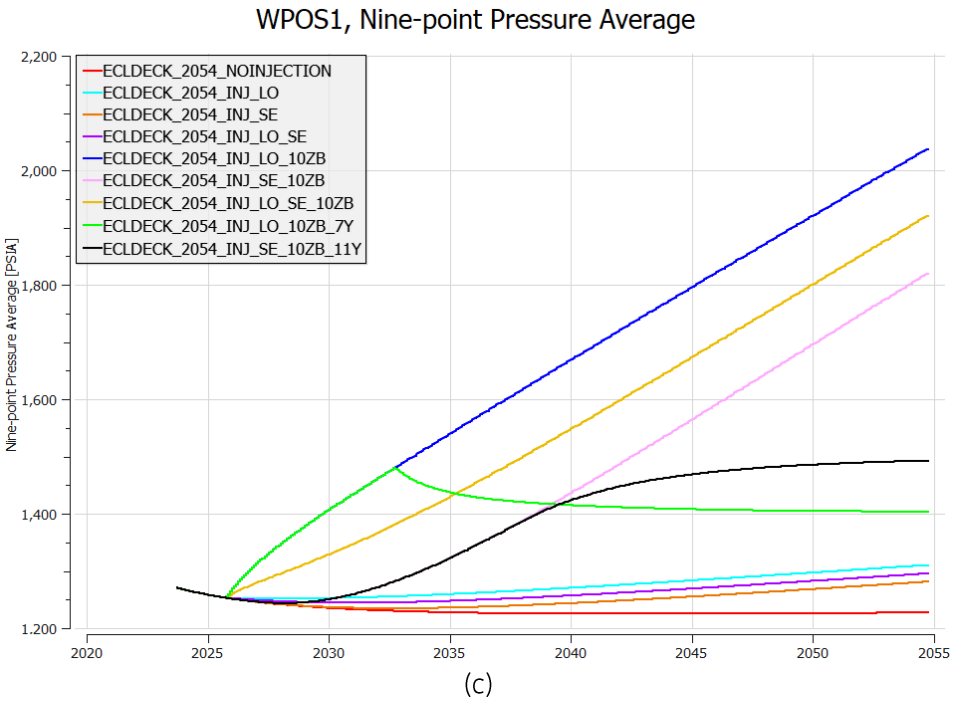

(c)

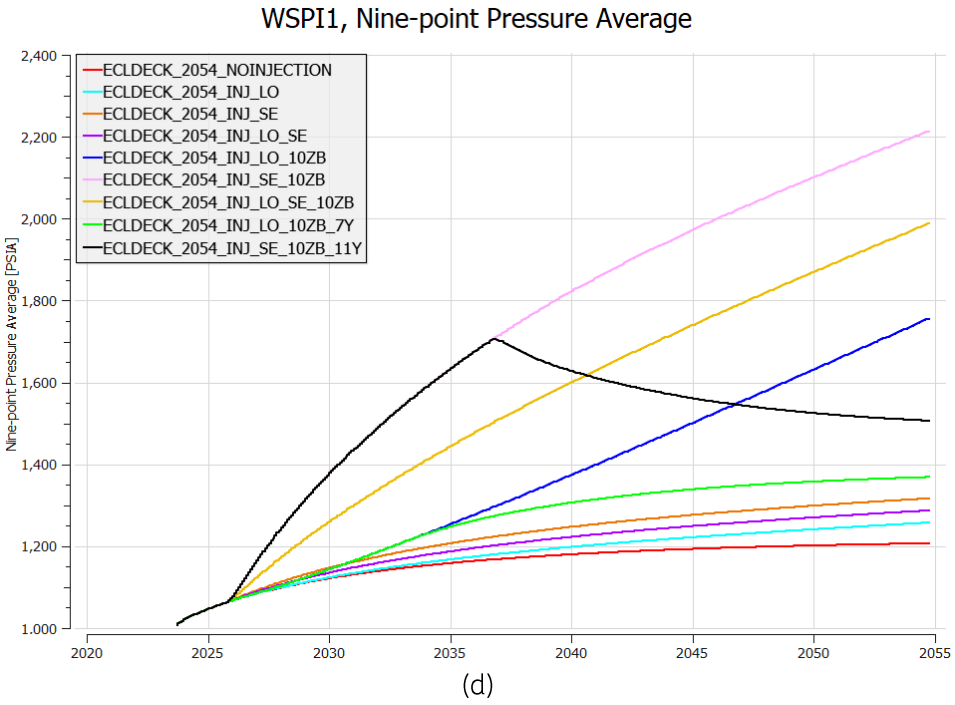

(d)

Figure 10 Near-well average simulated reservoir pressure around 4 wells from 4 different production regions that are not used for injection. (a) Amsweer 1, located in the East-Central region, (b) Eemskanaal 1, located in the Eemskanal region, (c) Ten Post 1, located in the Loppersum region, and Spitsbergen 1, located in the South-West region. Results are shown for the base case and all injection scenarios.

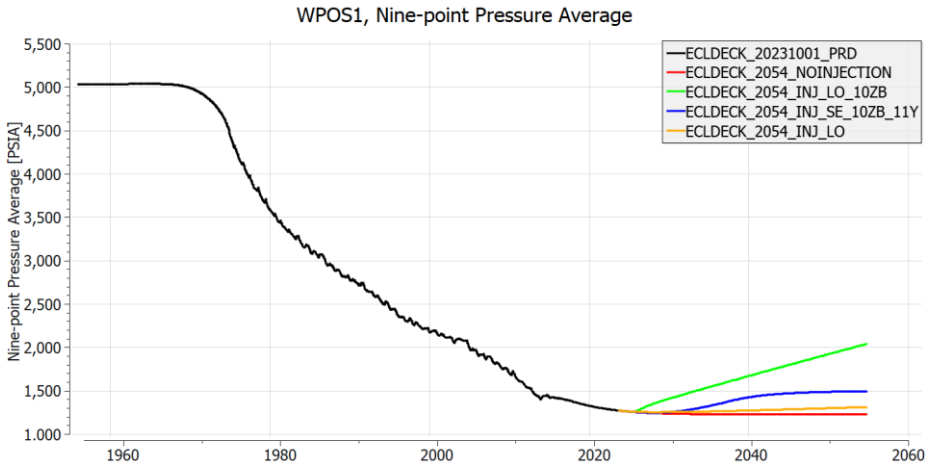

(a)

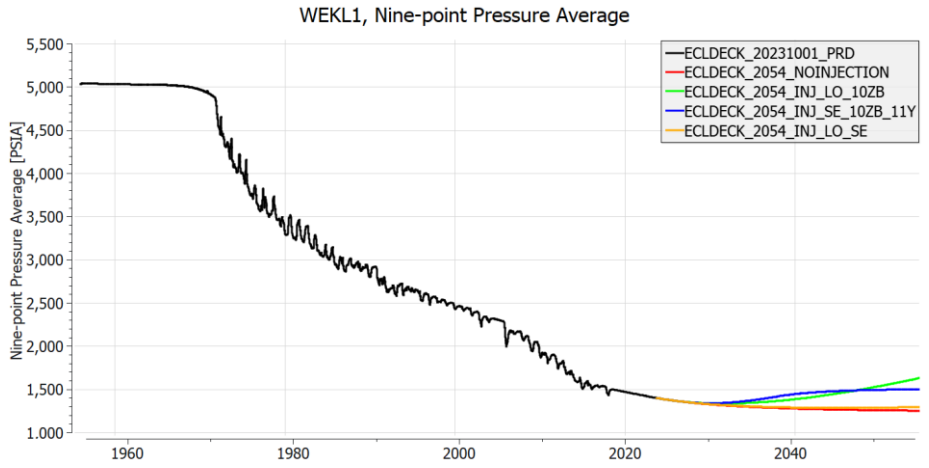

(b)

Figure 11 Near-well average simulated reservoir pressure around 2 wells from 2 different production regions that are not used for injection. (a) Ten Post 1, located in the Loppersum region, (b) Eemskanaal 1, located in the Eemskanal region. Results are shown for the production period (black line), the no-injection scenario (red line), two scenarios with 10ZB injection capacity, and one scenario with 1ZB injection capacity.

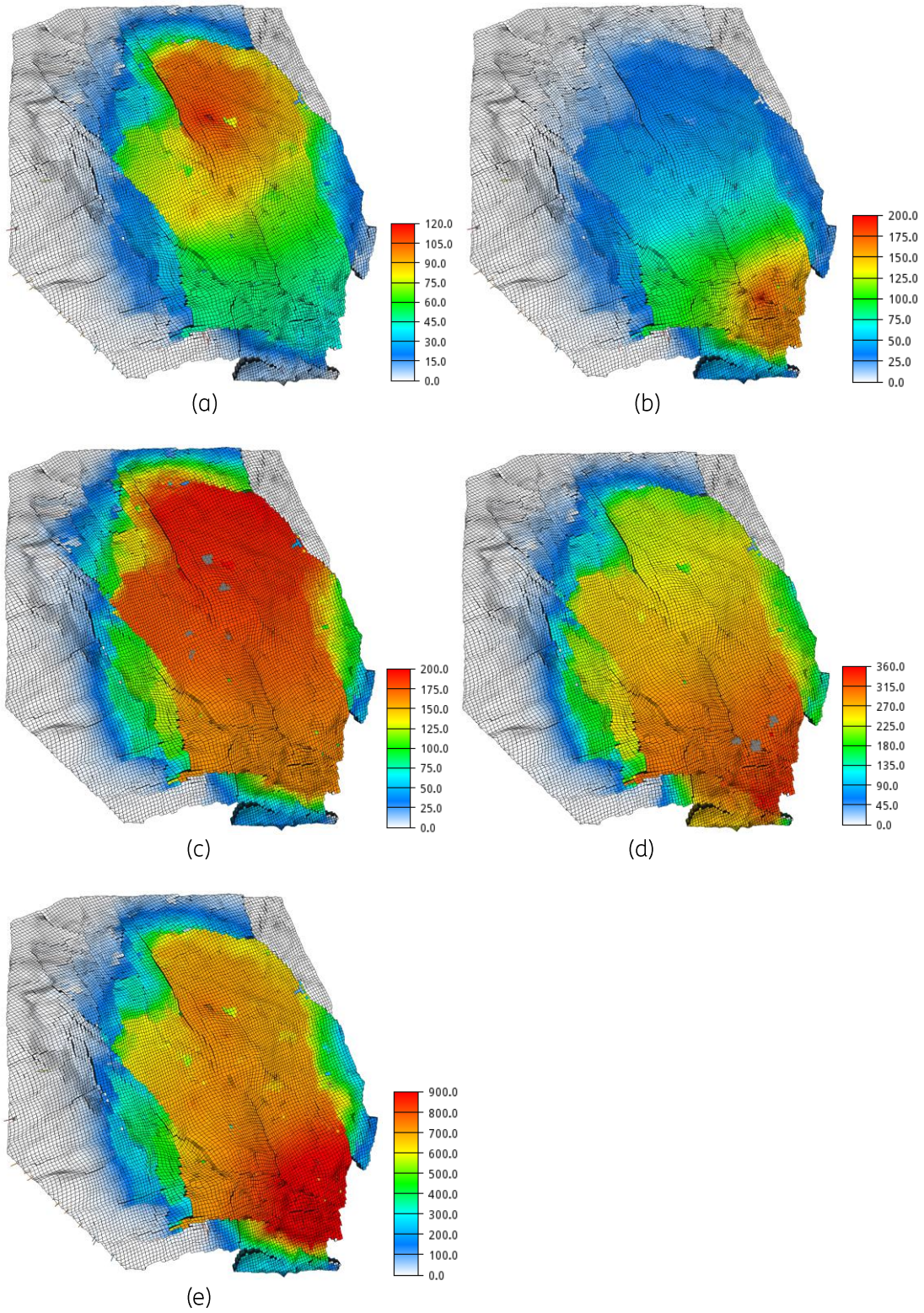

Figure 12 Pressure differences at the end of the simulation period (year 2054) relative to the Base Case (no injection). (a) LO, (b) SE, (c) LO_10ZB_7Y, (d) SE_10ZB_11Y, (e) LO_SE_10ZB. Note the different colour scales. Units are psi (100 psi ≈ 6.9 bar). The locations of active injection wells in the Loppersum and South-East regions are indicated by the clusters of grey dots in panels (c) and (d) respectively.

3.6 Compositional effects

A compositional Eclipse 300 (Schlumberger) model was created to evaluate the effect of gas composition on the expected pressure response. The model can be used to determine the N_2 injection volumes that would be required to achieve the same pressure results as simulated with injection of Groningen gas. A single-cell box model was created that was initialized at a pressure similar to the pressure in the Groningen field at the end of production. The input for the Eclipse 300 compositional simulation model was created using Petrel (Schlumberger) using the built-in components C_1 to C_6, representing methane, ethane, propane, butane, pentane and hexane, N_2 (nitrogen), CO_2 (carbon dioxide), and H_2O (water vapour). Mole fractions were taken from standardized average composition of Groningen natural gas (Gasunie, 1980). The parameters of the compositional model were calculated by Petrel using database values for critical pressure, temperature, Z factor etc. Results for simulations with injection of Groningen gas and injection of N_2 are shown in Figure 13.

The results suggest that injection of the same volume of nitrogen gas will result in a faster increase in pressure. In other words, in order to reach a desired reservoir pressure, a smaller surface volume of nitrogen gas is required than of Groningen gas. The ratio between the two curves increases from 1 at the initial time to 1.06 around 2030 and 1.14 at 2054. The simulation results obtained with Eclipse 100 reported earlier should therefore be interpreted as providing something like an upper bound on the volume of gas required to reach the simulated pressure states, or as providing an upper bound on the time required to reach a desired pressure state (or, more or less equivalently, reduce the seismicity to a desired level). Note that a pressure of around 2000 psi, reached here around simulation time 2030, is similar to the maximum pressure that was obtained in the Groningen injection scenarios, suggesting that errors due to compositional effects are smaller than 6%.

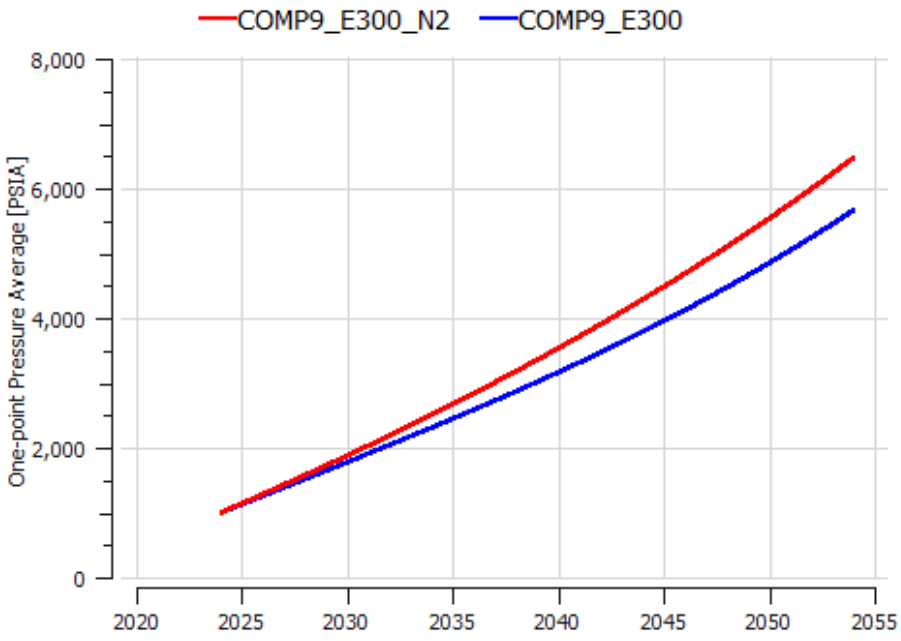

Figure 13 Comparison of single-cell pressure behaviour for a constant surface volume injection rate resulting from simulations with Eclipse 100 (gas properties from the NAM Eclipse model), Eclipse 300 with specification of Groningen gas composition and injection of Groningen gas, and Eclipse 300 with specification of Groningen gas composition and injection of N2.

3.7 Additional comments

In this chapter we have considered relatively simple scenarios for gas injection where we have assumed constant nitrogen generation and injection capacity. Future increases due to changes in gas production and usage, or even the addition of an additional nitrogen facility, could be imagined. Given the low pressures currently present in the field, and the relatively low volume injection rates that we consider here, pressures increases will approximately scale linearly with the average volume injected (as confirmed by the first parts of the curves in Figure 13 for pressures up to 2000 psi, and the last parts of the curves in Figure 10 after transient effects have more or less disappeared). This means that, given an average injection rate of e.g. 2 ZB, pressure increases relative to the no injection case at 2054 can be expected to be higher by approximately a factor 2 than the pressure increase obtained for an average injection rate of 1 ZB.

We have assumed that individual wells cannot inject at rates higher than their maximum historic gas production rates. These maximum production rates range from 0.2 to 1.2 ZB for wells in the LOPPZ region, and from 0.1 to 0.7 ZB for the wells in the South-East region. This means that the wells with the highest productivity (> 1 ZB) could already by themselves inject all nitrogen injected in the LO scenarios (Table 2). Note that nearly 60 wells were used for the scenarios where gas is injected in the South-East region. The high well productivity estimates imply that this number of wells could in principle be strongly reduced.

For completeness we note that a similar simulation as was used to produce Figure 13 but with the Eclipse 100 black-oil formulation results in a curve that does not exactly match the Eclipse 300 result for injection of Groningen gas. An explanation for the difference could lie in the gas formation volume factor, which in the Eclipse 100 deck may have been tuned by NAM to account for the presence of water vapour in the produced gas. However, practical experience has shown that these two simulators always tend to produce different results that require separate tuning of each type of model. It is also not known to the authors how accurate the density calculations of Eclipse 300 are for arbitrary gas compositions.

4 Hazard & Risk Analysis

4.1 Introduction

In this chapter we will investigate the effect of gas injection and the resulting pressure changes on the overall seismicity, seismic hazard and seismic risk. The seismicity, seismic hazard, and seismic risk is modelled by applying the *TNO Model chain for Groningen* (TNO, 2022). In the seismic source model used within the model chain, seismicity is only possible at locations and times in the field where the gas pressure is decreasing. Since nitrogen injection will cause an overall increase in the gas pressure, we expect to observe primarily beneficial effects of fluid injection. Any potentially negative effects (e.g. caused by reservoir cooling, or local development of tensile stresses due to high injection pressures) are currently not modelled and are therefore not considered in this study.

In this chapter we include a number of key figures. A full set of figures related to seismicity, seismic hazard, and seismic risk is included in Appendix A.

4.2 Model description

To calculate seismicity, hazard, and risk, we apply the *TNO Model chain for Groningen* (TNO, 2022, 2023b, 2023c) with the same model versions that were used for the 'analysis according to the most recent scientific insights' in the public Seismic Hazard and Risk Analysis 2023 (TNO, 2023):

- Seismic source model V6: Linear elastic reservoir response to pore pressure changes, leading to spatio-temporal Coulomb Stress Change field. This stress field controls the activity rate through an exponential rate model and the earthquake magnitudes though a stress-dependent Gutenberg-Richter b-value.
  The activity rate model and the magnitude model are calibrated over the period 1995-01-01 through 2023-02-28.
- Ground Motion Model V7 (Bommer et al., 2022)
- Fragility and Consequence model V7 with adjusted parameters to reflect the results of the TNO typology project. (Crowley et al., 2019; TNO, 2023)

For more details on the *TNO Model chain for Groningen* see (TNO, 2022).

The seismic hazard and risk calculation is based on time series of yearly snapshots of pore-volume weighted vertically averaged pressure grids, resulting from the simulations described in Chapter 3. The NAM Eclipse model does not provide the exact same historical gas pressures as the NAM internal reservoir model (MoRes) which has provided the pressure grids for all previous pSHRA model runs. Since the calibration of the source model is conditioned on the historical gas pressures (see TNO 2022 for a description of the source model calibration procedure), the calibrated source model posterior parameter distribution is slightly different compared to the pSHRA '23.

Therefore, the resulting seismicity hindcasts over the production period, as well as the seismicity forecast for the base case scenario (no gas injection) are also different from the pSHRA '23 results (TNO, 2023). For the purposes of this study, which compares different N_2 injection scenarios, this is not a concern, since we're interested in the magnitude of the effect of different N_2 injection scenarios on seismicity/hazard/risk compared to the 'no injection' base case.

4.3 Seismicity

For all scenarios detailed in Chapter 3, Table 2, we forecast the event rate until gas year 2052/2053, and provide a full seismicity forecast (including magnitudes, suitable for hazard and risk assessment) for the gas years 2024/2025 until 2036/2037. Since this study focusses on the impact of different nitrogen injection scenarios, which are clearly visible in the first 13 years of these scenarios, full seismicity forecasts, as well as hazard and risk calculations beyond 2036/2037 are not provided. In Appendix A Figure 14 to Figure 25, the temporal evolution of the forecasted event rate is shown for all modelled cases. A comparison to the reference case (the base case in which no injection occurs) is included. Figure 26 to Figure 27 show the spatio-temporal evolution of the full seismicity forecast used for hazard and risk analyses.

The main effects that can be seen are:

- Injecting more nitrogen leads to a faster reduction of seismicity in the forecasts. In the models where the equivalent of 10 Zuidbroek II facilities worth of N_2 production capacity are injected (10ZB), seismicity rapidly declines to zero expected events per year in 7 to 11 years, depending on the injection location (Figure 14, Figure 18, Figure 19). In contrast, in scenarios where the equivalent of 1 Zuidbroek II facility worth of N_2 production capacity is injected (1ZB), the decline in seismicity is slower and reaches zero expected events close after approximately 25 years of continuous injection (Figure 15, Figure 16, Figure 17).
- When considering the same injection volume, injecting in the Loppersum area leads to a faster reduction in seismicity compared to injecting the South-East. The seismicity reduction for injection of equal volumes in the Loppersum and South-East areas (cases LO_SE and LO_SE-10ZB) falls in between these two end-members (Figure 14, Figure 15, Figure 16, Figure 17, Figure 18, Figure 19).
- Although injection in the Loppersum area leads to a faster decline in seismicity compared to other tested spatial N_2 distribution scenarios, it is also associated with the largest increase in seismicity after injection stops (Figure 20). This is due to the pressure equilibration in the field that continues to occur after cessation of the injection. Injection in the Loppersum area maintains the spatial pressure differences in the field, which leads to gas flow to equilibrate pressures. In the current implementation of the seismic source model, any local gas pressure decrease leads to seismicity, even if that particular location has seen even lower gas pressures in the past. This is potentially a limitation of the current source model, and it is beyond the scope of this project to assess whether this particular feature is a realistic representation of the physics relevant for seismicity.

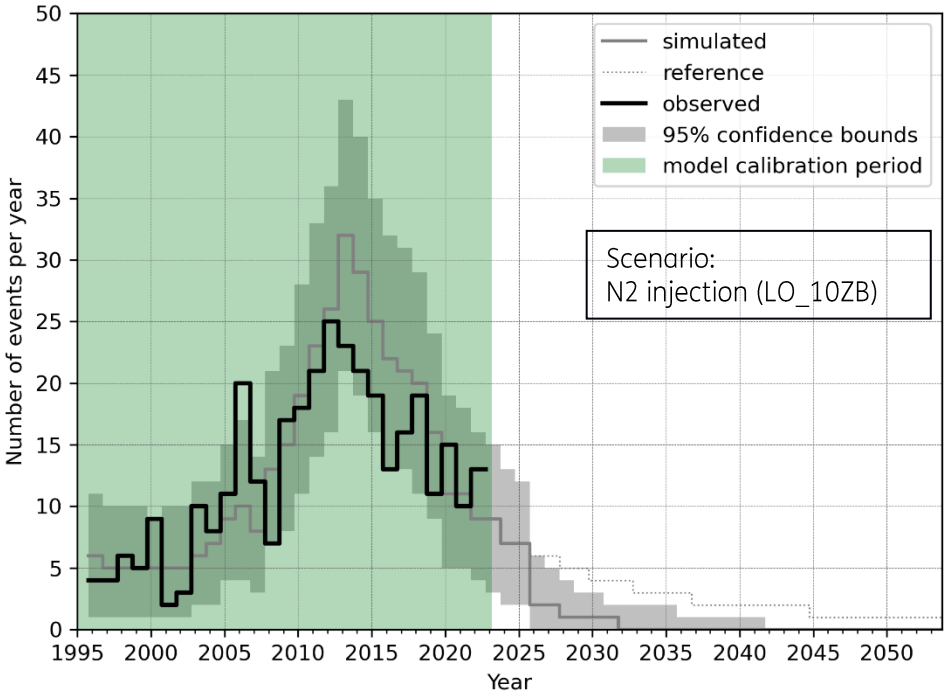

Figure 14: Number of events per year in the Groningen field of M1.5 and above for the LO_10ZB scenario. The solid grey line is the modelled expected number of events, the grey area gives the 95% confidence bounds per year. The solid black line is the data and the green area is the period over which the model is calibrated. The dotted reference line represents the base case for comparison.

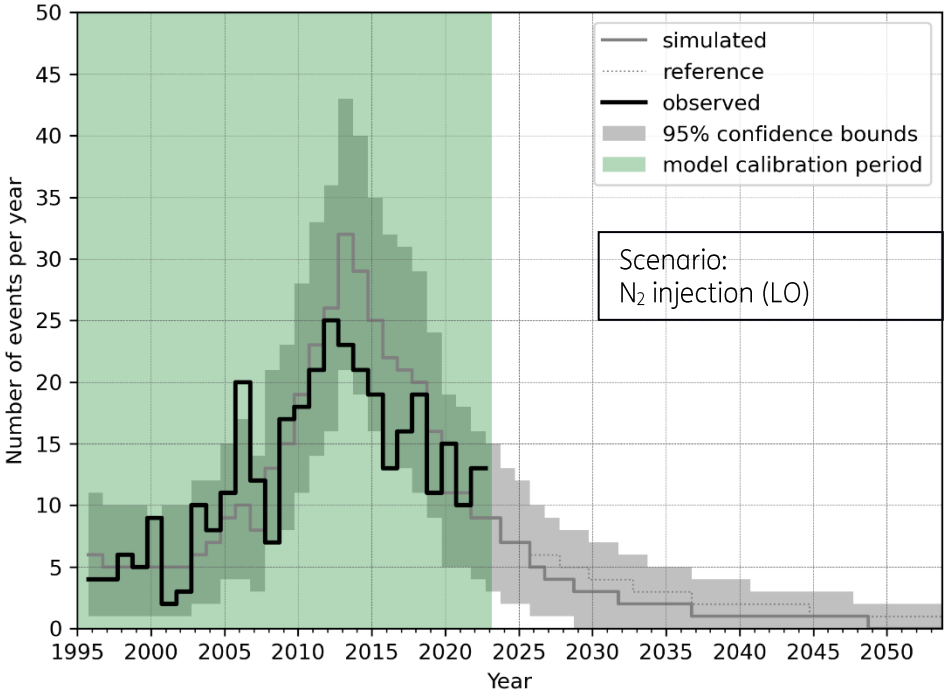

Figure 15: As Figure 14, except for the LO scenario. The dotted reference line represents the base case for comparison.

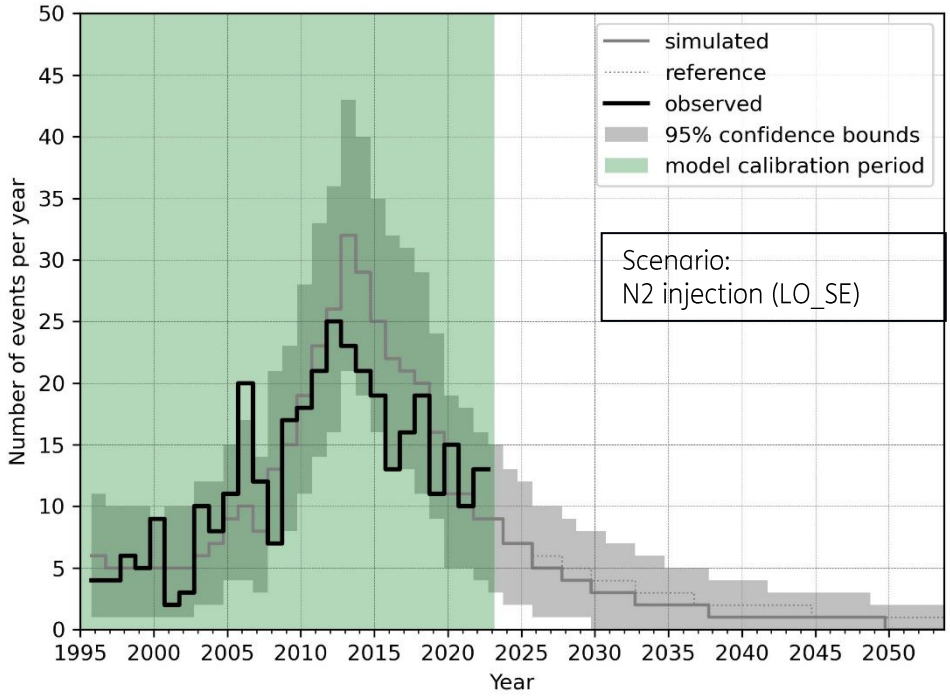

Figure 16: As Figure 14, except for the LO_SE scenario. The dotted reference line represents the base case for comparison.

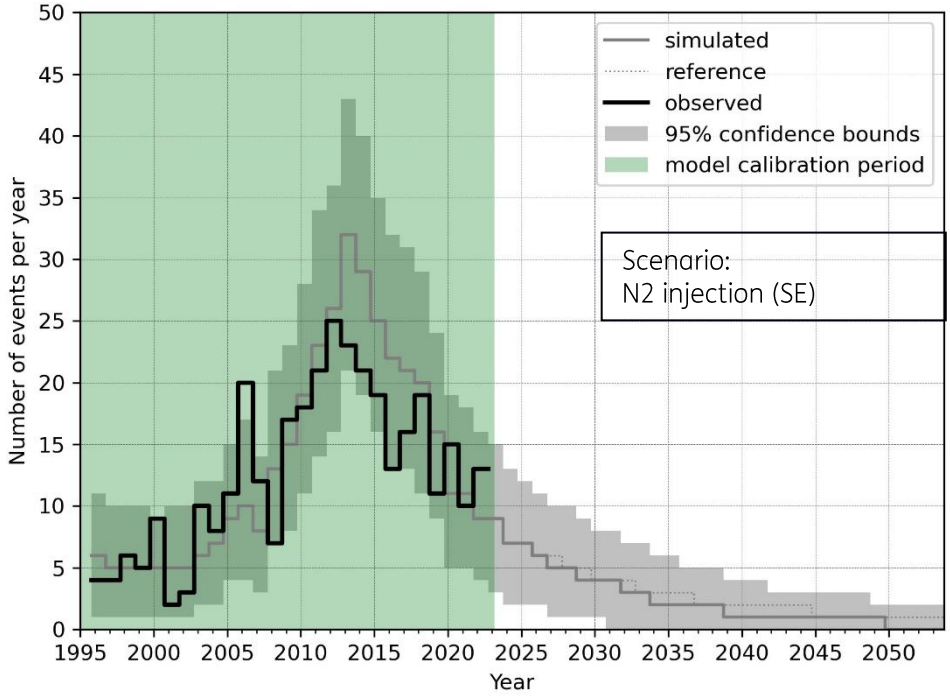

Figure 17: As Figure 14, except for the SE scenario. The dotted reference line represents the base case for comparison.

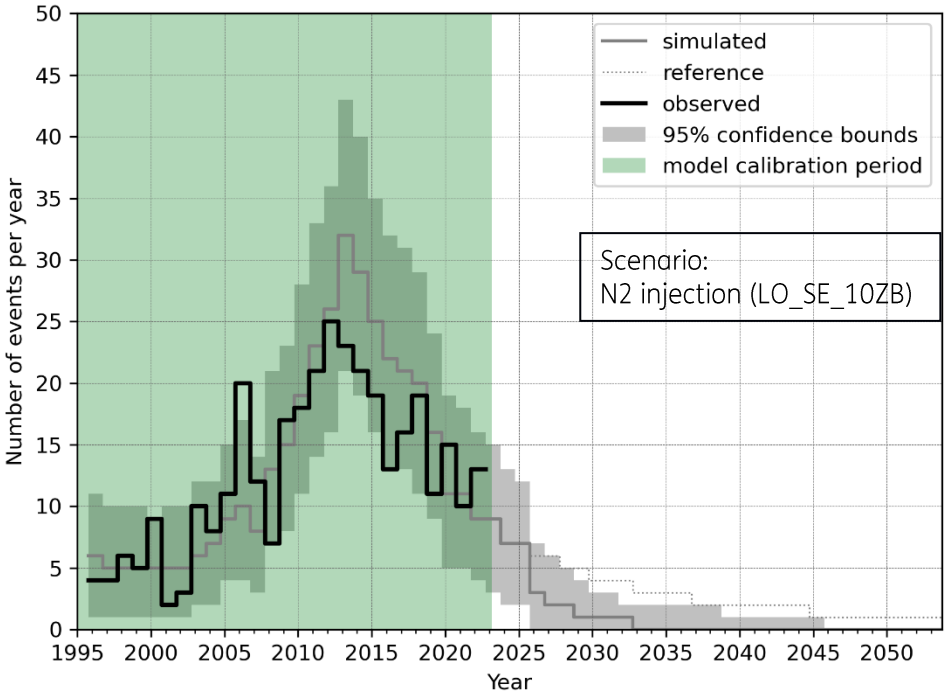

Figure 18: As Figure 14, except for the LO_SE_10ZB scenario. The dotted reference line represents the base case for comparison.

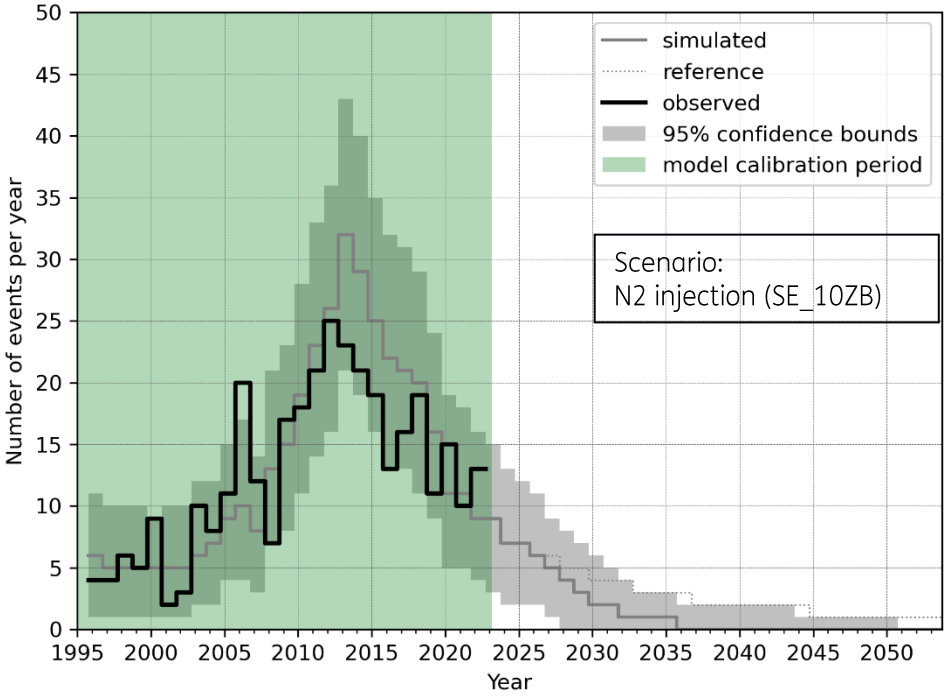

Figure 19: As Figure 14, except for the SE_10ZB scenario. The dotted reference line represents the base case for comparison.

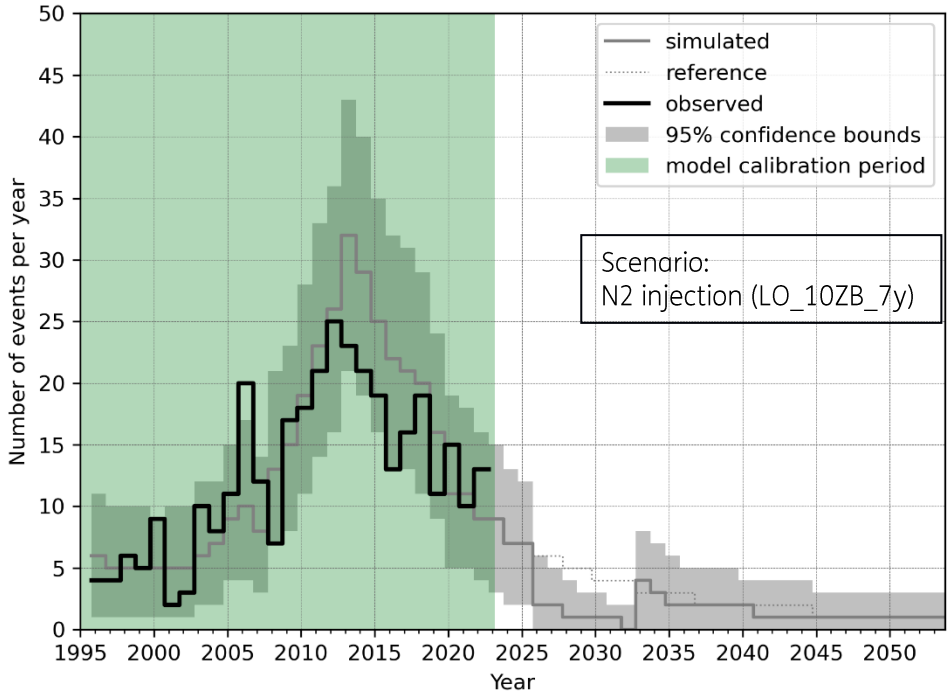

Figure 20: As Figure 14, except for the LO_10ZB_7y scenario. The dotted reference line represents the base case for comparison.

4.4 Hazard and risk

In Appendix A, Figure 46 to Figure 54 show the hazard maps (PGA for 475 year return period) for all cases. Their general pattern is comparable to that of the seismicity maps; the hazard is higher in areas with more expected earthquakes. The hazard maps also show the effects of the shallow subsurface (through the site response model in the Ground Motion Model), which can locally increase/decrease the hazard, depending on the mechanical properties of the shallow subsurface layers. Here, we show the hazard for the base case (Figure 21), the LO case (Figure 22), and the LO_10ZB case (Figure 23).

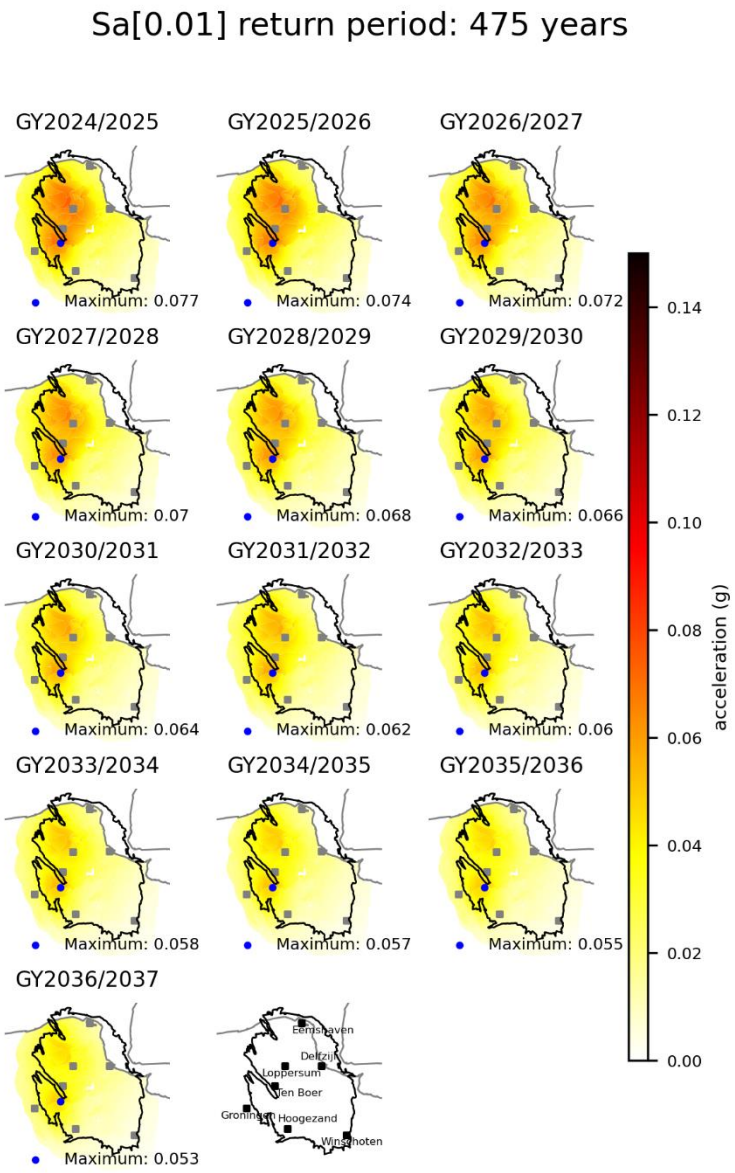

Figure 21: Peak Ground Acceleration (pseudo-spectral acceleration at 0.01 s) hazard map for a 475 return period (10% probability of exceedance in 50 years). The blue dot indicates the position of the largest hazard for each year. Base case (no injection).

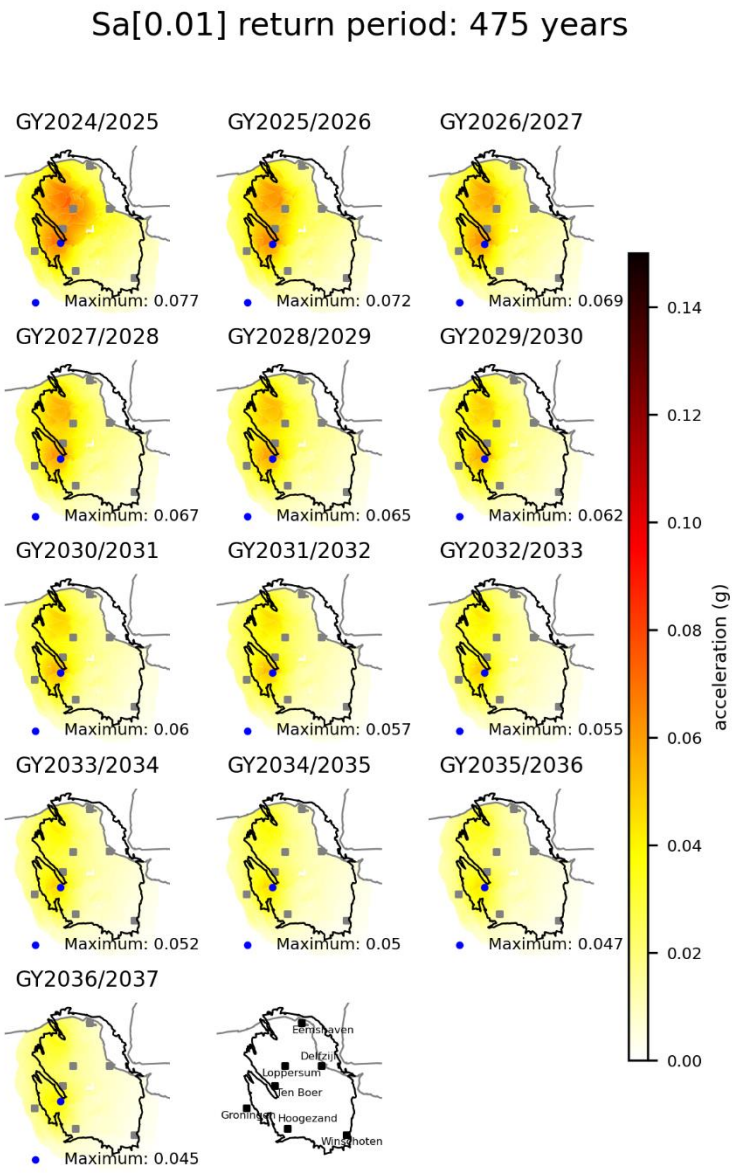

Figure 22: As Figure 21, except for the LO scenario

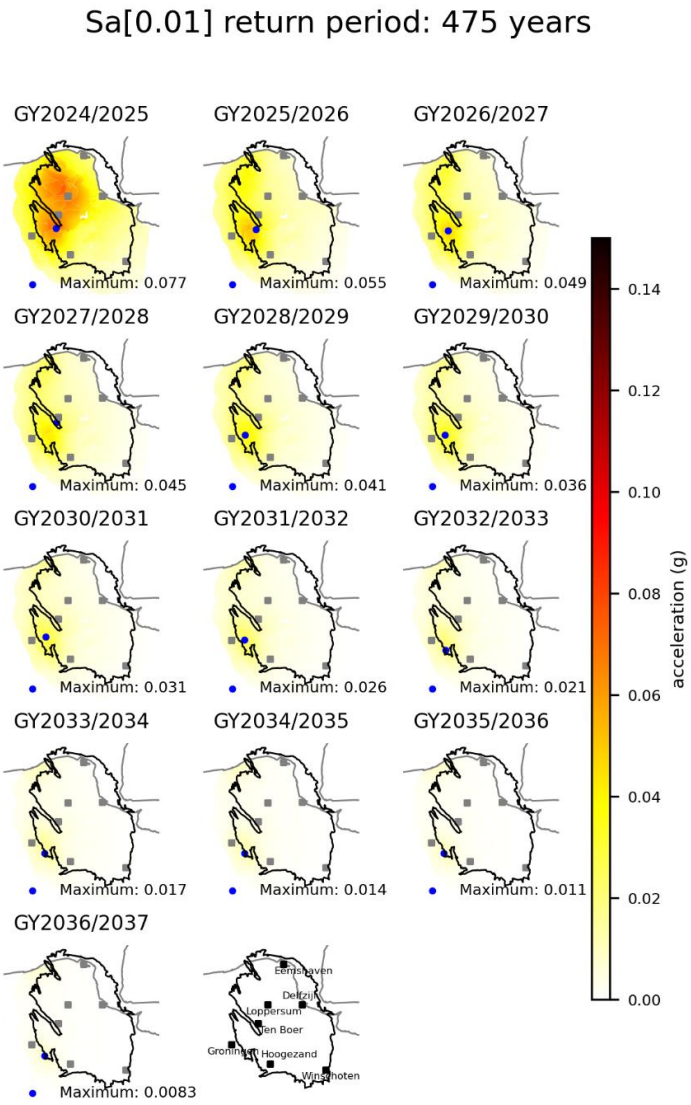

Figure 23: As Figure 21, except for the LO_10ZB scenario

In Appendix A, Figure 55 to Figure 67 show the risk exceedance curves for all gas years 2024/2025 until 2036/2037. Four of these figures are also shown below. Since the N_2 injection for all cases except the base case starts on 1 October 2025 (the first day of gas year 2025/2026), the risk is identical for all scenarios in gas year 2024/2025 (Figure 24). Over the subsequent years, we see a general reduction in the risk for all scenarios when compared to the base case. When N_2 is injected in the Loppersum area at a rate equivalent to the Zuidbroek II production capacity (1ZB), the number of buildings that do not conform to the safety norm (Local Personal Risk of 10^{-5} y^{-1} (Commisie Meijdam, 2015)) goes from ~500 to ~200 after 1 year of injection (Figure 25). The most pronounced reduction occurs when 10ZB is injected in the same area, resulting in a reduction to ~3 after only 1 year. However, if injection in this scenario is stopped after 7 years (when the expected event rate reaches zero), the number of buildings that don't conform to the safety norm goes back up to ~300 (Figure 26), due to the reappearance of seismicity associated with pressure redistribution in the gas reservoir. If the same volume of N_2 is modelled to be injected in the South-East clusters, the decline of seismic risk is less rapid. However, the increase in risk level associated with cessation of the N_2 injection is much less pronounced (Figure 27).

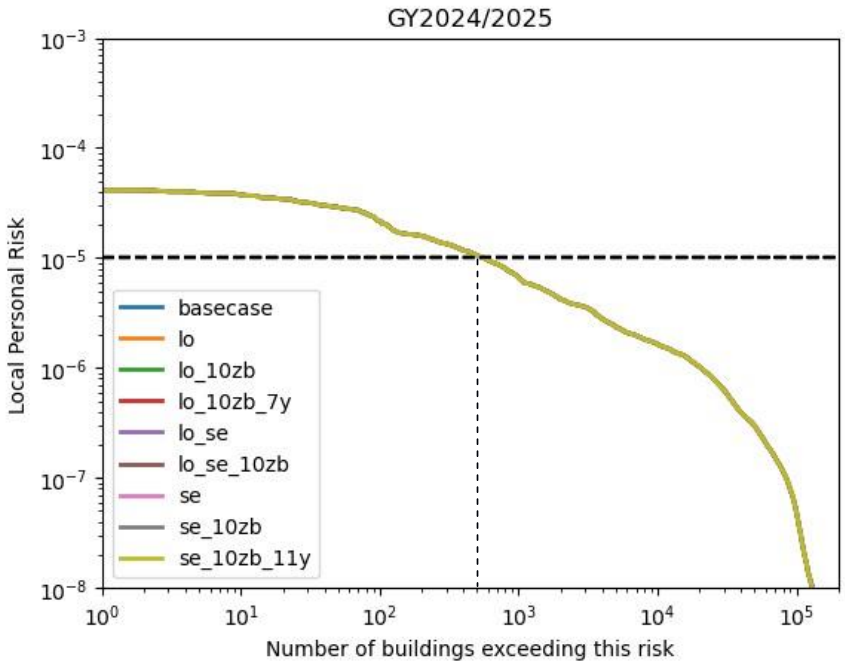

Figure 24: Risk exposure plot. Shows how many buildings (on the x-axis) are exposed to a given local personal risk (y-axis). Shows all scenarios considered for GY 2024/2025. Since N_2 injection starts on the 1st of October 2025 in all scenarios (1st day of gas year 2025/2026), the risk exposure is identical for all scenarios, leading to all the lines being on top of one another. Approximately 500 buildings exceed the Meijdam norm ($10^{-5}\,y^{-1}$) for all scenarios.

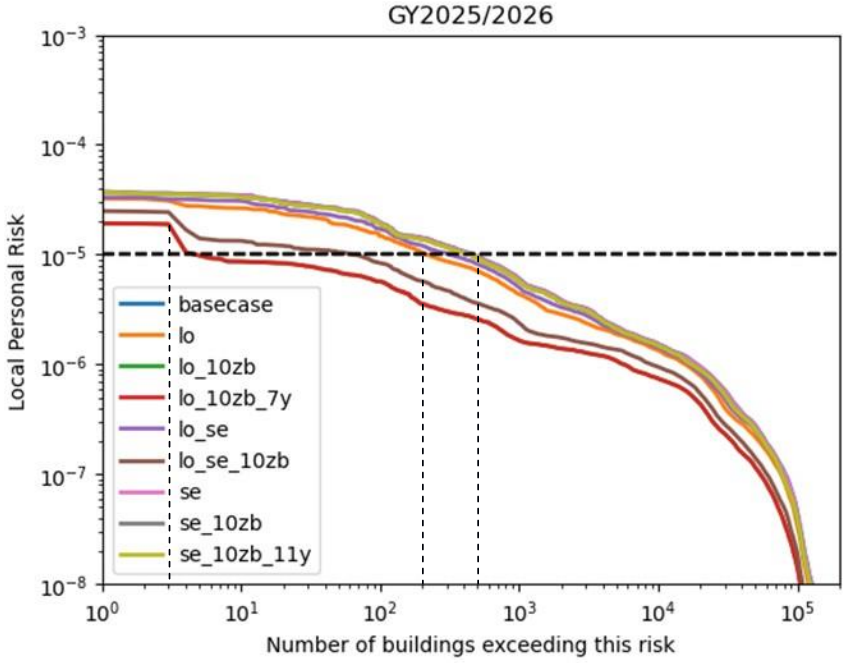

Figure 25: Risk exposure plot for GY 2025/2026. The risk profile decreases compared to previous year for all scenarios (including the base case), but with different amounts. For the scenarios where 10x the Zuidbroek II capacity of N_2 production is injected in the clusters around Loppersum (overlapping green and red curves), the number of buildings not conforming to the safety norm goes down to 3 buildings.

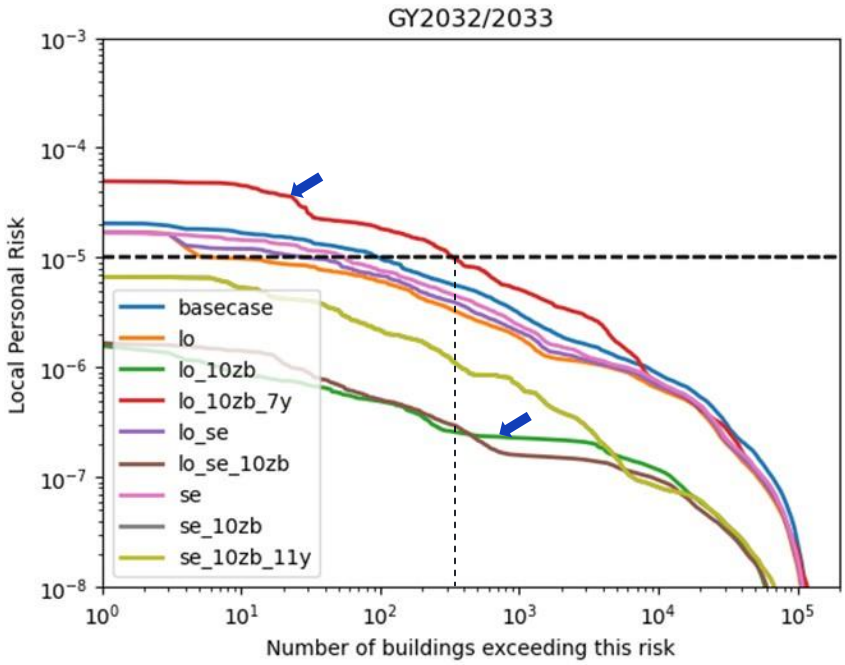

Figure 26: Risk exposure plot for GY 2032/2033. Note the large increase in risk for the lo_10zb_7y case, where nitrogen injection ceases on the 1 October 2032.

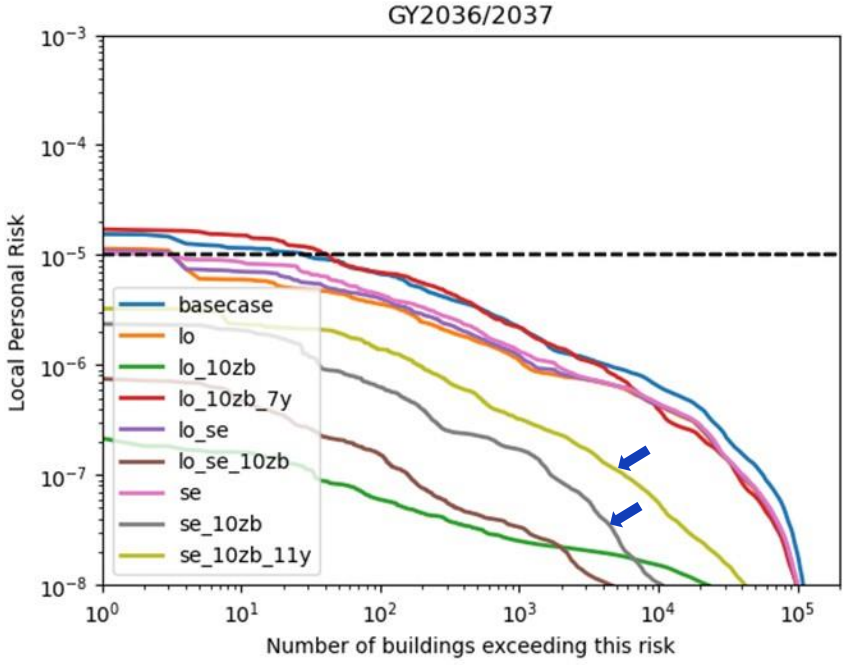

Figure 27 Risk exposure plot for GY 2036/2037. Note the increase of in risk for the se_10zb_11y case, where nitrogen injection ceases on the 1 October 2036. Despite the increase in risk, all buildings conform to the safety norm for this case.

4.5 Discussion and conclusions

Here, we have specifically investigated the potential positive effects of N_2 injection in the Groningen gas field on seismic event rate, seismic hazard, and seismic risk. We looked at two total volume scenarios to get a sense for the general response to different amounts of N_2 injection, and different spatial distributions, all under the assumption that the only effect of injection is on the gas pressure distribution, and that locally increasing the gas pressure leads to less seismicity at that location.

It is important to note that the seismic source model used in this study was developed with gas production in mind, and was calibrated on seismicity generated by gas production. As a result, the results obtained for different injection scenarios are automatically less well constrained. The source model may not include all physical mechanisms that are relevant in an injection scenario, and the model parameters are calibrated on a dataset that was collected when no gas injection was taking place. Nonetheless, these results give us first order indications on the effects of different quantities of N_2 injection, and the effects of the spatial distribution of that injection. In particular, they suggest that the potential positive effects of large-scale N_2 injection on both seismicity rate (the number of earthquakes per unit time) and seismic risk (the probability of loss of life due to seismicity) can be substantial compared to the 'no injection' base case.

For injection volume rates informed by estimated current N_2 production capacity (e.g. the LO scenario, in which 1x the annual nitrogen production capacity of the Zuidbroek II facility is injected in the Loppersum cluster) we see significant effects, both in terms of seismicity (Appendix A, Figure 29), hazard (Figure 22), and risk (Figure 25). For example, the number of buildings exposed to a risk level above the Meijdam norm (LPR $>10^{-5}$ y^{-1}) goes down from ~500 to ~200 after 1 year of injection, and to ~50 after 6 years of injection.

For the LO_10ZB scenario (inject 10 times the annual nitrogen production capacity of the Zuidbroek II facility in the Loppersum cluster), we see that the expected number of earthquakes of M1.5 and above goes down to zero after 7 years of injection (Figure 18). In the base case (no N_2 injection), the expected number of events does not reach zero at the end of our simulations (gas year 2053/2054) (Appendix A, Figure 28). For the LO_10ZB scenario, the number of buildings exposed to a risk level above the Meijdam norm (LPR $>10^{-5}$ y^{-1}) goes down to 3 after only 1 year of injection, while in the base case the number of exposed buildings remains ~500 (Figure 25; the blue line is hidden under the curves for the SE scenarios).

Injection scenarios that (partially) inject the nitrogen in the South-East clusters have less pronounced effects on seismicity, hazard, and risk on the short term, but potentially offer advantages on the longer term, since they reduce spatial gas pressure variability, and therefore are associated with less pressure equilibration once gas injection eventually ceases. In general, the injection scenarios modelled in this study are indicative of the approximate types of behaviour that can be expected under the set of modelling assumptions outlined at the beginning of this chapter. The scenarios represent broad classes of injection-related choices, mainly the injection volume/rate and spatial distribution of the injected N_2.

5 Explore seismic source model adjustments

5.1 Introduction

In this chapter, we investigate changes that can be made to the current seismic source model to include the potentially destabilizing (seismicity enhancing) effects related to nitrogen injection. Nitrogen injection causes pressure increase and temperature decrease in the reservoir. Although in general, induced seismicity can be caused by injection (e.g. fracking, wastewater disposal, Enhanced Geothermal Systems), in this case we do not expect significant effects of the pressure increase due to nitrogen injection on seismicity for the following reasons:

- The Groningen reservoir rock is very permeable, leading to modest near-well pore pressure increase when injecting (i.e. the near well pressure is reasonably well represented by the large-scale reservoir simulations). In fact, in our simulations, the bottom hole pressure of injection wells and the grid block average pressure of grid blocks with an injection well differ less than 0.1 MPa (1 bar). We therefore do not expect local failure around the well due to the pressure increase.
- In the stress field of the Groningen gas field, pressure increase is expected to stabilize the faults.
- Injection would be mainly aimed at stopping pressure decrease, rather than substantially increasing pore pressures compared to their present state. Mild pore pressure increase is already seen in some parts of the Groningen gas field for years. In these areas, seismicity is largely absent, suggesting that the current source model actually captures the reservoir response to moderate pore pressure increase rather well.

On the other hand, reservoir cooling would be associated with a decrease in horizontal stress and associated destabilization of fault. We therefore focus our efforts on adjusting the theoretical framework to deal with temperature changes.

The current source model is based on linear poroelasticity. We explore the theoretical foundations of linear poroelasticity with thermal effects in conjunction with its implementation on the model chain, to further examine their combined impact on induced seismicity.

5.2 Description of adjustments

Theory of linear poroelasticity combined with thermal effects: Linear poroelasticity describes the behavior of fluid-saturated porous materials under small deformation. It is based on principles such as conservation of mass, which ensures fluid balance within the pores, and conservation of momentum, which considers the balance of internal and external forces. The effective stress, according to Terzaghi's principle, is defined as the total stress minus the pore fluid pressure. Constitutive relations in this theory link stress σ and strain ε in the material, taking into account the interplay between the solid matrix and fluid pressure P_p.

The theory sets the basis for understanding more complex phenomena when additional factors like thermal effects are included. When thermal effects are incorporated, the theory extends to linear thermo-poroelasticity, addressing the thermal expansion/contraction of the solid matrix due to spatio-temporal variations in the temperature. Thus, the system of equations in index notation describing linear poroelasticity combined with thermal effects reads (Fjaer et al. 2008)

$$\sigma_{ij} = \frac{Ev}{(1+v)(1-2v)}\varepsilon_{vol}\delta_{ij} + \frac{E}{1+v}\varepsilon_{ij} + \alpha P_p \delta_{ij} + \frac{E}{1-2v}\alpha_T \Delta T \delta_{ij} \quad (1)$$

Where E, v, α, and α_T are the Young modulus, Poisson's ration, Biot's coefficient and linear thermal expansion coefficient, respectively. In the context of the model chain framework, ΔT is an input variable obtained from reservoir simulations that accounts for the spatio-temporal variations in the temperature field as fluid injection/production occur.

Uniaxial Strain Conditions

The seismic source model is based on uniaxial strain conditions, where strain is applied only in the vertical direction. This approach simplifies the material's response by focusing the analysis on stress and strain relations along the horizontal plane. Consequently, Equation (1) is rewritten to reflect changes in vertical and horizontal stresses as follows:

$$E\varepsilon_H = \Delta\sigma_H - v(\sigma_h + \sigma_v) - (1-2v)\alpha\Delta P_p - E\alpha_T\Delta T \quad (2.a)$$
$$E\varepsilon_h = \Delta\sigma_h - v(\sigma_H + \sigma_v) - (1-2v)\alpha\Delta P_p - E\alpha_T\Delta T \quad (2.b)$$
$$E\varepsilon_v = \Delta\sigma_v - v(\sigma_H + \sigma_h) - (1-2v)\alpha\Delta P_p - E\alpha_T\Delta T \quad (2.c)$$

With $\varepsilon_H = \varepsilon_h = 0$ under uniaxial strain conditions, the system simplifies further

$$\Delta\sigma_H = \Delta\sigma_h = \frac{1-2v}{1-v}\alpha\Delta P_p + \frac{H(1-2v)(1+v)}{(1-v)^2}\alpha_T\Delta T \quad (3.a)$$
$$\varepsilon_v = -\frac{1}{H}\alpha\Delta P_p - \frac{(v+1)}{(1-v)}\alpha_T\Delta T \quad (3.b)$$

Here, we assume $\Delta\sigma_v = 0$, because the vertical stress remains constant due to the constant weight of the overburden layers. For convenience, Equation (3.a) and (3.b) are expressed in terms of the uniaxial compaction modulus H. The uniaxial compaction modulus H is a measure of the material's stiffness under uniaxial strain conditions. The formula for the uniaxial compaction modulus H in terms of Poisson's ratio v and Young's modulus E is derived from the relationship between stress and strain under uniaxial conditions:

$$H = \frac{E}{(1-2v)(1+v)} \quad (4)$$

This relation comes from the generalized Hooke's Law and reflects the effect of Poisson's ratio on volumetric strain under uniaxial loading.

In the context of the source model framework, the uniaxial compaction modulus is a spatially varying model parameter. In other words, the amount of strain for a given amount of pore pressure change is not spatially constant, due to the spatial heterogeneity of the reservoir rock's material properties. We deem it likely that this implies that the reservoir rock would also not respond homogeneously to a given change in temperature. Here, we relate the sensitivity of the vertical strain to temperature change (given by α_T) to the uniaxial compaction modulus H.

An important feature to pay attention to is the relationship between the material stiffness E and the thermal expansion coefficient α_T. Generally, the stiffer the material, the less it expands or contracts with temperature changes. This trend is primarily due to stronger atomic or molecular bonds in stiffer materials, which resist deformation under both mechanical and thermal stresses. According to Le Bourhis (2014), there exists an inverse relationship between the thermal expansion coefficient (α_T) and Young's modulus (E). This relationship is expressed in terms of the uniaxial compaction coefficient as follows:

$$\alpha_T = \frac{a_T}{H} \tag{5}$$

where a_T is a new model parameter that has to be calibrated within the seismic source model. A prior range for this parameter could be defined based on the known range of α_T in Rotliegend sandstone rocks, and the range of values for H that are used in the current implementation of the seismic source model. Further calibration of the parameter a_T would have to be based on observations of either seismicity (or lack thereof) or subsidence, in combination with actual cold fluid injection and non-isothermal reservoir modelling.

5.3 Potential for further work

The updated source model could be implemented in the TNO Model Chain for Groningen, although the specifics depend on a number of factors:

- First of all, the currently derived method for including the effects of temperature change depends on a linearly elastic reservoir model. The model currently used for hazard and risk assessments (pSDRSA 2023) is in fact linearly elastic, but TNO has recommended including a non-linear rate-type compaction branch in the source model. Adding temperature effects to the rate-type implementation would be non-trivial.
- The calibration framework would have to deal with an additional parameter (a_T). We do not foresee that this would result in computational difficulties, even for the current 'brute-force' grid evaluation that is used for characterization of the parameter space.
- The model would have to be provided with a temperature forecast. These can be provided by reservoir simulators like Eclipse. To ensure that near-well effects are captured, it may be necessary to perform local grid refinement on the flow grids around the wells. Including a non-regular grid in the source model would require an additional update of the source model and some parts of the hazard and risk chain.

All in all, it appears feasible to update the linearly elastic source model to include temperature effects. Such a model could be calibrated in theory, although in practice this would require actual nitrogen injection (or at the very least temperature changes) to be performed. However, as stated above, we expect that the prior range of the new model parameter a_T can be relatively well-constrained based on existing data, suggesting that it may be possible to capture a range of expected outcomes in terms of seismicity to be calculated without further calibration.

5.4 Conclusions

We have discussed the theoretical basis for expanding the current linearly elastic seismic source model. Rather than assuming a single value for the thermal expansion coefficient, we have explored the connection between the thermal expansion coefficient and the uniaxial compaction modulus to include the expected spatially heterogenous impact of temperature on strains throughout the gas field. We expect that these alterations can be implemented in the TNO Model chain for Groningen, although not for more complicated compaction models such as rate-type compaction. Once implemented, forecasts that include the effect of temperature change could be produced, although they would necessarily be based on prior assumptions for the new model parameter a_T until this parameter can be calibrated on observed seismicity (or lack thereof) in combination with actual induced temperature changes in the reservoir.

6 Conclusions and recommendations

KEM-24b aimed to address the following research questions:

1. What can be learned from examples of fluid (including gas) injection in reservoirs similar to the Groningen reservoir?
2. Which injection scenarios for mitigating seismicity could be applied after production has stopped?
3. How can the existing Groningen SHRA (Seismic Hazard and Risk Assessment) model chain be adapted to include fluid injection?
4. What is the potential beneficial effect of fluid injection on the overall seismicity, seismic hazard and seismic risk?

Based on a literature review, we conclude that large-scale injection aimed at reducing seismicity in a previously heavily depleted gas field has not been done elsewhere. We judge that the closest analogous cases to the Groningen case (in terms of pressure history, expected possible geomechanical failure mechanisms, injection depth, and reservoir properties) are Dutch Underground Gas Storage (UGS) facilities. However, the relevance of these analogue cases for the Groningen case is limited, since UGS facilities are cyclically pressurized to pressures much higher than the depletion pressure and then depressurized again when the gas is produced. This is different from possible nitrogen injection in Groningen, where the goal would simply be to stop local pressure decrease wherever this is likely to result in seismicity, rather than large-scale re-pressurization as seen in UGS operations.

In this study, we specifically investigated the beneficial effects on seismic event rate, seismic hazard, and seismic risk associated with re-pressurization by N_2 injection in the Groningen gas field. We looked at two volume scenarios (1ZB and 10ZB) to get a sense for the general response to different amounts of N_2 injection, and different spatial distributions, all under the assumption that the only effect of injection is on the gas pressure distribution, and that locally increasing the gas pressure leads to less seismic activity at that location.

It is important to note that the seismic source model of the existing Groningen SHRA (Seismic Hazard and Risk Assessment) model chain used in this study was developed with gas *production* in mind, and was calibrated on seismicity generated by gas production. As a result, the results obtained for different *injection* scenarios are automatically less well constrained. The source model does not include all physical mechanisms that may be relevant in an injection scenario, especially those associated with temperature changes, and the model parameters are calibrated on a dataset that was collected when no gas injection was taking place. Nonetheless, we argue that this study should provide first order indications on the effects of different quantities of N_2 injection, and the effects of spatial distribution.

The model experiments suggest that, if gas volumes similar to the capacity of the Zuidbroek II nitrogen generation facility were available for large-scale injection, the positive effects on both seismicity rate (the number of earthquakes per unit time) and seismic risk (the probability of loss of life due to seismicity) could be substantial already after a single year of injection, when compared to the 'no injection' base case. In one scenario, the number of buildings exposed to a risk level above the Meijdam norm is reduced from approximately 500 after 1 year without injection to approximately 200 after 1 year of gas injection. Without injection this takes about 5 years. The effectiveness of injection depends on both the injection location and the total injected volume. The variability of seismic hazard and risk results between scenarios with the same amount of injected gas shows that there is room for optimization of spatial and temporal distribution of gas injection over the available wells. Further exploring this aspect was not part of the scope of this project. We have also not explored how a long-term injection strategy could be developed that includes eventually ending the N_2 injection. Such an 'exit-strategy' is clearly needed, as infinite injection in unfeasible from many perspectives, including physical considerations.

Although the current analyses only highlight positive effects of injection, we have discussed the theoretical basis for expanding the current seismic source model. We have explored the connection between the thermal expansion coefficient and the uniaxial compaction modulus to include the expected spatially heterogenous impact of temperature on strains throughout the gas field. We expect that these alterations can be implemented in the TNO Model chain for Groningen, although not (at least not in their current form) for more complicated compaction models such as rate-type compaction. Once implemented, forecasts that include the effect of temperature change could be produced, although they would necessarily be based on prior assumptions until the updated model can be calibrated with (lack of) observed seismicity during actual N_2 injection.

The results of this study suggest a number of possible further steps that could answer issues of both scientific and possibly practical interest:

- By incorporating the alterations suggested for the source model, it would be possible to study reservoir cooling effects as an additional driver of seismicity to the model.
- If the expected reductions in seismicity are judged to be valuable from either societal or economic perspective, the feasibility of the N_2 injection scenario's to minimize seismicity and seismic risk should be investigated in more detail. This would require collecting more detailed information about expected trends and fluctuations in the availability of N_2, and about the potential availability of wells and other infrastructure for transport and injection of N_2.
- Optimization of injection strategies can be done by numerical procedures that take costs and seismic risk into account as objectives (see e.g., Candela et al., 2022). Limitations posed by the available surface infrastructure could be included as constraints. Such an optimization exercise should consider how to adjust injection schemes to both decrease seismicity as rapidly as possible, while also reaching spatial pressure equilibrium within an acceptable timeframe.
- The usefulness of such follow-up activities should be based on an assessment of potential societal benefits, as could be done in a (Societal-)Cost-Benefit-Analysis (MKBA in Dutch).

References

Bommer, J.J., Stafford, P.J., Ruigrok, E., Rodriguez-Marek, A., Mtinalexis, M., Kruiver, P.P., Edwards, B., Dost, B., Van Elk, J. (2022) Ground-motion prediction models for induced earthquakes in the Groningen gas field, the Netherlands. J Seismol 26, 1157–118 https://doi.org/10.1007/s10950-022-10120-w

Bois, A.P., Mohajerani, M., Dousi, N. and Harms, S. (2013). Inducing earthquake by injecting water in a gas field: water-weakening effect. Society of Petroleum Engineers. http://doi.org/10.2118/166430-MS.

Buijze, L., Van Bijsterveldt, L., Cremer, H., Paap, B., Veldkamp, J.G., Wassing, B., Van Wees, J.-D., Van Yperen, G., Ter Heege, J., and Jaarsma, B., (2019). Review of induced seismicity in geothermal systems worldwide and implications for geothermal systems in the Netherlands. Netherlands Journal of Geosciences. 98. http://doi.org/10.1017/njg.2019.6.

Buijze L, Veldkamp H, Wassing B. (2023). Comparison of hydrocarbon and geothermal energy production in the Netherlands: reservoir characteristics, pressure and temperature changes, and implications for fault reactivation. *Netherlands Journal of Geosciences*;102:e7. http://doi.org/10.1017/njg.2023.6

Candela, T., C. Goncalves Machado, O. Leeuwenburgh, J. Ter Heege (2022). A physics-informed optimization workflow to manage injection while constraining induced seismicity: The Oklahoma case, Frontiers in Earth Science, 10:1053951. https://doi.org/10.3389/feart.2022.1053951

Cesca, S., Stich, D., Grigoli, F. *et al.* (2021). Seismicity at the Castor gas reservoir driven by pore pressure diffusion and asperities loading. *Nat Commun* **12**, 4783. https://doi.org/10.1038/s41467-021-24949-1.

Cesca, S., Stich, D., Grigoli, F. *et al.* (2022). Reply to: Multiple induced seismicity mechanisms at Castor underground gas storage illustrate the need for thorough monitoring. *Nat Commun* **13**, 3445 (2022). https://doi.org/10.1038/s41467-022-30904-5.

Cheng Y., W. Liu, T. Xu, Y. Zhang, X. Zhang, Y. Xing, B. Feng, Y. Xia, (2023). Seismicity induced by geological CO_2 storage: A review,Earth-Science Reviews, Volume 239, https://doi.org/10.1016/j.earscirev.2023.104369.

Commissie Meijdam (2015). Eindadvies Handelingsperspectief voor Groningen

Crowley, H., Pinho, R., Van Elk, J., Uilenreef, J., (2019) Probabilistic damage assessment of buildings due to induced seismicity. Bull. of Earthquake Eng. Volume 17, 4495-4516. https://doi.org/10.1007/s10518-018-0462-1

Davies, R., Foulger, G., Bindley, A., Styles, P. (2013). Induced seismicity and hydraulic fracturing for recovery of hydrocarbons. Mar Pet Geol 45:171–185.

Draganov, D., Naranjo, D., Polychronopoulou, K., and Weemstra, C. (2023). The potential of probabilistic moment-tensor inversions for the characterization of geothermal reservoirs in urban environments, EGU General Assembly 2023, Vienna, Austria, 24–28 Apr 2023, EGU23-14534, https://doi.org/10.5194/egusphere-egu23-14534.

Ellsworth, W. L. (2013). Science 341, 1225942, https://doi.org/10.1126/science.1225942.

Evans, K. F., A. Zappone, T. Kraft, N. Deichmann, F. Moia, (2012). A survey of the induced seismic responses to fluid injection in geothermal and CO_2 reservoirs in Europe. Geothermics 41, 30–54, https://doi.org/10.1016/j.geothermics.2011.08.002.

Foulger, G.R., Wilson, M.P., Gluyas, J.G., Julian, B.R., Davies, R.J. (2018). Global review of human-induced earthquakes. Earth Sci Rev. https://doi.org/10.1016/j.earscirev.2017.07.008.

Fugro (2022a). Effect of pressure maintenance by fluid injection on seismic risk (KEM24/IUC202003010) Umbrella Report A | 1020-169309.R01 01 | 30 September 2022.

Fugro (2022b). Effect of pressure maintenance by fluid injection on seismic hazard, Hazard analysis Report | KEM-24 Report C 172147-REP01-FNV_SHA_KEM24 03, September 2022.

Gasunie (1980). Physical properties of natural gas, NV Nederlandse Gasunie.

Grigoli, F. et al. (2017). Current challenges in monitoring, discrimination, and management of induced seismicity related to underground industrial activities: a European perspective. *Rev. Geophysics* **55**, 310–340.

KEM (2022). KEM-24 Research review, evaluation and interpretation of “Effect of pressure maintenance by fluid injection on seismic risk”.

KEM-19 (2022). KEM-19 Evaluation of post-abandonment fluid migration and ground motion risks in subsurface exploitation operations in the Netherlands – Phase 1, 1 July, 2022.

Kivi, I. R., Boyet, A., Wu, H., Walter, L., Hanson-Hedgecock, S., Parisio, F., and Vilarrasa, V. (2023). Global physics-based database of injection-induced seismicity, Earth Syst. Sci. Data, 15, 3163–3182, https://doi.org/10.5194/essd-15-3163-2023.

Mandal, R., Lui, S.K.Y. (2022). Interdependent effects of fluid injection parameters on triggered aseismic slip and seismicity. *Sci Rep* **12**, 20922. https://doi.org/10.1038/s41598-022-25239-6

McGarr, A. (2014). Maximum magnitude earthquakes induced by fluid injection. J Geophys Res Solid Earth 119:1008–1019. https://doi.org/10.1002/2013JB010597.

Mijnlieff, H.F (2020). Introduction to the geothermal play and reservoir geology of the Netherlands. *Netherlands Journal of Geosciences*. 2020;99:e2. http://doi.org/10.1017/njg.2020.2.

Muntendam-Bos A.G., Hoedeman G., Polychronopoulou K., Draganov D., Weemstra C., van der Zee W., Bakker R.R., and Roest H. (2022). An overview of induced seismicity in the Netherlands. Netherlands Journal of Geosciences, Volume 101, e1. https://doi.org/10.1017/njg.2021.14

NAM (2016). Groningen Pressure Maintenance (GPM) study – Progress report, February 2016.

NAM (2020). Seismic Hazard and Risk Assessment Groningen Field update for Production Profile GTS – raming 2020 March 2020, EP202003201727

NAM (2023a). Seismic threat assessment for Schoonebeek-Zechstein water injection. Report: EP202304200850, April 2023.

NAM (2023b). Groningen Dynamic Model update 2023. Report: EP202306200914.

Rubinstein, J.L. and Mahani, A.B. (2015). Myths and Facts on wastewater injection, hydraulic fracturing, enhanced oil recovery, and induced seismicity. Seismol Res Lett 86(4):1060–1067

Shapiro, S. A. and Dinske, C., 2009. Fluid-induced seismicity: pressure diffusion and hydraulic fracturing. Geophysical Prospecting 57: 301–310. https://doi.org/10.1111/j.1365-2478.2008.00770.x.

SodM (2023). Risico's voor mens en milieu door afvalstromen rondom injectielocatie Borgsweer, 30 mei 2023.

Suckale J. (2009). Induced seismicity in hydrocarbon fields. Adv Geophys 51:55–106.

TNO (2014). Literature review on injection-related induced seismicity and its relevance to nitrogen injection. TNO project report 2014 R11761, December 2014.

TNO (2015a). Injection-Related Induced Seismicity and its relevance to Nitrogen Injection: Description of Dutch field cases. TNO report 2015 R10906, November 2015.

TNO (2015b). Injection Related Induced Seismicity and its relevance to Nitrogen Injection: Modeling of geomechanical effects of injection on fault stability. TNO report 2015 R11259, November 2015.

TNO (2015c). Injection Related Induced Seismicity and its relevance to Nitrogen Injection: Main findings, recommendations and general guidelines. TNO report R11648, December 2015.

TNO (2022) Probabilistic Seismic Hazard and Risk Analysis in the TNO Model Chain Groningen. TNO 2022 R11052.

TNO (2023). [in Dutch] Publieke Seismische Dreigings- en Risicoanalyse Groningen gasveld 2023. TNO 2023 R10682.

TNO (2023b): https://github.com/TNO/SHRA-Groningen-seismic-source-model

TNO (2023c): https://github.com/TNO/SHRA-Groningen-hazard-risk-models

Vilarrasa, V., De Simone, S., Carrera, J. & Villaseñor, A. (2022). Multiple induced seismicity mechanisms at Castor underground gas storage illustrate the need for thorough monitoring. *Nat. Commun.*, https://doi.org/10.1038/s41467-022-30903-6.

Vörös R, Baisch S. (2022). Induced seismicity and seismic risk management – a showcase from the Californië geothermal field (the Netherlands). *Netherlands Journal of Geosciences*. 2022;101:e15. doi:10.1017/njg.2022.12

Warpinski, N.R., Du, J., Zimmer, U. (2012). Measurements of hydraulic-fracture-induced seismicity in gas shales. SPE Prod Oper 27:240–252.

Zang, A., Oye, V., Jousset, P., Deichmann, N., Gritto, R., McGarr, A., Majer, E., Bruhn D. (2014). Analysis of induced seismicity in geothermal reservoirs—an overview. Anal Induc Seism Geotherm Oper 52:6–21. https://doi.org/10.1016/j.geothermics.2014.06.005.996.

Zang, A., Zimmermann, G., Hofmann, H. *et al.* (2019). How to Reduce Fluid-Injection-Induced Seismicity. *Rock Mech Rock Eng* **52**, 475–493. https://doi.org/10.1007/s00603-018-1467-4.

Appendix A: Seismic hazard and risk assessment figures

Here we provide all figures related to the seismic hazard and risk assessment performed for all scenarios.

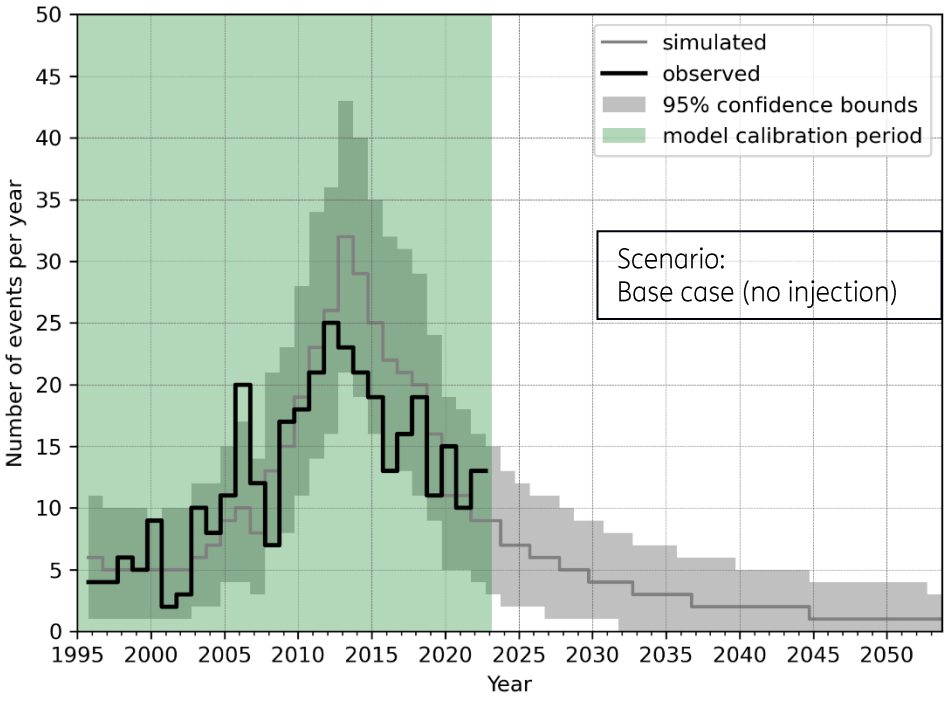

Figure 28: Number of events per year in the Groningen field of M1.5 and above. Base case (no N_2 injection). The solid grey line is the modelled expected number of events, the grey area gives the 95% confidence bounds per year. The solid black line is the data and the green area is the period over which the model is calibrated.

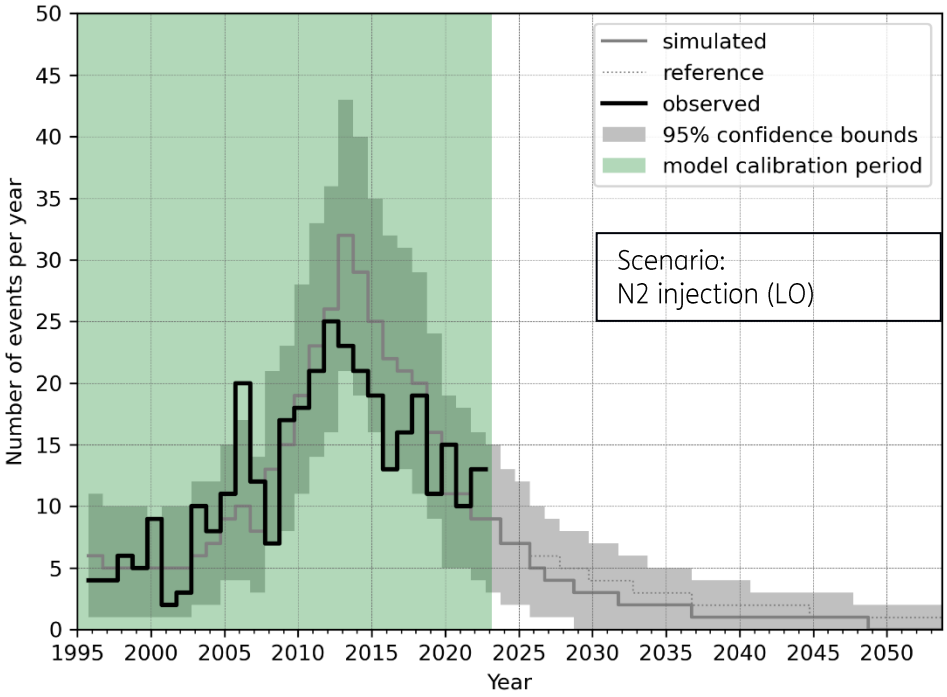

Figure 29: As Figure 28, except for the LO scenario. The dotted reference line represents the base case for comparison.

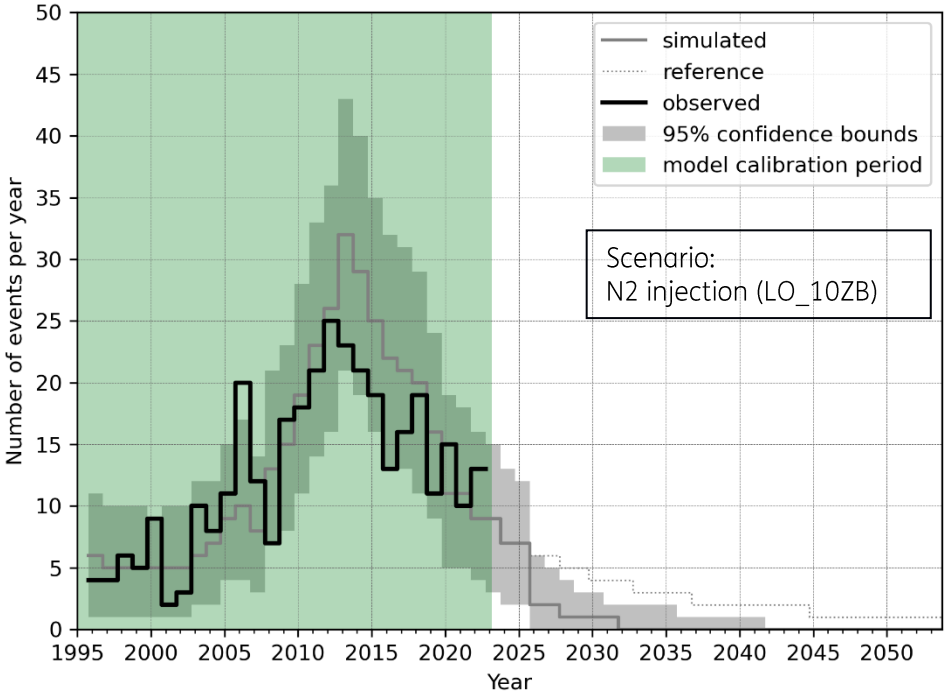

Figure 30: As Figure 28, except for the LO_10ZB scenario. The dotted reference line represents the base case for comparison.

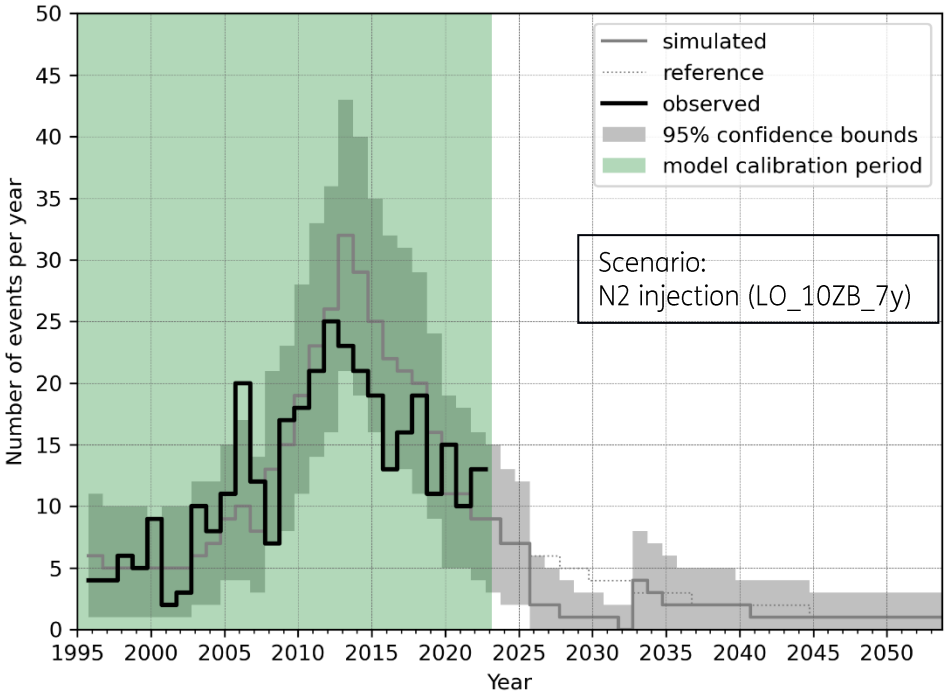

Figure 31: As Figure 28, except for the LO_10ZB_7y scenario. The dotted reference line represents the base case for comparison.

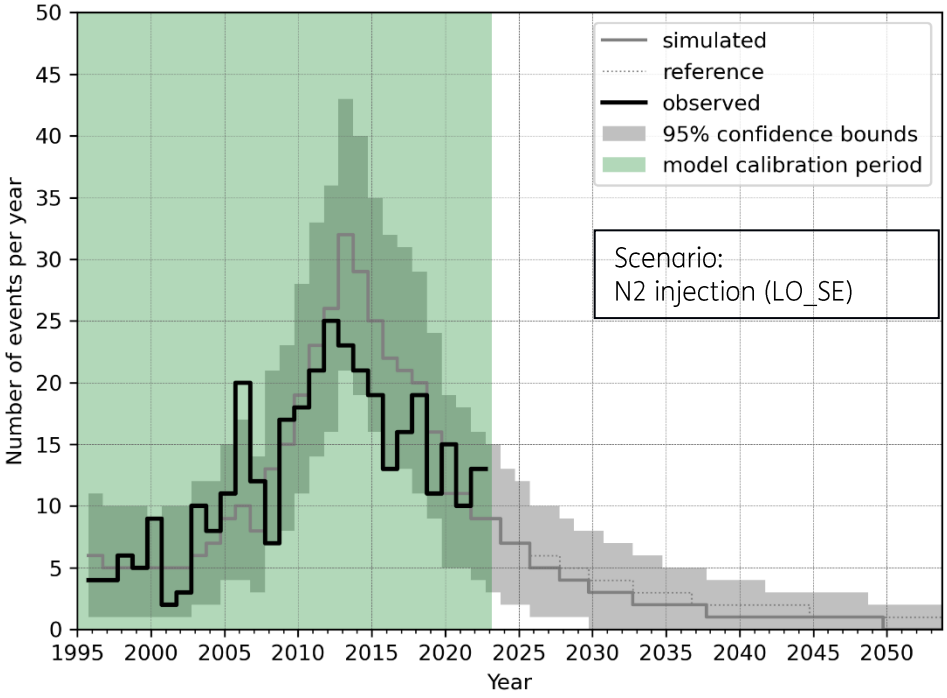

Figure 32: As Figure 28, except for the LO_SE scenario. The dotted reference line represents the base case for comparison.

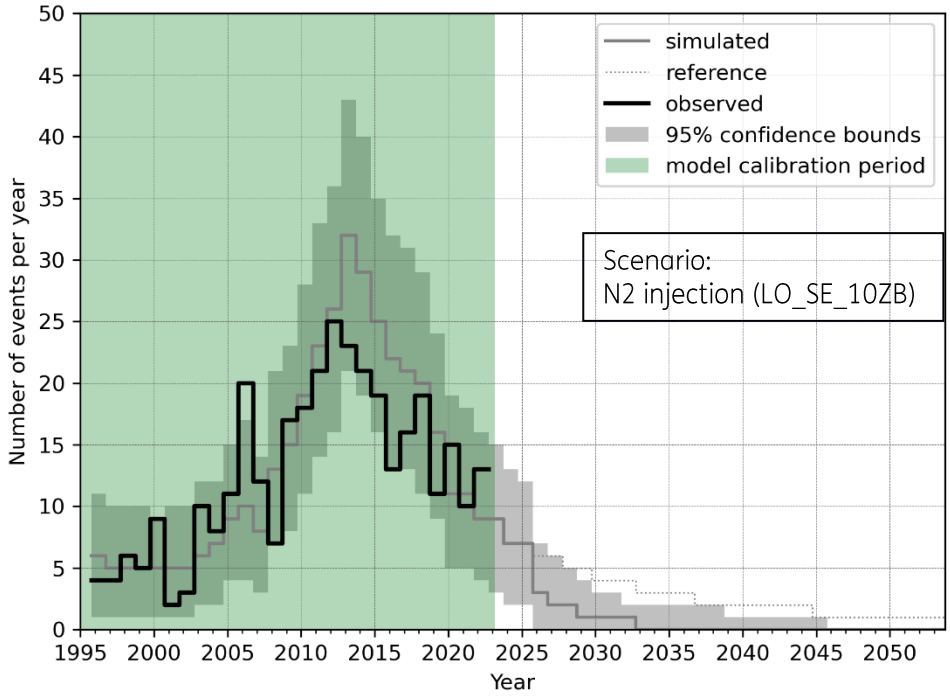

Figure 33: As Figure 28, except for the LO_SE_10ZB scenario. The dotted reference line represents the base case for comparison.

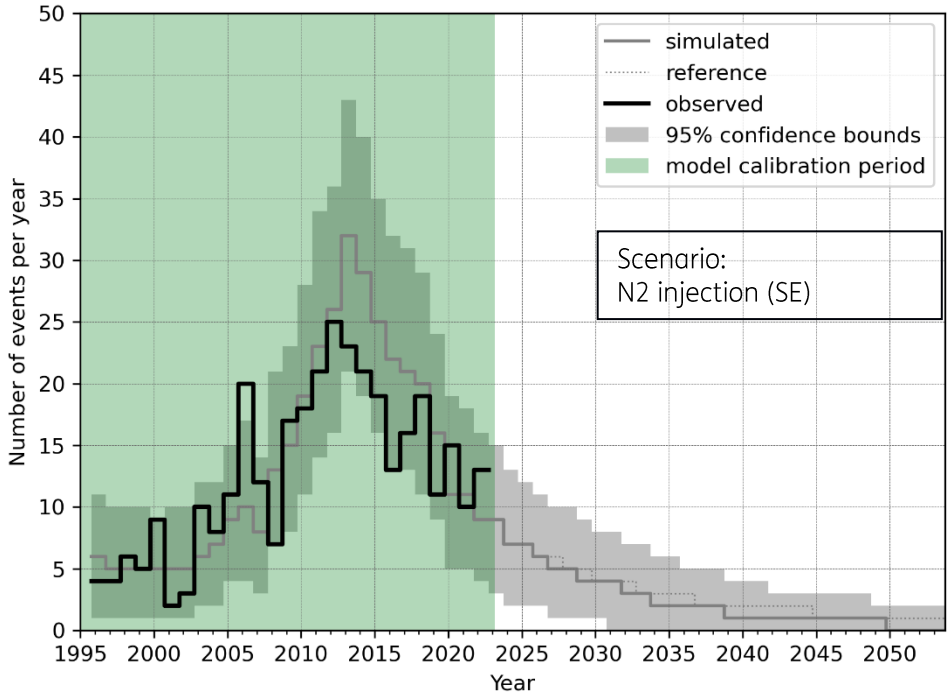

Figure 34: As Figure 28, except for the SE scenario. The dotted reference line represents the base case for comparison.

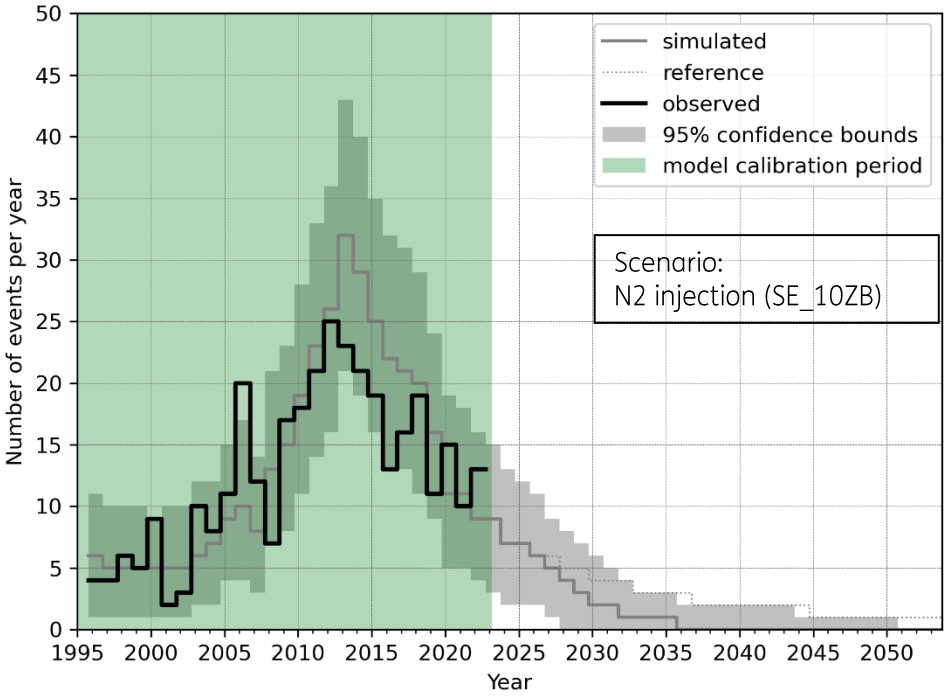

Figure 35: As Figure 28, except for the SE_10ZB scenario. The dotted reference line represents the base case for comparison.

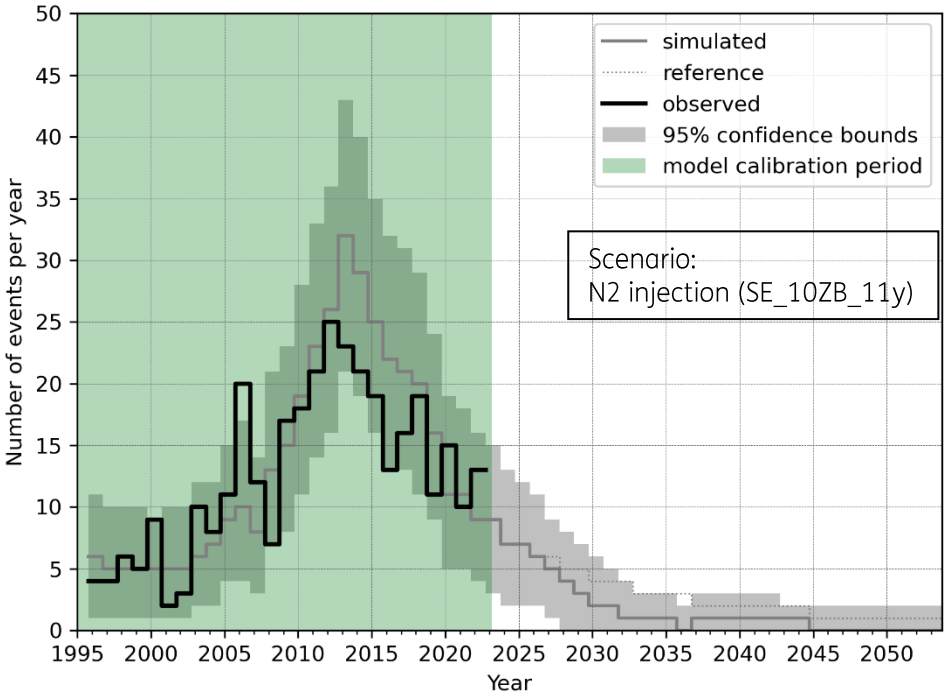

Figure 36: As Figure 28, except for the SE_10ZB_11y scenario. The dotted reference line represents the base case for comparison.

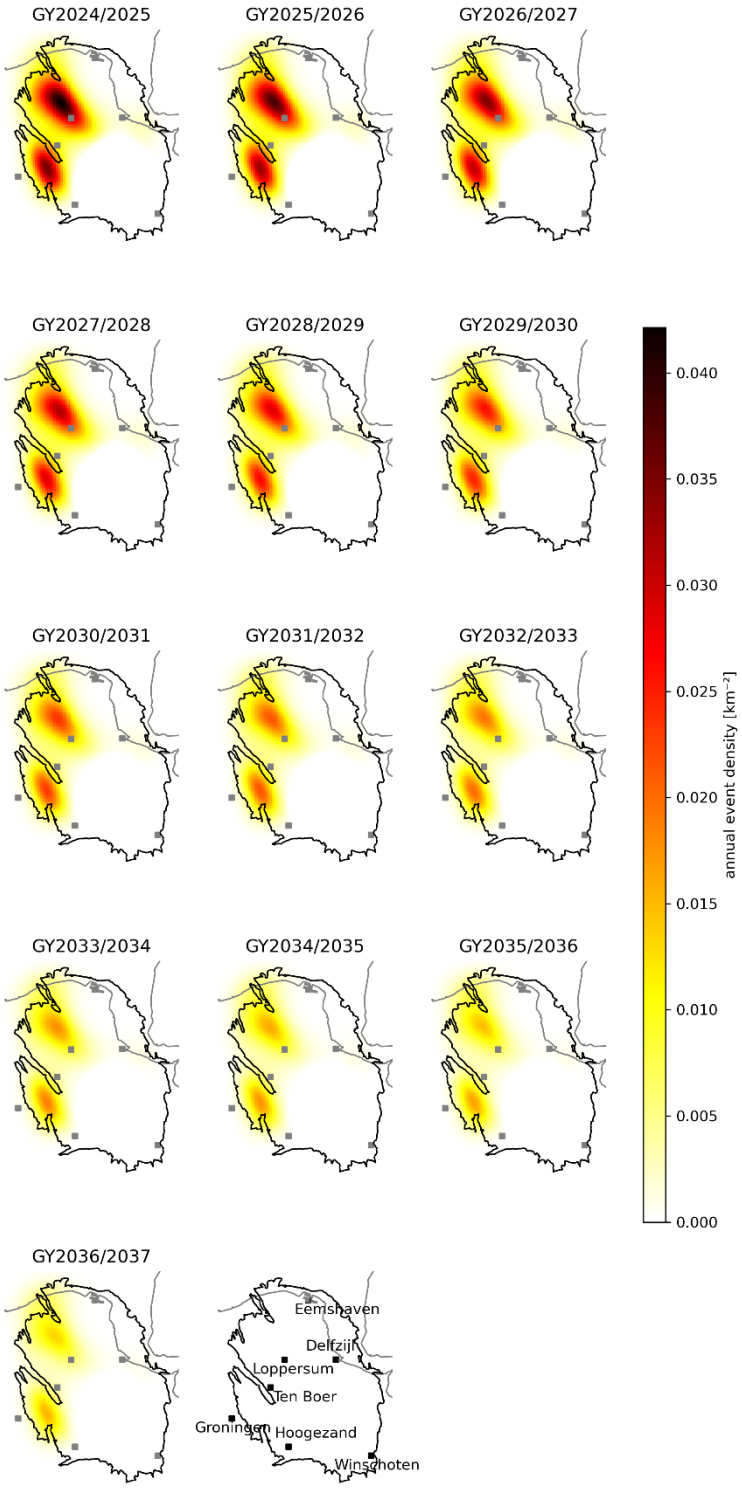

Figure 37: Annual spatial distribution of the seismicity for GY2024/2025 until GY2036/2037. The colour represents the annual expected number of events per square kilometre. Base case (no N_2 injection).

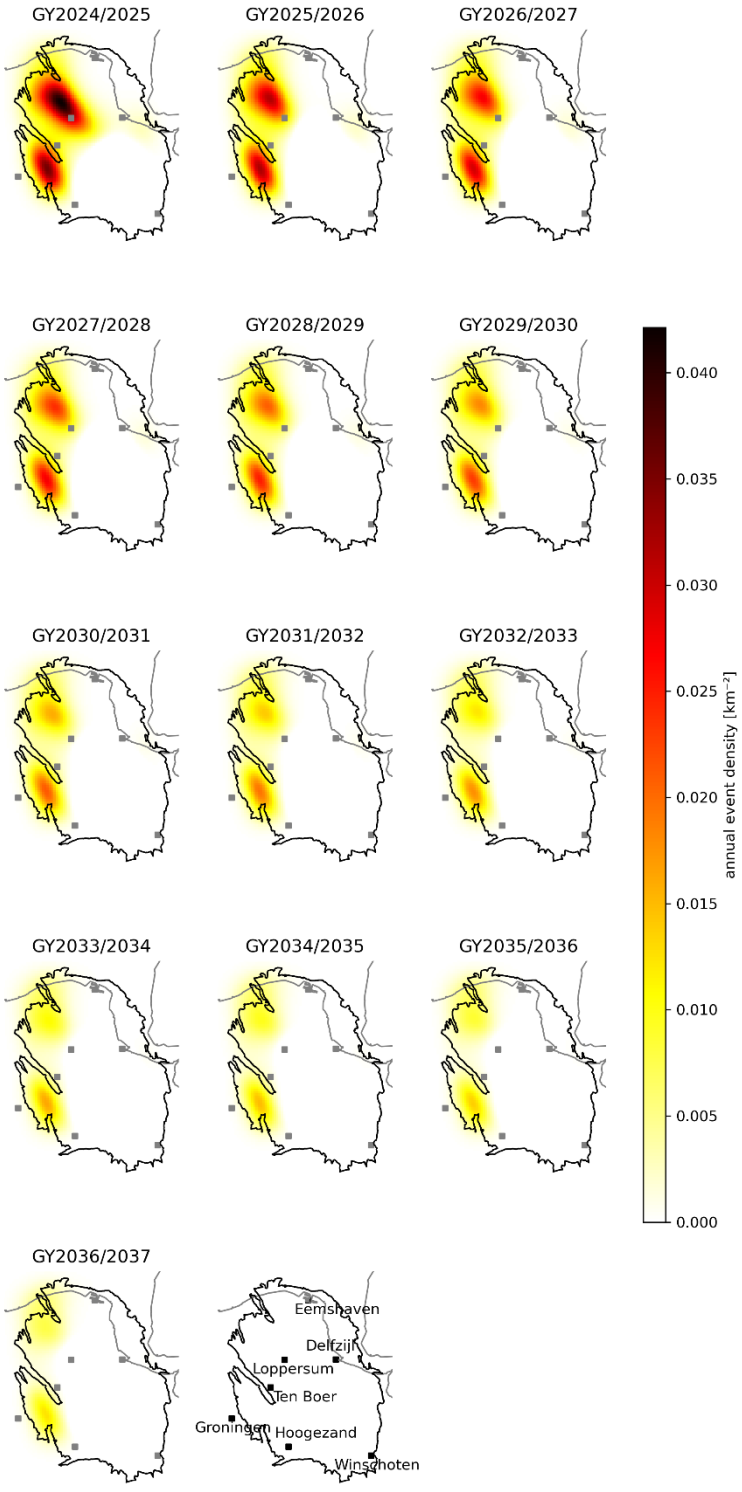

Figure 38: As Figure 37, except for the LO scenario

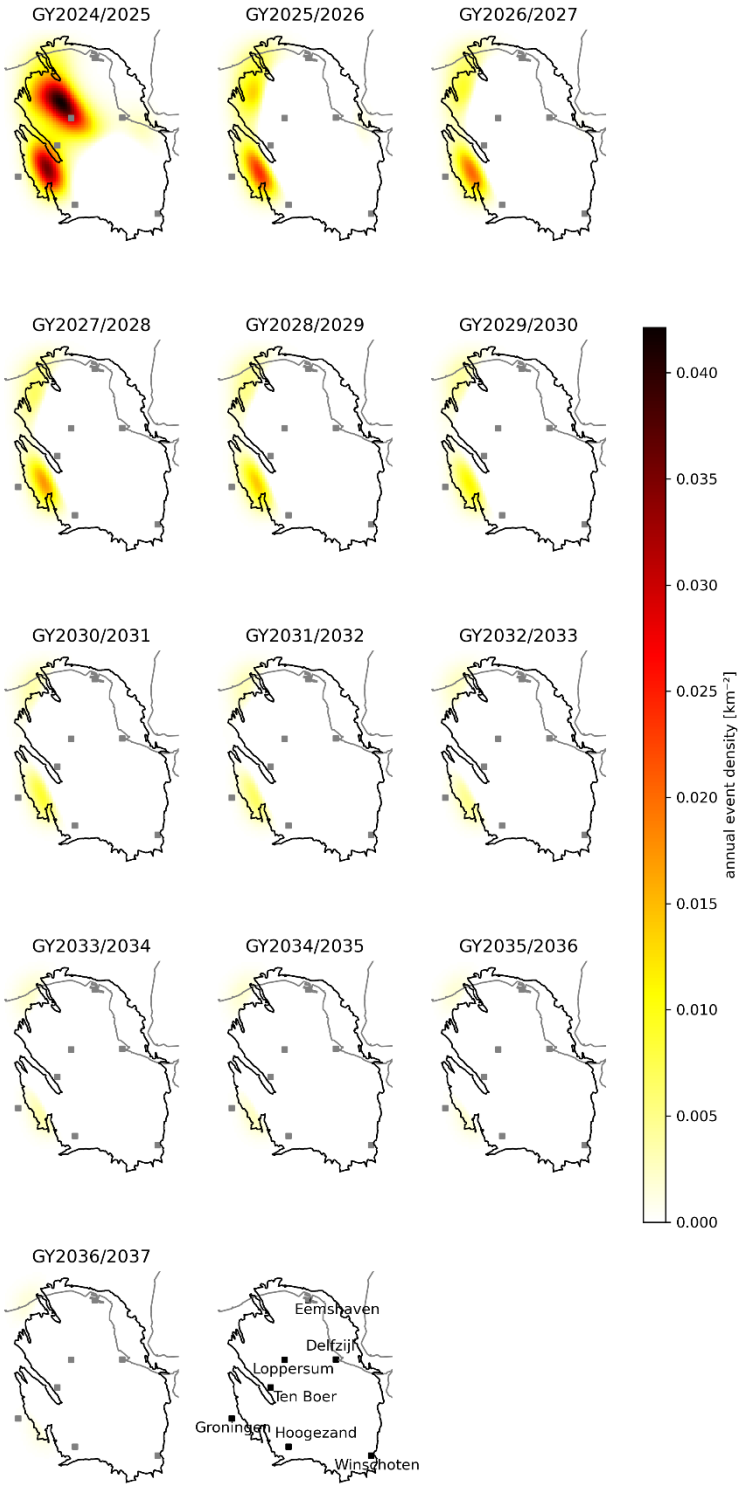

Figure 39: As Figure 37, except for the LO_10ZB scenario

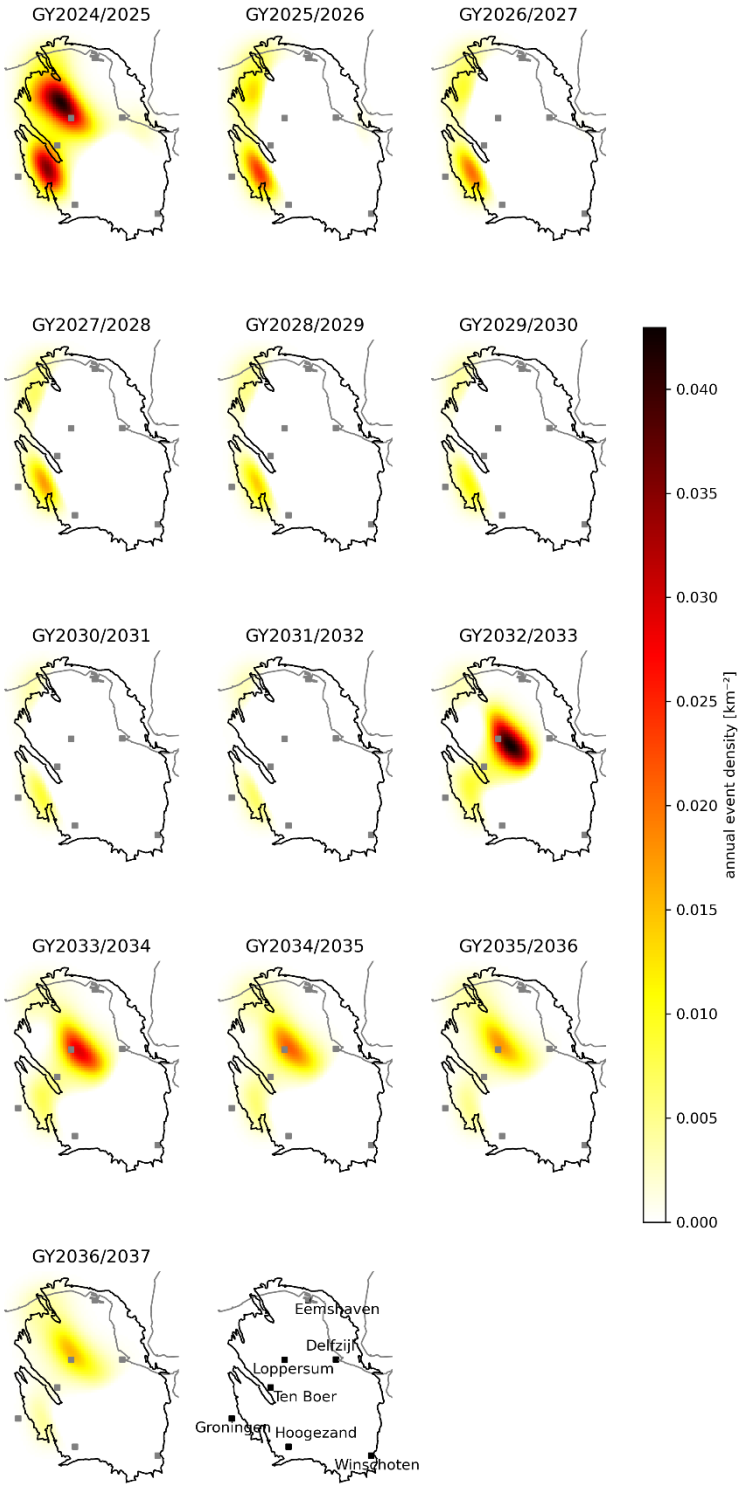

Figure 40: As Figure 37, except for the LO_10ZB_7y scenario

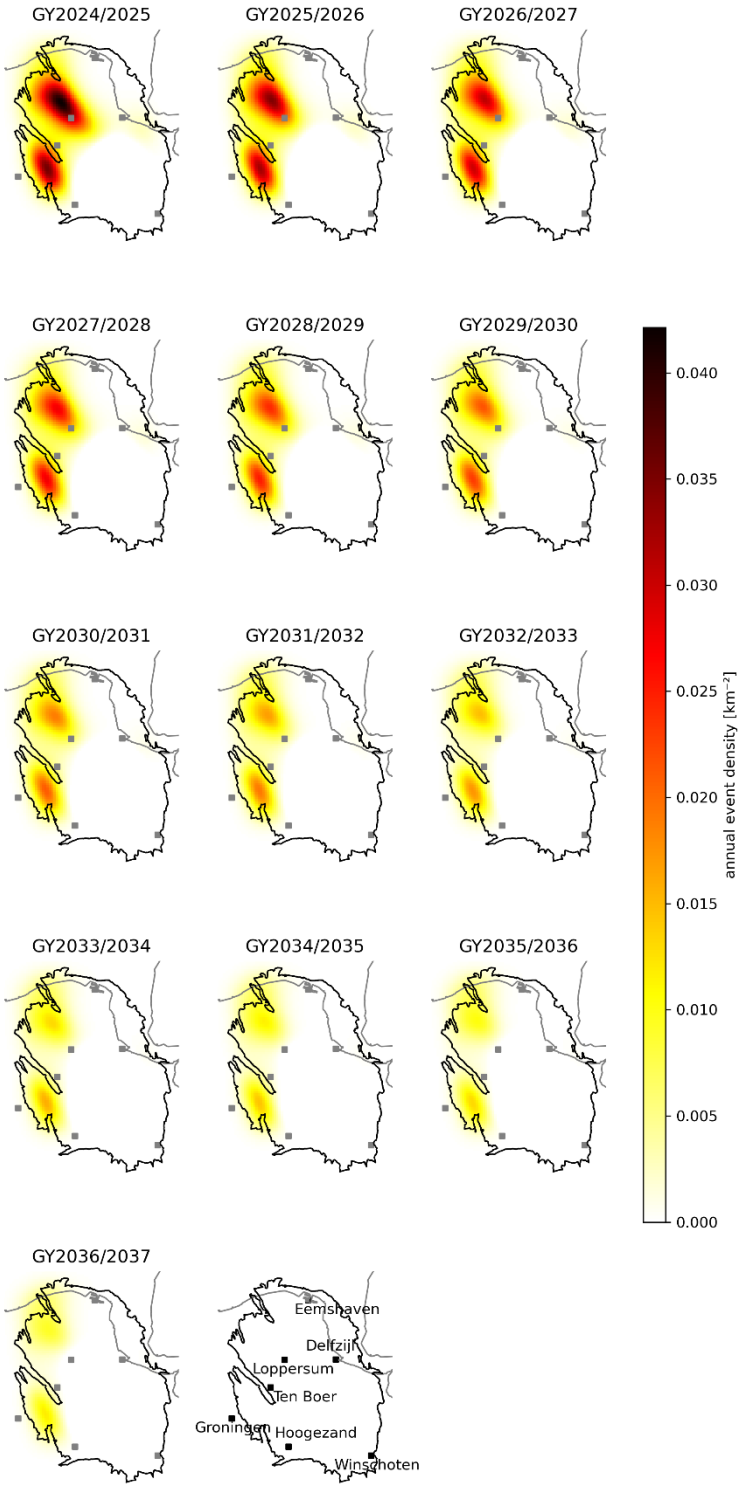

Figure 41: As Figure 37, except for the LO_SE scenario

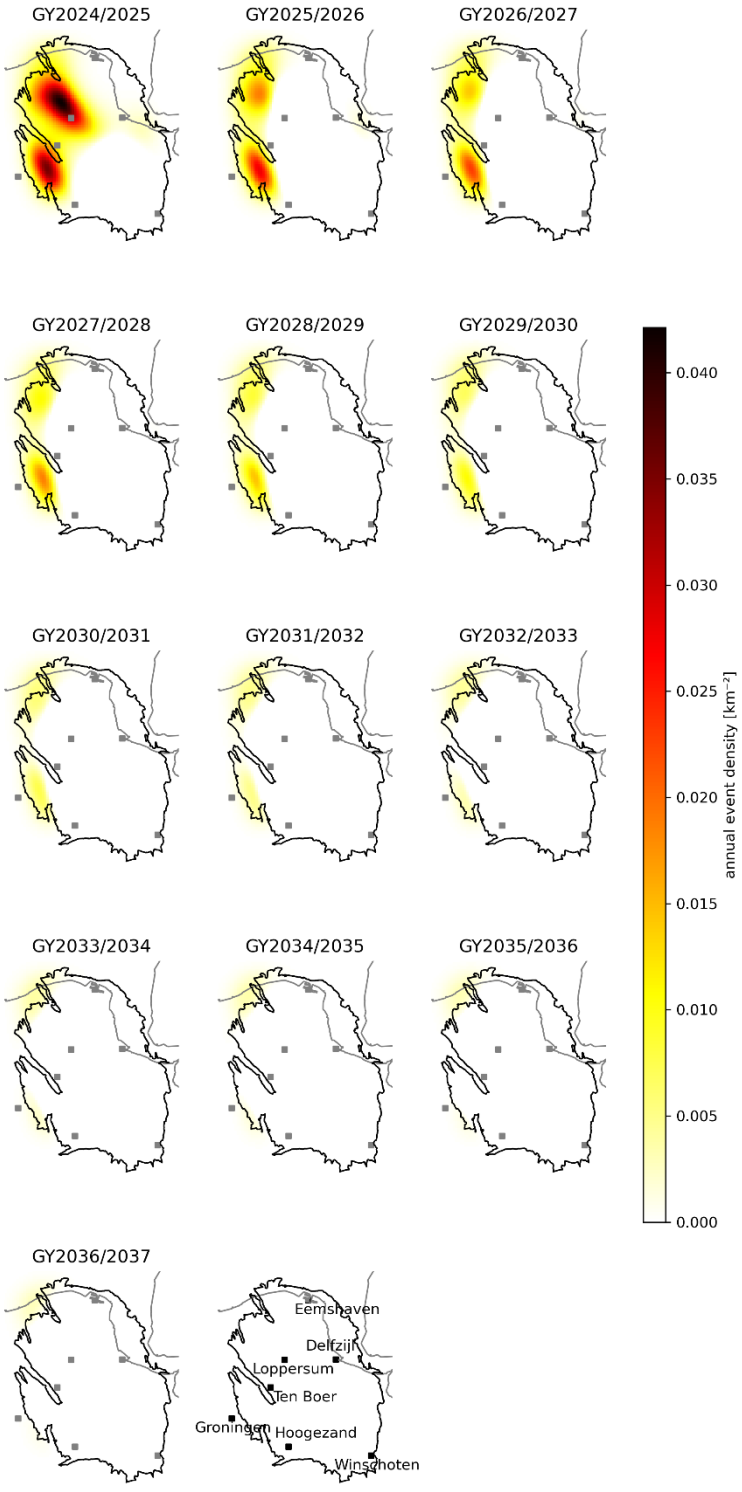

Figure 42: As Figure 37, except for the LO_SE_10ZB scenario

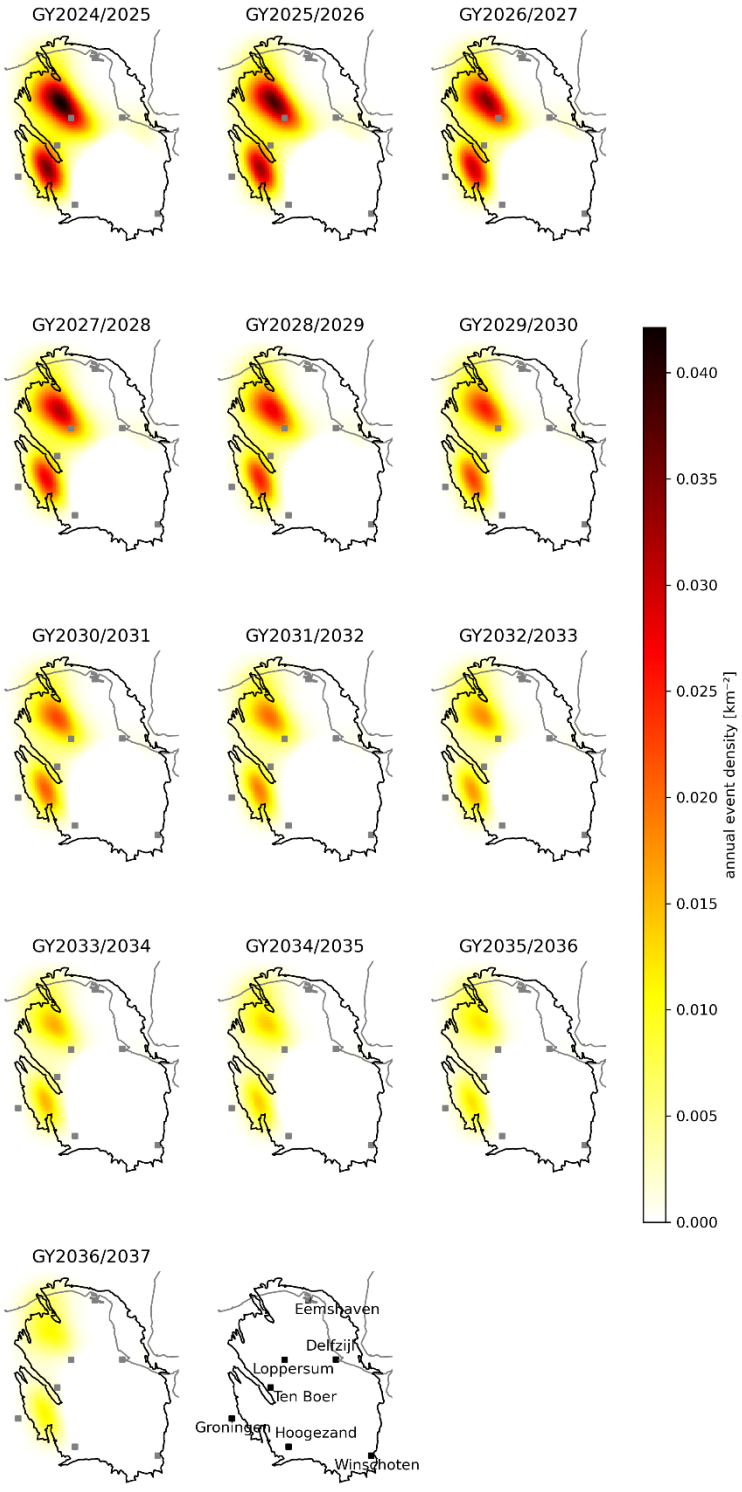

Figure 43: As Figure 37, except for the SE scenario

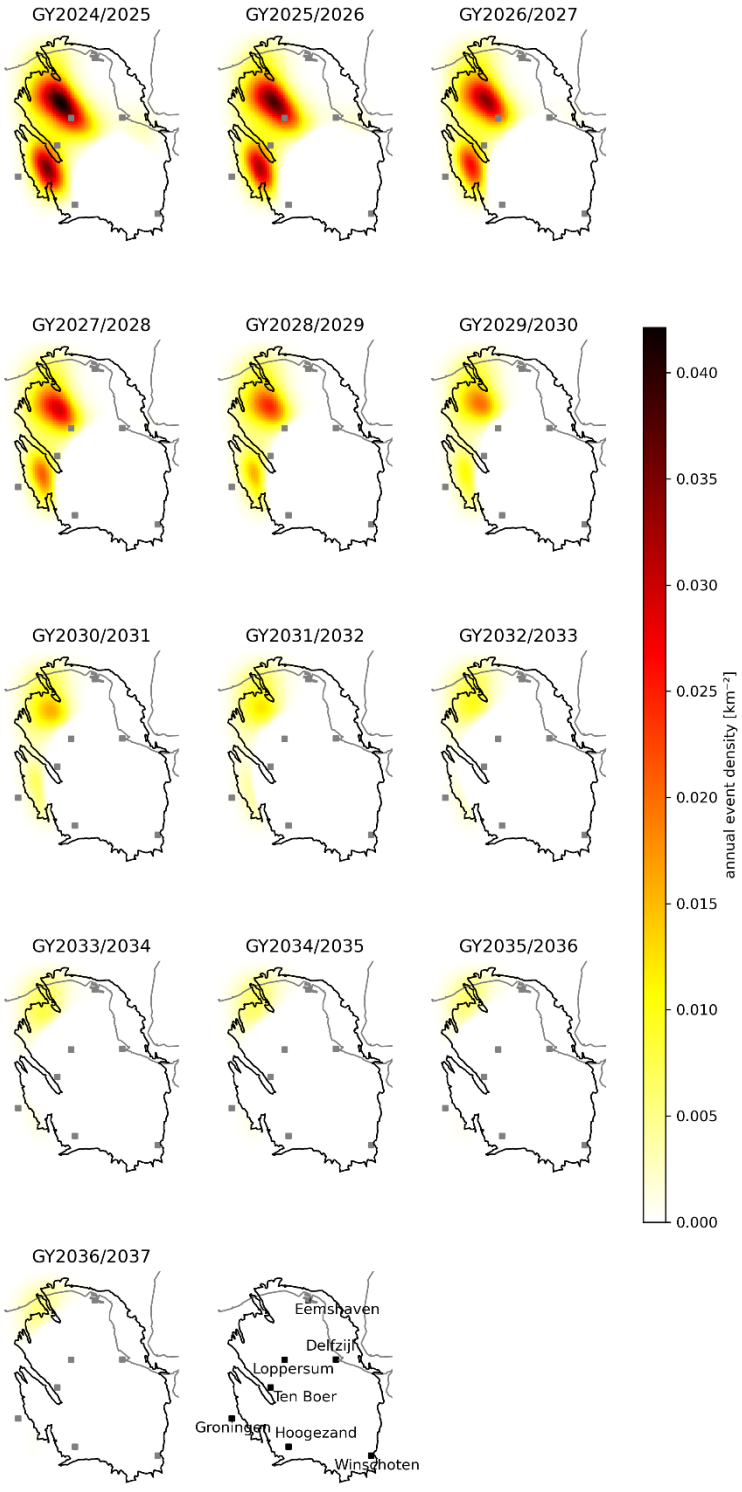

Figure 44: As Figure 37, except for the SE_10ZB scenario

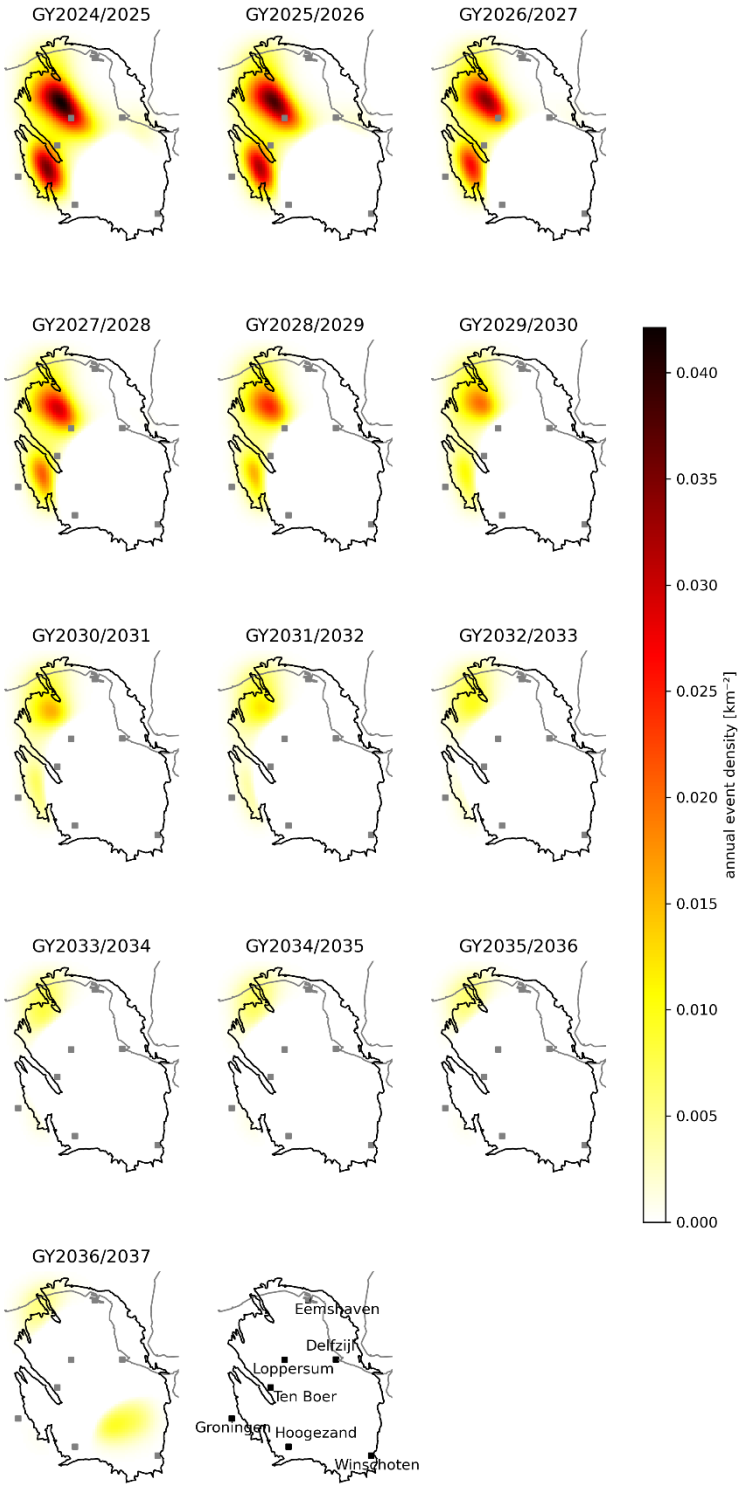

Figure 45: As Figure 37, except for the SE_10ZB_11y scenario

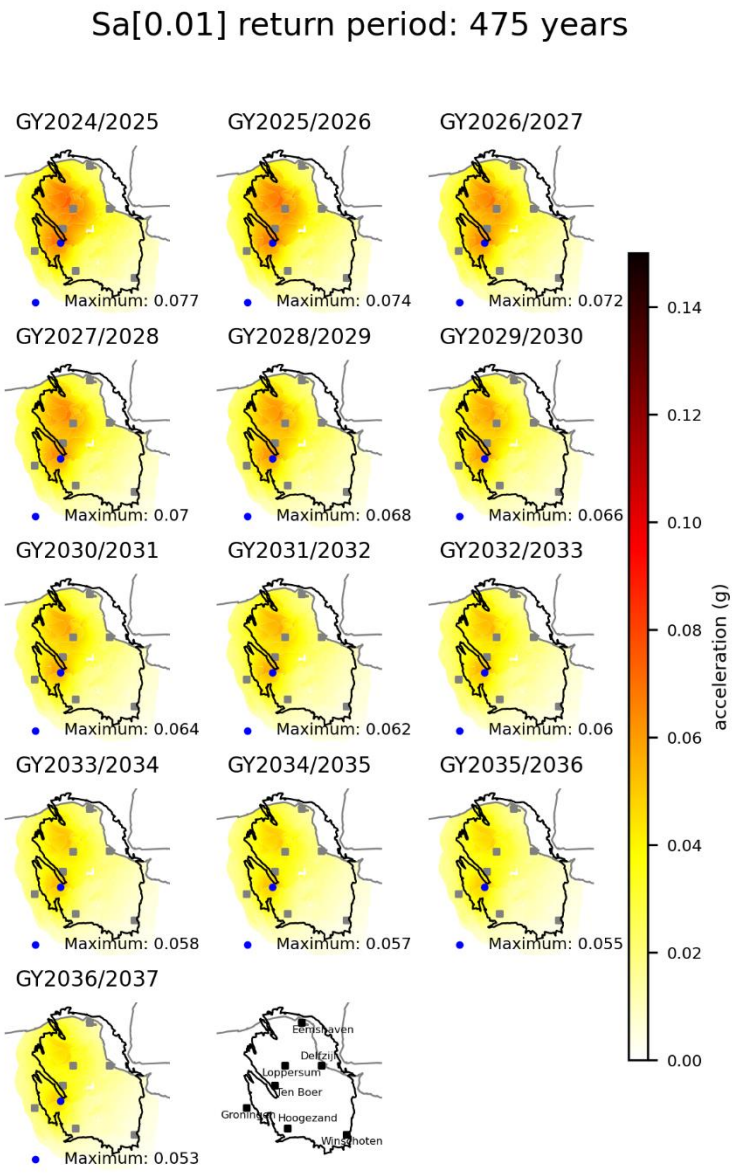

Figure 46: Peak Ground Acceleration (pseudo-spectral acceleration at 0.01 s) hazard map for a 475 return period (10% probability of exceedance in 50 years). The blue dot indicates the position of the largest hazard for each year. Base case (no N_2 injection).

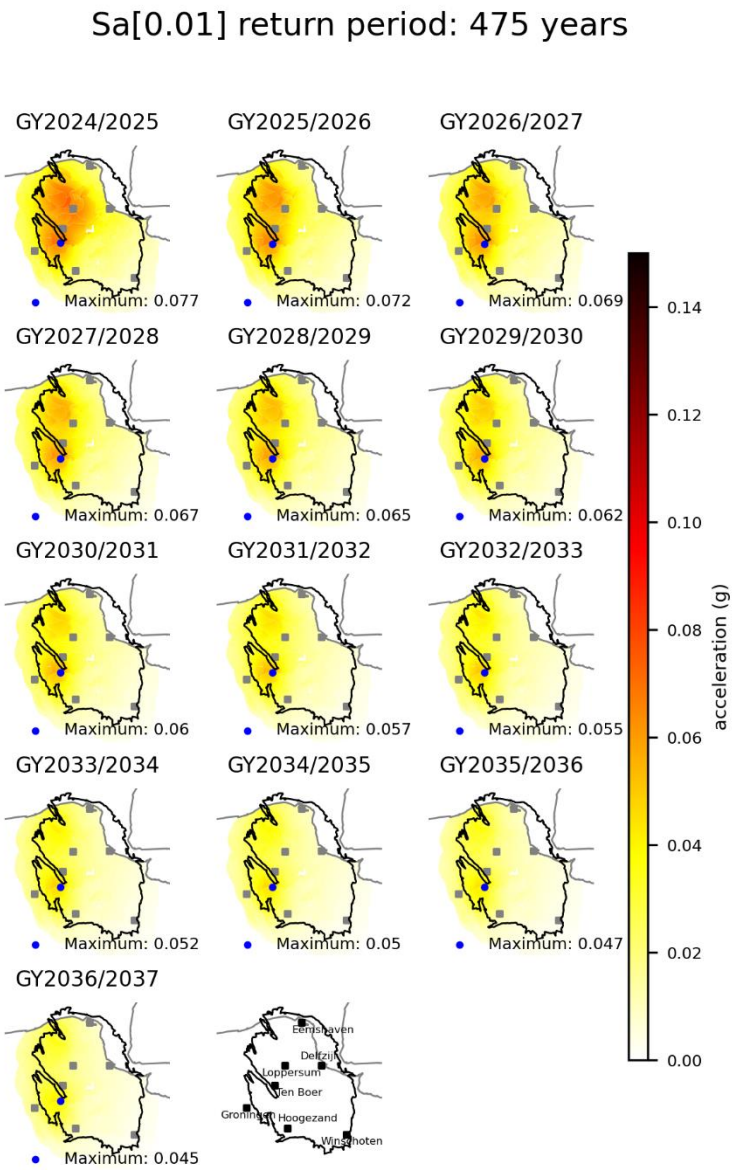

Figure 47: As Figure 46, except for the LO scenario

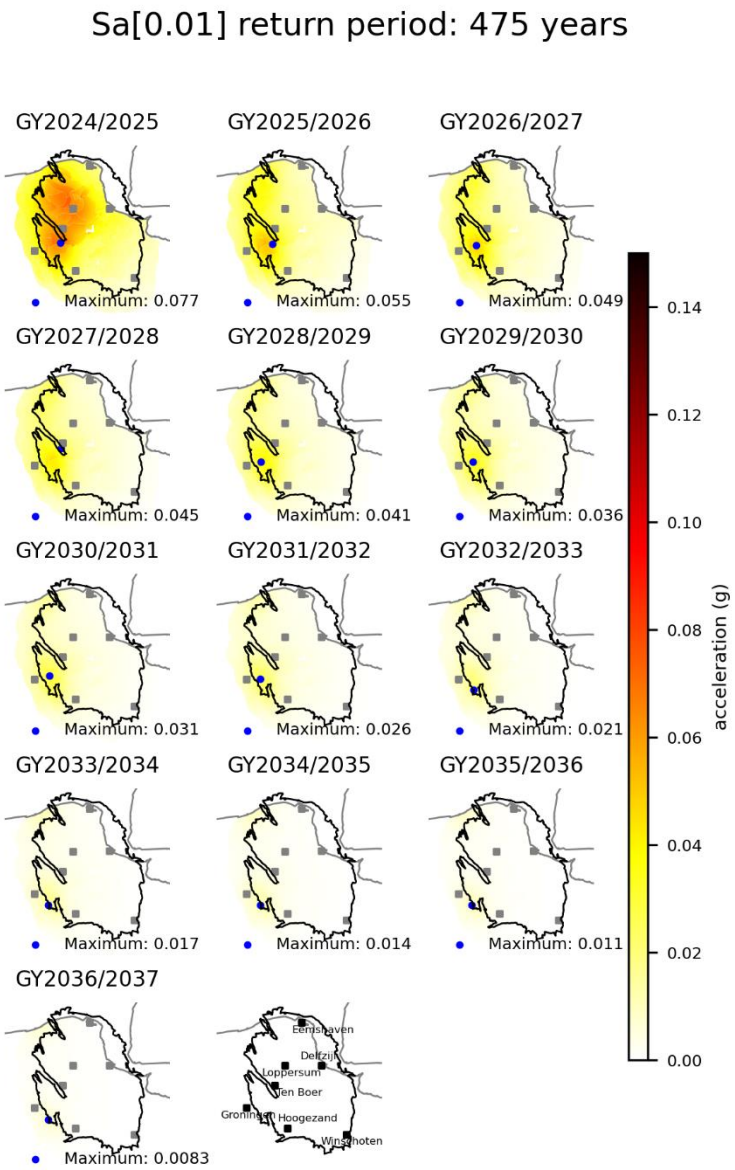

Figure 48: As Figure 46, except for the LO_10ZB scenario

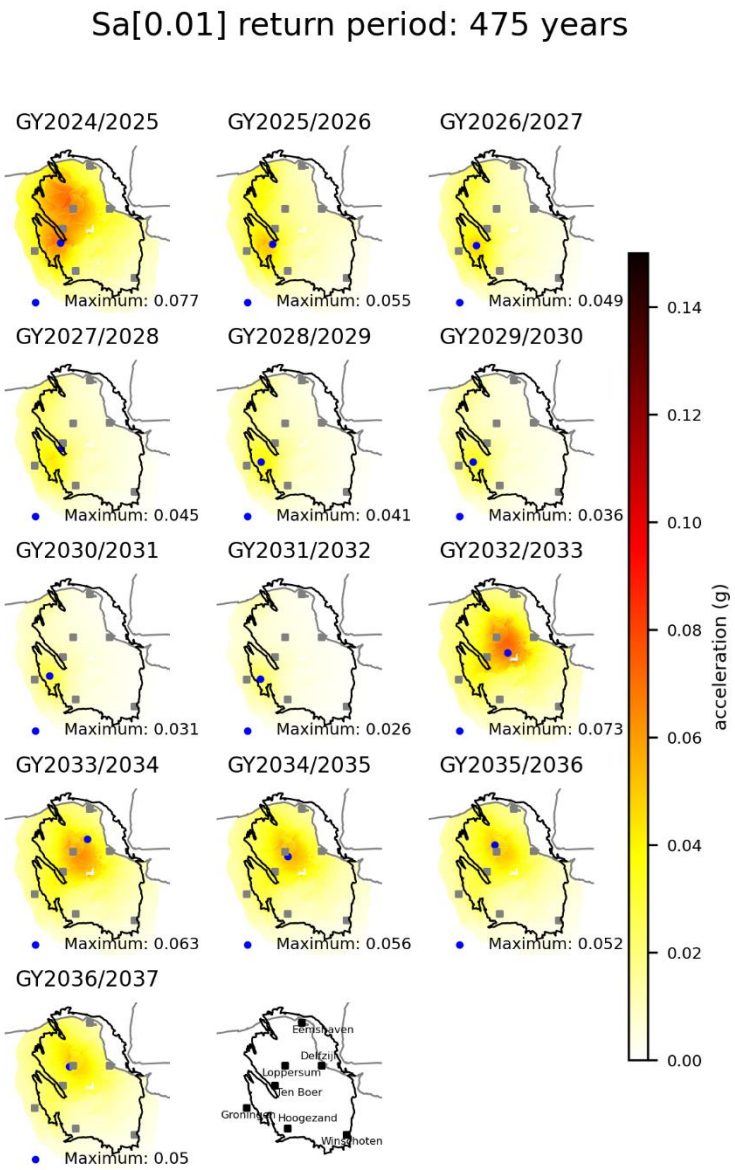

Figure 49: As Figure 46, except for the LO_10ZB_7y scenario

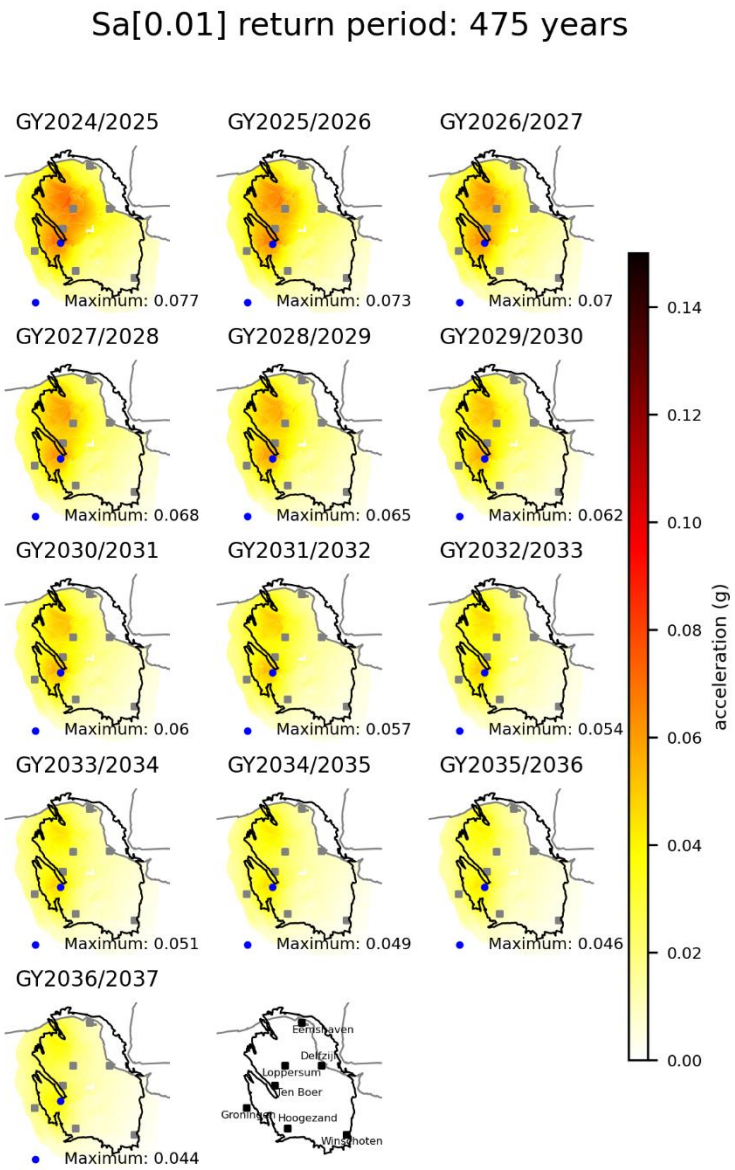

Figure 50: As Figure 46, except for the LO_SE scenario

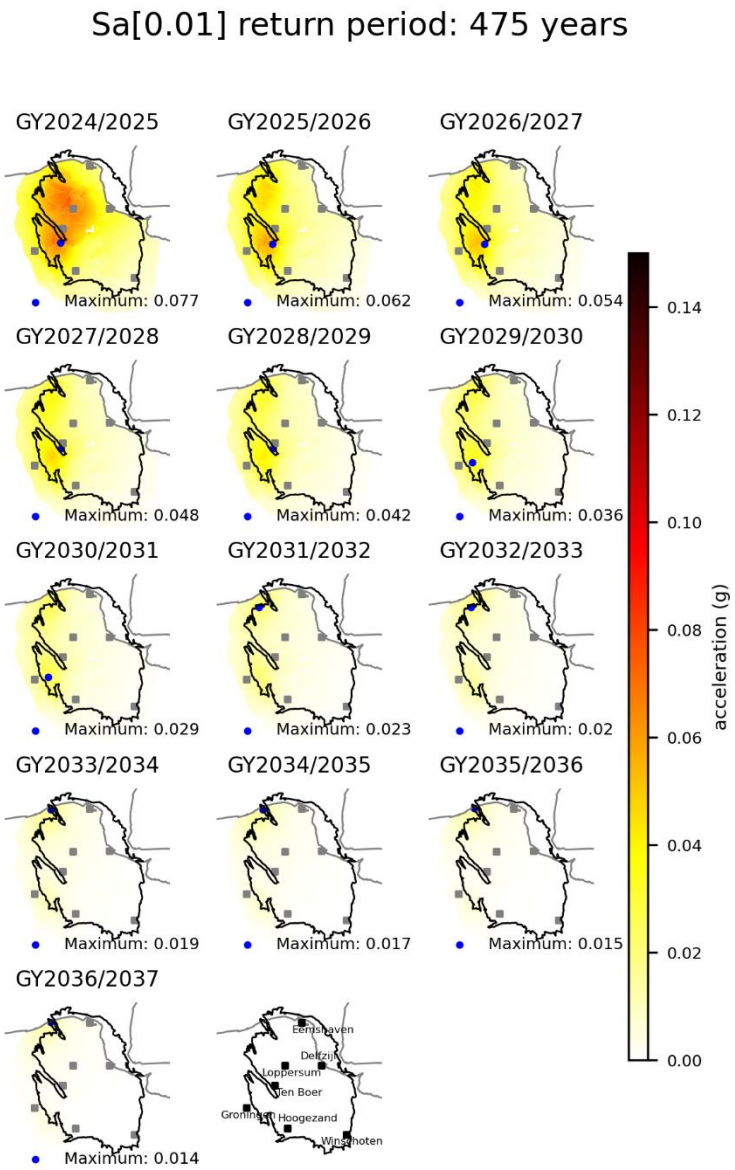

Figure 51: As Figure 46, except for the LO_SE_10ZB scenario

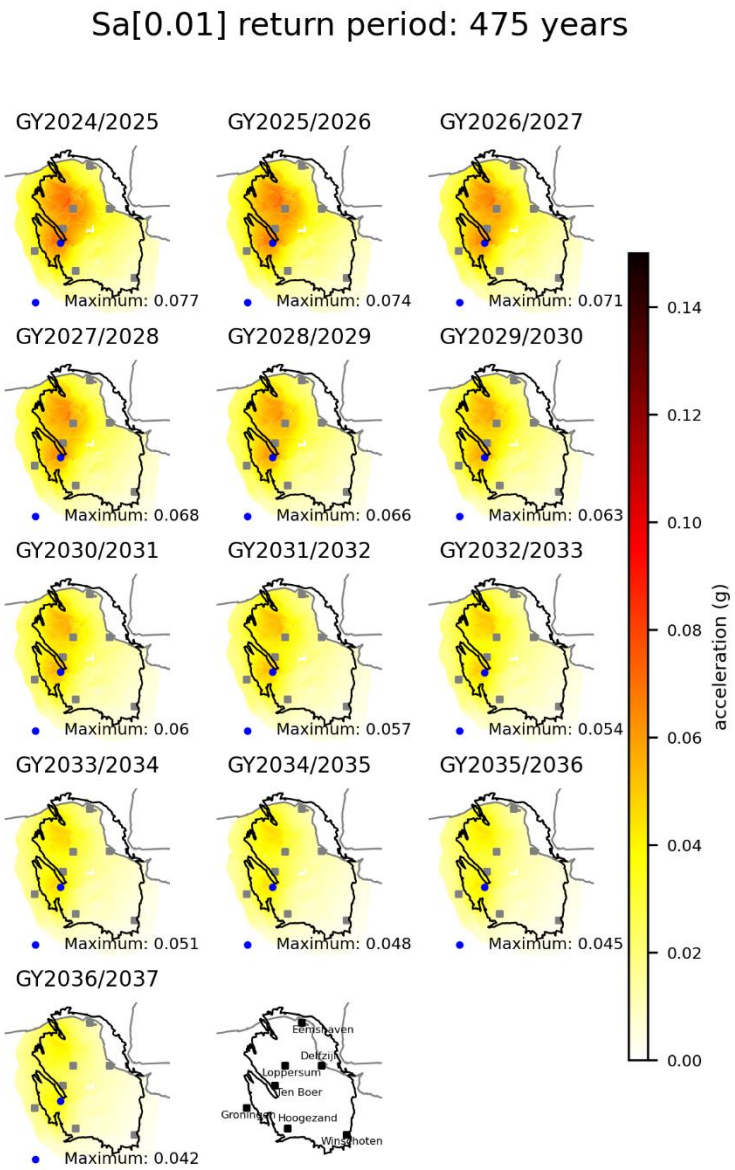

Figure 52: As Figure 46, except for the SE scenario

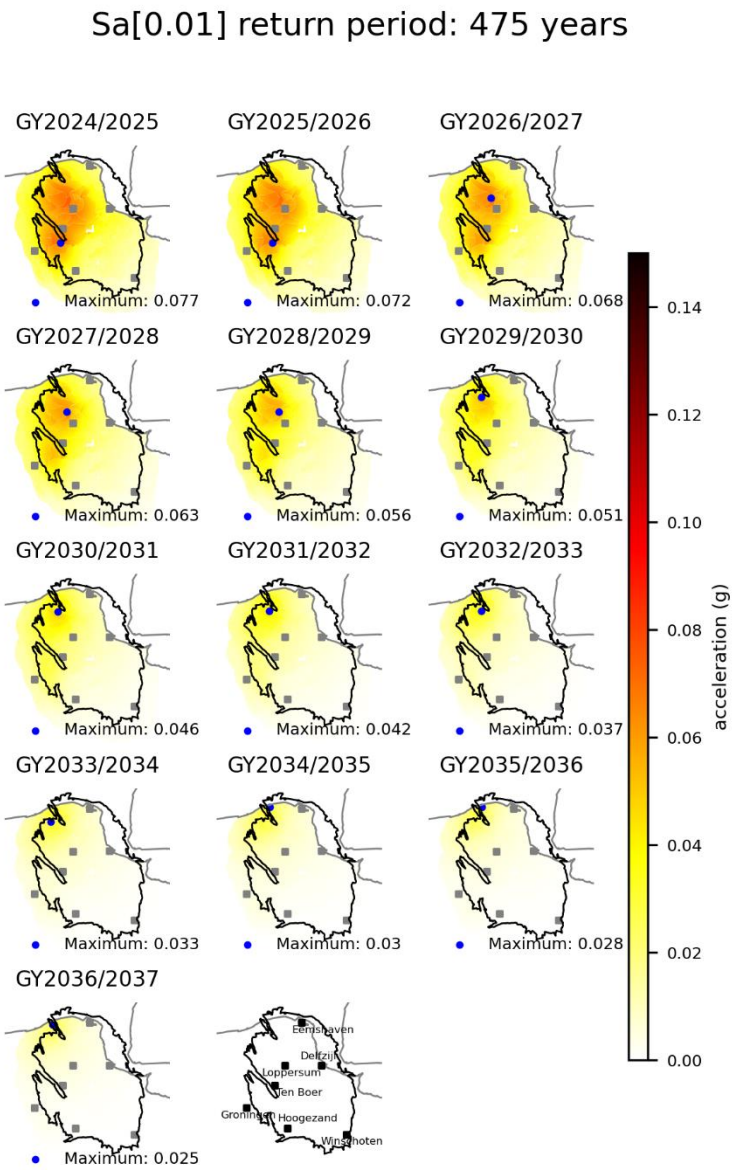

Figure 53: As Figure 46, except for the SE_10ZB scenario

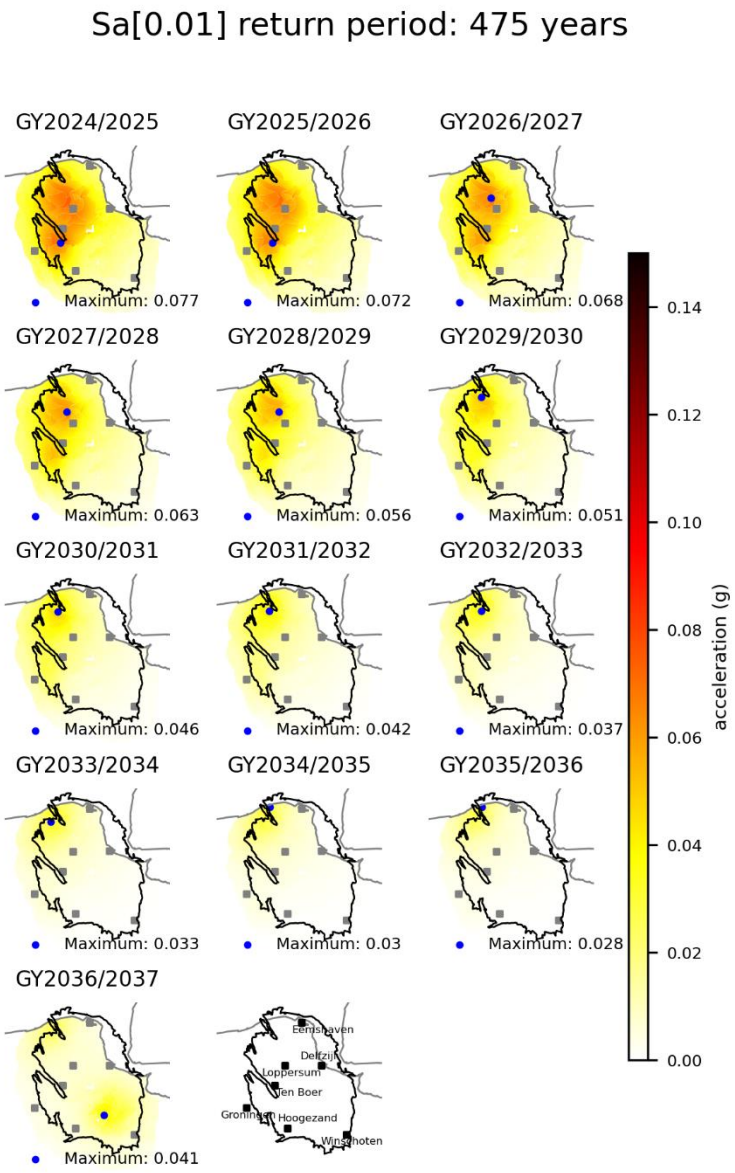

Figure 54: As Figure 46, except for the SE_10ZB_11y scenario

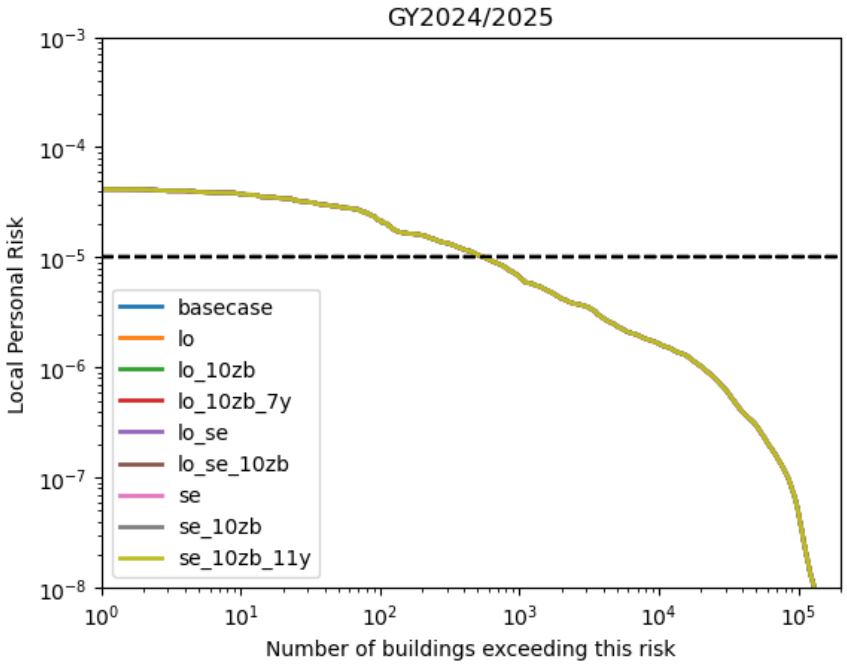

Figure 55: Risk exposure plot. Shows how many buildings (on the x-axis) are exposed to a given local personal risk (y-axis). Shows all scenarios considered for GY 2024/2025. Since N_2 injection starts on the 1st of October 2025 in all scenarios (1st day of gas year 2025/2026), the risk exposure is identical for all scenarios. Approximately 500 buildings exceed the Meijdam norm (10^{-5} y^{-1}) for all scenarios.

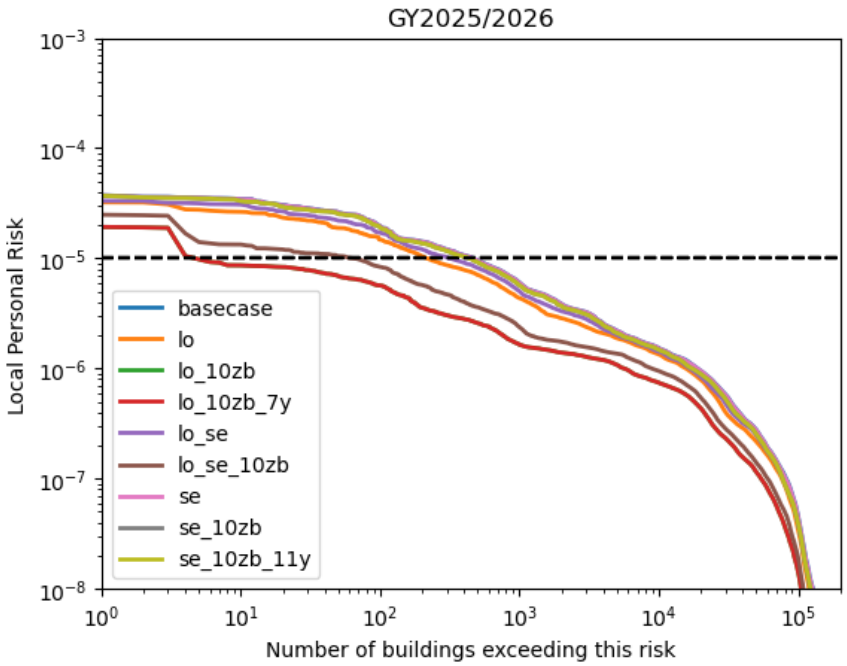

Figure 56: Risk exposure plot for GY 2025/2026. The risk profile decreases compared to previous year for all scenarios (including the base case), but with different amounts. For the scenarios where 10x the Zuidbroek II capacity of N_2 production is injected in the clusters around Loppersum, the number of buildings not conforming to the safety norm goes down to 3 buildings.

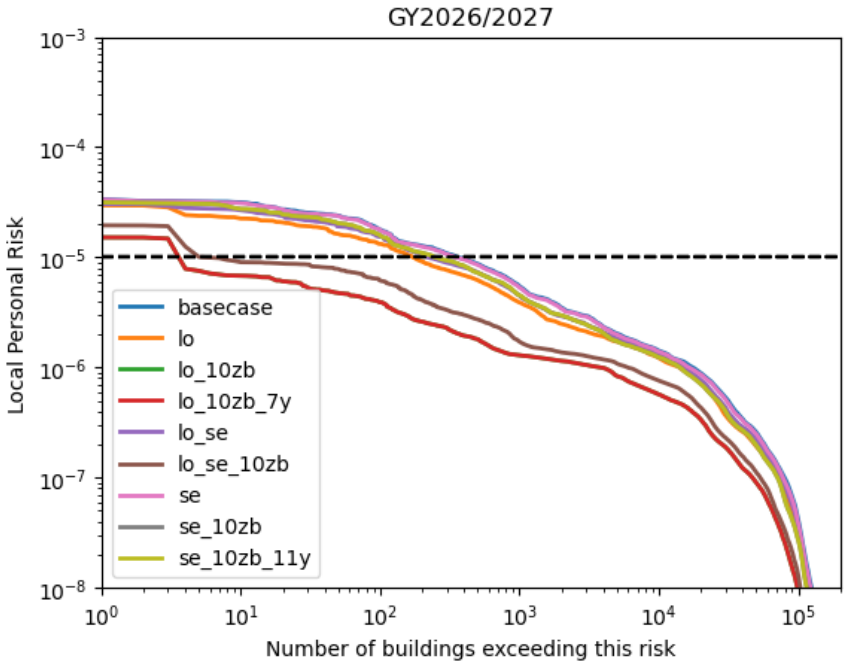

Figure 57: Risk exposure plot for GY 2026/2027. The risk profile decreases compared to last year for all scenarios (including the base case), but with different amounts.

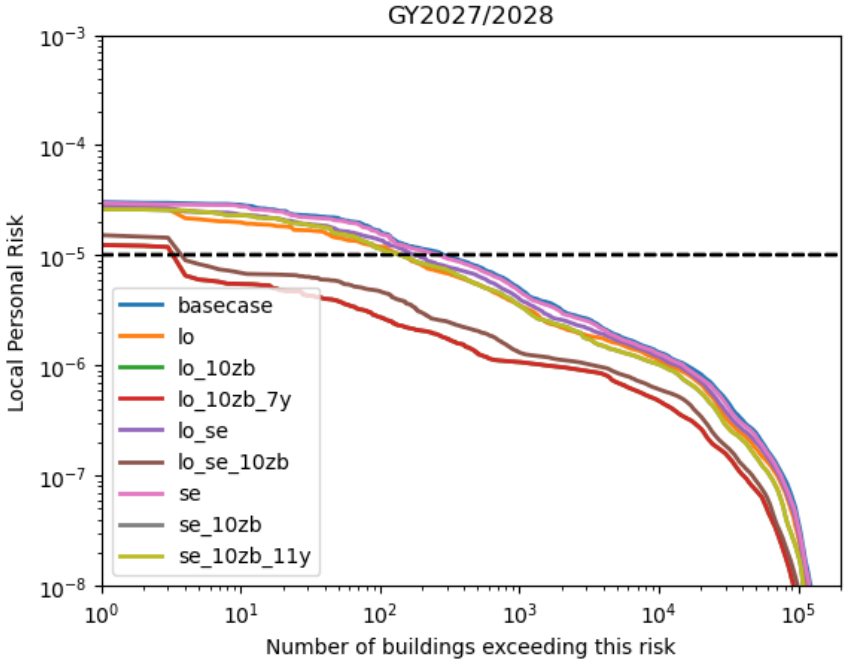

Figure 58: Risk exposure plot for GY 2027/2028. The risk profile decreases compared to last year for all scenarios (including the base case), but with different amounts.

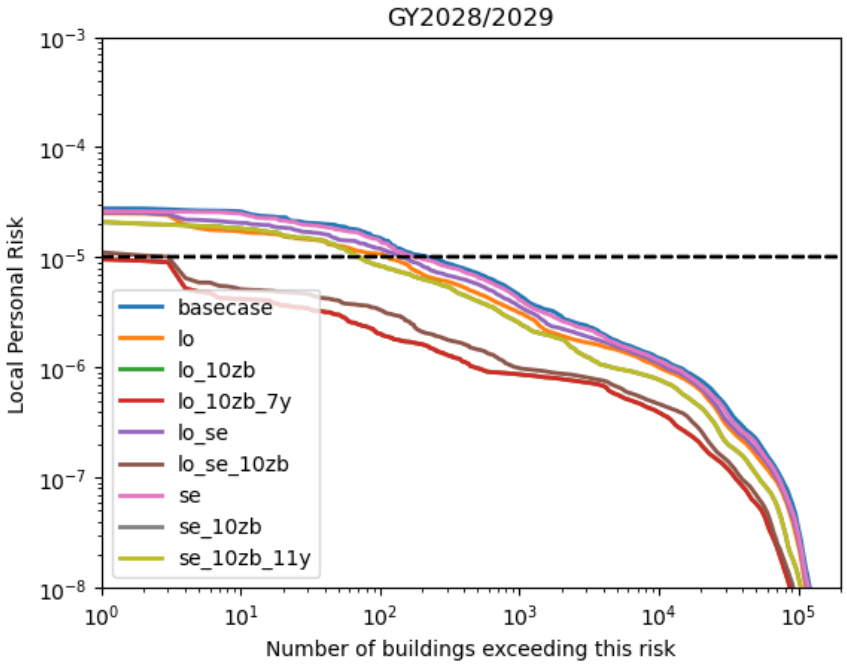

Figure 59: Risk exposure plot for GY 2028/2029. The risk profile decreases compared to last year for all scenarios (including the base case), but with different amounts.

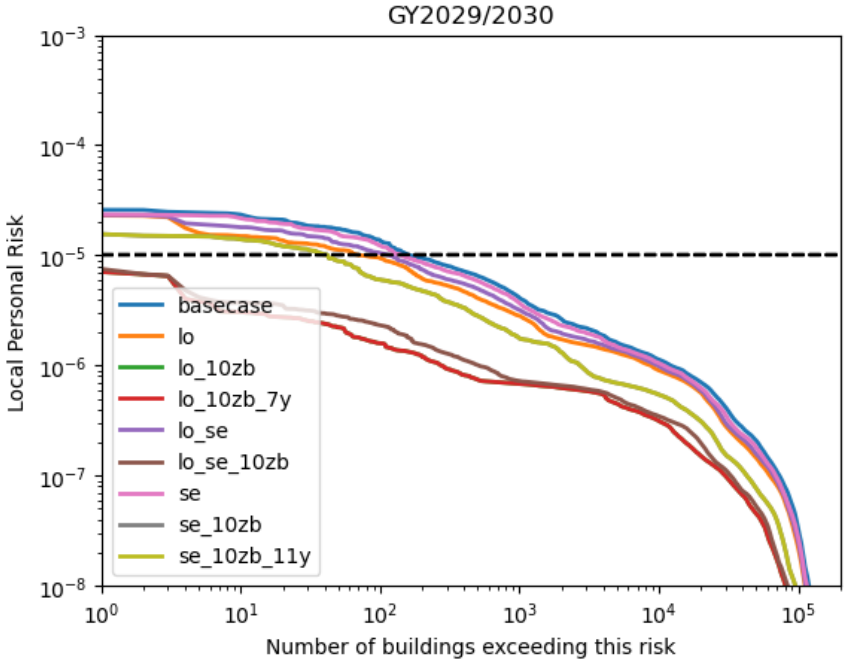

Figure 60: Risk exposure plot for GY 2029/2030. The risk profile decreases compared to last year for all scenarios (including the base case), but with different amounts.

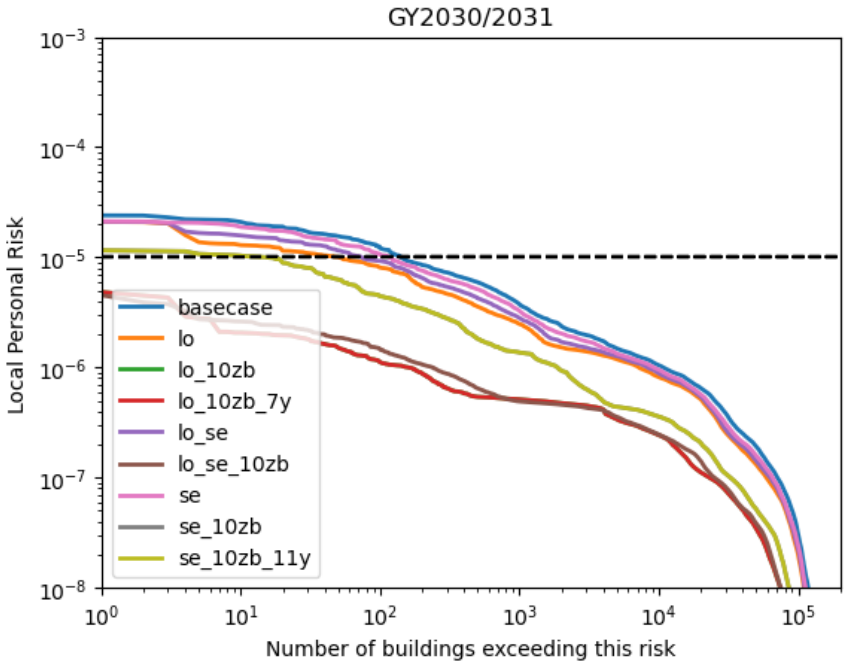

Figure 61: Risk exposure plot for GY 2030/2031. The risk profile decreases compared to last year for all scenarios (including the base case), but with different amounts.

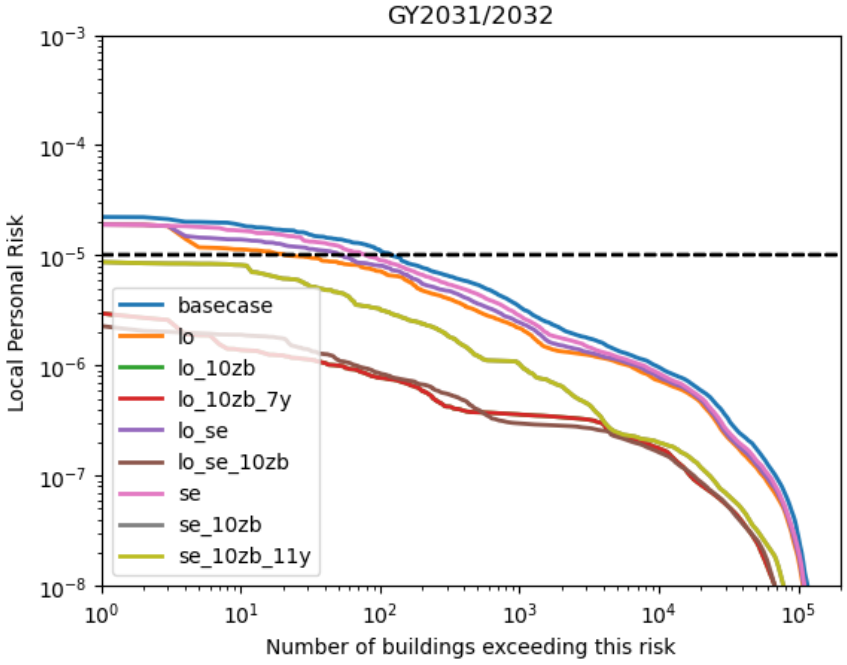

Figure 62: Risk exposure plot for GY 2031/2032. The risk profile decreases compared to last year for all scenarios (including the base case), but with different amounts.

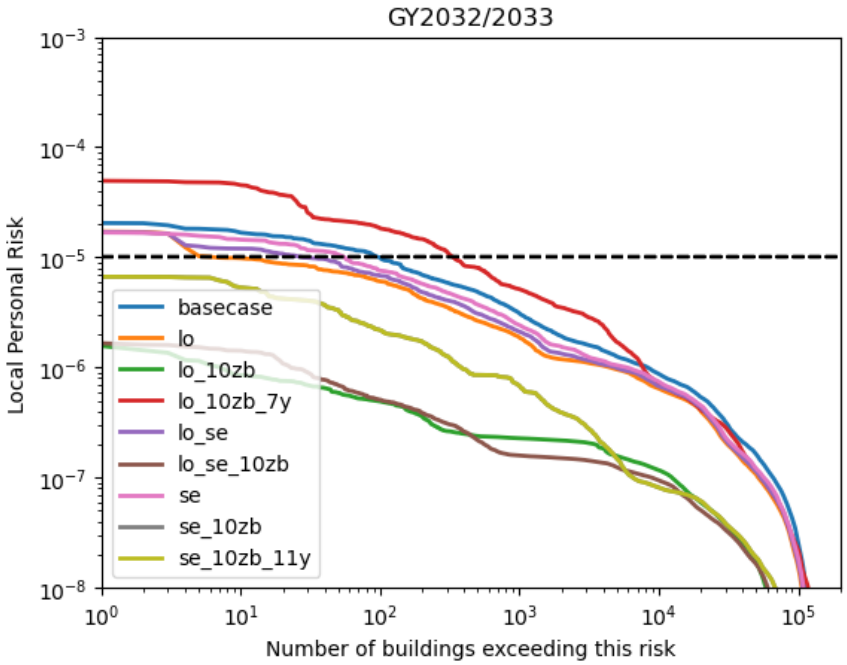

Figure 63: Risk exposure plot for GY 2032/2033. Note the large increase in risk for the lo_10zb_7y case, where nitrogen injection ceases on the 1 October 2032.

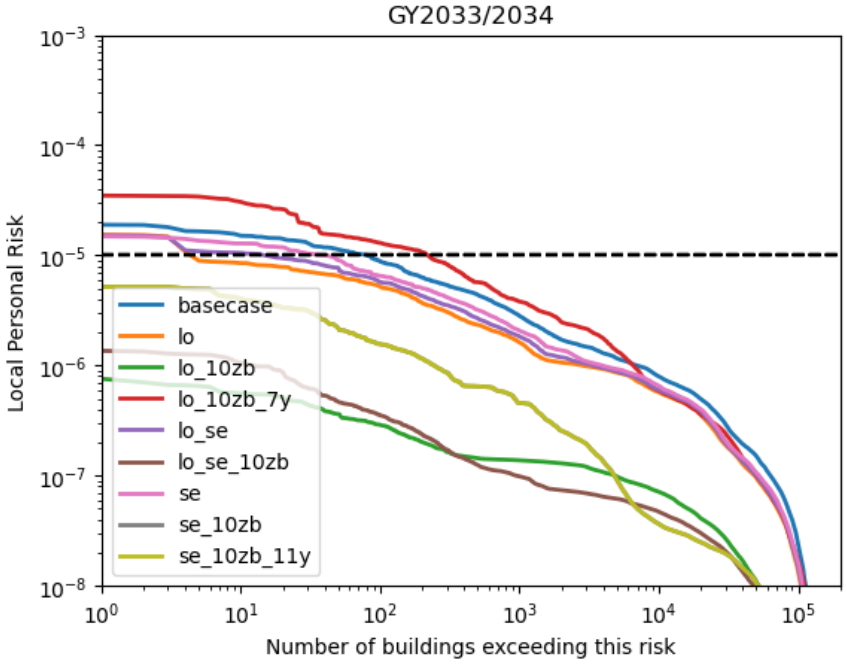

Figure 64 Risk exposure plot for GY 2033/2034. The risk profile decreases compared to last year for all scenarios (including the base case), but with different amounts.

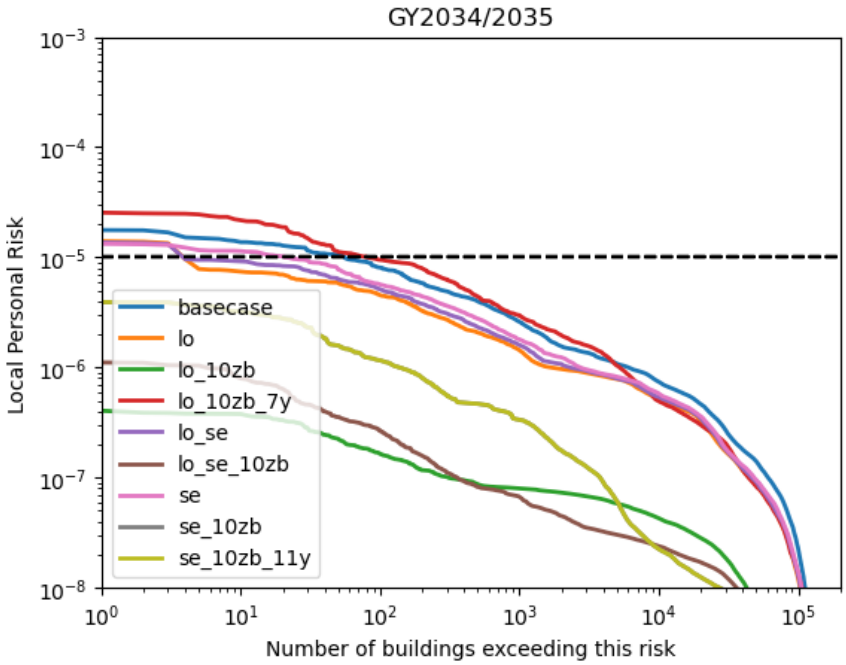

Figure 65 Risk exposure plot for GY 2034/2035. The risk profile decreases compared to last year for all scenarios (including the base case), but with different amounts.

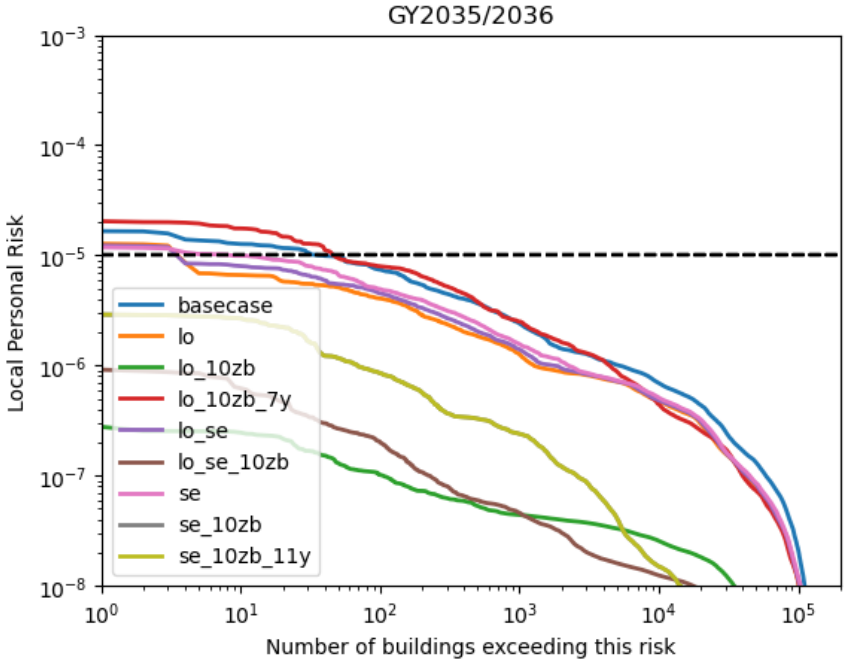

Figure 66: Risk exposure plot for GY 2035/2036. The risk profile decreases compared to last year for all scenarios (including the base case), but with different amounts.

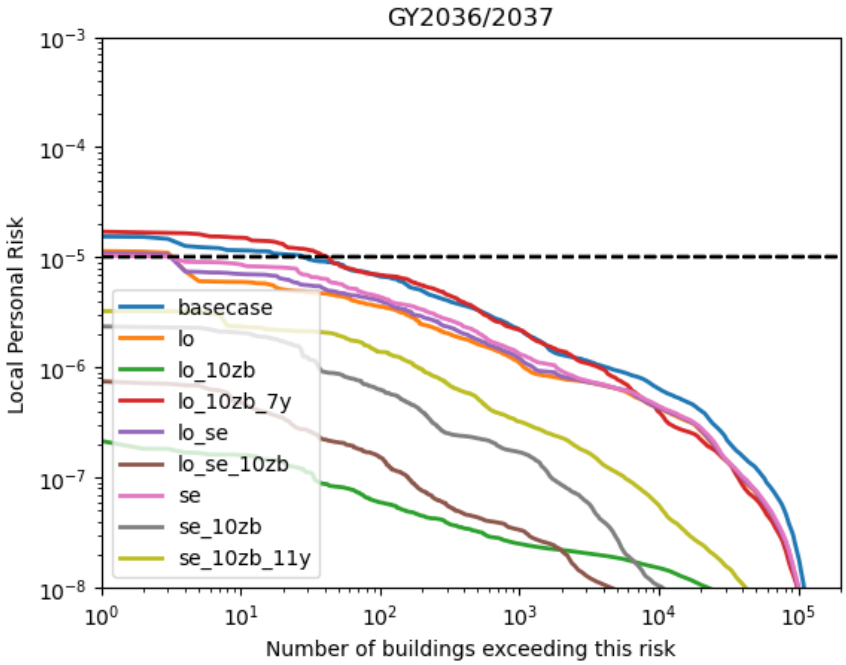

Figure 67 Risk exposure plot for GY 2036/2037. Note the increase of in risk for the se_10zb_11y case, where nitrogen injection ceases on the 1 October 2036. Despite the increase in risk, all buildings conform to the safety norm for this case.

Appendix B: Derivation of source model equations including fault offsets

In the main body of this report, we propose a method for including thermoelastic stresses. Here we show that this method can be applied in the full source model framework, which includes fault offsets as an 'amplification' term for stresses.

Following the Bourne & Oates (2017) conventions, contractive strains and compressive stresses are negative, pore pressure depletion is negative. In this context, it is sensible to define cooling as a negative temperature change. For an isotropic, homogeneous, linear, poro-thermo-elastic medium, the incremental total stress relationship with bulk strain may be written as:

$$\Delta\sigma_{ij} = \frac{E}{(1+\nu)}\left[\Delta\varepsilon_{ij} + \frac{\nu}{1-2\nu}\Delta\varepsilon_{kk}\delta_{ij}\right] - \alpha\Delta P\delta_{ij} - \frac{E}{1-2\nu}\alpha_T\Delta T\delta_{ij}$$

Following Bourne & Oates (2017) section 2.3.2 we get an expression for the vertically averaged strain tensor:

$$\bar{\varepsilon}_{ij} = \begin{pmatrix} \lambda_1 & 0 & 0 \\ 0 & 0 & 0 \\ 0 & 0 & \lambda_3 \end{pmatrix}$$

with

$$\lambda_{1,3} = \frac{\bar{\varepsilon}_{zz}}{2}\left(1 \pm \sqrt{1+\Gamma^2}\right)$$

where

$$\pm : \begin{cases} - & for\ \lambda_1 \\ + & for\ \lambda_3 \end{cases}$$

and Γ is the geometric gradient of the reservoir, which is large at faults.

Using this definition of the strain, we can write an expression for the change in the vertically averaged largest principle total stress σ_1 and the change in the smallest principle total stress σ_3:

$$\Delta\bar{\sigma}_{1,3} = \frac{E}{(1+\nu)}\left[\frac{1 \pm (1-2\nu)\sqrt{1+\Gamma^2}}{2(1-2\nu)}\right]\bar{\varepsilon}_{zz} - \left(\alpha\Delta P + \frac{E}{1-2\nu}\alpha_T\Delta T\right)$$

where

$$\bar{\varepsilon}_{zz} = \frac{1}{E}\frac{(1+\nu)(1-2\nu)}{1-\nu}\alpha\Delta P + \frac{1+\nu}{1-\nu}\alpha_T\Delta T$$

And therefore

$$\alpha \Delta P + \frac{E}{1-2\nu}\alpha_T \Delta T = \frac{\bar{\varepsilon}_{zz} E(1-\nu)}{(1-2\nu)(1+\nu)}$$

This allows us to write the stress changes in terms of $\bar{\varepsilon}_{zz}$:

$$\Delta\bar{\sigma}_{1,3} = \frac{E}{(1+\nu)}\left[\frac{1 \pm (1-2\nu)\sqrt{1+\Gamma^2}}{2(1-2\nu)}\right]\bar{\varepsilon}_{zz} - \frac{\bar{\varepsilon}_{zz} E(1-\nu)}{(1-2\nu)(1+\nu)}$$

$$\Delta\bar{\sigma}_{1,3} = \bar{\varepsilon}_{zz} E\left\{\left[\frac{1 \pm (1-2\nu)\sqrt{1+\Gamma^2}}{2(1-2\nu)(1+\nu)}\right] - \frac{(1-\nu)}{(1-2\nu)(1+\nu)}\right\}$$

This shows that the poro-elastic and thermo-elastic effects on the stress are fully encoded in the vertical strain signal.

For completeness, we'll derive the the incremental maximum shear and mean total normal stresses developed within the thin sheet, after which we can make use of the Bourne and Oates framework for the rest of the source model:

$$\Delta\tau = \frac{1}{2}(\Delta\sigma_1 - \Delta\sigma_3)$$

$$\Delta\sigma_n = \frac{1}{2}(\Delta\sigma_1 + \Delta\sigma_3)$$

$$\Delta\tau = \frac{1}{2}\left(\bar{\varepsilon}_{zz} E\left\{\left[\frac{1-(1-2\nu)\sqrt{1+\Gamma^2}}{2(1-2\nu)(1+\nu)}\right] - \frac{(1-\nu)}{(1-2\nu)(1+\nu)}\right\} - \bar{\varepsilon}_{zz} E\left\{\left[\frac{1+(1-2\nu)\sqrt{1+\Gamma^2}}{2(1-2\nu)(1+\nu)}\right] + \frac{(1-\nu)}{(1-2\nu)(1+\nu)}\right\}\right)$$

$$\Delta\tau = \frac{1}{2}\left(\bar{\varepsilon}_{zz} E\left[\frac{1-(1-2\nu)\sqrt{1+\Gamma^2}}{2(1-2\nu)(1+\nu)}\right] - \bar{\varepsilon}_{zz} E\left[\frac{1+(1-2\nu)\sqrt{1+\Gamma^2}}{2(1-2\nu)(1+\nu)}\right]\right)$$

$$\Delta\tau = -\bar{\varepsilon}_{zz} E\frac{\sqrt{1+\Gamma^2}}{2(1+\nu)}$$

$$\Delta\tau = -\sqrt{1+\Gamma^2}\gamma H\bar{\varepsilon}_{zz}$$

where

$$\gamma = \frac{1-2\nu}{2(1-\nu)} \text{ and } H = \frac{E}{(1-2\nu)(1+\nu)}$$

And similarly for $\Delta\sigma_n$:

$$\Delta\sigma_n = \frac{1}{2}\left(\bar{\varepsilon}_{zz} E\left\{\left[\frac{1-(1-2\nu)\sqrt{1+\Gamma^2}}{2(1-2\nu)(1+\nu)}\right] - \frac{(1-\nu)}{(1-2\nu)(1+\nu)}\right\} + \bar{\varepsilon}_{zz} E\left\{\left[\frac{1+(1-2\nu)\sqrt{1+\Gamma^2}}{2(1-2\nu)(1+\nu)}\right] - \frac{(1-\nu)}{(1-2\nu)(1+\nu)}\right\}\right)$$

$$\Delta\sigma_n = \frac{1}{2}\left(\bar{\varepsilon}_{zz}E\left(\left[\frac{2}{2(1-2\nu)(1+\nu)}\right] - \frac{2(1-\nu)}{(1-2\nu)(1+\nu)}\right)\right)$$

$$\Delta\sigma_n = \bar{\varepsilon}_{zz}E\left(\left[\frac{1}{2(1-2\nu)(1+\nu)}\right] - \frac{2(1-\nu)}{2(1-2\nu)(1+\nu)}\right)$$

$$\Delta\sigma_n = \bar{\varepsilon}_{zz}E\left(\frac{-(1-2\nu)}{2(1-2\nu)(1+\nu)}\right)$$

$$\Delta\sigma_n = -\frac{\bar{\varepsilon}_{zz}E}{2(1+\nu)}$$

$$\Delta\sigma_n = -\gamma H\bar{\varepsilon}_{zz}$$

These expressions are identical to the ones obtained by Bourne & Oates (2017), but have now explicitly included the thermal component in the vertically averaged vertical strain throughout the derivation.

Signature

Authorization release

Y.A. Schavemaker MSc
Research manager

Energy & Materials Transition

Princetonlaan 6
3584 CB Utrecht
www.tno.nl

TNO innovation for life

TNO innovation for life

KEM-19b
Evaluation of post-abandonment fluid migration and seismic hazard assessment in the southwest aquifer of Groningen

Part 1

TNO Public › TNO 2025 R10452
20 June 2025

Energy & Materials Transition
www.tno.nl
+31 88 866 42 56
info@tno.nl

TNO 2025 R10452 – 20 June 2025

KEM-19b
Evaluation of post-abandonment fluid migration and seismic hazard assessment in the southwest aquifer of Groningen

Part 1

Author(s)	S. Osinga, E. Peters, P. Fokker; D.A. Kraaijpoel, C.R. Geel, M. van Unen, J. Foeken, S. Peeters, S. Bottero

Classification report	TNO Public
Title	TNO Public
Report text	TNO Public
Appendices	TNO Public
Number of pages	154 (excl. front and back cover)
Number of appendices	5
Sponsor	The Dutch Ministry of Economic Affairs and Climate
Programme name	Kennisprogramma Effecten van Mijnbouw - KEM program
Project name	KEM-19b

Managementsamenvatting

Aan de zuidwestelijke grens is het Groningen gasveld verbonden met een groot aquifer (watervoerende laag) in de zuidelijke Lauwerszee Trog. Door de gasproductie uit het Groningen gasveld en een reeks kleine gasvelden aan de westkant van de trog, heeft deze aquifer te maken met nog steeds voortdurende drukverlaging. Het doel van deze studie is om onze kennis te vergroten over deze voortdurende drukverlaging en het potentieel voor toekomstige seismische activiteit in de aquifer als gevolg van deze drukverlaging.

Om dit te bereiken is een ensemble van geologische en dynamische simulatiemodellen van de aquifer gemaakt, inclusief de kleine gasvelden aan de westkant en een deel van de Groningen en Bedum velden aan de oostkant. Voor het ensemble werden compactie en bodemdaling gesimuleerd. Op basis van de overeenkomst met waargenomen druk in de kleine gasvelden en bodemdaling boven de aquifer, werd een subset van het ensemble geselecteerd om de drukverlaging en compactie in de aquifer van 2024 tot 2100 te voorspellen. In sommige gebieden van de aquifer, met name de aquifer net ten westen van Harkstede en van Ten Boer, werd de onzekerheid in de voorspelde drukverlaging aanzienlijk verminderd op basis van de waargenomen bodemdaling. De aquifer tussen het Roden veld en het Harkstede gebied ervoer duidelijk drukverlaging door gaswinning uit zowel het Roden als het Groningen veld, met name door de productie nabij Harkstede.

De voorspellingen van druk en compactie werden gebruikt als input om seismiciteit en seismische dreiging (grondbeweging) te bepalen voor de komende decennia. Hiervoor wordt de TNO Model Chain workflow, oorspronkelijk ontwikkeld voor het Groningen veld (TNO, 2020), toegepast op de zuidwestelijke aquifer. Deze toepassing vereist de uitbreiding van de twee belangrijkste bouwstenen: (1) het seismische bronmodel (SSM) en (2) het grondbewegingsmodel (GMM). Voor de Groningen modelketen zijn beide componenten specifiek ontworpen en gekalibreerd voor het Groningen veld. Een uitbreiding van de keten, om de zuidwestelijke aquifer op diepte en een groter blootgesteld gebied aan het oppervlak op te nemen, vereist zowel het in beeld brengen van nieuwe (meer) gegevens als een (her)kalibratie.

Ondanks de aanzienlijke onzekerheid met betrekking tot de aquiferdrukken, tonen de seismische voorspellingen gebaseerd op de verschillende ensembleleden, eenmaal gekalibreerd, allemaal zeer beperkte seismische activiteit in de zuidwestelijke aquifer in vergelijking met de verwachte voortdurende seismische activiteit in het Groningen veld. Dit is een belangrijk resultaat, omdat het aangeeft dat de aanzienlijke onzekerheid in de drukvoorspellingen niet vertaalt naar aanzienlijke onzekerheid met betrekking tot seismische activiteit. Ten slotte, vanwege de lage hoeveelheid voorspelde seismische activiteit in de zuidwestelijke aquifer, is er een zeer beperkte impact van deze nieuw gemodelleerde seismische activiteit op de seismische dreiging boven de zuidwestelijke aquifer. We concluderen dat de seismische dreiging blijft afnemen met toenemende afstand van het Groningen gasveld en dat de seismische activiteit van de zuidwestelijke aquifer zeer beperkt is en dit algemene beeld niet significant verandert.

Executive Summary

On its southwest border, the Groningen gas field is connected to an extensive aquifer in the southern Lauwerszee Trough. Due to the gas production from the Groningen gas field and a series of small gas fields on the west side of the trough, this aquifer has experienced, (and is still experiencing) pressure depletion. The objective of this study is to increase our knowledge on the ongoing pressure depletion in the aquifer and the potential for future seismic activity.

To achieve that, an ensemble of geological and dynamic simulation models has been created of the southwest (SW) aquifer including on the west side the small gas fields and on the east side a part of the Groningen and Bedum fields. For the ensemble, compaction and subsidence were also simulated. Based on the fit to observed pressure in the small gas fields and subsidence above the aquifer, a subset of the ensemble was selected to forecast the depletion and compaction in the aquifer from 2024 to 2100. In some areas of the aquifer, most notably the aquifer just west of Harkstede and of Ten Boer, the uncertainty in the forecasted depletion was considerably reduced based on the observed subsidence. The aquifer between the Roden field and the Harkstede area clearly experienced depletion due to gas exploitation from both the Roden and the Groningen fields, in particular from the production near Harkstede.

The forecast of pressure and compaction was used as input to produce seismicity forecasts and seismic hazard (ground motion) assessments for the coming decades. For this purpose, the TNO Model Chain workflow developed for the Groningen field (TNO, 2020) is applied to the SW aquifer. This application requires the extension of the two main building blocks: (1) the seismic source model (SSM) and (2) the ground motion model (GMM). For the Groningen model chain both components have been designed and calibrated specifically for the Groningen field. An extension to include the SW aquifer at depth, and a larger exposed area at the surface, requires both taking into account new (more) data, as well as a (re)calibration.

Despite the considerable uncertainty related to the pressures, once calibrated, the seismicity forecasts of the individual pressure model ensemble members all show very limited seismicity in the SW aquifer when compared to the expected ongoing seismicity in the Groningen field. This is an important result, as it indicates that the significant uncertainty in the pressure forecasts does not translate to significant uncertainty with regards to seismicity. Finally, due to the low level of forecasted seismicity in the SW aquifer, there is a very limited impact of this newly modelled seismicity on the seismic hazard above the SW aquifer. We have identified that the seismic hazard continues to decrease with increasing distance from the Groningen gas field and that the seismicity of the SW aquifer itself is very limited and does not significantly change this general picture.

Contents

Contents

1 Introduction

The Groningen gas field has been producing since the 1960's and the resulting pressure depletion has caused many induced seismic events. Due to the pressure depletion in the Groningen gas field, some of the surrounding aquifers are also depleting in pressure. Some of these aquifers extend quite far beyond the gas reservoir. One of these depleting aquifers is the SW aquifer of the Groningen gas field which is situated in the southern Lauwerszee Trough (Figure 1-1), a region where small-scale seismicity has been observed in recent times, likely caused by pressure depletion in the aquifer. The depletion in the aquifer is attributed not only to gas production from the Groningen gas field, but also to the small gas fields on the west side of the Lauwerszee Trough, in particular the Roden gas field (Molen et al., 2020).

The specific objective of this project is to focus on the aquifer in the southern Lauwerszee Trough and investigate the pressure depletion as well as the future potential seismic activity in the aquifer.

This project is a follow-up of the KEM-19 study "Evaluation of post-abandonment fluid migration and ground motion risks in subsurface exploitation operations in the Netherlands" carried out by TNO and Deltares and completed in 2022 (TNO-Deltares 2022).
In the KEM-19 study, the pressure depletion in the aquifers surrounding the Groningen gas field was investigated for the coming centuries. It was concluded, that the Groningen gas field is too large to be repressurized by its connected aquifers and that the connected aquifers will continue to decline in pressure, albeit at a slow pace.

This study focuses on the following research questions:
1. What will be the pressure depletion of the southwestern aquifer taking into account the depletion of Groningen gas field as well as the smaller gas fields in the Lauwerszee Trough?
2. What are the locations of smaller faults, and their orientation and throw in the southwestern aquifer?
3. What is the expected induced seismicity in the coming decades?
   a. What is the seismic hazard?
   b. How does this compare to the seismic hazard of the Groningen gas field?

This study aims to address key research questions through a modelling approach.
In KEM-19 project, a regional reservoir model was developed, encompassing the SW aquifer of the Groningen gas field in the Lauwerszee Trough. However, it did not include the smaller gas fields on the southwestern side of the Lauwerszee Trough. As a result, the KEM-19 model could not fully capture the aquifer's depletion, as it only reflected the pressure changes from the Groningen gas field. Additionally, the limited number of wells in the aquifer led to significant uncertainty.

In this follow-up project a local model is created that includes the SW aquifer, the surrounding small gas fields and a part of the Groningen field. Due to the lack of direct pressure measurements in the aquifer, subsidence is modelled for the area of interest and compared to observed subsidence. This approach is expected to significantly improve the quantification of the current pressure depletion and its evolution in the future, including associated uncertainties. To characterize uncertainties, an ensemble of models is used instead of a single

model. Special focus is on the characterization of smaller and larger scale faults, including fault orientation and throw, to be able to include them in a geological model and in the seismic source model. In order to produce seismic hazard (ground motion) estimates, the Ground Motion Model (GMM-V7) for Groningen is extended to cover the SW aquifer. Due to the similar structure of the deep subsurface, the main effort regarding the GMM update concerns extending the site-response model with an additional 81 spatial zones to account for the site-amplification characteristic of the shallow subsurface, which is highly variable in composition and structure.

The report is structured to address the research questions of this study. Following the introduction, in Chapter 2 the creation of the ensemble of geological (static) reservoir models is detailed, including the development of the reservoir's geometry and properties such as porosity, permeability and net-to-gross (NtG). Chapter 3 describes how the ensemble of geological models is extended to an ensemble of dynamic models to simulate the pressure history. It also covers the modeling of subsidence for the ensemble of models and the selection of a subset based on the fit to observed subsidence and pressures to forecast aquifer pressure. In Chapter 4, the required extension of the Ground Motion Model and Seismic Source Model is described. The extended version of the TNO Model Chain workflow developed for the Groningen field (TNO, 2020) is then applied to the SW aquifer. Finally, Chapter 5 presents the conclusions and recommendations derived from the study.

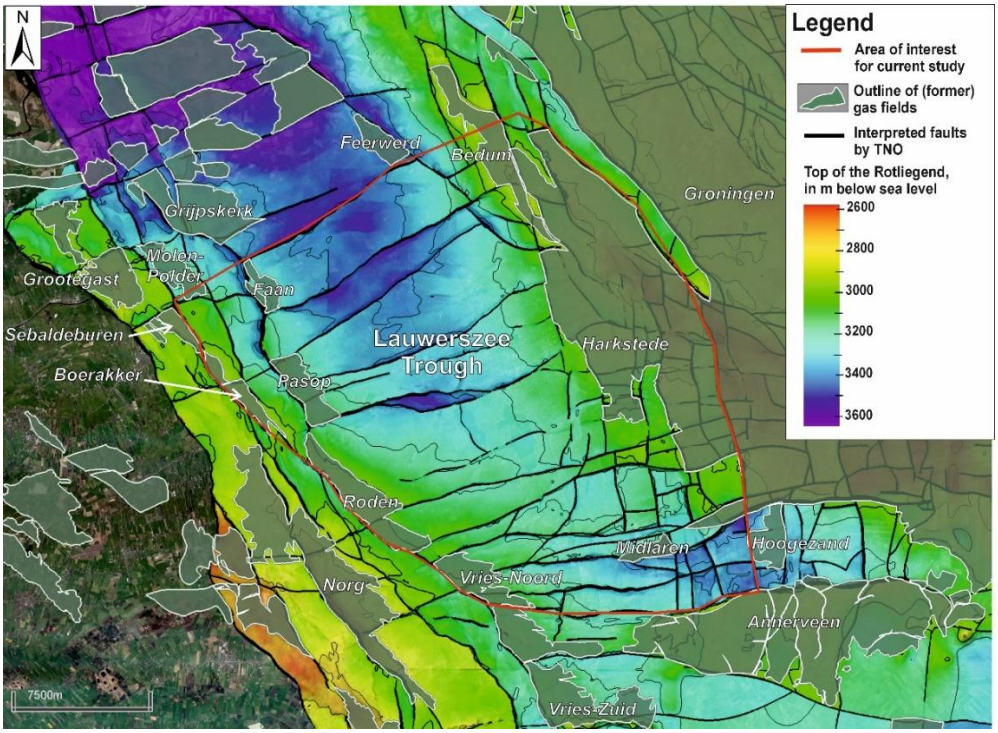

Figure 1-1 Overview image displaying the area of interest outlined in red and the locations of gas fields projected onto a depth map of the Rotliegend formation (warmer colors indicate shallower depths). The interpreted faults, shown in black, are based on TNO's (2023) internal geological model for the broader Groningen region.

2 Improved geological model SW aquifer of the Groningen field

2.1 Introduction

The main objective of this part of the study was to create an ensemble of geological models of the aquifer located southwest of the Groningen Field (Figure 2-1, Figure 2-2 and Figure 2-3) including the small gas fields on the west side and a relevant part of the Groningen gas field on the east. Special emphasis was placed on the characterization of both small and large-scale faults, including fault orientation and throw, and incorporating them in a geological reservoir model of the SW aquifer, which comprises the Slochteren Formation of the Groningen field.

The approach was as follows:

- Existing reservoir models and data sets were used as much as possible to model known reservoir characteristics and fault trends. To cover this point, first an introduction is given regarding the geological background, including the stratigraphy (paragraph 2.1.1), reservoir architecture (paragraph 2.1.2) and the structural development of the wider Groningen area (paragraph 2.1.3). Subsequently, the data and existing reservoir models are described that were used to construct the model for the current study (paragraph 2.2);
- The boundaries for the model are described and faults that were missing from the previous models were newly interpreted on 3D seismic data. Based on these additional fault interpretations, a new base case structural model was built (paragraph 2.3);
- A petrophysical analysis was done for the wells in the small gas fields on the west side of the Lauwerszee Trough (paragraph 2.4)
- An ensemble of geological models with properties was created using Gaussian simulation. First the methods regarding the property modelling are described (paragraph 2.5). Finally the modelling results are shown (paragraph 2.6).

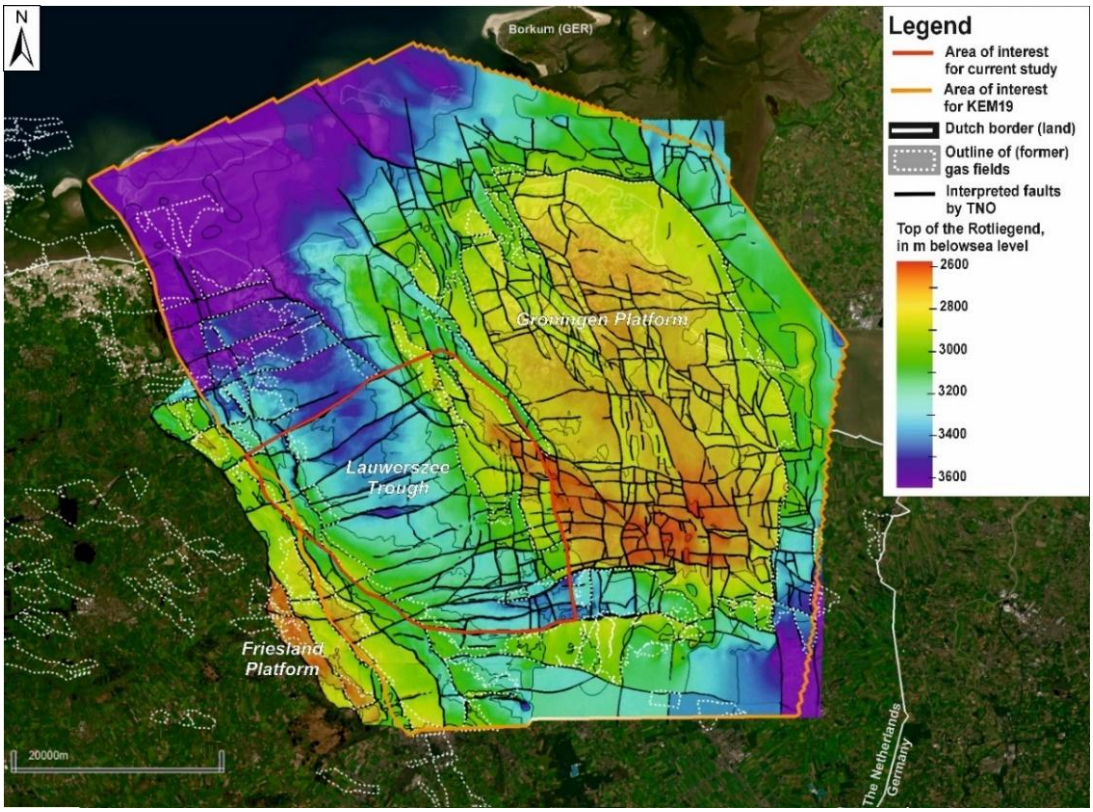

Figure 2-1 Area of Interest (red polygon) of the KEM-19b project projected onto a depth map of the Top of the Rotliegend (=Base Zechstein) with a fault interpretation by TNO. Warmer colours mean shallower depths, cooler colours mean larger depths. The thin black lines are contour lines which are present every 200 m. The interpreted faults (in black) are from TNO (2023) internal geological model for the wider Groningen area.

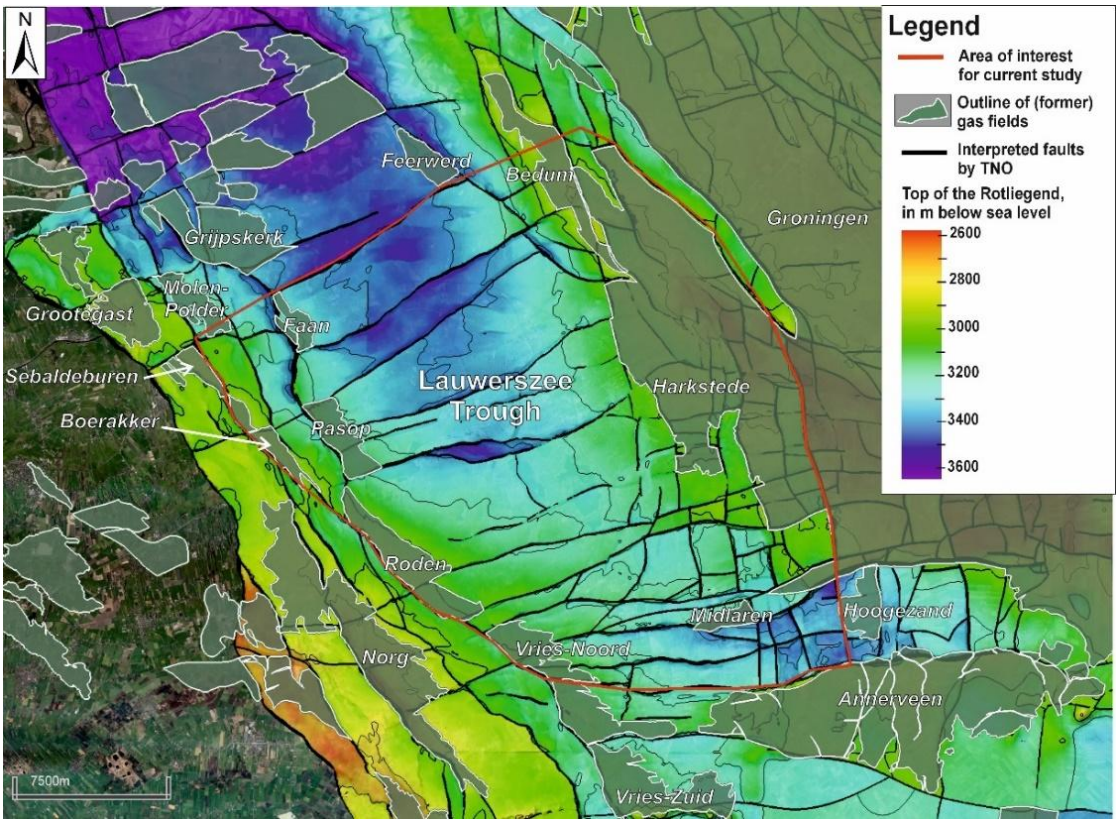

Figure 2-2 Overview picture showing the names and locations (green) of the gas fields in the area of interest projected on a depth map of the top of the Rotliegend (warmer colours indicate shallower depth). The red outline is the area of interest. The interpreted faults (in black) are from TNO (2023) internal geological model for the wider Groningen area.

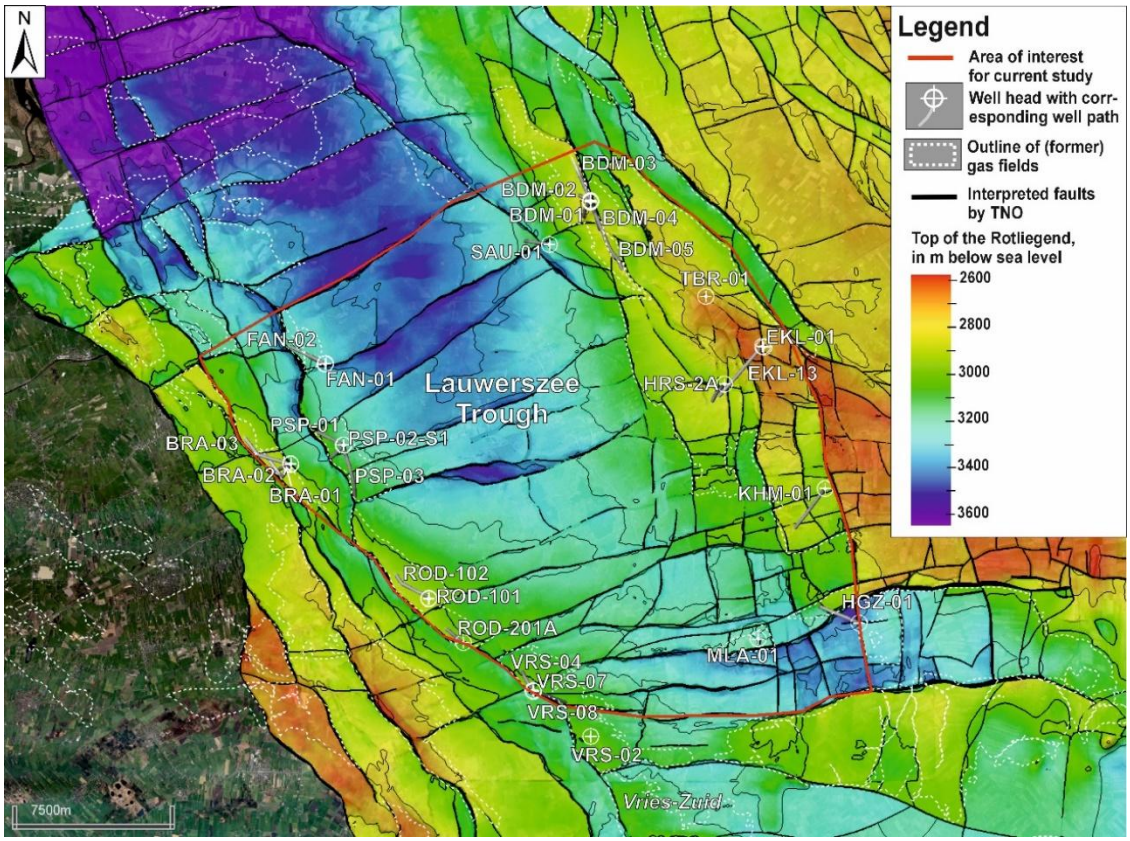

Figure 2-3 Overview picture showing the well names in the area of interest projected on a depth map of the top of the Rotliegend (warmer colours indicate shallower depth). The red outline is the area of interest. For the EKL cluster, only well EKL-1 is plotted for clarity. The dashed white lines indicate the outline of the gas fields. See Figure 2.2 for a clearer image of the position of the gas fields. The interpreted faults (in black) are from TNO (2023) internal geological model for the wider Groningen area.

2.1.1 Regional geological background and stratigraphy

The Late Permian sandstones of the Upper Rotliegend group comprise the Slochteren Formation, which can be subdivided into the Lower Slochteren and the Upper Slochteren Members (Figure 2-4). Around 80% of all the Dutch natural gas has historically been produced from more than 200 fields within this interval, including the large Groningen gas field (e.g. Kortekaas et al., 2023, see also Figure 2-2). The Upper Rotliegend siliciclastic sediments were deposited along the fringes of the Southern Permian Basin (SPB), which was an endorheic[1] basin during the Late Permian that stretched from the UK in the west towards Poland in the east (e.g. Fryberger et al., 2011, Figure 2-5). During deposition of the Upper Rotliegend Group, the SPB generally underwent gentle thermal subsidence (Ziegler, 1990; van Wees et al., 2000, Geluk, 2007). This gentle period of subsidence followed after a tectonic pulse, causing crustal thinning, widespread uplift, wrench tectonics and associated magmatism during the Latest Carboniferous and Early Permian (Ziegler, 1990; van Wees et al., 2000, Geluk, 2007). This tectonic phase is expressed in the current SPB-area as the Base Permian Unconformity (BPU), which reflects a hiatus in the geological record of around 40-60 million years between the sediments of the Late Carboniferous and the overlying Upper Rotliegend sediments (Geluk, 2007; Reijmer et al., 2017). Towards the south of SPB, continental collision occurred along the

[1] An endorheic basin is a self-contained basin that allows no water outflow to other bodies of water (such as rivers and oceans). Instead, the water drainage flow in an endorheic basin equilibrates through evaporation. Modern day examples of endorheic basins are the Caspian basin and the Dead Sea basin.

Rheic suture during roughly the same time period, leading to major uplift and the formation of the Variscan orogenic belt (e.g. Ziegler, 1990; Smit et al., 2018).
When the Upper Permian sands were deposited, the SPB was positioned around 20˚ N, causing an arid climate at the time (e.g. Glennie; 1972. Howell, and Mountney, 1997; Fryberger et al., 2011). Within this arid climate, sediments were transported by ephemeral river systems and by strong (generally easterly trade) winds, leading to a variety of lithofacies including fluvial, playa and aeolian deposits (e.g. Fryberger et al., 2011; de Jager & Visser, 2017; Bouroullec and Geel, in press). Aeolian deposits are generally considered the best reservoirs with an average porosity that exceeds 20% (e.g. De Jager & Visser, 2017; Kortekaas et al., 2023). The main source of sediments was the Variscan orogenic belt towards the south of the SPB, from which sediments were transported generally from south-southeast towards the north-northwest (e.g. Geluk, 2007; Fryberger et al., 2011, Van Ojik et al., 2012; Figure 2-6).

The overall subsidence of the SPB and the influx of sediments caused a progressive basal onlap configuration onto de paleo basin margins, where younger strata were deposited increasingly further southwards (e.g. Fryberger et al., 2011, De Jager & Visser, 2017, Figure 2-4). Overall, the sediments along the southern rim of the SPB, display a typical proximal to distal trend which is characterised by a shaling out towards the north ((e.g. Fryberger et al., 2011, De Jager & Visser, 2017, Kortekaas et al., 2023, Figure 2-7). Along the most proximal southern parts of the SPB, conglomerates are abundantly present, while further towards the north, the sandstones get increasingly intermixed with mudstones (Fryberger et al., 2013; De Jager & Visser, 2017, Figure 2-7). The distal deposits that are time-equivalent to the Slochteren. Fm. are part of the Silverpit Formation (e.g. Kortekaas et al., 2023, Figure 2-4, Figure 2-6 and Figure 2-7). A significant mudstone interval, which can be found also in more proximal parts of the SPB and represents a base level highstand, is formed by the Ameland Claystone Member, which separates the Lower Slochteren from the Upper Slochteren Members (Kortekaas et al., 2023, Figure 2-4 and Figure 2-7). Another base level highstand led to the deposition of the Ten Boer Claystone Member, which overlies either the Upper Slochteren Mb or the Slochteren Formation (Kortekaas et al., 2023, Figure 2-4 and Figure 2-7). In the most distal parts of the SPB (also referred to as the Silverpit Basin, Figure 2-6), also evaporites were deposited.

At the very end of the Permian, an abrupt flooding of the SPB occurred, leading to the deposition of the Kupferschiefer Formation. This flooding marks the end of the Upper Rotliegend Group and the onset of the deposition of the Zechstein Group, during which alternations of carbonates, evaporites and siliciclastics were deposited in several reoccurring cycles (e.g. Geluk, 2007; Patruno et al., 2017; Peeters et al., 2023). During deposition of the Zechstein Group, vast amounts of evaporites were deposited in the Groningen area. These evaporites were remobilised into a variety of salt structures during Mesozoic rifting (e.g. Ten Veen et al., 2012; Bouroullec et al., 2018). The presence of Zechstein salt also decouples the sub-salt deformation from the supra salt deformation in the wider Groningen area (Ten Veen et al., 2012; Bouroullec et al., 2018).

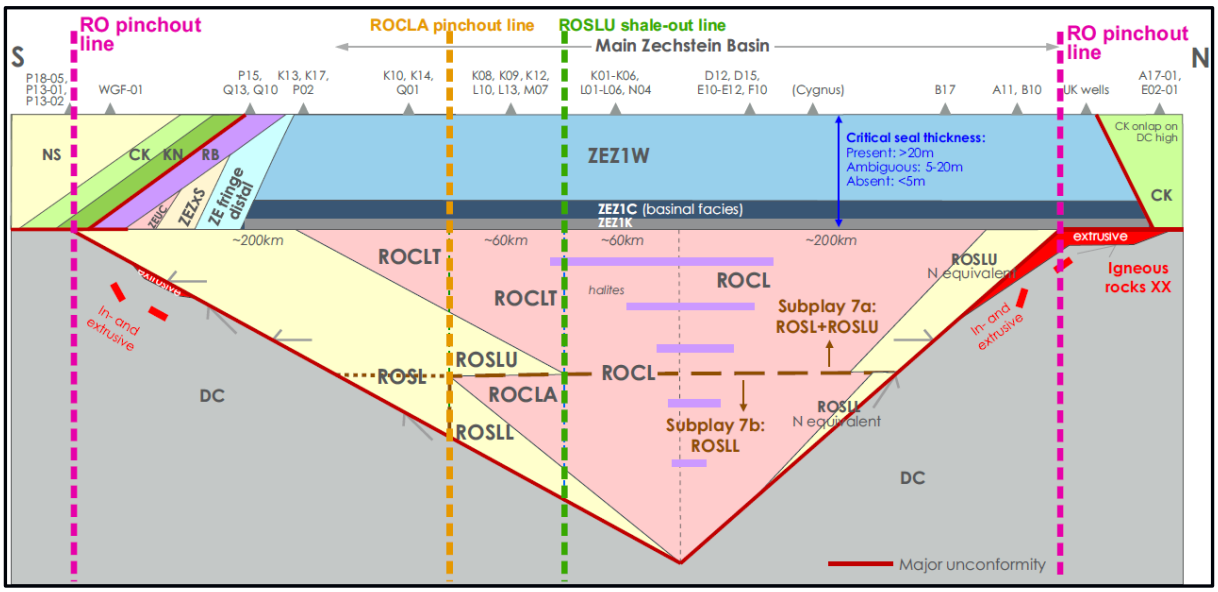

Figure 2-4 Stratigraphic scheme illustrating the vertical and lateral distribution of the Rotliegend Upper-, and Lower Slochteren sandstones. Abbreviations used: NS; North Sea Groups, CK; Chalk Group, KN; Rijnland Group, RB; Lower Germanic Trias Group, ROSL; Slochteren Fm. (sandstones), ROSLU; Upper Slochteren Mb., ROSLL; Lower Slochteren Mb., ROCLT; Ten Boer Claystone Mb., ROCLA; Ameland Claystone Mb., ROCL; Silverpit Formation (claystones), ZE; Zechstein Group; ZEZ1K; Coppershale Mb., ZEZ1C; Z1 Carbonate Mb., ZEZ1W; Z1 Anhydrite Mb., ZEZxS; Zechstein Fringe Sandstone Members (Z1-Z4), ZEUC; Zechstein Upper Claystone Mb. See the dashed black line in Figure 2-5 for the approximate location of this stratigraphic scheme. Figure from Kortekaas et al., 2023.

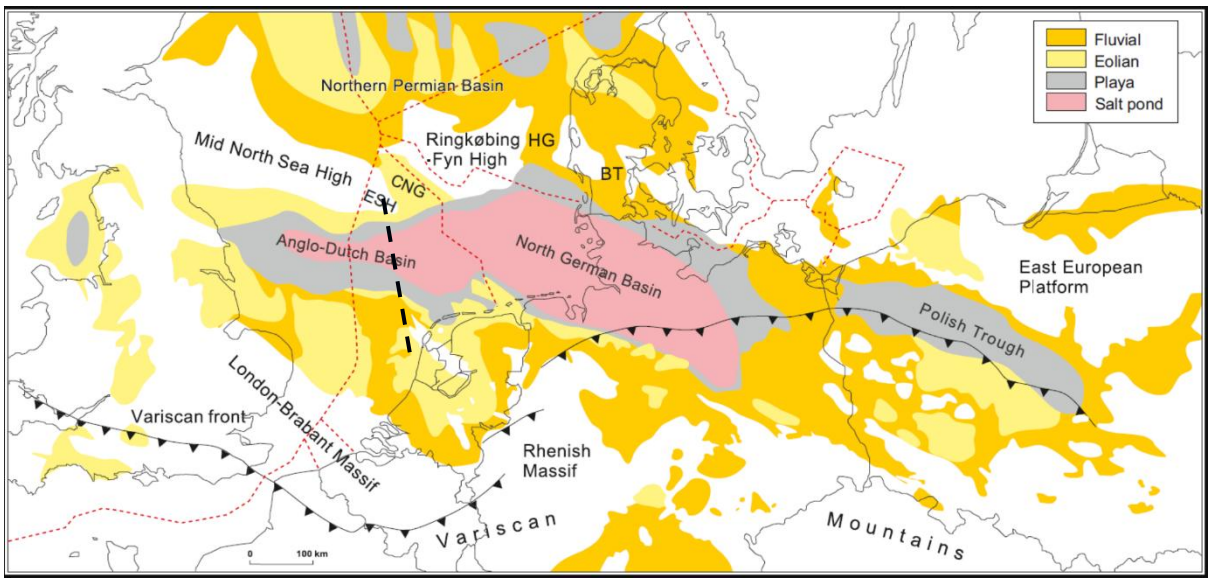

Figure 2-5 Generalised Gross Depositional environment map on the European scale, illustrating the outline of the Southern Permian Basin, which stretched from the UK in the west towards Poland in the east. Figure from Bouroullec and Geel, in press.

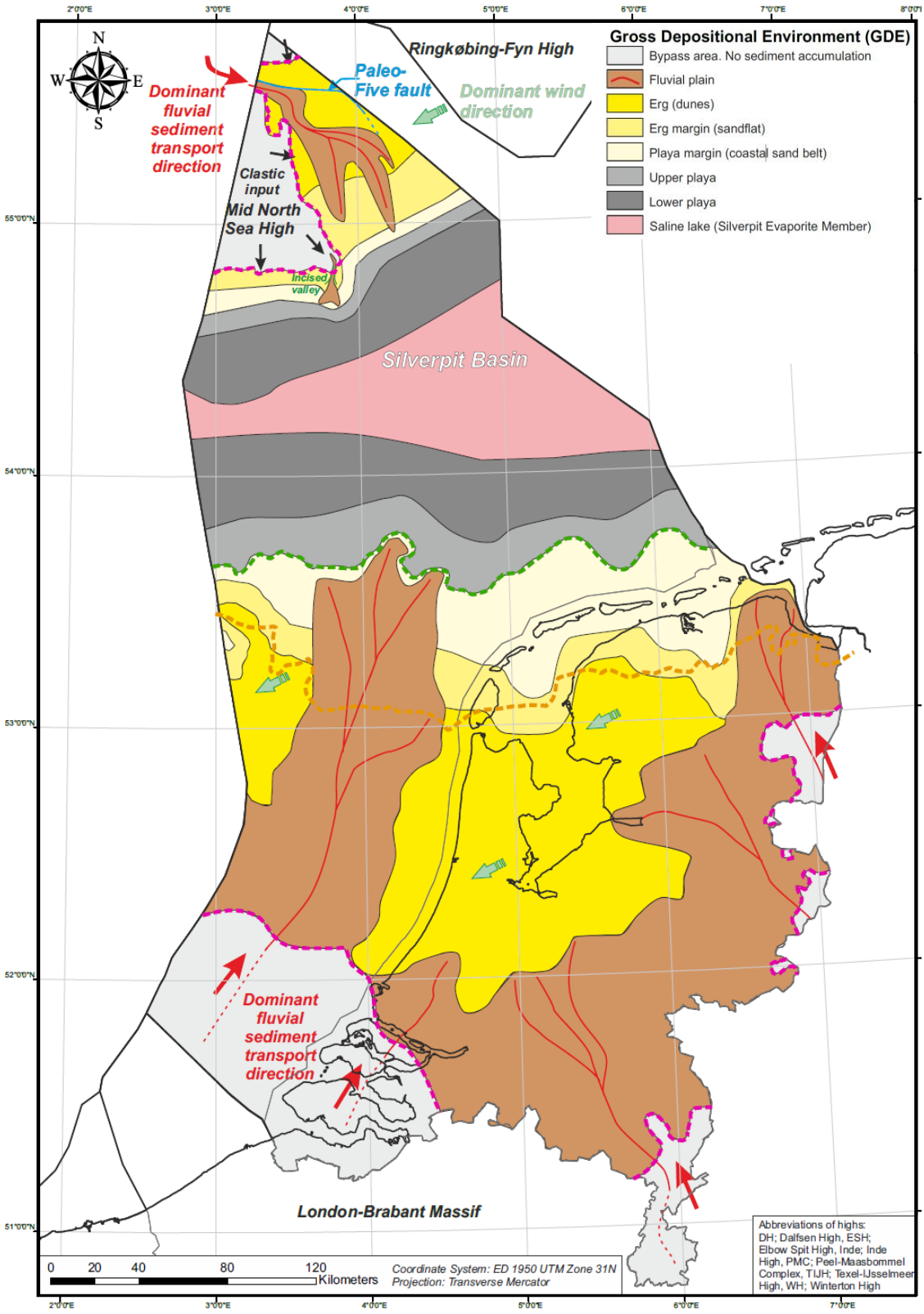

Figure 2-6 Generalised gross depositional environment (GDE) map for the Upper Slochteren Member of the Netherlands. Note that the fluvio-eolian reservoirs were deposited along the margins of Southern Permian Basin, while in the distal part of the SPB (referred to as Silverpit Basin), mainly mudstones and evaporites were deposited. General transport direction was from south to north. Figure from Kortekaas et al., 2023.

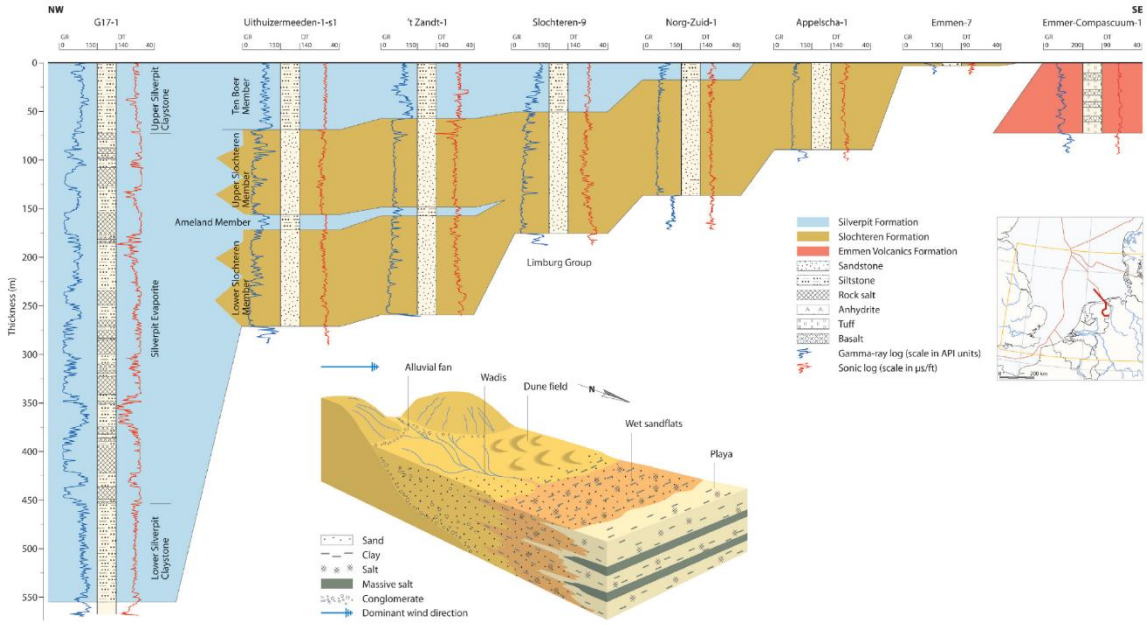

Figure 2-7 Lithological cross section displaying a proximal to distal trend from the offshore G17-1 well in the Silverpit basin (distal part of the system), towards the onshore wells in the wider Groningen area (proximal part of the system). Note that in the well SLochteren-9, Norg-Zuid-1, Appelscha-1 and Emmen-7, the Ameland Claystone Member is no longer present and the Upper and Lower Slochteren Members merge into a single succession of sand, which is then defined as the Slochteren Fm.. See also Figure 2.4. *Figure from Gast et al., 2010.*

2.1.2 Reservoir architecture in the wider Groningen area

The reservoir quality of the Slochteren reservoirs has been extensively studied in the wider Groningen area via thousands of core plugs (De Jager & Visser, 2017). Porosities vary typically from 10 to 24% and permeabilities generally vary between 1 to 1000 mD (Visser, 2012; De Jager & Visser, 2017). Attempts have been made for the extensively studied Groningen field to distinguish different facies within the sandstones, such as fluvial, aeolian and mixed fluvial-eaolian (e.g. Vissers et al., 2016; De Jager & Visser, 2017). Although the purely aeolian sandstones are characterised by the best reservoir properties, they only account for 1.5% of the sandstone facies, which has been attributed to repeated erosion of aeolian deposits, leading to a high degree of sorting but a low degree of preservation in the sedimentary record (Vissers et al., 2016). It is noted that when the degree of sorting is lower and some small amounts of finer-grained sediments are intermixed with the coarser-grained sediments, this only has a limited effect on the average porosities (De Jager & Visser, 2017). On the field scale, the best reservoir qualities can generally be found in the central part of the field. Towards the south, conglomeratic facies become more abundant and towards the north, the interval becomes more prone to mudstone intercallations that are interbedded with the sandstone intervals (e.g. Gast et al., 2010 Fryberger et al., 2011, De Jager & Visser, 2017, Figure 2-4). Besides the paleo depositional environment, also the diagenetic history usually exerts a major control on the reservoir quality. For the Groningen field, diagenesis generally did not have a significant negative impact on the reservoir quality (De Jager & Visser, 2017). Other Rotliegend fields are sometimes affected by early diagenetic processes such as the secondary precipitation of anhydrite or dolomite (Amthor and Okkerman, 1998; Van Hulten, 2006). Amthor and Okkerman (1998) found for the southern margin of the SPB that the combined

volume of dolomite and anhydrite cementation increases from south to north, following roughly the proximal to distal trend present in the paleo depositional environment (Figure 2-6). This is likely related to an increase in salinity and wetness of the system (i.e. episodically higher groundwater tables) from south to north (Amthor and Okkerman (1998). Although the current study area is positioned in a proximal part of the system, the risk for secondary precipitation of anhydrite and/or dolomite might increase northward.

Another diagenetic process that may (partly) plug the reservoir pores and deteriorate the reservoir quality is the formation of fibrous illite (Bjørlykke et al., 1995; Van Hulten, 2006; Gaupp and Okkerman, 2011). Illite occurs both as an authigenic clay mineral within the Upper Permian Rotliegend interval (e.g. Seemann, 1979), but may also form due to illitization of kaolinite, derived from Zechstein brines (Almon, 1979, Lanson et al., 1996, Van Hulten, 2006). The occurrence of fibrous illite occurs later in the diagenetic history at relatively higher temperatures and has been link to major phases of tectonic activity (e.g. Mesozoic rifting and/or Late Cretaceous/Early Cenozoic inversion), allowing Zechstein brines to be introduced in the Rotliegend system after faulting (Lanson et al., 1996). The majority of the Groningen field has been largely protected from fibrous illite formation, likely because of its limited maximum burial depth and/or early charge of gas (Gaupp & Okkerman, 2012; De Jager & Visser, 2017). For the current study area, this means that especially away from the Groningen field and the Groningen platform in general and into the Lauwerszee Trough, this secondary clay precipitation such as fibrous illlite precipitation may have had a negative impact on the reservoir quality.

2.1.3 Structural development of the wider Groningen area

The current study area covers the central part of the Lauwerszee Trough, the very eastern tip of the Friesland platform and the southwestern part of the Groningen platform (Figure 2-1). The Lauwerszee Trough was likely already a paleo low during the Early Carboniferous, when platform carbonates developed onto the adjacent Friesland and Groningen Highs (Kombrink et al., 2010; Van Hulten, 2012). At present, The Zechstein and Rotliegend Groups are positioned at greater depths within the Lauwerszee Trough than on the adjacent Groningen and Friesland platforms. The difference is generally around 400 - 800 meters (see Figure 2-1). The overlying space is mostly filled with a relatively thick interval of Triassic within the Lauwerszee Trough compared to the platform areas (GDN-v5). The Jurassic interval is absent both within the Lauwerszee Trough and on the platform areas and also the Cretaceous and Cenozoic intervals don't display any clear thickness trends (GDN-v5).

Like the rest of the current southern North Sea Area, the wider Groningen area has been affected by multiple deformation phase. Younger deformation phases often reactivated older structures, resulting in the complex fault pattern that is present today (See Figure 2-1). The main deformation phases within the area are:

- An Early Carboniferous phase of extensional tectonics, during which the approximately NW-SE oriented main bounding fault systems of the Lauwerszee Trough where active (e.g. Smit et al., 2018)
- A phase of Late Carboniferous-Early Permian inversion, widespread uplift, magmatism and wrench tectonics, resulting in the formation of the BPU (e.g. Geluk, 2007; Reijmer et al., 2017)
- A phase of Early Permian rifting, which created narrow syn-depositional grabens in Germany and possibly affected also the Ems Graben just east of the Groningen field

(De Jager & Visser, 2017). Syn-depositional faulting within the Groningen area has not been demonstrated for the Upper Rotliegend sediments (De Jager & Visser, 2017).

- Mesozoic extension and rifting. During the Triassic, a general east-west extension was present within the Southern North Sea Area. The thickness trend within the Lauwerszee Trough suggest that the main bounding fault systems were possibly active during this time (DGM V-5, Triassic thickness map). Mesozoic extension also triggered major halokinesis of the Zechstein evaporites (e.g. Bouroullec et al., 2018). It is most likely that, during this phase, faults at the Rotliegend level were most active, and created the patchwork of fault blocks that is observed at present (De Jager & Visser, 2017, Figure 2-1).
- A Late Cretaceous to Early Cenozoic phase of inversion, caused by Alpine compression. This phase mainly affected the Mesozoic rift Basin in the Southern North Sea Area, but some effect is present on the platforms area, including the wider Groningen area. Within the wider Groningen area, some fault reactivation of pre-existing trends can be observed, resulting in narrow pop-up and pull-apart blocks formed by NW-SE to more W-E striking faults (De Jager & Visser, 2017). Additionally, thinning of the upper part of the Paleogene over the Groningen field indicates that inversion during the Cenozoic to some extent also affected the Groningen platform (De Jager & Visser, 2017).

2.2 Data collection

The data collection started with a review of existing, publicly available, and in-house 3D reservoir models that cover the area of interest or are adjacent to it. The available models are:

- NAM reservoir model Groningen Field (2019) - a detailed, complex 3D reservoir model of the Groningen Field
- TNO KEM-19 - a relatively simple 3D reservoir model based on NAM and TNO-GDN.
- TNO internal model - NAM 3D reservoir model extended with additional seismic interpretations west of the Groningen Field.
- TNO ThermoGIS - a layer based model with reservoir properties for various aquifers, among which the Slochteren Formation (Lower Slochteren Member - ROSLL, Upper Slochteren Member - ROSLU), Ameland Member (ROCLA) and Ten Boer Member (ROCLT).

Figure 2-8 shows top views of three of these models with faults and the base of the Zechstein. Shortcomings and missing features of each model for the current project are readily identified. In the NAM reservoir model (2019) an area is missing on the western side and therefore it doesn't cover the full extent of the current study area. In addition, the faults that cross the Lauwerszee Trough do not extend far enough into the area of Interest. Additionally, not enough faults were interpreted in the Lauwerszee Trough in order to fully cover the objectives of the current study.

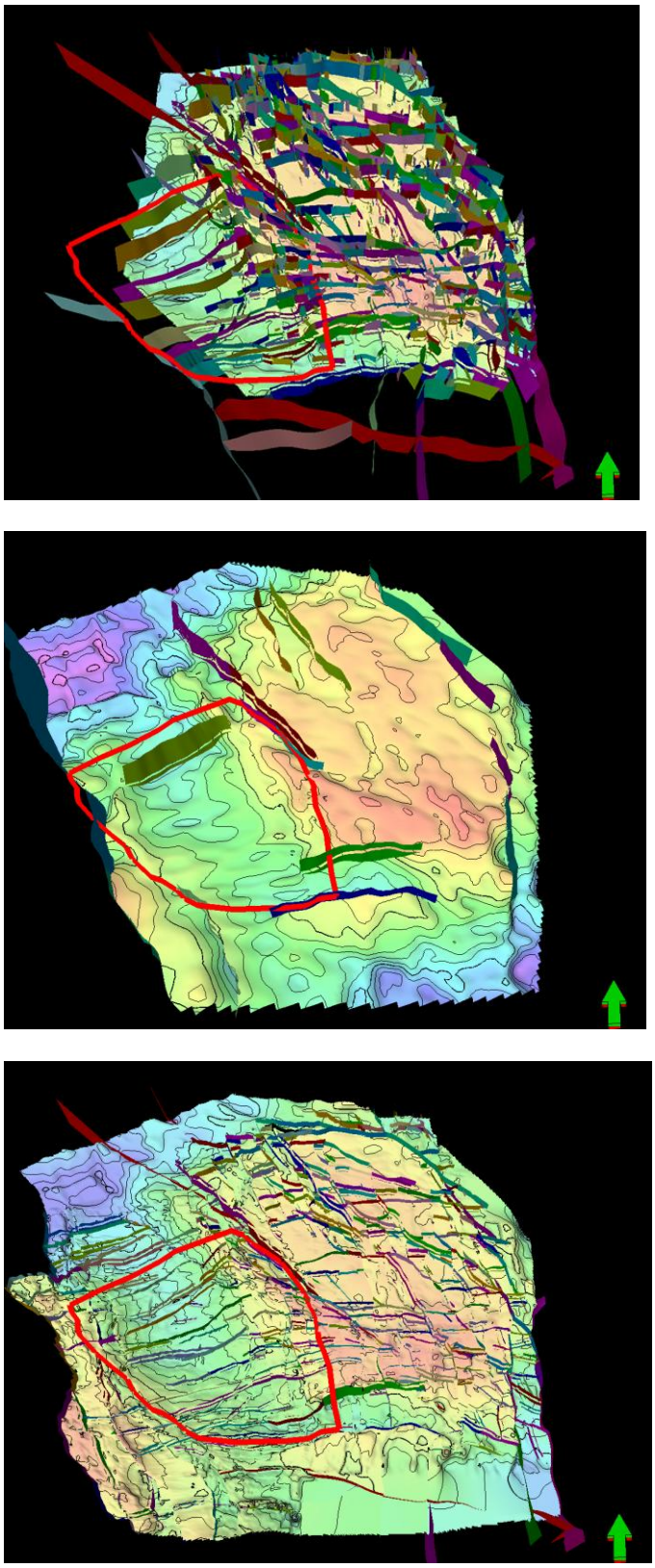

Figure 2-8 Low angle bird's-eye view, which enables to compare the extend and details of the existing models. For an impression of the scale see Figure 2-1 to Figure 2-3. Upper: NAM reservoir model (2019). Middle: TNO KEM-19 reservoir model (2021). Lower: TNO internal reservoir model (2023). The red polygon is the outline of the current area of interest. Green arrow indicates north.

The TNO KEM-19 reservoir model (2021) contains only a handful of faults (middle image in Figure 2-8), and lacks the detail needed within the Lauwerszee Trough. The TNO internal reservoir model (2023) was based on NAM's (2019) model for the area on the Groningen platform and had been extended toward the west, thereby covering also large parts of the Lauwerszee Trough and a minor part of the Friesland platform. This model is generally detailed enough and it covers the current area of interest. A limited number of smaller scaled faults in the Lauwerszee Trough is not incorporated in this model (Figure 2-8 bottom picture and Figure 2-14). Another point of attention for the TNO (2023) internal model is that its reservoir properties are likely too optimistic in the water zone since the simulation of the properties do not take into account differences in reservoir quality between the water and gas phase and changes with depth.

The model of choice to use as a starting point was TNO's internal model (2023) (Figure 2-9). The geometry (horizons, faults, grid cell size) was largely fit for purpose, but a few challenges remained. First of all, the set of faults needed to be checked on seismic and some smaller scaled faults needed to be added. Also the model boundaries needed to be selected before creating the static model. Subsequently a model grid was created via pillar gridding. In addition, a part of the Carboniferous underlying the Lower Slochteren Member needed to be added to the bottom of the model. This is needed to allow pressure depletion in the underlying Carboniferous interval (see also chapter 2.3).

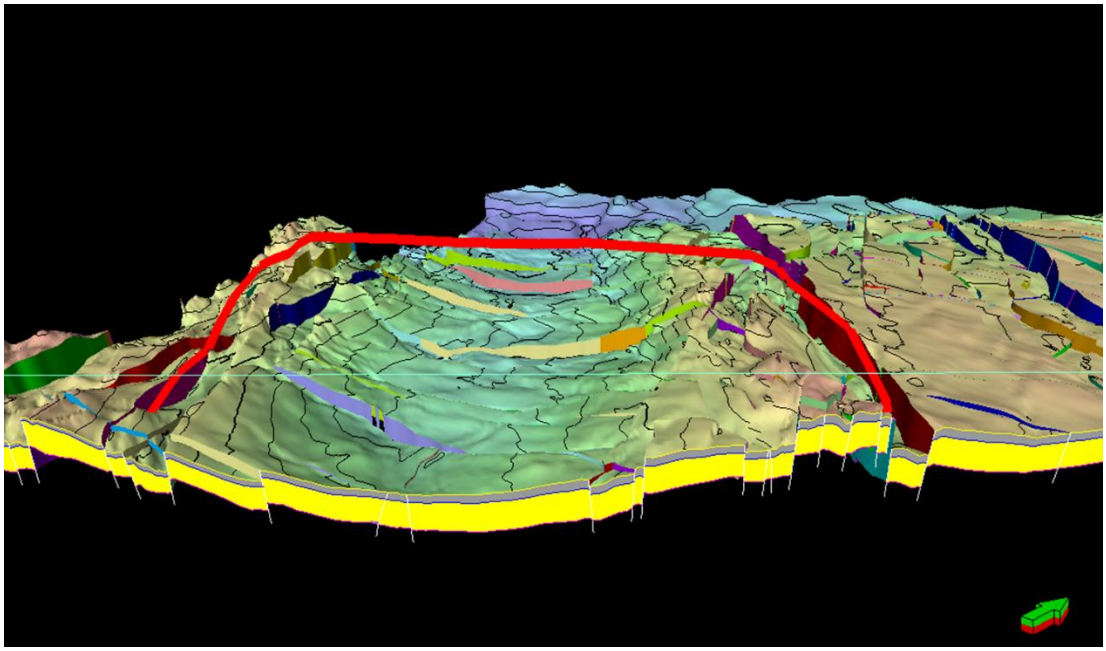

Figure 2-9 3D bird's-eye view of the geometry of the TNO internal model that was used as a starting point for the KEM-19b model. Yellow colour on the cross-section denotes the sandstones of the Slochteren Formation, the overlying grey represents the shaly Ten Boer Member. Note that the Ameland Member is not present this far south. Green arrow indicates north.

2.3 Construction of the fault model and grid

From the geological model (also called static reservoir model), a dynamic reservoir model will be created, which will be used to simulate the pressure depletion in this aquifer. This has a strong impact on the choice of the model area and boundaries, which will be discussed below. Ultimately, an ensemble of models will be created by varying reservoir properties. The geometry (i.e. faults and reservoir configuration) of the model, which is discussed in the

current chapter 2.3, will not be varied. The creation of the ensemble will be discussed in section 2.5.

Since there are no wells in the aquifer within the Lauwerszee Trough, the information for the aquifer needs to come from the gas fields on both sides of the aquifer: the Groningen and Bedum fields on the east and a series of small gas fields in the west (Figure 2-2 and Figure 2-3). These gas fields and the wells associated with it need to be included in the model to constrain the reservoir properties (porosity and permeability), to simulate the pressure depletion in the aquifer resulting from these small gas fields and to simulate the subsidence. As mentioned in the introduction, observed subsidence is used to reduce the uncertainty. The workflow of how this is done is explained at the start of Chapter 3. Only a small part of the Groningen field will be included to keep the size of the model limited and to allow a sufficiently detailed grid near the small gas fields. Keeping the size of the model limited is important because the uncertainty will be addressed by using an ensemble of models rather than a single model. Preferably the boundary of the model is located at faults with large offset which act as no flow boundaries, but that was not always possible. Below the detailed choices for the boundaries are described, based on the geological settings and the requirements for the dynamic model. The boundaries are no flow boundaries except when indicated otherwise.

The boundaries of the model were selected as follows:

- In the north, a large fault with large offset separating the northern part of the Lauwerszee Trough from the southern part is used as the main part of the boundary (Figure 2-2 and Figure 2-10). On the northwest side, the model boundary is formed by a number of faults bounding the Faan and Boerakker gas fields. In the north-east no suitable faults were available and the boundary of the model is in the Bedum field (Figure 2-2 and Figure 2-10). Therefore the Bedum field will be implemented as a pressure boundary condition.
- On the east side, two connected faults with large offsets separating the western periphery from the Groningen main field are selected as boundary. The offset of the faults is well visible in Figure 2-9 (i.e. the red fault and the purple fault) and Figure 2-10. The included part of the Groningen field will be implemented as a pressure boundary.
- To the south, the position of the boundary is taken as the south bounding fault of the graben between Groningen and Annerveen on the east side and on the west side by faults separating Vries North from Vries Central. The Annerveen field itself is not included in the model (Figure 2-2 and Figure 2-10), because it is not directly connected to the SW aquifer due to the deep graben.
- On the west side, the boundary is formed by a series of faults which close the small gas fields on the west and mostly have large offsets (Figure 2-2, Figure 2-9 and Figure 2-10).

The implementation of the Groningen and Bedum fields as pressure boundary conditions and the values used for the pressure will be discussed in more detail in paragraph 3.2. As top boundary condition, the base Zechstein is selected. For the bottom boundary, a part of the Carboniferous underlying the Lower Slochteren Member needed to be added to the bottom of the TNO model. This was done to allow pressure depletion in these layers. In the model area, the Lower Slochteren Member is underlain by various formations of the Limburg Group. This is simplified in the model.

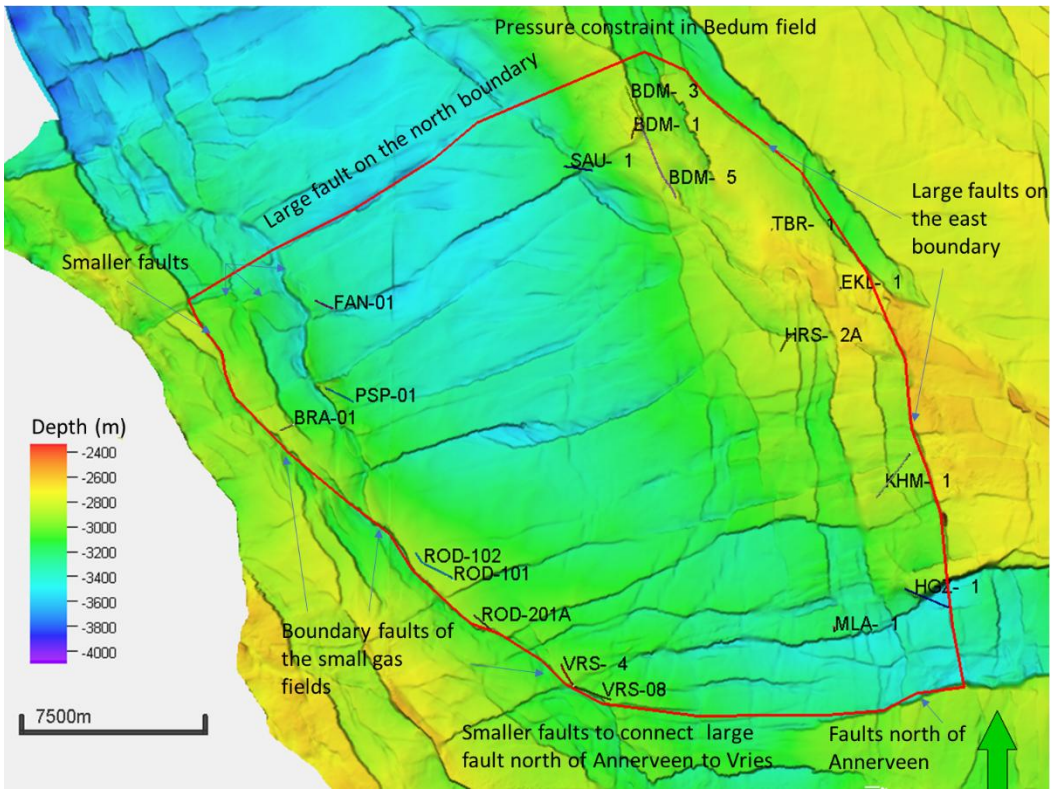

Figure 2-10 Top of the Rotliegend depth map. Red line is the outline of the area of interest. Green arrow indicates north.

As stated above, additional work on the faults was necessary. A check on the faults from TNO's internal model against a Variance cube (a seismic attribute that is frequently used to map faults) resulted in the identification of a number of minor, small scaled faults (i.e. both in terms of offset and lateral continuity) that are not incorporated in the TNO internal model (Figure 2-11). The majority of these faults have an approximately east-west strike that is oblique to the strike of the larger faults in the Lauwerszee Trough, which is generally WSW-ENE (Figure 2-12). These minor faults are most likely Riedel shear faults, which resulted from strike-slip movements. It is noted that not all minor faults have been incorporated in the current model. This is due to gridding limitations, and not due to seismic quality as the seismic quality is good.

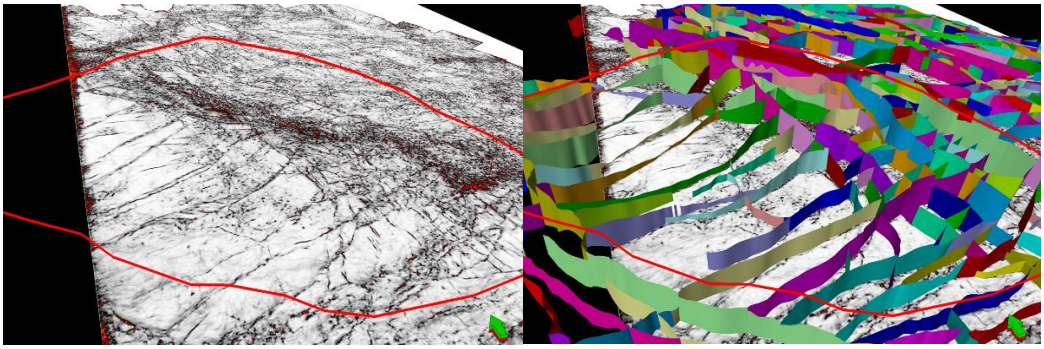

Figure 2-11 **Left:** Bird's-eye view showing a depth slice of the 3D Groningen seismic survey at ~3500 m depth. Right: the same time slice overlain by faults from TNO's internal model (2023). Note that some smaller faults are missing from the model. The red polygon is the outline of the area of interest.

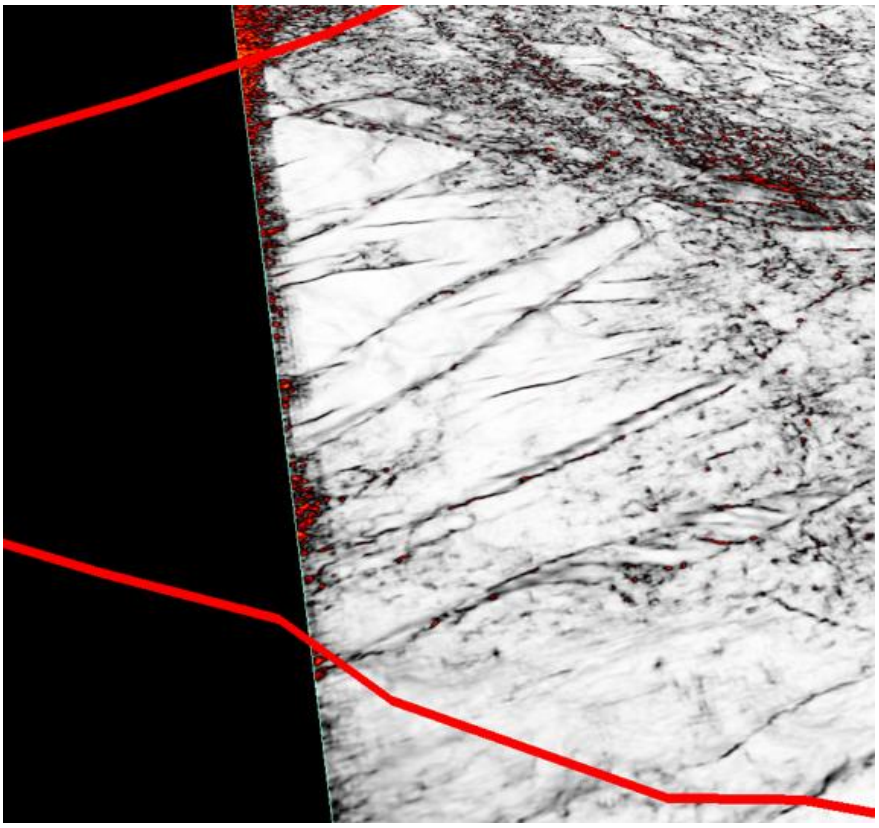

Figure 2-12 Detail of Figure 2-11 left, showing the oblique strike of the smaller faults with respect to the larger faults, most likely the result of strike-slip movements. A mall pull-apart structure is present the foreground. The red polygon is the outline of the area of interest.

In addition to fault interpretation on the Groningen seismic cube, additional faults needed to be interpreted on seismic cubes west of the Groningen cube. Figure 2-13 shows a map with the outlines of all seismic cubes that cover the area of interest. Apart from the Groningen cube, these include 5 seismic surveys:

- Grootegast L-123 (1985)
- Grootegast L-128 (1985)
- Lauwerszee (1983)
- Broek (1992)
- Eext (1992)

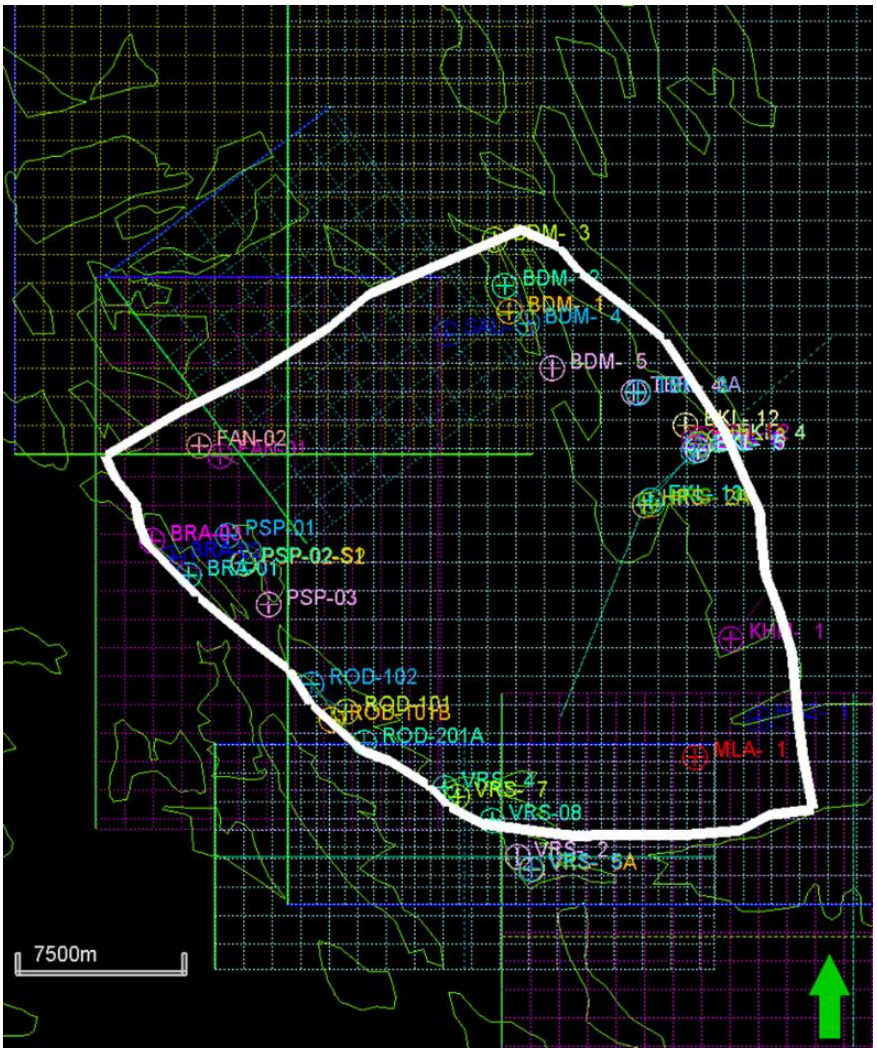

Figure 2-13 Overview of seismic surveys and wells in the area of interest (white polygon). Green arrow indicates north.

For the area of interest, a pillar grid with increment of approximately 150x150 m (Figure 2-14, top map) was created. The pillar grid is a 3D grid based on the fault information (the fault model) and is structured based on the pillars describing the fault geometry. The selected horizontal resolution of ~150 x 150 m is a compromise between the accurate representation of the faults and the small gas fields on the one hand and a feasible number of grid cells required for the reservoir simulations in WP 2. To create the 3D grid to be used for reservoir simulations, the pillar grid is combined with information from the relevant horizons. The top of the model is the top of the Ten Boer Member (ROCLT). The other horizons are the top of the Upper Slochteren Member (ROSLU), the Ameland Member (ROCLA) and top and base of the Lower Slochteren Member (ROSLL). The bottom of the model is 60 m below the base of the Lower Slochteren Member to allow pressure depletion in the underlying formations from the Limburg Group of the Carboniferous. This is less than the thickness of the Limburg Group that is included in the NAM Groningen model. However in the south of the Groningen field, these units are gas bearing and are known to be connected to the gas bearing units of ROSLL above. This is not the case in the aquifer area and lower permeability and connectivity is expected.

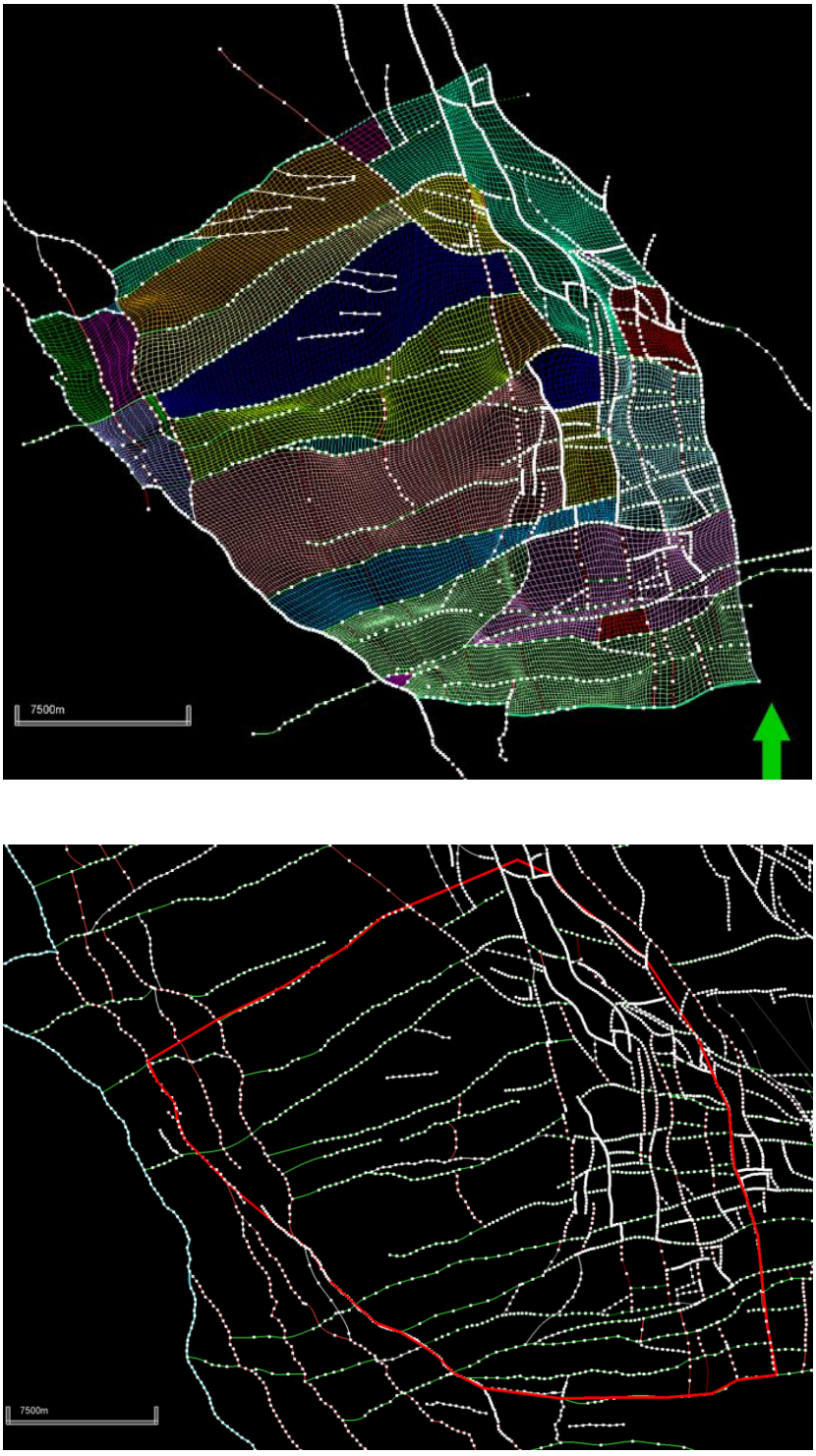

Figure 2-14 Top Figure: Map view of the pillar grid of the area of interest resulting from the combination of existing large fault model and some newly interpreted small faults in the current project. Bottom Figure: Map view of the fault pattern in a pillar gridding configuration of the internal TNO (2023) project. The bold (light) red polygon indicates the outline for the area of interest for the current project.

The horizons are created based on a combination of seismic interpretation and well tops. The top of the Rotliegend was derived from seismic interpretation performed during the modelling of the NAM geological model (2019; for the Groningen platform area) and during the TNO internal modelling (2023; for the Lauwerszee Trough and the most eastern part of the Friesland platform). The intra-Rotliegend layering was based on well tops, which were adopted from the NAM geological model (2019) and the TNO's internal geological (2023). These well tops were picked based on well-log data during the modelling of the aforementioned models. It is noted that the following wells were not incorporated in the TNO internal (2023) geological model: FAN-01, FAN-02, PSP-02, PSP-03 and VRS-08. The well data from these wells, including well logs, well deviation paths, and well tops, were downloaded from nlog.nl, imported into the Petrel project and subsequently used for the update of the geological model.

To achieve a consistent grid, the model construction was undertaken by adding the thickness of the individual zones (derived from well tops) to the top of the model (i.e., the top of the Ten Boer Member (ROCLT), derived from seismic interpretation). The zone layering is presented in Table 2-1. Because most gas is produced from the Upper Slochteren Member (ROSLU), this zone has the highest resolution (i.e. average thickness of 8 m per layer, see Table 2-1). The Ameland Member (ROCLA) is a relatively thin, largely mudrock-dominated interval layer. The ROCLA pinches out towards the south, which reduces the average thickness of the layer. Nevertheless, it was modelled explicitly because it can affect the communication between Upper and Lower Slochteren Members.

Table 2-1 Overview of the layering of the geological 3D grid

Zone	Number of layers	Average thickness of the layers
ROCLT	2	27 m
ROSLU	15	8 m
ROCLA	1	3 m
ROSLL	5	11 m
Carboniferous	2	31 m

In total the geological 3D grid has 143 x 160 x 25 grid cells resulting in 572,000 cells.

In the centre of the model there were a few cells with negative volume due to pinching out of cells near faults. This has been solved for the simulation grid by setting these cells to inactive. Because the cells are in the aquifer the impact of the volume is not relevant. The connectivity is marginally reduced, but because these cells are located near low-permeable fault, the impact is negligible.

2.4 Review petrophysical properties and update

2.4.1 Data and methods

The NAM Groningen reservoir model (2019) does not contain wells outside the Groningen Field. Therefore, in order to populate the extended model with reservoir properties (porosity, net-to-gross, permeability), a petrophysical evaluation of selected wells in the southern

part of the Lauwerszee Trough and on the eastern side of the Friesland platform has been conducted (Figure 2-2 and Figure 2-9).

Table 2-2 provides an overview of the selected wells with available log data. Main target intervals for the evaluation are the Ten Boer, the Slochteren and the underlying Carboniferous formations. For some wells, porosity (ϕ), permeability (k) and net-to-gross (NtG) data are available from ThermoGis_v2.2 (a single averaged ϕ, k or NtG over the (entire) Slochteren Formation).

Table 2-2 Selected wells for petrophysical evaluation with available log data. Reported property data (NtG, ϕ, k) are adopted from ThermoGIS_v2.2 and represent the average Slochteren (ROSL) reservoir interval.

Field	Well name	Alternative well name	Usable logs	Evaluated [Y/N]	Comment	ThermoGis_v2.2 Eff. porosity [%] ROSL	ThermoGis_v2.2 permeability [mD] ROSL	ThermoGis_v2.2 NtG [%] ROSL
Roden	ROD-101		GR, DENS, Sonic, Resistivity	Y	Ten Boer, Slochteren (RO) & Maurits (DC) formations evaluated	16.7	25	95.3
	ROD-101-S1		no logs available	N	Undifferentiated below Zechstein, RO-DC well tops not interpreted			
	ROD-101-S2		GR, Sonic, Resistivity	N	No density logs	20.0		
	ROD-102		GR, NEU, DENS, Sonic, Resistivity	Y	Ten Boer, Slochteren (RO) & Maurits (DC) formations evaluated	18.3		74.1
	ROD-201		-	N	well TD in Ommelanden-Chalk			
	ROD-201-S1		GR, NEU, DENS, Sonic, Resistivity	Y	Ten Boer, Slochteren (RO) & Maurits (DC) formations evaluated	16.8		
Vries*	VRS-4	VRS-401	GR, NEU, DENS, Sonic, Resistivity	Y	Ten Boer, Slochteren (RO) & Limburg Group (DC) formations evaluated	16.4		82.6
	VRS-7	VRS-402	GR, NEU, DENS, Sonic, Resistivity	Y	Ten Boer & Slochteren (RO) formations evaluated. TD in Slochteren	16.3		75.0
	VRS-8	VRS-403	GR, NEU, DENS, Sonic, Resistivity	Y	Ten Boer & Slochteren (RO) formations evaluated. TD in Slochteren			
Pasop	PSP-01		GR, DENS, Sonic	Y	Ten Boer, Slochteren (RO) & Ruurlo (DC) formations evaluated	17.5	33	89.6
	PSP-02		GR	N	Undifferentiated below Zechstein, RO-DC well tops not interpreted			
	PSP-02-S1		GR, DENS, Sonic	Y	Ten Boer, Slochteren (RO) & Limburg Group (DC) formations evaluated			
	PSP-02-S2		GR	N	No density logs	17.1		
	PSP-03		GR, Sonic	N	No density logs			
Boerakker	BRA-01		GR, DENS, Sonic	Y	Ten Boer, Slochteren (RO) & Ruurlo (DC) formations evaluated	18.1		81.4
	BRA-02		GR, DENS, Sonic	Y	Ten Boer & Slochteren (RO) formations evaluated. TD in Slochteren	16.9		67.0
	BRA-03		GR, DENS, Sonic	Y	Ten Boer & Slochteren (RO) formations evaluated. TD in Slochteren	16.7		86.0
Faan	FAN-01		GR, DENS, Sonic, Resistivity	Y	Ten Boer & Slochteren (RO) formations evaluated. TD in Slochteren			
	FAN-02		GR, Sonic	N	Ten Boer & Slochteren (RO) formations evaluated. TD in Slochteren			

* VRS-02, VRS-05, VRS-09, VRS-10 are outside the study area

Because the Slochteren formation is a nearly pure sandstone formation, porosity is calculated from the Density log without applying a shale correction:

$$\varphi = \frac{\rho_{matrix} - \rho_{bulk}}{\rho_{matrix} - \rho_{fluid}}$$

with ρ_bulk = RHOB log, ρ_matrix=2.66 g/cm^3, ρ_fluid = 1.05 g/cm^3.

Porosity was calculated using the Petrel calculator. Permeability was calculated in each well based on the porosity log and by applying a poro-perm relationship. In ThermoGIS a standard, countrywide poro-perm relationship is used to calculate permeability from porosity (https://www.thermogis.nl/porositeit-en-permeabiliteit). However, for the wells in the present study, poro-perm relationships were derived (where possible) for each field using poro-perm data reported in the NLOG core plug database (https://www.nlog.nl/sites/default/files/thematische_data/nlog_poroperm.xlsx). Both a porosity correction (0.92) as well as a Juhasz correction (Juhasz, 1986) on permeability data have been applied.

The core-plug data is also used to test whether different porosity-permeability relationships are required for either gas or water bearing intervals in the Slochteren formations.

For each evaluated well a net-to-gross (NtG) was determined using cut-offs on the GR and porosity in line with NAM . Net reservoir is taken as GR<60 gapi and porosity > 0.04.

2.4.2 Petrophysical evaluations

2.4.2.1 Ten Boer and Slochteren formations

Log evaluations have been conducted for the wells listed in Table 2-2. Evaluated results have been, where porosity-permeability measurements are available, cross checked with the core plug data (Figure 2-15). Generally a good match was achieved between the density derived porosity data and the coreplug data. In 0, the porosity-permeability log data per well is provided.

In order to check how the density derived porosities compare to porosities from the NAM Groningen reservoir model, two random wells (EKL-04 and AMR-01) were selected from the Groningen model. In each well, the porosity was calculated based on the density log only, and compared to existing porosity logs in the Groningen model. It is hereby assumed that in the Groningen model a full integrated petrophysical evaluation has been conducted for the wells using all available logs (GR, NEU-DENS, sonic, density). For well EKL-04, also the Ten Boer formation porosities were re-calculated in order to check if the effect of not incorporating a shale correction in the porosity determination of the wells in Table 2-2.

Density derived porosities generally compare well to those derived from the Groningen reservoir model (Figure 2-16). For porosities > 15%, the density porosity generally slightly overestimate the porosity by ~10% (Figure 2-16 A and C). Differences in porosity > 15% may be related to regional and depth variation, sand/shale distribution in the wells but are generally considered negligible when the logs are upscaled for the reservoir model.

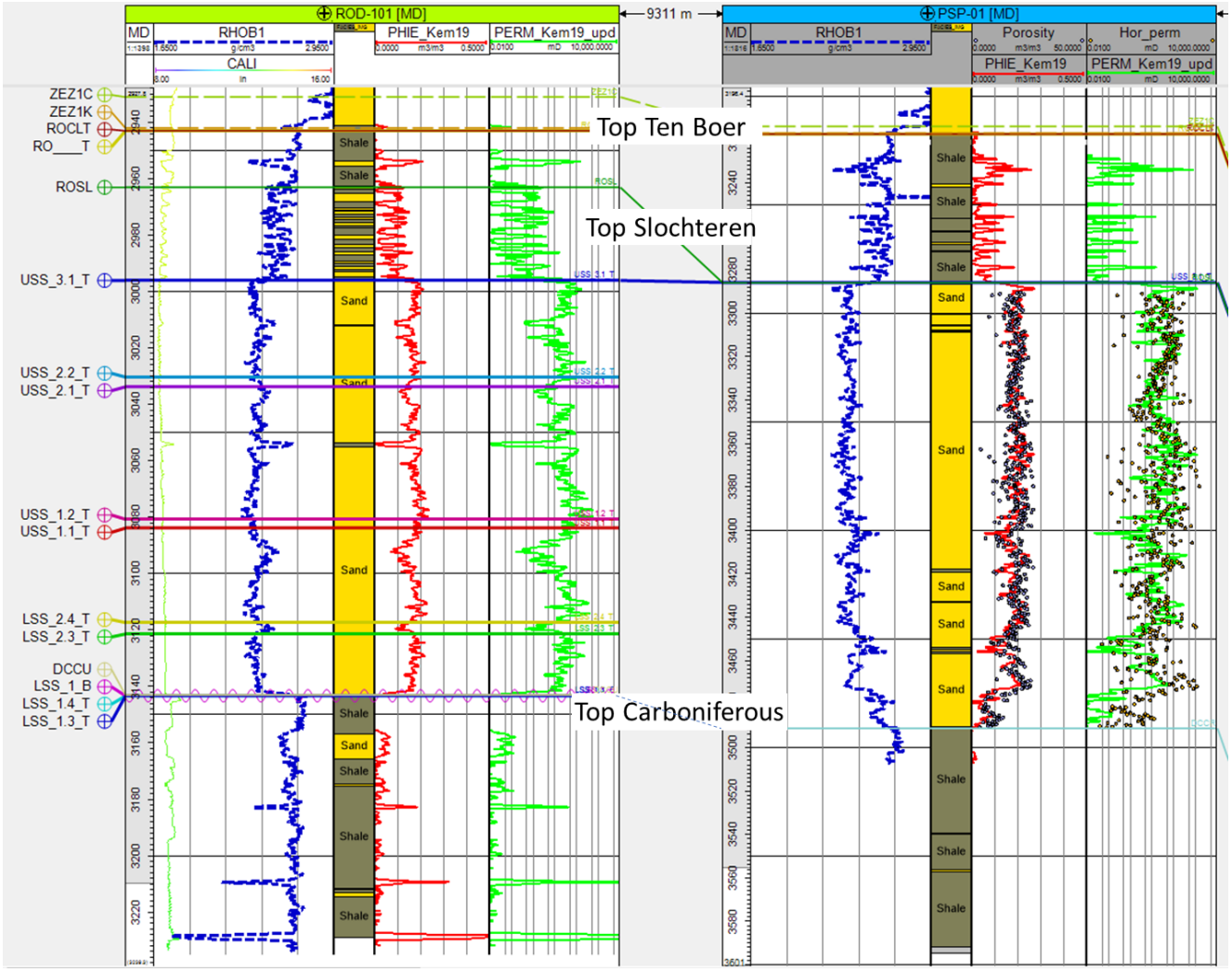

Figure 2-15 Well corelation panel with examples of evaluation results of well ROD-101 and PSP-01. ROSL coreplug measurements (https://www.nlog.nl/sites/default/files/thematische_data/nlog_poroperm.xlsx) are shown for PSP-01 to compare to calculated porosity and permeability logs.

In order to assess whether the assumption to neglect the shale correction is valid, the Ten Boer porosities in well EKL-04 were calculated using the density log and compared to the Groningen reservoir log values. In the Groningen model, cut-offs are applied to the porosity data (if ϕ <0.04 and if ϕ>0.34 then porosity is set to undefined), hence only the more sandy intervals are present in the Groningen model in the Ten Boer interval. Despite this, also the Ten Boer density derived porosities compare well to the Groningen model porosity data in this well. For porosities > 15%, the density porosity generally slightly overestimate the porosity by ~10% (Figure 2-16 B).

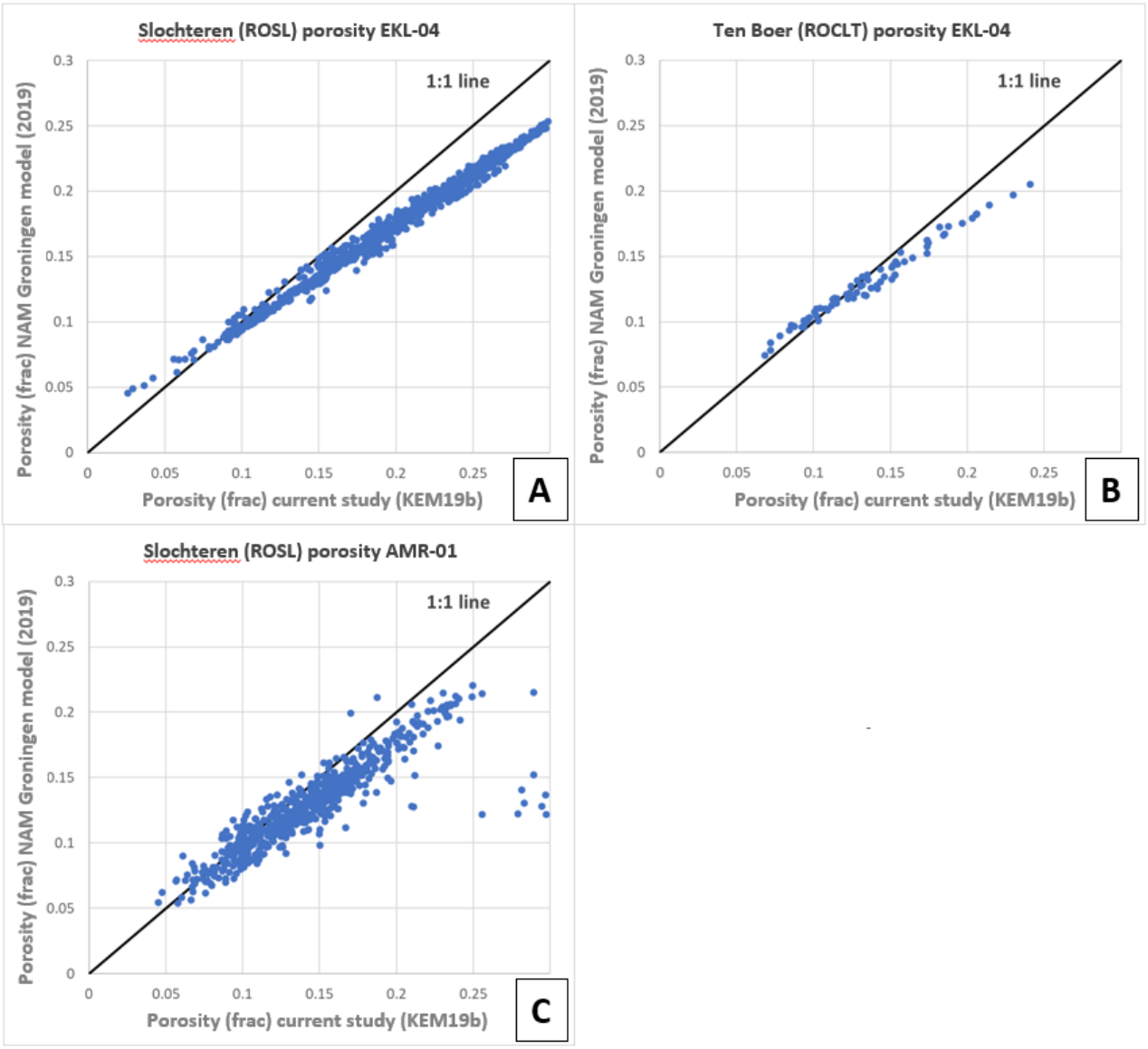

Figure 2-16 Comparison between porosities derived from the NAM Groningen reservoir model (2019) and porosity calculated based on density logs for two randomly selected wells from the Groningen Field. A and B are for well ERK-04 for respectively Slochteren (ROSL) and the Ten Boer (ROCLT) formations. C for well AMR-01 (only Slochteren interval).

Permeability was calculated from the density derived porosity logs using a field-specific poro-perm relationship for Pasop (PSP-01) and Roden (ROD-101 & ROD-202-S1), see Figure 2-17 and Table 2-3.

Wells from the Vries field had only a limited number of coreplug measurements (n = 6) for the Slochteren interval. In some of the Vries wells, a significant amount of coreplug data from the Ten Boer Formation was available, however using these data for the Slochteren interval would underestimate the poro-perm relationship. For wells in the Boerakker and Faan fields, no coreplug data is available. For the evaluated wells in these fields, the poroperm relationship from PSP-01 was used (Table 2-3).

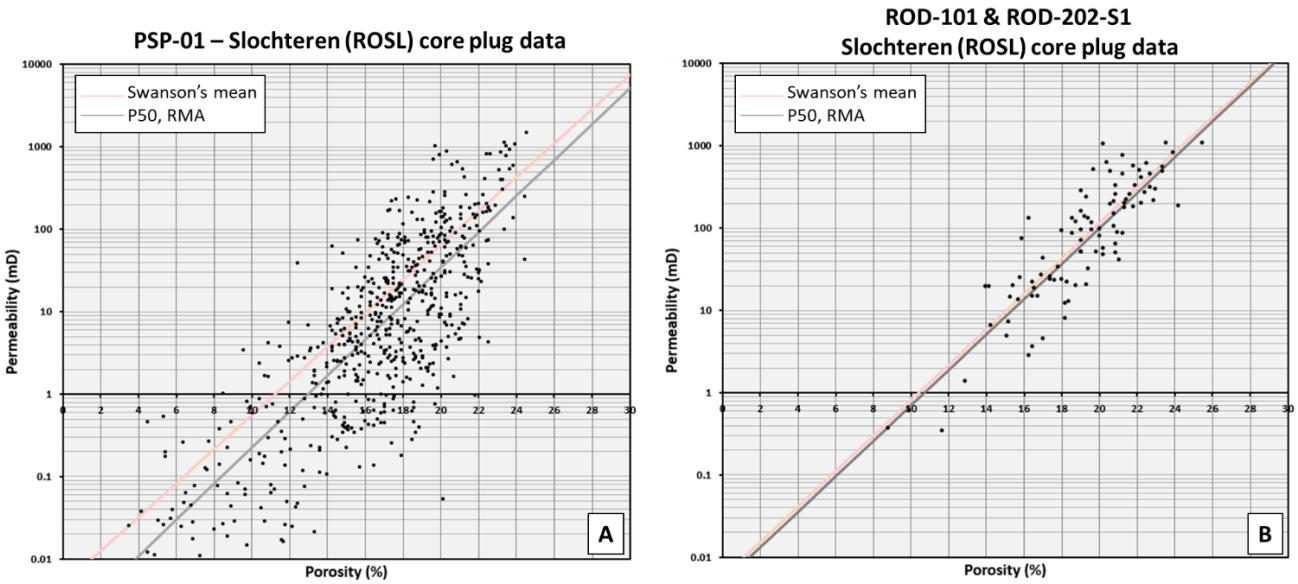

Figure 2-17 Slochteren (ROSL) porosity-permeability plot based on coreplug data from well PSP-01 (A) and wells ROD-101 & ROD-202-S1 (B). For all calculated poro-perm relationships, the P50 – reverse mean average (RMA) was adopted. A Juhasz (1986) correction and a porosity correction of 0.95 have been applied to all coreplug data.

Table 2-3 Derived porosity-permeability relationship for wells in the study area.

Well	Poro-perm relationship	Formation
PSP-01	k = 0.001477 * exp^(0.5020*PHIE)	ROSL
ROD-101	k = 0.0060275 * exp^(0.4839*PHIE)	ROSL
ROD-201-S1		
Vries	6 coreplug measurements in ROSL; PSP-01 poro-perm used	ROSL
Faan	Insufficient coreplug data; poro-perm relationship of PSP-01 was	
Boerakker		

In order to assess the effect of water versus gas bearing intervals on the calculated permeability, the coreplug data from PSP-01 (most coreplug dense well in the study area) is plotted above and below the Gas-Water Contact (GWC, Figure 2-18. The GWC in PSP-01 resides at 3123 m (m NAP) or 3443 m MD.

No clear distinction between porosity-permeability data from below and above the GWC is observed (Figure 2-18). Separate porosity-permeability relationships were derived based on coreplug data below and above the GWC. The resulting calculated permeabilities show minimal differences and have negligible (<5%) effect on the calculated permeabilities.

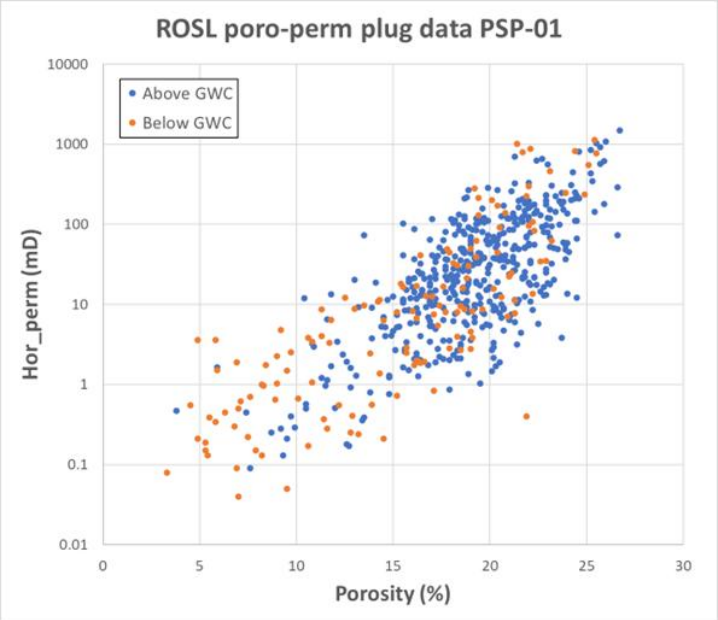

Figure 2-18 Slochteren coreplug data from well PSP-01 separated into above and below the Gas-Water contact (GWC) at 3123 m (m NAP) or 3443 m MD.

2.4.2.2 Carboniferous formations

The aquifer properties of the Carboniferous units directly underlying the Slochteren formations (Pasop and Boerakker: Ruurlo Formation; Vries: De Lutte Formation; Roden: Maurits Formation) were assessed by incorporating core plug data alone. Often log coverage over these Carboniferous intervals is poor to absent, hence it is not possible to do a meaningful evaluation.

Coreplug data from wells in the study area are only available for the Pasop field (PSP-01). Plug data from the Vries Field is available for one well outside the study area (VRS-101). To further expand the plug database for the Carboniferous units, two wells from nearby fields were selected (Grijpskerk: GRK-03 and Saaksum: SSM-02).

A summary of available plug data is provided in Table 2-4.

NtG cannot be calculated from the coreplug and/or available log data. Therefore, following the NAM Groningen reservoir model, a constant NtG of 0.2 is adopted.

Table 2-4 Summary of available coreplug data for Carboniferous units in and in close proximity to the study area.

Field	Well	Unit	ϕ - porosity (%)					k - permeability (mD)				
			min	max	avg	median	nr coreplugs	min	max	avg	median	nr coreplugs
Grijpskerk	GRK-03	DC	2.4	19.3	8.1	8	19	0.02	5.94	0.94	0.06	16
Saaksum	SSM-02											
Pasop	PSP-01	Ruurlo	4.2	7.8	6.08	6.3	26	0.03	0.53	0.17	0.08	5
Vries	VRS-101	De Lutte	3.3	13.8	8.94	9.3	36	0.3	26.0	6.64	3.00	29

2.5 Property modelling

The result of property modelling will be an ensemble of geological models representing the uncertainty in the reservoir properties that serves as input for dynamic reservoir flow simulations. For creating the ensemble several properties are varied, namely:

- Porosity, net-to-gross and horizontal permeability
- Vertical permeability as a fraction of the horizontal permeability
- Vertical permeability of the Ameland Member (ROCLA)
- Baffle[2] for vertical flow between the Slochteren and the Carboniferous units
- Transmissivity of the faults

Porosity, net-to-gross and permeability are varied over the entire field per ensemble member using Gaussian random function simulation. The details of this will be discussed below. The details of how the other properties are varied, is discussed in Section 3.3, where the creation of the ensemble of reservoir models is discussed.

Upscaling well logs
All wells logs in the model area need to be upscaled to the resolution of the grid before they can be used for the property modelling. This applies to both the wells of the small gas field interpreted in this project and to the logs of the wells of the NAM Groningen model. For the wells interpreted in this project outliers where removed by applying cut-offs to the porosity data: if $\phi < 0.04$ and if $\phi > 0.35$ then porosity is set to undefined following the NAM workflow.

For all wells inside the model area, the logs of porosity, NtG and permeability were upscaled to the vertical resolution of the grid. For the upscaling arithmetic averaging was used for all three properties, also permeability. Since parallel flow to the well is the most relevant flow pattern, arithmetic averaging is the most appropriate upscaling method. No weighting was applied.

Porosity
Reservoir properties are based on well log data which are predominantly from the gas fields. Only two wells have been drilled in the aquifer, namely HAR-01 and SAU-01 and of these two, only SAU-01 has sufficient data to estimate porosity. Properties in the deep Lauwerszee Trough are most likely not as good as in the surrounding gas fields because of the presence of dolomite cement and illite fibers (see paragraph 2.1.2). In addition, there is generally a bias in the wells because they are targeting better quality rocks. NAM therefore has used inversion of the seismic data to improve the porosity estimates in areas with few wells (de Zeeuw and Geurtsen, 2018). It is beyond the scope of the current project to do this for the Southern Lauwerszee Trough. Instead, a porosity-depth relation will be included to ensure lower values in the deeper aquifer. This will be explained in more detail below.

As discussed in paragraph 2.1.2, there might be a decrease in reservoir properties from south to north. The small gas fields do not reflect this trend. The fields with the best reservoir quality are Roden and Pasop (see Figure 2-2 for locations of the fields), whereas Vries, which is more to the south doesn't have very good reservoir quality. This also depends however on the depth of the gas-water contact compared to the Upper and Lower Slochteren Members. Therefore

[2] An area that reduces or obstructs the flow, for example a layer; semi-permeable barrier.

no directional orientation has been implemented because there is not enough information to support such a decision.

Porosity is simulated using Gaussian random function simulation with the upscaled well logs as main input. A spherical variogram has been used with a sill of 1 and nugget of 0.001. The range settings used for the variogram are shown in Table 2-5. In the NAM Groningen static model, the ranges for the variogram are smaller, mostly around 3000 to 5000 m and the sill ranges from ~1 to 1.5. The reason for the larger ranges used in this project is the lack of wells in the Lauwerszee Trough.

For Ameland and Ten Boer Members, the petrophysical analysis is less appropriate because no shale correction was applied to the density log derived porosities (it is assumed that the Slochteren Formation is predominantly sandstone). The Ameland Member will be adjusted during base model tuning and is varied in the ensemble. To the north of the model area, the Ameland Member causes a clear barrier between the Upper and Lower Slochteren Members (Landman, 2023). In the model area, the thickness is mostly less than 5 m and is not expected to hydraulically separate the Upper from the Lower Slochteren.

As a result of the small number of logs penetrating the Carboniferous formations, the distribution to be used for the Gaussian simulation is taken with an average porosity of 0.08 rather than from the upscaled well logs.

Table 2-5 Settings for the Gaussian random function simulation of the porosity

	mean	Standard deviation	range	Variogram Range (major/minor/vertical)
ROCLT	From upscaled logs			15000/15000/15
ROSLU	From upscaled logs			15000/15000/30
ROCLA	From upscaled logs			15000/15000/10
ROSLL	From upscaled logs			15000/15000/15
DC	0.08	0.04	0.02-0.2	15000/15000/30

As secondary variable in the Gaussian simulation, a porosity-depth relation is used which is treated as a local varying mean (with normal score transform). The porosity-depth relation for the Upper Rotliegend members is based on the change of porosity with depth in ThermoGIS for the Upper Rotliegend and is shown in Figure 2-19. Below, insufficient information was available to derive a pore-depth curve. The curve for the modelled Carboniferous interval used and shown in Figure 2-19 is based on the available core data in Table 2-4 and the information available in (Zeeuw and Geurtsen, 2018b).

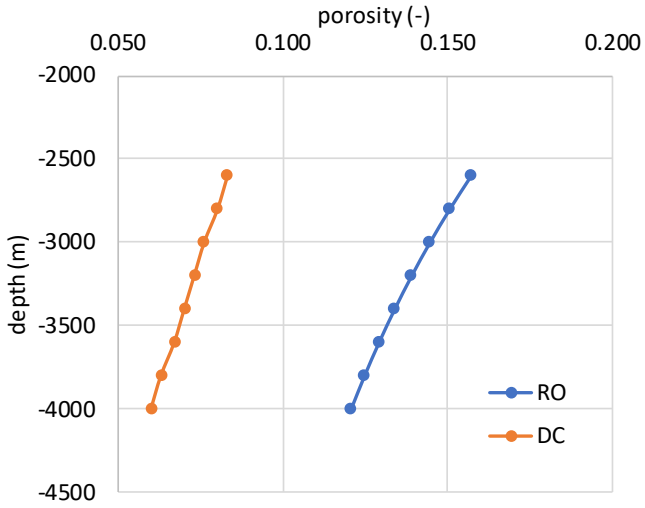

Figure 2-19 Porosity-depth relations used for the Upper Rotliegend members (RO) and Carboniferous units (DC).

Net-to-gross (NtG)
NtG is also simulated using Gaussian random function simulation with the same settings as used for porosity in Table 2-5, with the exception of the values for the Carboniferous. Due to a paucity of data, a constant value of 0.2 is used in the entire model area for all ensemble members. In addition, to avoid grid cells with very low volume which are set to inactive during the simulation, NtG was minimized on a value of 0.03.

Permeability
Permeability is simulated using Gaussian random function simulation with co-kriging of porosity as the secondary variable (using locally varying mean). In this case a lognormal distribution is used instead of the distribution from the well logs. To avoid unrealistically high permeability in some of the layers that distort the flow modelling, the maximum value is limited for some formations. See Table 2-6 for the values used.

For the Carboniferous, a normal distribution is used instead of lognormal, to reduce the occurrence of high values. The ranges of permeability are based on the NAM Groningen model (Zeeuw and Geurtsen, 2018b).

The vertical permeability is calculated as a fraction of the horizontal permeability. To determine a range of realistic values for this fraction, the NAM Eclipse model for the Groningen gas field was investigated. The NAM Eclipse model[3] has been made publicly available in 2023 through https://public.yoda.uu.nl/geo/UU01/8JYW40.html). This model shows a range of values in anisotropy because it is an upscaled model. The permeability in this model shows less anisotropy for higher permeability. For a horizontal permeability (kh) of around 1 mD, the most common value for the vertical permeability (kv) is ~0.1 mD resulting in kh/kv ~ 10. At kh = 100 mD, kv ≈ 30 mD resulting in kh/kv ~ 3. However, the grid cell height is generally less in the NAM model than in the model developed in this project, which implies higher anisotropy in this model than in the NAM model. Based on this information, a range of kh/kv from 5 to 15 for the ensemble was used (See section 3.3 for more information on the sampling for the ensemble). For the base model a value of 10 has been used.

[3] Dynamic model (Eclipse version) to predict the formation pressure response to gas extraction in the Groningen gas field, The Netherlands, P. Tummala, NAM, 2023.

Table 2-6 Settings for the Gaussian random function simulation of the permeability

	mean	Standard deviation	Range	Variogram Range (major/minor/vertical)
ROCLT	From upscaled logs			15000/15000/15
ROSLU	From upscaled logs		0.74 – 3000	15000/15000/30
ROCLA	From upscaled logs		0.63 – 500	15000/15000/10
ROSLL	From upscaled logs		0.03 – 1000	15000/15000/15
DC	0.3	0.2	0.02 – 50	15000/15000/30

Fault transmissivity multipliers
The fault transmissivity is calculated by the simulation software based on the juxtaposition of the formation and the permeability of these formations. However, the transmissivity of faults often differs from this value. In the Groningen area many faults are known to have very low transmissivity. Therefore, initial fault transmissivity multipliers were set to 0.1. Subsequently, for all faults for which information was available, the multipliers were set manually. Information was derived from the NAM Groningen model on the east side and the small gas fields on the west. The faults in this project were matched by name to the faults in the NAM model. The multipliers listed in different versions of the NAM Groningen dynamic model were compared and a value selected based on the different values. Also the range to be used for the ensemble sampling were based on it. Due to changes in the different NAM models over time and differences in naming, not all fault multipliers could be determined this way. In addition the NAM dynamic model has a stair-step grid and a different resolution than the model created in this project. Differences in multipliers therefore, can be expected between the two models. The remaining fault multipliers, including those on the west side of the model, were tuned in the base model (Section 3.2.2.6).

The list of multipliers per fault is presented in Appendix B (Table B-3).

2.6 Results

Figure 2-20 and Figure 2-21 show the geometry of the model in two cross-sections. The cross-section from north-west to south-east (Figure 2-20) illustrates the change in thickness of the Upper Rotliegend units. The cross-section from south-west to north-east (Figure 2-21) shows the difference in faults on the east side near Harkstede and on the west side near the Roden gas field.

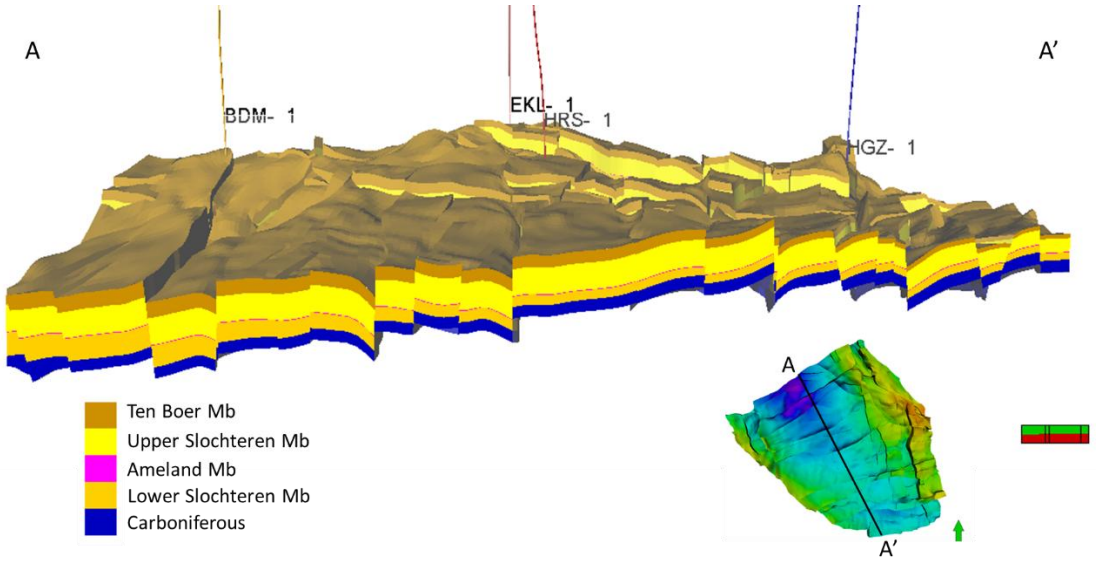

Figure 2-20. North-west to south-east cross-section showing the five modelled zones.

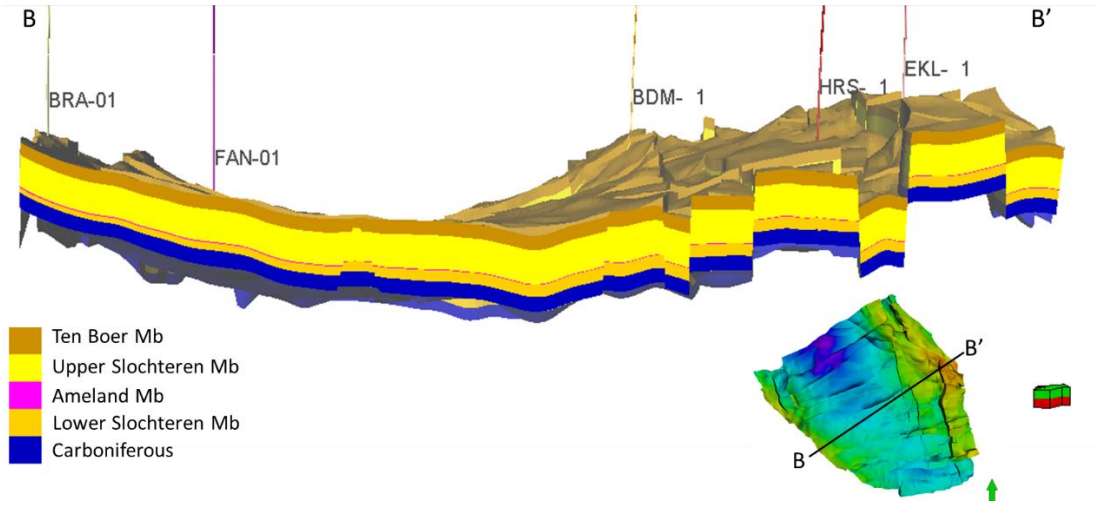

Figure 2-21 South-west to north-east cross-section showing the five modelled zones.

In total the geological model has 177 faults, excluding the boundary faults. More than 50% of these faults have a throw of less than 40 m, but a small number of faults has large throws of more than 300 m (Figure 2-22). These are predominantly the long faults with a west-south-west to east-north-east orientation. There are also a few in the Harkstede area on the edge of the Groningen field. Please note that the faults with the largest throw are poorly visible in Figure 2-22, because the throw exceeds the total thickness of the model, especially in the south of the model. Please see for example the cross-section in Figure 2-20 to see these faults. The majority of faults added in this study are short, east-west oriented faults in the northern part of the model area (Figure 2-14). On the east side of the model area (near the Groningen field), the fault interpretation was already very complete.

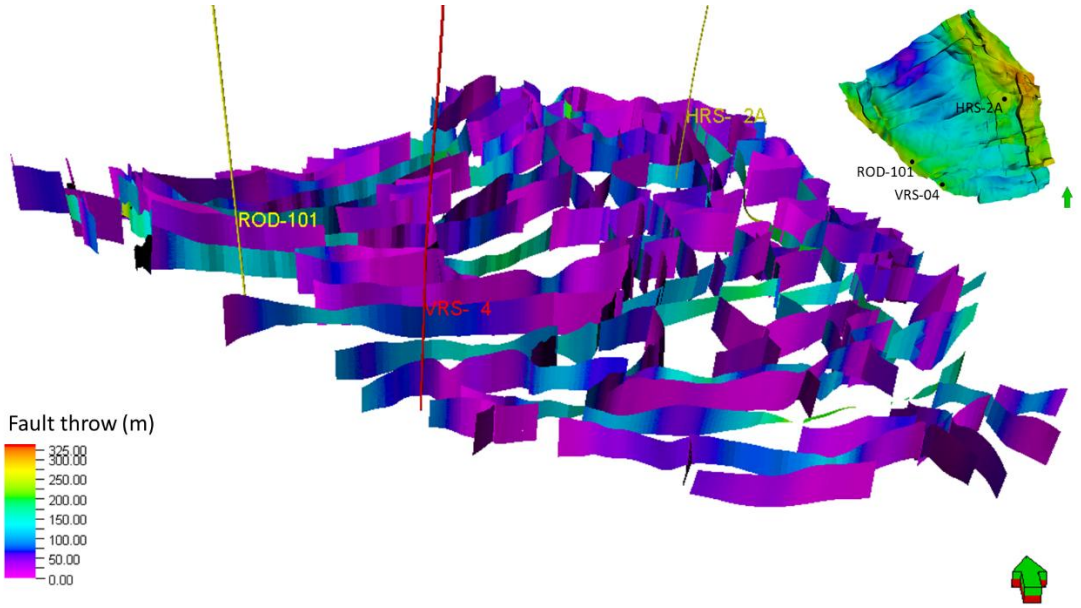

Figure 2-22 Fault throw (m) of the interpreted faults. Three wells have been added for orientation purposes. z-axis is increased by a factor of 5. Green-red arrow indicates north (green on top, red at bottom).

In Figure 2-23 an example of the porosity of the top of the ROSLU is presented as an illustration. Overall, the distribution of the properties is quite smooth as can be expected from the long ranges that were used for the variogram. Figure 2-24 shows two cross sections. One approximately south-west to north-east and the other north-west to south-east. Also shown are the grid cells around the wells which are determined by upscaling of the well logs. These values determine to a large extent the distribution of the simulated porosity. The cross section from south-west to north-east, which goes from Roden to the Groningen field, clearly shows the reduction of the porosity with depth between the gas fields. The cross section from north-west to south-east goes through the aquifer and becomes thinner in the south-east.

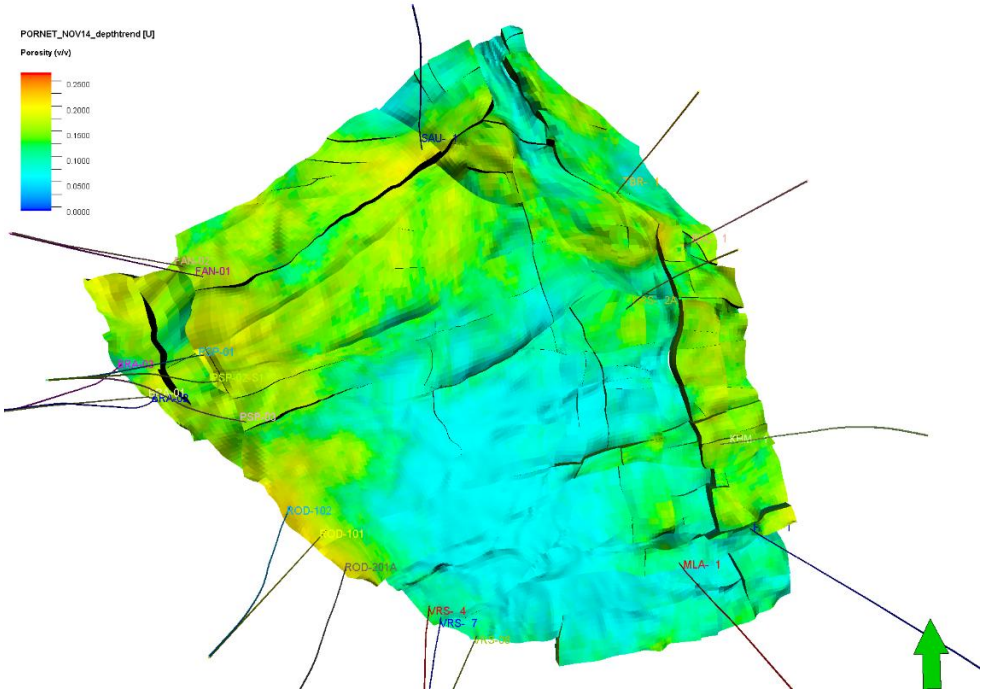

Figure 2-23 Example of the porosity of the top of the ROSLU. Green arrow indicates north.

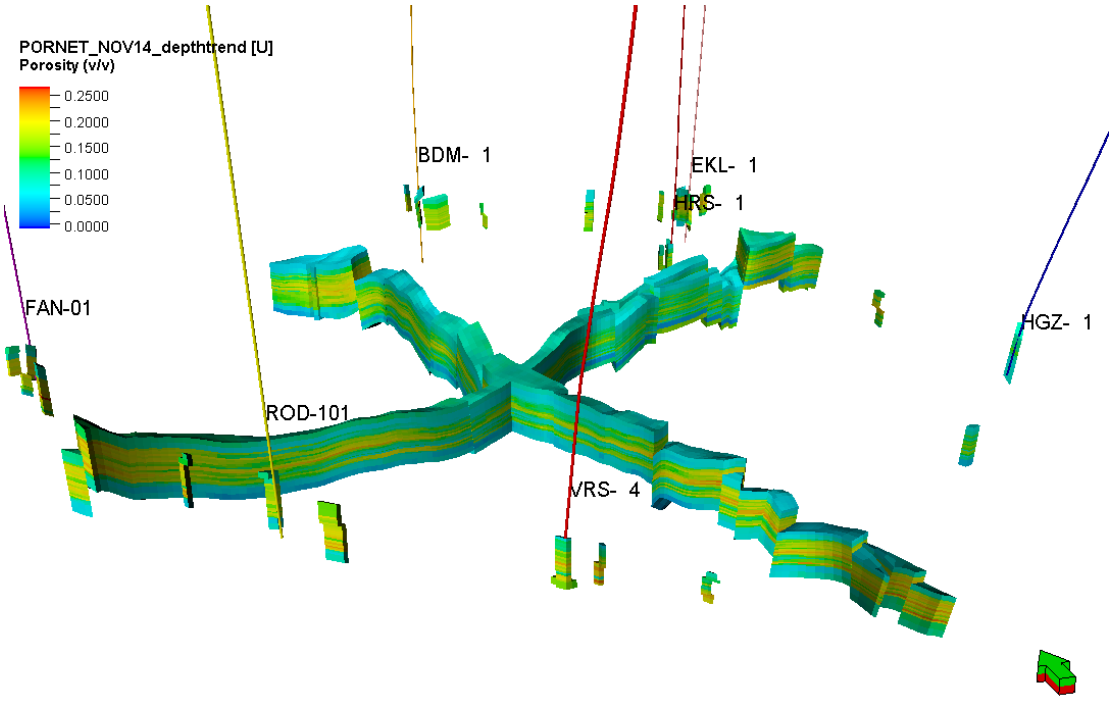

Figure 2-24 Example of the simulated porosity in two cross-sections. Also shown are the upscaled grid cells near the wells that are the input to the Gaussian simulation. For orientation a number of key wells are shown. Green-red arrow indicates north (green on top, red at bottom).

Porosity-depth trends where implemented as locally varying mean to ensure a decreasing trend of porosity with depth. Figure 2-25 shows the resulting trend lines from an example of the simulated porosity with depth. The implemented curves from Figure 2-19 have been added. This shows that the variability in the resulting trends is quite large. Porosity in the Ten Boer Member (ROCLT) is much lower, but the trend is similar. Upper Slochteren has the best properties, which decrease little with depth. The spread around the trend lines is large though: the correlation coefficient ranges from -0.23 for the Lower Slochteren Member to -0.51 for the Carboniferous units. The high porosity at shallow depth for the Carboniferous units is the result of relatively high porosity encountered in the VRS-4 well, which influences the area around the well.

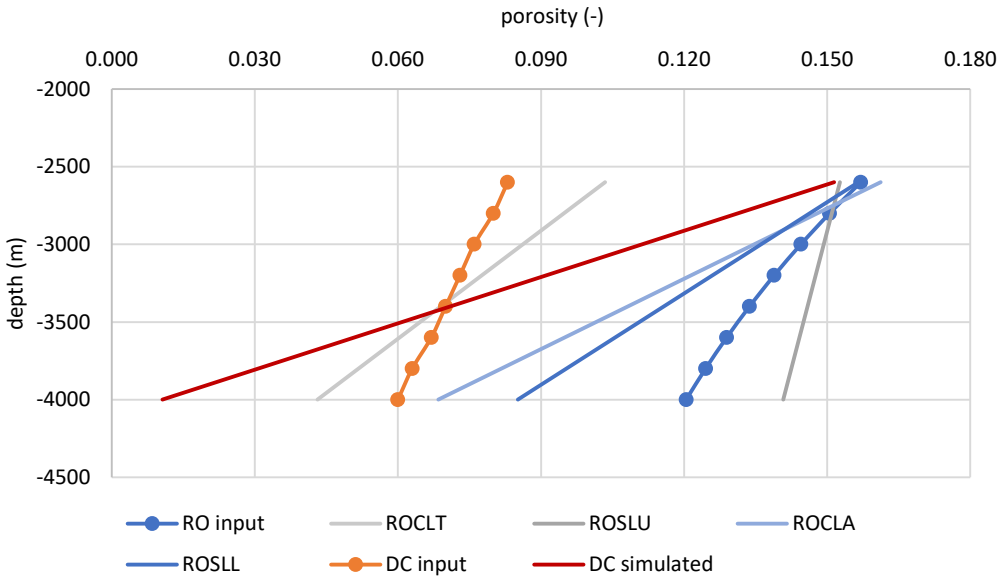

Figure 2-25 Porosity-depth trends from an example of the simulated porosity (linear trend lines of porosity versus depth) and the input porosity-depth relations used as a local varying mean for the Upper Rotliegend (RO) and Carboniferous units (DC) (curves with dots).

Permeability is simulated with co-kriging of porosity as the secondary variable and thus follows the trends of porosity, which is clear from a comparison of Figure 2-23 and Figure 2-26. The apparent variability in the aquifer is due to the logarithmic scale which enhances the variability of the small values.

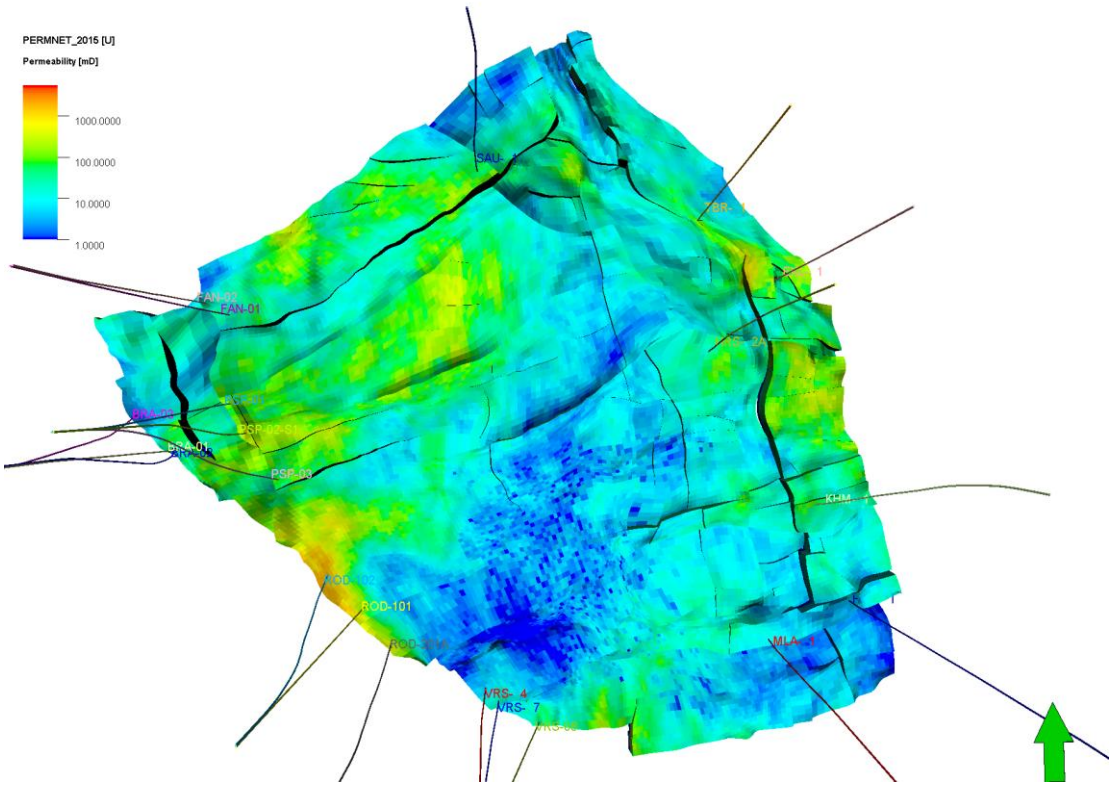

Figure 2-26 Example of the permeability of the top of the ROSLU. Green arrow indicates north.

3 Post-abandonment pressure depletion

3.1 Objectives and approach

The objective of this part of the study is to generate pressure forecasts for the SW aquifer of the Groningen gas field for the period 2024-2100. To achieve this, an ensemble of dynamic reservoir simulation models is developed based on the ensemble of geological models. The workflow is illustrated in Figure 3-1. This ensemble of dynamic models is used to simulate the pressure history based on historical production data. Subsequently, the ensemble of pressure simulations (of the historical period) is used to calculate an ensemble of compaction and subsidence simulations. Based on the match to observed pressure in the small gas fields on the west side of the aquifer and to observed subsidence, a subset of the ensemble is selected for the forecast period. Finally, the selected subset of the ensemble is simulated over the period 2024 - 2100 to provide the required forecasts of pressure and compaction.

Before creating the ensemble of reservoir models, first a base dynamic model is created. The base model uses a single geological realization with a fixed seed for the porosity, NtG and permeability.
The base model has been tuned to reflect the general behaviour of gas production and pressure at the well data. Since the primary purpose of the model is to predict pressure behaviour in the aquifer, a detailed analysis and history match of each of the small gas fields is out of scope of this study. The focus has been on reproducing typical behaviour (like pressure recovery after shutin) rather than a detailed pressure match and to focus on behaviour that impacts the aquifer rather than those only affecting pressure at the well.

In this chapter the creation and tuning of the base model is described in Section 3.2. Following this, the development and the results of the ensemble of dynamic reservoir simulation models and the simulations of compaction and subsidence are discussed in Sections 3.3 and 3.4. Finally, Section 3.5 presents the selection of the subset of ensemble members used for the forecast period and the resulting forecasts .

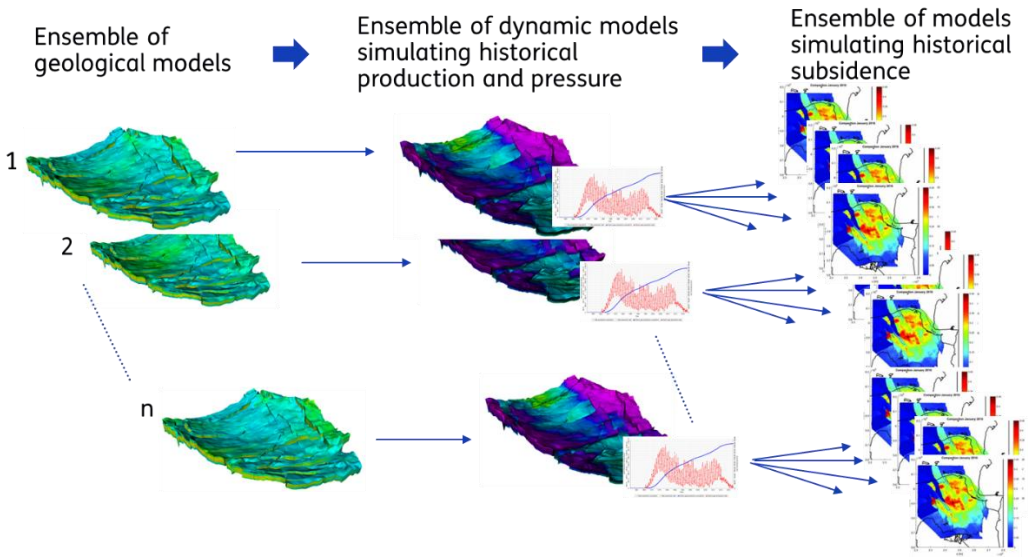

Figure 3-1 Illustration of the workflow used in this chapter. An ensemble of geological and dynamic reservoir simulation models is created, where each geological model is used to create one dynamic reservoir simulation model. The output of each dynamic model is subsequently used to create multiple simulations of compaction and subsidence.

3.2 Base reservoir model

3.2.1 Input

In this section the input used to build the base reservoir model is discussed. One of the realizations of the ensemble of geological models is used as base, which is the realization created with the following seeds (Petrel version 2022.7): 10004 for porosity, 6600 for permeability and 25114 for NtG. The porosity and permeability are illustrated in Figure 2-23 and Figure 2-26.

Capillary pressure and relative permeability

For the relative permeability and capillary pressure information, the curves from the NAM Eclipse 100 (by Schlumberger) dynamic reservoir model of the Groningen gas field have been used, but in a simplified way. NAM has made the Eclipse™ model publicly available in 2023[4] through https://public.yoda.uu.nl/geo/UU01/8JYW40.html together with a Petrel geo-model. The model is based on the existing MoReS model. The NAM Eclipse™ dynamic model has a separate set of relative permeability and capillary pressure curves for each porosity class (0.01 per class) for each formation. In this study, a single set of curves has been used, namely the curve for the average porosity of that formation:

- ROCLT and DC: average porosity is 0.08.
- ROSLU: average porosity is 0.15
- ROSLL + ROCLA: average porosity is 0.12

The curves that have been used are shown in Figure 3-2.

[4] Dynamic model (Eclipse version) to predict the formation pressure response to gas extraction in the Groningen gas field, The Netherlands, P. Tummala, NAM, 2023.

Two aspects of the curves are important to discuss: gas below free water level (GBFWL) and the permeability in the water zone.

In the Groningen area, gas below the free water level (GBFWL) is found in many wells. NAM included this GBFWL in the dynamic models, because it affects the pressure depletion and thus the compaction and subsidence (Zeeuw and Geurtsen, 2018b). The impact of the gas is two-fold: the permeability of the aquifer is reduced due to the presence of the gas and the effective compressibility of the aquifer is increased resulting in less pressure decline for the same flow to the gas field. The NAM Eclipse dynamic model has 2% GBFWL (i.e. gas saturation is 0.02 below FWL) in the Rotliegend formation. The same approach is followed in this study. In some of the logs in the small gas fields, also evidence was found of GBFWL, for example in ROD-102.. Therefore, in the entire model area, in the Ten Boer (ROCLT) and Upper Slochteren (ROSLU), 2% GBFWL was added for 30 m below the free water level (FWL). This is implemented in the model by assigning relative permeability curves that end at Sw=0.98. The curves from the NAM Eclipse model have been used at the average porosity of the formation (Figure 3-3). The gas is not mobile and capillary pressure is zero. It should be noted that the irreducible water saturation (at which Krw=0.2 in Figure 3-2) has changed as well. This does not affect the results, because only the end-point is used of these curves.

From information from logs and history matching in the Groningen gas field, it is known that the permeability in the water zone is generally lower than in the gas zone. This is possibly caused by continuing diagenesis in the areas where water is present compared to gas-filled zones. Because most logs used for the property modelling are from the gas zone, this is not well represented in the simulated reservoir properties in the water zone (Section 2.5). Here the approach followed by NAM is used, which is to reduce the endpoint of the relative permeability curve of water to 0.2 (Figure 3-2). This is essentially a multiplier on the permeability in the water zone. The benefit of this approach is that the multiplier is applied in one go to all relevant areas (i.e. all areas with high water saturation), also in the capillary fringe, which is the transition zone between water and gas zones.

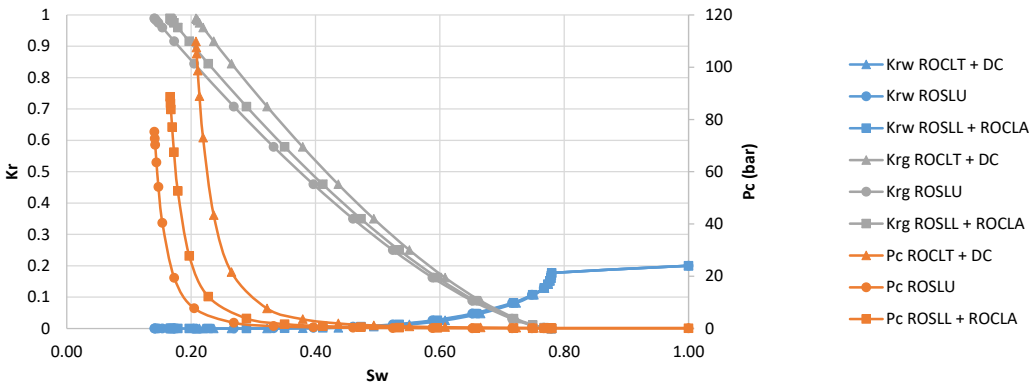

Figure 3-2 Relative permeability and capillary pressure curves used in the dynamic reservoir model.

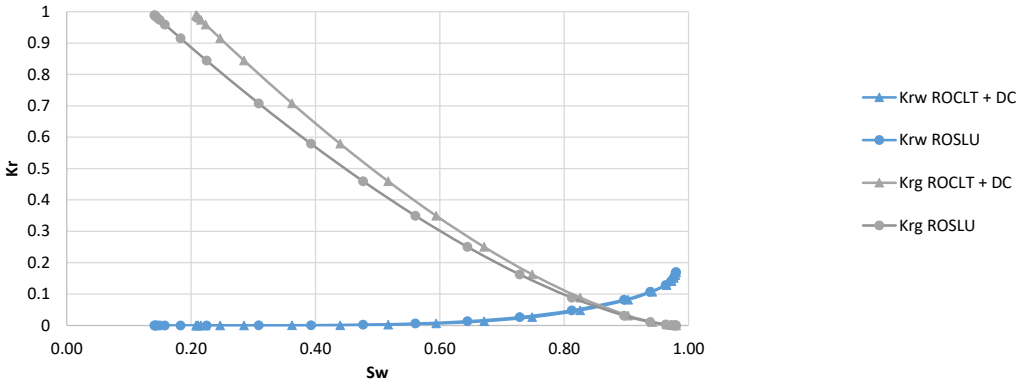

Figure 3-3 Relative permeability used in the dynamic reservoir model for the zone with GBFWL of 30 m thickness below the FWL.

Gas composition

Public information on gas composition was downloaded from nlog.nl (http://www.nlog.nl/sites/default/files/thematische_data/nlog_gascompos.xlsx). Information is available for the following wells in the area of interest: ROD-101, ROD-101-S2, ROD-102, PSP-01, BRA-01 (see Figure 2-3 for well locations). Each of the small gas fields has a different gas composition, but the available data show that Roden, Boerakker and Pasop (see Figure 2-2 for the locations of the small gas fields) have similar composition with the amount of methane in the range of 80.5 to 82.5 mol-% and an amount of N_2 of around 11 mol-%. Therefore, it was decided to use the gas composition of the Roden field for the Boerakker and Pasop fields as well. For Faan no data is available, but since it is close to Boerakker and Pasop, also the gas composition of the Roden field was used.

For Vries-North, no wells are listed in the information on nlog.nl, however, in Vries-Central, just south of Vries-North, information is given for well VRS-201. This composition has a higher methane content than the small gas fields to the north (Roden, Boerakker and Pasop) and a relatively small amount of nitrogen. The composition for well VRS-201 is used for the gas properties of Vries-North.

The composition of the Groningen gas has 86 mol-% CH_4 and 14 mol-% N_2. This is also used for Bedum, although this field has less N_2 (4 to 5 mol-%). This simplification is allowed because both fields are implemented as pressure constraints. The description of the implementation as pressure constraints is discussed later in this section under "*boundary conditions*".

The gas compositions used are given in Appendix B (Table B-1). The properties for these compositions are derived using the correlations from (Dranchuk and Abou-Kassem, 1975) for the Z-factor and (Carr et al., 1954) for gas viscosity which are the default correlations as used by Petrel v2022.7.

Water composition

For the water composition a single value for the salinity for the entire model area is used: 280.000 ppm NaCl. Molen et al. (2020) used a value of 200,000 ppm for the Roden field, but Burkitov et al (2016) used 280,000 for the Groningen field. The latter is assumed to be more accurate and more representative of the aquifer and is used for the entire model area. The viscosity and density at 100°C were used based on the Petrel default correlations: (Spivey and McCain, 2003) for density and (Kestin et al., 1981) for viscosity. The viscosity is 0.63 cP at reservoir conditions. The brine density at Eclipse standard conditions is 1215.9 kg/m^3 and at

reservoir conditions (100°C and 345 bar) it is 1179 kg/m^3. The compressibility is 2.8E-5 1/bar. All values are close to the values used in the NAM Eclipse model and listed in (Burkitov et al., 2016).

Pore volume compressibility
The pore volume compressibility is based on the values used for the NAM Groningen model and listed in (Burkitov et al. 2016) and depends on porosity. The same basic approach was used in later versions of the NAM model (Landman, 2023), enhanced with a multiplier estimated during the history match. The corrections based on history matching on the Groningen side of the model have not been applied. For each of the main formations (ROCLT, ROSLU etc) of model, the average porosity was determined and the pore volume compressibility estimated from Figure 42 of Burkitov et al., 2016. Because the variability was quite small for the range in average porosity from 0.08 to 0.15, a single values of 2.5E-5 1/bar has been used. Please note that this is not the value used in the modelling of compaction and subsidence in Section 3.4, where different compaction models are used (see Section 3.4.2). The impact of the pore volume compressibility on the flow simulation is small which justifies the use of a single, averaged value of compressibility.

Initial conditions
It is assumed that the entire area is in pressure communication and that the initial pressure is consistent throughout the model area. Initial water pressure is taken as 344 bar at 3000 m depth, based on the pressure in the Groningen and Roden fields. For input in the simulator the pressure is recalculated to the depth of the Free Water Level (FWL) using a density of 1178 kg/m^3. The values used are listed in Appendix B.

The FWL values for the small gas fields are based on the most recent field review document of the respective fields as available on NLOG. The FWL values for the Groningen model are based on the values from Groningen dynamic model update V7 (Landman, 2023). The values for the Bedum field are based on (Geurtsen et al., 2020). See Appendix B for the values used.

The model simulations do not include thermal modelling and therefore a constant reservoir temperature of 100°C is used throughout the model, which is the estimated temperature at ~3 km depth. This mainly affects the fluid properties.

Boundary conditions
The position of the boundaries of the model was discussed in paragraph 2.3. Most boundaries can be implemented as no-flow boundaries, because they are positioned at large bounding faults, except on the east side. On the east side of the model is the Groningen gas field. Only part of the gas field is incorporated in the model, to keep the size of the model limited and allow more detail in the aquifer and small gas fields. Since the pressure in the part of the Groningen gas field that is incorporated in the model is influenced by production outside of the model, the pressure in the east part of the model will be imposed. This is done by running the production wells in this area on a pressure constraint. This means that the bottom hole pressure in the well is set and that the amount of reservoir fluids (gas and/or water) that can be produced is simulated based on the bottom hole pressure.

For the bottom hole pressure (BHP) constraint of the production wells on the east side of the model (see Figure 2-3), the simulated bottom hole pressure from the NAM Groningen MoReS dynamic model is used. These have been made available with the NAM Groningen Eclipse model. In this case the output from the MoReS model rather than the Eclipse model was used, because the Eclipse model deviates from the MoReS model in the western periphery (TNO, 2024) and the MoReS model fits the observations better. The match of the MoReS model is

within a few bar for most wells (Landman, 2023), which is sufficiently accurate for the purpose of this model. Using pressure observations rather than model output is not possible, because the observations do not cover the entire area and time period.

Wells and dynamic data
For all the wells in the small gas fields on the west side of the model area (Vries-North, Roden, Pasop, Boerakker and Faan (Figure 2-2), the following data was collected:

- Well path and completions
- Well gas and water production rates
- Static pressure measurements

Most information is available on NLOG.nl. The completions were provided by NAM, as was the gas and water production of wells prior to 2003, which are not available on NLOG. The static pressure measurements are based on public information available online: https://nam-feitenencijfers.data-app.nl/embed/component/?id=gasdruk#tab-overig, enhanced by the information in (TNO, 2023a) and in public field review documents.

The simulation model is run with annual time steps. This is sufficiently accurate for the relatively slow response of the aquifer. It does mean however that detailed pressure behaviour in the small gas fields is not represented. Please note that the static pressure measurements are approximated by the pressure in the grid block containing the top perforation. Because the model is run with annual time steps, it is not possible to simulate the reservoir pressure during a shutin explicitly. The gas production for the small gas fields is available on a monthly basis in Nm^3. For the simulation they are recalculated to sm^3 and aggregated to annual time steps.

For the wells on the east side of the model, the well paths were available in the NAM Groningen geological model that was used as input for the geological models in this project. The completions were imported from the NAM Groningen Eclipse model. As mentioned during the discussion of the boundary conditions, the BHP constraints for the production wells were taken from the NAM Groningen MoReS model. For each well on the east side, the simulated BHP is available at daily time steps for the entire model period. For the Eemskanaal-cluster (EKL, Figure 2-3) not all wells are incorporated in the model, because the interference between the wells caused numerical instability in the model. The observation wells HRS-2A, MLA-1 and SAU-1 are also included in the model. More information on these wells is provided in Section 3.2.2.6.

For all the wells in the model, the completions could not always be implemented at the depth at which they are in reality. Because the grid is relatively coarse, perforations that are placed in a (thin) layer with high permeability in reality, will be in a thicker, lower permeability layer in the model. In this case, implementing the actual perforated thickness results in underestimation of the productivity. In these cases, the length of the perforated intervals are adjusted to fit the coarser grid.

3.2.2 Tuning of the base model

To be able to tune the base model to the dynamic data, part of the data is used as input and part as observations. All the wells in the small gas fields are run on gas production targets. The static pressure measurements and, to a lesser extent, the water production are used as

observations. Because of the relative coarseness of the models compared to the size of the small gas fields, the water inflow measurements are difficult to reproduce. In particular the vertical resolution is a limiting factor, because it is chosen relatively coarse for simulation of a very large aquifer, rather than for simulation of small gas fields, where vertical details are more relevant.

The estimates of the GIIP (Gas Initially In Place) were mostly based on the field review reports ("winningsplannen"), which are available on nlog.nl for all Dutch gas fields.

3.2.2.1 Roden

The Roden gas field is the most important of the small gas fields in the context of this project: the gas field is one of the larger gas fields and has a well connected aquifer, which extends to the Groningen gas field (around Harkstede)(Figure 3-4). Also important is the fact that in the Roden south block (which is produced via well ROD-201), static pressure measurements were continued almost 30 years after production had been stopped (Figure 3-5). During this period, a significant pressure increase was observed which was attributed to aquifer inflow (Molen et al., 2020). Also in the north block considerable pressure increase was observed after production stop.

The Roden field has three wells which were producing from 1976 to 2003 (Figure 3-5). The Slochteren Formation has good reservoir properties and the connected aquifer has very few faults. The pressure has increased in the south block by around 100 bar from the time of the shutin of the well ROD-201 in 1985 to 2000. In the north block the pressure recovery after shutin is at least 88 bar. The prior estimates of the GIIP was 8 NBCM (8.5 sBCM) for the north block and 1.5 NBCM (1.6 sBCM) for the south block based on (Molen et al. 2020) and the field review of 2003.

Because of challenges in matching the observed pressure recovery, a mass balance approach was employed to estimate the required aquifer size. This estimation based on the equilibrated pressure (i.e. the pressure after the gas field and aquifer are in equilibrium again after production), the estimated GIIP and gas production. For the equilibrated pressure, the final pressure was assumed. For the south block, this resulted in an estimated size of the aquifer twice the size of the aquifer in the reservoir model. Since the uncertainty in the size of the aquifer in the reservoir model was not that large, probably the GIIP estimate is inaccurate. For the north block, the aquifer size appeared to be approximately correct if GIIP was somewhat lower than estimated.

Much better solutions could be simulated by assuming a higher GIIP in place for the south block (consistent with the static model), slightly lower GIIP for the north block (also consistent with the static (geological) model) and that part of the gas in both blocks is available as so-called 'slow gas'. This is gas that is for example located behind fault with low transmissivity or in low permeability deposits. It was investigated whether gas below FWL or gas from ROCLT (Ten Boer Member) could be responsible for this behaviour, however neither of these options had sufficient effect. After re-examining the seismic data, it was concluded that there are several locations in which low-offset faults could be present in the gas fields. Implementing these as semi-permeable baffles improved the pressure behaviour considerably. The position of the baffles is shown in Appendix B.

From the pressure behaviour it is clear that pressure communication between the north and south block is limited. This is consistent with the NAM Groningen dynamic models in which the

large SW-NE oriented faults are mostly assumed to have low permeability (e.g. Zeeuw and Geurtsen, 2019).

The results of the base model in which the above changes are implemented are plotted in Figure 3-6 and Figure 3-7. The estimated GIIP and pore volume multiplier are given in the summary table of the base model (Table 3-1).

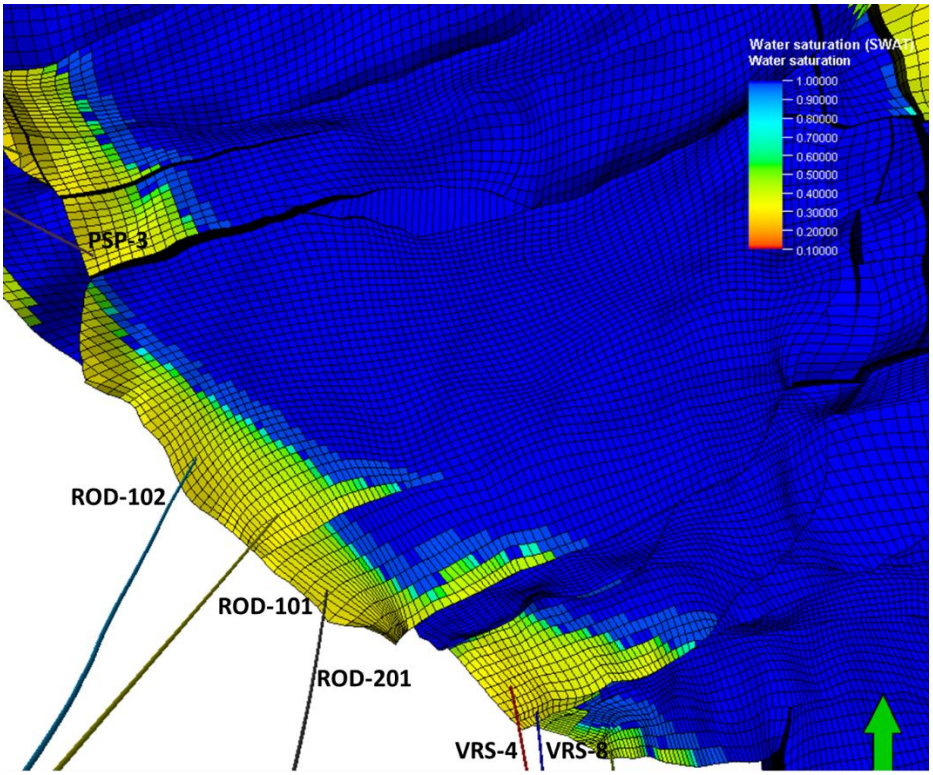

Figure 3-4 Top of the Roden gas field showing water saturation and the three wells ROD-102 and ROD-101 in Roden North and ROD-201 in Roden South. An overview of the initial water saturation in the entire model is presented in Figure 3-15.

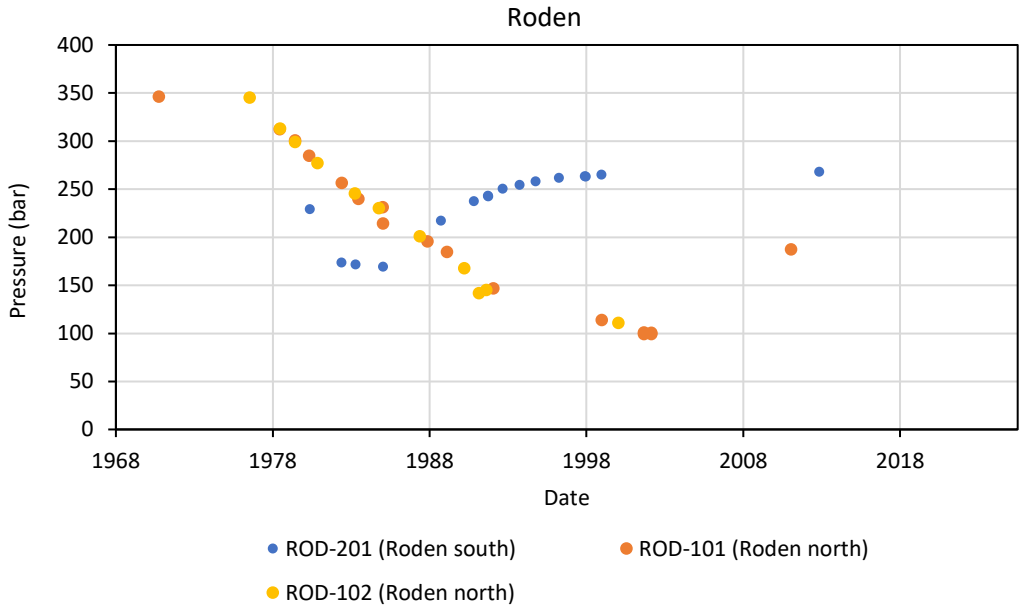

Figure 3-5 Observed static pressure in the Roden field. Roden north is produced via wells ROD-101 and ROD-102 and Roden south via well ROD-201.

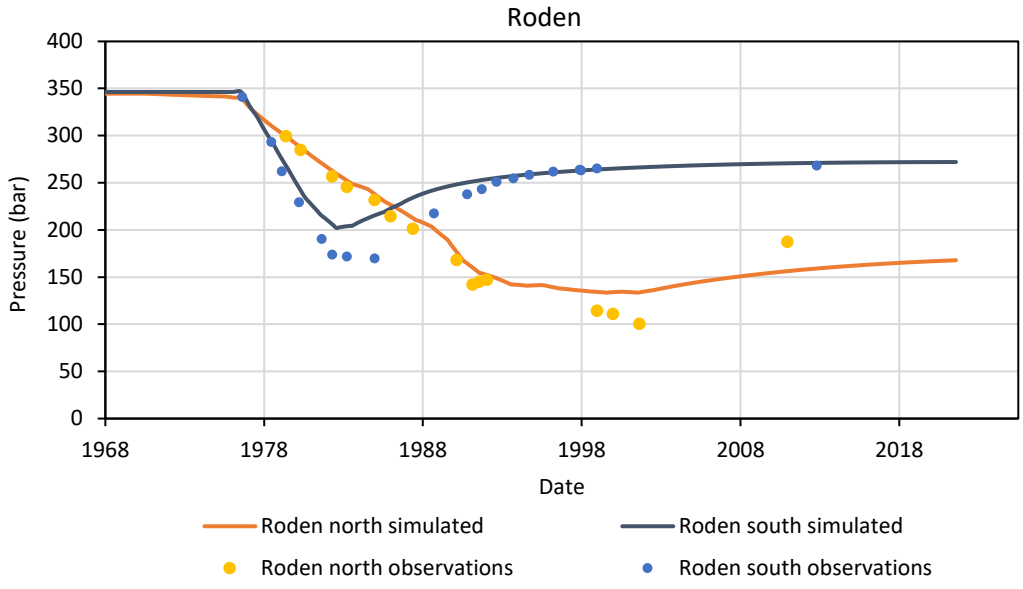

Figure 3-6 Base model results for the Roden gas field showing the static pressure observations (observations), and the simulated reservoir pressure in the grid blocks containing the wells (simulated).

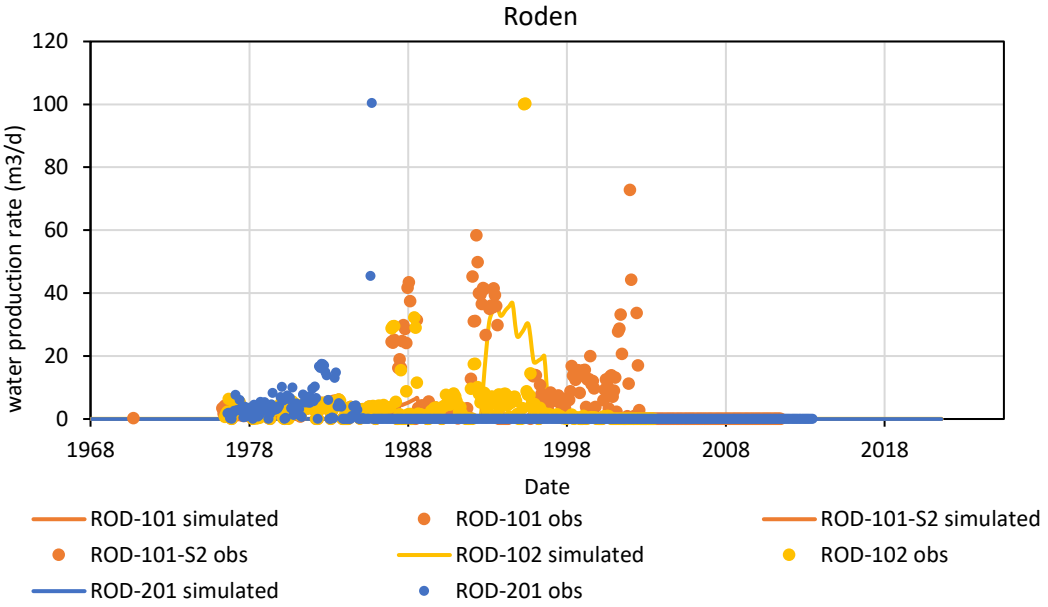

Figure 3-7 Base model results for the Roden gas field showing the water production observations and simulations per well. ROD-101 was replaced in 1989 by the sidetrack ROD-101-S2.

3.2.2.2 Vries North

The gas field Vries North is produced from three wells: VRS-4 (VRS-401 on nlog.nl), VRS-7 (VRS-402 on nlog.nl) and VRS-8 (VRS-403 on nlog.nl) and has lower productivity than the Roden field. The initial model had far too much water production and too little drawdown, indicative of an overestimation of the size of the connected aquifer. A smaller aquifer was also shown in NAM, 2021 in the model used for long term subsidence forecasts which includes the connected aquifers in a coarse way. NAM, 2021 illustrates (in their Figure 3) that the fault density is much higher in the Vries aquifer than in the Roden aquifer which might explain the lower connectivity since many faults in this area have reduced transmissivity. Because it was not feasible to include all faults, a number of baffles was implemented in the same way as in the Roden field to reduce the connectivity in the aquifer. The baffles are show in Figure B-14 in Appendix B. The position of the baffles was based on indications of the presence of faults from the seismic data and the structure map by NAM.

The static GIIP was lower than the GIIP estimate from NAM and was adjusted using a pore volume multiplier. The estimated GIIP and pore volume multiplier are given in the summary table of the base model (Table 3-1).

The results of the base model are shown in Figure 3-8 (pressure) and Figure 3-9 (water production). VRS-4 and VRS-7 are located in the same fault block and the static pressure measurements were only reported for the fault block and not for each well separately.

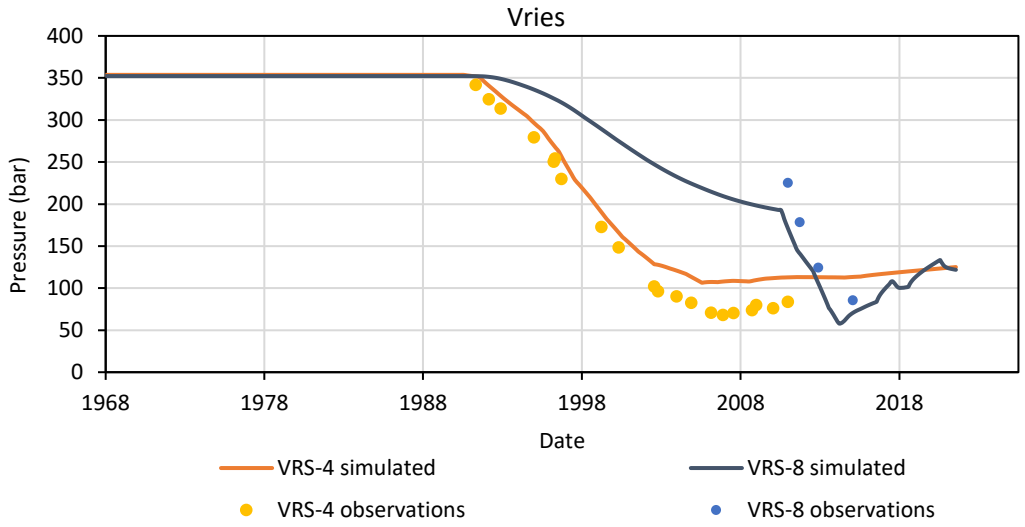

Figure 3-8 Base model results for Vries North showing the static pressure observations (observations), and the simulated reservoir pressure in the grid blocks containing the wells (simulated). VRS-7 is located in the same fault block as VRS-7.

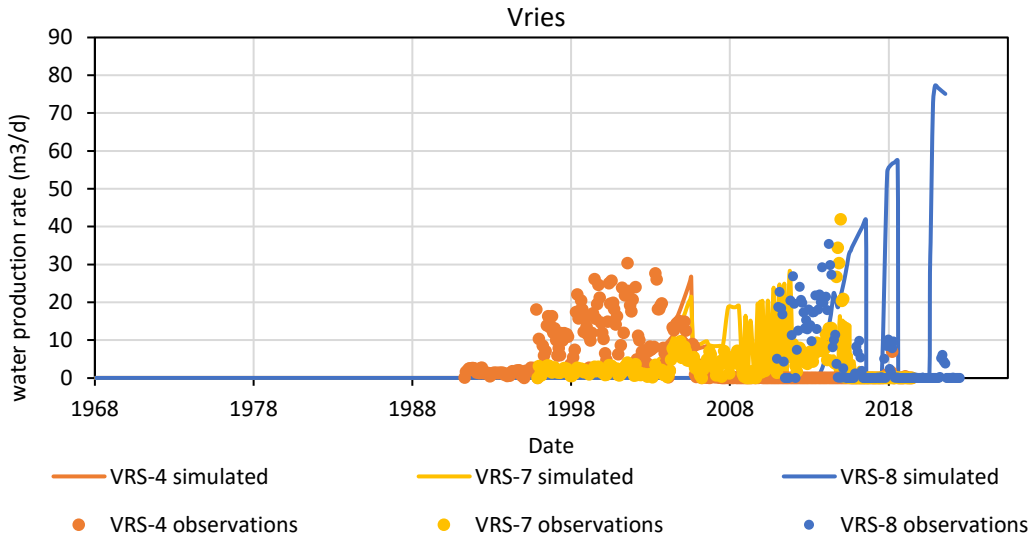

Figure 3-9 Base model results for Vries Noord showing simulated and observed water production for all three wells.

3.2.2.3 Pasop

Pasop is a small gas field just to the north of Roden. It is produced from three wells (PSP-01, PSP-02-S2 and PSP-03. The field has good productivity like Roden, but is highly compartmentalised with a ~400 m wide, high block in which the wells are located. The wells are produced intermittently to avoid formation water production. The amount of gas initially in place is too large, which could be related to the fact that not all static GIIP is accessible from the wells due to the highly compartmentalised nature of the field. It could also be related to an inaccurate representation of the details of the faults and the top of the reservoir due to

the relatively coarse grid. The GIIP is reduced via a pore volume multiplier. In addition the transmissivity of the faults is adjusted to better predict the pressure drawdown. Based on the NAM structural map, two faults were missing which were added as baffles (Figure B-14 in 0). The pressure results of the base model are shown in Figure 3-10. In the model no water production rate is simulated. Observed water production rates are substantial for PSP-01 (50 to 200 sm^3/d) but only for a short period in 2006 and 2007. The model was too coarse to reproduce this.

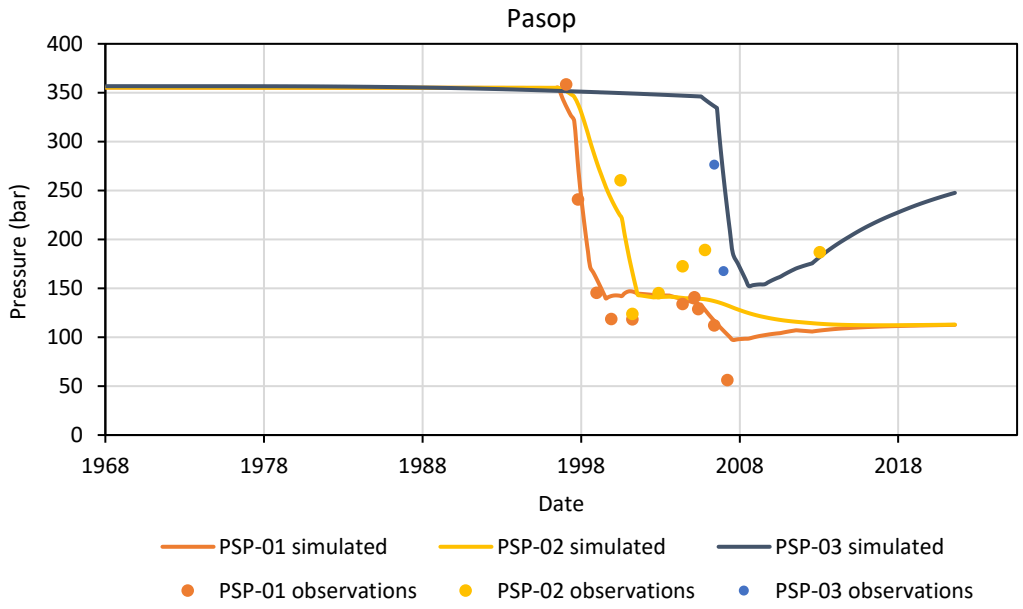

Figure 3-10 Base model results for Pasop showing the static pressure observations (observations), and the simulated reservoir pressure in the grid blocks containing the wells (simulated).

3.2.2.4 Faan

The Faan gas field is to the north of the Pasop field and produced via wells FAN-01 and FAN-02 from 2008. The field is highly compartmentalized and consists of at least three compartments. The FAN-01 well is located in the Faan main block, FAN-02 in the west block. The Faan main block is connected to the SW aquifer. In the model developed in this project, the internal faults are missing. The GIIP in the static model is considerably larger than the dynamically estimated GIIP and the pressure decline in the wells was thus predicted very poorly. The model was matched by adding baffles roughly at the locations of the missing faults and reducing the size of gas zone via a pore volume multiplier. The connection to the SW aquifer appears to be overestimated in the model and has been reduced by means of a baffle around the contact. The results for the pressure are shown in Figure 3-11. In the model no water production rate is simulated. Observed water production rates were small (max 30 sm^3/d for one date).

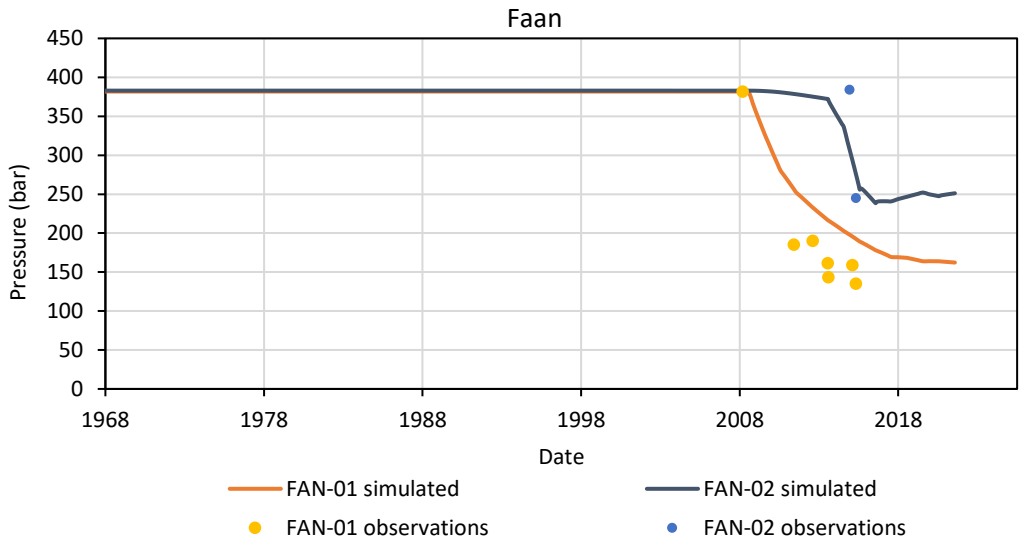

Figure 3-11 Base model results for Faan showing the static pressure observations (observations), and the simulated reservoir pressure in the grid blocks containing the wells (simulated).

3.2.2.5 Boerakker

The Boerakker gas field is located on the far north-westerly tip of the model and hardly influences the pressure in the SW aquifer, since it is not connected to it. The main reason to include it is the prediction of the subsidence: the pressure drawdown at Boerakker creates a subsidence bowl that influences the Pasop and Roden fields. The field is produced via two wells: BRA-02 and BRA-03. The static GIIP is considerably smaller than the NAM estimate (Table 3-1), which is corrected using a pore volume (PV) multiplier on the compartment containing BRA-2 and a separate PV multiplier on the block containing BRA-3. The PV multiplier on the block containing BRA-3 is 0.55 and is not varied in the ensemble. The results are shown in Figure 3-12.

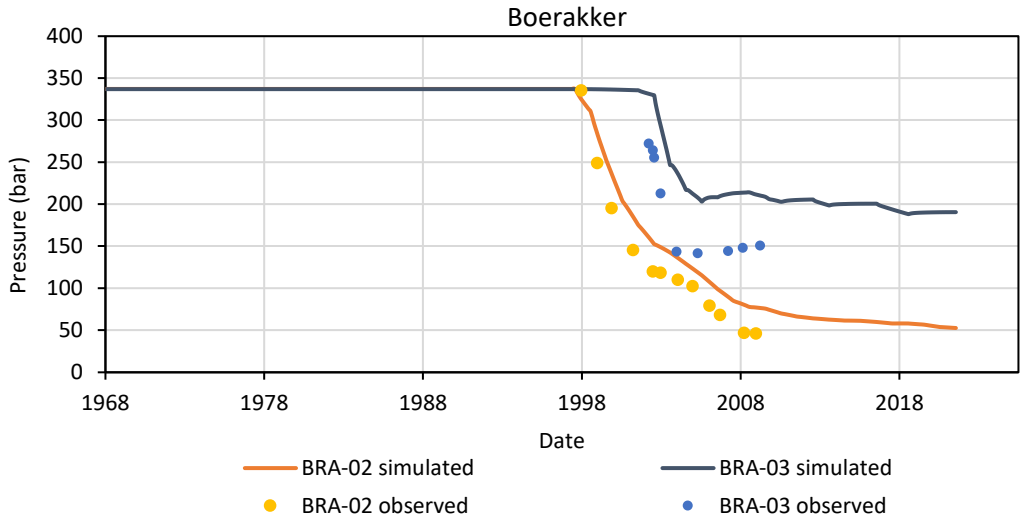

Figure 3-12 Base model results for Boerakker showing the static pressure observations (observations), and the simulated reservoir pressure in the grid blocks containing the wells (simulated).

3.2.2.6 Groningen side

On the east side of the model are the Groningen and Bedum fields in which the wells are run on pressure constraint, because the pressure is not only determined by production from the wells incorporated in the model created here, but also from outside the model area as mentioned in paragraph 2.3. Only the pressure measurements in the following wells can be used for tuning: HRS-2A, MLA-1 and SAU-1, because they are further from the boundary (Figure 2-3). The NAM Groningen MoReS model was matched using additional types of, such as PNL (Pulsed Neutron Lifetime) data which give information on the water level rise. Most of this is in the main Groningen area, but PNL data are available in the Harkstede block, which show a water level rise. This information has only been included in a qualitative way by checking if the water level rises in the base model.

The most important parameters used for tuning the model are fault transmissivity multipliers. The initial settings for the fault transmissivity multipliers are discussed in Section 2.5. These settings resulted in a slight overestimation of the pressure drawdown in the Harkstede block (well HRS-2A) prior to 2006 when well EKL-13 starts producing. A small reduction in connectivity to the EKL cluster and increased connectivity to the aquifer were sufficient to get a good match in HRS-2A (Figure 3-13). The fast pressure recovery of the NAM model after the stop of the production in early 2014, was not reproduced in the reservoir model developed in this study.

Pressure drawdown at well MLA-1 was underestimated with the initial settings. This was attributed to a lack of connectivity to the region with well HGZ-1 which depletes as a result from production in the Groningen field. An increase in the relevant fault multipliers improved the match sufficiently (Figure 3-14). Well SAU-1 was matched sufficiently well with the initial settings (367 bar compared to the observed 372 bar).

It should be noted that the south-west periphery of the Groningen field is the most complicated area of the Groningen field (Zeeuw and Geurtsen, 2019) and that a full

representation of all the behaviour is not feasible in this setting. Also NAM had difficulty matching this area. For example to achieve a history match in KHM-1 (Figure 2-3, between the EKL-cluster and HGZ-1), Landman (2023) was forced to implement time-varying fault multipliers to achieve a satisfactory history match.

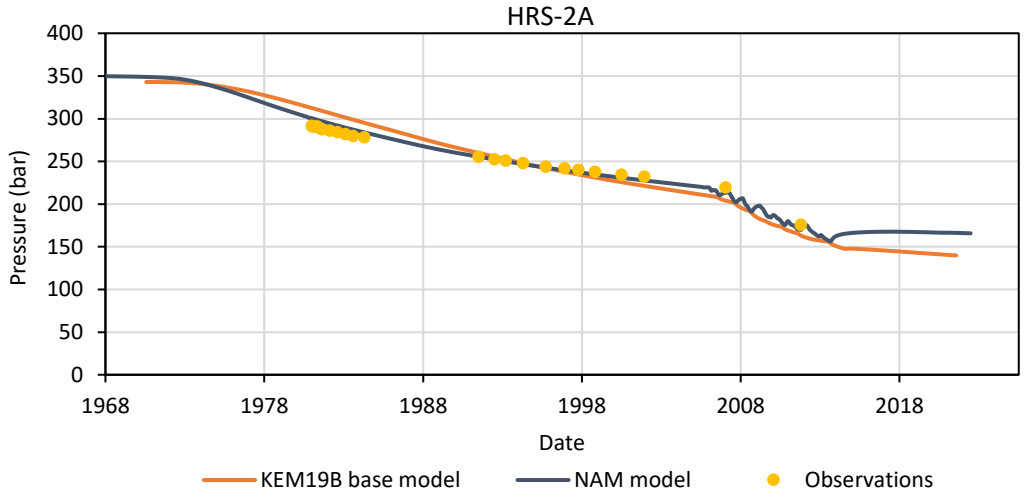

Figure 3-13 Pressure at HRS-2A from the base model, from the NAM Mores model and observations.

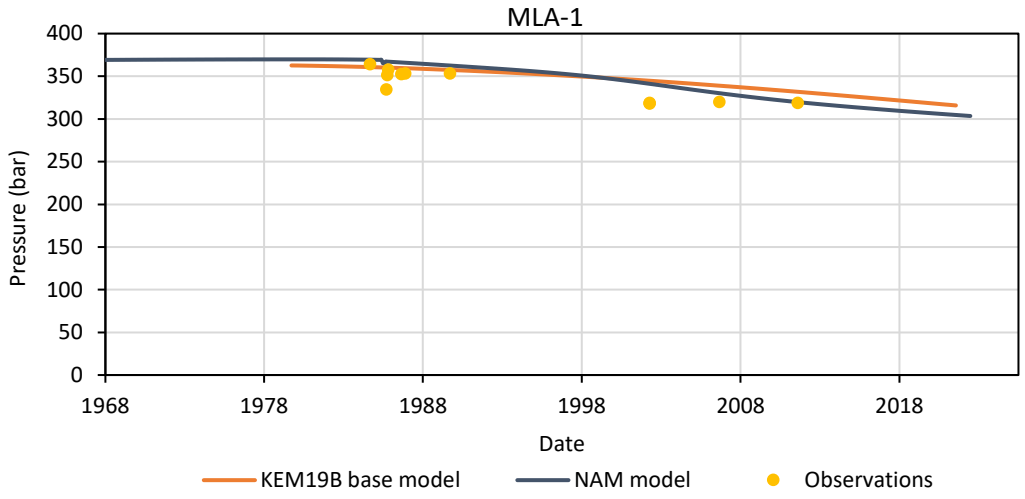

Figure 3-14 Pressure at MLA-1 from the base model, from the NAM Mores model and observations.

3.2.3 Results base model

Table 3-1 gives an overview of the GIIP of the static base model prior to application of the pore volume multiplier, the GIIP of the dynamic base model (incl. gas BFWL which is ~5% for most fields) and estimates by NAM based on field reviews. The value listed in the table is not the mean of the ensemble, but the value of the single realization selected as base model. The

ensemble results are presented in the next section. Figure 3-16 shows the simulated pressure in the base model at the end of the historical period (1 Jan 2022 in this study). Clearly visible in blue is the depleted aquifer that is connected to Roden. The other aquifers are less depleted.

Table 3-1 Estimated GIIP values (BCM in sm^3) for the base model compared to the estimates derived from the field reviews by NAM

	Static GIIP	Pore volume multiplier	dynamic GIIIP (incl GBFWL)	NAM GIIP
Vries-Noord	3.1	1.4	4.6	4.8
Roden-Noord	7.3	1.0	7.7	8.5**
Roden-Zuid	3.2	1.17	3.9	1.6
Boerakker	2.6	1.81*	3.9	4.8
Pasop	6.4	0.61	4.1	3.9
Faan	3.7	0.3	0.9	1.4
Noordlaren	0.3	0.83	0.2	0.2

* For the main compartment containing BRA-1 and BRA-2, BRA-3 has multiplier 0.55.
** For the Roden field, NAM estimates are available for the entire field only. The division is based on (Molen et al., 2020).

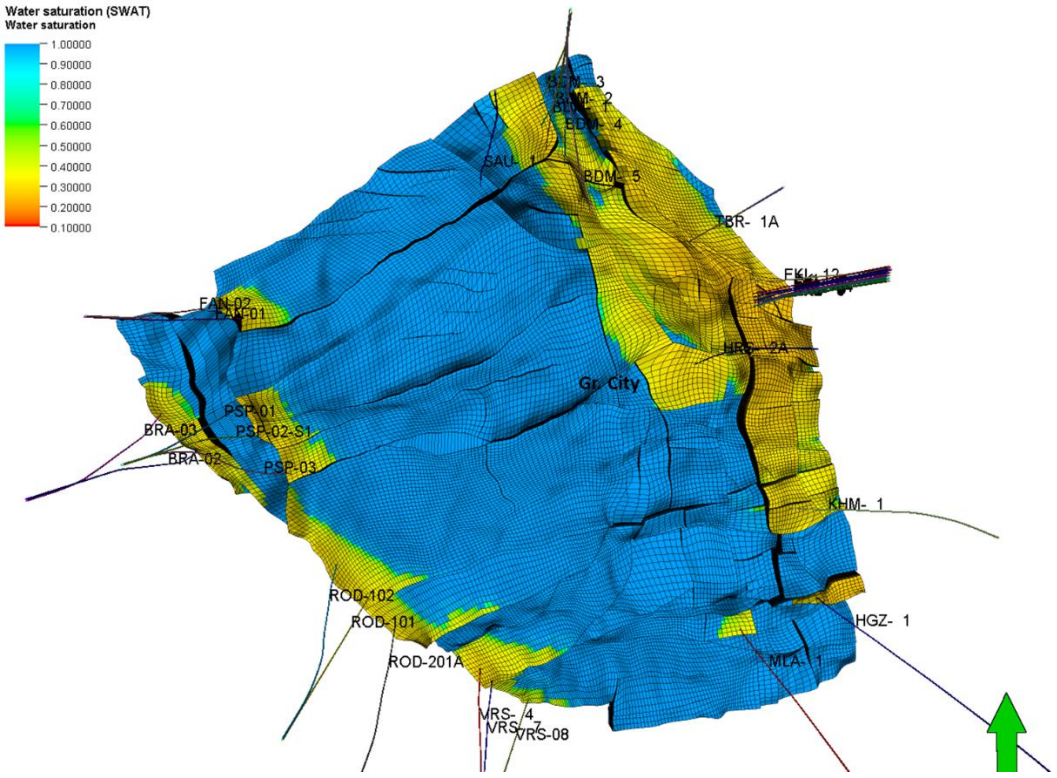

Figure 3-15 Initial water saturation distribution in the model area of the base model. Green arrow indicates north.

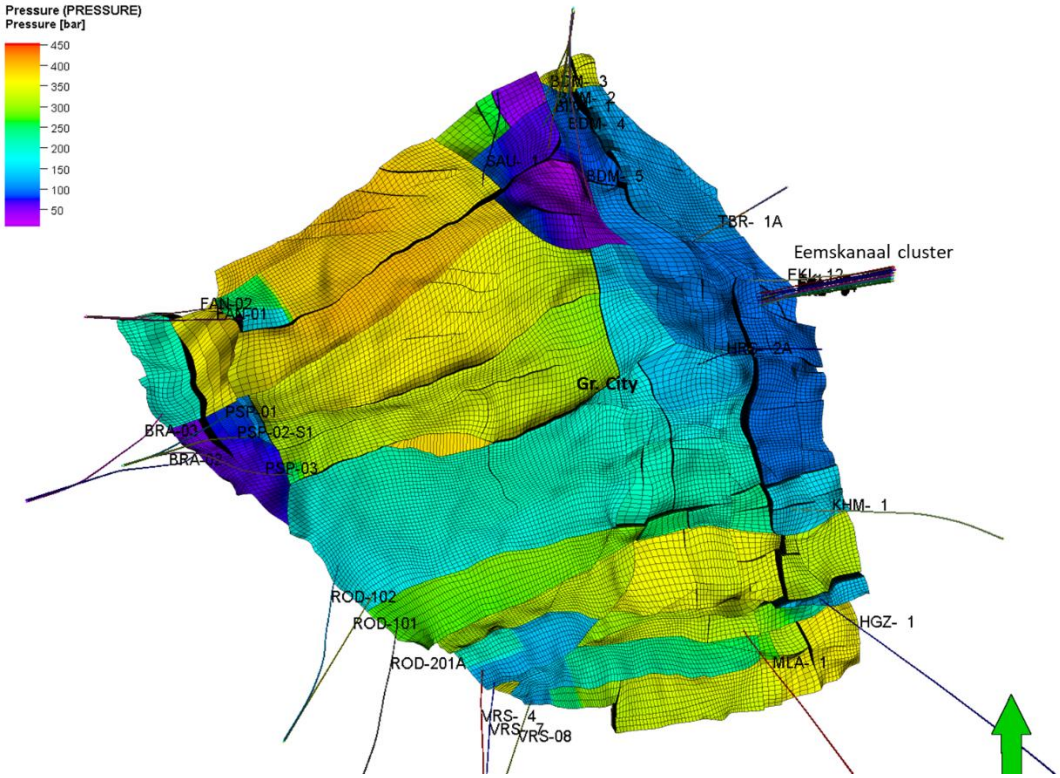

Figure 3-16 Top view of the pressure at the end of the history period (1 January 2022) for the base model. Green arrow indicates north.

3.3 Ensemble of reservoir models

3.3.1 Ensemble input settings

The following properties are varied to create the ensemble of 100 reservoir model realizations:

- NtG, porosity and permeability via Gaussian simulation (discussed in section 2.5)
- Vertical permeability as a fraction of the horizontal permeability
- Vertical permeability of the Ameland member (ROCLA)
- Multiplier on the permeability between the Slochteren and the Carboniferous formations following (Zeeuw and Geurtsen, 2018b): layer 23
- Transmissivity of the baffles to horizontal flow from the base model (faults implemented as baffles in the small gas fields)
- Fault transmissivity

Although the main sources of uncertainty have been included in the ensemble, the set is not complete. Sources of uncertainty that have not been included are for example structural uncertainty and the relative permeability. In part, such uncertainties have not been included because they are more difficult to implement, but mainly because the impact is similar to uncertainty that has been included, like structural uncertainty and porosity which both affect the GIIP.

Adjustment of the gas-initially-in-place (GIIP) for the ensemble
For the base model, pore volume multipliers per small gas field were implemented to get an acceptable GIIP and history match in the wells. Due to the variations in NtG and porosity, the GIIP is different for each member (model realization) of the ensemble. Due to these differences, application of the same pore volume multipliers as in the base model to all ensemble members does not lead to an acceptable history match for the ensemble. An alternative would be to apply a pore volume multiplier to each ensemble member that results in the same GIIP-values for all ensemble members. This is not a good alternative, because it underestimated the uncertainty. Therefore, to preserve variation in the ensemble but have the correct range, the pore volume multipliers are calculated for each ensemble member separately. The multipliers are calculated in such a way that the range from the ensemble is normalised to the expected GIIP range based on 'observations'. The 'observations' of the GIIPs are values estimated by NAM and during the tuning of the base model. Thus if a member has a GIIP of for example 10% above the minimum of the initial range, it will be adjusted to a value 10% above the minimum of the 'observed' range.

The multipliers are calculated based on the static GIIP values calculated using the porosity and NtG from the ensemble and the average gas formation volume factor from the base model. The procedure is illustrated in Figure 3-17. $GIIP_{ens}$ refers to the values from the static ensemble prior to the adjustment. $GIIP_{obs}$ refers to the range in GIIP values to which the GIIPs are corrected and which are based on the observations. Table 3-2 lists the values for the GIIPs for the small fields.

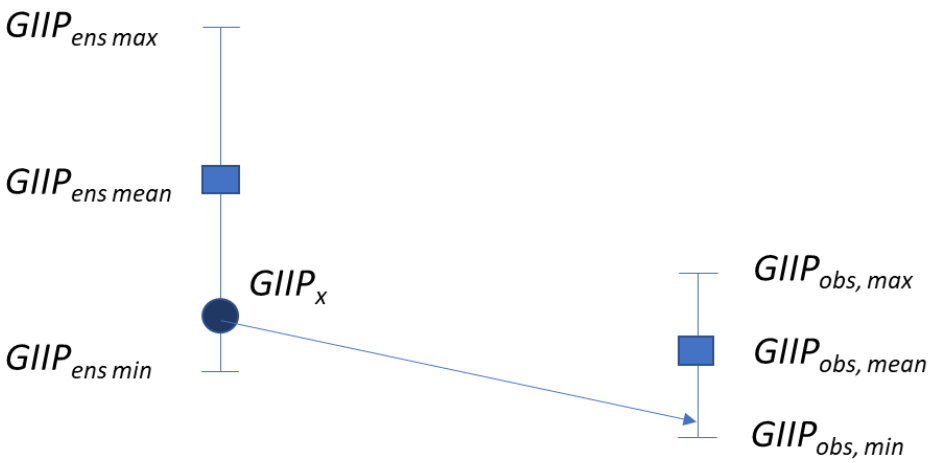

Figure 3-17 Illustration of the procedure for the adjustment of the GIIP of each of the small gas fields in the ensemble while preserving variability for ensemble member x.

Thus for each pore volume multiplier in the model, the following equation (eq. 1) is used:

$$PVMULT_x = \frac{GIIP_{obs,\ mean} + \left(\frac{(GIIP_x - GIIP_{ens,\ mean})}{GIIP_{ens,\ range}} GIIP_{obs,range} \right)}{GIIP_x} \qquad \text{eq. 1}$$

Where:

$PVMULT$: pore volume multiplier
GIIP : Gas Initially In Place

Subscripts:
x : small gas field or sector identifier
y : ensemble member number
ens : the static ensemble prior to the application of the multiplier
obs : values to which the GIIPs are corrected (based on observations)
mean : arithmetic average
range : maximum value – minimum value

For Vries, Roden Boerakker and Noordlaren , the static GIIP estimate is close to the dynamic GIIP without GBFWL. For Faan and Boerakker, the dynamic GIIP of the base model is lower, because some changes were implemented in the tuning phase that are not in the static model.

Table 3-2 Static GIIP (sBCM) values of the ensemble prior to the adjustment using multipliers ($GIIP_{ens}$ in Figure 3-17) and which were used for determining the multipliers for the ensemble ($GIIP_{obs}$ in Figure 3-17). These GIIP values don't include the GBFWL and the manual changes to the dynamic model in the tuning phase for Boerakker and Faan.

	Static GIIP of the ensemble			Range ('obs') used to calculate the pore volume multiplier		
	min	mean	max	min	mean	max
Vries-Noord	2.8	3.1	3.6	4.1	4.3	4.7
Roden-Noord	6.7	7.5	8.3	7.1	7.4	7.9
Roden-Zuid	2.9	3.2	3.4	3.2	3.7	4.2
Boerakker	2.6	2.9	3.3	4.4	4.8	5.1
Pasop	5.6	6.4	7.0	3.4	3.9	4.4
Faan	3.6	3.9	4.3	1.0	1.1	1.3
Noordlaren	0.2	0.3	0.3	0.1	0.2	0.3

Sampling for the ensemble
The other parameters that are varied for the ensemble (except for the fault transmissivity multipliers, see below) are sampled from a uniform distribution with ranges as given in Table 3-3. The values used in the base model are added for comparison.

Table 3-3 Minimum and maximum of the range of the uniform distribution from which the parameters are sampled.

	Base model	min	max
Anisotropy (kh/kv)	10	5	15
Multiplier on kv ROCLA	0.01	0.002	0.032
Multiplier on kv layer 23	0.001	0.0002	0.0032
Baffles set 1	0.01	0.005	0.02
Baffles set 2	0.001	0.0005	0.002
Baffles set 3	0.0002	0.0001	0.0003

Fault transmissivity multipliers
The fault transmissivity multipliers have also been varied for the ensemble. The workflow is however different from the other parameters that have been varied. Like the other parameters, a value has been set in the base model for each multiplier. However for the variation in the ensemble, the faults have first been grouped in 'logical' geographical groups, like for example the group of faults that controls the flow between the Eemskanaal cluster and the Harkstede block. The division of the faults over the groups can be found in Appendix B. Group 0 is not varied in the ensemble. For all other groups of faults a random value is sampled from a uniform distribution with ranges as specified in Table B-5 in 0. The random value is raised to the power 10 before multiplying with the fault multiplier from the base model:

$$Fault\_mult_x = fault\_mult\_base * 10^{random\ value\ of\ the\ group} \quad \text{eq. 2}$$

Simulation
The ensemble and base model have been developed in Petrel and Eclipse (by Schlumberger NV (SLB.com)). However for simulation of the ensemble, open source simulator OPM flow (https://opm-project.org/) has been used. For the base model, it was checked that the results of OPM flow are in line with those from Eclipse.

3.3.2 Ensemble results

Table 3-4 shows the results of the dynamic GIIP of the ensemble for the small gas fields. The dynamic GIIP is calculated in the dynamic model and deviates from the static GIIP because the gas formation volume per grid cell is used instead of the average and the gas below free water level is included. Figure 3-18 and Figure 3-19 show the reservoir pressure for the Roden field and HRS-2A respectively for the ensemble as examples. Further pictures are provided in Appendix B. The spread for HRS-2A is larger than for the Roden field, because there was less pressure information to constrain it. The subsidence data will be used to select the better fitting ensemble members. The calculation of the subsidence and the workflow to select the members will be discussed in the next section.

Table 3-4 Dynamic GIIP values from the ensemble

GIIP (BCM sm3)	Dynamic GIIP ensemble		
	min	mean	max
Vries-Noord	4.2	4.5	4.9
Roden-Noord	7.5	7.9	8.3
Roden-Zuid	3.5	4.0	4.5
Boerakker	3.6	4.0	4.4
Pasop	3.6	4.1	4.7
Faan	0.8	1.0	1.1
Noordlaren	0.1	0.2	0.3

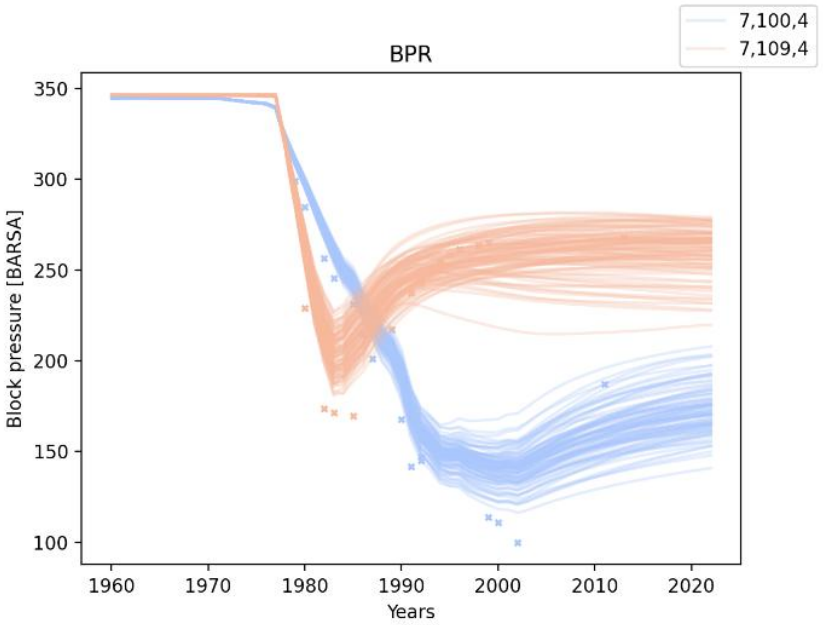

Figure 3-18. Ensemble of reservoir pressures (at BHP depth) of the Roden gas field for the historical period. Blue curves represent the Roden north block and red is Roden south. Stars indicate static pressure measurements.

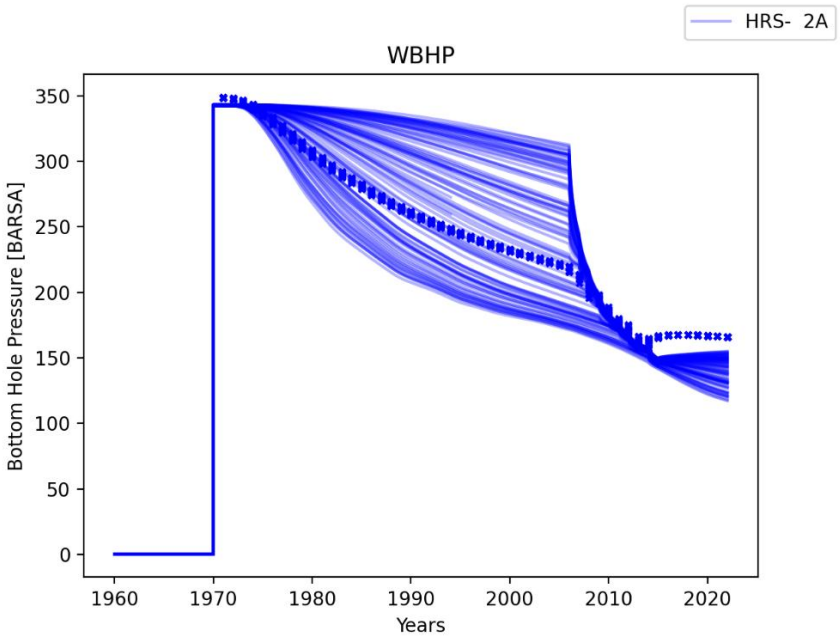

Figure 3-19 Ensemble of BHP (bottom hole pressure) for HRS-2A. Stars indicate output from the NAM MoReS model which were used as measurements.

3.4 Compaction and subsidence

Aquifer pressure changes cause compaction by the changes in effective stress associated with them. This compaction causes surface movement – which can be measured. In this Section we document how we have employed subsidence measurements to reduce the uncertainty of the pressure distribution in the aquifer and to discriminate probabilities of the ensemble members. The tool that we use is ESIP (acronym for Ensemble Subsidence Interpretation and Prediction), an inhouse tool targeted at the use of surface movement data for reservoir characterization, deploying an ensemble data assimilation approach (Candela et al, 2022).

3.4.1 Surface movement data

We have evaluated two sources of surface movement data. The first is the data provided by Rijkswaterstaat. These contain benchmark heights through time, of the primary benchmark network. However, the benchmarks located in the region above the Groningen SW aquifer are quite limited and none of them contain numbers outside the timespan 1980 – 2000.

We therefore also evaluated data provided by NAM, which are the data that they have used for their own interpretation of subsidence in the northern Netherlands. The dataset spans the time interval between 1964 and 2018 and contains more benchmarks: also the secondary benchmarks are incorporated. The secondary benchmarks have been constructed specifically for the determination of surface movement due to gas production in the region. Therefore, the network of benchmarks is much more dense. In addition, the time window at which benchmark heights have been determined is much larger and a good coverage of the complete history during the gas production of Groningen until 2018 could be provided. We have thus used the NAM data in this study.

The reservoir model output that we used for this study is the pressure decline in the SW aquifers only. We have therefore selected only the benchmarks that are not influenced by parts of the gas fields which are not in the pressure output maps. All gas-production-related surface movements in the selected benchmarks can thus be attributed to the pressures in the models detailed above. The locations of the benchmarks that were used are represented in Figure 3-20.

ESIP uses double differences of height measurements. Our input contained interpreted heights for each location. These had been produced by comparing single height differences between benchmark locations and comparing them to a benchmark that is assumed stable. Using those is equivalent to double differences under the condition that the error model is propagated and incorporated in a covariance matrix. This covariance matrix, however, was not available.

NAM have employed an adapted use of the measurement error model upon a motivation of "model error" – possible unmodeled features causing mismatches between model results and measurements (NAM report, 2021). They assume this error is larger for larger displacements; they add a variance of $\sigma_0 + \alpha \cdot dh$ to the covariance, with σ_0 of the order of 0.5 – 0.6 cm^2; α of the order of 0.03 cm and dh the modeled displacement. These numbers make the covariance matrix almost diagonal, so the NAM treatment provides a qualitative argument for using a diagonal covariance matrix. However, our inversion procedure is different from theirs: we use a "Red Flag" approach (Nepveu, Kroon et al, 2010), therefore we use the measured displacements rather than the modeled displacements for the additional variance determination. In the assimilation procedure we use height differences of subsequent times;

not the total displacements since the first measurement campaign in which that point was evaluated.

We deploy the measurements in a parameter estimation exercise. Ensemble methods like those that we use often suffer from ensemble collapse if the number of data points is large (Van Leeuwen, 2009): the spread of the outcome then is too small in view of the data uncertainty. The ensemble collapse can be removed by increasing the variance of the data considerably. We arrived at acceptable numbers of sizeable model realization probabilities with $\sigma_0 = 1\ cm^2$; $\alpha = 1\ cm$. We comment on this below.

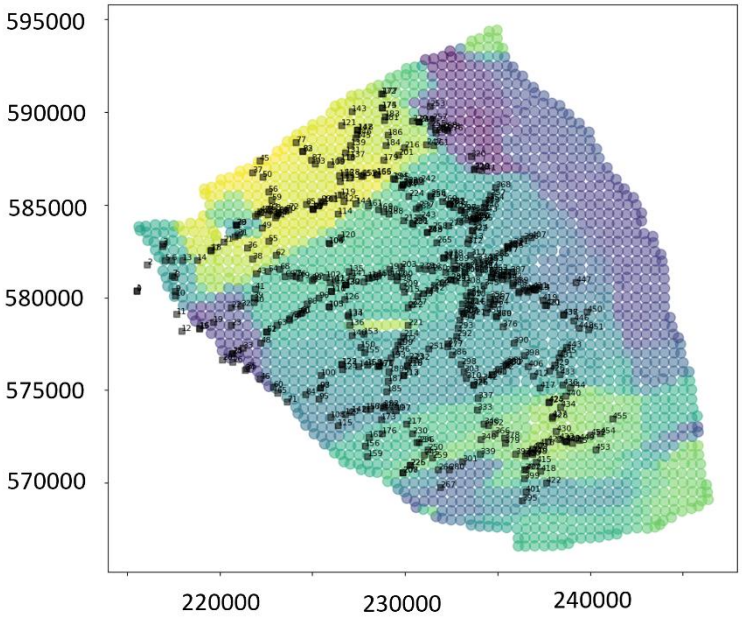

Figure 3-20 Selected benchmarks above the SW Groningen aquifer. The background color signifies the pressure depletion in the SW aquifer (darker colors indicate more decline); we see larger pressure declines towards the NE-E border, where the aquifers are bounding the Groningen field, and to the W-SW border where the aquifers bound some of the smaller fields.

3.4.2 Screening of mechanical parameters with the Red Flag method

We have deployed the Red Flag method for our parameter estimation exercise (Nepveu et al, 2010). In the Red Flag method, first an ensemble of realizations is created. Then each ensemble member is assigned a scaled probability, based on the mismatch between the ensemble's calculated subsidence and the measured subsidence.

We used four compaction models: a linear model, a bi-linear model, a time-decay model and a rate-type compaction model (Candela et al, 2022; see also the next sections). For each compaction model we construct 10 random realizations of the driving parameters within their bandwidth, for each of the 100 reservoir models. For each of the four compaction models this results in an ensemble of 1000 surface movement predictions at all locations.

For the influence function we used a Geertsma-Van Opstal function (Opstal, 1974). This function calculates the subsidence bowl for a center of compression at the depth of the compacting reservoir in a homogeneous subsurface, with an underlying rigid basement. The parameters in this function are the given depth of the compacting source, the depth of the basement, and the Poisson's ratio of the subsurface. The subsidence model calculates the total influence of all compacting grid cells of the reservoir simulator by superposition. The data with which the model realizations are compared contain 2829 differences at 457 locations.

The compaction coefficient is dependent on the porosity. The starting value for our compaction coefficient is (Candela et al, 2022)

$$c_{m0}[10^{-5}bar^{-1}] = 267.3 \cdot \phi^3 - 68.72 \cdot \phi^2 + 9.85 \cdot \phi + 0.21$$

The compaction coefficient is calculated for each grid cell in the reservoir simulation.

3.4.2.1 Linear compaction model

The thickness change of a grid cell in the linear compaction model under uniaxial strain conditions is a simple linear function of the pressure depletion:

$$\frac{\Delta V_{linear}}{V} = f_{cm} \cdot c_{m0} \cdot dP$$

With the use of the linear compaction model we apply a single multiplication factor f_{cm} to the starting value to maintain the porosity dependence. We have first have determined the range in which the compaction parameters should be. We started with a range of 0.3-1.0 for the compaction coefficient multiplication factor; for the Geertsma-Van Opstal parameters we started with 4000-7000 m depth for the rigid basement and a fixed value of 0.25 for the Poisson ratio.

The 1000 ensemble members are evaluated in the customized Red Flag algorithm, resulting in a scaled probability for each realization. The screening phase of the Red Flag method employs a variance that is increased by a factor of 10, because otherwise the exercise results in ensemble collapse with only a single realization surviving with sensible probability.

Figure 3-21 visualizes the results. In Figure 3-21a we see the probability for each realization vs the realization number. Every reservoir realization corresponds to 10 realizations in this plot, arranged with numbers 0-9; 10-19 for reservoir realizations 1, 2, etc. We see that some reservoir realization perform better than others, however, there is considerable scatter and the probability within every set of 10 for a reservoir realization is largely varying. When plotting the probabilities against the compaction parameters , we conclude, somewhat intuitively, that the f_{cm} (Figure 3-21b) should be in the range 0.5-0.6; the rigid-basement depth (Figure 3-21c) should be larger than 5000 m. Even within these ranges, the majority of the members have small probability, apparently because the corresponding reservoir realizations are suboptimal.

We reran the Red Flag algorithm with the narrower distribution of these starting values, in order to obtain a larger number of members with relatively large probability and a more precise determination of the fitness of the underlying reservoir realizations. To our reassurance, the best realizations remained largely the same ones. In Section 3.5.1 we will further discuss how we proceed to selecting cases for forecasting. The measured and modelled displacements in 20 of the 457 locations is reproduced in Figure 3-22. The

assignment of probabilities based on the match of ensemble member predictions with the data indeed improves the fit considerably. This was also the case for the benchmarks not shown here.

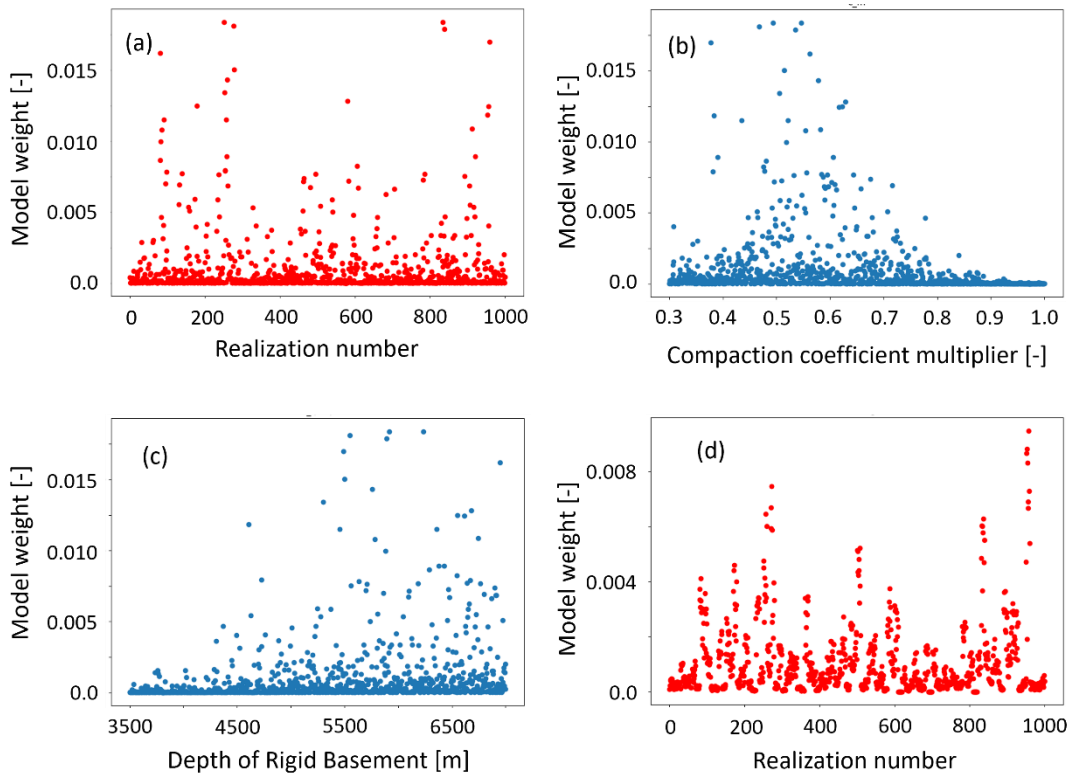

Figure 3-21 Model weights of the model realizations for the linear compaction model plotted against (a) realization number; (b) compaction coefficient multiplication factor; (c) depth of the rigid basement. (d) weights with better constraint starting values

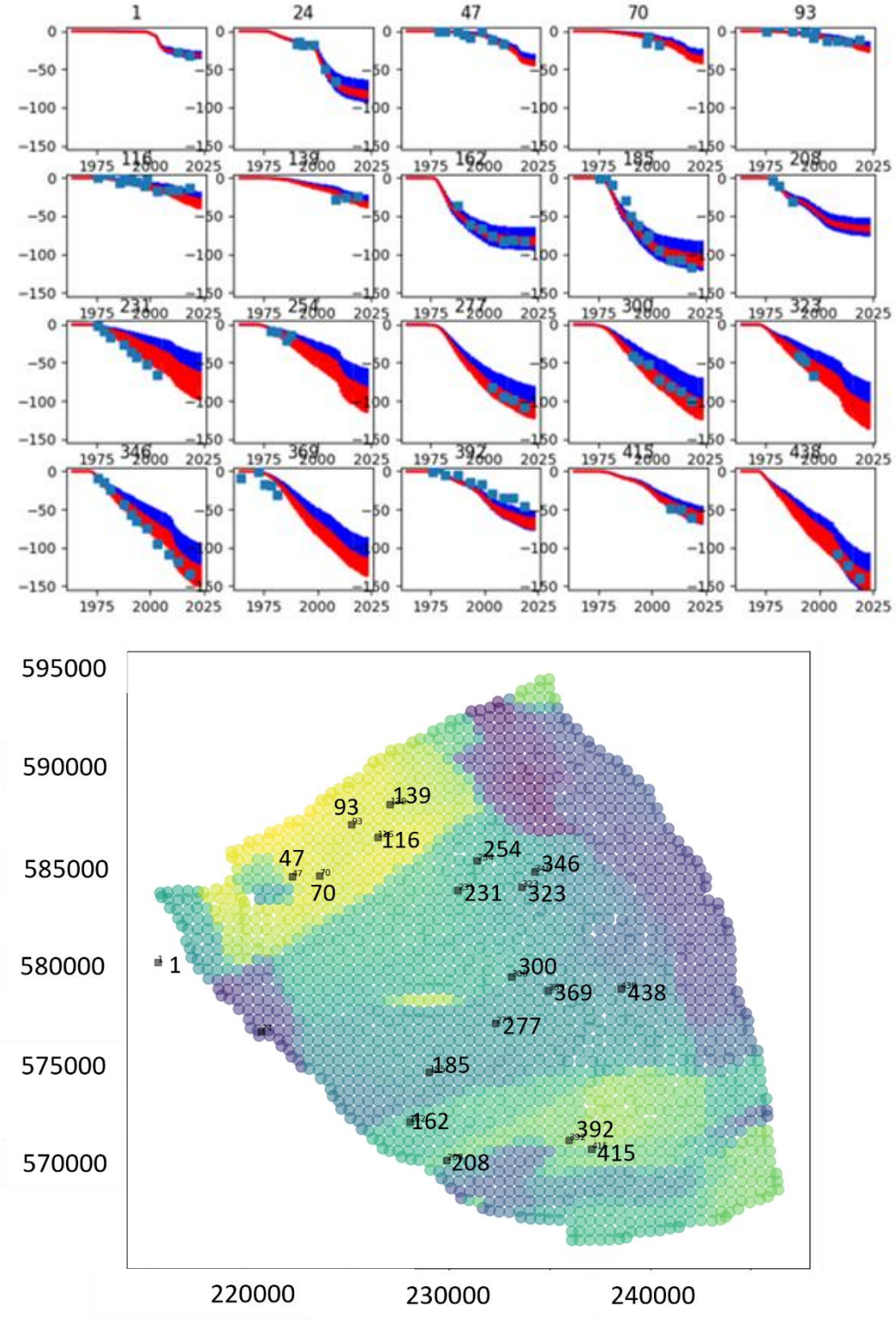

Figure 3-22 Top: Traces of the displacements (in mm) at 20 selected benchmarks. Blue: Prior mean including uncertainty; Red: Posterior mean including uncertainty, based on Red Flag output. Symbols: Measured displacements. Bottom: positions of the represented benchmarks, with the colors indicating the last pressure drawdown of realization 96 (darker colors indicate more drawdown).

3.4.2.2 Alternative models

A similar procedure was followed with the bilinear compaction model, a model with different values for the compaction coefficient for pressures larger and smaller than a transition pressure. Compaction model parameters are here the compaction coefficients f_{cm1} and f_{cm2} for smaller and for larger depletion pressures, and the pressure value P_{trans} at which the transition occurs:

$$\frac{\Delta V_{bilinear}}{V} = \begin{cases} f_{cm1} \cdot c_{m0} \cdot (P_0 - P) & (P \geq P_{trans}) \\ f_{cm1} \cdot c_{m0} \cdot (P_0 - P_{trans}) + f_{cm2} \cdot c_{m0} \cdot (P_{trans} - P) & (P < P_{trans}) \end{cases}$$

We refer the compaction coefficients again to the starting values c_{m0} with a multiplication factors f_{cm1} and f_{cm2}. We found that the first compaction coefficient (the one working at smaller depletion pressures) was similar to the single coefficient in the linear compaction model (f_{cm1} in the range 0.5 – 0.6) and that the rigid basement should be deep. The results were insensitive to the transition pressure and the second compaction coefficient. This is related to the range starting value for the transition pressure, between 180 and 270 bar, which is reached for only very few points in the aquifer. We therefore do not use the bilinear compaction model in the remainder of this study.

The time-decay model employs a delayed action of pressure depletion to compaction (Mossop, 2012). The relative compaction of a grid cell with volume V, subject to a pressure step change dP at time t_0, is given by

$$\frac{\Delta V_{tdecay}}{V} = f_{cm} \cdot c_{m0} \cdot dP \cdot \frac{1}{\tau} \exp\left[-\frac{t - t_0}{\tau}\right]$$

An evolving pressure is included through a time convolution of the pressure development with this function. The model parameters are the multiplication factor for the compaction coefficient c_m and the characteristic time constant τ.

Starting with a broad distribution of f_{cm} and τ of 0.1 – 2 and 0.1 – 40 years we see a clear correlation between them when plotting the ranked probabilities in a cross-plot. The realizations ranking higher are distributed along a band ranging from (f_{cm}, τ) ~ (0.5, 0) to (2.0, 25) (Figure 3-23). However, a number of resampling exercises led to an optimum range of f_{cm} between 0.5 and 0.6 and τ between 0.1 and 1. This is virtually equivalent to results of the linear compaction model, because a decay of 1 year and less can hardly be seen on the scale of the measurements. Also the results for the rigid basement was similar: it should be deep to the extent that its effect at the surface can not be seen.

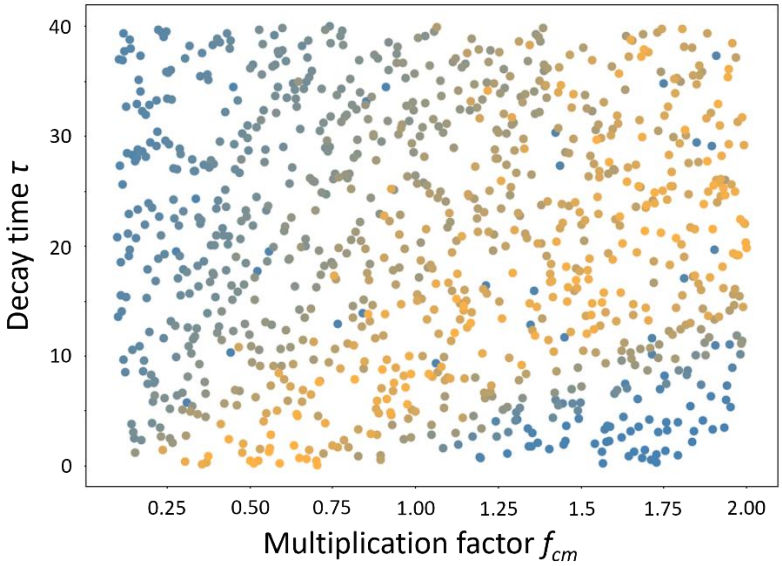

Figure 3-23 Crossplot of decay time vs multiplication factor for the compaction coefficient, with realizations in the broad test of the time decay model. Colors from yellow to blue indicate the ranking from high to low probability.

The rate type compaction model employs two contributions to compaction: an immediate response and a delayed response that depends on the rate of pressure depletion. The model is well documented in Candela et al (2022) and Pruiksma et al (2015) and utilizes three material parameters ($c_{m,ref}, c_{m,d}, b$) and one state parameter ($\dot{\sigma}'_{ref}$ Results of a screening of the parameters yielded values of $c_{m,ref}$ between 0.3 and 0.6; $c_{m,d}$ between 0.6 and 0.9, b between 0.01 and 0.02 and $\log \dot{\sigma}'_{ref}$ between -6 and -3. This is in line with the values reported by NAM (NAM report, 2021). Except for the value of $c_{m,ref}$, the outcome is not discriminating. This is due to the relatively small values for the depletion in the aquifer, while the distinction of the rate type compaction model with regard to the linear compaction model is mainly for larger values of the depletion. We will therefore not use the rate type compaction in the remainder of the report.

3.4.2.3 Synthesis of the Red Flag model results

The Red Flag methodology has been deployed with an inflated variance, in order to avoid ensemble collapse. We judge this allowable since we only use the method to identify the best reservoir model realizations at this stage; and ensemble collapse is known to pose a major problem if many data points are available.

All compaction models yielded reasonable values for their parameters. At the same time the Red Flag approach yielded a clear distinction between reservoir models. The models with the largest probabilities were consequently the same for all compaction models, and the optimal value for the rigid basement was found to be large. The selection of the best realizations to pursue further is documented in Section 3.5.1.

3.5 Forecast of the post-abandonment pressure

3.5.1 Selection of model realizations

Before making the selection for the model realizations to be used for forecasting, first it is discussed why some reservoir models from the ensemble are more probable based on the observed subsidence than others (in other words: fit the data better). Figure 3-24 shows the pressure in the model with the highest probability based on the subsidence (member 96). Comparison with the pressure of the base model in Figure 3-16, shows that the main change is in the aquifer north of the Roden aquifer which is connected to the small gas field Pasop to the west and the Ten Boer area to the east. In particular on the east side of this aquifer (near the Ten Boer area), the pressure is expected to be considerably lower than in the base model. The pressure depletion in the middle of the aquifer is less certain: the posterior ensemble of the subsidence still shows a relatively large range of ~5 cm at the end of the history period (Figure 3-22).

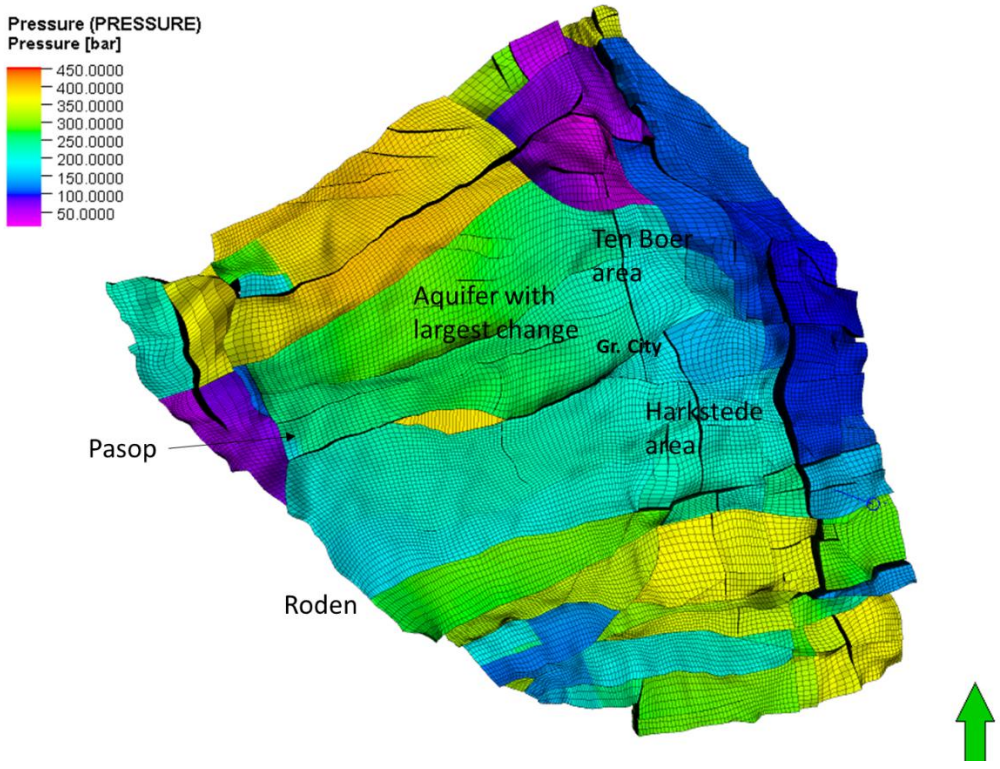

Figure 3-24 Top view of the pressure at the end of the historical period (1 Jan 2022) for the model with the highest probability based on the subsidence (96).

In order to make a selection of the model realizations that fit the observations best, the probability based on the subsidence needs to be combined with a measure for the fit to the pressure data. Therefore the Root Mean Squared Error (RMSE) of the static pressure observations was calculated for the all the wells of the small gas fields and HRS-2A and MLA-1. First the RMSE was calculated per well and then the values per well were averaged to arrive at one RMSE per model realization.
Figure 3-25 shows a plot of both the probability and the RMSE per model realization. This shows no correlation between the two measures. Because the pressure was already used to

tune the base model, it was decided to base the selection of the best fitting models (which are to be used for forecasting) on the fit to the subsidence more than on the fit to the pressure. The following thresholds were used to get a reasonable number of models.

- The threshold for the probability based on subsidence is 0.015
- The threshold for RMSE of the pressure is 51 bar

This means that ensemble members with a probability higher than 0.015 and RMSE lower than 51 bar are selected. The selection is illustrated in Figure 3-25 by the red outline. This results in a selection of 22 models from the total of 100.

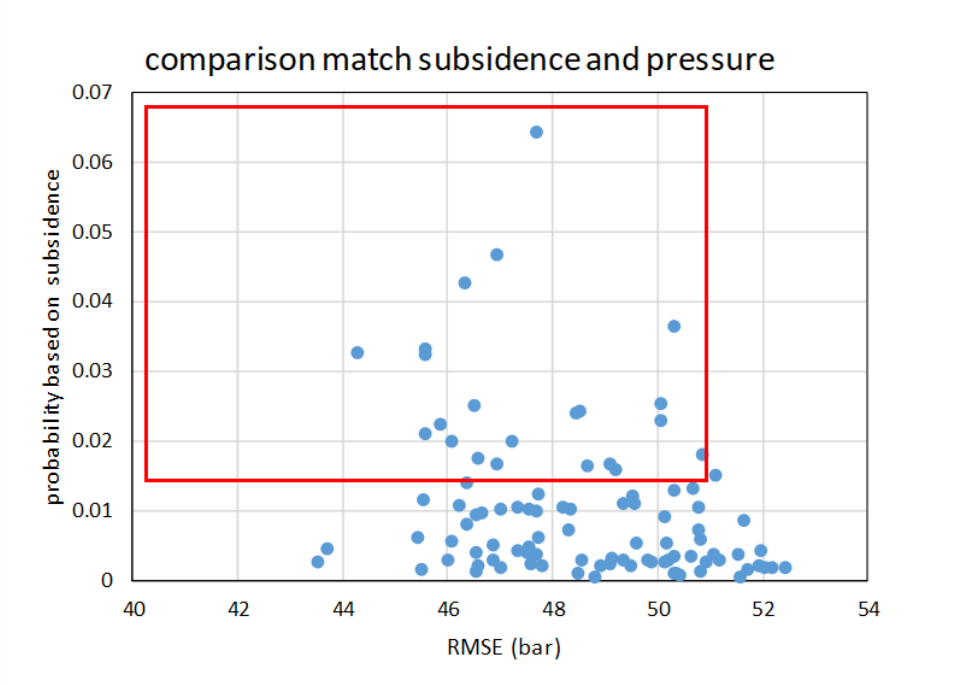

Figure 3-25 Probability of the model realizations based on the subsidence plotted against the averaged RMSE for the reservoir pressure. The red square indicates the model realizations selected for prediction.

3.5.2 Constraints for the forecast period

To simulate the post-abandonment pressure, the selected model realizations need to be run forward in time to the year 2100. To do this, well constraints are required, both for the small gas fields and the Groningen side. For the small gas fields, the constraints are simple. Except for well FAN-01, all wells were closed before 1/1/2024. The production data from 2022 and 2023 are taken from NLOG.nl, where necessary. Based on the publicly available 'Winningsplan' for Faan, well FAN-01 is expected to cease production in 2025. Production as listed in the 'Winningsplan' for the mid case is implemented for 2024 and 2025.

On the east side of the model, constraints need to be decided upon for Bedum and the Groningen wells. The required pressure constraints for the Eemskanaal wells are based on the results of the base case model from the KEM24b project (TNO, 2024), which is based on the NAM Eclipse model. The original KEM24b model was run to 2054, but the run was extended to 2100 for this project. To achieve the pressure decline due to the equilibration with the rest of the Groningen field, the wells were opened for gas production in the model.

For the wells in the western periphery (HGZ-1 and KHM-1), the historical results of the KEM24b model are not in line with the NAM MoReS model and the model developed in this project. Unfortunately, no predictions are available from the NAM MoReS model. So for both wells, a pressure decline was defined based on expert judgement. For HGZ-1 it was assumed that the well will fully equilibrate with the Groningen field, because the pressure was already close to the Groningen pressure (Figure 3-26). For well KHM-1, which probably depletes via the Eemskanaal area rather than the Groningen main field (Landman, 2023), the pressure constraint is set to go down to 125 bar and then further deplete via Eemskanaal.

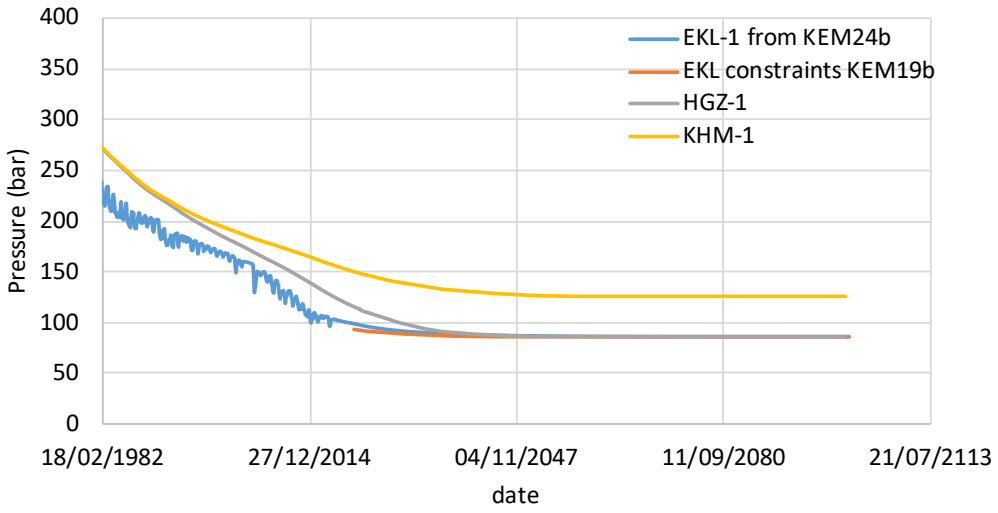

Figure 3-26 Pressure constraints for the Eemskanaal wells (EKL constraints KEM19b), HGZ-1 and KHM-1.

Based on the production plan for Bedum, the abandonment pressure for the field is 35 bar and shutin is expected in 2030. Therefore the pressure constraints for all wells are gradually declined to a pressure of 35 bar and the field is shutin on 1-1-2030. Well BDM-4 had already dropped below 35 bar in 2021, so no more gas was produced from this well.

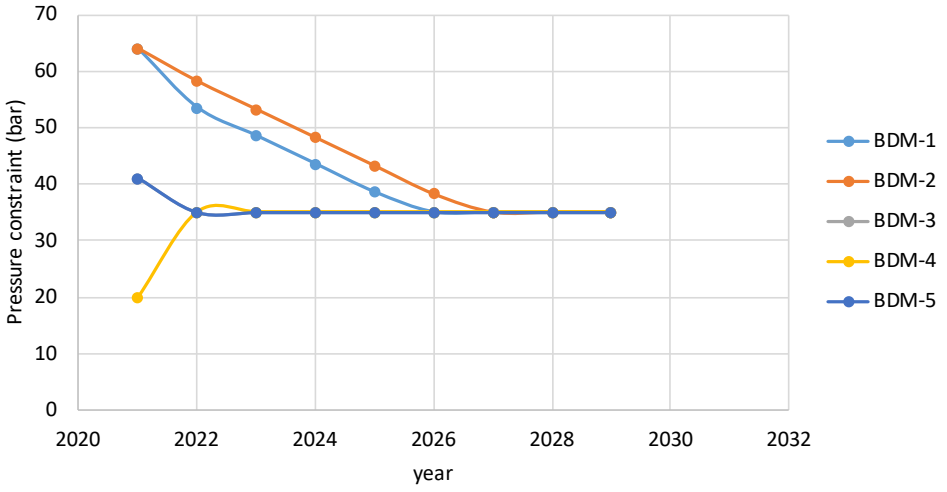

Figure 3-27 Pressure constraints for the Bedum field.

3.5.3 Results

The entire ensemble of 100 members is simulated over the entire time period from 1960 to 2100. The reason for simulating and showing the entire ensemble is that this shows how the selected ensemble members are distributed over the initial ensemble. An example is shown in Figure 3-28 for HRS-2A. Each curve represents the pressure at HRS-2A of one model realization. The blue curves are the model realizations that were not selected for the prediction period. The black curves are the ones that are selected (see Section 3.5.1 for the selection criteria). The red curve is the most probable model realization based on the subsidence (number 96). The vertical blue line marked "2022" indicates the point in time when we move from history to forecast mode. The black curves are distributed over the entire ensemble, which indicates that the ensemble is not biased and the uncertainty cannot be further reduced based on the subsidence observations at the locations where the base model was already tuned using pressure observations. The best overall fitting member (most probable member 96 in the red curve) shows very little drawdown in the early period which conflicts with the pressure observations in the well (see Figure 3-13 and Figure 3-19): a good overall fit doesn't imply a good fit for each individual well.

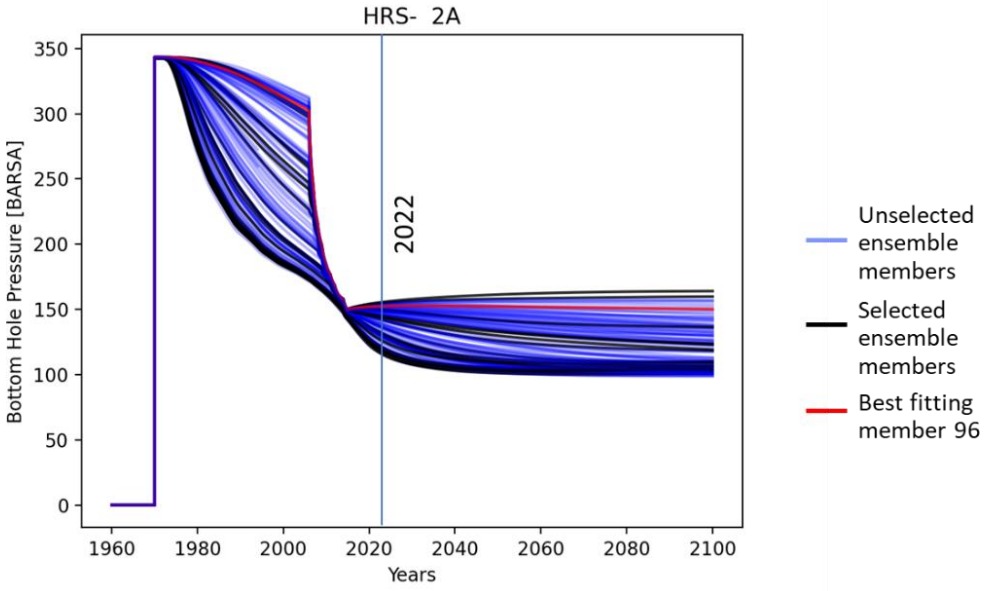

Figure 3-28 Pressure at HRS-2A for the period 1960 to 2100. Black and red curves are the selected model realizations, where the red curve is the best fitting member 96. Blue curves are the model realizations that do not fit sufficiently well to data to be used for prediction.

A second example is shown in Figure 3-29 for the Roden field for the north and south block. For both Roden north and south, the selected ensemble members span the entire range of the ensemble, again indicating no bias. For Roden south a decline in pressure is predicted after the earlier rebound for many of the ensemble members. This is due to slow depletion from adjoining aquifers and gas fields. The results from the other small gas fields and wells are shown in Appendix B.

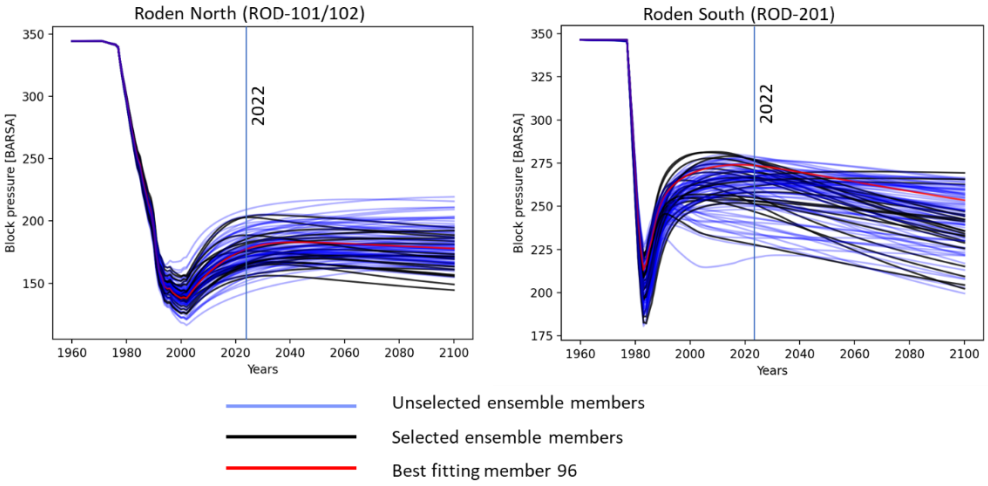

Figure 3-29 Pressure in the Roden field in the north and south blocks for the period 1960 to 2100. Black and red curves are the selected model realizations, where the red curve is the best fitting member 96. Blue curves are the model realizations that do not fit sufficiently well to data to be used for prediction.

Results in the aquifer

Up to this point, all the presented results are from either small gas fields or the Groningen field. To better understand the results within the aquifer, the pressure over time for a series of points from north to south in the aquifer is plotted in Figure 3-30 and Figure 3-31. Figure 3-30 shows the pressure in the northern part of the aquifer, while Figure 3-31 shows the pressure in the southern part. The red dots indicate the position in the aquifer. The map shows the pressure at the end of the history period (in 2022) for the best fitting member 96. The legend of the curves is as in Figure 3-28 and Figure 3-29. The most northerly two points, which are in the aquifer connected to Faan and Bedum, have limited depletion overall (30 to 40 bar) and the ensemble shows no bias. However for the two points to the south ((85,47,4) and (87,56,4)) which are in the aquifer connected to Pasop, the selected model realizations in black are exclusively in the lower part of the graph indicating that the observed subsidence points to more pressure depletion than the prior ensemble. For both points, the best fitting member (in red) is the curve that has most depletion. Clearly in this part, using the subsidence had added value. In Figure 3-29, the two points near Harkstede ((86,96,4) and (110, 100, 4)) are the locations with the largest depletion, which is supported by the subsidence. In fact, most of the selected curves are in the lower part of the graph. The point (110,122,4) further south has the largest spread in the results from any of the points and is poorly constrained both by wells and by subsidence.

In Figure 3-32 the depletion is shown for the best fitting member 96 for the years 2022, 2060 and 2100. All calculated with respect to the pressure before the start of production in 1960. The figure shows the ongoing depletion in the aquifers and some recovery in pressure in some small gas fields like Bedum (in the north-east), Faan (in the north-west) and Vries (south-west). Overall the largest depletion that is reached in the aquifer is around 200 to 220 bar in the Harkstede/Ten Boer area or a decrease of about 60% of the initial pressure. The figure also shows the relatively uniform depletion in the aquifers between the Roden field and Harkstede and the more variable depletion in the south part of the model.

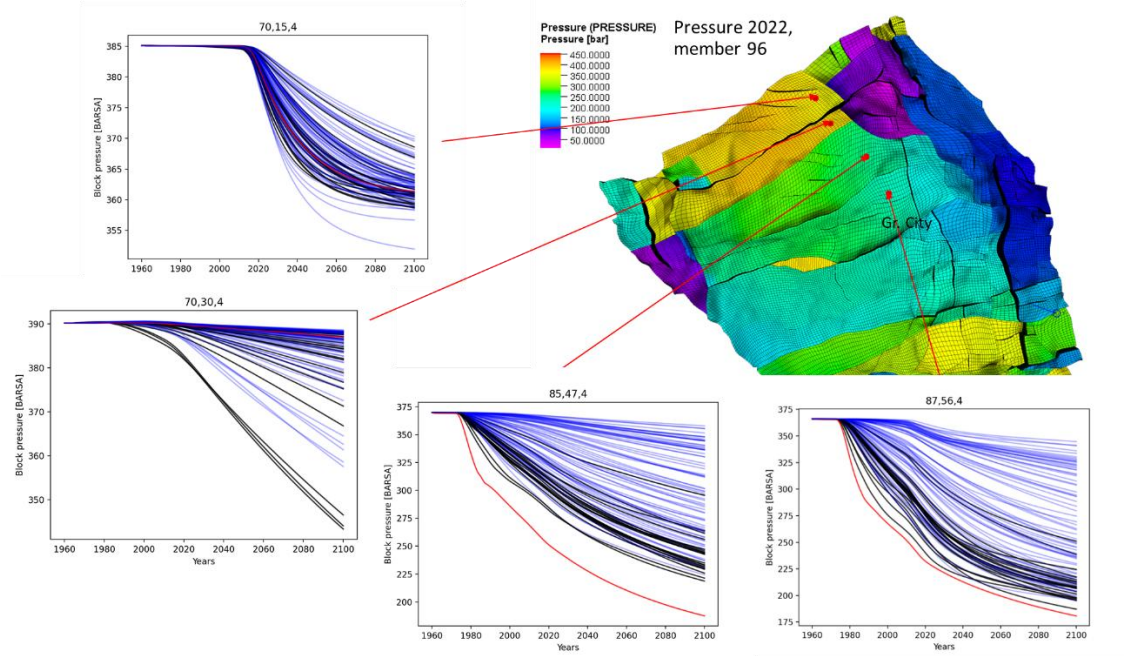

Figure 3-30 Pressure for four locations in the northern part of the aquifer for the period 1960 to 2100. The red dots indicate the position in the aquifer for which the line plots are. The legend of the curves is as in Figure 3-28 and Figure 3-29. The map shows the pressure at the end of the history period (in 2022) for the best fitting member 96. The number on top of the graph is the grid block.

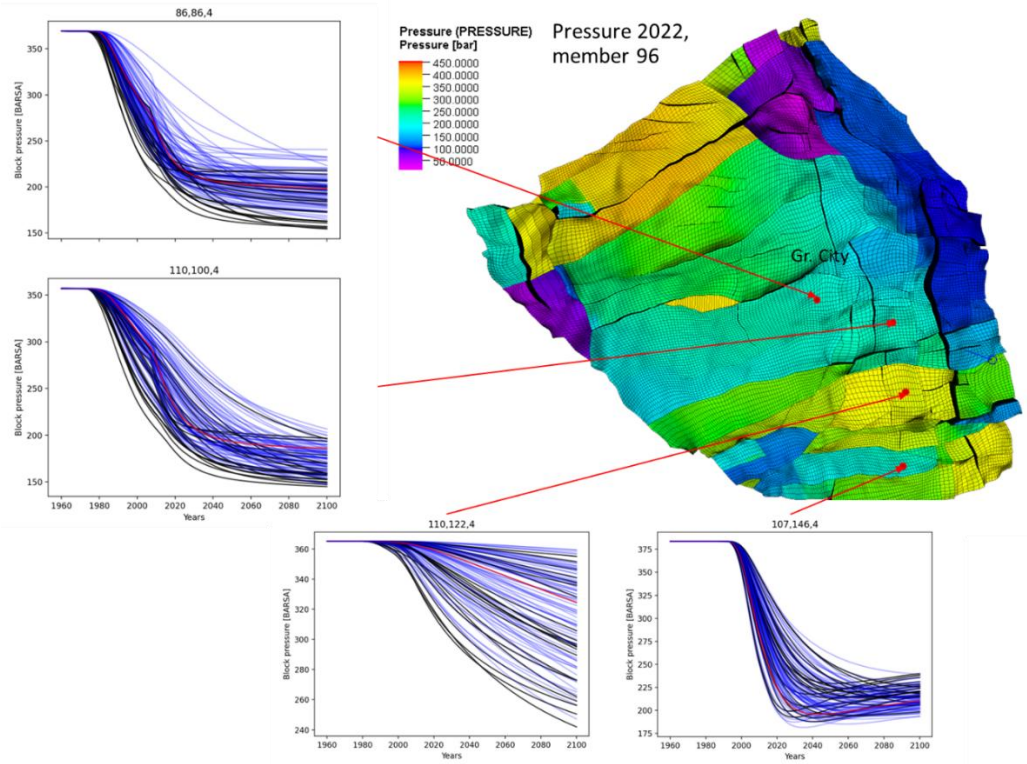

Figure 3-31 Pressure for four locations in the southern part of the aquifer for the period 1960 to 2100. The red dots indicate the position in the aquifer for which the line plots are. The legend of the curves is as in Figure 3-28 and Figure 3-29. The map shows the pressure at the end of the history period (in 2022) for the best fitting member 96. The number on top of the graph is the grid block.

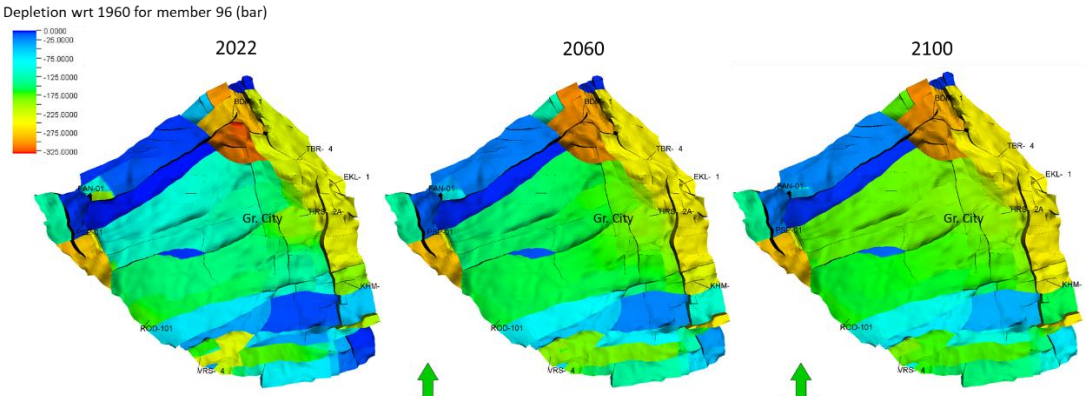

Figure 3.32. Depletion in 2022, 2060 and 2100 with respect to 1960 for the best fitting member 96

3.6 Discussion and conclusions

The current study has resulted in the forecast of pressure depletion for an ensemble of 22 out of 100 members in the SW aquifer of Groningen gas field in the southern Lauwerszee Trough. The ensemble was ranked based on static pressure measurements in the small gas fields and observations of surface movement measurements above the aquifer. The surface movement measurements have helped making this ranking by discriminating the models according to how the calculated surface movements fit the measured ones. The better constrained reservoir properties facilitate a better estimate of seismicity that is still to be expected, as the main outcome of the complete study.

The forecasted depletion on the east side of the aquifer is dominated by the Groningen field (Figure 3-32), although the production from the Roden field likely has caused depletion in this area in the period before 2000 (Figure 3-31 subfigure '86,86,4'). After that the depletion due to production near Harkstede (from EKL-13) dominated the pressure depletion. The aquifer between the small gas field Pasop (just North of Roden) and the Groningen field, also shows considerable depletion, but based on the timing of the drawdown this appears to be caused more by production from the Groningen field, in particular the Eemskanaal cluster, than from Pasop. The other small gas fields appear to have a more local influence.

Reservoir model
During the tuning of the base model, additional faults or baffles were interpreted compared to the faults interpreted during the seismic interpretation. Some of these were small compared to the resolution of the current model, while some were very poorly visible in the seismic data, probably because of small fault offset. This suggests that also in the aquifers, the fault interpretation is not complete.

It should be realised that the focus of this model is the SW aquifer. Even though the small gas fields and the west part of the Groningen model are part of the model area and some effort was made to simulate these parts correctly, the model does not represent this sufficiently well for detailed analysis. In particular, in the Groningen and Bedum gas fields, the pressure predictions from the NAM models are more accurate and better constrained by data.

Although considerable effort was invested in making a reliable estimate of the possible pressure range and constraining the uncertainty, the uncertainty that remains in some areas

is still considerable. Sometimes this is due to model limitations: for example the area near Midlaren is relatively close to the boundary of the model and the surface movement is influenced by the Groningen Main field and the Annerveen gas field (Figure 3-20 and Figure 2-2). This means that only a few surface movement observation points could be included in this area. The impact of the Annerveen field was also not included on the pressure depletion, because the field is separated from the model area by a fault with a very large offset isolating the Annerveen field from the aquifer to the north.

Comparison with NAM results
To guide the history match despite the lack of measurements, NAM assumed that the depletion in SW aquifer should be larger than 90 bar based on the earthquakes in the aquifer at Paddepoel and Eelderwolde (Zeeuw and Geurtsen, 2018b). This is based on the observation in gas fields that the possibility of seismicity is negligible when the pressure drop is less than 28% of the initial pressure (Staatstoezicht op de Mijnen, 2016; Thienen-Visser, 2012) The depletion of the aquifer connected to Roden was expected to be more than 100 bar in the entire aquifer by 2006. In the model developed in this project, depletion in the Roden aquifers in 2006 is estimated around 140 to 160 bar, so in agreement with the assumptions by NAM.
For the Groningen Long term Subsidence Forecast (NAM, 2021), NAM has also matched a simplified aquifer model to surface movement data. For the aquifer connected to the Roden North gas field, they estimated a drawdown of around 120 to 140 bar in 2020, which is slightly lower than the estimates in this project (140 to 160 bar depletion for the best fitting member 96). In the Roden south block, the estimated drawdown is 70 to 80 bar for both models. The aquifer connected to the Pasop field is simulated differently in the two models: the connectivity is higher in the KEM19B model than in the NAM model with a drawdown of ~100 bar compared to ~50 bar in the NAM model in the middle of the aquifer. Overall the results align quite well taking into account the overall uncertainty.

Subsidence modelling
For the surface movement estimates there are still steps for improvement possible. These are related to the shortcomings of the present study and we will list them here.

The main problem with the procedure followed in this study is concerned with the Red Flag method itself. It is known that a particle filter (which is the more common name for our Red Flag method) is prone to ensemble collapse if many data points are available (Van Leeuwen, 2009). The 2829 difference measurements that we have is indeed a large number in that respect and a straightforward application of the method resulted in a single ensemble member with all probability collected in it. This was the case for any single compaction model and set of starting parameters that we employed. We have addressed this point in two ways: by reducing the discriminating power of the method through an inflation of the data variance, and by resampling of the parameter space. Inflation of the data variance is not scientifically underpinned but was only meant to identify more than a single realization as the outcome of the procedure. The obvious alternative of increasing the ensemble size in order to obtain a more dense sampling of the parameter space was not feasible because of the associated requirement of making many reservoir model realizations and the large computation times involved. Resampling after first testing a broad distribution and focusing this to a narrower one, on the other hand, is warranted and was successfully deployed.

An alternative would be to use a different data assimilation method. In other studies we have used the Ensemble Smoother with Multiple Data Assimilation (ES-MDA) (Fokker, Wassing et al, 2016; Fokker, Gunnink et al, 2019). ES-MDA uses a linear superposition of the prior models and model parameters to construct an update. We have fixed reservoir simulations that cannot be changed and of which the parameters have not been schematized in the procedure.

Updating only the compaction and geomechanical parameters would therefore be inappropriate since the surface movement data predictions on which these updates are based are originating from different reservoir realizations. The updated parameter values would be applied to the original reservoir model realizations which have not been assimilated.

A single-step Ensemble Smoother could possibly circumvent this shortcoming of the combination of ES-MDA with our ensemble of reservoir models. The single-step Ensemble Smoother does not require a re-run of the model, and assimilated forecasts could be constructed in the same way as the assimilated parameter values. It is certainly a way forward that deserves to be attempted.

The second fruitful way forward that we envisage makes use of the fact that only a small number of realizations of the reservoir model have survived the Red Flag approach of the current study. Each of these can then be treated separately and subjected to a data assimilation or inversion exercise in order to constrain the best set of parameters for that particular realization, in combination with the compaction model selected. Such an exercise is feasible, with some 40 inversion exercises: 4 compaction models for each of the 10 most probable realizations. Upon completion of those exercises the user can decide which combination of reservoir model with compaction model fits best.

In any case, the way forward will involve considerable expert knowledge and expert judgement. This is the fate of the necessary sequence of models ranging from geological to reservoir to compaction finally to surface movement. For the purpose of using surface movement data in order to improve seismicity estimates, however, we deem the approach that was followed in the present study sufficient.

4 Seismicity analysis and seismic hazard assessment

4.1 Objectives

The objective of this part of the study is to provide a forecast of the induced seismicity rate, and the corresponding seismic hazard assessment for the coming decades in the SW aquifer of Groningen. For this purpose, the TNO Model Chain workflow developed for the Groningen field (TNO, 2020) is applied to the SW aquifer. This application requires the spatial extension of the two main building blocks: (1) the seismic source model (SSM) and (2) the ground motion model (GMM). For the Groningen model chain both components have been designed and calibrated specifically for the Groningen field. An extension to include the SW aquifer at depth, and a larger exposed area at the surface, requires both taking into account new (more) data, as well as a (re)calibration.

In Section 4.2 we describe the theory and methodology used to achieve the model extensions and generate the results. The results are presented in Section 4.3, and discussed in Section 4.4.

4.2 Seismicity analysis and hazard

4.2.1 Seismic hazard analysis

In this section we provide a brief summary of seismic hazard analysis and its relation to the seismic source and ground motion models. For more details the reader is referred to TNO(2020) or general introductions such as Baker et al. (2021).

Let us define the seismicity rate λ as the expected number of earthquakes per unit time, per unit space (area, or volume) and per unit magnitude. The seismicity rate function will, in general, depend on time t, spatial dimensions x, representing the location of the hypocentre, and magnitude m, and hence, can be expressed as a parameterized function accordingly: $\lambda(t, x, m)$. Furthermore let us define the distribution of a certain ground motion attribute, such as peak ground acceleration (PGA) or spectral acceleration (SA), say g, at a surface location y, in terms of its survival function (probability of exceedance) S_G. In general, this distribution will depend on the subsurface conditions at the surface location (e.g. the local shear wave velocity profile) represented by a zone-index ζ, the magnitude of the earthquake, and the distance to the earthquake rupture r. The ground motion distribution can thus be presented as a conditional distribution: $S_G(g|\zeta, r, m)$.

Seismic hazard as a consequence of the seismicity rate distribution introduced above can be defined as the rate of exceedance $R_G(g|y,t)$, obtained by integrating over the rupture distance, space and magnitude dimensions:

$$R_G(g|y,t) = \iiint S_G(g|\zeta(y),r,m) f_R(r|x,y,m) \lambda(t,x,m) dr dm dx.$$

Here, f_R represents the probability density function of the rupture distance. This distribution quantifies the rupture model, which describes the distribution of possible rupture lengths and orientations extending from the hypocentre conditional on the location and magnitude of the earthquake. For more details on the rupture model the reader is referred to TNO (2020). In the current project, the rupture model is adopted identically from the Groningen model chain. To arrive at an annual probability of exceedance $P_G(g|y)$ two more steps are required. First, the rate needs to be integrated over the span of a year, and then, based on the Poisson assumption, the probability $P_G(g|y)$ of at least one exceedance in this period can be defined as the complement of the probability of no exceedance. Under the assumption that all events are independent (Poisson assumption) the waiting time for the next event follows an exponential distribution. This means that the probability that no event occurs within a year is equal to the probability that the waiting time exceeds one year. Hence, we get:

$$P_G(g|y) = 1 - \exp\left(-\int R_G(g|y,t)\, dt\right),$$

where the integration over time relates to the specific time period of one year. Again, for more details, see TNO (2020) or Baker et al. (2021).

In the following sections we describe how we define the seismicity rate distribution $\lambda(t,x,m)$ using the Seismic Source Model (SSM, Section 4.2.2) and the conditional ground motion distribution represented by survival function $S_G(g|\zeta,r,m)$ using the Ground Motion Model (GMM, Section 4.2.3). Results in the form of seismicity and hazard maps will be provided in the Results (Section 4.3).

4.2.2 Seismic source model

The seismic source model is tasked with providing the seismicity rate λ as the expected number of earthquakes per unit time, per unit area and per unit magnitude. The seismicity rate function depends on time t, spatial dimensions x, representing the location of the hypocentre, and magnitude m. The seismic source model used in his study was developed for the Groningen gas field and has been extensively described in previous publications (Bourne and Oates, 2017; TNO, 2020). Here, rather than applying the model to the SW aquifer only, we spatial *extend* the Groningen source model to include the SW aquifer. This way, we get a spatially continuous seismicity model to incorporate in the seismic hazard calculation. This is desirable from a physical perspective, since seismicity within the bounds of the Groningen gas field affect the hazard calculation above the SW aquifer and vice-versa.
The input needed for the source model consists of:

- Reservoir compressibility
- Reservoir pressures through time
- Fault locations and properties, including the fault throw and reservoir thickness at fault

All these inputs are readily available for the area covered by the Groningen gas field. For the SW aquifer, and ensemble of the reservoir compressibility and reservoir pressures has been obtained in this study. This was covered in Chapter 3. Both the reservoir compressibility and reservoir pressures are described as 2D ‘map-view’ grids, without accounting for the depth dimension. This follows the ‘thin-sheet’ geometry assumption that underlies the Groningen source model (Bourne and Oates, 2017).

The structural model used to generate the dynamic model in Chapter 3 contains the fault locations, including the fault throws and reservoir thickness at fault. These were extracted and converted to the same format as the faults in the Groningen reservoir, where faults are represented by their location in map view as a collection of points, with their throw and reservoir thickness as attributes at each point.
With the required inputs available for both the Groningen gas field and the SW aquifer, the next step is to merge them.
For the compressibility and reservoir pressures, there is some overlap between the KEM19b reservoir model and the pressures available for the Groningen gas field. In other words, the original Groningen gas field reservoir model contains a pressure forecast for part of the SW aquifer, and the KEM19b reservoir models contain pressure forecasts for part of the Groningen gas field. For the locations that spatially overlap, we have chosen to populate the combined model according to the following logic: if the location falls within the mapped outline of the Groningen field, the Groningen reservoir model is used, while all locations outside this polygon are populated using the KEM19b model. We believe this choice most closely honors the original purpose of each reservoir model; the Groningen reservoir model was created to model pressures within the gas field, while the KEM19b models were created to model pressures in the aquifer.
Combining the two fault datasets was slightly more involved, due to the nature of fault data. Individual faults are represented as a collection of points. In order to properly incorporate these points in the seismic source model, it is not only important to know which point belongs to each fault, but also the distance to their neighboring point(s) and therefore their 'order' within the fault. A simple way to maintain this structure would be to simply add the two fault databases together. However, this would result in faults that are present in both models to be 'double counted' and since fault density is an important metric for the seismicity model, this is not desirable. We therefore do the following:

1. For each fault in the original Groningen database, we check whether for each of its constituent points whether it falls within the area covered by the KEM19b pressure model. If the fault is fully outside the KEM19b area, we label it *keep*. If it falls fully within the KEM19b area, we label it *dismiss*. If it partially falls within the KEM19b area, we label it for manual checking (Figure 4.1a).
2. Since the faults from the KEM19b fault database only cover the KEM19b area, we can now add the faults from the original Groningen model labelled *keep* and the KEM19b fault database, without any double counted faults (see Figure 4.1b).
3. The faults labelled *check* are inspected individually. For these faults, it is possible that they partially represent a fault that is already included in the KEM19b model, and should therefore be dismissed in the overlapping section. This is done on a fault-by-fault basis (see Figure 4.1c).

The result is a combined fault database that contains all faults that were present in the original Groningen fault model and the KEM19b fault model, but without any 'double' counting of faults or parts of faults.

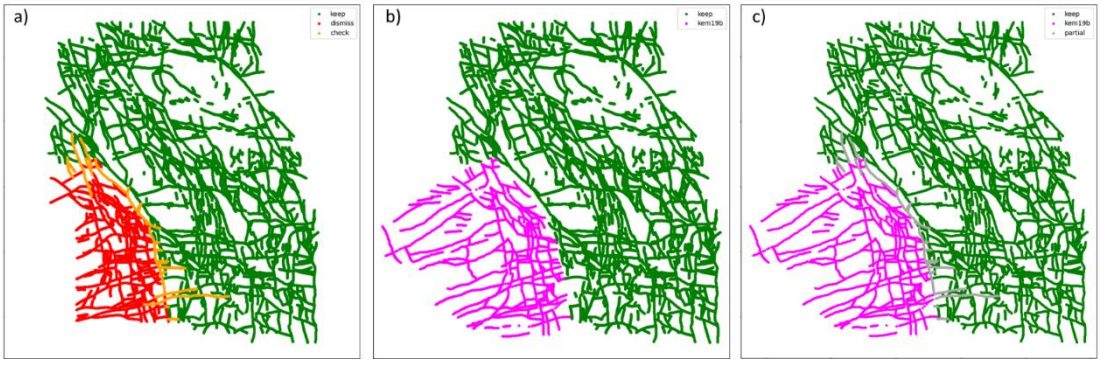

Figure 4-1: Three stages of merging the original Groningen and KEM19b fault databases. Subfigure (a) shows the curation of the original dataset, subfigure (b) the combination of the mutually exclusive sets, and (c) the inclusion of curated faults at the boundary

As described in Section 3.5.1, 22 reservoir models were selected to represent the uncertainty in pressure evolution of the SW aquifer. Each pressure realization comes with its corresponding compressibility realization which need to be multiplied with a factor between 0.5 and 0.6 to obtain the final compressibility map. To represent a low, medium, and high compressibility scenario, we here choose 0.51, 0.55, and 0.59. This means that a total of 66 sub-surface realizations are used for calibration and forecast.
To calibrate the seismic source model, a Bayesian framework is applied (TNO, 2020). The data used to infer the posterior distribution of model parameters consists of all 371 recorded earthquakes of M1.5 and above in the period 1995-01-01 until 2024-04-30 (KNMI, 2024). Of these, 12 events fall within the SW aquifer, while the remaining 359 fall within the Groningen field outline.
The calibration is performed for each reservoir compaction realization (see Chapter 3) independently. For each realization, a well-defined posterior distribution is obtained. Although not identical, the posterior parameter distribution are very similar between the 66 realizations. It's also interesting to note that the posterior parameter distributions that are obtained are fairly similar to the one obtained on the 'base' reservoir model. This means that adding the SW aquifer to the model does not significantly change our understanding of the physical parameters of the seismicity-controlling processes, and conversely, that our understanding of the seismicity based on the Groningen reservoir does a reasonable job of explaining the observed seismicity in the SW aquifer.

4.2.3 Ground motion model

For the ground motion model of KEM19b we adopt the general approach of the GMM-V7 ground motion model for the Groningen field as developed by Bommer et al. (2021). GMM-V7 is a probabilistic model in the sense that it provides probability distributions of ground motion attributes conditional on the three predictor variables, introduced in Section 4.2.1, being the magnitude m, the distance to the rupture plane r and zone-index or -identifier ζ. The latter represents the variety of physical properties associated with a specific geological zone in which the surface point where the ground motion is realized is located. The ground motions attributes of interest are the spectral accelerations, which encode the hypothetical response of idealized buildings with a set of specific resonance periods. In risk assessment practice, the spectral response of actual buildings can be predicted in terms of these idealized spectral accelerations. These assessments, however, are not part of the current work.

The ground motion model (Bommer et al., 2021) consists of two main components:

1. A *reference ground motion* model that expresses the distribution of spectral accelerations at a reference level at approximately 800 m depth below the surface, i.e., the bottom of the North-Sea lithostratigraphic unit. This part of the model is ergodic, in the sense that all lateral and directional variations in ground motions due to heterogeneities in the subsurface properties and rupture processes are summarized in a predictive model conditioned only on earthquake magnitude and rupture distance.
2. A *site response* model that expresses the amplification and/or damping of ground motions propagating upwards from the reference level to the surface. This model is only partially ergodic, in the sense that it does takes into account spatial variations of the physical properties of the local soils by using a regional zonation. For GMM-V7 a total of 160 zones are defined on the basis of geological characterization. See Kruiver et al. (2017a) for het methodology applied for an earlier version of the model.

For the KEM19B project we have made the decision to adopt the first component, the ergodic reference ground motion model, identically from the Groningen GMM-V7. This is warranted because of the proximity of the SW aquifer to the Groningen field and the reality that there is no additional information available to constrain the model beyond that what was used for GMM-V7.
For the second component, the site response model, however, additional information is required since its geographic domain of application explicitly extends beyond the contours considered in GMM-V7.
Figure 4.2 shows the geographic domain of the aquifer in relation to the domain of the Groningen model chain and the GMM-V7 model.

The extension of the site response model involves the following 4-step work plan:
1. Interpretation and characterization of geological features of the shallow subsurface and construction of regional zonation (Kruiver et al., 2017a),
2. Generation of (stochastic) ensembles of representative shear-wave velocity profiles for every zone (Kruiver et al., 2017b),
3. Numerical analysis of wave amplification for all generated shear-wave velocity profiles using a stochastic sample of representative input motions (Kruiver et al., 2017b, Rodriguez-Marek et al., 2017),
4. Calibration of the non-linear amplification model (Rodriquez-Marek et al., 2017, Bommer et al., 2021).

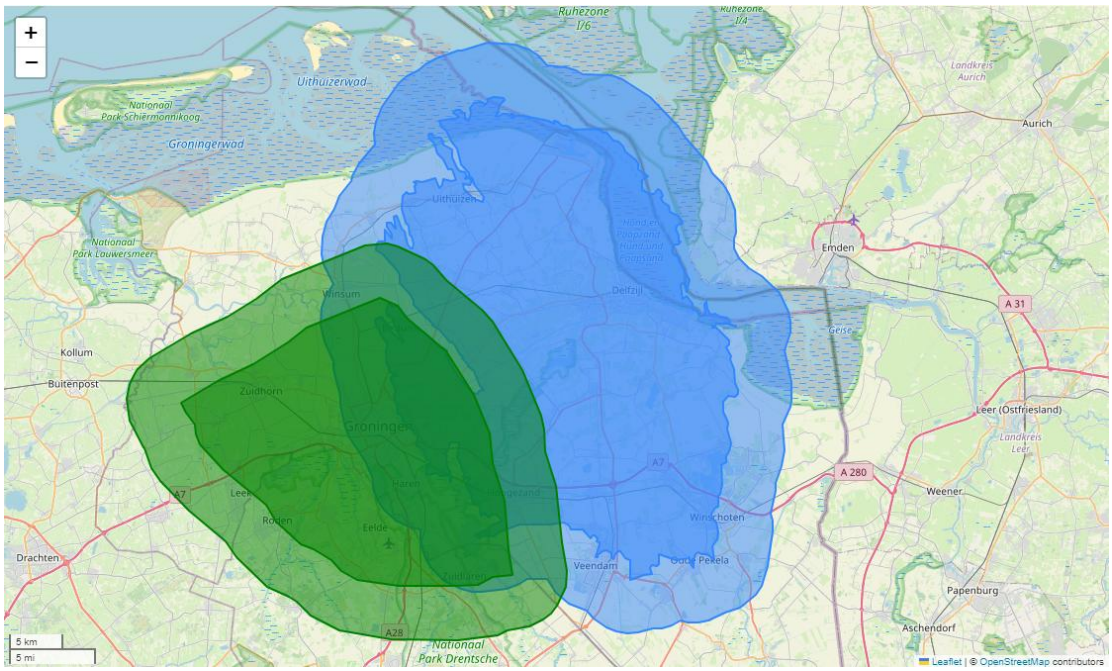

Figure 4-2: Geographic regions involved in the seismic hazard assessment for the Groningen field (blue) and the KEM19-B SW aquifer (green). The darker patches represents the subsurface domains. The lighter areas represent a five km buffer that demarcates the spatial extent of the site response model.

Step 1 above was already completed by the earlier work in the context of the Groningen GMM project. Figure 4.3 shows both the geological zonation obtained for the work described in Kruiver et al. (2017a) and the KEM-19B project area. It shows that a small fraction of the site response region has not yet been covered by a geological zone. We have decided to designate this region a separate zone. A complete KEM-19B zonation has been constructed by first determining the geometric intersection of the geological zonation and the KEM-19B site response area, and second determining the geometric complement with the existing GMM-V7 zonation. The final zonation is displayed in Figure 4.4. It contains 81 new zones in addition to the 160 zones adopted from GMM-V7.

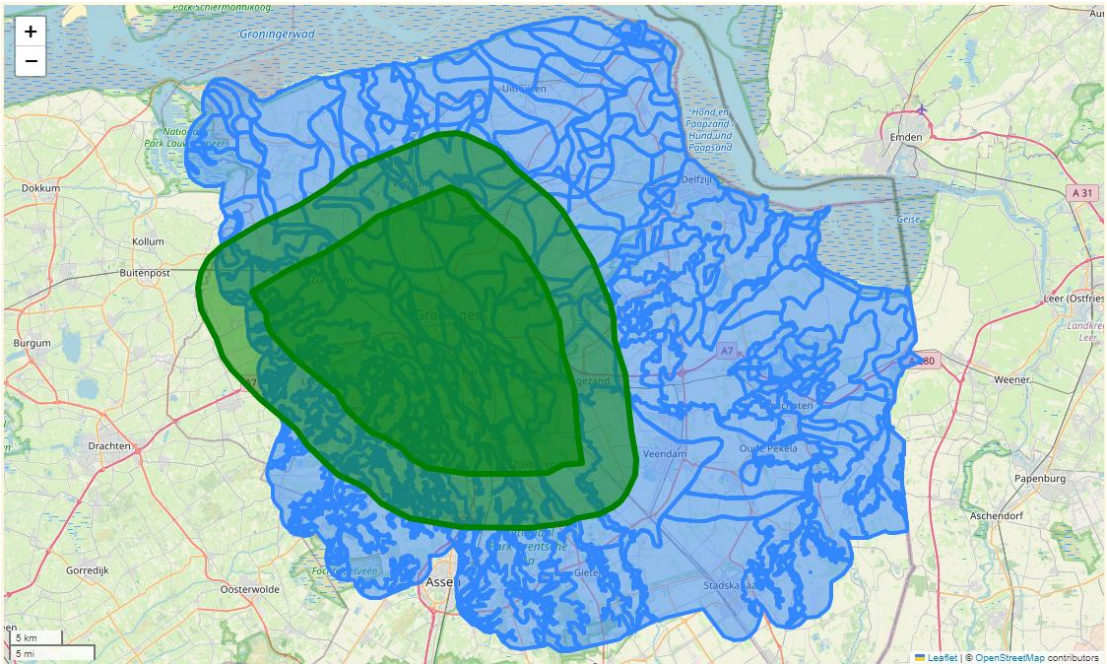

Figure 4-3: Kem 19-B geographic region against in the background the geological zonation obtained for the Groningen GMM project (Kruiver et al., 2017a).

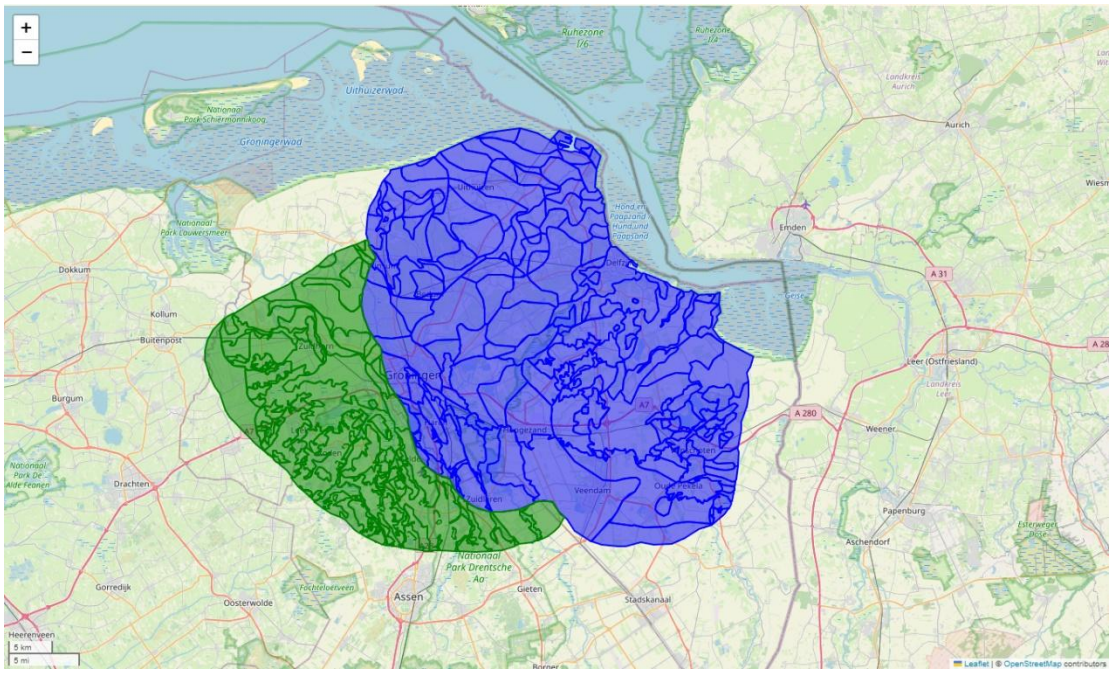

Figure 4-4 Site response zonation of GMM-V7 in blue, and the extension provided by the KEM-19B project in green.

Steps 2 and 3 of the work plan have been executed by Deltares and reported in Appendix E They have largely followed the work flow that they used in their contribution to GMM-V7 (Bommer et al., 2021). As an output of their work they have delivered stochastic sets of synthetic amplification data organised per KEM-19B site response zone.

Step 4 of the work plan involves the calibration of a predictive amplification model using the data obtained in Step 3. During the execution of this step it became clear that it within the

current project we are not able to completely reproduce the workflow of GMM-V7, as described in Bommer et al. 2021 (Chapter 8) for two reasons. First, the description of the workflow in Bommer et al., is insufficient to fully reproduce it as it depends on undocumented algorithmic choices. Second, it turns out that calibration has been by using a combination of both linear and equivalent-linear simulations, where the linear simulations are used to calibrate the linear part of the model and the equivalent-linear simulations for the non-linear. However, for the KEM-19b project only the equivalent-linear simulations have been performed. In principles it is possible to perform an independent calibration, but that will produce inconsistencies between the GMM-V7 and the KEM-19b parts of the ground motion model. Since the main focus of the project is to study effects of changes in the source distribution, a conflation with changes in the ground motion model appears undesired.

Instead of an independent calibration, we have chosen to infer the site amplification model for each KEM-19b zone by selecting the best fitting (maximum likelihood) model out of the 160 GMM-V7 models. This appears a reasonable compromise between adaptation and consistency. An example of the inferred models is shown in Figure 4.5. The fact that the new zone functions are fairly distributed among the original GMM-V7 options provides confidence that the original distribution is sufficiently wide. In addition an example map view of the linear amplification is provided in Figure 4.6.

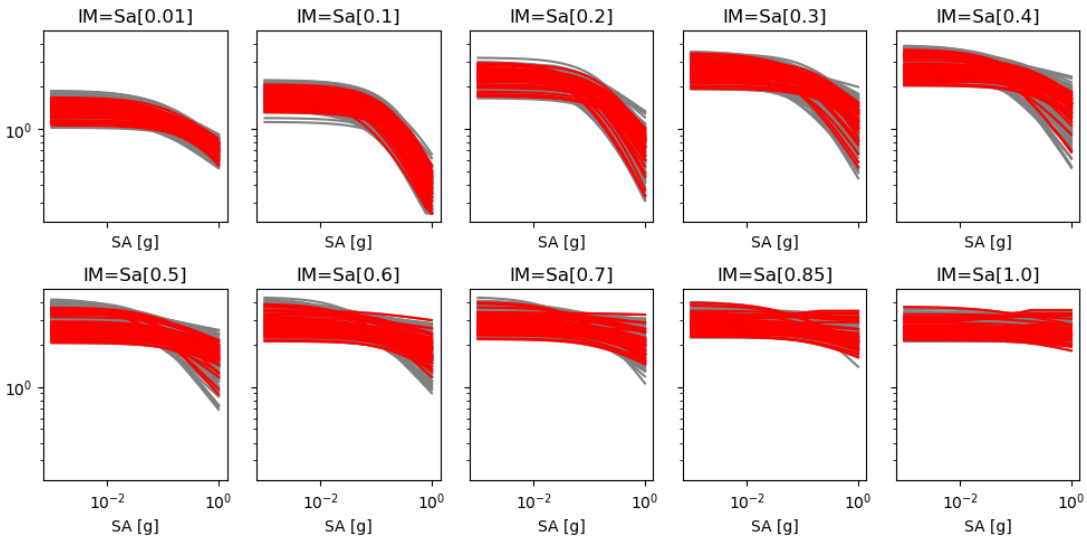

Figure 4-5 Median site amplification as a function of reference spectral acceleration per spectral component for all zones. The grey curves represent the 160 zones of the GMM-V&, while the red curves represent the 81 new zones for KEM-19B. The curves are produces for an earthquake of magnitude 4.5 at distance of 15 km, to be able to compare to Figure 8.8 in Bommer et al. (2021).

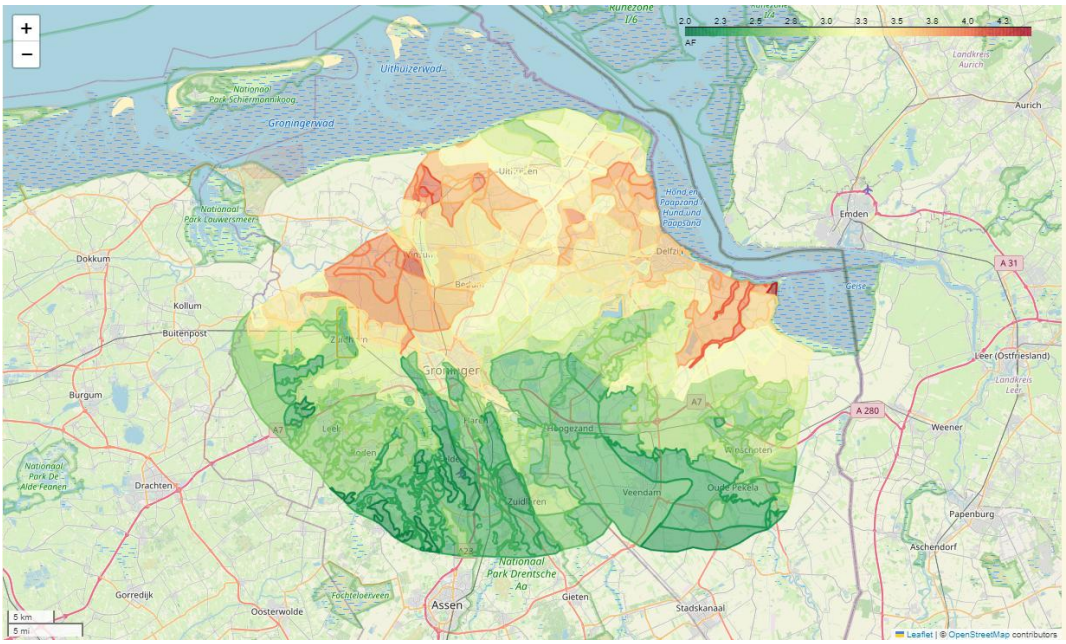

Figure 4-6: Linear amplification response per zone for spectral acceleration at a period of 0.6s (Sa[0.6]), for an earthquake of magnitude 4.5 at 5 km distance.

4.3 Results

The calibrated source models (all 66 realizations) can be used to forecast seismicity into the future, based on the spatio-temporal pressure forecast of each model (see Section 4.2.2 for details). Although there is quite a range of pressure scenarios contained in the ensemble, the ensemble of seismicity forecasts is significantly less wide. In fact, both the spatial and temporal signature of the 66 seismicity forecasts look remarkably similar, not just to each other, but also to the seismicity forecasts generated in the past for the Groningen gas field (TNO, 2023b). It is difficult to strictly speak of 'seismicity in the SW-aquifer' versus 'seismicity in the Groningen field. This is for two reasons. First, the pressures in the SW-aquifer and the Groningen field influence each other, and consequently the resulting vertical strains and seismicity are interconnected as well. Second, the spatial smoothing that is an inherent part of the seismic source model further blurs the clear distinction between the two areas. It is therefore more sensible to view the models as a whole: the Groningen gas field models (TNO, 2023b) on one hand, and the models of the Groningen gas field plus the SW-aquifer on the other hand (this work).

In the calibration period (1995-01-01 until 2024-04-30) a total of 371 M1.5+ events occurred in the area covered by the Groningen gasfield and the SW aquifer (black lines in Figure 4.7). Of these, 12 happened in the SW aquifer, outside the boundaries of the Groningen gas field. The calibrated models hindcast a total of ~5.1 events in this area. It is important to realize that the calibration attempts to find the best fitting model in space and time. Any sub-section of the model, whether in space or time or both, is likely to either overpredict or underpredict compared to the data. However, since this study specifically focusses on the SW aquifer, we believe it's important to further explore the nature of the mismatch between model and data. Of the 12 events observed in the SW aquifer, 6 appear to be directly related to the gas fields of Roden and Vries (see Table 11). Although these gas fields are included in the KEM19b pressure model, our model was aimed at representing the aquifer and the uncertainty in the pressure distribution within the aquifer, rather than the gas fields that are connected to the aquifer. It may therefore be reasonable to expect that our model does not capture these seismic events well. The remaining 6 events do occur within the 'true' aquifer portion of the model. This number compares well to the ~5.1 events hindcasted by our calibrated model.

Table 5: Events in the SW aquifer during the calibration period.

Date	Latitude	Longitude	Magnitude	Description
1996-09-02	53.147	6.422	2.1	Roden (Roden gas field)
1996-12-28	53.107	6.505	1.9	Bunne (Vries gas field)
1996-12-28	53.111	6.502	1.8	Bunne (Vries gas field)
2006-09-06	53.189	6.522	1.8	Aquifer
2009-01-01	53.095	6.718	1.5	Aquifer
2011-06-05	53.176	6.612	1.5	Aquifer
2012-08-09	53.183	6.613	1.5	Aquifer
2013-07-08	53.305	6.542	1.6	Aquifer
2017-03-06	53.327	6.571	1.6	Aquifer
2020-09-27	53.122	6.496	1.8	Winde (Vries gas field)
2023-08-22	53.117	6.495	1.6	Winde (Vries gas field)
2023-08-23	53.117	6.496	1.7	Winde (Vries gas field)

Here, we show the ensemble mean forecast (equal weight applied to all ensemble members, Figure 4.7). Although the SW aquifer is included in the model, it is barely visible due to the small amount of seismicity forecasted. The main reason for the lack of forecasted seismicity in the SW aquifer is the relatively limited pressure decline (and associated vertical strain) in this region. In the seismic source model, there is a linear relation between vertical strain and incremental Coulomb stress. The relation between incremental Coulomb stress and seismicity rate is exponential. This means that the amount of seismicity resulting from a given amount of pressure decline depends heavily on the local reservoir pressure: the lower the pressure, the more seismicity results from a given amount of pressure decline. The slow and limited pressure decline in large parts of the SW aquifer (slow and limited compared to the Groningen gas field) means that the seismicity rate in this region is expected to remain low in the future: in the 30 years that the forecast covers (GY 2024/2025 until GY 2053/2054) the number of expected events of M1.5 and above within the entire region (gas field + SW aquifer) is 43.04 (ensemble standard deviation: 0.55). In the same time period, the total number of expected events of M1.5 and above within the SW aquifer is 2.24 (ensemble standard deviation: 0.17).

Table 6: Forecasted event rates in the entire model, and the SW aquifer area specifically.

Gas year	Total event rate (M1.5+)	SW aquifer event rate (M1.5+)
2024/2025	4.25	0.12
2025/2026	3.70	0.11
2027/2028	3.24	0.11
2028/2029	2.87	0.10
2029/2030	2.54	0.10
2030/2031	2.26	0.09
2031/2032	2.03	0.09
2032/2033	1.82	0.08
2033/2034	1.65	0.08
2034/2035	1.52	0.08
2035/2036	1.40	0.07
2036/2037	1.31	0.07
2037/2038	1.22	0.07
2038/2039	1.14	0.07
2039/2040	1.07	0.07
2040/2041	1.01	0.07
2041/2042	0.95	0.07
2042/2043	0.90	0.07
2043/2044	0.82	0.06
2044/2045	0.82	0.06
2045/2046	0.78	0.06
2046/2047	0.74	0.06
2047/2048	0.71	0.06
2048/2049	0.68	0.06
2049/2050	0.65	0.06
2050/2051	0.63	0.06
2051/2052	0.59	0.06
2052/2053	0.57	0.06
2053/2054	0.55	0.05

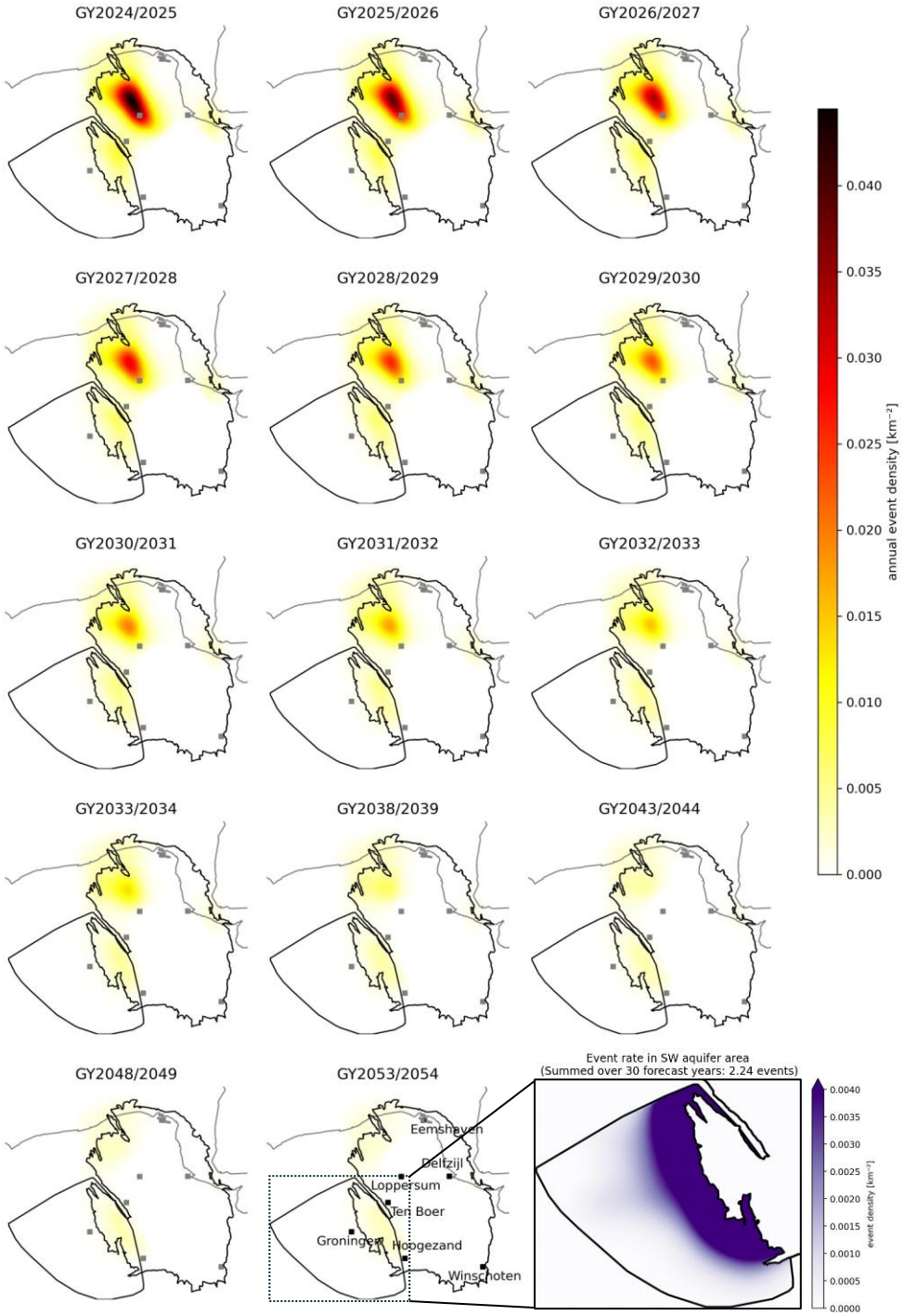

Figure 4-7 Ensemble mean seismicity forecast for the Groningen gas field and the SW aquifer combined. The forecasted seismicity in the SW aquifer is low for all forecasted years and the individual ensemble member forecasts all look very similar to the ensemble mean. The extent of the Groningen field outline and the SW aquifer model is shown in black solid lines. In the bottom-right, we show a zoom-in on the SW aquifer, with a different color scale. This sub-figure shows the total event density over 30 years, indicating that the event rate is highest close to the Groningen gas field. It is important to note that compared to the Groningen gas field, the event rate in the SW aquifer is much lower, as can be seen in the annual figures with the yellow-red color scale.

With the extended ground motion model (including the site-response model) available, the seismic hazard (annual probability of exceedance of spectral accelerations per selected surface point) can be calculated. This is the seismic hazard related to the ongoing pressure development in the aquifer under study, as well as in the Groningen gas field. Conversely, the extended seismic source model also influences the seismic hazard that is calculated for the original area under consideration of the Groningen pSHRA. However, due to the low seismicity rates forecasted in the SW aquifer, the impact of the extended source model is limited, both in the area covered by the original GMM-V7 model and in the area added in this study. In Figure 4.8, we show a comparison between the hazard calculated using the base reservoir model as described in Chapter 2, and the hazard calculated using the spatial extension of the reservoir model including the SW aquifer. Both hazard calculations use the same source model and ground motion model (besides the spatial extension). This comparison conveys that the spatial extension of the source model to include the SW aquifer does not increase the hazard compared to before in the area that was previously already included in the hazard calculation. In fact, in the area west of the city of Groningen, the hazard actually decreases. This is a direct result of the updated source model forecasting less events in this region, which in turn stems from the model being calibrated on a different spatial region (now including the SW aquifer). Although the updated spatial distribution appears to better match the observed events, this is in some way a 'lucky' outcome since no explicit effort was made to improve the spatial match; the underlying source model is unchanged in terms of its representation of physics.
The hazard in the newly considered area above the SW aquifer is very much in line with what could be expected based on simple extrapolation of the pSDRA 2023 results. In Figure 4.9, we include an overview of the hazard maps (PGA, 475 year return period) for up to gas year 2053/2054. The individual hazard maps are included in Appendix D.

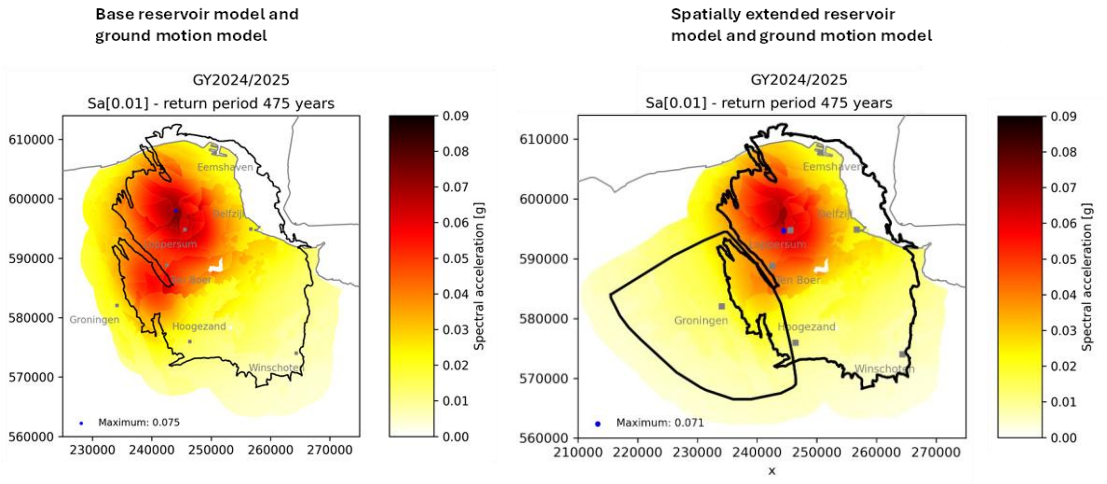

Figure 4-8 Hazard maps for PGA at 475 years from the pSDRA 2023 (TNO, 2023b) and the current study (KEM19b).

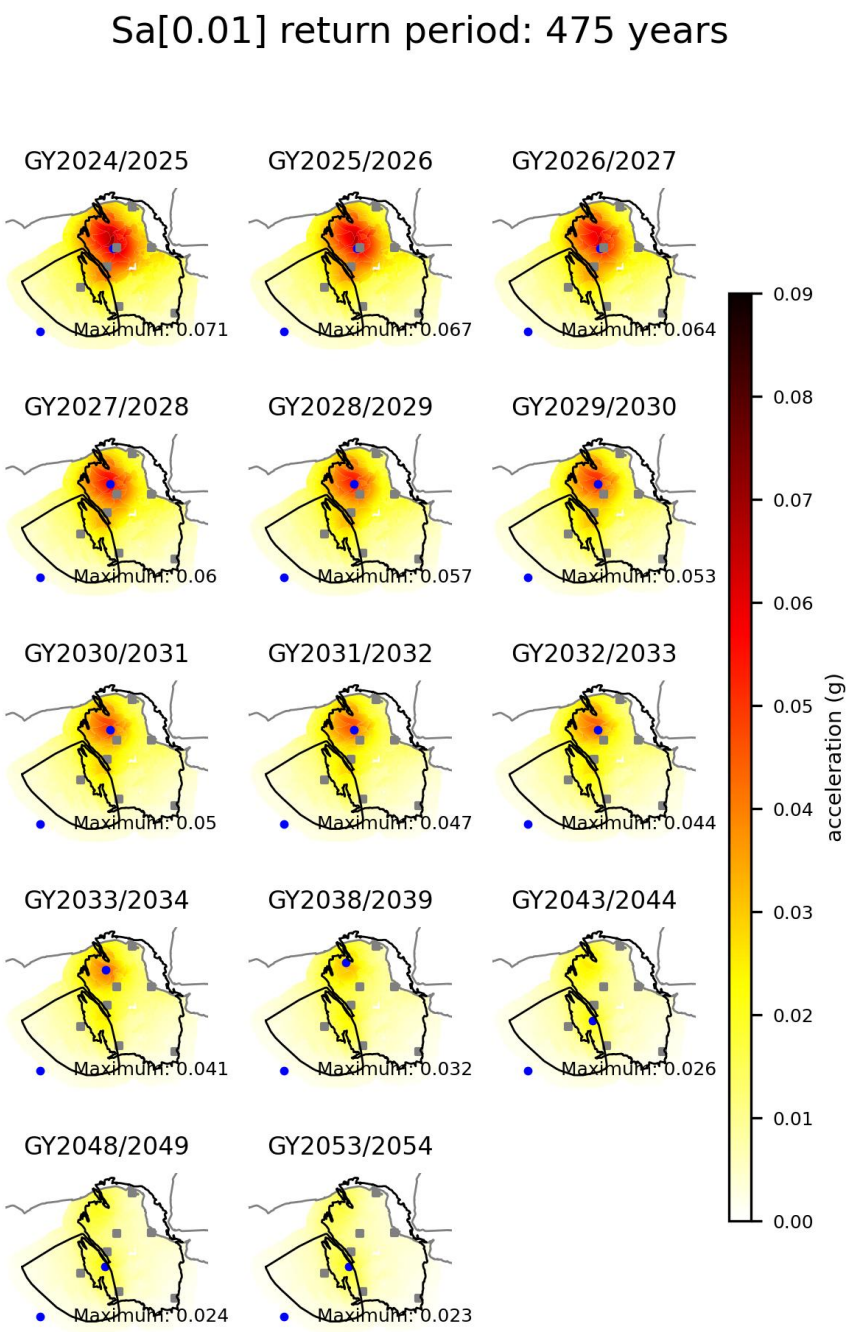

Figure 4-9: Hazard maps for PGA at 475 years for the coming gas years.

4.4 Discussion and conclusions

The work presented in this chapter shows we have been able to successfully extend both the Ground Motion Model and the Seismic Source Model for the Groningen area to include the SW aquifer. Even though this project focusses on the seismicity and seismic hazard resulting from pressure changes in the SW aquifer, an important feature of our modelling throughout is the consistency in approach and models between the original Groningen seismicity & seismic hazard assessment, and those for the SW aquifer. Adding the site response model and extending the subsurface models required some implementation choices to be made. However, we do not expect these choices to significantly impact the results of either the seismicity forecast or the seismic hazard calculations. Using the results from Chapter 3, we incorporate the significant uncertainty in both the past and future pressure evolution of the SW aquifer through an ensemble of pressure models. For each ensemble member, we successfully calibrated the seismic source model for the combined SW aquifer and the Groningen gas field, with a posterior parameter distribution that is similar to that obtained for the Groningen field alone. This means that the model parameters that get significant weight in forecasting the seismicity for the Groningen gas field also get significant weight in the combined model, indicating that the model captures the relevant physics. Despite the considerable uncertainty related to the pressures, once calibrated, the seismicity forecasts of the individual pressure model ensemble members all show very limited seismicity in the SW aquifer when compared to the expected ongoing seismicity in the Groningen field. This relatively small uncertainty surrounding the number of induced events in the SW aquifer stems from the subsidence inversion, which allows us to forecast the expected vertical strain (the product of pressure depletion and compaction coefficient, which in the end drives seismicity in the model) with much more certainty than the pressure depletion itself. This is an important result, as it indicates that the uncertainty in the pressure forecasts does not translate to uncertainty around seismicity. Finally, due to the low level of forecasted seismicity in the SW aquifer, there is a very limited impact of this newly modelled seismicity on the seismic hazard above the SW aquifer. In fact, the hazard in the 81 zones that were added to the site response model in this study is equal or lower than the hazard on the former western edge of the site response model. That means that this study did not identify a 'previously missed' zone of increased seismic hazard due to seismicity in the SW aquifer, but rather that we've identified that the seismic hazard continues to decrease with increasing distance from the Groningen gas field and that the seismicity of the SW aquifer itself is very limited and does not significantly change this general picture.

5 Conclusions and recommendations

This study addressed the following research questions:

1. What will be the pressure depletion of the southwestern aquifer taking into account the depletion of Groningen gas field as well as the smaller gas fields in the Lauwerszee Trough?
2. What are the locations of smaller faults, and their orientation and throw in the southwestern aquifer?
3. What is the expected induced seismicity in the coming decades?
   a. What is the seismic hazard?
   b. How does this compare to the seismic hazard of the Groningen gas field?

These can be answered as follows:

1. The current study has resulted in the forecast of pressure depletion for an ensemble of 22 out of 100 flow models in the SW aquifer of Groningen gas field in the southern Lauwerszee Trough. The model ensemble was ranked based on static pressure measurements in the small gas fields and observations of subsidence above the aquifer. The surface movement measurements have helped making this ranking by discriminating the models according to how the calculated surface movements fit the measured ones. The forecast of the depletion on the east side of the aquifer is dominated by the Groningen field, although the production from the Roden field likely has caused depletion in this area in the period before 2000. After that the depletion due to production near Harkstede (from EKL-13) dominated the pressure depletion. The aquifer between the small gas field Pasop (just North of Roden) and the Groningen field, also shows considerable depletion, but based on the timing of the drawdown this appears to be caused more by production from the Groningen field, in particular the Eemskanaal cluster, than from Pasop. The other small gas fields appear to have a more local influence.

2. The smaller faults in the aquifer, which were interpreted in this project, are mainly short faults with east-west orientation and a small throw of less than 40 m. In general, the large faults (both in length and offset) are oriented west-south-west to east-north-east. Near the Harkstede area (the transition of the Groningen field to the aquifer) has several north-south faults with large off-set.

3. The expected induced seismicity in the SW aquifer, taking into account the considerable uncertainty in the pressure depletion, is low (see Figure 4.7). We obtain a total of 2.24±0.17 expected events of M1.5 and above within the south west aquifer in the 30 years that the forecast covers (GY2024/2025 until GY 2053/2054). For context, the number of expected events of M1.5 and above for that same time period within the entire region is 43.04±0.55.
   a. The seismic hazard in the 81 added site-response regions above is relatively low, with a PGA value of 0.02g or below (see Figure 4.9).

b. These hazard levels are comparable to those in the southeast region of the Groningen earthquake area, or around Hoogezand (see Figure 4.9).

Recommendations

The forecasted seismicity in the SW aquifer and associated seismic hazard at the surface is relatively low, despite the relatively large uncertainty range in the underlying pressure forecasts. Therefore, in the context of this study (seismicity related to pressure changes in the SW aquifer due to its connection to the Groningen gas field), no major effort is currently recommended to further reduce uncertainty. It is recommended to keep monitoring the subsidence above the aquifer, in particular near just west of Harkstede and Ten Boer, to check that the subsidence remains within the ranges forecasted by the ensemble of models.

In case of future activities in the aquifer, however, more detailed analysis might be required. In that case, the workflow could be improved in several ways:

- The largest added value is in particular a joint history match of the reservoir and subsidence model based on pressure and subsidence measurements.
- If a joint history match is not feasible, several improvements to the two step approach are also possible. These are discussed in paragraph 0.
- Future human activities in the aquifer will likely impact the pressure and temperature fields in the aquifer. Assessing the magnitude and spatial footprint of the changes in these fields will be a crucial part of updating the seismicity model and consequently of updating the seismic hazard assessment.
- The current seismic source model uses for both the Groningen gas field and the SW aquifer (in this study), assumes a so called ‘thin-sheet’ geometry, which is based on the large horizontal extent of the reservoir compared to its thickness, and the relatively smooth spatial changes (small spatial gradients) of pressure and temperature. If future operations lead to violation of these assumptions, for example by introducing relatively large temperature gradients, the source model may need to be updated to account for these changes.

In addition to improvements to the workflow, the low availability of pressure data in the aquifer remains a point of attention, especially in the context of potential future activities in the aquifer.

6 References

Amthor, J.E., Okkerman, J., 1998. Influence of Early diagenesis on reservoir quality of Rotliegende Sandstones, Northern Netherlands. AAPG Bulletin, V2, No.12, p. 2246-2265.

Baker, J., Bradley, B., & Stafford, P. (2021). Seismic Hazard and Risk Analysis. Cambridge: Cambridge University Press.

Bjørlykke, K., Aagaard, P., Egeberg, P.K., Simmons, S.P. 1995. Geochemical constraints from formation water analyses from the North Sea and the Gulf Coast Basins on quartz, feldspar and illite precipitation in reservoir rocks. In: J. Cubitt M., W. England A. (Eds.), The geochemistry of reservoirs, 86, Geological Society, London, pp. 33-50

Bommer, J.J., B. Edwards, P.P. Kruiver, A. Rodriguez-Marek, P.J. Stafford, B. Dost, M. Ntinalexis, E. Ruigrok and J. Spetzler, (2019). V6 Ground-Motion Model (GMM) for Induced Seismicity in the Groningen Field.

Bommer, J.J., B. Edwards, P.P. Kruiver, A. Rodriguez-Marek, P.J. Stafford, M. Ntinalexis, E.Ruigrok and B. Dost (2021). V7 Ground-Motion Model for Induced Seismicity in the Groningen Gas Field. Revision 1, 29 September 2021, 273 pp

Bourne, S. J., Oates, S. J. 2017. Extreme threshold failures within a heterogeneous elastic thin sheet and the spatial-temporal development of induced seismicity within the Groningen gas field. *Journal of Geophysical Research: Solid Earth*, 122, 10,299–10,320

Bouroullec, R., Verreussel, R.M.C.H., Geel, C.R., De Bruin, G., Zijp, M.H.A.A., Körösi, D., Munsterman, D.K., Jansse, N.M.M., Kerstholt-Boegehold, S.J., 2018. Tectonostratigraphy of a rift basin affected by salt tectonics: synrift Middle Jurassic–Lower Cretaceous Dutch Central Graben, Terschelling Basin and neighbouring platforms, Dutch offshore. Geological Society, London, Special Publications, 469. In: Kilhams, B., Kukla, P. A., Mazur, S., McKie, T., Mijnlieff, H. F. & Van Ojik, K. (eds) Mesozoic Resource Potential in the Southern Permian Basin. https://doi.org/10.1144/SP469.22

Burkitov, U., H. van Oeveren and P. Valvatne, 2016. Groningen Field Review 2015. Subsurface Dynamic Modelling Report. https://www.nam.nl/feiten-en-cijfers.html.

Candela, T.G.G., Chitu, A.G., Peters, E., Pluymaekers, M.P.D., Hegen, D., Koster, K. and Fokker, P.A., 2022. Subsidence induced by gas extraction: A data assimilation framework to constrain the driving rock compaction process at depth. *Frontiers in Earth Science,* **10**, pp. 1-18.

Carr, N.L., Kobayashi, R., and Burrows, D.B.: 'Viscosity of Hydrocarbon Gases Under Pressure,' Trans. AIME (1954) 201, 264-272

De Jager, J., Visser, C., 2017. Geology of the Groningen field – an overview. Netherlands Journal of Geosciences – Geologie en Mijnbouw. 96-5, s3-s15. Doi: 10.1017/njg.2017.22

DGM-deep V5 on- and offshore | NLOG

Dranchuk and Abou-Kassem: 'Calculation of z-Factors for Natural Gases Using Equations of State,' JCPT (July-Sept. 1975) 34-36.

Fokker, P.A., Gunnink, J.L., Koster, K. and De Lange, G., 2019. Disentangling and Parameterizing Shallow Sources of Subsidence: Application to a Reclaimed Coastal Area, Flevoland, the Netherlands. *Journal of Geophysical Research: Earth Surface,* **124**(5), pp. 1099-1117.

Fokker, P.A., Wassing, B.B.T., Van Leijen, F.J. and Hanssen, R.F., 2016. Application of an ensemble smoother with multiple data assimilation to the Bergermeer gas field, using PS-InSAR. *Geomechanics for Energy and the Environment,* **5**, pp. 16-28.

Fryberger, S., Knight,R., Hern, C., Moscariello, A. & Kabel, S., 2011. Rotliegend facies, sedimentary provinces and stratigraphy, Southern Permian Basin UK and the Netherlands: A review with new observations. In Grotsch, J. & Gaupp, R., (eds). The Permian Rotliegend Of The Netherlands. SEPM Special Publication 98, pp. 51-88.

Gast, R.E., Dusar, M., Breitkreuz, C., Gaupp, R., Schneider, J.W., Stemmerik, L., Geluk, M.C., Geißler, M., Kiersnowski, H., Glennie, K.W., Kabel, S. & Jones, N.S., 2010. Rotliegend. In: Doornenbal, J.C. and Stevenson, A.G. (editors): Petroleum Geological Atlas of the Southern Permian Basin Area. EAGE Publications b.v. (Houten): 101-121.

Gaupp, R., Okkerman, J.A., 2011. Diagenesis and reservoir quality of Rotliegend sandstones in the Northern Netherlands – A Review. SEPM Special Publications 98:193-226, in the book: The Permian Rotliegend of The Netherlands.

Geluk, M.C., 2007. Permian. In: Wong, Th. E., Batjes, D.A.J. & de Jager, J., (eds). Geology of the Netherlands. Royal Netherlands Academy of Arts and Sciences: 63–83.

Geurtsen, L., A.J. Landman, G. Ketelaar, 2020. Groningen abandonment – Surveillance requirements. Nederlandse Aardolie Maatschappij B.V. EP number: EP202006201318.

Glennie, K.W., 1972. Permian Rotliegendes of Northwest Europe interpreted in light of modern desert sedimentation studies. American Association of Petroleum Geologists Bulletin. 56: 1048–1071.

Hernandez, E.O., 2023. Memo: KEM 19-B: Extended site response analysis to the south-west aquifer of the Groningen gas field. Deltares, 11209407-000-BGS-0001

Howell, J. And Mountney, N., 1997, Climatic cyclicity and accommodation space in arid to semi-arid depositional systems: an example from the Rotliegend Group of the UK southern North Lea, in Ziegler, K., Turner, P., and Daines, S.R., eds., Petroleum Geology of the Southern North Sea: Future Potential: Geological Society of London, Special Publication 123, p. 31–61.

Kestin, Khalifa, & Correia, 'Effect of Pressure on the Viscosity of Aqueous NaCl Solutions in the Temperature Range 20-150degC,' J. Chem. Phys. Ref. Data, Vol 10, No. 1, 1981, p 71.

KNMI 2024, https://rdsa.knmi.nl/abcws/event/query?eventtype=induced&format=csv. Last accessed 2024-12-20.

Kombrink, H., Van Lochem, H., Van der Zwan, K.J., 2010. Seismic interpretation of Dinantian carbonate platforms in het Netherlands; implications for the palaeogeographical and structural development of the Northwest European Carboniferous Basin. Journal of the Geological Society 167: 99-108.

Kortekaas, M., R. Bouroullec, S. Peeters, M. van Unen, M. Swart, D. den Hartog Jager, E. Wiarda, M. Nolten, and K. Beintema. 2023. Play 7 Rotliegend. https://www.geodeatlas.nl/pages/play-7-rotliegend

Kruiver, P.P., van Dedem, E., Romijn, R., de Lange, G., Korff, M., Stafleu, J., Gunnink, J.L., Rodriguez-Marek, A., Bommer, J.J., van Elk, J. &Doornhof, D., 2017b. An integrated shear-wave velocity model for the Groningen gas field, The Netherlands. Bulletin of Earthquake Engineering 15 (9): 3555–3580

Kruiver, P.P., Wiersema, A., Kloosteman, F.H., de Lange, G., Korff, M., Stafleu, J., Buscher, F., Harting, R. & Gunnink, J.L., 2017a. Characterisation of the Groningen subsurface for hazard and risk modelling. Netherlands Journal of Geosciences / Geologie en Mijnbouw.

Landman, A J., 2023. Groningen Dynamic Model Update 2023. NAM. Includes: Landman, A.J. and C. Visser, 2023. Groningen Dynamic Model Update V7. NAM B.V. EP202306200914

Molen, J. van der, E. Peters, F. Jedari-Eyvazi and S.F. van Gessel, 2020. Dual hydrocarbon–geothermal energy exploitation: potential synergy between the production of natural gas and warm water from the subsurface. *Netherlands Journal of Geosciences*, Volume 98, e12. https://doi.org/10.1017/njg.2019.11

Mossop, A., 2012. An Explanation for Anomalous Time Dependent Subsidence, *46th US Rock Mechanics / Geomechanics Symposium*, June 24-27, 2012 2012, pp. 1-8

NAM, 2021. Groningen long term subsidence forecast. NAM-report EP202008201822, version 2.

Nepveu, M., Kroon, I.C. and Fokker, P.A., 2010. Hoisting a Red Flag: An Early Warning System for Exceeding Subsidence Limits. *Mathematical Geosciences,* **42**(2), pp. 187-198.

Opstal, G. H. C. Van, 1974. The effect of base-rock rigidity on subsidence due to reservoir compaction, *Proceeding 3 of the International Society of Rock Mechanics Congress, Advances in Rock Mechanics* 1974.

Patruno, S., Reid, W., Jackson, C.A-L. and Davies, C., 2017. New insights into the unexploited reservoir potential of the Mid North Sea High (UKCS quadrants 35-38 and 41-43): a newly described intra-Zechstein sulphate-carbonate platform complex. In: Petroleum Geology of NW Europe: 50 Years of Learning – Proceedings of the 8th Petroleum Geology Conference. Geological Society, London.

Peeters, S.H.J., Geel, C.R., Garland, J., Bouroullec, R., 2023. Seismic and petrographic characterisation of the Zechstein Hauptdolomit platforms around the Elbow Spit High, Dutch offshore. Journal of Petroleum Geology 46(3): 361-382. https://doi.org/10.1111/jpg.12842

Pruiksma, J.P., Breunese, J.N., Van Thienen-Visser, K. and De Waal, J.A., 2015. Isotach formulation of the rate type compaction model for sandstone. *International Journal of Rock Mechanics and Mining Sciences,* **78**, pp. 127-132.

Reijmer, J.J.G., ten Veen, J.H., Jaarsma, B., Boots, R., 2017. Seismic stratigraphy of Dinantian carbonates in the southern Netherlands and northern Belgium. Netherlands Journal of Geosciences – Geologie en Mijnbouw, 96-4, 353-379. https://doi.org/10.1017/njg.2017.33

Rodriguez-Marek, A., Kruiver, P.P., Meijers, P., Bommer, J.J., Dost, B., van Elk, J. & Doornhof, D., 2017. A regional site-response model for the Groningen gas field. Bulletin of the Seismological Society of America 107 (5): 2067–2077

Smit, J., Van Wees, J-D. and Cloetingh, S., 2018. Early Carboniferous extension in East Avalonia: 350 My record of lithospheric memory. Marine and Petroleum Geology. 92, 1010-1027. Doi: 10.1016/j.marpetgeo.2018.01.004

Spivey, J.P. and McCain, W.D., Jr.: 'Recommended Correlations for Fluid Property Estimation,' unpublished September 2003

Staatstoezicht op de Mijnen (2016) Methodiek voor risicoanalyse omtrent geïnduceerde bevingen door gaswinning. Tijdelijke leidraad voor adressering MBB.24.1.P, versie 1.2

Ten Veen, J.H., van Gessel, S.F., den Dulk, M., 2012. Thin- and thick-skinned salt tectonics in the Netherlands; a quantitative approach. Netherlands Journal of Geosciences – Geologie en Mijnbouw, 91-4, 447-464.

Thienen-Visser, K. van, Nepveu, M. & Hettelaar, J. (2012) Deterministische hazard analyse voor geïnduceerde seismiciteit in Nederland. TNO rapport 2012 R10198.

TNO 2020. Probabilistic Seismic Hazard and Risk Analysis in the TNO Model Chain Groningen. TNO2020 R11052 | 3

TNO 2023b, Publieke Seismische Dreigings- en Risicoanalyse Groningen gasveld 2023. TNO R10682

TNO, 2023a. Berekende bodemdaling ten gevolge van de gaswinning uit het Groningen veld en de gasopslag Norg. TNO 2023 R10900.

TNO, 2024. KEM-24b: Preliminary assessment of beneficial effects of nitrogen injection in depleted reservoirs. TNO 2024 TNO 2024 R11366.

Van Hulten, F.F.N., 2006. Reservoir quality distribution as tool for better exploration prospect evaluation and estimation of the resource base in the Netherlands. In: Hulten, F.F.N. van & Lutgert, J.E. (comp.). Tight gas fields in the Netherlands, workshop EBN-TNO.

Van Leeuwen, P.J., 2009. Particle filtering in geophysical systems. *Monthly Weather Review,* **137**(12), pp. 4089-4114

Van Ojik, K., Böhm, A.R., Cremer, H., Geluk, M.C., De Jong, M.G.G., Mijnlief, H.F. & Nio, S.D., 2012. The rationale for an integrated stratigraphic framework kof the Upper Rotliegend II depositional system in the Netherlands. In: Grötsch, J. & Gaupp, R. (eds): The Permian Rotliegend of the Netherlands. SEPM Special Publication No. 98. SEPM (Tulsa, Oklahoma, USA): 37–48.

Van Wees, J.-D., SEPHENSON, R.A., Ziegler, P.A., Bayer, U., McCann, T., Dadlez, R., Gaupp, R., Narkiewicz, M., Bitzer, F. and Scheck, M., 2000. On the origin of the Southern Permian Basin, Central Europe. Marine and Petroleum Geology, 17, 43-59.

Visser, C.A., 2012. Groningen Field Review 2012; static modelling and hydrocarbon volume determination. Published under 'Feiten en cijfers', available at www.nam.nl

Visser, C.A., Porter, R.J & Solano Viota, J.L, 2016. On the implementation of sedimentological data in porosity modelling of the Groningen field. Published under 'Feiten en cijfers', available at www.nam.nl

Zeeuw, Q. de and L. Geurtsen, 2018a. Groningen Dynamic Model Update 2018. Includes: Zeeuw, Q. de and L. Geurtsen, 2018. Groningen Dynamic Model Update 2018 – V5. NAM B.V. Zeeuw, Q. de and L. Geurtsen, 2018b. Groningen Dynamic Model Update 2019. https://www.nam.nl/feiten-en-cijfers.html. Includes: Zeeuw, Q. de and L. Geurtsen, 2018. Groningen Dynamic Model Update 2018 – V6. NAM B.V. EP201809202872

Signature

TNO › Energy & Materials Transition › Utrecht, 7 July 2025

Appendix A Petrophysical results

Calculated log data (porosity, ϕ, permeability, k, and net-to-grass, NtG)) for wells in the Roden, Pasop, de Vries, Boerakker and Faan fields. .

Each well panel follows similar layout: Track 1 = depth (MD, measured depth, depth along hole); Track 2 = input density log (RHOB/RHOB1) and other relevant logs , e.g. Caliper (CAL) and/or Gamma Ray (GR/GR100), Track 3 = sand/shale as proxy for NtG (clean sand calculated from GR < 60), Track 4 = calculated porosity log, Track 5 = calculated permeability log. Porosity is calculated from the density log (RHOB). Permeability is calculated from the porosity log using field specific poro-perm relationships. See section 2.4 for details.

Well tops follow the Stratigraphic Nomenclature (ZEZ1K = Coppershale member, ROCLT = Ten Boer Member, ROSL = Slochteren Formation, DCCU = Maurits Formation) or the NAM Groningen Model (RO__T, USS_** and LSS_**) naming convention.

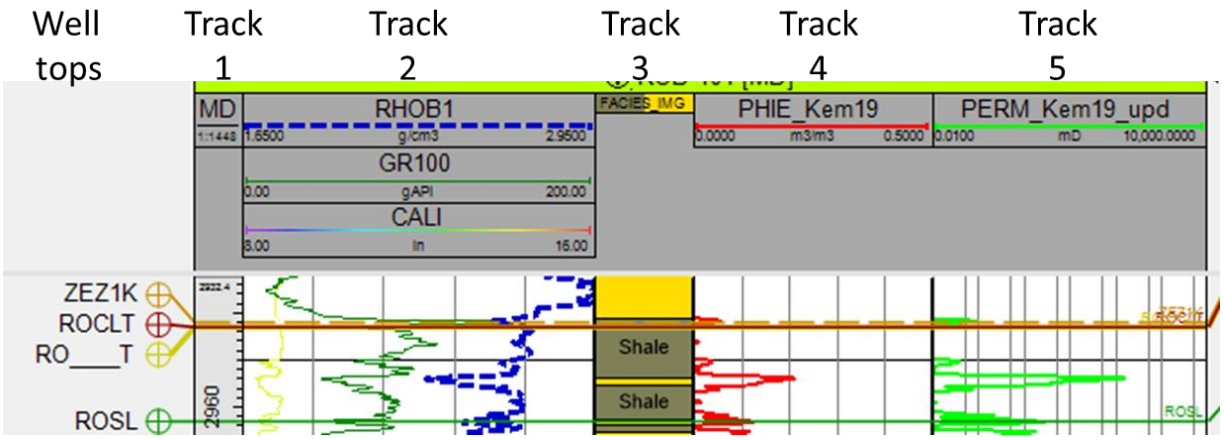

Figure 6-1: Example of a well panel with input and calculated porosity & permeability logs. See text for explanation on well tops and Track 1 – 5.

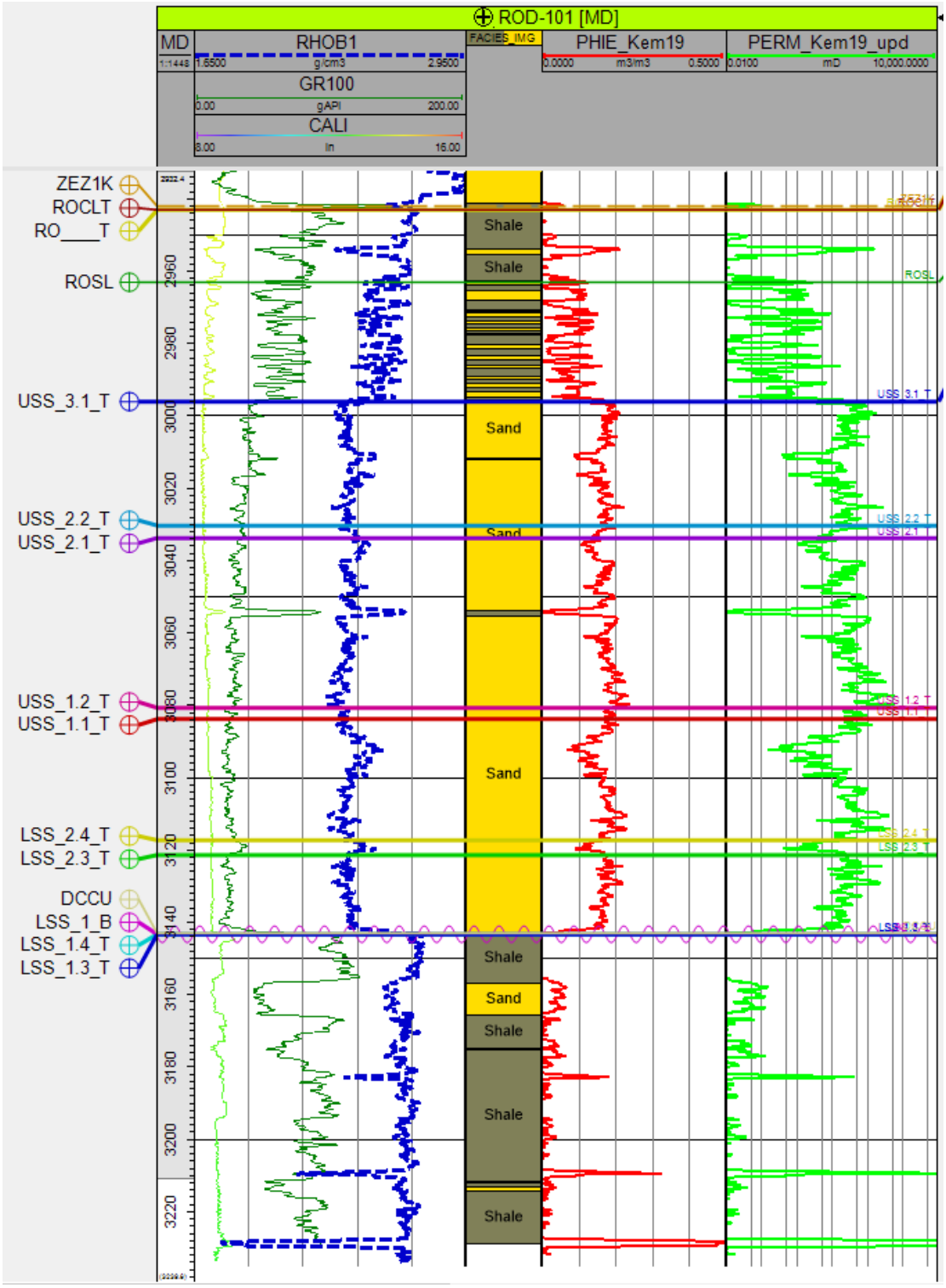

Figure 6-2: Well panel for well ROD-101.

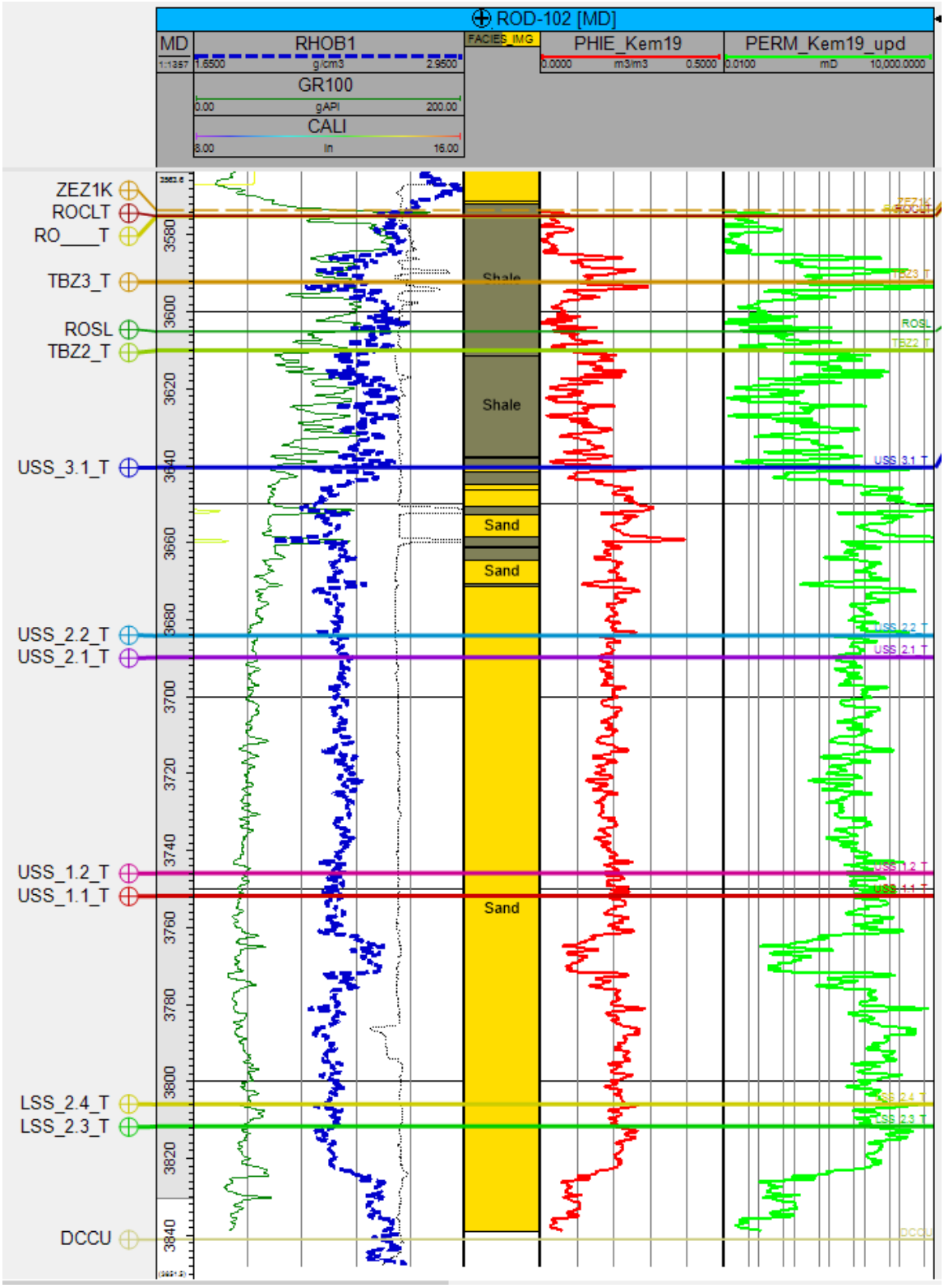

Figure 6-3: Well panel for well ROD-102.

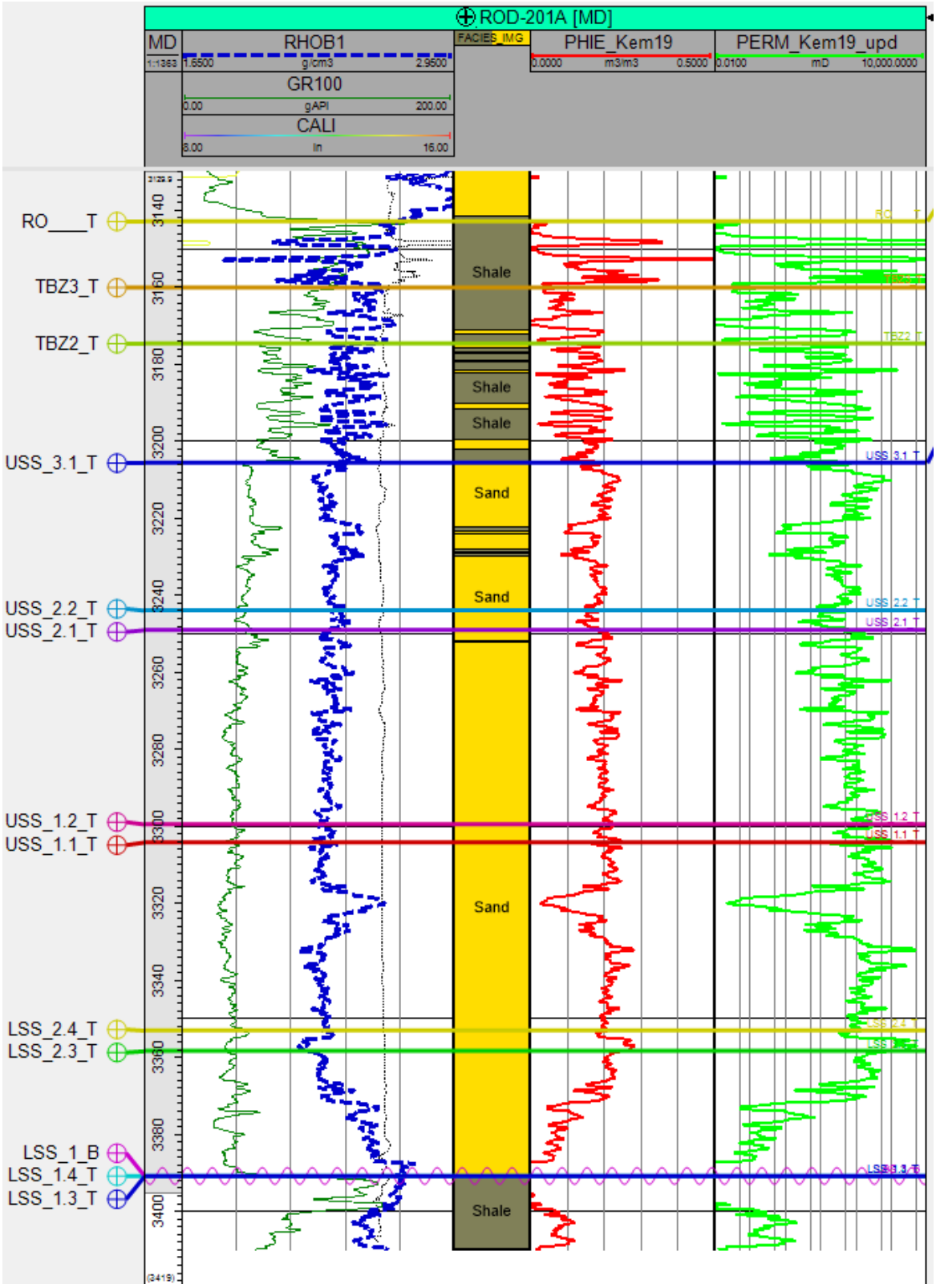

Figure 6-4: Well panel for well ROD-201-S1 (ROD-201A).

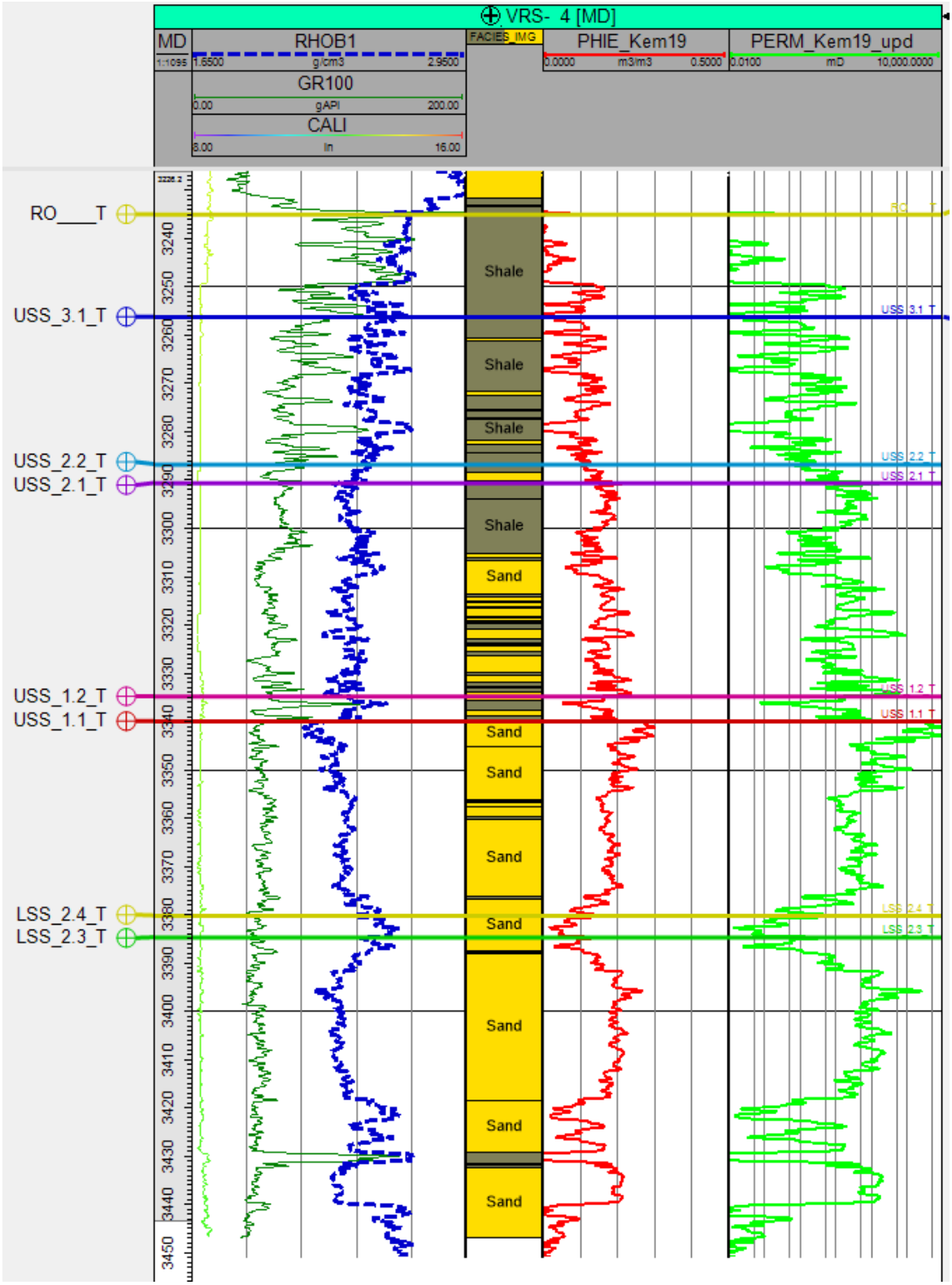

Figure 6-5: Well panel for well VRS-04 (VRS-401).

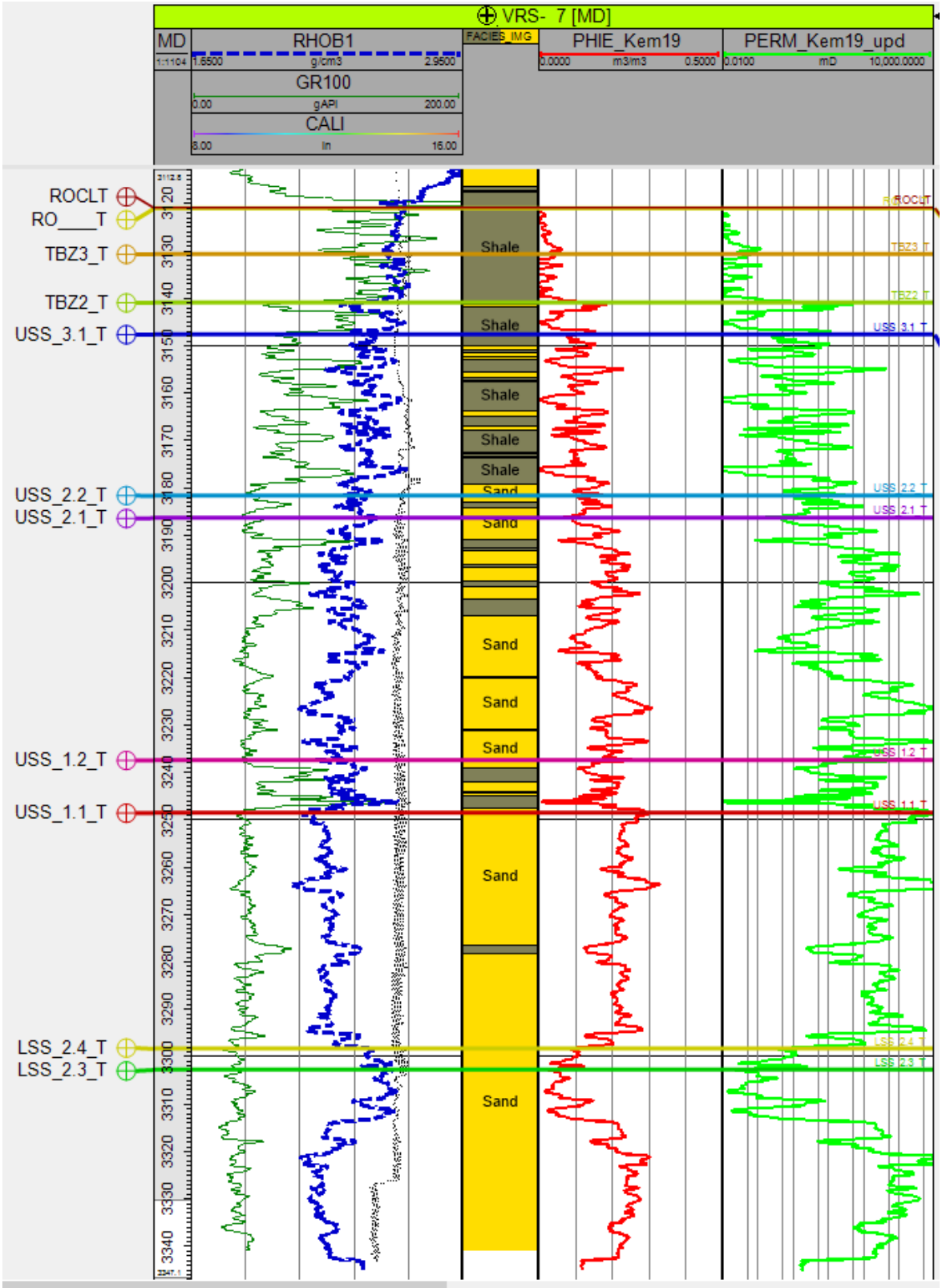

Figure 6-6: Well panel for well VRS-07 (VRS-402).

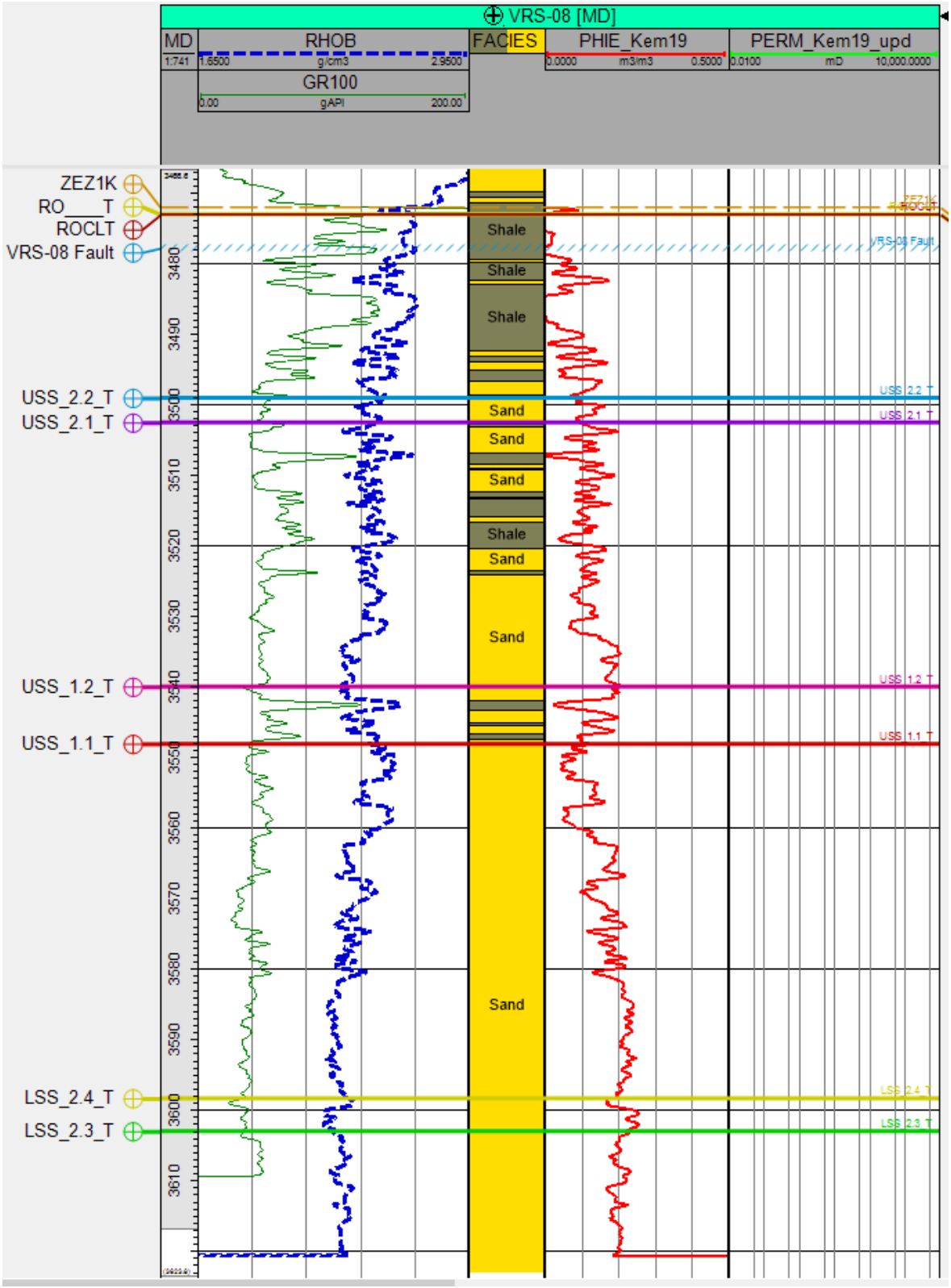

Figure 6-7: Well panel for well VRS-08 (VRS-403).

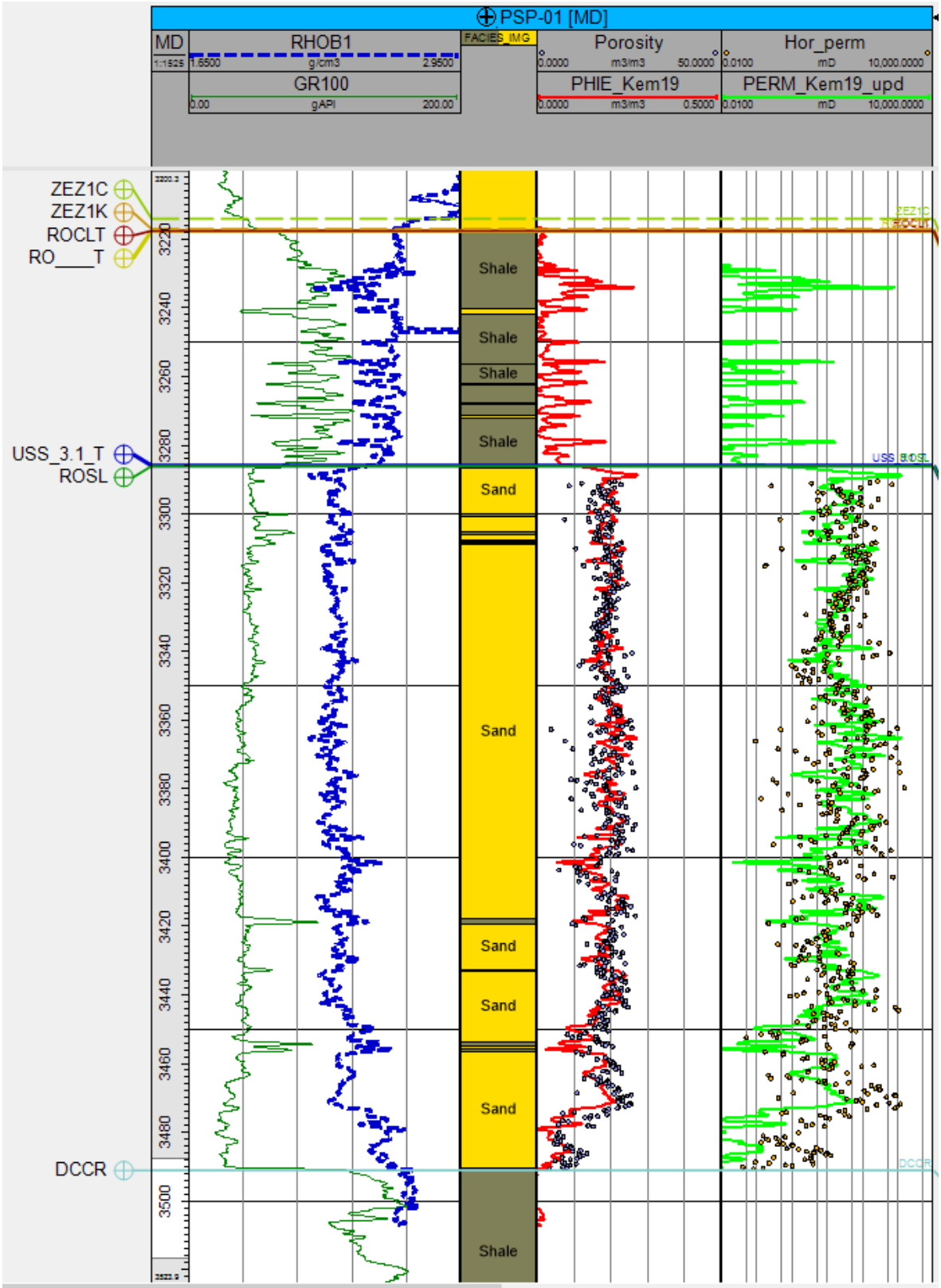

Figure 6-8: Well panel for well PSP-01. In Track 4 and 5, coreplug measurements are plotted, which show a good corelation between calculated log data and measured coreplug data.

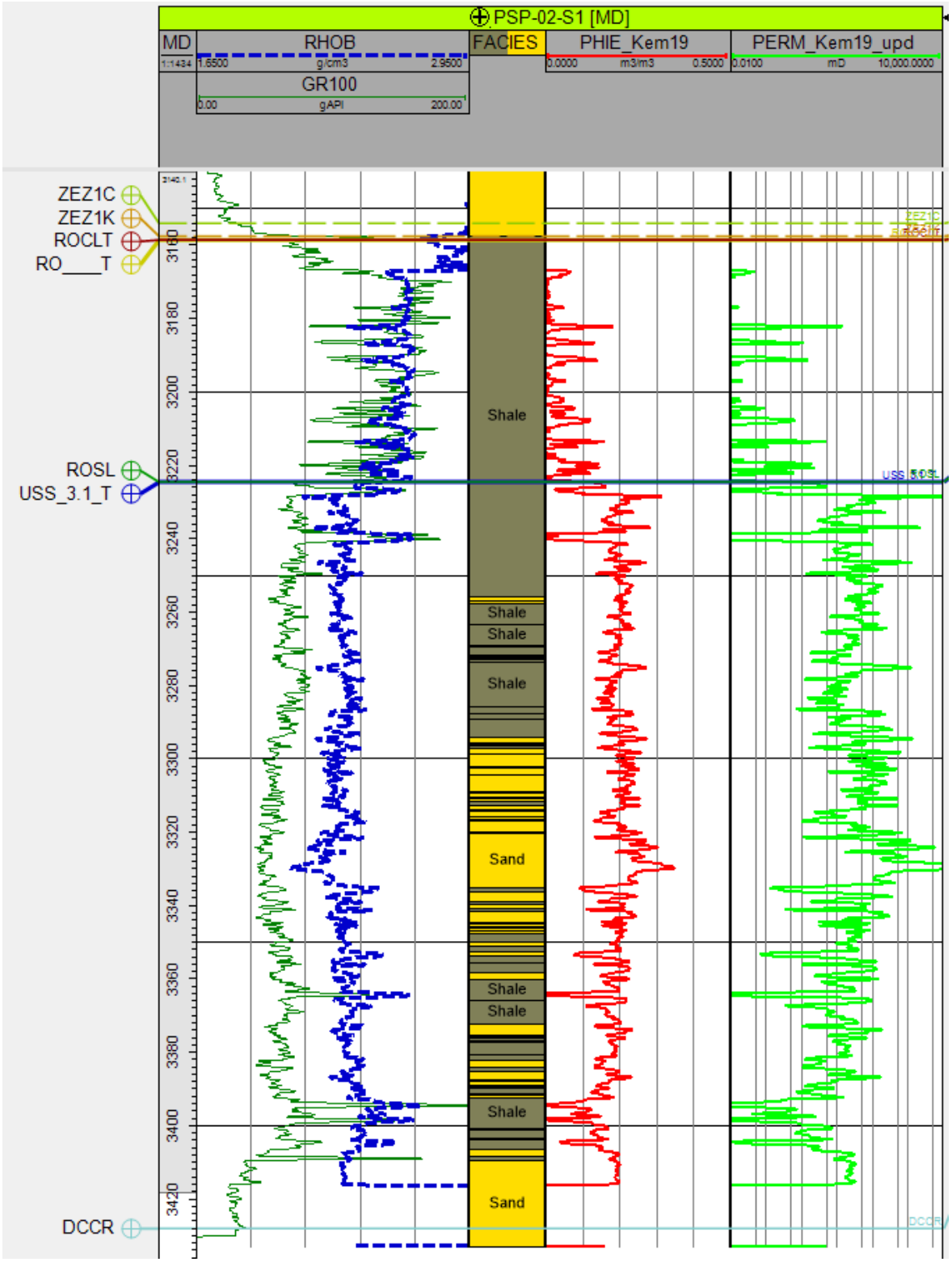

Figure 6-9: Well panel for well PSP-02-S1.

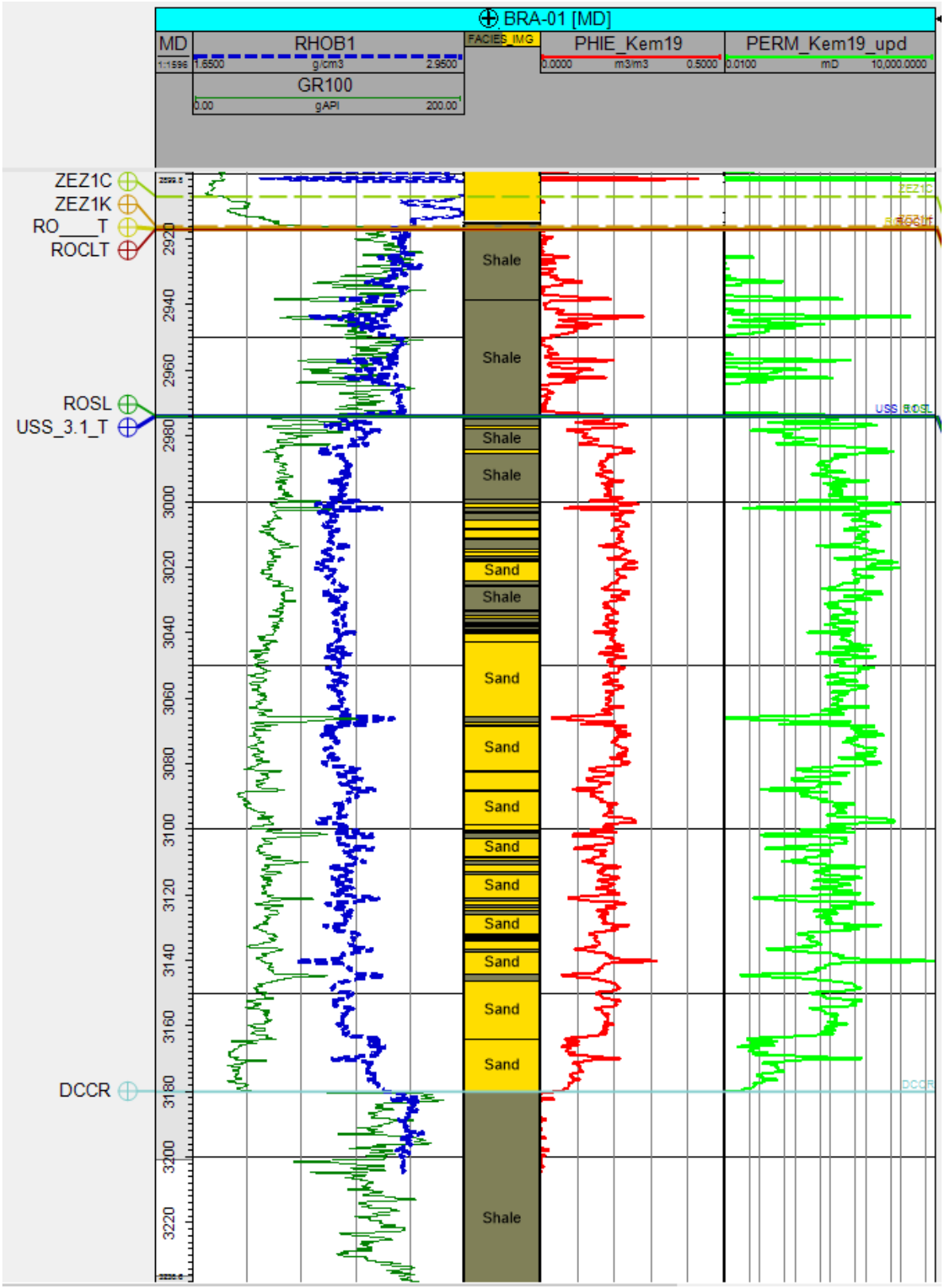

Figure 6-10: Well panel for well BRA-01.

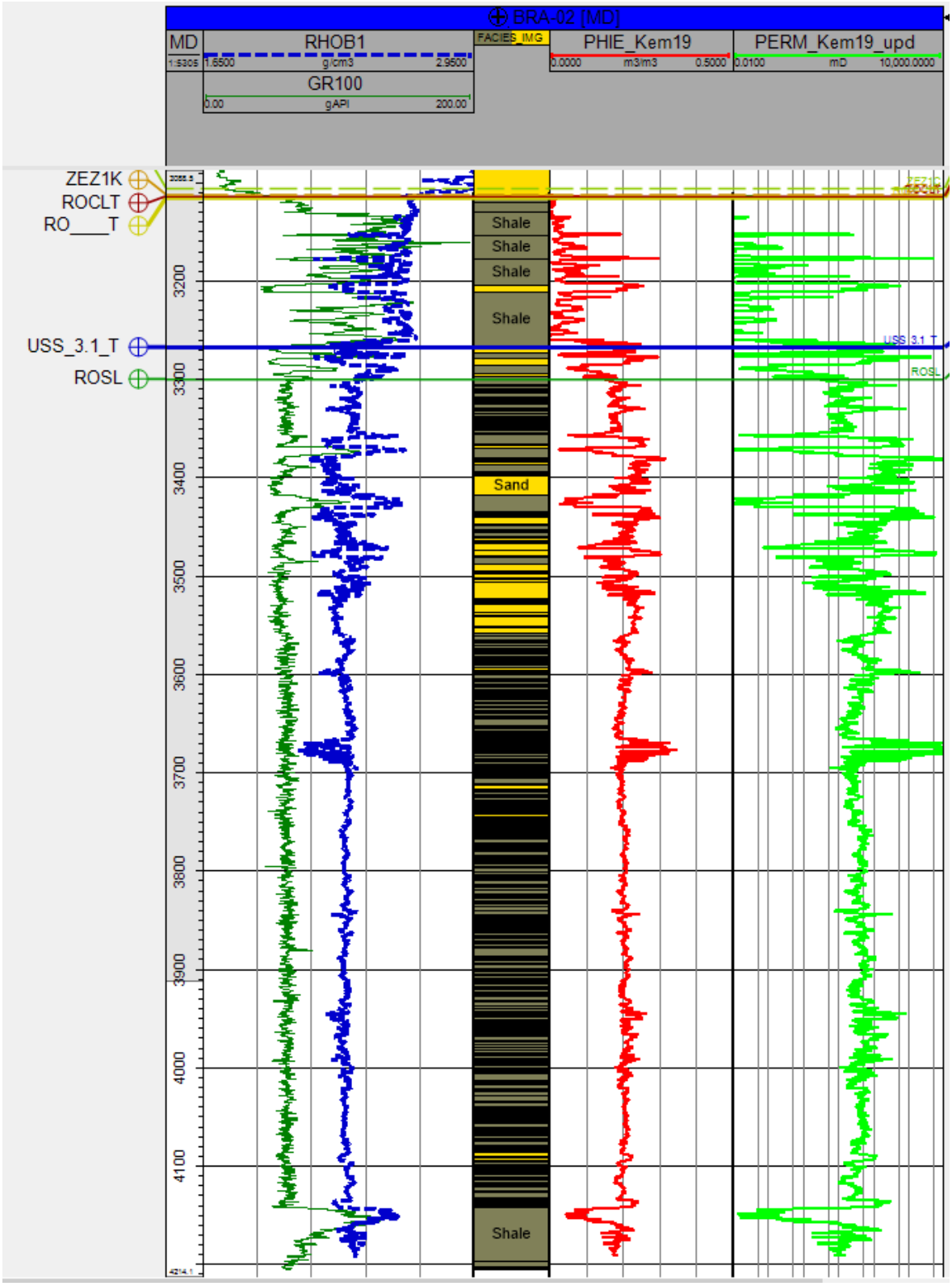

Figure 6-11: Well panel for well BRA-02.

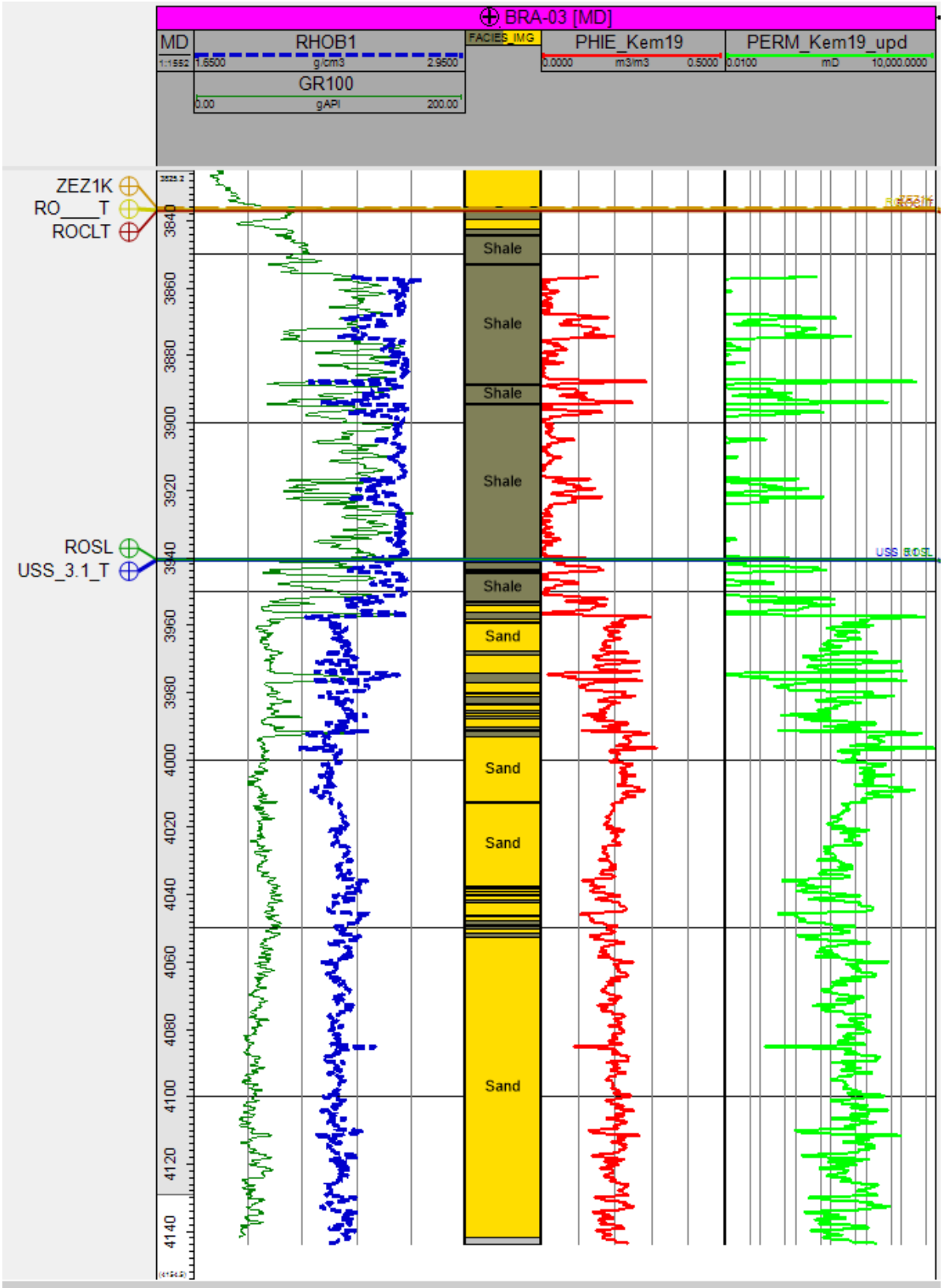

Figure 6-12: Well panel for well BRA-03.

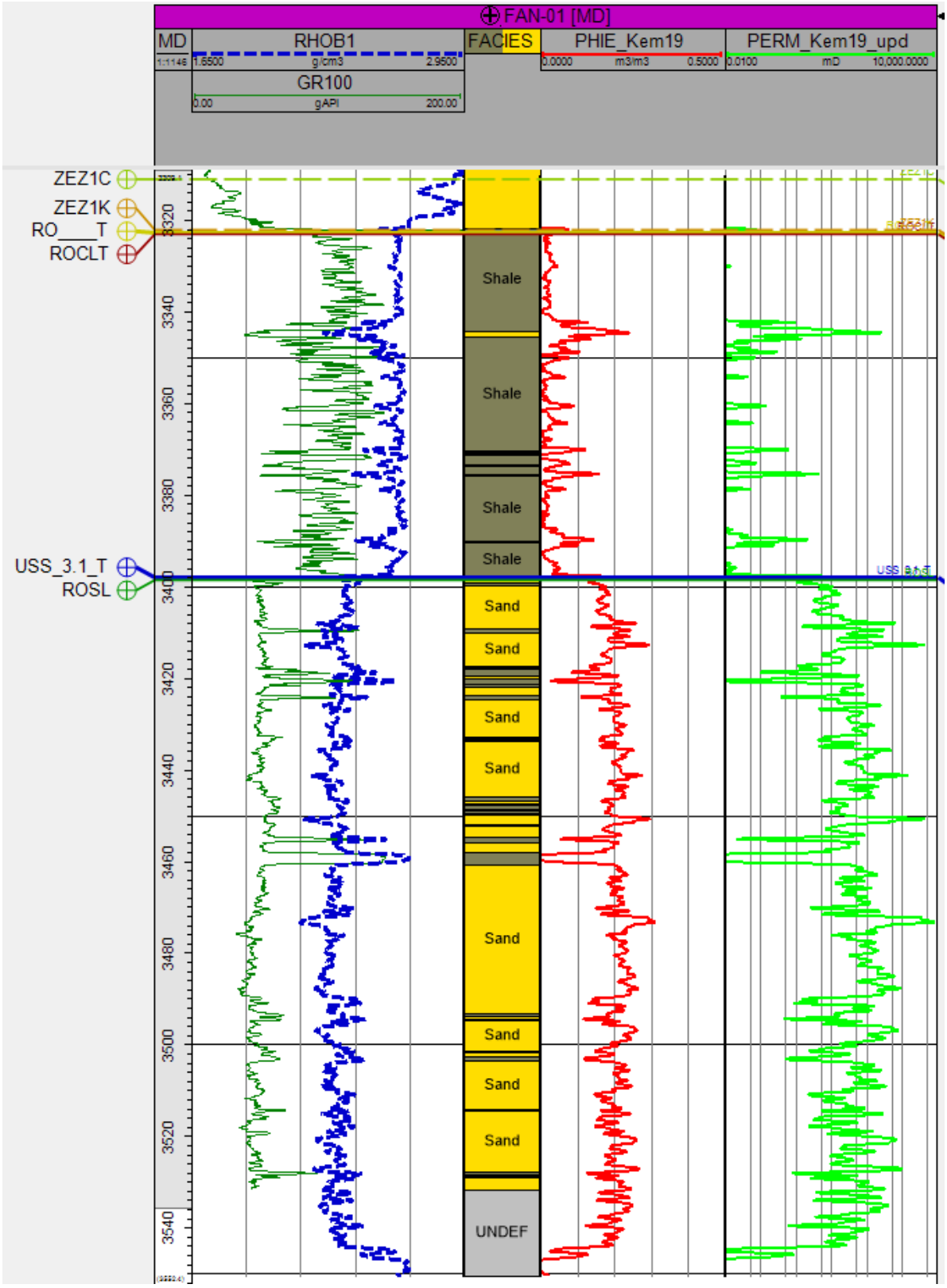

Figure 6-13: Well panel for well FAN-01.

Appendix B Input base model and ensemble

Table B-1 Gas composition used to create tables from correlations

	Roden, Pasop, Boerakker and Faan	Vries Noord	Groningen and Bedum
Methane (C1)	0.8119	0.8735	0.86
Ethane (C2)	0.0411	0.0409	-
Propane (C3)	0.0155	0.011	-
Iso-butane (iC4)	-	0.0036	-
Normal-butane (nC4)	0.0068	-	-
Iso-pentane (iC5)	-	0.0015	-
Normal-pentane (nC5)	0.0025	-	-
Hexanes (C6)	0.0013	0.0005	-
Heptanes plus (C7+)	0.0009	-	-
Carbon dioxide (CO_2)	0.01	0.007	-
Nitrogen (N_2)	0.11	0.062	0.14
Gravity (sg air)	0.667	0.625	0.644

Table B-2 Free water levels of the small gas fields and east side of the Groningen field.

	Free water level (m TVDSS)	Pressure at FWL (bar)
Areas without gas	2500	286.28
Roden	3021	346.42
Vries-Noord block 4	3108	356.47
Vries-Noord block 5 (with well VRS-08)	3075	352.66
Pasop	3123	358.20
Boerakker	2949	338.11
Faan	3346	383.94
Bedum	3002	344.23
Eemskanaal	2996	343.54
Harkstede and Kolham area	3016	345.85
Hoogezand	3030	347.46
Midlaren	3173	363.97

Table B-3 Overview of the faults in the model, including the Fault Group and multiplier of the base model (please note that in the Petrel fault names, some duplicates appear in this table, because the folder structure is not included here)

Name Petrel	Name Eclipse	Group	Multiplier
INT_29	'INT_29'	0	0.1
fault interpretation 5	'FAULTINT'	0	0.1
Fault 2	'FAULT2'	0	0.1
mFS18_Fault_52	'MFS18_FA'	5	1
mFS18_Fault_20	'MFS18__1'	0	0.1
mFS18_Fault_6	'MFS18__2'	0	0.1
mFS18_Fault_5	'MFS18__3'	0	0.1
Fault 3	'FAULT3'	0	0.001
mFS18_Fault_21	'MFS18__4'	0	0.1
B31	'B31'	0	0.00001
B35	'B35'	3	0.06
B36	'B36'	0	0.00001
B37	'B37'	5	0.03
B39	'B39'	3	0.03
B52a	'B52A'	0	0.00001
B53	'B53'	0	0.1
B55	'B55'	0	0.00001
B56	'B56'	0	0.00001
B58	'B58'	0	0.00001
B59a	'B59A'	0	0.00001
B60	'B60'	2	0.01
B64	'B64'	0	0.00001
INT 31	'INT31'	0	0.001
INT 32	'INT32'	0	0.00001
INT_24	'INT_24'	3	0.1
INT_25	'INT_25'	3	0.1
INT_26	'INT_26'	10	0.00001
INT_27	'INT_27'	11	0.00001
M10	'M10'	12	0.1
M11	'M11'	5	0.003
M12	'M12'	3	0.1
M16	'M16'	0	0.1
M19	'M19'	0	0.1
M22	'M22'	7	0.00001

Name Petrel	Name Eclipse	Group	Multiplier
M23	'M23'	0	0.001
M24	'M24'	0	0.00001
M27	'M27'	4	0.003
M28	'M28'	0	0.1
M29	'M29'	11	0.00001
M33	'M33'	0	0.00001
M35	'M35'	0	0.1
M74	'M74'	10	0.00001
M9	'M9'	5	0.001
M9b	'M9B'	10	0.00001
B57	'B57'	4	0.1
mFS9_Fault_9	'MFS9_FAU'	0	0.1
M30	'M30'	6	0.1
M68_E	'M68_E'	0	0.02
M31_E	'M31_E'	0	0.00001
M31_W	'M31_W'	11	0.0001
mFS17_Fault_5	'MFS17_FA'	3	0.1
mFS17_Fault_14	'MFS17__5'	12	0.1
mFS17_Fault_1	'MFS17__6'	3	0.1
mFS18_fault 21a	'MFS18__7'	6	0.1
mFS18_Fault_1	'MFS18__8'	0	0.1
mFS18_Fault_11	'MFS18__9'	0	0.1
mFS18_Fault_18	'MFS18_10'	12	0.1
mFS18_Fault_3	'MFS18_11'	0	0.1
mFS18_Fault_31	'MFS18_12'	6	0.06
mFS18_Fault_34	'MFS18_13'	12	0.1
mFS18_Fault_35	'MFS18_14'	0	0.1
mFS18_Fault_36	'MFS18_15'	0	0.1
mFS18_Fault_45	'MFS18_16'	0	0.1
mFS18_Fault_7	'MFS18_17'	0	0.1
mFS18_Fault_9	'MFS18_18'	0	0.1
mFS18_Fault_22_(See comments)	'MFS18_19'	0	0.1
mFS16_Fault_2	'MFS16_FA'	1	0.03
mFS16_Fault_20	'MFS16_20'	3	0.1
mFS16_Fault_24	'MFS16_21'	3	0.1
mFS16_Fault_25	'MFS16_22'	3	0.1
mFS16_Fault_26	'MFS16_23'	3	0.1
mFS16_Fault_32	'MFS16_24'	0	0.1

Name Petrel	Name Eclipse	Group	Multiplier
mFS16_Fault_41	'MFS16_25'	0	0.1
mFS16_Fault_43	'MFS16_26'	3	0.1
mFS16_Fault_45	'MFS16_27'	9	0.00001
mFS16_Fault_50	'MFS16_28'	0	0.1
mFS15_Fault 56	'MFS15_FA'	0	0.1
mFS15_Fault_10	'MFS15_29'	0	1
mFS15_Fault_107	'MFS15_30'	0	0.1
mFS15_Fault_11	'MFS15_31'	3	0.1
mFS15_Fault_112	'MFS15_32'	4	0.01
mFS15_Fault_12	'MFS15_33'	0	0.1
mFS15_Fault_16	'MFS15_34'	0	1
mFS15_Fault_17	'MFS15_35'	0	0.1
mFS15_Fault_18	'MFS15_36'	0	0.1
mFS15_Fault_19	'MFS15_37'	0	0.1
mFS15_Fault_21	'MFS15_38'	0	0.1
mFS15_Fault_22	'MFS15_39'	0	1
mFS15_Fault_26	'MFS15_40'	0	0.1
mFS15_Fault_27	'MFS15_41'	0	0.1
mFS15_Fault_3	'MFS15_42'	3	0.1
mFS15_Fault_31	'MFS15_43'	0	0.1
mFS15_Fault_33	'MFS15_44'	0	0.1
mFS15_Fault_35	'MFS15_45'	0	0.1
mFS15_Fault_36	'MFS15_46'	0	0.1
mFS15_Fault_4	'MFS15_47'	3	0.1
mFS15_Fault_43	'MFS15_48'	0	1
mFS15_Fault_44	'MFS15_49'	4	0.1
mFS15_Fault_44a	'MFS15_50'	0	0.1
mFS15_Fault_49	'MFS15_51'	0	0.1
mFS15_Fault_5	'MFS15_52'	3	0.1
mFS15_Fault_50	'MFS15_53'	0	1
mFS15_Fault_9	'MFS15_55'	0	0.1
mFS15_Fault_Extra 3	'MFS15_56'	0	0.1
mFS15_Fault_Extra2	'MFS15_57'	0	0.1
mS15_Fault_63	'MS15_FAU'	0	0.1
mFS15_Fault_48 (See comments)	'MFS15_58'	0	1
mFS15_Fault_15	'MFS15_59'	0	1
mFS15_Fault 34	'MFS15_60'	0	0.1
mFS10_fault_46	'MFS10_FA'	0	0.1

Name Petrel	Name Eclipse	Group	Multiplier
mFS10_Fault_47	'MFS10_61'	0	0.04
mFS10_Fault_48	'MFS10_62'	0	0.1
mFS10_Fault_49	'MFS10_63'	0	0.1
mFS9_Fault_20	'MFS9__64'	0	0.1
mFS9_Fault_22	'MFS9__65'	0	0.1
mFS9_Fault_27	'MFS9__66'	0	0.00001
mFS9_Fault_28	'MFS9__67'	0	0.00001
mFS9_Fault_29	'MFS9__68'	0	0.1
mFS9_Fault_31	'MFS9__69'	0	0.1
mFS9_Fault_37	'MFS9__70'	0	0.1
mFS9_Fault_44	'MFS9__71'	0	0.1
Bedum Aquifer fault 1	'BEDUMAQU'	7	0.00001
M68_W (delete)	'M68_W(DE'	7	0.00001
Fault interpretation 2	'FAULT_72'	9	0.00001
Fault interpretation 3	'FAULT_73'	9	0.00001
Fault interpretation 4	'FAULT_74'	9	0.00001
Fault interpretation 5	'FAULT_75'	0	0.1
Fault interpretation 7	'FAULT_76'	8	0.1
Fault interpretation 8	'FAULT_77'	8	0.1
Fault interpretation 10	'FAULT_78'	8	0.1
Fault interpretation 11	'FAULT_79'	12	0.001
Fault interpretation 12	'FAULT_80'	11	0.00001
Fault interpretation 13	'FAULT_81'	0	0.01
Fault interpretation 24	'FAULT_82'	0	0.1
Fault interpretation 29	'FAULT_83'	10	0.00001
Fault interpretation 30	'FAULT_84'	10	0.00001
Fault interpretation 32	'FAULT_85'	9	0.00001
Fault interpretation 29 (Depth 1)	'FAULT_87'	9	0.00001
Fault interpretation 35 (Depth 1)	'FAULT_89'	0	0.00001
Fault interpretation 39 (Depth 1)	'FAULT_91'	0	0.0003
Fault interpretation 40 (Depth 1)	'FAULT_92'	0	0.1
Fault 8	'FAULT8'	9	0.00001
Fault 9	'FAULT9'	0	0.1
Fault 15	'FAULT15'	0	0.1
Fault interpretation 1	'FAULT_94'	0	0.01
Fault interpretation 2	'FAULT_95'	0	0.01
Fault interpretation 6	'FAULT_96'	0	0.01
Fault interpretation 4	'FAULT_97'	0	0.00001

Name Petrel	Name Eclipse	Group	Multiplier
Fault 1_VRS-08	'FAULT1_V'	11	0.00001
Fault 4_VRS-08	'FAULT4_V'	11	0.00001
PSP EBF	'PSPEBF'	13	0.00001
Fault 1	'FAULT1'	0	0.00001
Riedel 1	'RIEDEL1'	0	0.01
Riedel 2	'RIEDEL2'	0	0.01
Riedel 3	'RIEDEL3'	0	0.01
Faan fault	'FAANFAUL'	0	0.00001
Fault 4	'FAULT4'	0	0.01
Fault 5	'FAULT5'	0	0.01
Fault 6	'FAULT6'	0	0.00001
Fault 7	'FAULT7'	1	0.01

Table B-4 Definition of the fault groups for applying multipliers in the ensemble.

Group	Description	Faults (Petrel name)
0	Don't vary	All faults not listed below
1	Between BDM/HRS –aq	Fault 7, mFS16_Fault_2
2	Gron-HRS	B60
3	HRS-Rod-aquifer	B35, INT_24, M12, INT_25, mFS16_Fault_20, mFS16_Fault_24, mFS16_Fault_25, mFS16_Fault_26, mFS17_Fault_1, mFS16_Fault_43, mFS15_fault_11, mFS15_fault_3, mFS15_fault_4, mFS15_fault_5, B39, mFS17_Fault_5
4	EKL-HRS block	M27, B57, mFS15_Fault_112, mFS15_Fault_44
5	KHM,HAR block E-W	B37, M9, mFS18_Fault_52, M11
6	HGZ-MLA connection	mFS18_fault_21a, M30, mFS18_Fault_31
7	BDM-Aq	M22, Bedum Aquifer fault 1, M68_W (delete)
8	N-S faults ROD/PSP aq	Fault interpretation 7, Fault interpretation 8, Fault interpretation 10
9	Large E-W faults, N	Fault interpretation 29 (Depth 1), Fault interpretation 32, Fault interpretation 4, Fault 8, Fault interpretation 2, Fault interpretation 3, mFS16_Fault_45
10	Large E-W faults, M	Fault interpretation 29, Fault interpretation 30, INT_26, M74, M9b

11	Large E-W faults, S	M29, M31_W, Fault 1_VRS-08, Fault 4_VRS-08, Fault interpretation 12
12	Vries aq dir. west	Fault interpretation 11, mFS17_Fault_14, M10, mFS18_Fault_34, mFS18_Fault_18
13	PSP EBF	PSP_EBF

Ranges of the uniform distribution from which the fault multipliers per group are samples for creating the ensemble

Table B-5 Ranges of the uniform distribution from which the fault multipliers per group are samples for creating the ensemble.

Group	range min	range max
0	n.v.t.	n.v.t
1	-1	1
2	-1	1
3	-1	1
4	-1	1
5	-1	1
6	-1	1
7	-1	1
8	-3	1
9	-1	2
10	-1	2
11	-1	2
12	-1	1
13	-1	1

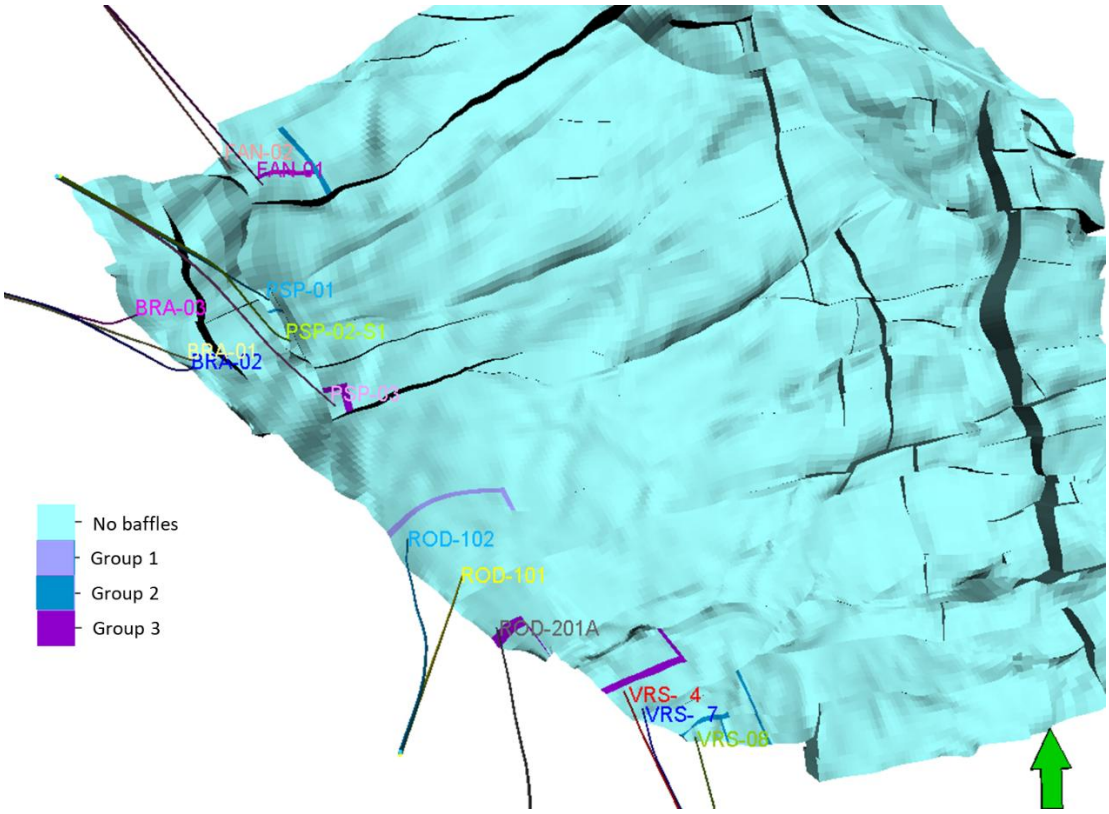

Figure B-14 Baffles implemented in the small gas fields during tuning. See Table 3-3 for the permeability values used for the base model and the ensemble.

Appendix C Results ensemble

C.1 Ensemble results history

Per block or small gas field the block pressure (BPR) is plotted:
Roden north block (ROD-101/ROD-101B and ROD-102): 7, 100, 4
Roden south block (ROD-201A): 7, 109, 4
Vries Noord (block with VRS-4 and VRS-7): 24, 140, 3
Vries Noord (block with VRS-8): 24, 151, 4
PSP-01: 13, 43, 4
PSP-02-S1: 13, 47, 4
PSP-03: 15, 66, 4
FAN-01: 14, 22, 4
FAN-02: 13, 16, 4
BRA-1 and BRA-2: 6, 39, 4
BRA-3 (listed as A-3-OPM): 1, 28, 4
Well Bottom hole pressure (WBHP) for HRS-2A and MLA-1.
Water production rate is plotted for all wells of the small gas fields

Every line represent a model realization. Crosses indicate measurements.

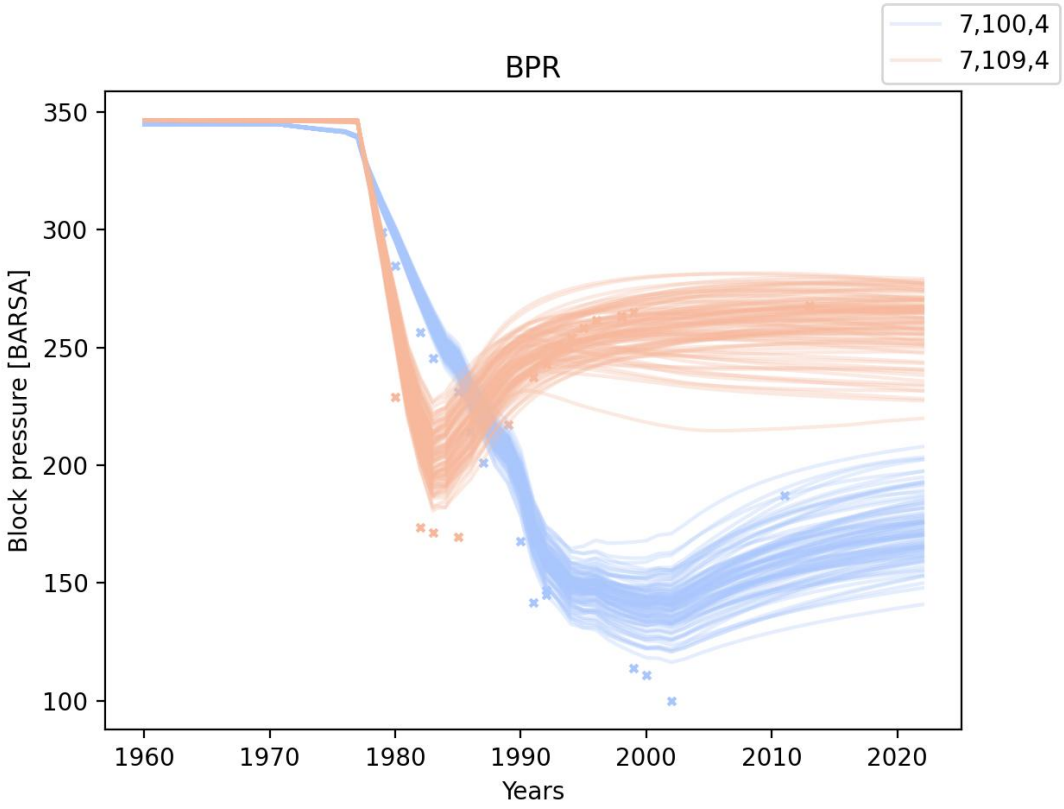

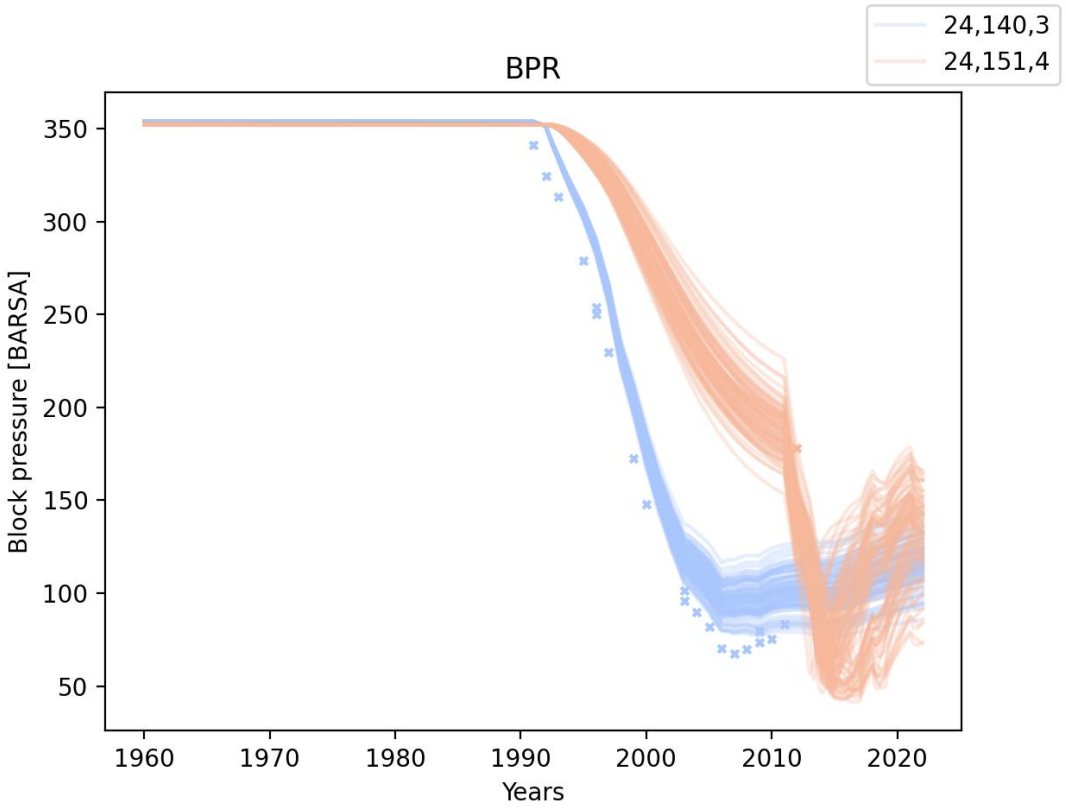
24,140,3
24,151,4
BPR
Block pressure [BARSA]
350
300
250
200
150
100
50
1960
1970
1980
1990
2000
2010
2020
Years

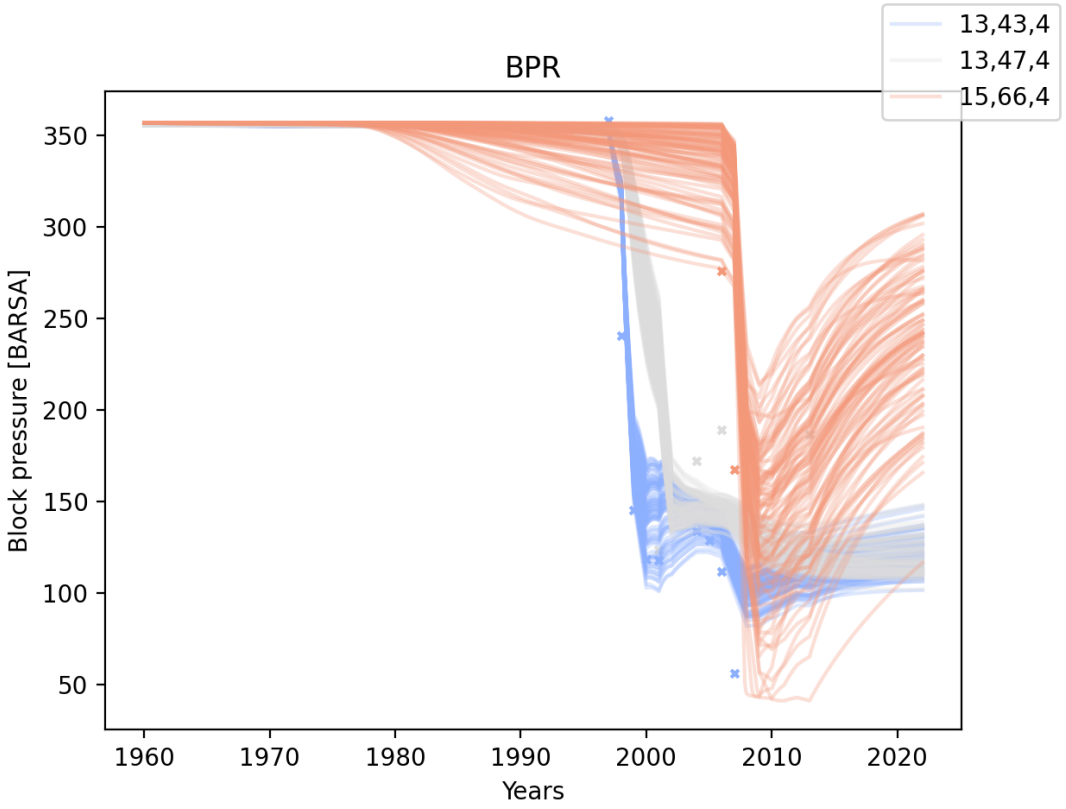
13,43,4
13,47,4
15,66,4
BPR
Block pressure [BARSA]
350
300
250
200
150
100
50
1960
1970
1980
1990
2000
2010
2020
Years

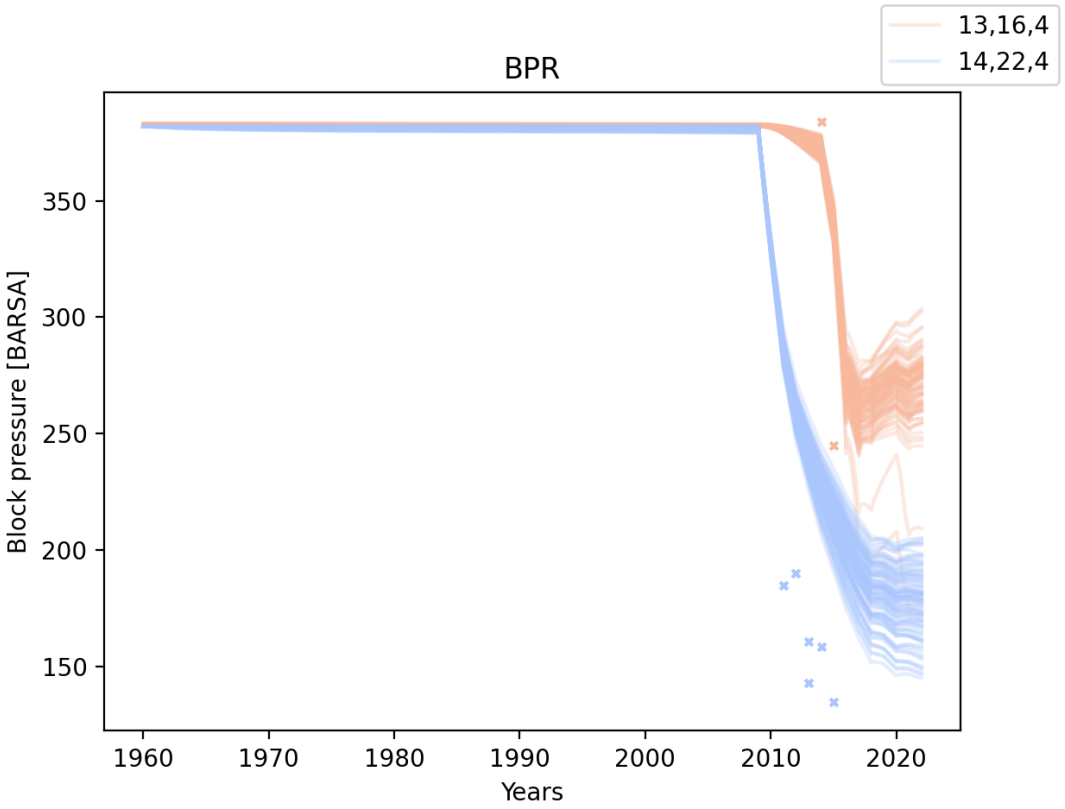
13,16,4
14,22,4
BPR
Block pressure [BARSA]
350
300
250
200
150
1960
1970
1980
1990
2000
2010
2020
Years

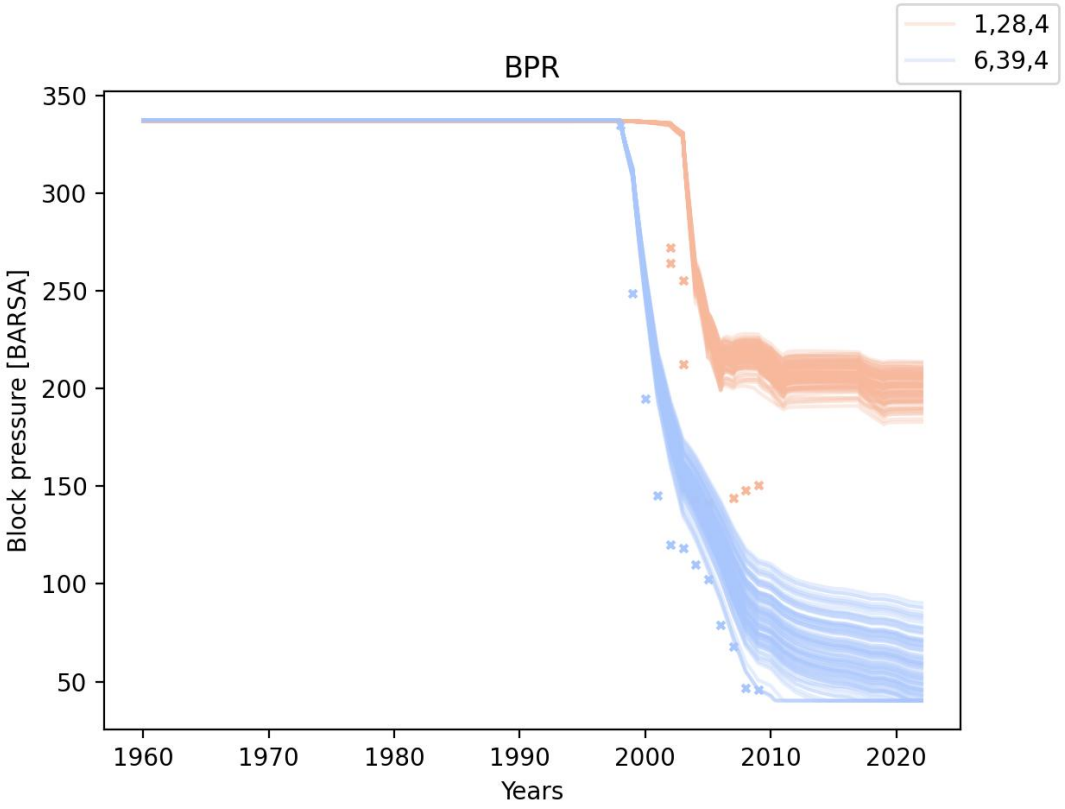
1,28,4
6,39,4
BPR
Block pressure [BARSA]
350
300
250
200
150
100
50
1960
1970
1980
1990
2000
2010
2020
Years

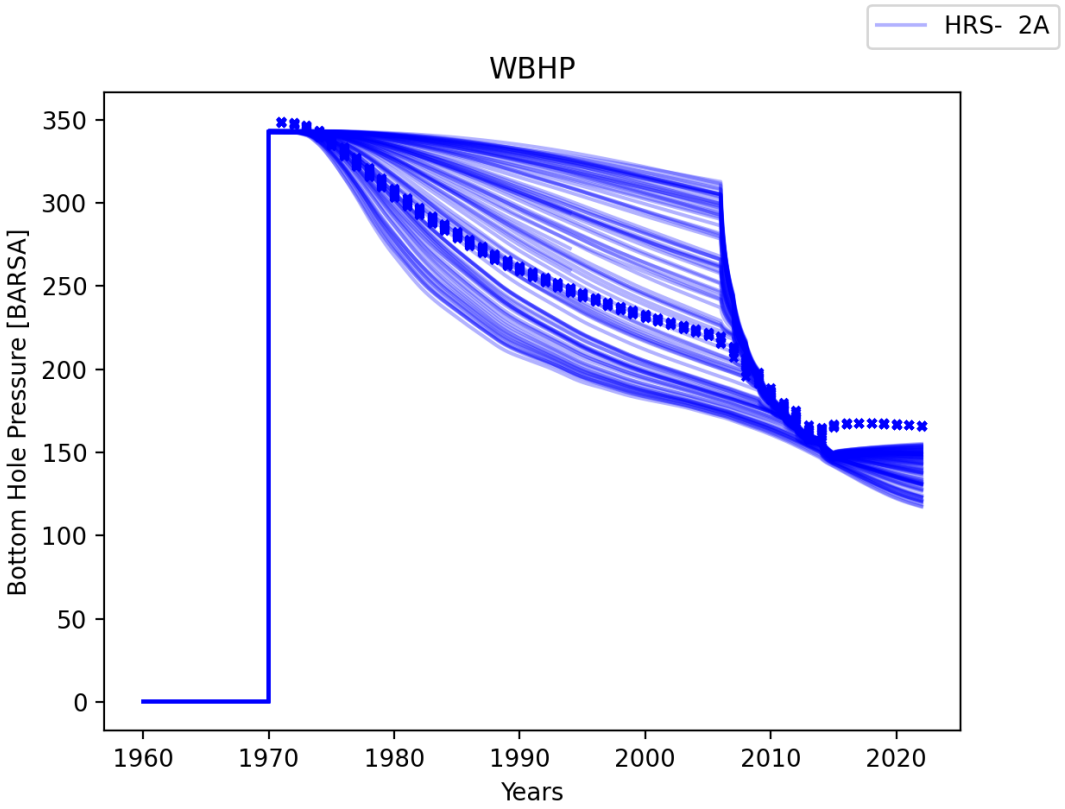
HRS- 2A
WBHP
Bottom Hole Pressure [BARSA]
350
300
250
200
150
100
50
0
1960
1970
1980
1990
2000
2010
2020
Years

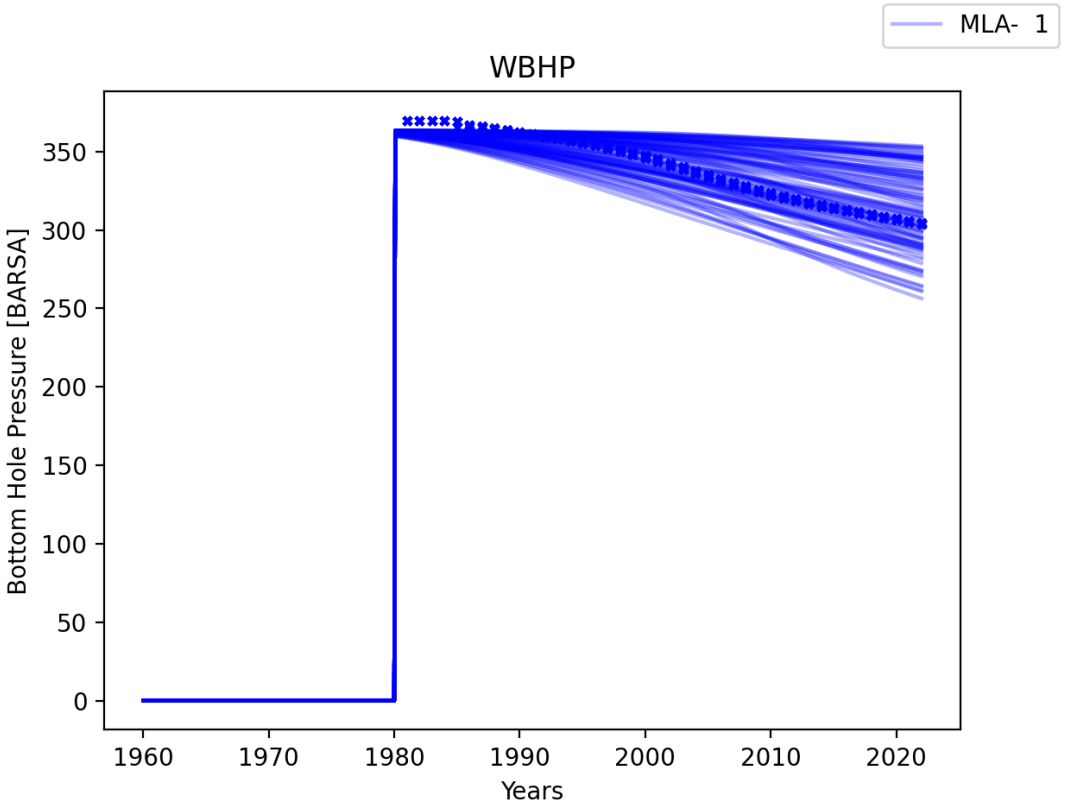
MLA- 1
WBHP
Bottom Hole Pressure [BARSA]
350
300
250
200
150
100
50
0
1960
1970
1980
1990
2000
2010
2020
Years

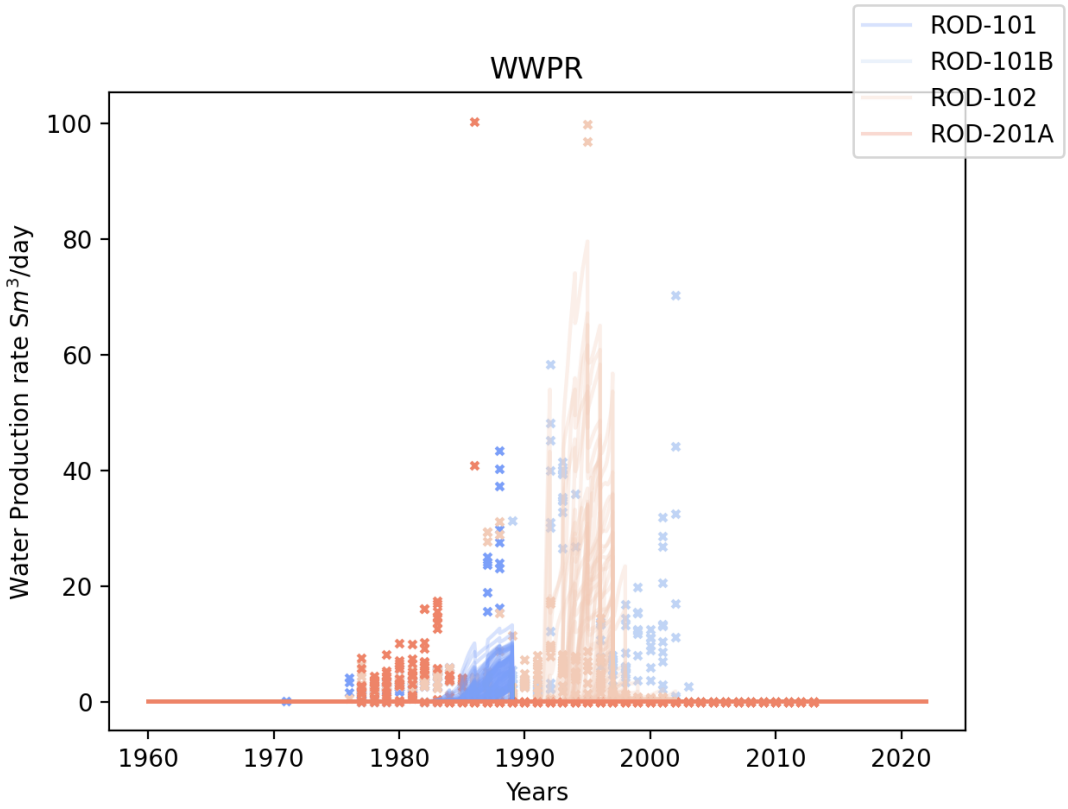
WWPR
ROD-101
ROD-101B
ROD-102
ROD-201A
Water Production rate Sm^3/day
0
20
40
60
80
100
1960
1970
1980
1990
2000
2010
2020
Years

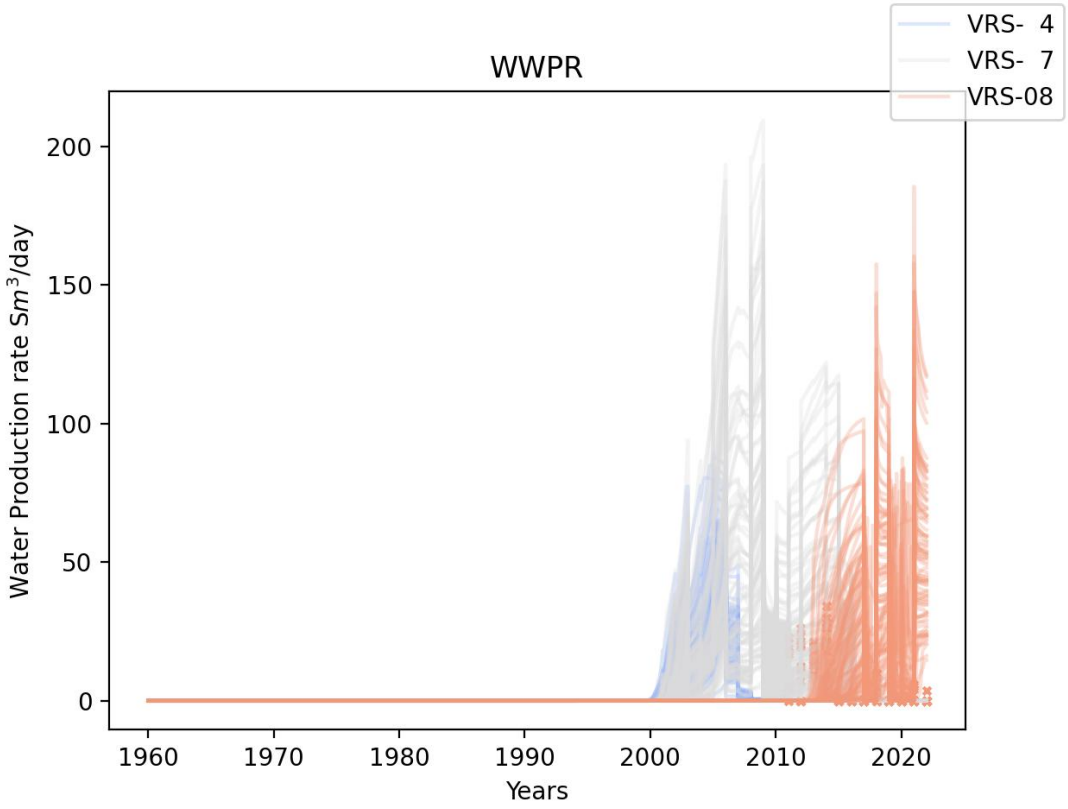
WWPR
VRS- 4
VRS- 7
VRS-08
Water Production rate Sm^3/day
0
50
100
150
200
1960
1970
1980
1990
2000
2010
2020
Years

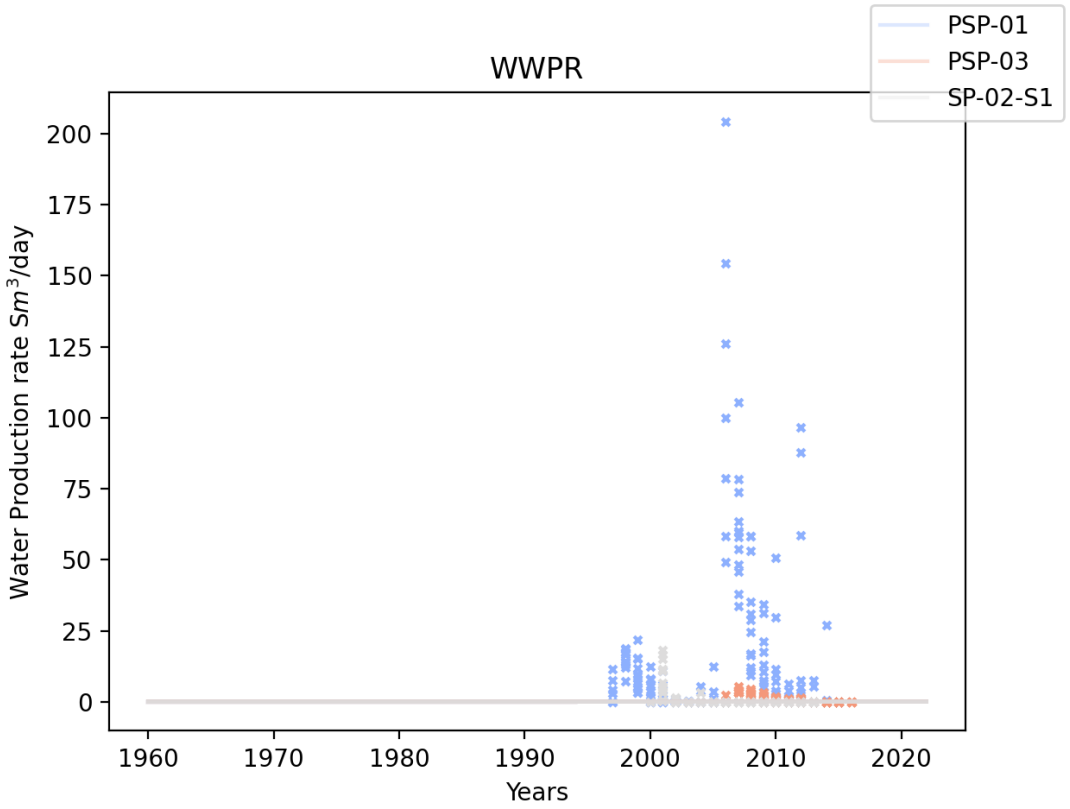
WWPR
PSP-01
PSP-03
SP-02-S1
Water Production rate Sm^3/day
0
25
50
75
100
125
150
175
200
1960
1970
1980
1990
2000
2010
2020
Years

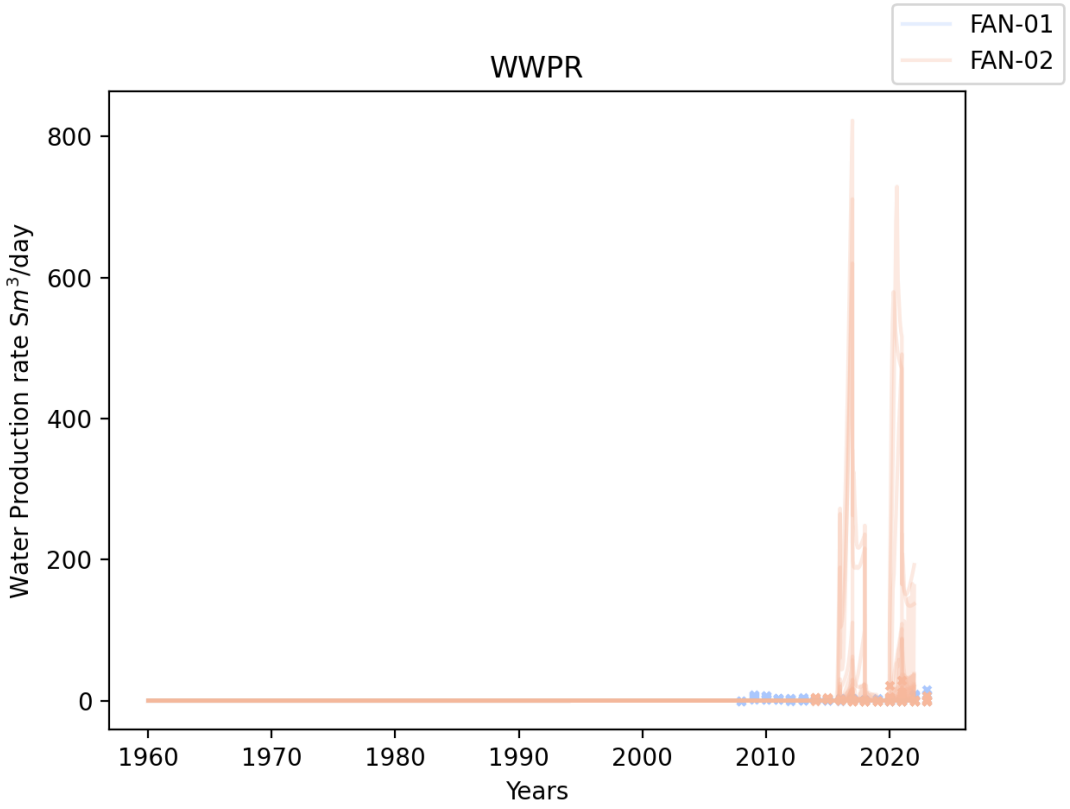
WWPR
FAN-01
FAN-02
Water Production rate Sm^3/day
0
200
400
600
800
1960
1970
1980
1990
2000
2010
2020
Years

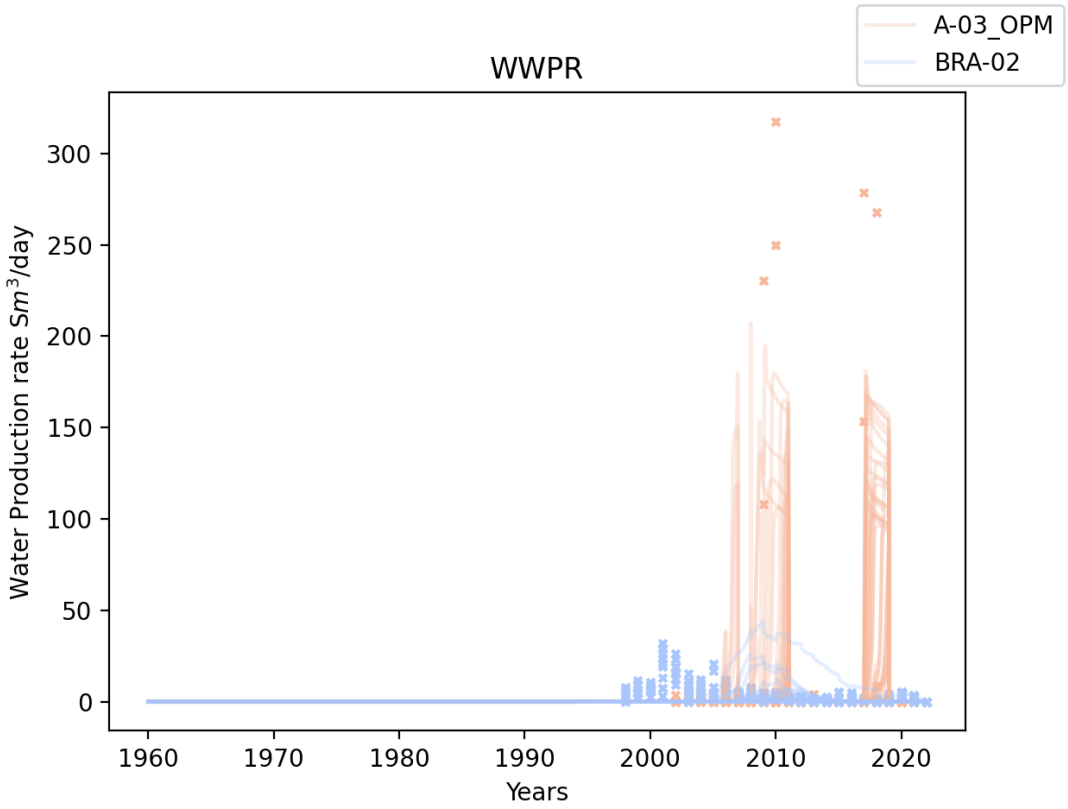

C.2 Ensemble results prediction

Ensemble results for both the historical and prediction period of the pressure. Black and red curves are the model realizations from which the predictions will be used ifor the seismicity analyses because they fit better to the observations (pressure and subsidence). The red curve is the best fitting member 96. Blue curves are the model realizations that do not fit sufficiently well to data to be used for the seismicity analysis. See the start of the appendix which block represents which field.

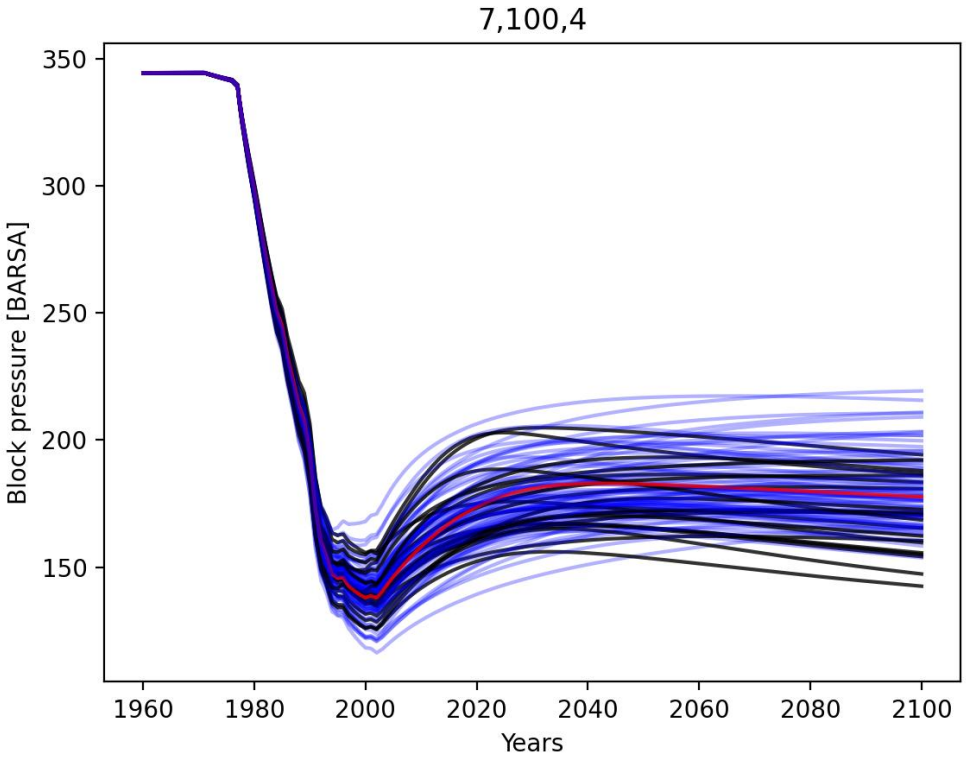
7,100,4
Block pressure [BARSA]
350
300
250
200
150
1960
1980
2000
2020
2040
2060
2080
2100
Years

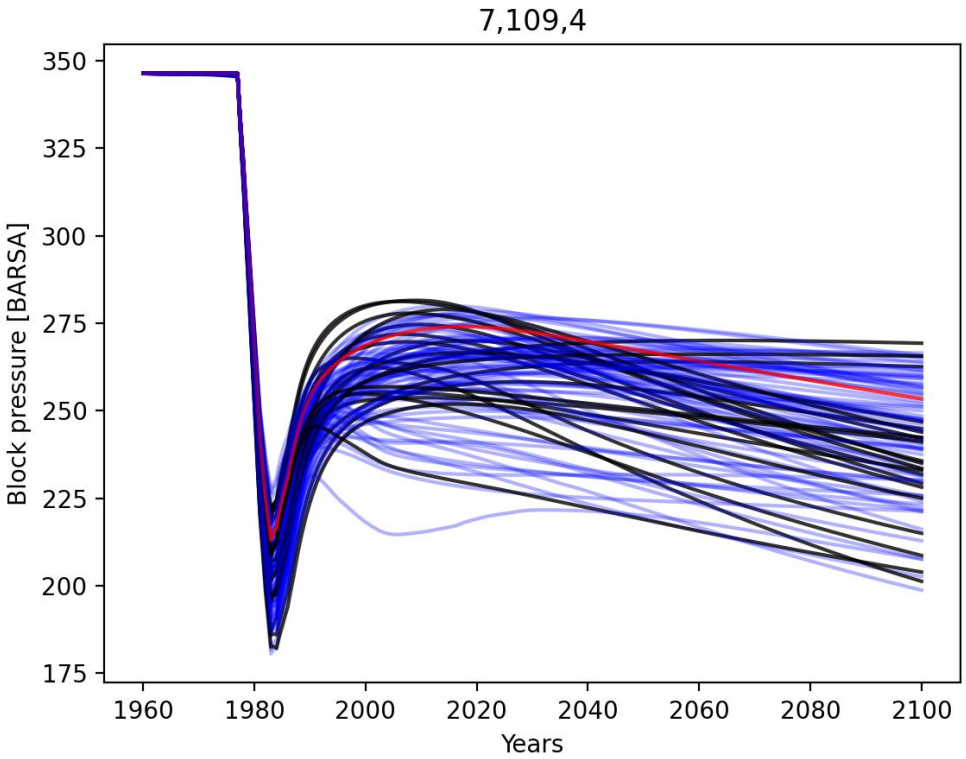
7,109,4
Block pressure [BARSA]
350
325
300
275
250
225
200
175
1960
1980
2000
2020
2040
2060
2080
2100
Years

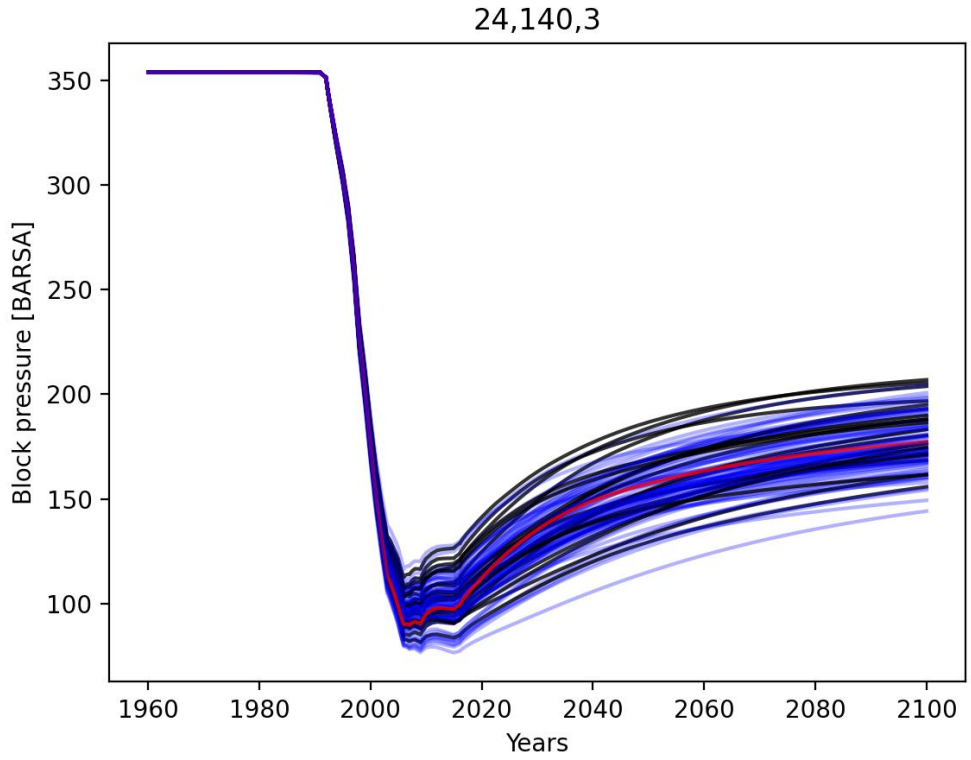
24,140,3
Block pressure [BARSA]
350
300
250
200
150
100
1960
1980
2000
2020
2040
2060
2080
2100
Years

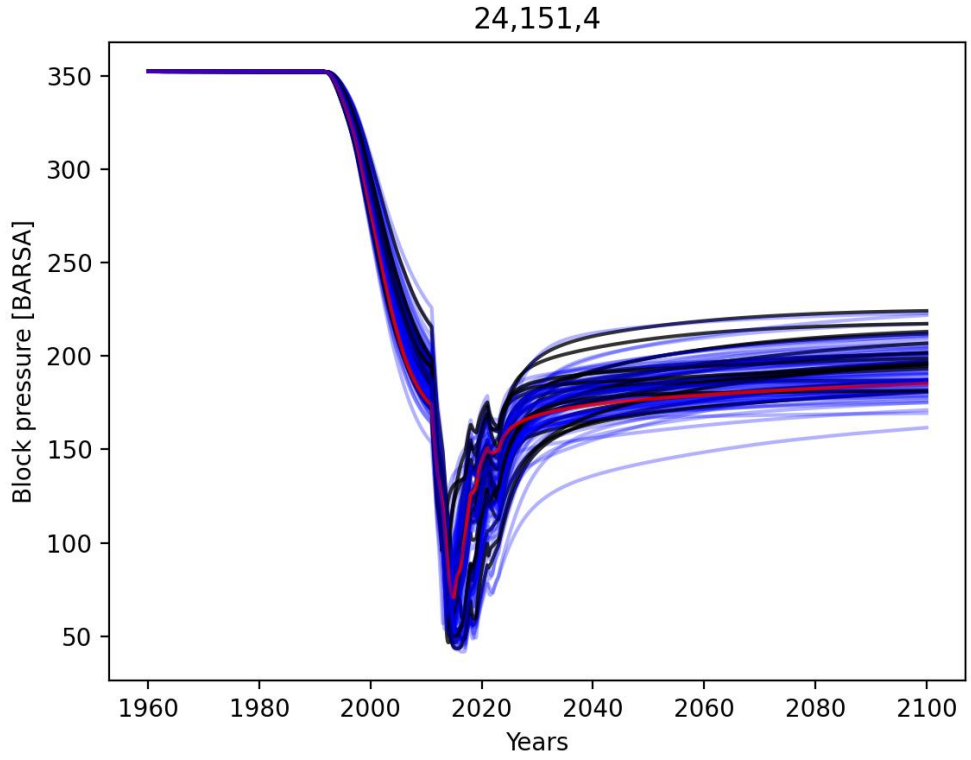
24,151,4
Block pressure [BARSA]
350
300
250
200
150
100
50
1960
1980
2000
2020
2040
2060
2080
2100
Years

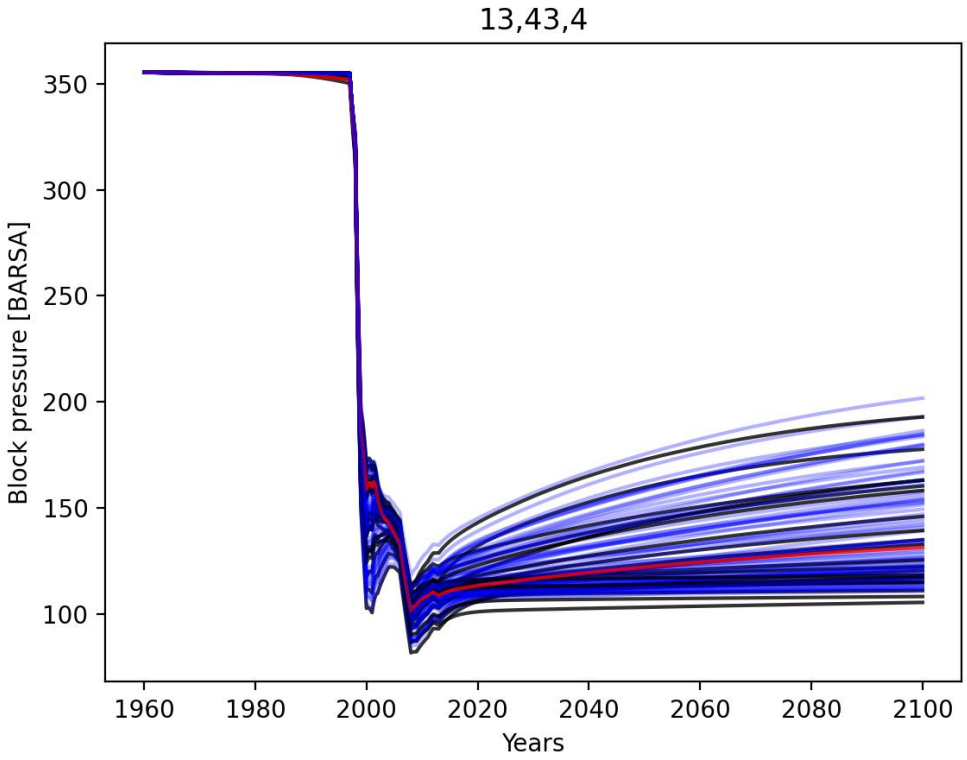
13,43,4
Block pressure [BARSA]
350
300
250
200
150
100
1960
1980
2000
2020
2040
2060
2080
2100
Years

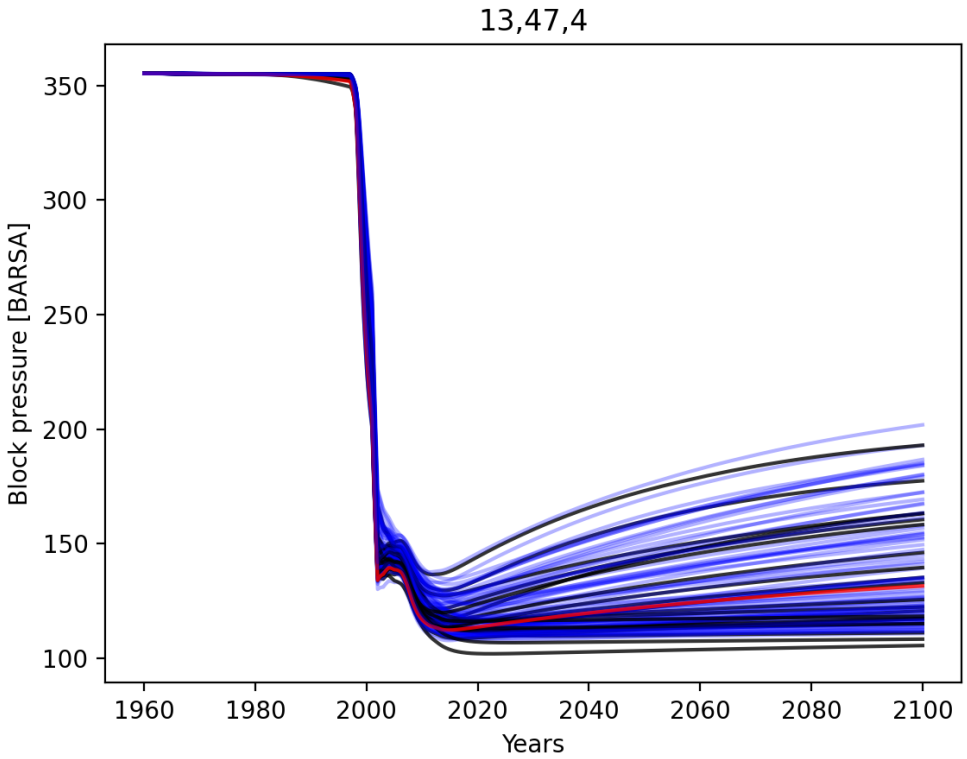
13,47,4
Block pressure [BARSA]
350
300
250
200
150
100
1960
1980
2000
2020
2040
2060
2080
2100
Years

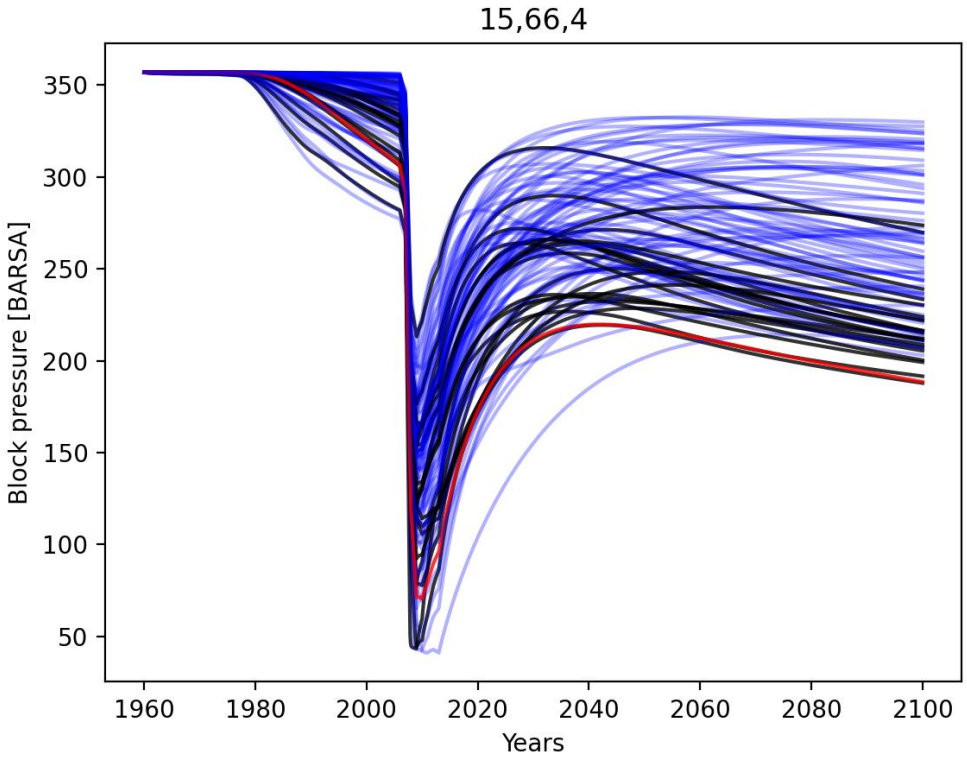
15,66,4
Block pressure [BARSA]
350
300
250
200
150
100
50
1960
1980
2000
2020
2040
2060
2080
2100
Years

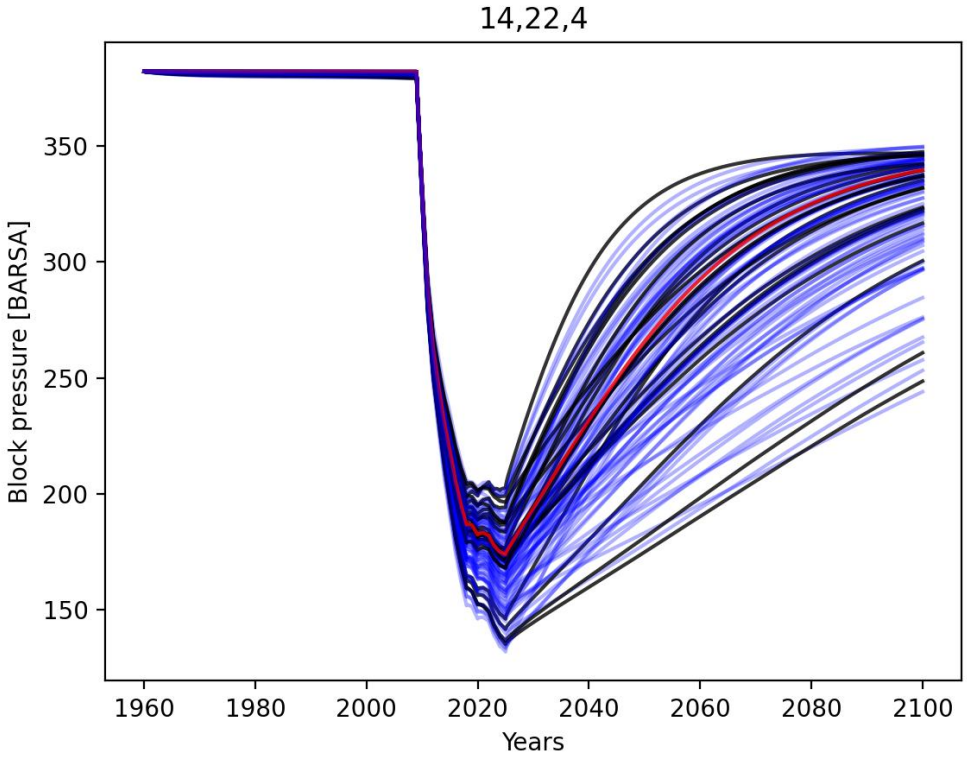
14,22,4
Block pressure [BARSA]
350
300
250
200
150
1960
1980
2000
2020
2040
2060
2080
2100
Years

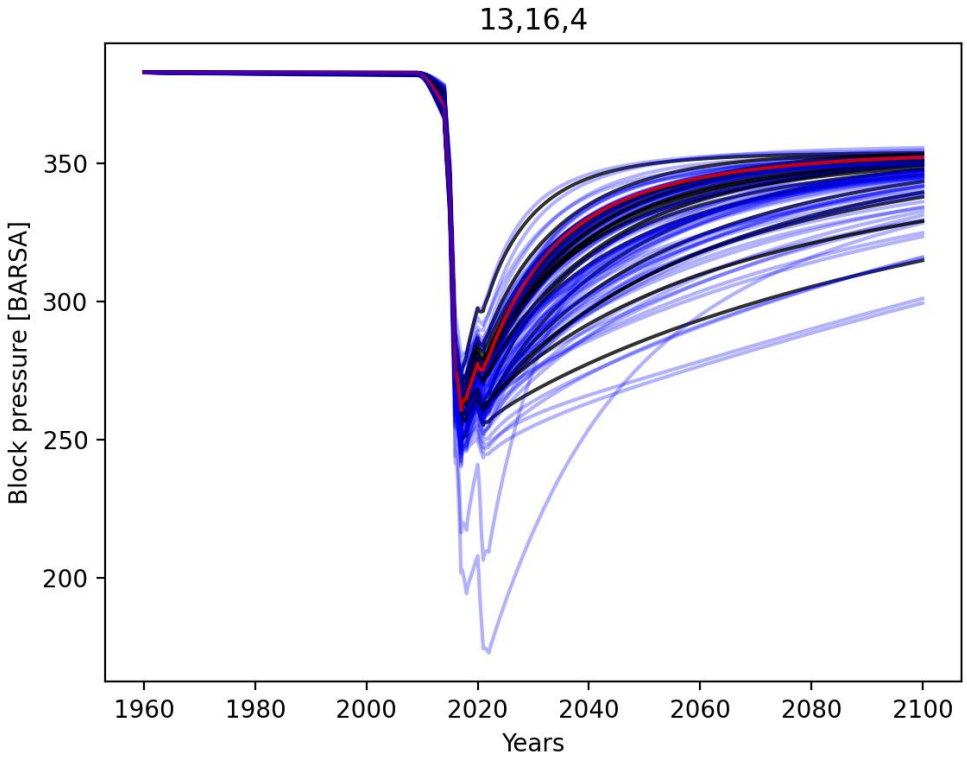
13,16,4
Block pressure [BARSA]
350
300
250
200
1960
1980
2000
2020
2040
2060
2080
2100
Years

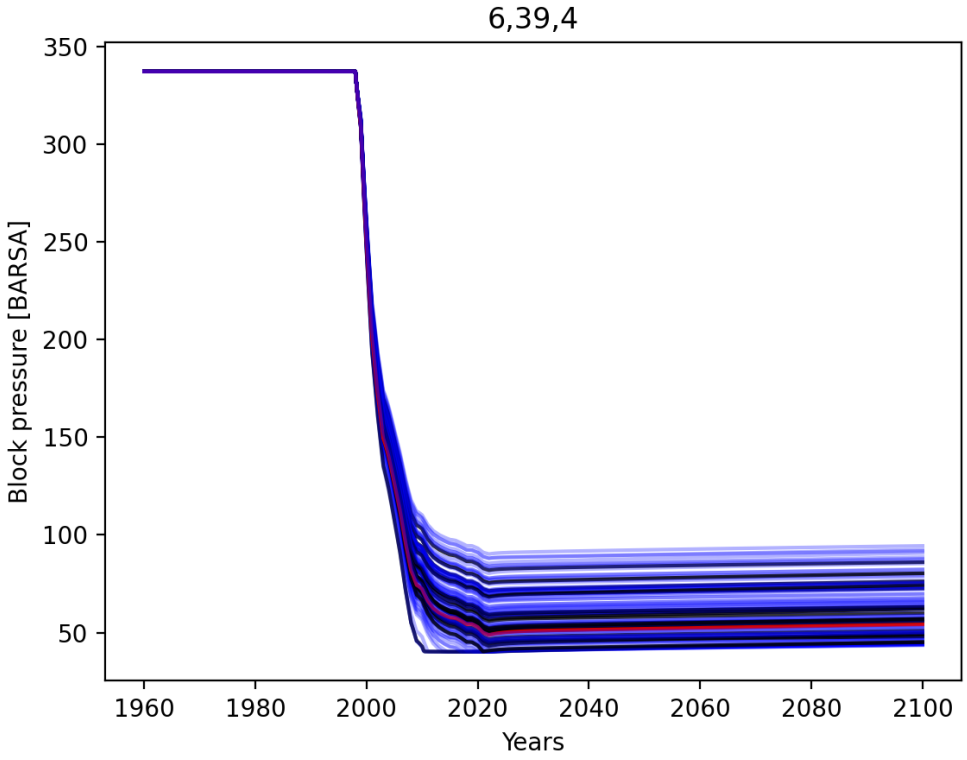
6,39,4
Block pressure [BARSA]
350
300
250
200
150
100
50
1960
1980
2000
2020
2040
2060
2080
2100
Years

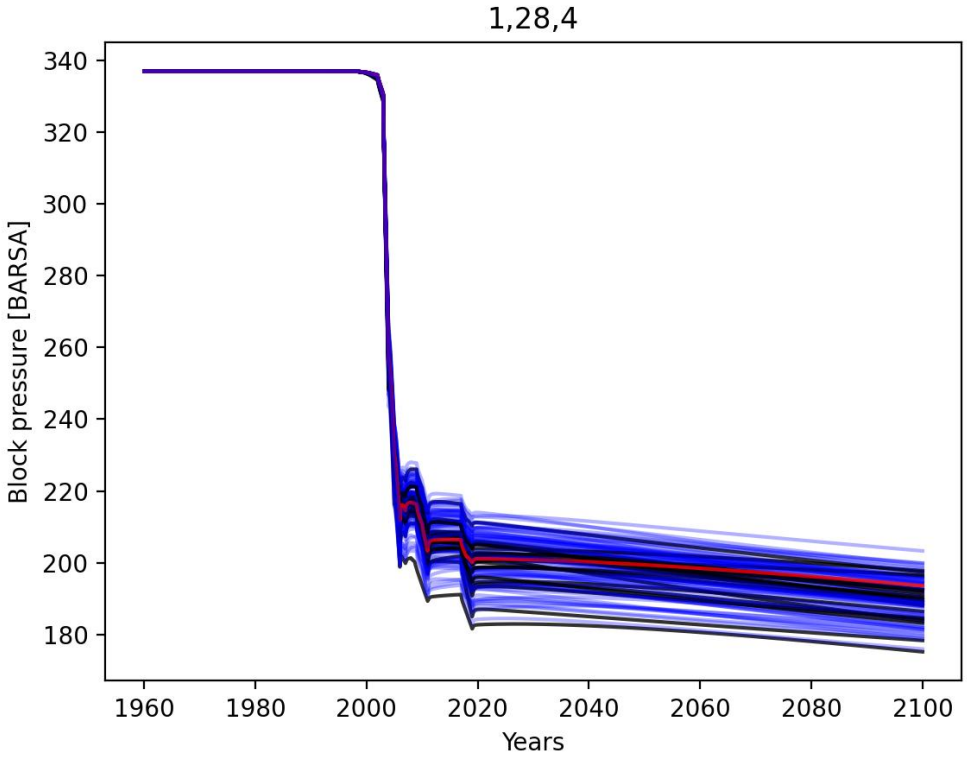
1,28,4
Block pressure [BARSA]
340
320
300
280
260
240
220
200
180
1960
1980
2000
2020
2040
2060
2080
2100
Years

Appendix D Hazard results for individual years

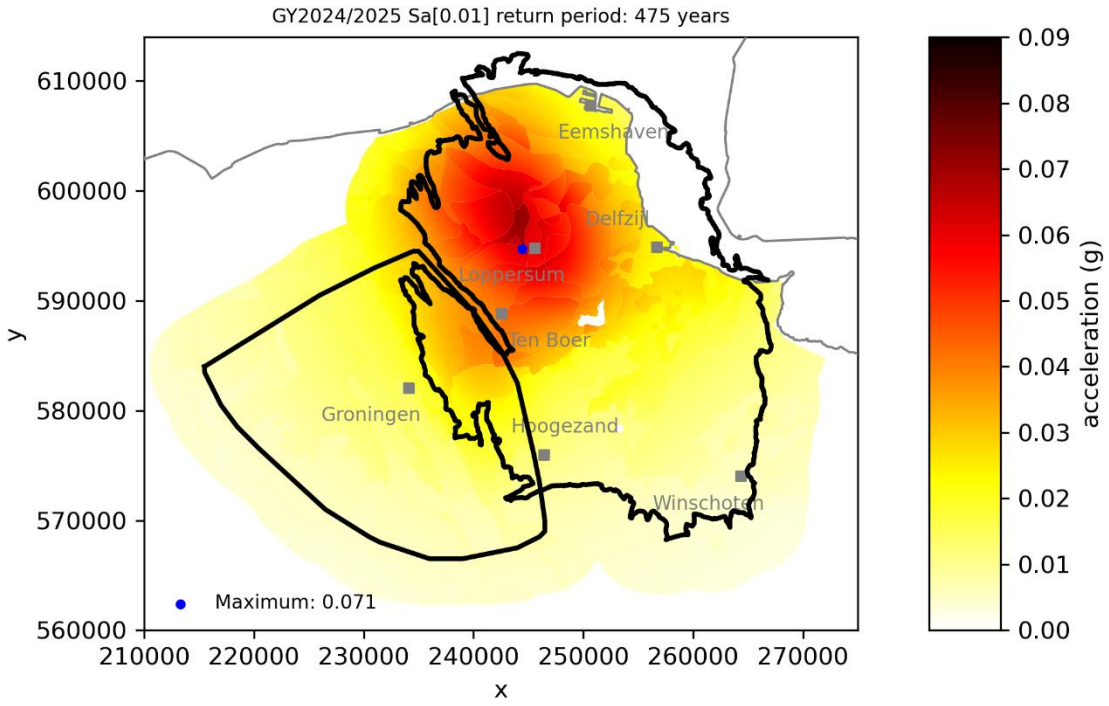

Figure D.1: Hazard maps for PGA at 475 years for gas year 2024/2025

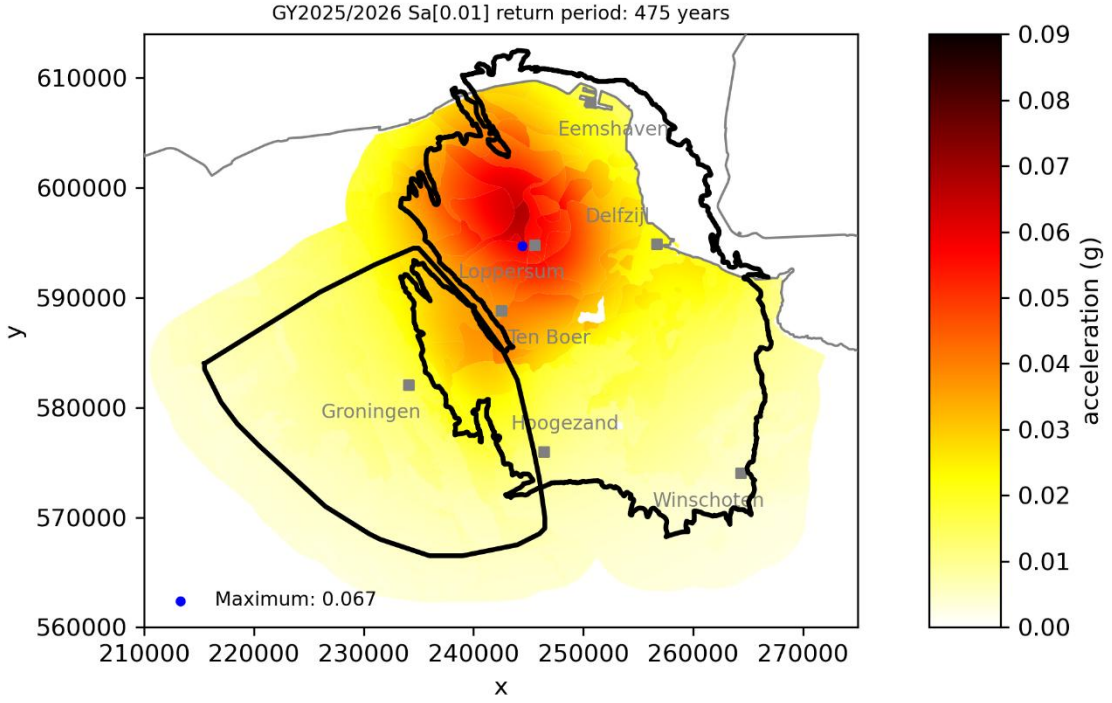

Figure D.2: Hazard maps for PGA at 475 years for gas year 2025/2026

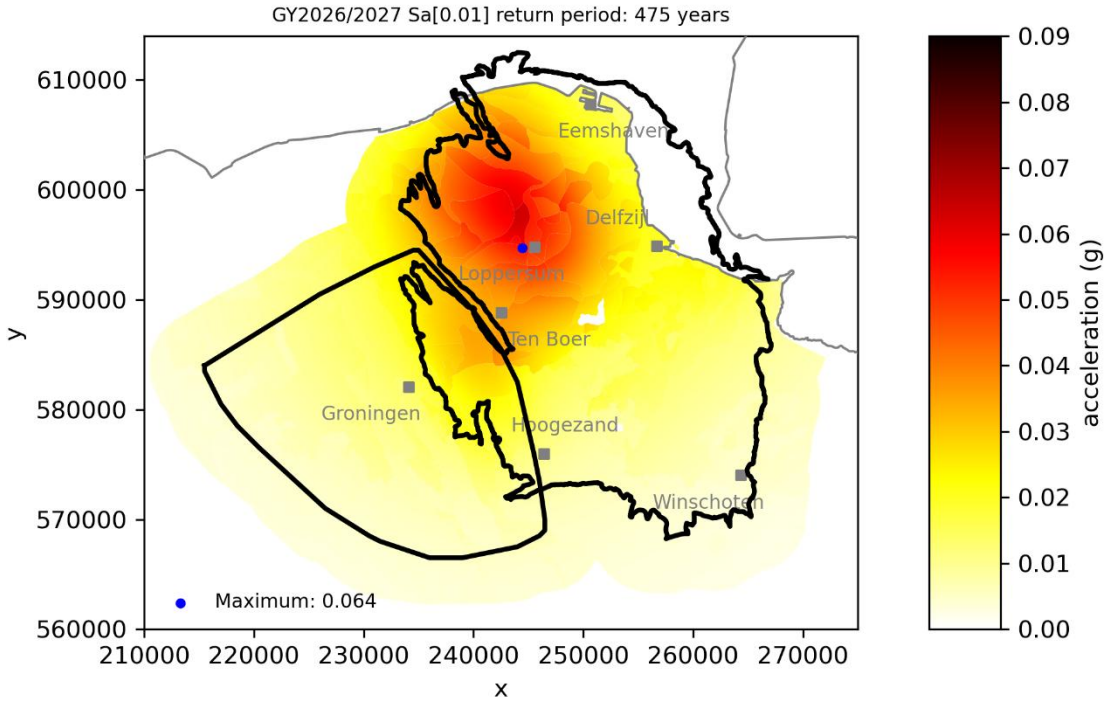

Figure D.3: Hazard maps for PGA at 475 years for gas year 2026/2027

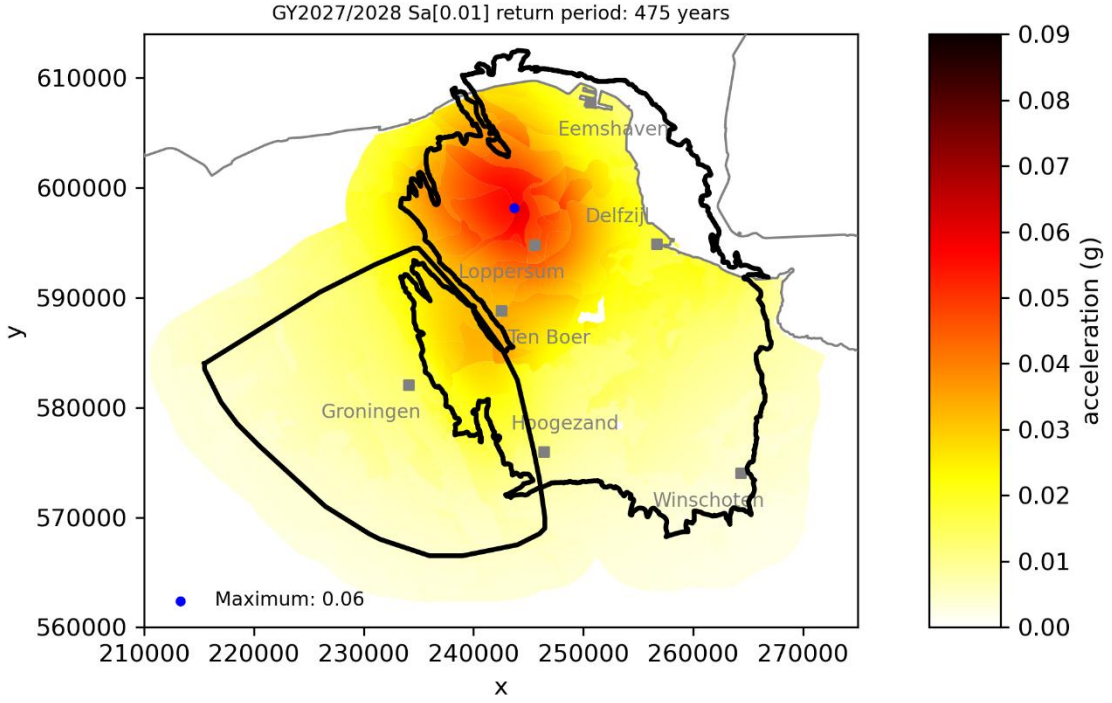

Figure D.4: Hazard maps for PGA at 475 years for gas year 2027/2028

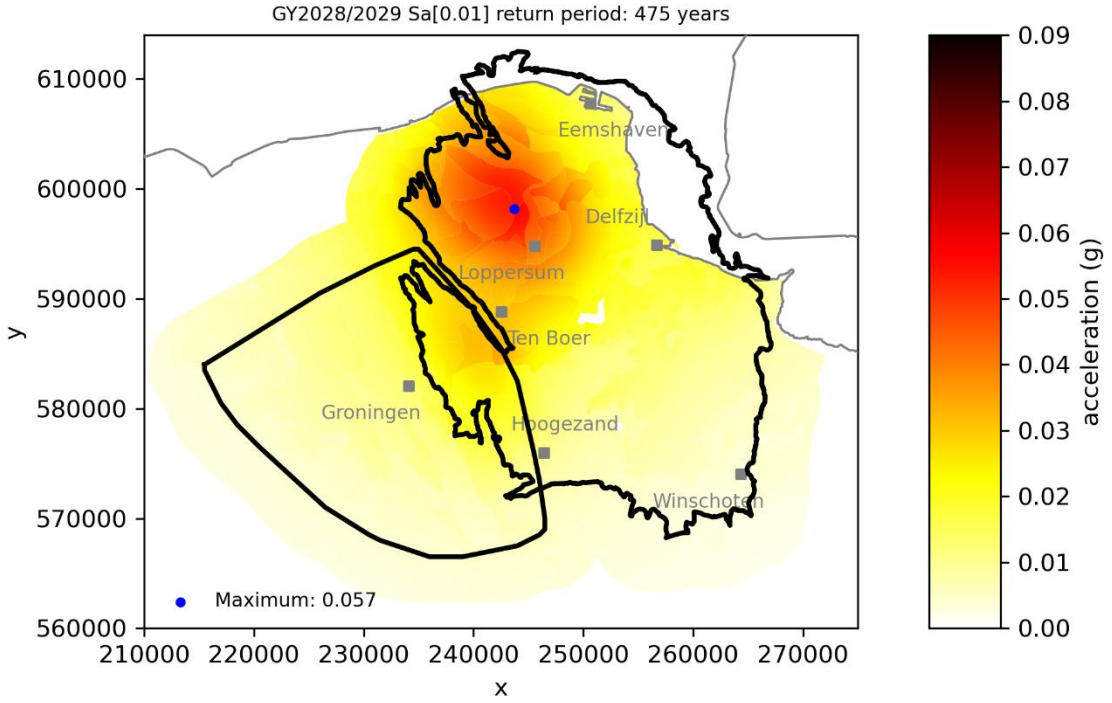

Figure D.5: Hazard maps for PGA at 475 years for gas year 2028/2029

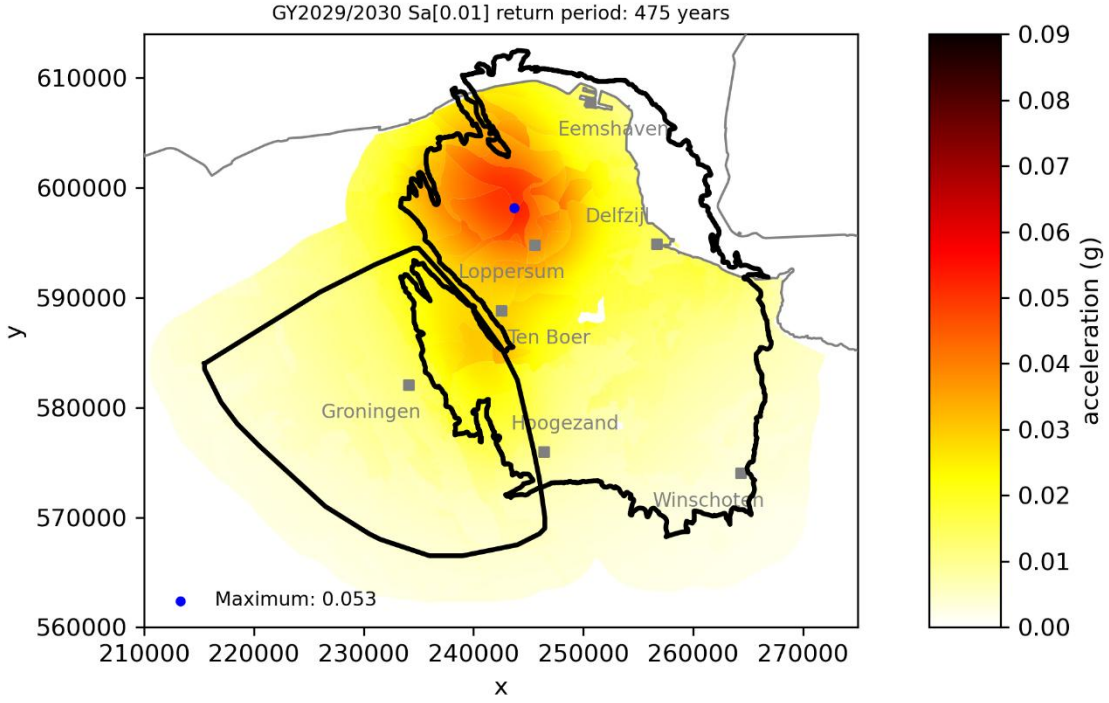

Figure D.6: Hazard maps for PGA at 475 years for gas year 2029/2030

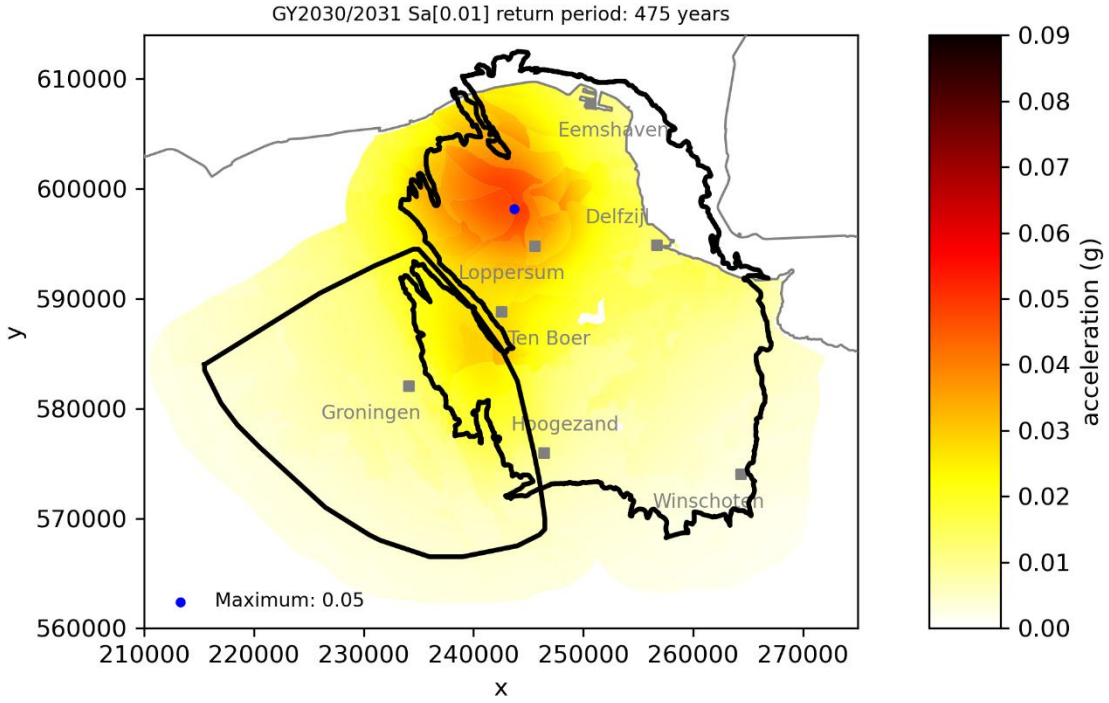

Figure D.7: Hazard maps for PGA at 475 years for gas year 2030/2031

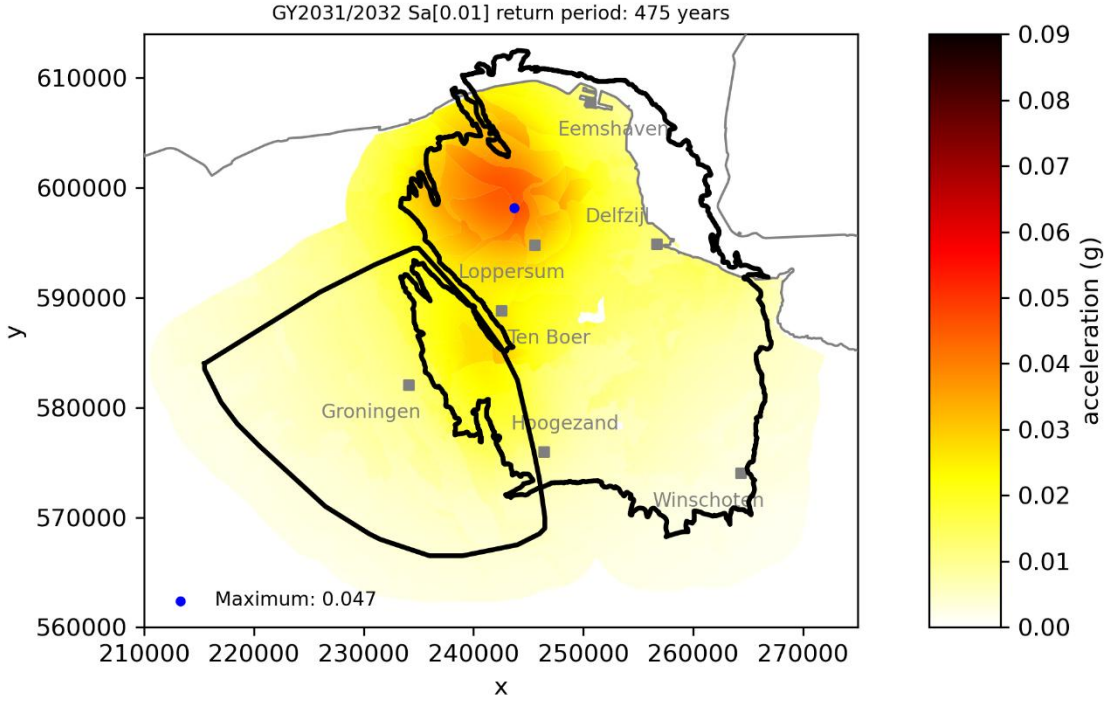

Figure D.8: Hazard maps for PGA at 475 years for gas year 2031/2032

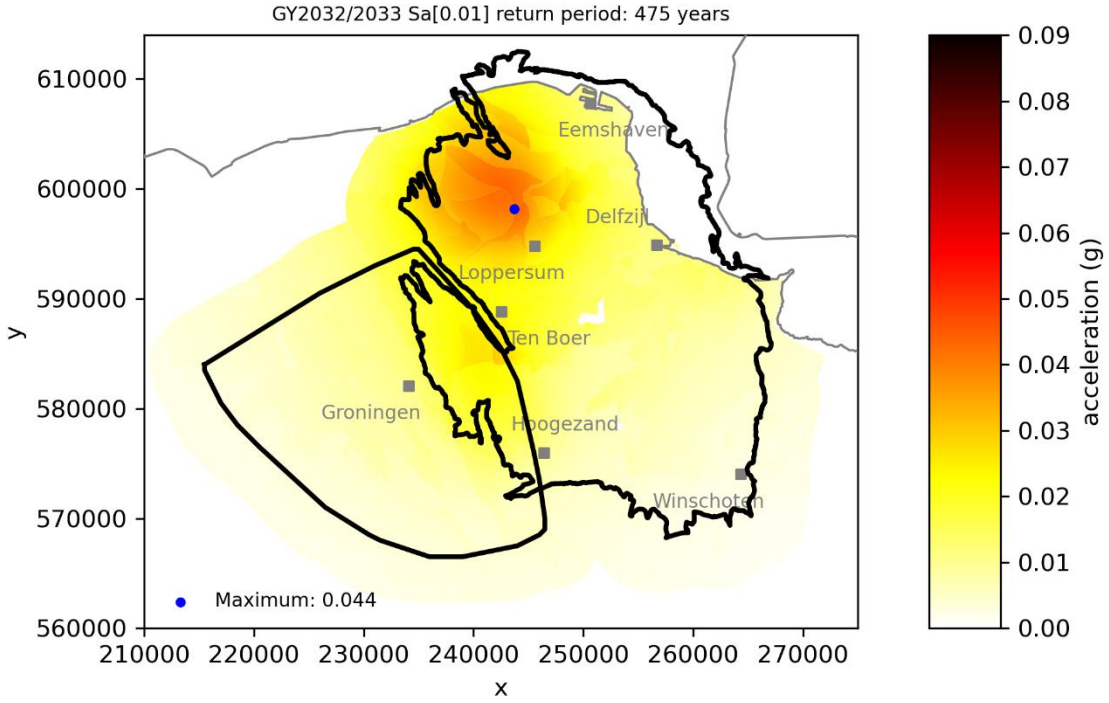

Figure D.9: Hazard maps for PGA at 475 years for gas year 2032/2033

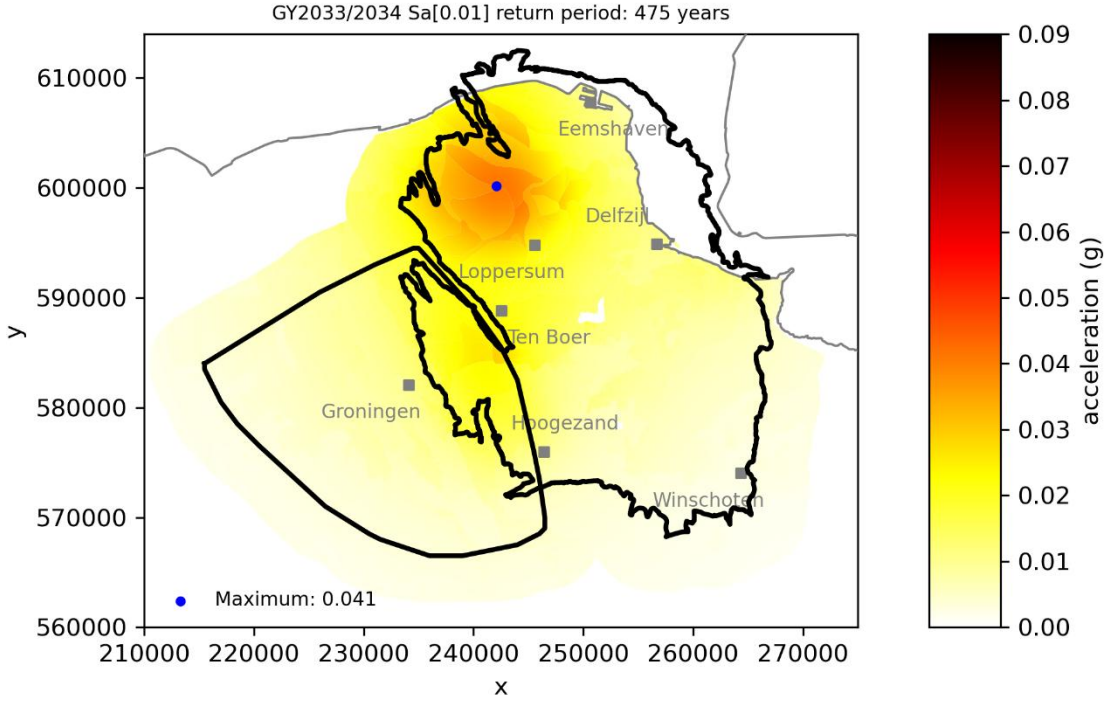

Figure D.10: Hazard maps for PGA at 475 years for gas year 2033/2034

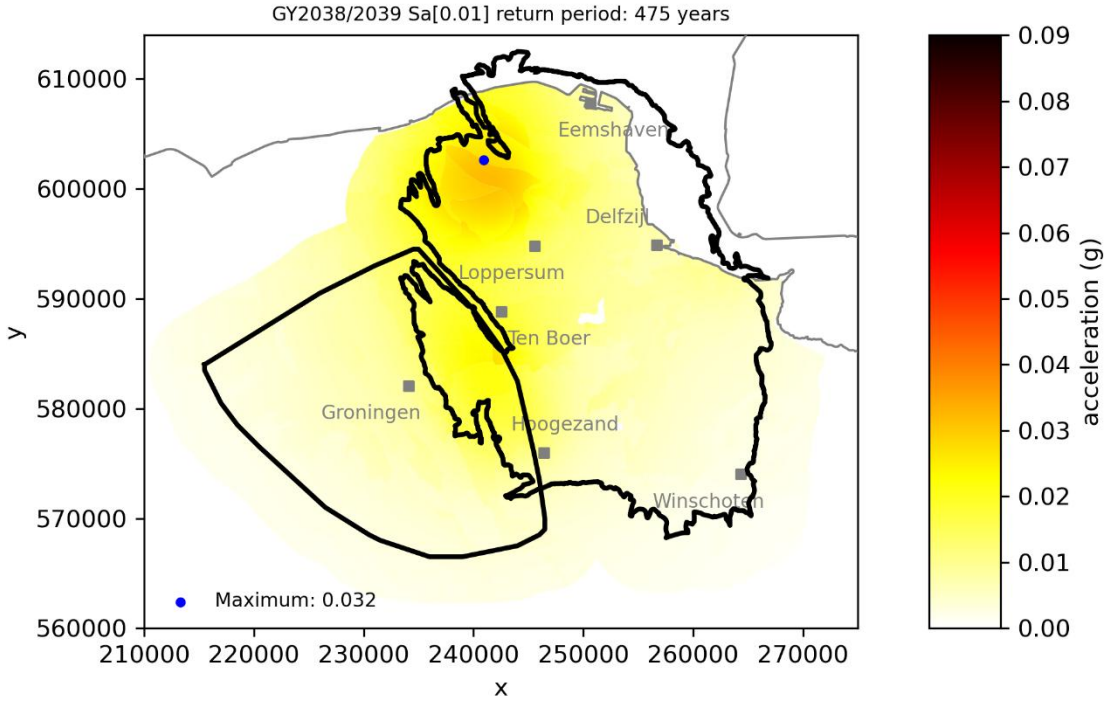

Figure D.11: Hazard maps for PGA at 475 years for gas year 2038/2039

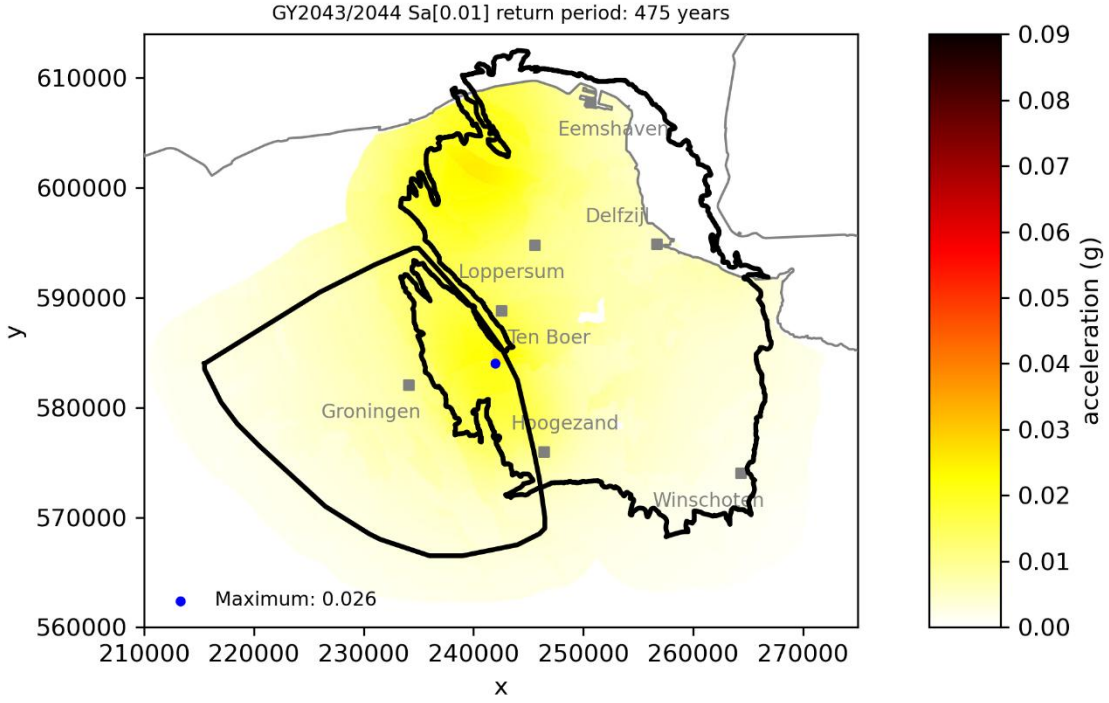

Figure D.12: Hazard maps for PGA at 475 years for gas year 2043/2044

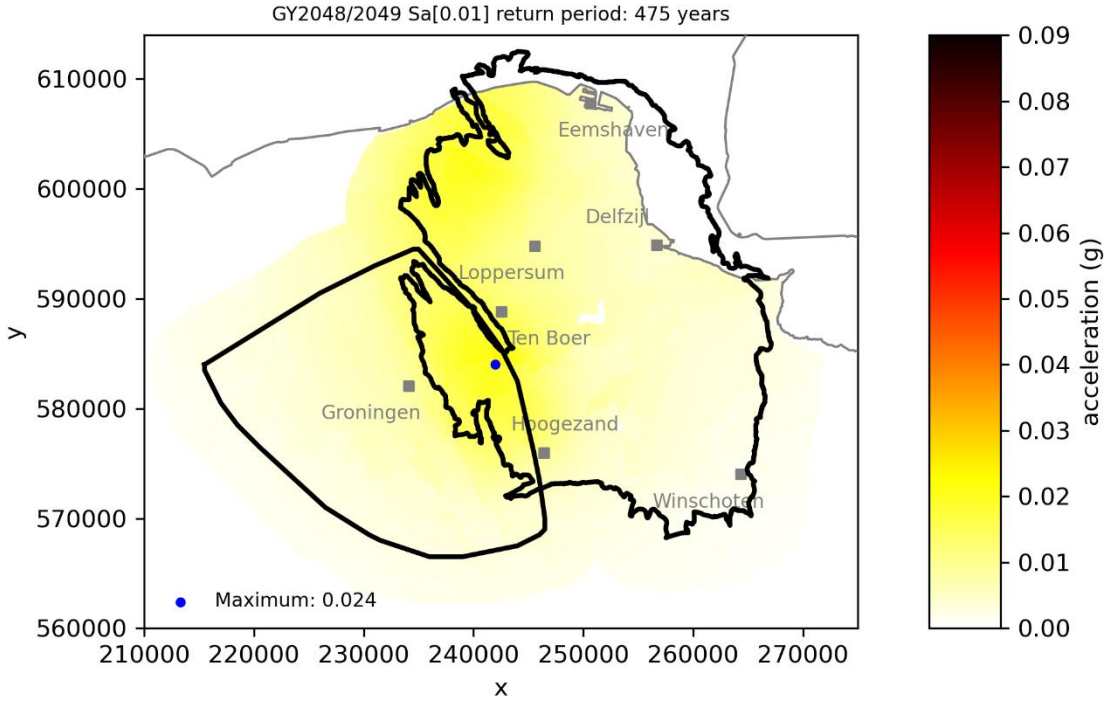

Figure D.13: Hazard maps for PGA at 475 years for gas year 2048/2049

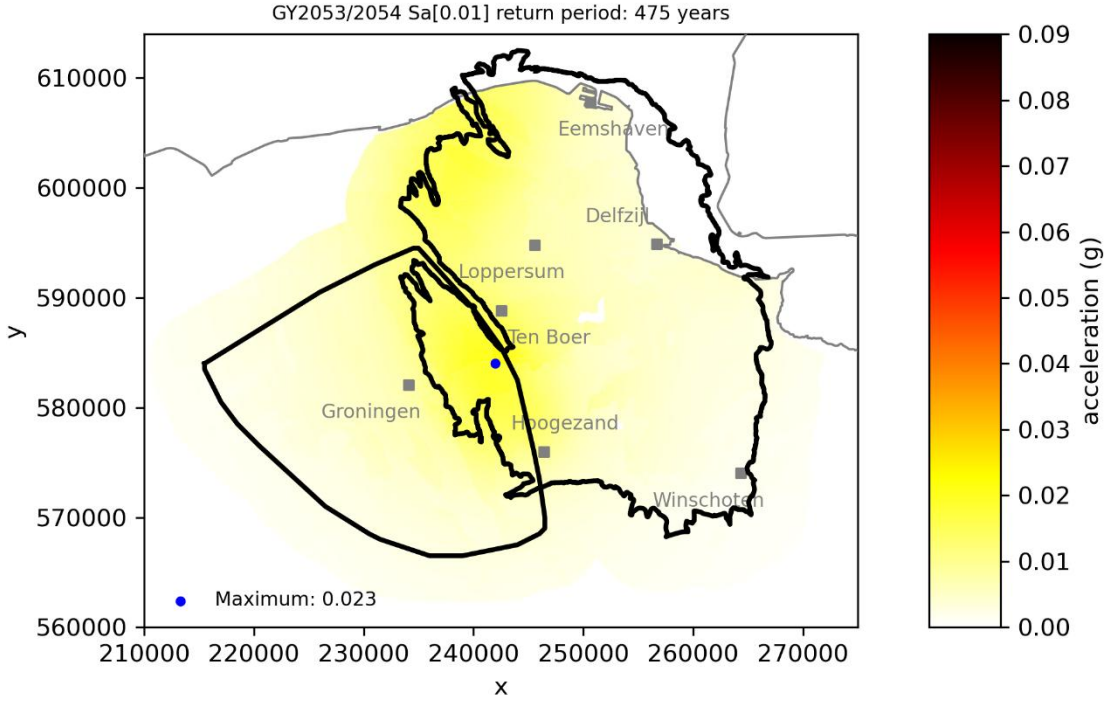

Figure D.14: Hazard maps for PGA at 475 years for gas year 2053/2054

Appendix E Extended site response analysis to the SW aquifer of the Groningen gas field

This work has been conducted and reported by Deltares as part of the KEM-19b project.

E.1 Introduction

In this memo we describe the methodology followed to produce the geological model including the data sources and criteria established for merging the different model sections. The report also contains a description and explanation of the shear-wave velocity profile (Vs) construction and the choices made regarding the available data sources. Finally, we summarize of the parameters used to produce the amplification factors through STRATA.

E.2 Methodology

E.2.1 Shear-wave velocity profiles (Vs)

The profiles used need the following information to calculate the amplification factor: mean Vs value, sampled Vs value and 'soil type': a combination of stratigraphy and lithology.

In the Groningen Ground Motion Model (GMM) Vs profiles were reconstructed using the following approach and data (for details see Bommer et al. 2021):
From surface level to NAP -50 m, soil type and Vs were derived from and related to the GeoTOP model from TNO Geological Survey Netherlands (TNO-GSN).
Soil type below NAP -50 m: is related to an expert schematization of the subsurface per geological zone with a stochastic approach, till the base of the Breda Formation (this is the base of the Upper North Sea Group). The Middle and Lower North Sea group were treated as one soil type; at the base of this unit, the top of Cretaceous, bedrock was modelled.
Vs below NAP -50 m: is based on two models: MEI – till 125 m - and Sonic – till bedrock. MEI values are used till the depth where it is higher than the Vs from the Sonic data, below that depth Sonic values are used. Vs at bedrock was fixed 1400 m/s.

For the KEM-19b area the MEI and Sonic models of the Vs values are not available – only in the overlapping area – and no expert schematization is available or part of the current study. Therefore, an alternative approach is followed to construct the profiles in the KEM-19b area, which is described in Section E.2.1.1 and E.2.1.2.

E.2.1.1 Shear-wave velocity profiles (Vs) for KEM-19b area

For the KEM study area the MEI and Sonic data are not available, except for the overlapping area with the Groningen GMM (Figure E 2.1). Therefore, in the entire KEM area, Vs profiles have been based on the values from the Groningen area. No correlation was found between soil type and Vs in the Groningen GMM, however, until the base of the Breda Formation there is a relatively small variation in the Vs values. The Vs shows a linear relation with depth, with an inflection point at NAP -350 m (Figure E 2.2). For the profiles in the KEM-19b area the mean Vs values up to the base of the Breda Formation uses the average values (blue line), for the sampled Vs value a random draw from a normal distribution is used, using presented averages

and standard deviations. In Table E1 and Table E2 all values for the MEI and Sonic Vs can be found.

Below the base of the Breda Formation, the Vs values don't show a linear relationship with depth. They show a typical pattern where Vs increases from the base of the Breda Formation to the top of the Brussels Sand Formation – a subunit within the Middle and Lower North Sea group. From the top to the base of the Brussels Sand Formation the Vs decreases. Below the base the Brussels Sand Formation, till the bedrock, the Vs has an almost constant value with relatively small spread (Figure E 2.3).
For the KEM-19b area the Vs value at the top of the Brussels Sands is related to the Vs value at the base of the Breda Formation, based on the values in the overlapping area this is a factor 1.077 (so Vs is 7.7% higher). The Vs is increased linearly between the base of the Breda Formation and the top of the Brussels Sands. The Vs below the Brussels Sands has an average Vs of 594.52 (m/s) with a standard deviation of 24.78. From the top to the base of the Brussels Sands the Vs is decreased linearly (to 594.52 m/s). Below the Brussels Sands the average value is used till bedrock, where Vs is fixed at 1400 m/s.

On four selected Vs profiles from the Groningen GMM the linear transfer function is calculated for 1) the mean Vs profile, 2) the sampled Vs profile and 3) the Vs profile as reconstructed using the above described method (see Figure E 2.4). These results show that the reconstructed profiles, even if deviating from the Vs mean profile, give a very similar transfer function, and show less variation than the sampled Vs profile. The latter has largest differences with the mean Vs in the upper part, which is based on GeoTOP (this part of the profile is constructed by TNO-GSN).

E.2.1.2 Soil type for the KEM19-b area

For the KEM area the vertical boundaries and soil type are based on three geological models from TNO-GSN: Digital Geological Model (DGM), REGIS II and DGM Deep. The Brussels Sands Formation boundaries were only used to reconstruct the Vs values (see previous section). The DGM model was adjusted by TNO-GSN for the KEM area including newly mapped base of the Peelo Formation.
The DGM has information on the stratigraphical units up to the base of the Breda Formation. The lithology is not available, but for most formations only one type of lithology is expected like in the schematization for the Groningen GMM. Only in the Peelo Formation and the Oosterhout Formation both a sandy lithology and a clayey lithology is expected. To include these, the clayey units from REGIS II were included: Peelo clay unit 1 and unit 2 (lithology 'clay' used for soil type), Oosterhout complex unit and clayey unit 1 (lithology 'clayey sand' used for soil type). For the depth of the bedrock, the DGM deep boundary of base of the Middle and Lower North Sea group was used.

Between the different geological models (minor) inconsistencies were present at some locations in the study area. These were corrected as follows:
The REGIS II units were corrected with the updated DGM boundaries: either units were entirely removed if the Peelo base was deeper, otherwise the top or base were adjusted to the Peelo base depth;
At locations where the Brussels Sands base is absent but the top is present, the unit was assumed absent;
Where Brussels Sands top is shallower than the base of the Breda Formation, the top is changed to the same depth as the base of the Breda Formation;

Where the bedrock depth is shallower than the base of the Breda Formation, the top is changed to the same depth as the base of the Breda Formation.

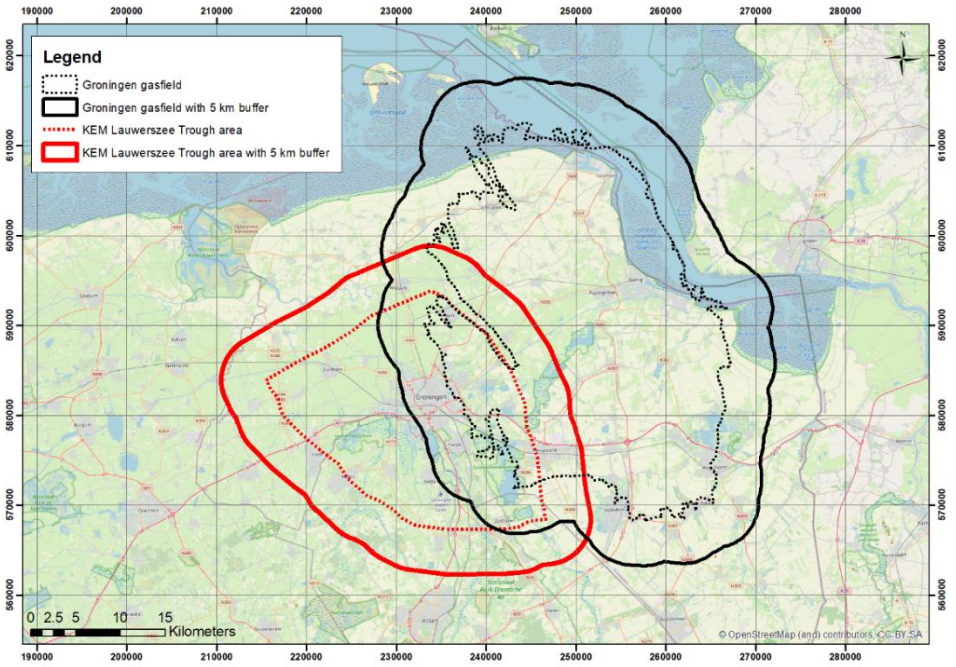

Figure E 2.1: Map of the KEM Lauwerszee Trough, study area in this report, and the Groningen area

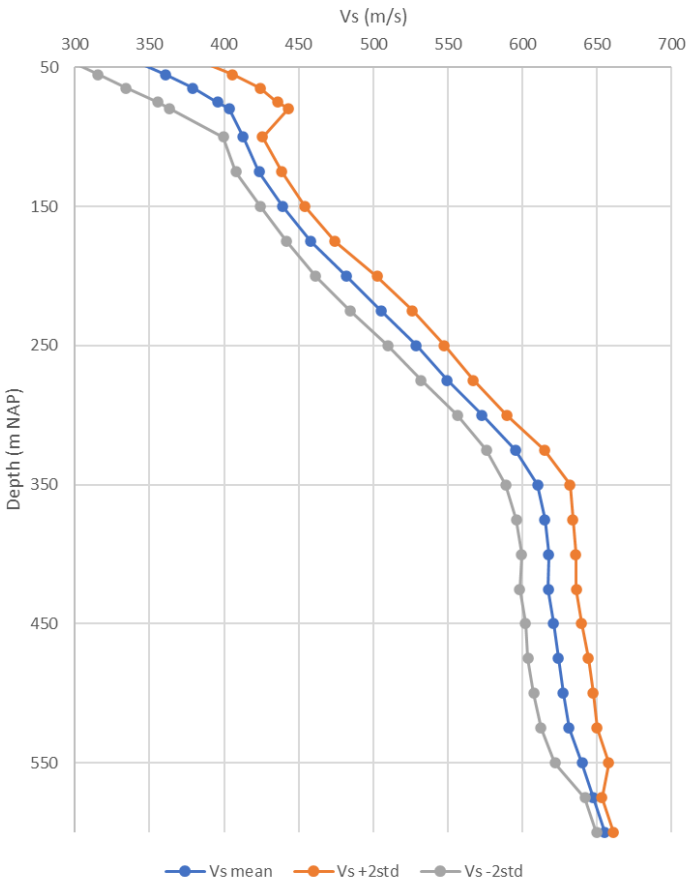

Figure E 2.2: Vs profile based on MEI and Sonic data, the blue line is the average Vs at specified depth, grey and orange lines are respectively average minus two standard deviations and average plus two standard deviations.

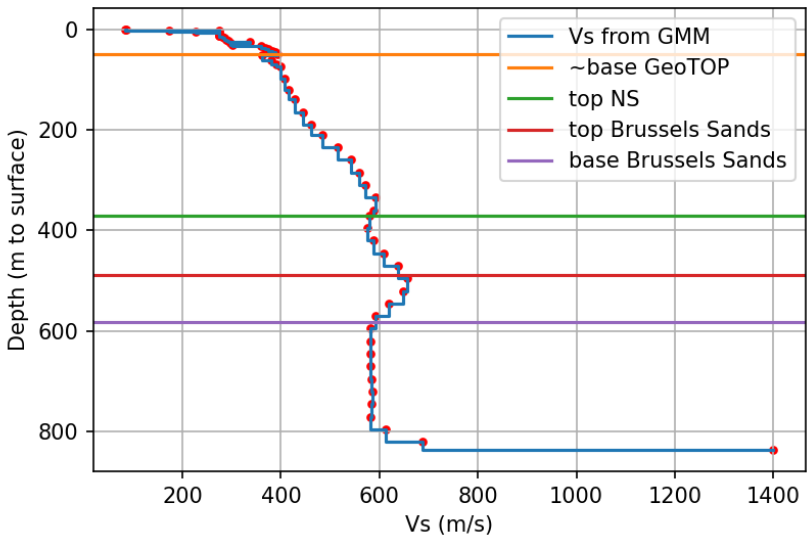

Figure E 2.3: Example of a Vs profile from the Groningen GMM (at x=236050, y=574250). NS is the Middle and Lower North Sea group, depth taken from the DGM Deep geological model (TNO-GSN). Top and base of Brussels Sands are based on the mapped surfaces from TNO-GSN

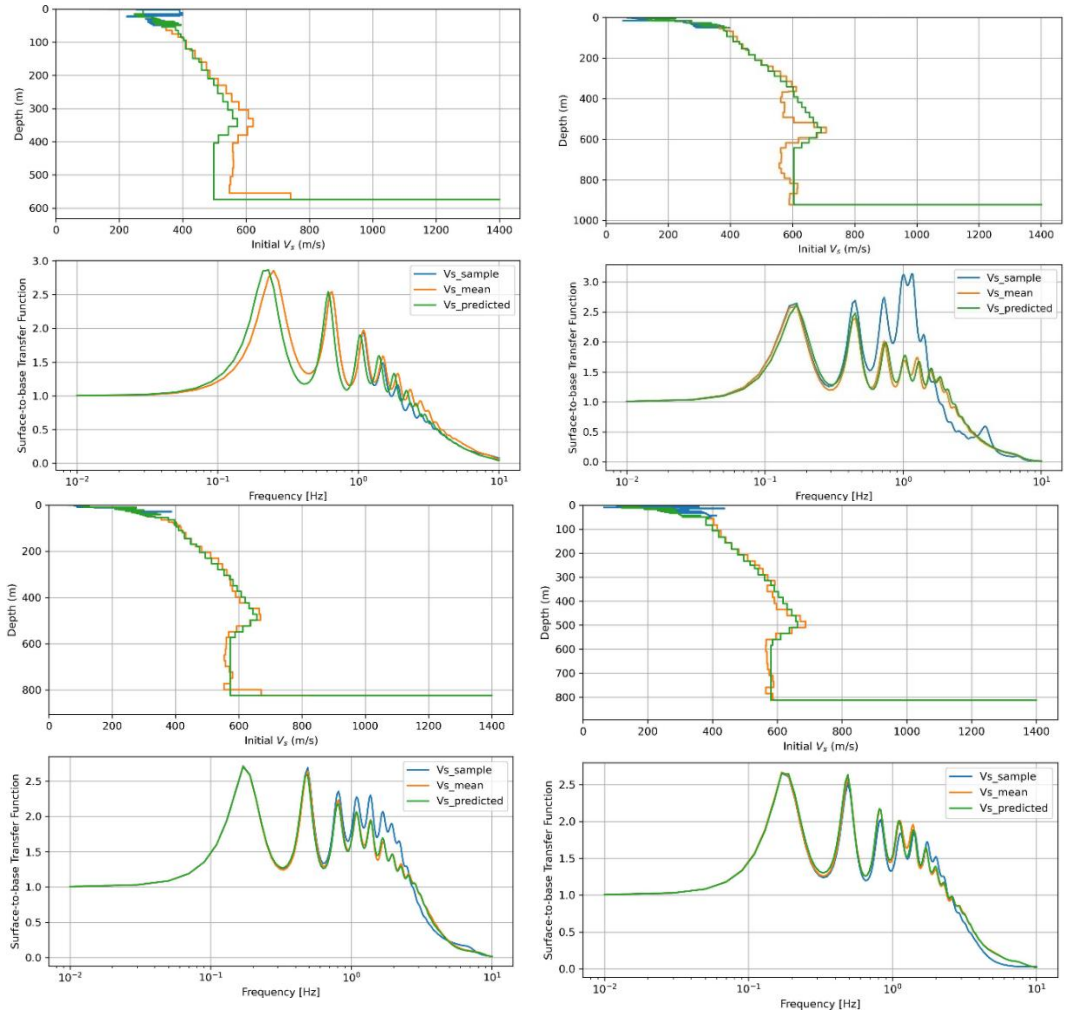

Figure E 2.4: Effect of four selected profiles on the linear transfer function.

E.2.1.3 Geological zonation

The boundaries of the geological zonation have been created by TNO-GSN and delivered as a shapefile. These zones are used to group the final results of the STRATA calculations, but have no influence on the creation of the Vs profiles or the calculation of the amplification factor. Since the results are analyzed per zone, a minimum number of profiles should be within each zone. In the Groningen GMM zonation the smallest zone had 45 locations, this was used as a minimum for the new study area. Zones with less locations were therefore merged with neighboring zones based on expert judgement, taking into account a.o. the general geological sequence. In Table E3 the remapped zones are given.

E.2.2 Summary of input parameters for STRATA calculations

The site response calculations are performed using the STRATA workflow version 7 implemented in Groningen area. The main output are the amplification factors computed for all profiles per zone. The computations are carried out considering two scenarios, namely: (1) Vs mean and (2) Vs sample. In the study area one soil type is present which is absent in the Groningen GMM: the Maassluis Formation. This formation occurs in the western part of the study area between the Peize-Waalre Formation and the Oosterhout Formation. Within the study area the formation has a limited thickness. The soil properties for this formation are taken from those of the Oosterhout Formation and Breda Formation.

Calculation Dmin per geological zone:

$$D_{fact} = \begin{cases} 1.7 & \text{for } V_{S30} \leq 119.6\ m/s \\ \exp\left(5.2874 - 0.9942 \ln\left(V_{S30}\right)\right) & \text{for } 119.6\ m/s < V_{S30} \leq 204.0\ m/s \\ 1 & \text{for } V_{S30} > 204.0\ m/s \end{cases}$$

Equation from Bommer et al. (2021).

E.3 Summary of results

E.3.1 Description of Vs profiles derived for the new area

In total 105,192 profiles in the study area were created till the bedrock. Visual inspection of the final results is performed on the locations overlapping with the Groningen GMM. The new approach give a good match for the upper part of the profile, up to the base of the Breda Formation. The part below shows larger deviations from the original profile, but still resembles it quite well and good enough to have relatively small effect on the linear transfer function (see also Section E.2.1.1). Some differences are caused by a different depth of the base of the Breda and the depth of the bedrock between the values used in this study and in the Groningen GMM. These surfaces were remapped for the Groningen GMM area specifically and not available for the entire KEM study area. Three examples of profiles are given in Figure E 3.1.

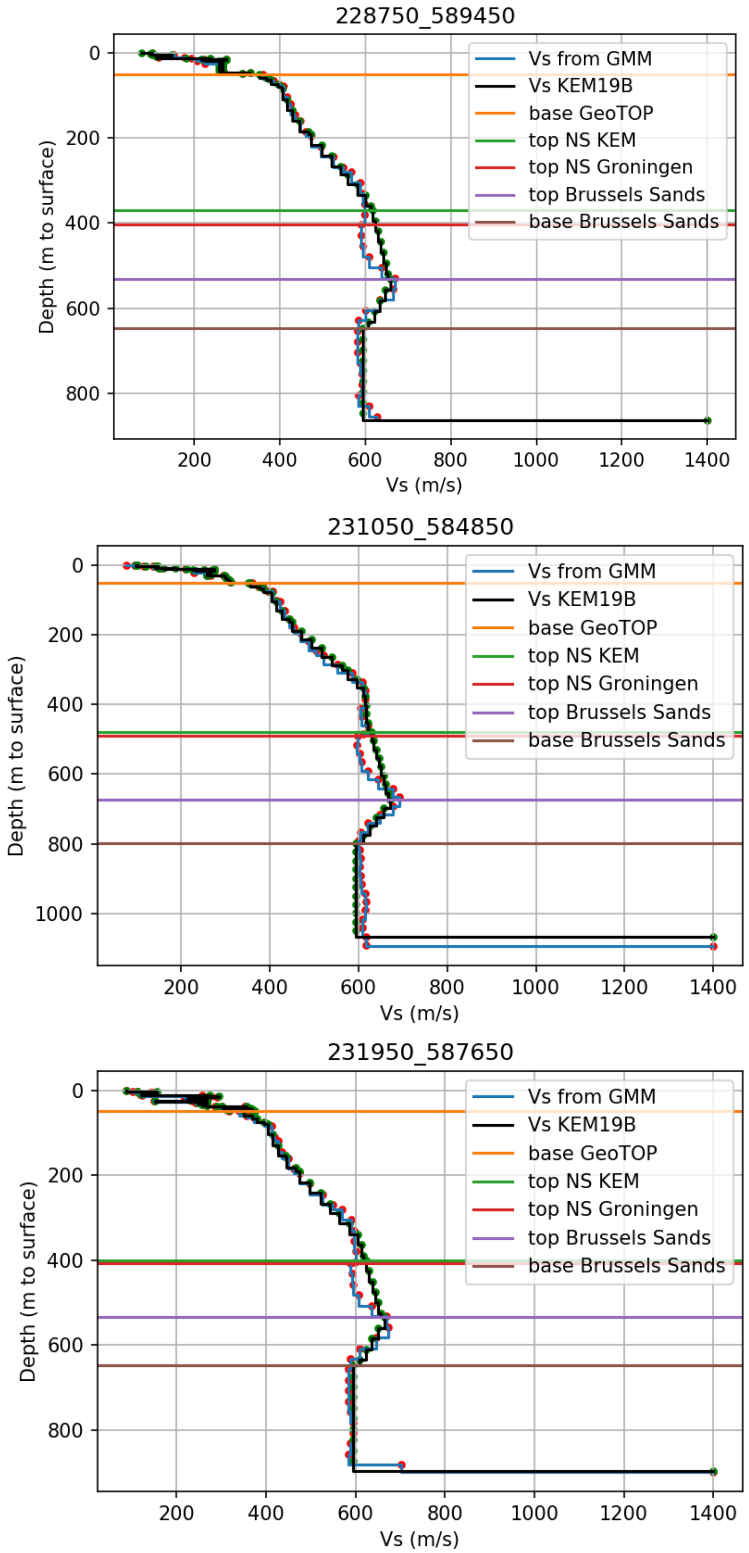

Figure E 3.1: Examples of reproduced Vs profiles (showing Vs mean) for three locations (coordinates in titles)

E.3.2 Description of STRATA input files

The STRATA outputs are generated with Python. The Python generated STRATA file is a combination of multiple data sources:

- GeoTOP model from TNO Geological Survey Netherlands.
- Digital Geological Model (DGM), REGIS II and DGM Deep.
- Derived VS profiles (paragraph E2).

The STRATA file is a .csv file that contains the following data columns:

- Location', 'X', 'Y': X and Y coordinates of the data location.
- Thickness: The thickness of individual layers.
- Depth: All data is interpolated or calculated for this depth interval.
- Stratigraphy, Lithology, and Soil Type: Formations are described in 'Stratigraphy'. The lithology that corresponds to this 'Stratigraphy' is set in the 'Lithology' and the 'Soil Type' is a combination of both.
- Vs mean: The mean S-wave velocity for each depth is dependent on the Soil Type. For the first 50 meters, this mean S-wave velocity comes from GeoTop. For the data below GeoTop, the mean VS is derived as described in paragraph 2.
- Vs sample: The sample S-wave velocity is a random draw from a normal distribution generated using the VS mean and the standard deviation. For the first 50 meters, this data is from GeoTop, for the deeper data, these values are derived as described in Section E.2.

The STRATA file is built up using the following workflow:

- GeoTop data is split for every unique location. The GeoTop data is translated into the STRATA file format and forms the first framework of the output.
- For every location, the depth is interpolated until the bedrock formation. Until the depth of the boundary between the MEI and Sonic data, the depth resolution of the data is set to 10 meters. Below, the resolution of the data is set to 25 meters. Every formation boundary is added in between the interpolated depths.
- The S-wave velocity is interpolated based on the depth of the key formation boundaries.
- Using the mean velocity data and the standard deviation, the sample VS is calculated for every given depth.
- Formation markers are interpolated between their base and top, corresponding lithologies are assigned and the soil type can be constructed using both values.
- Because of possible mismatches in the Geotop and MEI dataset for geological boundaries, it is possible that an unrealistic geological sequence is generated: Peelo-Appelscha-Peelo. From a geological viewpoint, this sequence is impossible and therefore, the Appelscha formation is removed from the dataset and replaced by Peelo.
- The output is generated per location and saved per geological zone defined by TNO.

E.3.3 Description of STRATA output files

The STRATA output files consists of text files that contain amplification factors per zone, computed for Vs mean and Vs sample. Each file contains the following relevant information: the name of the zone, X and Y coordinates, Earthquake Magnitude, epicentral distance, spectral acceleration of outcrop rock for various periods, and amplification factors for 24

structural periods between 0.01 – 5.0 seconds. An example of amplification factors for a single structural period is provided in Figure E 3.2.

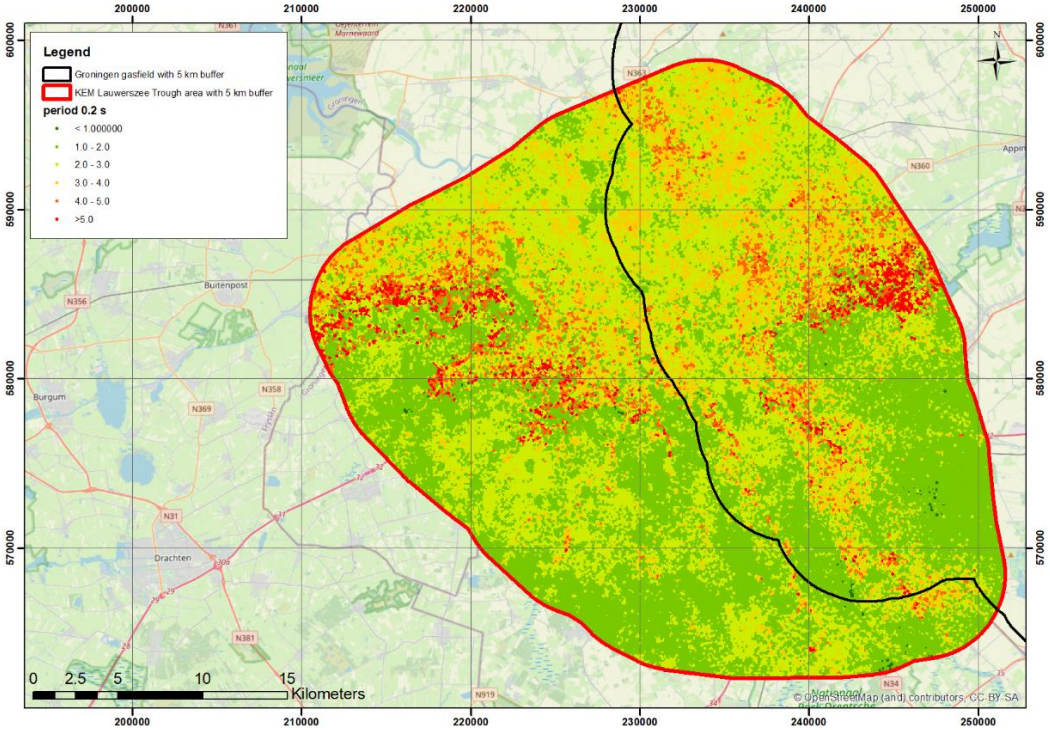

Figure E 3.2: Amplification factor based on mean Vs profiles for a period of 0.2 seconds.

Table E 1 Mean values and standard deviations of the MEI Vs model

Depth	Vs mean	Vs standard deviation
25	270.70	14.98
35	305.90	18.97
45	339.60	21.60
55	360.53	22.48
65	379.17	22.44
75	395.71	19.96
85	411.81	17.12
95	431.52	13.78
105	451.32	10.70
115	474.34	8.14

Table E 2 Mean values and standard deviations of the Sonic Vs model

Depth	Vs mean	Vs standard deviation
50	388.73	4.50
75	401.06	4.76
100	412.61	6.53
125	423.33	7.75
150	439.33	7.49

175	458.07	8.14
200	482.05	10.30
225	505.26	10.49
250	528.67	9.45
275	549.52	8.70
300	572.81	8.25
325	595.22	9.72
350	610.28	10.83
375	614.93	9.45
400	617.60	9.10
425	617.19	9.46
450	620.76	9.40
475	623.95	10.07
500	627.48	9.96
525	631.13	9.40
550	639.87	9.04
575	647.58	2.83

Table E 3 Remapped geological zones

Old zone ID	New zone ID
5	504
7	93
38	309
40	308
43	310
100	155
191	185
193	185
224	189
225	189
229	587
277	25
486	517
491	560
493	553
494	494
497	564
500	558
502	567
503	567
506	567
513	504

516	504
518	504
519	505
534	484
535	484
537	498
538	498
539	498
540	498
545	498
546	498
551	504
552	494
554	498
555	504
557	505
561	504
565	507
572	498
574	495
584	564
585	564
586	558

Energy & Materials Transition

Princetonlaan 6
3584 CB Utrecht
www.tno.nl

TNO innovation for life

TNO innovation for life

KEM-19b Seismicity estimates for potential subsurface operations

Part 2

TNO Public › TNO 2025 R10452
20 June 2025

TNO 2025 R10452 – 20 June 2025

KEM-19b
Seismicity estimates for potential subsurface operations

Part 2

Author(s)	S.Osinga, P.Fokker, S. Bottero

Classification report	TNO Public
Title	TNO Public
Report text	TNO Public
Number of pages	44 (excl. front and back cover)
Number of appendices	0
Sponsor	The Dutch Ministry of Economic Affairs and Climate
Programme name	Kennisprogramma Effecten van Mijnbouw - KEM program

Managementsamenvatting

Dit rapport beschrijft onderzoek naar de aardbevingseffecten van mogelijke toekomstige geothermische operaties in de zuidwestelijke aquifer van het Groningen gasveld aan de hand van verschillende benaderingen.

Allereerst onderzoeken we de ruimtelijke variabiliteit in *seismiciteitsneiging* (d.w.z. de neiging van het systeem om aardbevingen te genereren als reactie op poriedruk- en temperatuurveranderingen) met behulp van het Groningen seismische bronmodel waarin compactie gerelateerd is aan seismische gebeurtenispercentages. We tonen aan dat het gebied met de hoogste seismiciteitsneiging zich net ten noorden van de stad Groningen bevindt en zijn positie in de loop van de tijd niet verandert. Deze relatief hoge seismiciteitsneiging is het gevolg van relatief lage poriedrukken en grote verticale spanningen in dit gebied, gecombineerd met de aanwezigheid van in kaart gebrachte breuken. Dit resultaat is algemeen toepasbaar en is niet afhankelijk van het operationele ontwerp van een specifiek geothermisch project.

Daarnaast onderzoeken we de ruimtelijke omvang en de grootte van spanningsveranderingen die gepaard gaan met druk- en temperatuurveranderingen als gevolg van typische geothermische operaties en hoe deze worden beïnvloed door poriedrukdaling voorafgaand aan de start van de geothermische operaties. Deze onderzoeken zijn van belang omdat de ZW-aquifer van het Groningen gasveld een daling van de poriedruk ervaart als gevolg van de historische gasproductie in het Groningen veld. De spanningsveranderingen bepalen of breuken kunnen worden geheractiveerd, wat hier wordt aangenomen als indicatief voor geïnduceerde seismische slip. Over het algemeen vinden we dat de belangrijkste thermo-elastische spanningsveranderingen geassocieerd zijn met het gekoelde volume van de aquifer gecentreerd rond de injector, tot 1,5 keer de straal van de gekoelde zone (d.w.z. de afstand van de injectieput tot de rand van het gekoelde reservoirvolume). Poro-elastische effecten zijn minder belangrijk in de context van de ZW-aquifer. Heractivering van breuken is ook voornamelijk geconcentreerd in deze gekoelde zone. Daarom is het belangrijk om zowel het gekoelde volume als de geometrie van breuken die kunnen worden geheractiveerd en seismogeen kunnen zijn, in kaart te brengen. De straal van het gekoelde reservoirvolume hangt af van het volume geïnjecteerd koud water, de hoogte van de permeabele zone en de thermische eigenschappen van de vloeistof en de rots. We stellen methoden voor om de gekoelde reservoirzone te monitoren, waaronder puttesten, pulstesten en DTS. De delen van de aquifer waar de poriedruk hoog zijn gebleven zijn doorgaans iets stabieler, minder vatbaar voor breukheractivering en dus minder seismogeen. Dit hangt echter af van de gekozen geomechanische parameters (specifiek de Poisson's ratio en de Biot-constante).

Ten slotte is het belangrijk om het verzet van een breuk te beoordelen wanneer deze aanwezig is in de gekoelde zone (of zone met verminderde poriedruk) van een geothermisch veld. Een verzet gelijk aan de dikte van de aquifer, waarbij de top van het hangend blok op dezelfde diepte ligt als de basis van het liggend blok, maximaliseert het effect van drukdaling en koeling op de geïnduceerde spanningen. Dit geldt alle mogelijke hellingen van de breuk.

Over het algemeen is het belangrijk om onzekerheden in invoerparameters mee te nemen in een projectspecifieke analyse van geothermische operaties. In deze studie worden een aantal

belangrijke invoerparameters geïdentificeerd: de oorspronkelijke in-situ spanningsstaat, de wrijvingskenmerken van de breuk, en elastische moduli.

Het hier beschreven werk heeft zich explicitet gericht op generieke resultaten die breed toepasbaar zijn op alle potentiële geothermische projecten en vormt geen directe input voor een specifiek project. Vanwege hun brede toepasbaarheid kunnen de resultaten van dit project echter dienen als belangrijke input voor studies gericht op dergelijke projecten.

Executive Summary

We investigate the effects on seismicity of potential future geothermal operations in the southwest (SW) aquifer of the Groningen gas field using a number of different approaches.

First, we investigate the spatial variability in *seismicity propensity* (i.e. the tendency of the system to generate earthquakes in response to pore pressure and temperature changes) utilizing the Groningen seismic source model framework in which compaction is related to seismic event rates. We show that the area with the highest seismicity propensity is just north of the city of Groningen and does not change its position through time. This relatively high seismicity propensity stems from relatively low pore pressures and large vertical strains in this area, combined with the presence of mapped faults. This result is generally applicable and does not depend on the operational design of any particular geothermal project.

Second, we investigate the spatial extent and magnitude of stress changes associated with pressure and temperature changes due to typical geothermal operations and how these are influenced by pore pressure decline prior to commencing the geothermal operations. These investigations are of interest since the SW aquifer of the Groningen gas field is experiencing pore pressure decline due to the historical gas production in the Groningen field. The stress changes determine whether faults can be reactivated, which is assumed here as being indicative for induced seismic slip. In general, we find that the main thermo-elastic stress changes are associated with the cooled volume of the aquifer centered around the injector, reaching up to 1.5 times the cooled-zone radius (i.e. distance from injection well to the edge of the cooled reservoir volume). Poro-elastic effects are less important in the context of the SW aquifer. Reactivation of faults is also mainly concentrated in this cooled zone. Therefore it is important to map both the cooled volume and the geometry of faults that may be reactivated and may be seismogenic. The radius of the cooled reservoir volume depends on the volume of injected cold water, the height of the permeable zone and the thermal properties of the fluid and the rock. We suggest methods to monitor the cooled reservoir zone, including well testing, pulse testing and DTS. Non-depleted parts of the aquifer are typically slightly more stable, less prone to fault reactivation, and hence less seismogenic. However, this does depend on the geomechanical parameters chosen (specifically on the Poisson's ratio and Biot constant).

Finally, it is important to assess the offset of a fault when it is present in the cooled or depressurized zone of a geothermal field. An offset equal to the aquifer thickness, with the top of the hanging wall at the same depth as the bottom of the footwall, maximizes the effect of depletion and cooling on the induced stresses. This is the case for the complete range of values for the dip of the fault.

In general, uncertainties in input parameters are important to consider and should be taken into account in any project-specific analysis of geothermal operations. A number of key inputs is identified in this study: virgin in-situ stress state, fault frictional properties, elastic moduli.

The work described here has focused on generic results that are broadly applicable to all potential geothermal projects and is no direct input for a particular operation. However, due to their broad applicability, the results from this project can serve as important input to studies targeted at such operations.

Contents

Contents

1 Introduction

This report is part of the KEM-19b project, which focusses on the behavior of the southwest (SW) aquifer of the Groningen gas field. In report KEM-19b Part-1 (TNO 2025 R10452) we have reported on the geological modelling, reservoir flow modelling, seismicity analysis and seismic hazard assessment. The main focus of that work is on the long-term pore pressure evolution of the aquifer, and the corresponding effects on seismicity and seismic hazard.

The final research question of the KEM19b project focusses on the potential use of the SW aquifer of the Groningen gas field as a source for geothermal energy. In particular, this part of the study aimed to address the following research questions:

1. What areas are more prone or less prone to induced seismicity due to possible geothermal exploitation?
2. To what extend would a possible future geothermal exploitation of the aquifer impact the seismic potential of the aquifer? At what distance from a possible geothermal operation is the magnitude of stress change negligible?

The first question is addressed in Chapter 2 of this report, where we look at the SW aquifer's tendency to respond seismically to stress changes, utilizing the Groningen seismic source model framework. We call this tendency for seismicity the *seismicity propensity*. In particular, we focus on how the *seismicity propensity* varies spatially. This investigation therefore allows us to draw conclusions on which parts of the SW aquifer are expected to respond more/less seismically to geothermal operations, without having to make assumptions about the operational parameters of the geothermal project.

The second question in fact contains a number of sub-questions:

a. What is the expected magnitude of the stress changes associated with a geothermal project?
b. What is the spatial extent of these stress changes?
c. How are they impacted by the fact that the SW aquifer's pore pressure is declining over time due to the past gas extraction of the Groningen gas field?

These questions are addresses in Chapter 3, where we employ two semi-analytical tools (PANTHER and SRIMA) to investigate the stress changes around a geothermal project, under a range of different geomechanical parameters. Fault reactivation as a result of stress changes is taken as indicative for the induced seismicity potential.

2 Seismicity propensity

2.1 Introduction and approach

One of the main research questions for this project is 'What areas in the SW aquifer are more prone or less prone to induced seismicity due to possible geothermal exploitation?' Although the extent and magnitude of stress changes due to geothermal operations will critically depend on the specifics of the project, we can still identify areas that are more sensitive to stress changes without making reference to any specific project, or any specific operational parameters. We do this by applying a uniform forcing (a pore pressure change of a given amount), and calculate induced seismicity rates based on this, utilizing the Groningen seismic source model framework which relates reservoir compaction to seismicity rates. This will result in a map with an expected event rate for an identical amount of 'external forcing' at all locations in the SW aquifer. Such a continuous map indicates which areas are more and less prone to induced seismicity in general, and therefore also to induced seismicity due to a geothermal project. Although we apply a uniform pore pressure change (rather than a uniform temperature change), within the context of the Groningen seismic source model these quantities are actually interchangeable. This can be shown by considering the proposed update to the seismic source model for Groningen which includes temperature effects (TNO, 2024b). The derivations in that report show that the original Groningen seismic source model, in which vertical strain at offset faults generates seismicity, can be extended by including the temperature-dependent strain in the vertical strain term:

$$\varepsilon_v = -\frac{1}{H}\alpha\Delta P_p - \frac{(\nu+1)}{(1-\nu)}\alpha_T\Delta T \tag{1}$$

where ε_v is the vertical strain, H is the uniaxial elastic modulus, α is Biot's coefficient, ν is Poisson's ratio, α_T is the thermal expansion coefficient, ΔP_p is the pore pressure change (depletion defined as negative), ΔT is the temperature change (cooling defined as negative).

To show that an arbitrary pressure change is in fact interchangeable with an equivalent temperature change we define a new model parameter a_T^* (purely for convenience):

$$a_T^* = H\alpha_T \tag{2}$$

Substitution of (2) into (1) gives:

$$\varepsilon_v = -\frac{1}{H}\alpha\Delta P_p - \frac{(\nu+1)}{(1-\nu)}\frac{a_T^*}{H}\Delta T \tag{3}$$

We can then (again for convenience) define $a_T = a_T^*\frac{\nu+1}{1-\nu}$ to obtain

$$\varepsilon_v = -\frac{1}{H}\alpha\Delta P_p - \frac{1}{H}a_T\Delta T \tag{4}$$

And finally:

$$\varepsilon_v = -\frac{1}{H}(\alpha\Delta P_p + a_T\Delta T) \tag{5}$$

This shows that, for the purposes of calculating vertical strain ε_v, an arbitrary change in temperature without changing the pore pressure ($\Delta T = C, \Delta P = 0$, where C is an arbitrary value for ΔT), can be replaced with an equivalent change in pressure without changing the temperature ($\Delta P = \frac{\alpha_T}{\alpha} C, \Delta T = 0$). In the context of the Groningen seismic source model (Bourne and Oates, 2017), ε_v at offset faults (through Coulomb stress change ΔC) is the driver for seismicity. In this model, a given amount of vertical strain leads to the same stress change ΔC, regardless of whether the vertical strain is caused by a pore pressure change or temperature change. This is due to the 'amplification' of stresses at offset faults (see Bourne and Oates 2017 for details) in the simplified 'thin-sheet' geometry.

By applying this approach of equivalent pressure and temperature change, we are implicitly assuming that the assumptions behind the Groningen seismic source model, which was developed for dealing with pressure changes, remain valid in the context of temperature changes. Specifically, we assume that the induced strains are primarily uniaxial in nature, which is a sensible assumption in the context of pore pressure-induced strains in a laterally extensive, highly permeable reservoir, remains true for geothermal operations.
We acknowledge that strains induced by typical geothermal operations are less uniaxial in nature, due to their relatively large spatial temperature gradients. However, we believe that for a first-order assessment of seismicity propensity, the chosen approach is sensible and valid. After all, we are investigation *seismicity propensity* which can be seen as an expression of the probability of encountering faults that are near failure and only need a small stress disturbance for failure to occur. In the case of the SW aquifer of the Groningen field, to what extent faults are near failure is determined by their stress history, which is determined by pressure depletion. In other words, although the uniaxial strain assumption may not be fully valid for modelling the stress disturbance caused by geothermal operations, it is a valid assumption to describe the stress history of the faults, and therefore of their propensity for failure and seismicity.

2.2 Results

Here we choose to apply a spatially uniform 1 MPa pressure depletion (approximately equivalent to a 5 °C cooling for typical parameter choices), to identify where in the SW aquifers the combination of reservoir stiffness (H), pressure depletion, and fault geometry is most prone to the generation of induced seismicity. The magnitude of the depletion (1 MPa) is arbitrary in some sense, since we're interested in evaluating how different parts of the reservoir respond to *the same* forcing. We here choose an equivalent forcing that is expected to be reached by any geothermal project (5°C cooling) to investigate the spatial differences in seismicity propensity. Since the relation between vertical strain and the rate of induced seismicity is exponential, it is possible that this spatial picture changes when the reservoir pressures evolve though time. We therefore apply the 1 MPa depletion at two points in time, once in 2025, and once in 2053 (the final year of the pore pressure simulations). To account for the uncertainty in pore pressures and reservoir compressibility, we apply this depletion to all 66 vertical strain ensemble members and show the mean ensemble result. The calibration of the source model is performed on each ensemble member individually. For details, see the other report on KEM19-b (TNO, 2024a).
The seismic source model contains a spatial smoothing step, which smooths the incremental Coulomb stress changes on faults, before calculating the seismicity rate. This means that each fault segment influences the seismicity rate in the surrounding area (several kilometers in practice). This has two consequences that are undesirable from the perspective of the

research question at hand. First, it means that even though the loading (pressure change) is only applied in the aquifer, the stresses reach into the Groningen gas field. Because of the past depletion in the reservoir, and the exponential relation between stress changes and seismicity, this means that the loading in the aquifer mostly affects the seismicity within the Groningen gas field. The second consequence is that the seismicity rate forecast resulting from a uniform pressure depletion is spatially rather smooth. However, for this particular research question, we are interested in finding the fault locations that are particularly prone to seismicity. For these reasons, the spatial smoothing of incremental Coulomb stress changes is omitted in the forecasting. This results in more specific field locations which 'light up' as being prone to the generation of seismicity upon stress changes due to their stress history, compressibility, fault throw and fault density. For visualization purposes, we do apply a smoothing kernel with a small standard deviation (500m, 1 pixel) to the resulting seismicity rates to obtain a continuous seismicity propensity map (Figure 1). In addition, in Figure 2 a map with a different color scale is shown to provide a more detailed view of the seismicity propensity map for parts of the SW aquifer that are difficult to see in Figure 1.

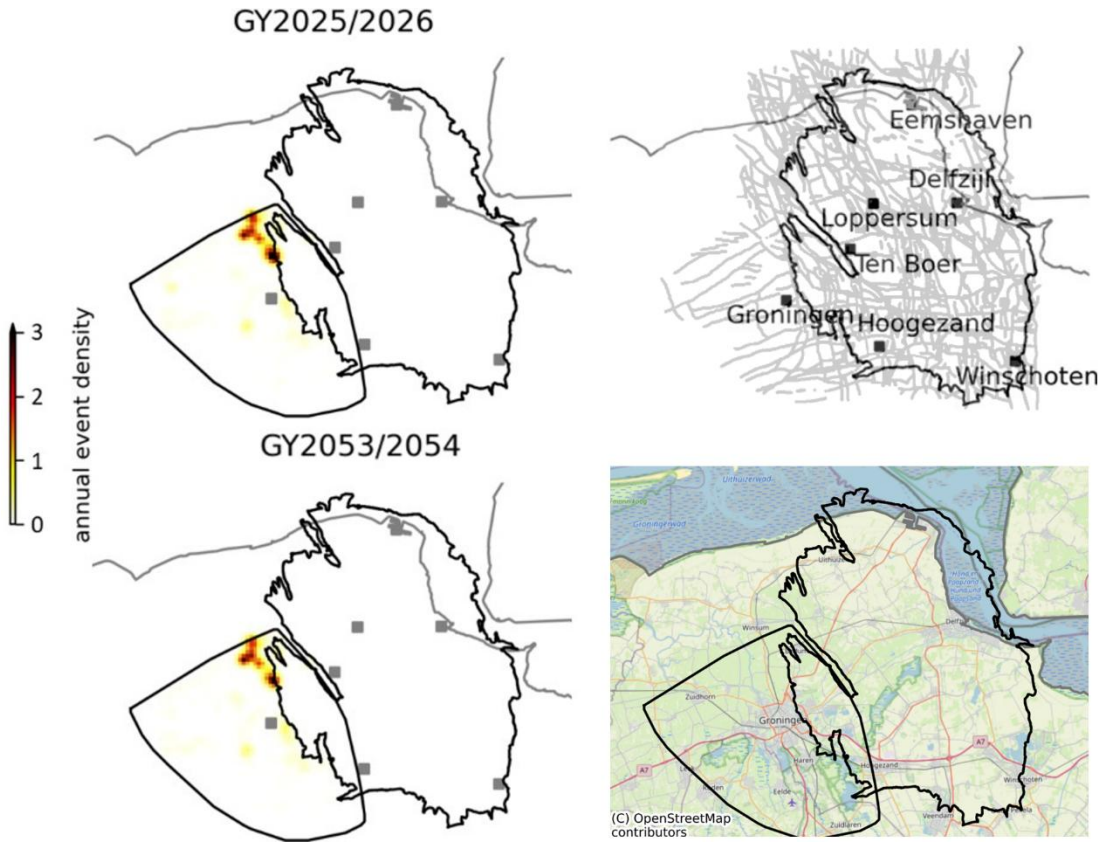

Figure 1: Relative seismicity propensity (arbitrary scale). Generated by applying a 1MPa pressure depletion throughout the entire SW aquifer for gas year 2025/2026 and 2053/2054. Model is calibration is identical to that described in Chapter 4 of the KEM19b report (Part I). The pressures outside the SW aquifer are kept constant and faults within the Groningen field are not considered in the seismicity calculation.

The resulting maps show that the seismicity propensity of the SW aquifer does not vary significantly with time. Given the same loading, the area just north of the city of Groningen is expected to be the most prone to seismic activity. This is largely explained by the high pressure depletion in this area (Bedum field), leading to comparatively high Coulomb stress development compared to other areas in the SW aquifer. Due to the exponential relation between Coulomb stress and seismicity rate, a similar amount of loading has a larger effect on seismicity in this area.

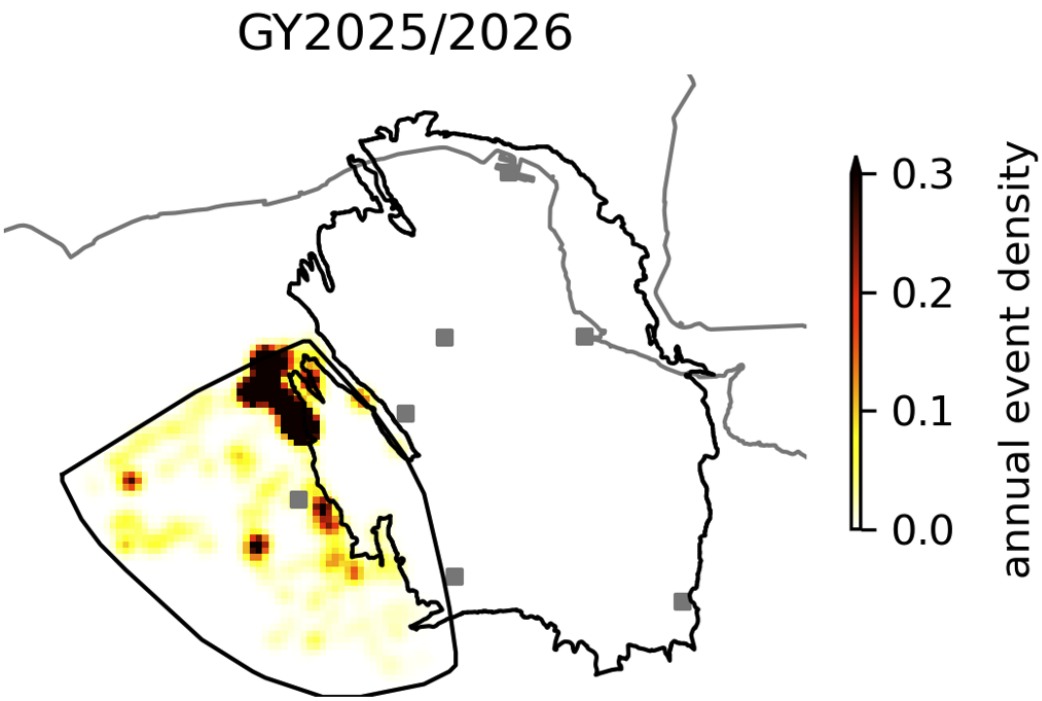

Figure 2: As Figure 1, but with the color scale maximized at 10% of the full scale. This allows for more detail to be shown in areas more to the southwest. It is important to note that due to the 'clipping' of the color scale, areas that appear black may represent different values (i.e. the seismicity propensity around Bedum is still significantly higher than the seismicity propensity in the east and southwest of the city of Groningen, despite both showing the same color on this map). This figure is meant to show relative differences in the SW aquifer that are difficult to see in Figure 1, due to the impact of the area around Bedum.

3 Extent and magnitude of the stress impact of geothermal operations

3.1 Introduction

The areal extent, temperature and permeability of the SW aquifer make it a potential target area for geothermal energy. A pressing question is how geothermal operations would change the probability of induced seismicity of the area. We have seen (TNO 2025 R10452) that the depletion of the aquifer due to equilibration with the surrounding gas fields causes a change in the probability of induced seismicity. Geothermal energy operations introduce more pressure changes since water will be injected (local pressure increase) and produced (local pressure decrease). In addition, temperature changes around the injection wells will occur as the reinjected fluids are usually 10's of degrees cooler than the initial reservoir temperature. Both pressure and temperature changes impact the total and effective stresses. These stress changes change the potential for fault reactivation, and, assuming fault reactivation results in seismic fault slip, will consequently change the seismic potential of the area. We here report on an initial assessment of the magnitude of the stress changes and fault reactivation.

As a first step we wish to investigate to what extent a possible future geothermal exploitation would impact the probability of induced seismicity by making a first-order assessment of both its area of influence and its magnitude of influence.

In order to assess the influence of a geothermal project on seismicity, the ideal approach would be to incorporate the ensuing stress changes into the model determined above. However, due to the large number of operational variables involved (production/injection rates, re-injection temperature, doublet configuration and location), this is infeasible to do in a generic non-project specific sense. In addition, the seismicity proxy 'smoothed incremental Coulomb stress' is difficult to interpret as a 'physical' quantity. This makes it difficult to superpose any stress changes derived outside of the Groningen source model framework to the Groningen source model. Also, the effective stress changes resulting from a geothermal project in a sandstone reservoir as the Slochteren Sandstone Member are fundamentally different from those resulting from depletion. First of all, even though in both cases stress changes can be destabilizing, for cooling the effective stresses become less compressive, and for depletion the effective stresses become more compressive. Second, the space-time behavior is different because thermo-elastic stress changes develop in a cooling rock volume progressively growing in size, whereas poro-elastic stress changes from depletion occur gradually over the entire reservoir as the pressure changes (Buijze et al. (2023); Mathur et al. (2024)). Still, the initial state of stress or initial fault criticality and the fault characteristics are crucial input in both cases.

We therefore have chosen to assess the impact of a 'typical' geothermal project in the Groningen SW aquifer, starting from the situation where the aquifer has been depleted with regard to the virgin pressures. We use the semi-analytic mechanical models SRIMA (Seal and Reservoir Integrity Mechanical Analysis, developed at TNO, Buijze et al. (2022), https://www.nlog.nl/sdra-geothermie-integriteit-afdichtend-pakket) and PANTHER v0.7

(Buijze et al. (2022), https://github.com/TNO/PANTHER). SRIMA models both pressure and temperature effects on the stresses for a radially symmetric case. PANTHER models pressure and temperature effects on the stresses on a fault in a vertical plane-strain situation in which a reservoir crosses a dipping fault with an offset between the two sides.

3.2 Definition of the base cases

The starting situation of the geothermal base cases is the depleted SW aquifer. For the reservoir characteristics (depth, thickness, permeability, porosity) we take values given earlier (TNO 2024a).
Important properties are the elastic parameters. For the virgin in-situ stresses we take values from Bakx et al. (2022). We take a value of 22.6 MPa/km for the gradient of the lithostatic vertical stress; 17.8 MPa/km for the gradient of the minimum in-situ stress in the target sand layers and 18.3 MPa/km in the overlying and underlying, more claystone-rich layers. Elastic moduli have been shown to vary considerably with porosity, and sandstones from the Groningen gas field have even been shown to behave partly inelastic (Pijnenburg et al. (2018)). We use a base case value of 14 GPa but account for a range of 7 – 20 GPa. For Poisson's ratio we take a value of $\nu = 0.15$. Heat flow properties (heat capacity; thermal conductivity) are given representative numbers. Parameter values are presented in Table 1.

For the connection with induced seismicity, we evaluate the induced stresses in terms of change of the Coulomb Failure Function (ΔCFF) and Shear Capacity Utilization (SCU) on a fault. The two measures are defined as:

$$\Delta CFF = \Delta\tau - f_s \Delta\sigma_n'$$
$$SCU = \left|\frac{\tau}{C + f_s \sigma_n'}\right| \quad (6)$$

in which τ is the shear stress, C the cohesion, f_s the friction coefficient and σ_n' the effective normal stress. ΔCFF signifies how the stress changes with respect to the Mohr-Coulomb failure envelope, with positive values indicating the stress gets closer to failure, and negative values indicating the stress becomes more stable. The SCU measures the ratio of the shear stress with respect to the failure stress, with 1 as the critical value at which the shear stress equals the fault shear strength and reactivation occurs. We also define a typical fault geometry at critical orientation close to the injection well (150 m distance), but not intersected by it.
One of the most important input parameters that are analyzed are the starting values for the in-situ stresses, which are different from the virgin in-situ stresses because of the depletion of the aquifer. This depletion varies over the aquifer area spanning a range of 0 – 20 MPa. However, the distribution is relatively smooth, and we make the approximation of uniaxial compaction in order to calculate the starting stresses when starting a geothermal operation in a depleted area. Such compaction involves a constant total vertical stress and a decrease of the total horizontal stresses with a stress path coefficient (ratio of total horizontal stress change with respect to pressure change):

$$\gamma_h = \frac{\Delta\sigma_h}{\Delta P} = \alpha_p \frac{1 - 2\nu}{1 - \nu} \quad (7)$$

Typical Mohr diagrams for uniaxial compaction are drawn in Figure 3 for the starting pressure equal to the virgin pressure, and for values of the depletion of 5, 10, 15 and 20 MPa and a friction coefficient of 0.55. The rather small values of Poisson's ratio in combination with a large value of 1.0 for the Biot constant result in a value of γ_h=0.824 and a movement of the

Mohr circle towards the failure line upon depletion (Figure 3a). For a larger value of Poisson's ratio or a smaller Biot constant, depletion can result in movement away from failure. Figure 3b. The uniaxial compaction due to cooling moves towards the failure line much more dramatically (the arrows) than the movement due to the depletion (from blue to red circles).
We consider a typical geothermal doublet where hot water is produced and cold water is injected. We only assess the stresses around the injector since here the destabilization is largest due to increased pressures and decreased temperatures. For the thickness and permeability of the SW aquifer, we consider an average injection rate of 300 m^3/hr at an injection temperature of 35°C.
An important parameter in the assessments following is the size of the cooled zone. The upper limit of the radius of the cooled zone, which is the value when there is no leakage of heat to the seal and the base, is given by (Buijze et al, 2022).

$$r_{cooled}^{max} = \sqrt{\frac{V_{inj}}{H\pi} \cdot \frac{\rho_w c_w}{\rho_r c_r}} \tag{8}$$

Here, $V_{inj} = Q_{inj} \cdot t$ in the volume of injected fluid; H the height of the aquifer zone; ρ_w and ρ_r are the densities of the injected fluid and of the gross rock; and c_w and c_r are their respective heat capacities. In most of the cases this value can serve as a good estimate.

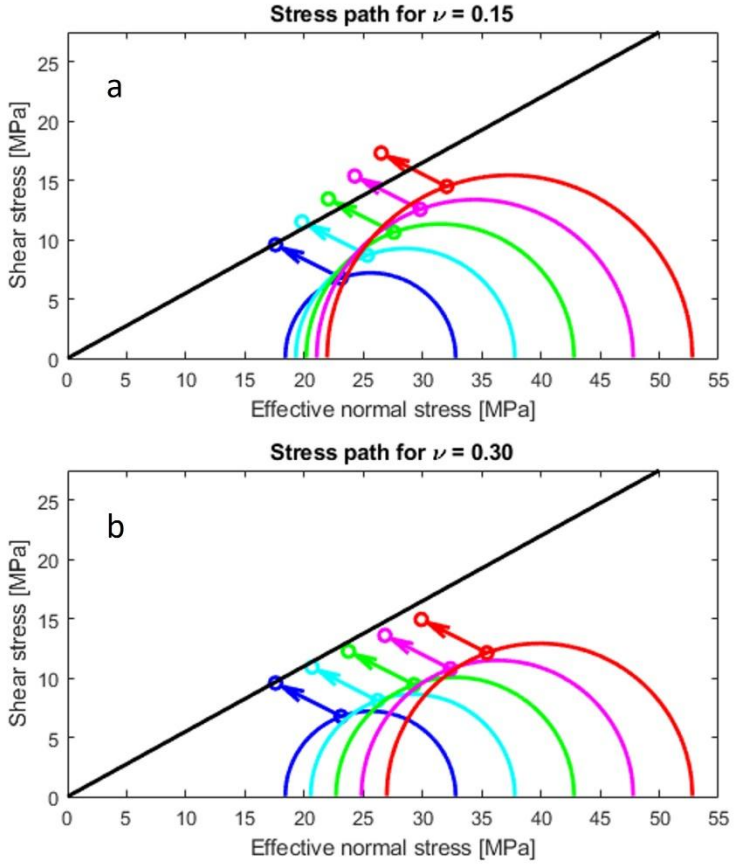

Figure 3 Typical stress path during uniaxial depletion and subsequent cooling. Mohr circles represent tractions on planes with different orientation. The depletion is 0, 5, 10, 15, 20 MPa for the blue, cyan, green, magenta and red circles. Geothermal injection is assumed to yield 0.5 MPa pressure increase, 7 MPa decrease of the principal horizontal stress and 1 MPa decrease of the principal vertical stress. Top and bottom figures represent Poisson ratios of 0.15 and 0.30, respectively.

3.3 SRIMA

3.3.1 The Tool

The assessment of potential seismicity requires the calculation of induced changes of pressures, temperatures, associated stress changes, the potential reactivation of faults, estimate of a maximum magnitude and the propagation of seismic waves to the surface. Due to large uncertainties in the input and the inherent irregular behaviour of seismicity, such calculations should ideally be performed stochastically. The tool SRIMA (acronym for Seal and Reservoir Integrity Mechanical Analysis) has been designed and developed for this purpose. It is a tool that calculates the above for radially symmetric geometries with injection in a reservoir layer that is sandwiched between a seal and a base layer. In the current study we have used it as a tool to test sensitivity of pressures, temperatures, induced stresses and reactivation potential to the input parameters.
The radial symmetry of SRIMA (Figure 4) deploys three layers. Advection of heat and a steady-state pressure solution is modelled in the reservoir. In the overlying and underlying layers, vertical diffusion of heat and pressure are modelled according to diffusivity laws in drained rock. Stresses are calculated for these geometries based on linear poro-thermo-elasticity, to be combined with the starting stresses in order to arrive at total and effective stress fields. From those, the increase in Coulomb Failure Function, ΔCFF, and the Shear Capacity Utilization SCU are calculated (Eq. 6). The calculations can be performed either in points on a line (for faults potentially present at those points at most critical orientation) or on a pre-defined fault plane. We limit the SRIMA evaluation to these outcomes; the connection to seismicity will be made outside SRIMA in the next Section of this report. For a more extensive description of SRIMA we refer to Buijze et al. (2022); Fokker, et al. (2023); Fokker & Wassing (2019).

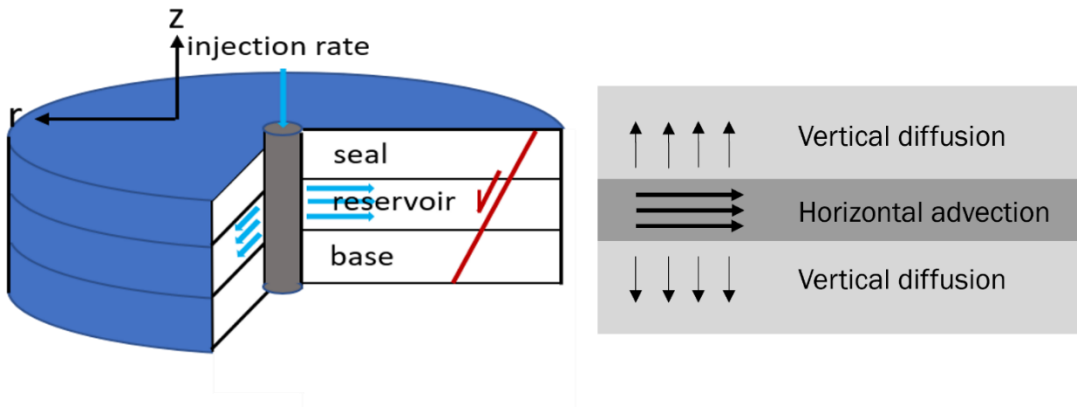

Figure 4 SRIMA geometry: Radially symmetric with injection over entire reservoir interval. Darcy flow and advection in the reservoir layer; diffusion above and below.

3.3.2 The model cases

SRIMA results were output at three different geometries: on a vertical line at the edge of the injection well; on a horizontal line starting from the wellbore into the aquifer in the middle of the reservoir; and on the pre-defined fault at 150 m distance from the well. For the vertical and horizontal lines, stochastic calculations were performed as well, to assess the influence of various uncertain parameters on measures that connect to induced seismicity.
The base case model outcomes involve calculations with five values of the starting aquifer pressure: 35 MPa (virgin pressure), 30, 25, 20 and 15 MPa, with corresponding initial horizontal stresses in the reservoir calculated through Eq. 7, assuming no initial pressure diffusion into

seal and base. These values have been chosen to represent the pore pressures at different positions in the SW aquifer. The values of the input parameters are reproduced in Table 1. The values for the virgin aquifer and the values after depletion represent the base cases; the value ranges for stochastic calculations have been used for Monte Carlo drawings of those parameters. Note further that the stress contrasts are chosen to reduce the stress in the aquifer layer, and that fault strike is not in the table since there is no horizontal stress anisotropy.

Table 1 SRIMA input parameters: Base Case values for virgin and for depleted aquifer; and ranges used.

Input parameter	Values for Virgin Aquifer	Values after depletion	Values for Stochastic calculations
Top depth	3000 m		3000 m
Thickness	300 m		150 – 400 m
N/G	70%		70%
Fault Dip	60°		
Reservoir temperature	100°C		100°C
Reservoir pressure at top	35 MPa	30 / 25 / 20 / 15 MPa	25 MPa
Pressure Contrast Seal To Reservoir	0 MPa	-5 / -10 / -15 / -20 MPa	-10 MPa
Pressure contrast Reservoir to Basement	0 MPa	5 / 10 / 15 / 20 MPa	10 MPa
Salinity	200,000 ppm		200,000 ppm
Permeability	100 md		50 – 500 md
Porosity	20%		20%
Heat capacity (saturated rock)	850 J/kg.K		850 J/kg.K
Thermal conductivity (saturated rock)	1.1 W/m.K		1.0 – 5.0 W/m.K
Minimum horizontal stress at top reservoir	53.4 MPa	49.28 / 45.16 / 41.05 / 36.93 MPa	42 – 48 MPa
Stress contrast Seal to Reservoir	-1.5 MPa	-4.12 / -8.24 / -12.35 / -16.47 MPa	-8 MPa
Stress contrast Reservoir to Basement	1.5 MPa	4.12 / 8.24 / 12.35 / 16.47 MPa	8 MPa
Vertical stress at top reservoir	67.8 MPa		67.8 MPa
Maximum / minimum horizontal stress ratio	1.0		1.0
Max hor. stress azimuth	135°		135°
Young's modulus	14 GPa		7 – 20 GPa
Poisson ratio	0.15		0.05 – 0.35
Biot constant	1.0		1.0
Linear thermal expansion coefficient (saturated rock)	1.0 10^{-5} K^{-1}		1.0 10^{-5} K^{-1}
MC friction coefficient	0.55		0.5 – 0.7
Cohesion	0 MPa		0 – 4 MPa
Residual friction	0.45		

Injection rate	300 m³/hr		300 m³/hr
Injection temperature	35 °C		20 – 50 °C
Injection duration	25 yr		25 yr

3.3.3 Stress changes with depth

With the low value of Poisson's ratio ($\nu = 0.15$), Biot constant equal to 1 and a friction coefficient of 0.55, depletion results in a stress moving closer to failure (see also Figure 3). The pressure and stress profiles for three of these cases (0, 10, and 20 MPa depletion prior to geothermal injection), along a vertical line close to the injection well, are represented in Figure 5, for the moment of starting cold-water injection and after 1, 5, and 25 years of injection. The pressure changes in the seal and the base are due to the minimum allowable value for the permeability and the assumption of drained conditions. After one year of injection and later, the SCU in the aquifer at the location of the well exceeds unity at the upper and lower aquifer boundaries; the effect is stronger for lower starting pressures (more prior depletion). SCU in the seal and the base quickly diminish with distance to the interface with the aquifer.

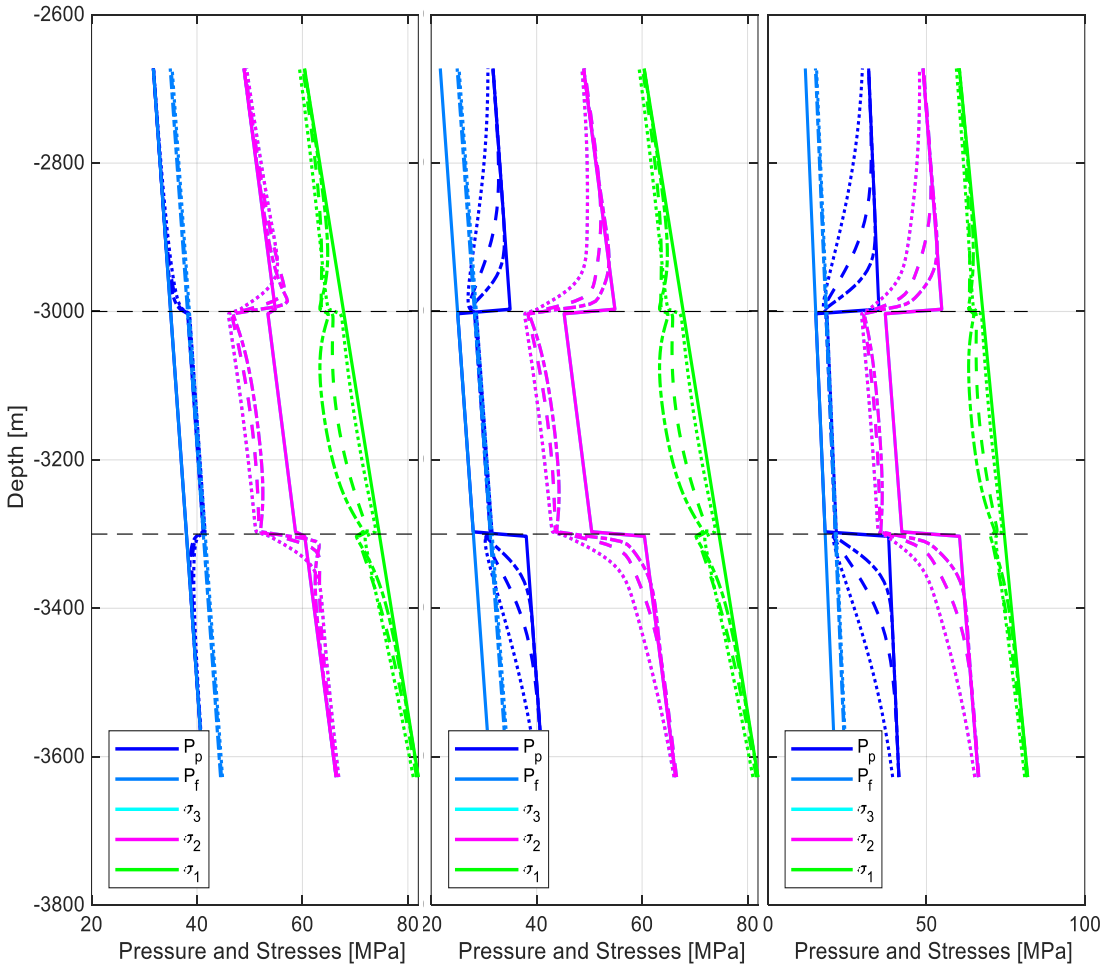

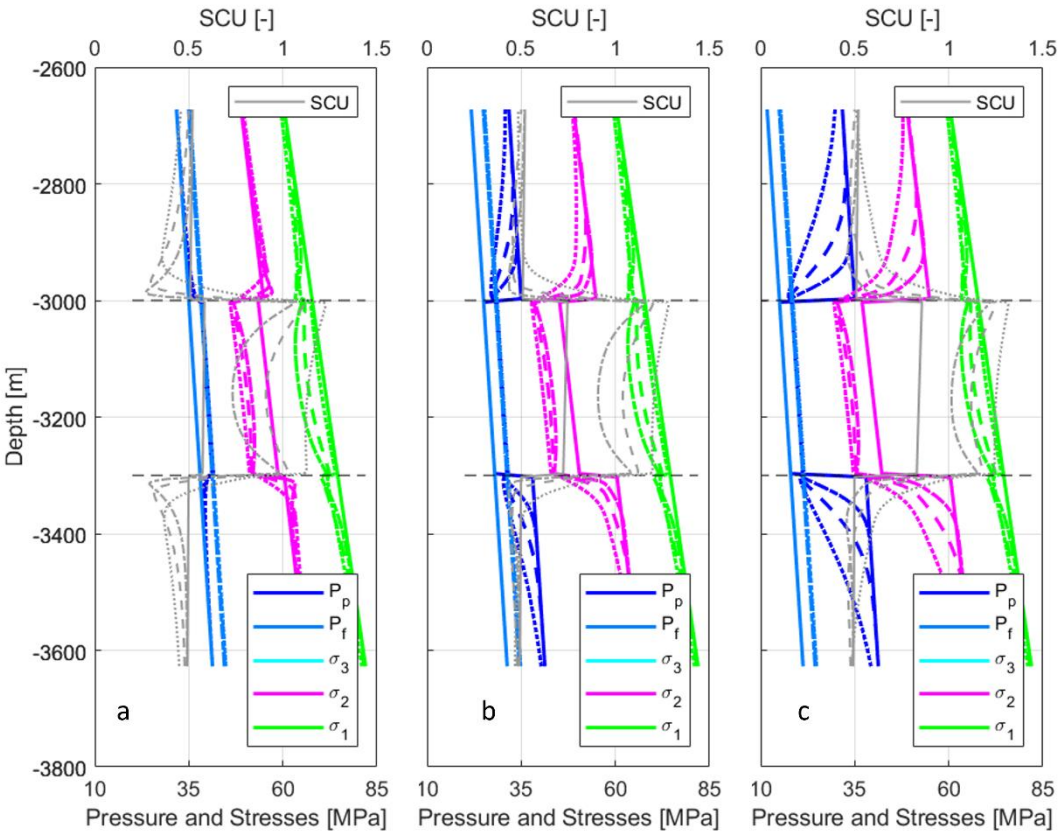

Figure 5 Pressure and stress profiles, and associated SCU along a vertical line close to the injection well. Starting pressure in the aquifer is 35, 25, and 15 MPa (a, b, c). The drawn curves are the starting pressures and stresses; the dashed and dotted ones are the profiles after 1, 5, and 25 years of injection.

3.3.4 Stress changes with distance from the well

An important question concerns the relative contributions of pressure and temperature to the stress changes, for faults at different distances from a geothermal injection well. We want to assess the area of influence and the magnitude of influence of geothermal projects on seismicity. Therefore, we also evaluate the induced stresses and shear capacity on a horizontal line in the aquifer, indicating how they change with distance from the well.

The pressure and temperature *changes* do not depend on the starting pore pressure in the aquifer. Consequently, the starting pressure also has no influence on the induced stress *changes*, including the change in the Coulomb Failure Function. In Figure 6 – Figure 8, the induced changes are presented. A number of observations can already be made from these figures. In the first place, while the cooled-zone radius propagates into the aquifer with injection time, the pressure profile hardly changes (Figure 6). Only a small effect from the larger viscosity of the cooled fluid can be seen because the cooled zone is growing with time. In addition, the pressure changes are concentrated around the wellbore, while the temperature changes reach much further into the aquifer. This has a direct influence on the distribution of the poro-elastic and thermo-elastic stresses. The poro-elastic stresses (right pane in Figure 7) are concentrated around the wellbore; the thermo-elastic stresses (left pane in Figure 7) reach much further into the aquifer, as do the temperature changes. In addition, the difference in shape of the pore pressure perturbation and temperature perturbation make the influence of temperature more important than the influence of the pressure. Clearly, this

balance may shift when input parameters are chosen differently – as an example, the pressure disturbance and the associated poro-elastic stresses are inversely proportional to the permeability and will increase with decreasing permeability.

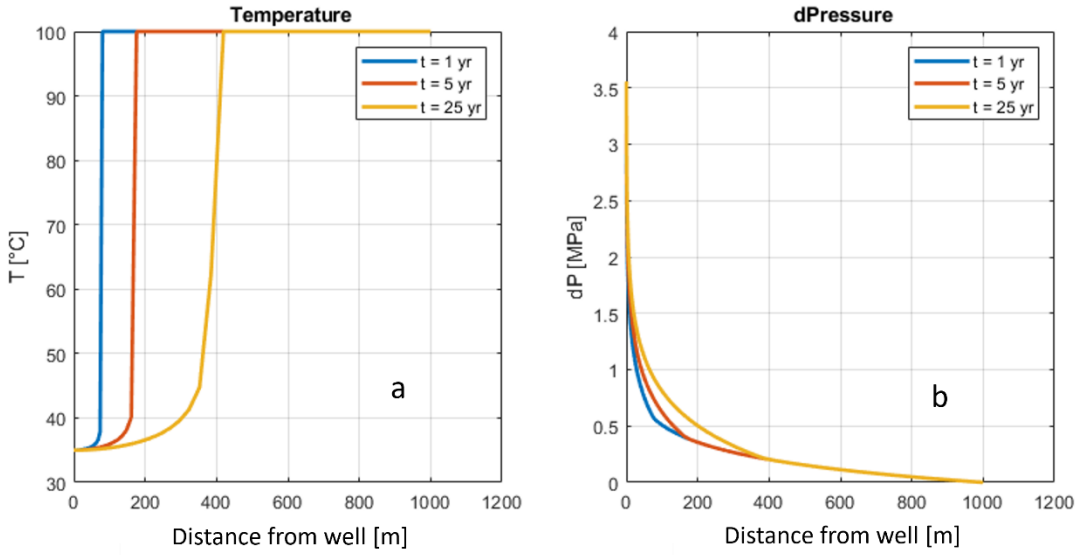

Figure 6 Temperatures (a) and pressure changes (b) in the aquifer. Different colours indicated different times during injection.

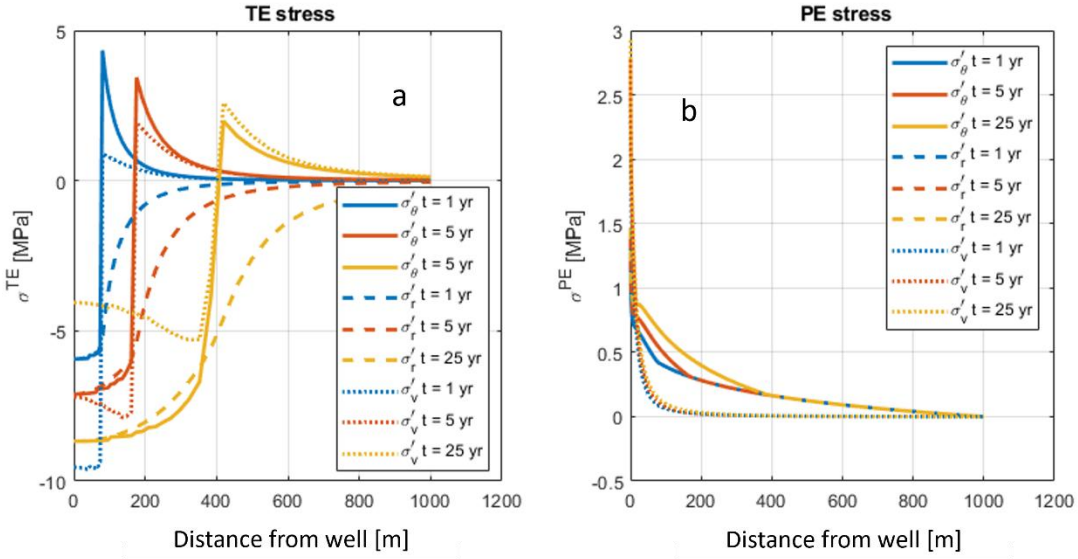

Figure 7 Induced thermo-elastic (a) and poro-elastic (b) stress changes . Colours indicate time since start of injection (1, 5, and 25 years with blue, yellow and red). Line type indicates stress direction (solid curves: tengential; dashed curves: radial; dotted curves: vertical).

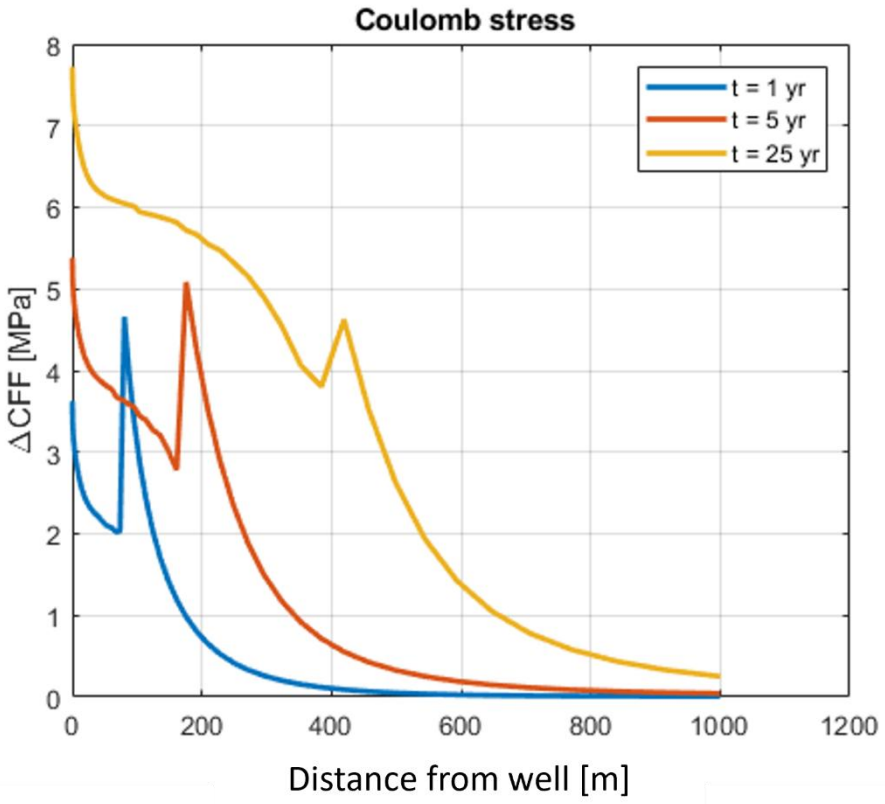

Figure 8 Induced increase in the Coulomb Failure Function as a function of distance to the injection well, for multiple time steps.

An important measure in this analysis is the Coulomb stress. Figure 8 presents the induced changes in the Coulomb Failure Function (ΔCFF, Eq. 6) at a horizontal line in the middle of the aquifer. We see that the *ΔCFF* profile generally follows the cooled zone of the aquifer (cf Figure 6). Close to the wellbore there is an additional effect of the pressure increase that is taking place there. Beyond the cooled zone, ΔCFF diminish to values below 1 MPa at 1.5 – 2 times the radius of the cooled zone. There is a peak in ΔCFF at the cooled-zone radius. This is due to the fast change in temperature with distance at this position, which remains to be present even for longer times, and the associated fast changes in tangential and vertical stresses at the cooled-zone radius. The background of this behavior is the large injection rate, which makes the flow of thermal energy advection-controlled (Nield & Bejan (2006)).
When the induced stress changes are combined with the starting (post-depletion) stress field, the Shear Capacity Utilization (SCU) can be determined. The outcome of this calculation depends on the starting situation. We therefore present in Figure 9 the SCU for aquifer starting depletion of 0, 10, and 20 MPa, for each case after 1, 5, and 25 years of injection. We see that for longer injection times the SCU increases in magnitude and extent. We also see for the larger depletion pressures the starting value of SCU is larger. Regions in the aquifer where more depletion is present at the start of injection show a larger radius for the area where the SCU values are larger than unity. The maximum radii for which SCU is larger than unity are presented in Figure 10.

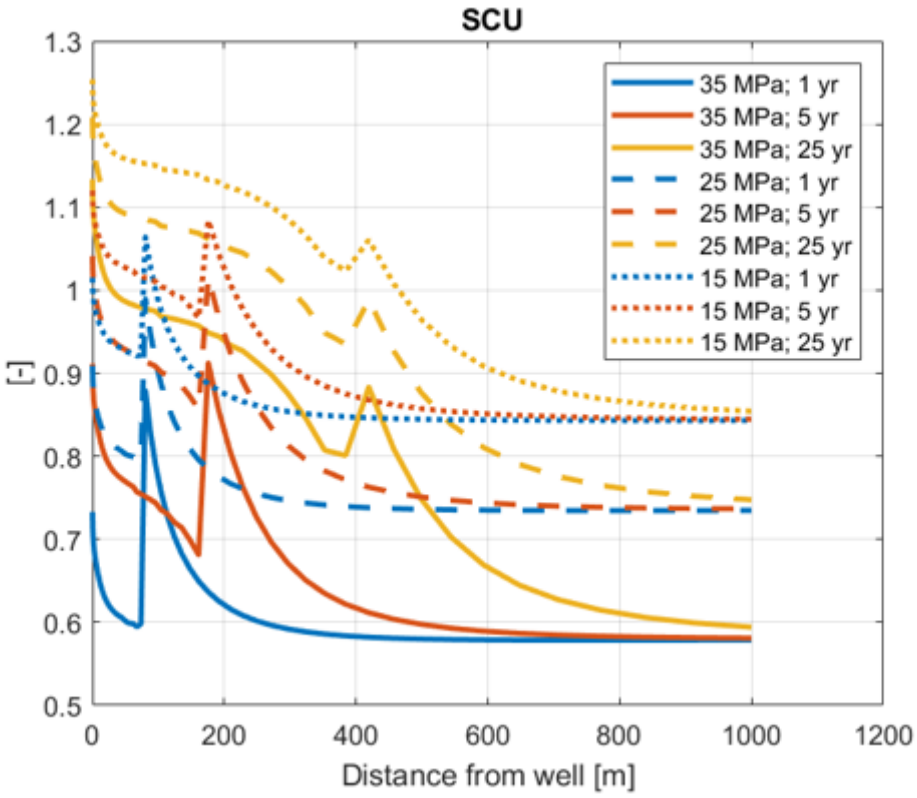

Figure 9 Shear Capacity Utilization (SCU) for the base case calculations after different times of injection (1, 5, 25 years) and for different starting pore pressures (35, 25, 15 MPa) in the aquifer.

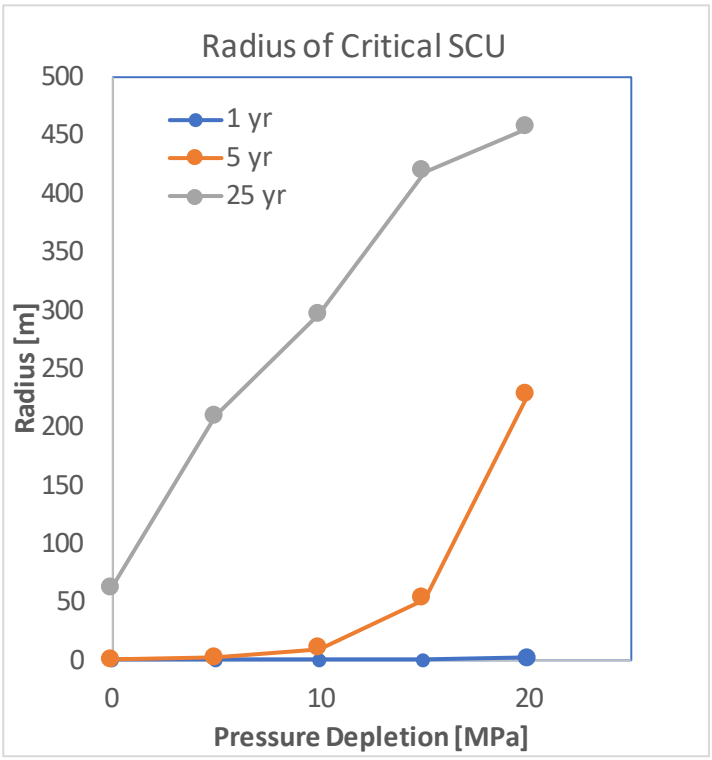

Figure 10 Radius of Critical SCU for different times vs starting depletion of the aquifer.

3.3.5 Stress changes on a predefined fault plane

The modeled fault position at 150 m from the wellbore, along with an indication of the size of the cooled volume, is provided in Figure 11. We give some outputs on the fault for the case starting with 10 MPa depletion. Figure 12 shows how the pressure change and temperature on the fault plane develop. The pressure increase grows with time due to the increased area flooded with low-temperature, high-viscosity water. The cooled zone has not yet reached the fault after one year but a large part of the fault is cooled in subsequent years. While the poro-elastic stress changes are small (maximum 0.7 MPa change of the principal values) and mainly limited to the area near the well, the thermo-elastic stress changes are considerable (Figure 13). They cause the majority of the effect on the stability measures on the fault: the change in ΔCFF and the resulting SCU (Figure 14). The chosen orientation of the fault is near critical; as a result, this is the worst case in the context of fault reactivation. For faults with different orientations, the induced stresses are less critical. The change in ΔCFF does not depend strongly on the dip angle when varying it between 52° and 69°; the SCU decreases substantially when moving away from the critical fault orientation. This is demonstrated in Figure 15 and Figure 16.

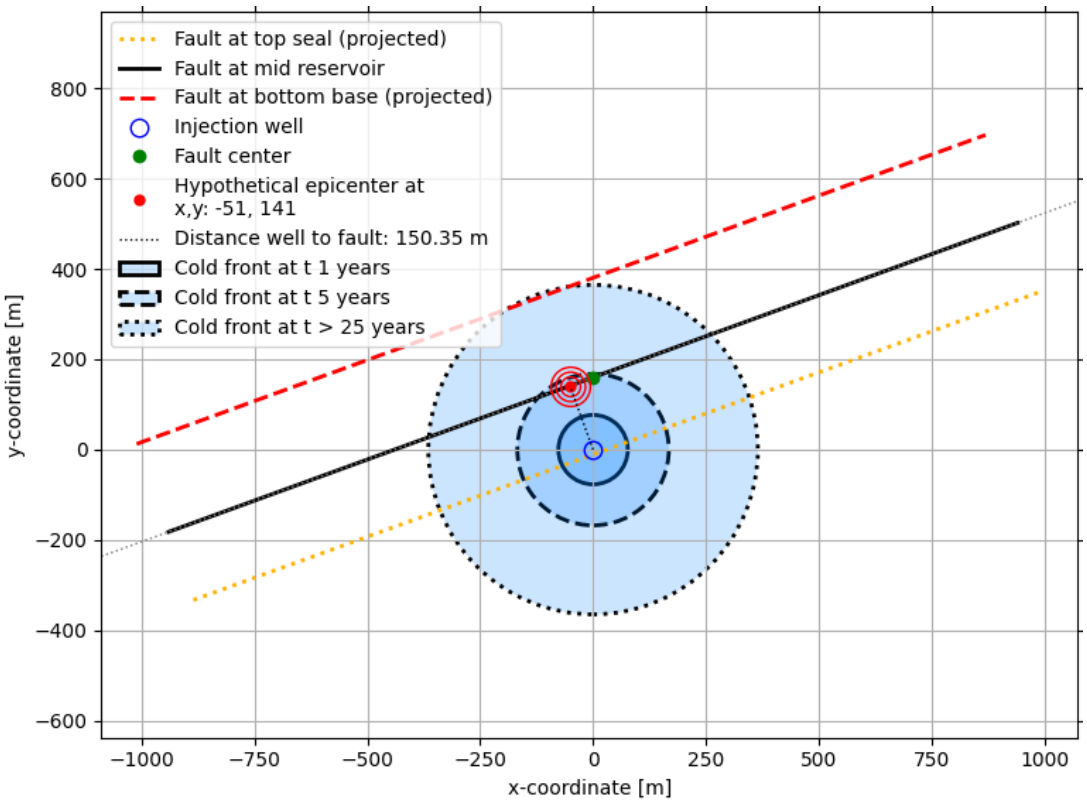

Figure 11 Position of the modelled fault plane with respect tot the injection well and the cooled zone after 1, 5, and 25 years of injection.

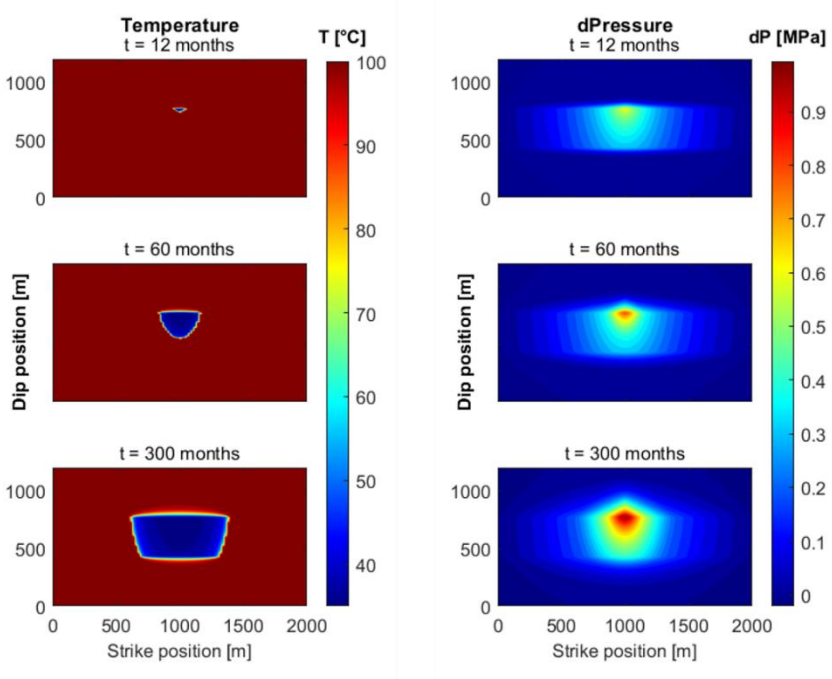

Figure 12 Pressure change and temperatures on the fault.

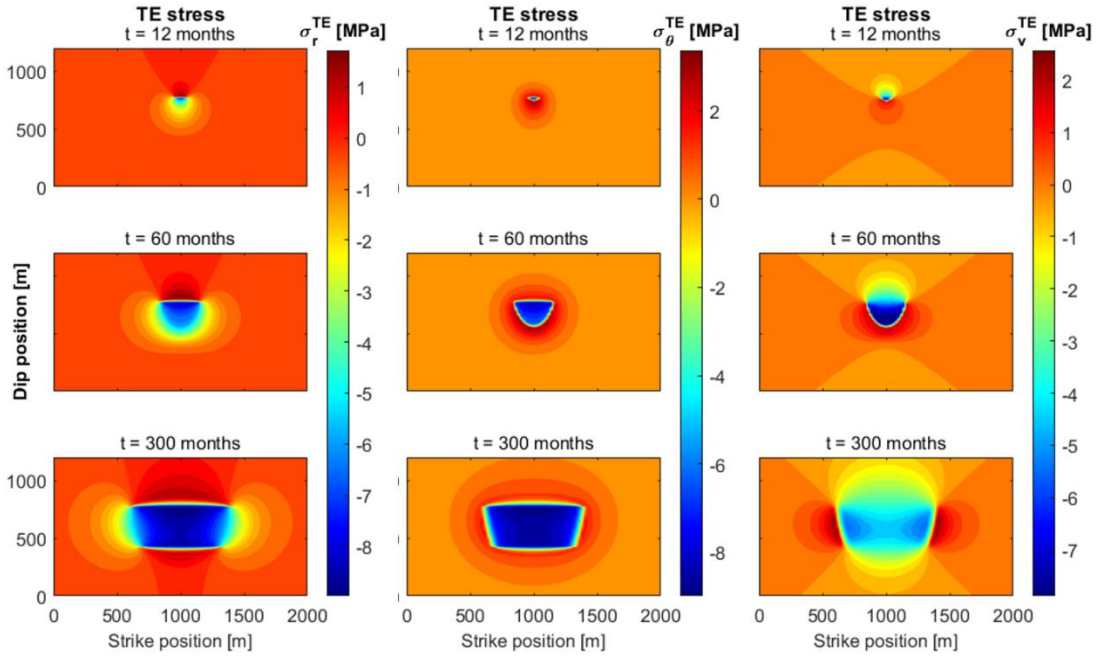

Figure 13 Induced thermoelastic stresses on the fault plane: radial, tangential and vertical stresses for the case with 10 MPa depletion.

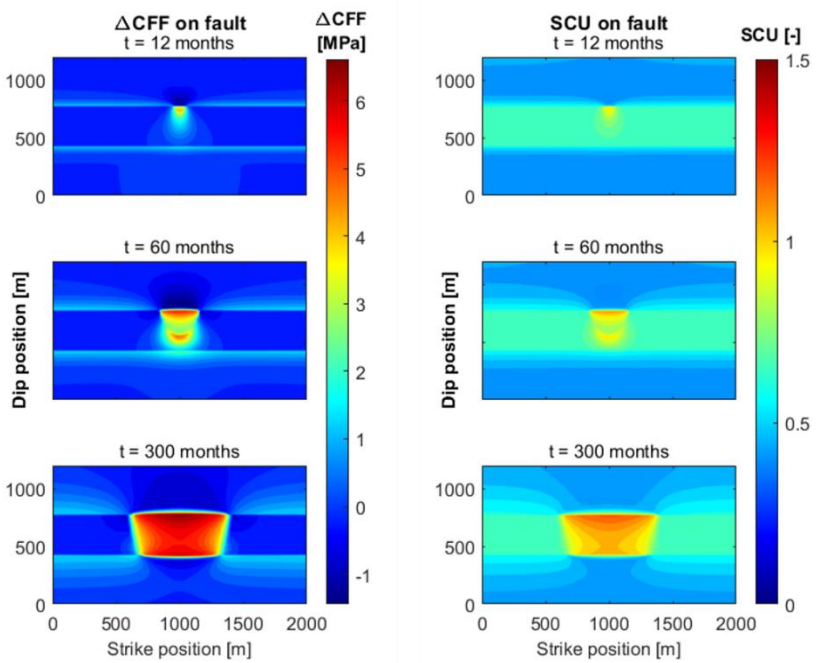

Figure 14 Stress measures on the fault: Change in Coulomb Failure Function (ΔCFF) and Shear Capacity Utilization (SCU) for the 10 MPa depletion case and a fault orientation of 60°.

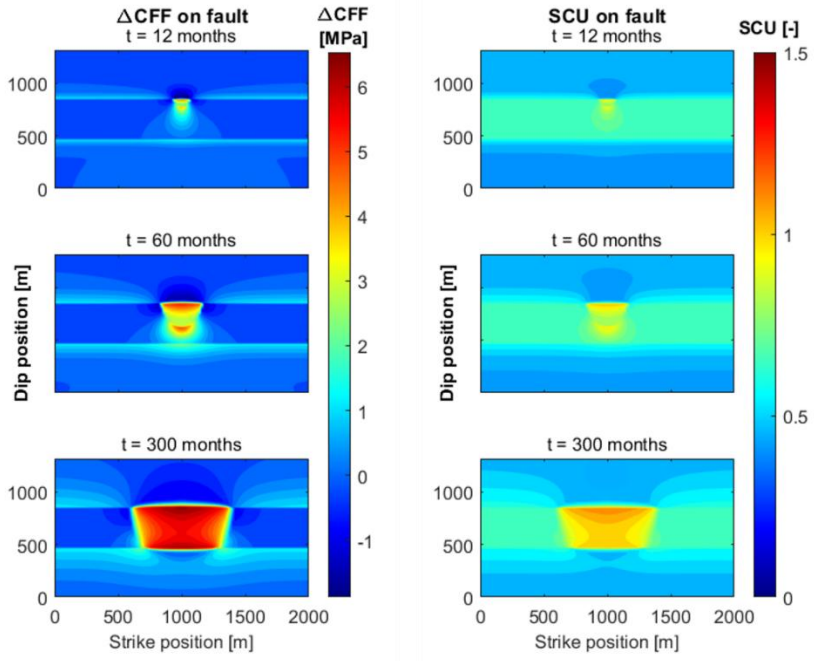

Figure 15 Stress measures on the fault: Change in Coulomb Failure Function (ΔCFF) and Shear Capacity Utilization (SCU) for the 10 MPa depletion case and a fault orientation of 52°.

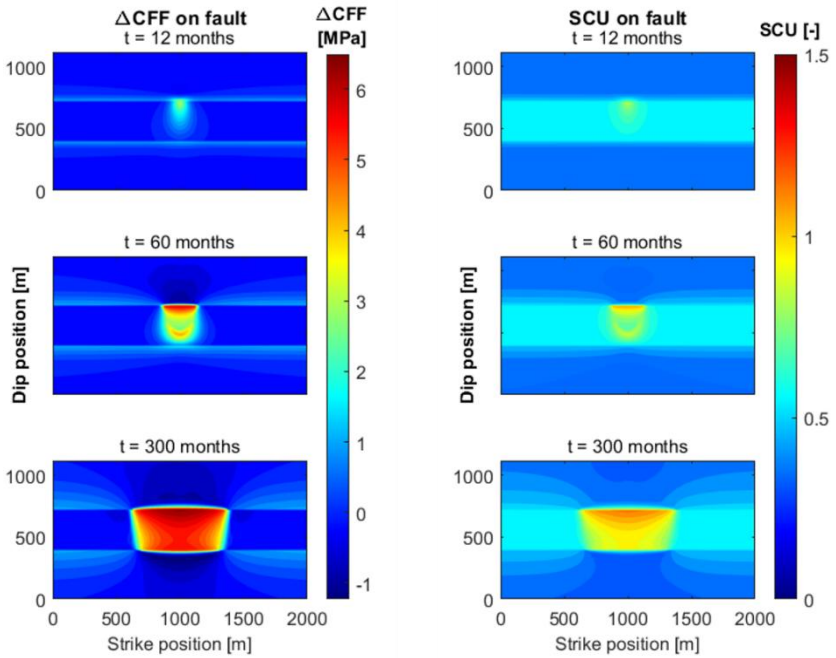

Figure 16 Stress measures on the fault: Change in Coulomb Failure Function (ΔCFF) and Shear Capacity Utilization (SCU) for the 10 MPa depletion case and a fault orientation of 69°.

3.3.6 Stochastic analysis for calculations vs depth

We want to obtain insight in the range of outcomes that are possible with the uncertainty of the input parameters, and to uncover their respective influence. We first performed such analysis on a vertical line, starting from the base case in Section 3.3.3, with a starting value for the aquifer pressure of 25 MPa (10 MPa depletion). The vertical line allows to investigate the effect in overburden and base. For the stochastic analysis, 1000 model values for all uncertain parameters in the last column of Table 1 were drawn randomly within their confidence range.

For the stochastic calculations, a number of measures are present in SRIMA that connect to induced seismicity. The most important for the calculations on a vertical line is the vertical extent to which $SCU > 1$. This is an indication for possible height growth of fault reactivation in the seal. Figure 17 shows the probabilities of reaching certain heights, for all simulations. Less than 10% of all cases show reactivation more than 15 m into the seal, even after 25 years.

Figure 18 shows how the activated cases relate to the driving parameters. In this figure we have ranked the results against the uncertain parameters. First, the propagation of reactivation into the seal has been determined, for each ensemble member. Then, for each input parameter that was varied in the stochastic analysis (e.g. H_{res}, k_{res}) the results were binned in 9 bins, spanning the full range between the minimum and maximum value of the parameter that was explored in the stochastic analysis. Per bin, the normalized fraction of model results for a certain value of the reactivation penetration are indicated with the different colors. The lowest bin represents the cases without reactivation, then we have bins with values smaller than 1.9 m; between 1.9 m and 3.8 m, etc. For instance, within the first E_{seal} bin between 7 and 8.4 GPa, we see no reactivations. For the last E_{seal} bin between 18.6 and 20 GPa, more than 50% of the model runs show fault reactivation to distances beyond 8.3 m from the boundary. This indicates that with increasing E_{seal} the probability that fault reactivation will occur at a certain distance into the seal increases.

The strongest correlations are found for the Young's modulus in the seal, the friction parameters and the injection temperature. This can be well understood since larger moduli in the seal cause larger thermoelastic stresses in the seal, and the same holds for larger temperature differences. The friction parameters control how prone possible faults are to failure at given stress.

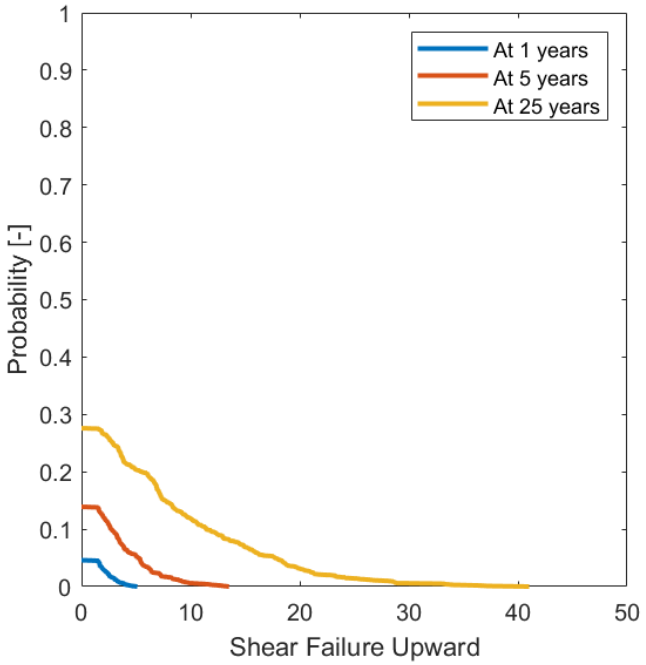

Figure 17 Probability of reactivating the seal upwards from the aquifer beyond the distances on the x-axis. Less than 30% show failure in the seal, even after 25 years.

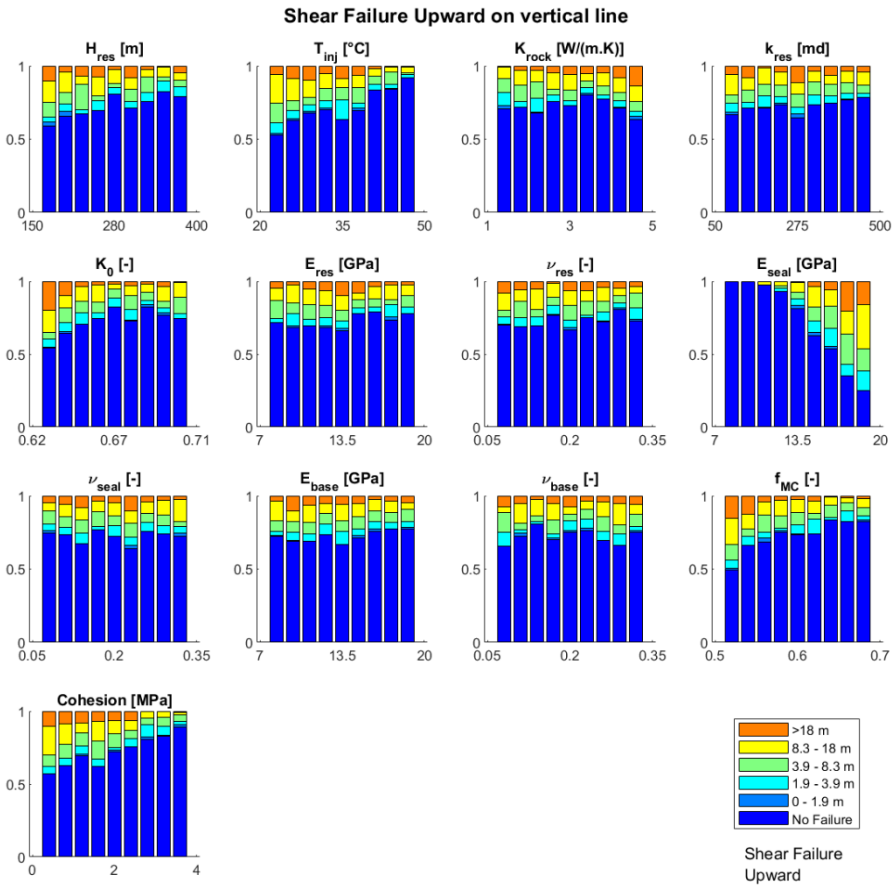

Figure 18 Distribution of the shear failure into the seal against variation of the uncertain parameters. The 13 subplots show the results according to a specific parameter: reservoir thickness (H_{res}), injection temperature (T_{inj}), rock thermal conductivity (K_{rock}), reservoir permeability (k_{res}), horizontal / vertical stress ratio (K_0), reservoir Young's modulus (E_{res}), reservoir Poisson ratio (ν_{res}), seal Young's modulus (E_{seal}), seal Poisson's ratio (ν_{seal}), base Young's modulus (E_{base}), base Poisson ratio (ν_{base}), Coulomb friction parameter (f_{MC}) and cohesion. For each input parameter shown in the subplots, the model runs have been grouped into 9 equally sized bins. Within each bin, the coloured bars indicate the fraction of model results within a certain range of upward shear failure. A correlation is found where the distribution of the sub-bins colours depends on the parameter bin values on the horizontal axes. The strongest correlations are found for the Young's modulus in the seal, the friction parameters and the injection temperature.

3.3.7 Stochastic analysis for calculations vs distance from the well

We now proceed to the results of the stochastic calculations on a horizontal line. These calculations were performed to assess the sensitivity of the extent and magnitude of induced stress changes and SCU to the input parameters and their uncertainties. Again, an ensemble of 1000 realizations was constructed based on the uncertainty of the parameters indicated in Table 1. The most critical depth for reactivation is close to the boundaries of the aquifer. Therefore we have taken a horizontal line at that depth, i.e. 10% of the aquifer thickness below its upper boundary.

A fault is considered to be reactivated if the Shear Capacity Utilization (SCU, Eq. 6) is larger than unity. For every ensemble member, a plot of SCU and the increase in Coulomb Failure

Function, ΔCFF, like those in Figure 8 and Figure 9 can be constructed. From these profiles we determine the largest distance between a fault and the injection well where SCU equals unity and the fault can be reactivated (r_{fault}) as a first measure for potential seismicity. We also determined the largest distance where ΔCFF is larger than 1 MPa ($r_{CFF\text{-}1MPa}$). The latter was quite intuitively chosen as a maximum radius of considerable induced stress changes. In principle, even small changes in the order of tidal influence on the stress can trigger a seismic event if the stress before geothermal injection is close to failure, therefore the usage of ΔCFF may be limited. Both measures are also compared with the radius of the cooled zone, which was determined as the distance where the temperature is the average between injection temperature and original aquifer temperature. Figure 19 and Figure 20 show the result.

Figure 19 (left) shows that the probabilities of criticality increase with time. After 1 year, only 20% of the cases show any criticality; this number increases with time, but remains smaller than 50% after 25 years. At the same time, more and more cases show criticality at larger distances. This increase is strongly correlated with the growth of the cooled zone (Figure 19 right). A clear step occurs at the cooled-zone radius: the number of cases with criticality at larger distances rapidly decreases.

The "maximum radius with considerable ΔCFF" also grows with time, and all cases show considerable ΔCFF within the cooled zone – hence the start of the curves at values slightly above unity in Figure 20 (right). Beyond that value the probabilities decrease, and for some cases a considerable ΔCFF can even be reached at 3 times the cooled-zone radius after 1 year; decreasing to less than 2.5 times after 25 years.

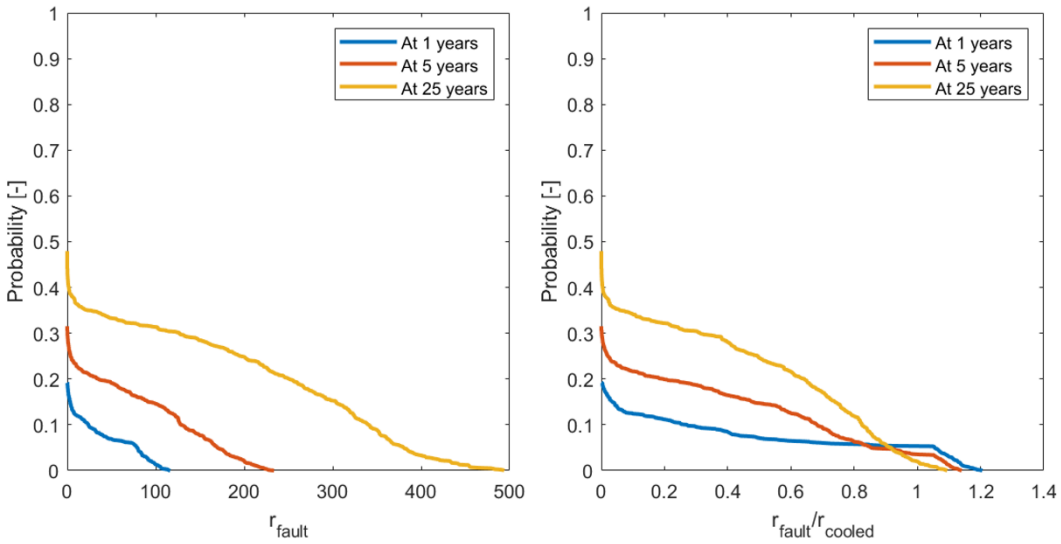

Figure 19 Probability of finding $SCU > 1$ at given distances to a fault (left) and at the relative distance (right). For distances larger than 1.2 times the cooled-zone radius, the stress is non-critical for all the cases.

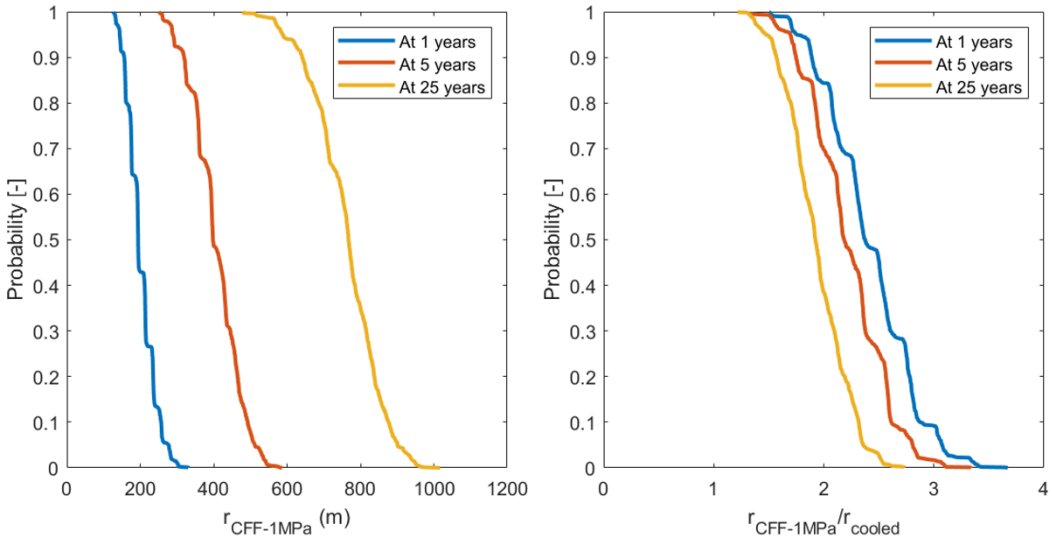

Figure 20 Probability of finding considerable ΔCFF at the given distance to the well (left) and at the relative distance (right). All cases experience considerable ΔCFF within the cooled zone. Considerable ΔCFF can occur up to 3 times the cooled-zone radius after a year, decreasing to 2.5 times the cooled-zone radius after 25 years.

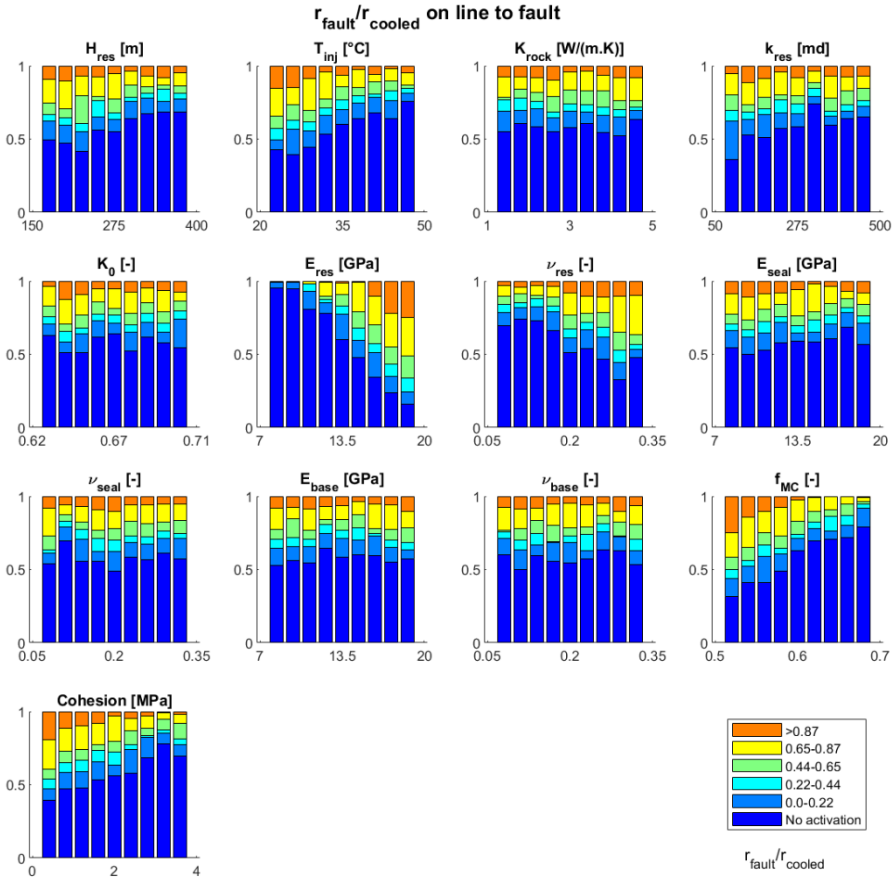

Figure 21 Distribution of the relative radius of criticality against variation of the uncertain parameters. Input values are in the bins on the horizontal axes of the subplots; the resulting values for these values are

ordered in coloured sub-bins ranging from small to high values. A correlation is found where the colour distribution of the sub-bins is depends on the parameter bin values on the horizontal axes. See for a discussion the main text in the report.

Now the question is appropriate which are the most important uncertainties and what is their influence. This is investigated by comparing the outcome of the calculations with the input parameters. We present the analysis for the relative fault distance for criticality and for the relative maximum radius of considerable ΔCFF in Figure 21 and Figure 22. In these figures we have ranked the results against the uncertain parameters, similar to the analysis in Figure 18. First, the measure that is investigated (r_{fault}/r_{cooled}; $r_{CFF\text{-}1MPa}/r_{cooled}$) has been determined for each ensemble member. Then, for each input parameter that was varied in the stochastic analysis the results were binned in 9 bins, spanning the full range between the minimum and maximum value of the parameter that was explored in the stochastic analysis. Per bin, the normalized fraction of model results for a certain value of the evaluation measure are indicated with the different colors.

For the fault distance for criticality (Figure 21) we firstly see a clear correlation with the geomechanical parameters of the aquifer. A larger elastic modulus, larger Poisson ratio and a smaller stress ratio all increase the probability of a large critical radius considerably. The probability of finding larger critical radii is also increased by more critical friction parameters: smaller Mohr-Coulomb friction coefficient or smaller cohesion. Finally, a smaller injection temperature and associated larger thermoelastic stresses increase the probability of finding larger critical radii.

A slightly different picture evolves from the analysis of relative maximum considerable ΔCFF. The friction parameters here have no influence, which is understood because they are not part of the calculation of ΔCFF. Injection temperature, elastic modulus and stress ratio have similar effect as they have on the radius of criticality. Noteworthy here is the influence of the aquifer thickness. Larger thicknesses increase the probability of finding larger values for ΔCFF. This is related to the height / radius ratio of the cooled zone. The effect is not seen in the radius of criticality since it is often closer to the cooled-zone radius, which decreases the effect of the thickness of the cooled zone.

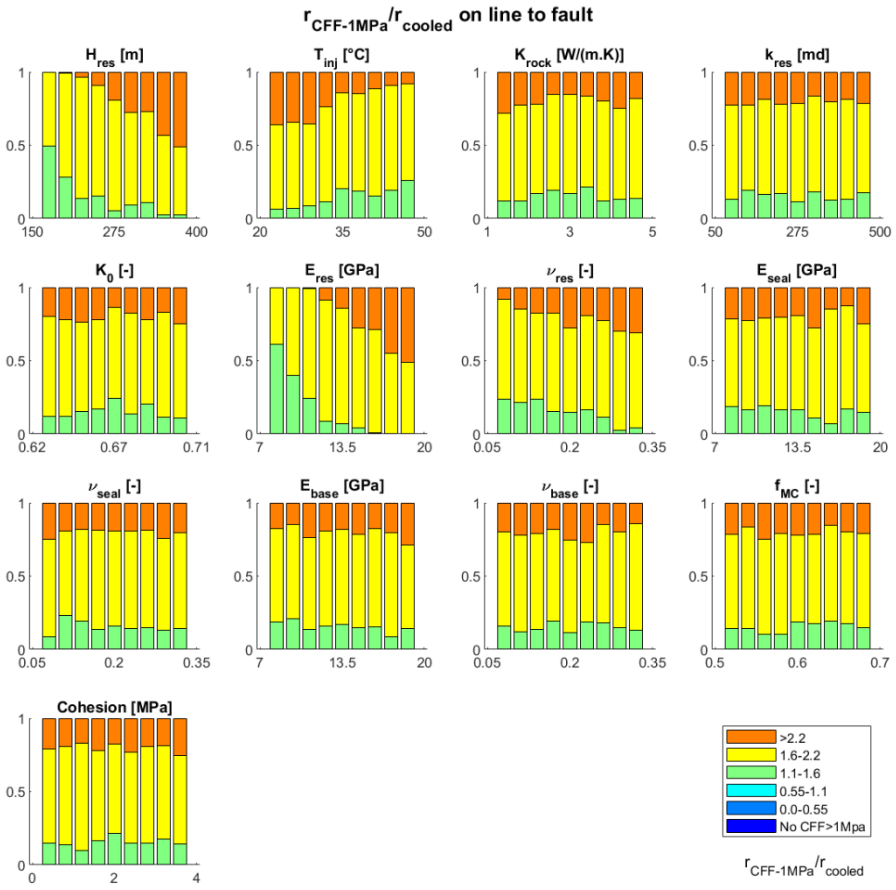

Figure 22 Distribution of the relative radius of considerable ΔCFF against variation of the uncertain parameters. Input values are in the bins on the horizontal axes of the subplots; the resulting values for these values are ordered in coloured sub-bins ranging from small to high values. A correlation is found where the distribution of the coloured sub-bins is depends on the parameter bin values on the horizontal axes. See for a discussion the main text in the report.

3.4 PANTHER

The PANTHER cases deploy the same subsurface parameters as the SRIMA cases. Only the geometry is different: while SRIMA uses radial symmetry, in PANTHER plane-strain conditions are utilized (no strain in the out-of-plane direction). PANTHER has been developed to model the effect of a depleting or cooling reservoir on the stresses and the Shear Capacity Utilization (SCU) of a fault, while the fault offsets the reservoir parts on either side (Figure 23).
We investigate the effect of both pressure depletion and cooling. While the pressure changes due to injection are relatively small with respect to the typical depletions already experienced due to the earlier depletion, and localized in the direct vicinity of the injection well, the effect of the pressure difference with the bounding layers due to depletion is significant. In addition, the distinction is important between cases where seal and base are subject to pressure diffusion or not. Cooling is applied uniformly over the reservoir, with thermal diffusion to the seal and base. We used a value of 10 MPa pore pressure reduction with respect to virgin conditions and 55°C temperature reduction.

PANTHER models a cross section of a reservoir, with a fault dipping under an angle θ and having an offset between the footwall and the hanging wall. Our focus is on the effect of the offset because this cannot be modelled in SRIMA. With respect to the SRIMA simulations, the offset has only an effect if it introduces a distortion of the stress fields with respect to the case without offset – which is only the case when there are pressure or temperature differences with respect to the bounding layers. Therefore, the simplification to the 2D geometry is warranted for this study: it mimics the situation of a fault well within the distorted temperature or pressure field. Besides the effect of the offset for a critical dip angle, we also evaluate the effect of the dip angle itself, and the relationship between the two.

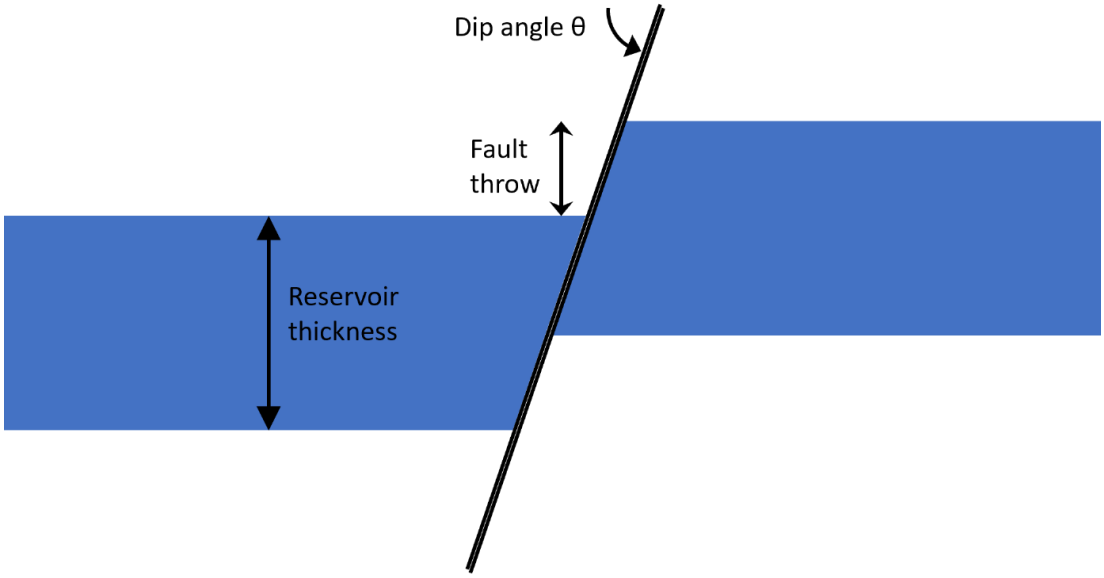

Figure 23 Geometry of PANTHER simulations. The picture show a situation with positive offset: the hanging wall is deeper than the footwall

A typical result is provided in Figure 24. The stresses are calculated for a 300 m thick reservoir that is cut in two parts by a 60° dipping fault with a throw of 150 m. The center depth is 3150 m; the two parts of the aquifer are assumed unbounded in the direction away from the fault. Thermal diffusion into the bounding layers causes a smoothing of the induced thermo-elastic stresses; pressure diffusion is not taken into account in this simulation and the lower pressure in the aquifer results in stress concentration at the upper and lower boundaries of the two parts of the aquifer. When slip is allowed to reduce the shear stress to the Mohr-Coulomb failure envelope, the SCU is maximized on unity and some slip develops in that zone.
We now proceed to discussing some of the sensitivities that we studied. Figure 25 demonstrates the effect of depletion without diffusion, for a range of values for the fault throw. We see the stress concentrations at the four boundary levels of the two sides of the aquifer. The largest effect of the fault throw is when the throw equals the aquifer thickness, i.e. when the upper boundary of the hanging wall is at the same depth as the lower boundary of the footwall. Hydraulic diffusion removes the stress concentrations, but the global behavior is maintained (Figure 26). Cooling (Figure 27) has a similar effect as depressurization on the total stresses – however, fault reactivation is controlled by the effective stresses. As a result, we see a decrease of the effective normal stress working on the fault in the middle of the zone for the thermal cooling case, while we see an increase in effective normal stress for the depressurization case. Furthermore, the magnitude of the induced stresses and the SCU by cooling are larger than those by depressurization for this case.

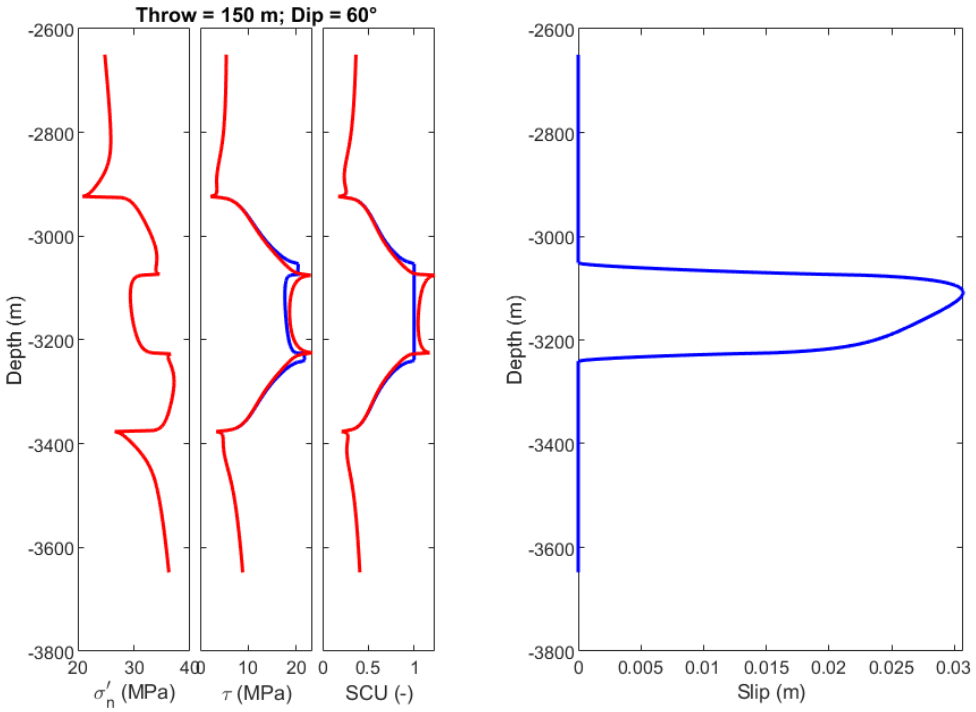

Figure 24 Typical example of stresses and SCU (left) and slip (right) calculated on a fault that is dipping with 60° and offset with 150 m. Effects of temperature and pressure are included; no pressure diffusion into the bounding layers is assumed. Red curves: no slip calculated (purely elastic); blue curves: slip is allowed to happen and to relax the stress down to $SCU = 1$.

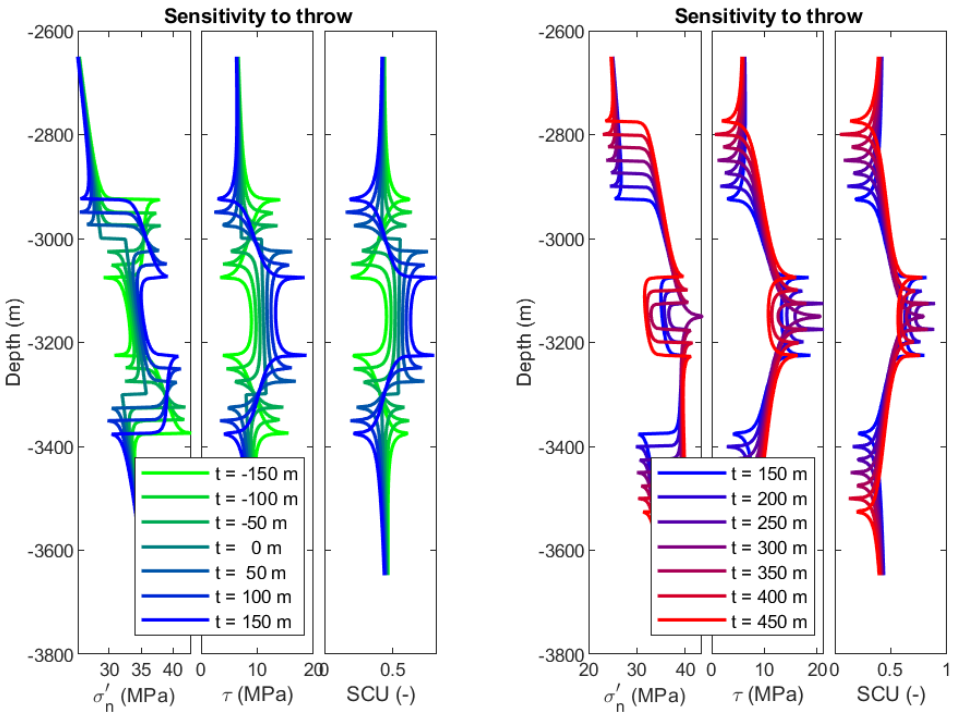

Figure 25 Simulations of normal effective stresses, shear stresses and SCU for 10 MPa reservoir depletion without diffusion. Left: fault offsets between -150 m (reverse displacement) and 150 m (normal displacement). Right: normal fault offsets between 150 m and 450 m.

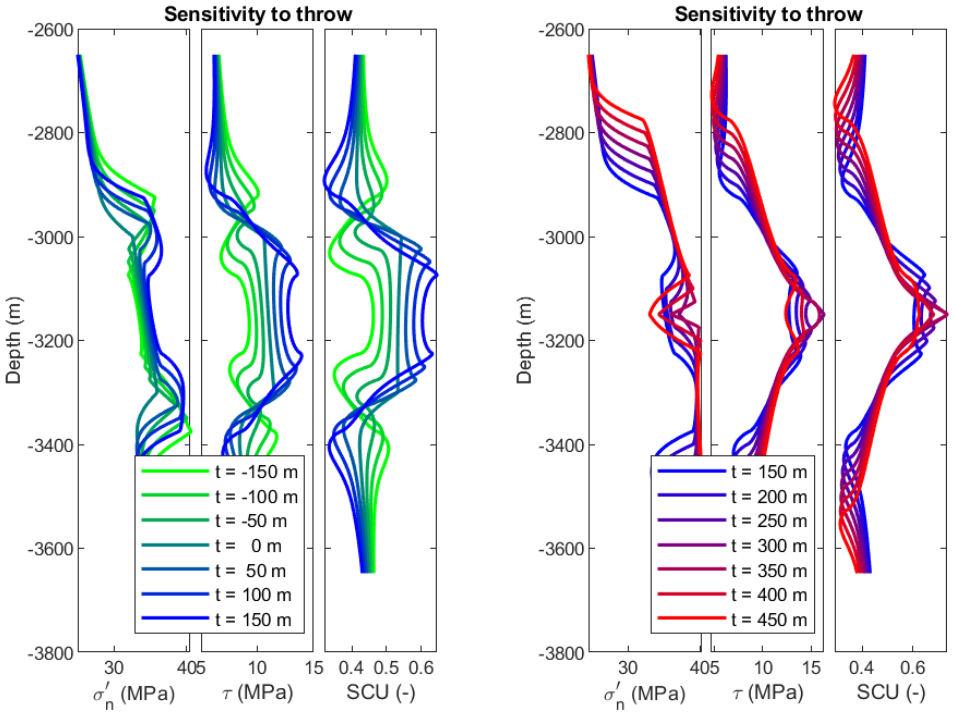

Figure 26 Simulations for reservoir depletion with diffusion, after 25 years, Same identification of curves as in Figure 25.

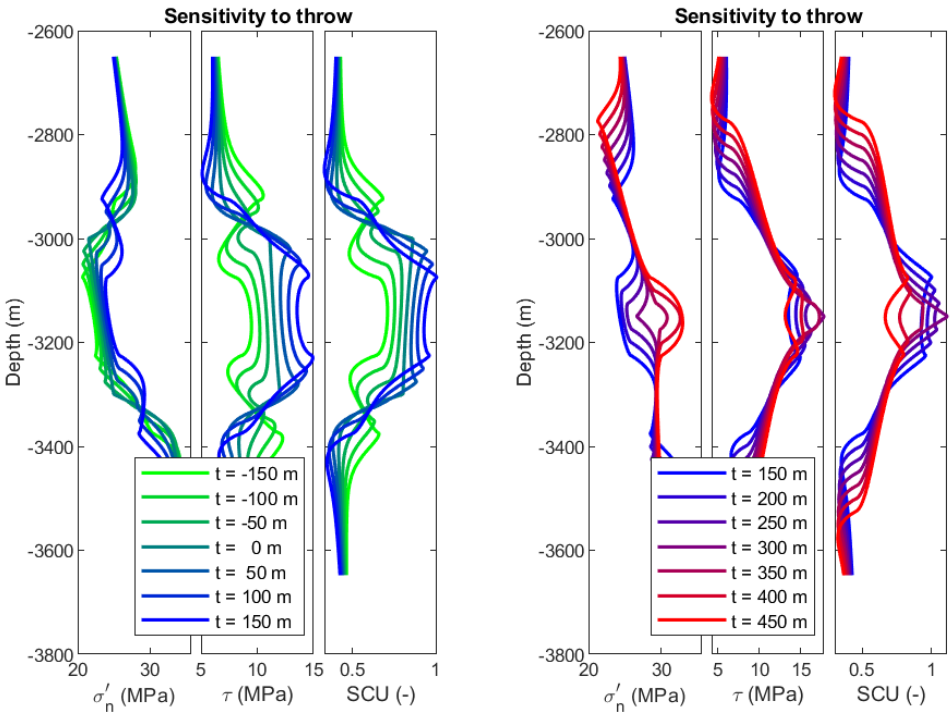

Figure 27 Simulations for 55°C reservoir cooling for 25 years, Same identification of curves as in Figure 25.

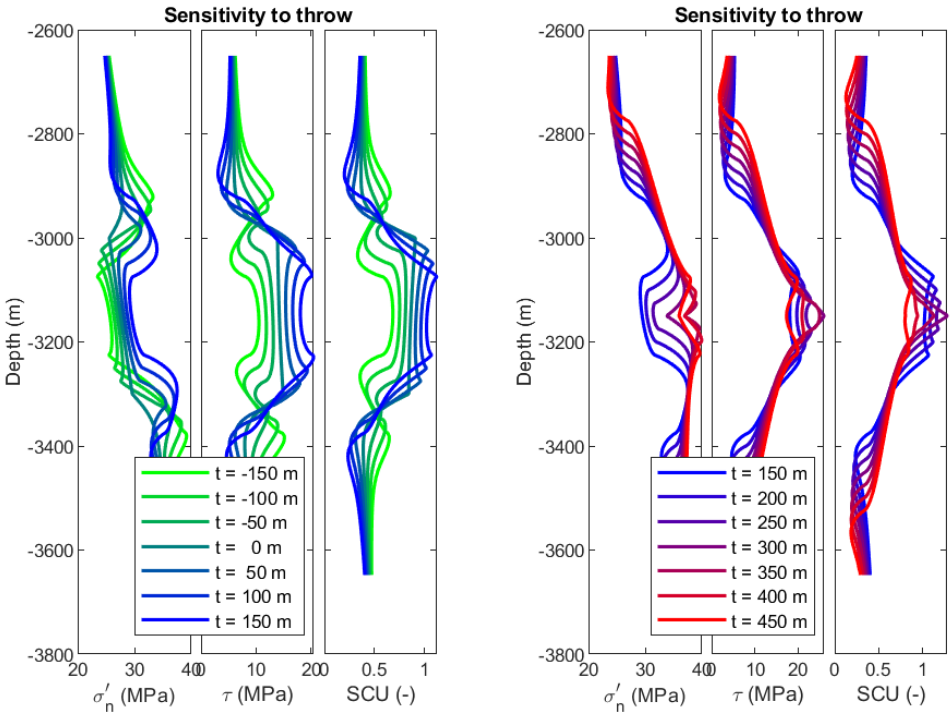

Figure 28 Simulations for 25 years combined reservoir depletion (10 MPa reduction) and cooling (55°C temperature decrease). Same identification of curves as in Figure 25.

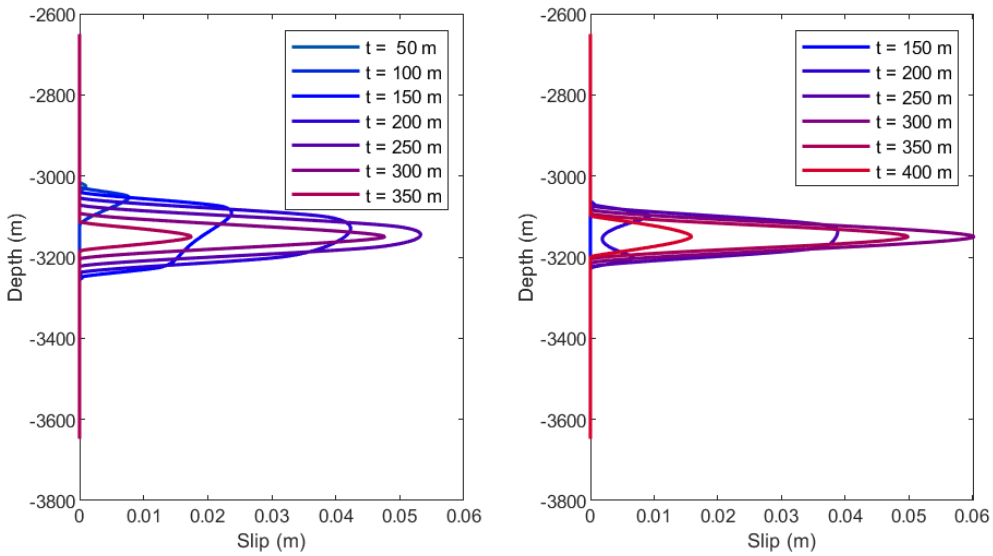

Figure 29 Slip for combined depletion and cooling of the aquifer . Left: 60° dip. Right: 80° dip. Only those cases are shown that exceed the reactivation criterion ($SCU > 1$) and consequently show slip.

The combined effect of depletion and cooling is presented in Figure 28. Generally speaking, SCU is increased between the upper boundary of the upper aquifer and the lower boundary of the lower aquifer, i.e. over most of the depths where a pressure or temperature disturbance is present. When compared to zero offset, negative offsets (the hanging wall being shallower than the footwall) cause smaller increase of SCU; positive offsets (normal displacement with the hanging wall deeper than the footwall) cause a larger increase of SCU in the region where the aquifer intervals overlap. The maximum values for SCU occur for an offset equal to the aquifer thickness (i.e. 300 m), at the depth where the upper boundary of the hanging wall touches the lower boundary of the footwall. We see that for a throw between 50 and 400 m, the SCU exceeds unity. When the slip calculation option is enabled, we observe (Figure 29, left) that slip takes place mainly at the upper boundary of the hanging wall when the throw is small; it becomes larger for larger throws and reduces again when the two reservoir parts do not overlap anymore.

The stress response on the fault depends heavily on the fault dip. Figure 30 shows the fault stresses and resulting SCU for faults dipping at 40° and 80°, respectively. While the absolute values for the smaller dip of 40° decrease and slip conditions are not reached, values for the 80° dip remain high and cause reactivation. Figure 29 (right) shows how the slip values for the 80° dip compare to the 60° dip base case: they are slightly less, and more concentrated in the centre of the fault zone.

This dip angle dependency is further explored in Figure 31. The figures show the elastic responses to pressurization and cooling for dips ranging between 30° and 90°, for fault throws of 0, 150, and 300 m. The cases with throws of 150 and 300 m and dips near to the critical angle show SCU exceeding unity and consequently slip when that option is enabled. Most slip is observed for the case where the throw equals the aquifer thickness and the upper boundary of the hanging wall touches the lower boundary of the footwall (Figure 32).

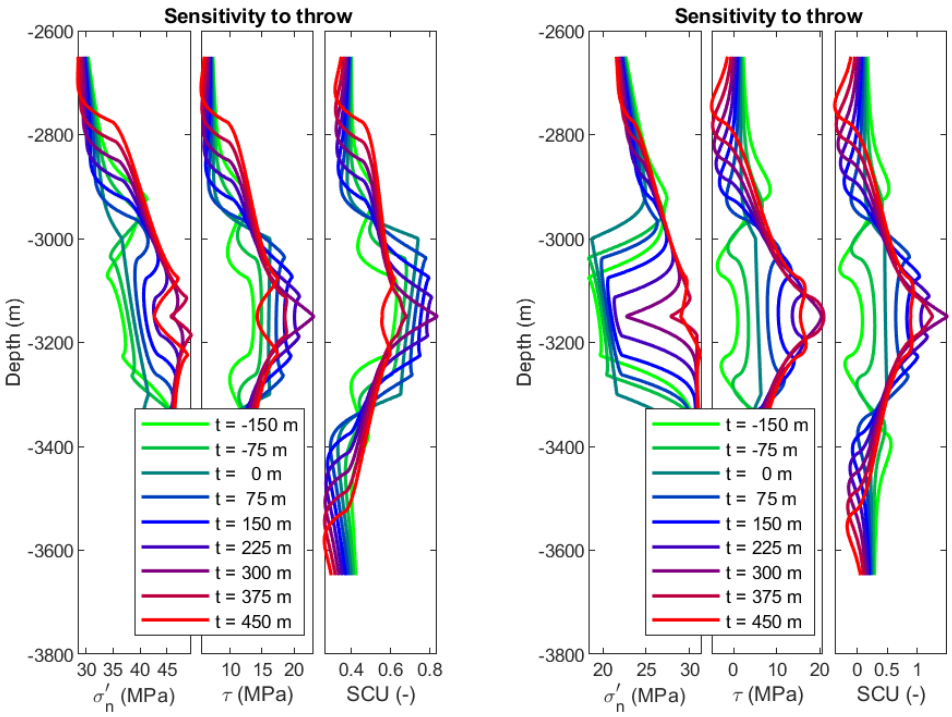

Figure 30 Simulations for 25 years combined depletion and cooling. Left: 40° dip. Right: 80° dip

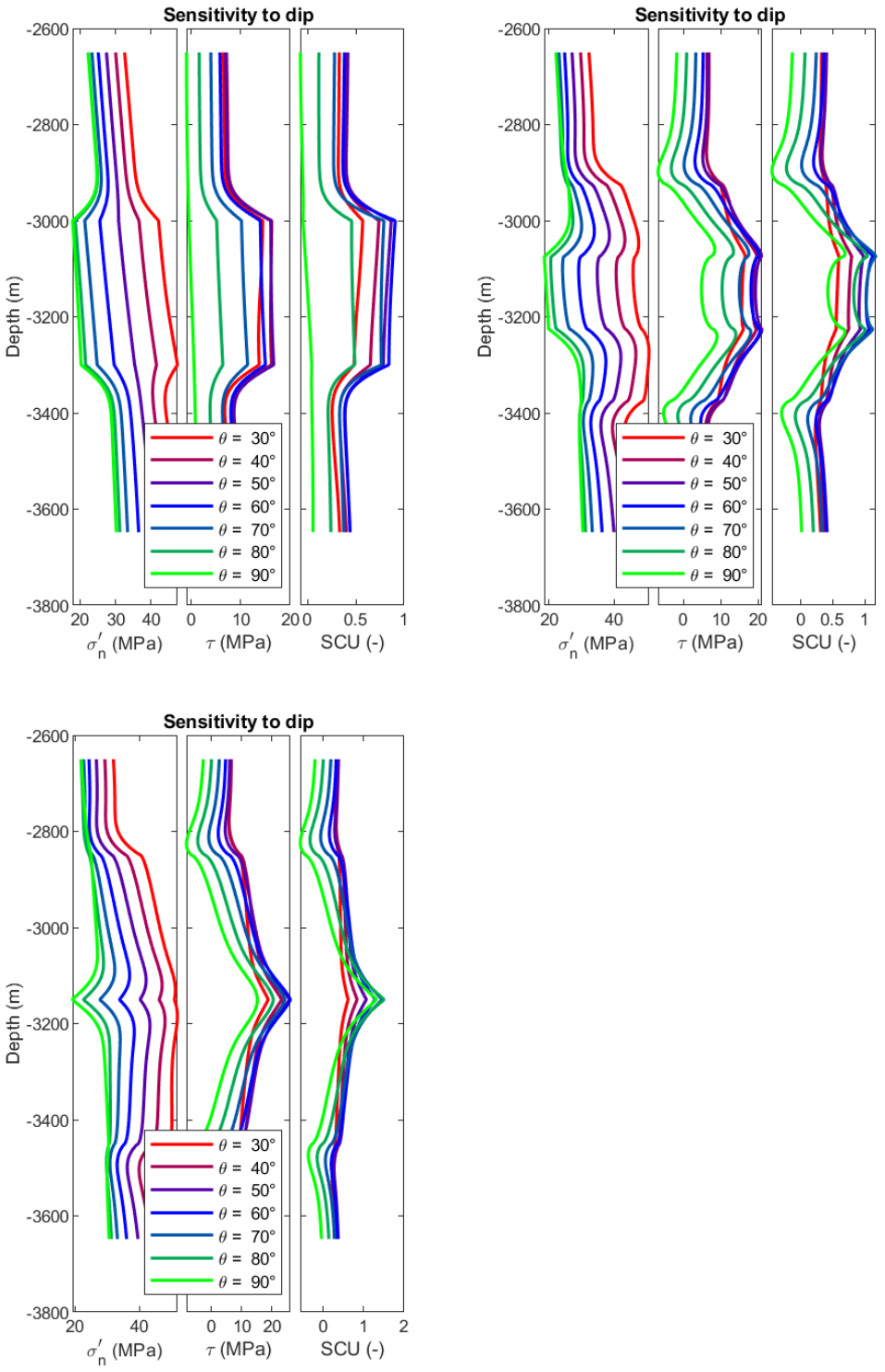

Figure 31 Simulations for 25 years combined depletion and cooling with different dip. Throw is 0 m (top left); 150 m (top right); 300 m (bottom).

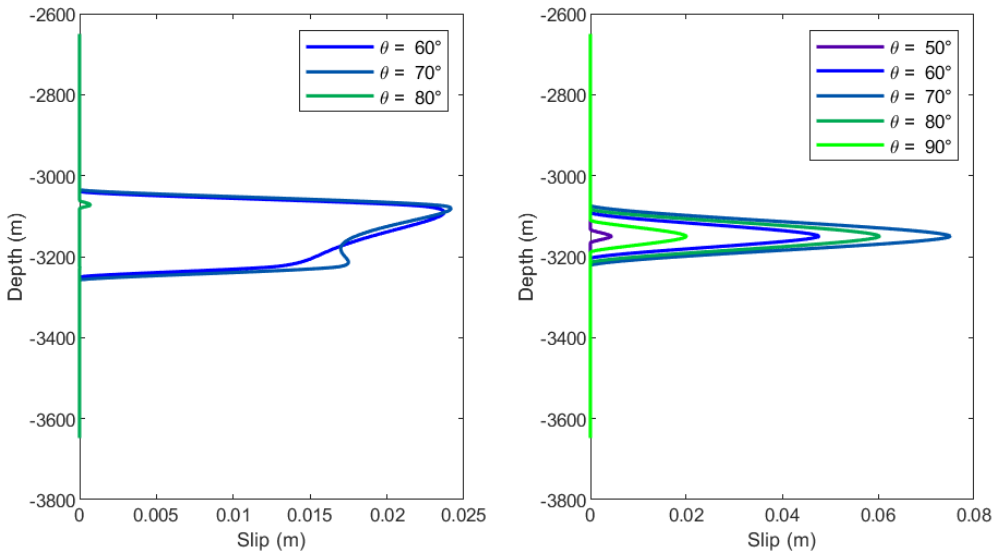

Figure 32 Slip for simulations with different dip. Left: throw = 150 m. Right: throw = 300 m

From the PANTHER analysis we conclude that it is important to assess the offset of a fault when it is present in the cooled or depressurized zone of a geothermal field. An offset equal to the aquifer thickness, with the top of the hanging wall at the same depth as the bottom of the footwall, increases the effect of depletion and cooling on the induced stresses. This is the case for the complete range of values for the dip of the fault. The offset of the aquifer depth at the two sides of a fault therefore constitutes an important parameter in the analysis of potential seismicity. It can considerably increase the probability of failure.
Depletion of the aquifer has a negative effect on SCU for the low values of Poisson ratio and the high values for the poro-elastic constant that we deployed. Aquifer depletion brings faults closer to the critical value. This is in line with the results obtained with SRIMA above (Figure 3 and Figure 9). The introduction of a fault offset amplifies the effect of the depletion. This is visualized in Figure 28 and Figure 29. It introduces stress concentrations at the upper and lower boundaries of the aquifer. These peaks are relieved when pressure diffusion into seal and base is incorporated, but the overall effect of offset on the stresses does not disappear. The total effect is demonstrated in Figure 24.

3.5 Concluding remarks

We have investigated the impact of a typical geothermal operation in the SW aquifer, where pressure depletion had earlier taken place due to equilibration with the depleted gas fields connected to it. A typical geothermal operation involves the construction of a well doublet, with long-term injection of cold water in the injection well. This injection causes a local pressure increase and a propagating cooled volume around the injector. Both the increase of the pressure and the decrease of the temperature induce stress changes, and thereby change the probability of reactivating pre-existing faults. In the case of seismic fault reactivation this would translate into a change in probability of seismicity in the area. It was the objective of the present study to make first-order estimates of these effects.
An important observation is that the temperature development during geothermal operations initiates effects that are different in character from the effects of the pressure depletion that happened prior to geothermal injection. The changes in total stress are similar, because the poro-elastic and thermo-elastic additions to the elastic response in the constitutive equation are identical in character. However, seismicity is controlled by the effective stress, i.e. the

difference between total stress and pore pressure. Figure 3 presents the two effects in a Mohr diagram: pressure and temperature changes cause a movement of the stress that works on a fault plane in different directions. A treatment of temperature effects that is separate from pressure effects is required.

The main thermo-elastic effects are happening in the cooled zone of the aquifer and around it, up to 1.5 times the radius of the cooled zone. Reactivation of faults is also mainly concentrated in this region. Therefore it is important to map both the cooled volume and the geometry of faults that may be seismogenic. The radius of the cooled reservoir volume depends on the volume of injected cold water, the height of the permeable zone and the thermal properties of the fluid and the rock. It is possible to monitor the propagation of the cooled zone with well testing and with pulse tests (Fokker, P. A. et al. (2021)). Distributed temperature sensing (DTS) in nearby wells can also be very helpful, as was demonstrated by Dinkelman et al. (2022). For the characterization of fault locations and geometries, common geological and geophysical methods are available and need to be deployed; we refer to earlier Chapters of this report, where we performed these investigations for the current study.

A fault that offsets the two adjacent parts of the aquifer shows different seismogenic response than a fault without offset. For a fault with normal displacement, the increase in Coulomb Failure Function (ΔCFF) and associated Shear Capacity Utilization (SCU) in the reservoir are larger than for zero offset. This effect is at its maximum when the top of the hanging wall is at the same depth as the bottom of the footwall. The effect is, however, only present in the cooled or pressurized part of the aquifer. Depletion of the aquifer in combination with a fault offset increases SCU, because additional stress concentrations are generated at the top and bottom interfaces of the two aquifer parts at the location of the fault. Faults with a considerable offset that are located within the projected cooled region around an injection well therefore pose an additional threat to geothermal operations and should be investigated individually. From the present study, an offset of less than 1/3 of the layer thickness seems to be on the safe side.

The stresses at the start of possible geothermal operations in the SW Aquifer depend on both the virgin stresses and on the depletion due to pressure equilibration with the surrounding gas reservoirs, which has been studied above. Non-depleted parts of the aquifer can therefore be considered slightly more stable and less seismogenic. This balance, however, depends on the parameters chosen. As an example, higher Poisson's ratio and lower poro-elastic constant reverse the destabilization tendency of depletion to a stabilizing tendency.

The effect of injection rate is not expected to be large within the range of expected permeabilities and projected rates of injection. The contribution of the pressure increase due to the Darcy flow in the aquifer is moderate, as was shown by the limited sensitivity of the results to permeability (Figure 18, Figure 21 and Figure 22). Indeed, reducing permeability has a similar effect on the pressure change as increasing the injection rate. The largest effect of the injection rate will be by the associated size of the cooled zone. The volume of cooled rock is linearly dependent on the volume of injected cold water, and hence on the duration of the injection operations. In the same way, the thickness also affects the size of the cooled zone. However, the effect of thickness is magnified by the influence of the vertical / horizontal dimension ratio on the induced stresses: thicker zones result in less critical stresses.

There is still considerable uncertainty on a number of the key input parameters: virgin stresses, fault frictional properties, elastic moduli. These uncertainties propagate into an uncertainty in the expected stress changes, including the increase in Coulomb Failure Function and the Shear Capacity Utilization. A prior analysis of potential geothermal operations always needs to take into account these uncertainties. A general conclusion of this study is that the radius inside which stress changes are considerable is limited to 1.5 times the radius of the cooled zone, for which a good estimate can be given by Eq. (8).

4 General discussion and conclusions

The work performed here focusses on the impact of potential geothermal operations in the SW aquifer of the Groningen gas field. The research questions are aimed at generic questions relevant for all operations in this area. Consequently, the work has focused on generic results that are broadly applicable to all potential geothermal projects. This also means that the results of this work are not sufficiently project-specific to serve as direct input to an SHRA for a particular operation. However, due to their broad applicability, the results from this project can serve as important input to such an SHRA.

The *seismicity propensity* map in Chapter 2 shows that, regardless of project design, there are areas that are more and less prone to seismicity under the same loading. This does not imply that projects cannot be safely executed in the high propensity areas, nor that projects in the low propensity area cannot generate significant seismicity. It does however mean that, given a certain project design, the expectation is that that same project will lead to more seismicity in some areas than in others. This is relevant information for both individual geothermal projects, who may or may not have a degree of flexibility in the planning of their location, and for governmental and regulatory bodies who may be interested in the spatial and temporal planning of several geothermal projects. The calculations in Chapter 2 are based on the assumption that the assumptions behind the Groningen seismic source model, which was developed for dealing with pressure changes, remain valid in the context of temperature changes. Specifically, a given amount of vertical strain leads to the same stress change ΔC, regardless of whether the vertical strain is caused by a pore pressure change or temperature change. This is due to the 'amplification' of stresses at offset faults (see Bourne and Oates 2017 for details) in the simplified 'thin-sheet' geometry. Note that in the analyses in Chapter 3, stresses are computed along faults while taking into account a more complex geometry. In these models, temperature changes lead to a different stress path than pore pressure changes and can no longer be converted into an equivalent pore pressure change by using vertical strain as an intermediate quantity. In the context of assessing regional seismicity propensity, we argue that using the best available seismic source model for the region (i.e. the Groningen seismic source model) is a sensible choice, and hence we can use the equivalence between pore pressure and temperature changes in this context. In the context of assessing the stress impact of potential geothermal operations in terms of their extent and magnitude, we believe the tools applied in Chapter 3 are better suited.

In Chapter 2, we further assume that the induced strains are primarily uniaxial in nature, which is a sensible assumption in the context of pore pressure-induced strains in a laterally extensive, highly permeable reservoir, remains true for geothermal operations. Although strains induced by typical geothermal operations are less uniaxial in nature, due to their relatively large spatial temperature gradients, we believe that for a first-order assessment of seismicity propensity, the chosen approach is sensible and valid. We are investigating *seismicity propensity,* which can be seen as an expression of the probability of encountering faults that are near failure and only need a small stress disturbance for failure to occur. In the case of the SW aquifer of the Groningen field, to what extent faults are near failure is determined by their stress history, which is (up to now) determined by pressure depletion. In

other words, although the uniaxial strain assumption may not be fully valid for modelling the stress disturbance caused by geothermal operations, it is a valid assumption to describe the stress history of the faults, and therefore of their propensity for failure and seismicity.

The work presented in Chapter 3, on the extent and magnitude of stress changes induced by the geothermal project, contains valuable input for any geothermal project. The main geomechanical effects of interest are related to the injection well. Although the spatial extent of influence and the magnitude of the stress changes depend on the local mechanical parameters and the project specifications, the result that the main effects are closely tied to the cooled zone is generally valid. Similarly, the result that pressure depletion prior to commencing geothermal operations leads to less stable or more seismogenic circumstances applies in general and is useful to consider during project design.

The main conclusions of this report can be summarized as follows:

- The area with the highest seismicity propensity is just north of the city of Groningen and does not change its position through time. It's closely related to the pore pressure depletion in the Bedum gas field (Figure 1).
- The main thermo-elastic effects are associated with the cooled volume of the aquifer centered around the injector, reaching up to 1.5 times the radius of the cooled zone. Reactivation of faults is also mainly concentrated in this region.
- Poro-elastic effects depend on injection rate, permeability and thickness of the injection layer. However, the uncertainties and operational boundaries of these numbers make their effects generally less important than thermoelastic effects in the context of the SW aquifer.
- For a project-specific seismicity study, it is important to map both the cooled zone and the geometry of faults that may be seismogenic. We suggested methods to monitor the cooled reservoir volume, including well testing, pulse testing and DTS.
- It is important to assess the offset of a fault when it is present in the cooled or depressurized zone of a geothermal field. An offset equal to the aquifer thickness, with the top of the hanging wall at the same depth as the bottom of the footwall, maximizes the effect of depletion and cooling on the induced stresses. This is the case for the complete range of values for the dip of the fault. Non-depleted parts of the aquifer are typically slightly more stable and less seismogenic. However, this does depend on the geomechanical parameters chosen (specifically on the Poisson's ratio and poro-elastic constant), and on the presence of faults with offset.
- Uncertainties in input parameters are important to consider and should be taken into account in any project-specific analysis of geothermal operations. A number of key inputs have been identified in this study: virgin in-situ stress state, fault frictional properties, elastic moduli.

References

Bakx, E., Buijze, L., & Wassing, B. B. T. (2022). Formation, lithology and region-specific stress field in the Netherlands. TNO Utrecht.

Buijze, L., Fokker, P. A., & Wassing, B. B. T. (2022). Quantification of induced seismicity potential of geothermal operations: Analytical and numerical model approaches. TNO Utrecht.

Buijze, L., Veldkamp, H., & Wassing, B. (2023). Comparison of hydrocarbon and geothermal energy production in the Netherlands: reservoir characteristics, pressure and temperature changes, and implications for fault reactivation. Netherlands Journal of Geosciences, *102*, e7.

Dinkelman, D., Carpentier, S. F. A., Koenen, M., Oerlemans, P., Godschalk, B., Peters, E., Van Wees, J. D. A. M.High temperature aquifer thermal energy storage performance in middenmeer, the netherlands: Thermal monitoring and model calibration. 17-21 October 2022

Fokker, P. A., Salina Borello, E., Viberti, D., Verga, F., & Van Wees, J. D. (2021). Pulse testing for monitoring the thermal front in aquifer thermal energy storage. Geothermics, *89* doi:10.1016/j.geothermics.2020.101942

Fokker, P. A., Buijze, L., & Pluymaekers, M. P. D. (2023). SRIMA: Background Information of Python tool.

Fokker, P. A., & Wassing, B. B. T.A fast model for THM processes in geothermal applications. 11-14 June 2019

KEM-19b. Evaluation of post-abandonment fluid migration and seismic hazard assessment in the South-West aquifer of Groningen. TNO 2025 R10452

KEM 24-b. Preliminary assessment of beneficial effects of nitrogen injection in depleted reservoirs. TNO 2024 R11366

Mathur, B., Hofmann, H., Cacace, M., Hutka, G. A., & Zang, A. (2024). Thermo-hydro-mechanical simulation of cooling-induced fault reactivation in Dutch geothermal reservoirs. Netherlands Journal of Geosciences, *103*, e1.

Nield, D. A., & Bejan, A. (2006). *Convection in porous media* Springer.

Pijnenburg, R. P. J., Verberne, B. A., Hangx, S. J. T., & Spiers, C. J. (2018). Deformation Behavior of Sandstones From the Seismogenic Groningen Gas Field: Role of Inelastic Versus Elastic Mechanisms. Journal of Geophysical Research: Solid Earth, *123*(7), 5532-5558. doi:10.1029/2018JB015673

Signature

TNO › Energy & Materials Transition › Utrecht, 7 July 2025

Energy & Materials Transition

Princetonlaan 6
3584 CB Utrecht
www.tno.nl

TNO innovation for life

Ministerie van Klimaat en Groene Groei

Klimaat en groene Groei

Auteur
[redacted]

TER BESLISSING
Datum
25 juni 2025

Kenmerk
KGG / 99635118

RT 0000109210

Kopie aan

Bijlage(n)
5

Aan de Minister van Klimaat en Groene Groei
Cc de Staatssecretaris Herstel Groningen

nota
TER BESLISSING

Kamerbrief aardbevingen in en rondom het Groningenveld

Parafenroute

[redacted]

Aanleiding

Afgelopen januari heeft de NAM gerapporteerd over de seismiciteit in Groningen in kalenderjaar 2024. Deze was het laagst van de afgelopen 20 jaar. Daarnaast zijn er recentelijk meerdere onderzoeken uitgebracht die betrekking hebben op aardbevingen in en rondom het Groningenveld. Eén van deze onderzoeken is KEM24b, waarvan staatssecretaris Vijlbrief op 16 april 2024 in een debat met de Eerste Kamer heeft toegezegd deze met de Eerste Kamer te delen. Deze Kamerbrief bevat een update van de seismiciteit in en rondom het Groningenveld in 2024 en een duiding van deze recent uitgekomen onderzoeken. De brief wordt zowel naar de Eerste als naar de Tweede Kamer verzonden.

Geadviseerd besluit

U wordt geadviseerd om de bijgevoegde brieven aan de Eerste en Tweede Kamer te ondertekenen.

Kernpunten

- In januari 2025 heeft de NAM een rapportage uitgebracht over de seismiciteit in 2024. Uit deze rapportage blijkt dat de seismiciteit dat jaar in lijn met de verwachtingen uit de publieke Seismische Dreiging en Risico Analyse (pSDRA) afneemt, en dat de sinds 2014 afnemende trend dit jaar doorzet. Het aantal aardbevingen was in 2024 het laagst van de afgelopen 20 jaar.
- Recentelijk zijn verschillende onderzoeken gepubliceerd over aardbevingen in en rondom het Groningenveld:
    - In oktober 2024 heeft TNO het onderzoek KEM24b aan KGG opgeleverd. Dit onderzoek gaat over stikstofinjectie in het Groningenveld met als doel aardbevingen te verminderen. Deze brief bevat een toelichting van de resultaten uit dit onderzoek en een uitleg

waarom het demissionaire kabinet niet verder inzet op stikstofinjectie in het Groningenveld.
    - In juli 2025 heeft TNO het onderzoek KEM19b opgeleverd. Hierin is onderzoek gedaan naar seismiciteit in de watervoerende laag (aquifer) ten noorden aangrenzend aan het Groningenveld en andere kleine gasvelden. Er is gekeken naar de kans op bevingen door toekomstige drukdaling in de aquifer als gevolg van (historische) gaswinning uit de omliggende velden. Daarnaast is gekeken naar het verband van eventuele seismiciteit met potentiële toekomstige activiteiten in de aquifer (met name geothermie). Specifiek de aquifer nabij Warffum is niet in dit onderzoek betrokken (deze ligt ten westen van het Groningenveld).
    - Er is onderzoek gedaan naar de mogelijke oorzaken van de hoger-dan-verwachte seismiciteit in de periode 2021 tot 2023 door de NAM en door TNO. Het KEM-subpanel en SodM hebben gekeken naar de resultaten van de NAM. SodM komt na de zomer met een advies wat o.a. hier betrekking op zal hebben. Het demissionaire kabinet wacht dit advies af voordat zij verdere stappen zet op dit onderwerp.
- In het kader van maatregel 49 wordt het seismisch meetnetwerk van het KNMI verdicht. Dit zal ook betrekking hebben op de regio rondom het Groningenveld. Er wordt verwezen naar een toekomstige Kamerbrief die de Kamer binnenkort in meer detail over de verdichting van het meetnetwerk zal informeren.
- De inhoud van de Kamerbrief is vooraf gedeeld en afgestemd met TNO, SodM, en BZK.